Modelling rock slope behaviour and evolution with reference to Northern Spain and Southern Jordan

Simon Brett Nelis

MODELLING ROCK SLOPE BEHAVIOUR AND EVOLUTION WITH REFERENCE TO NORTHERN SPAIN AND SOUTHERN JORDAN

VOLUME 2

SIMON BRETT NELIS

Ph.D. THESIS 2004

Contents of Volume 2

List of Figures and Plates

The figures in this thesis include output from the UDEC computer simulation software and from the laboratory testing of rock. The output consists of two-dimensional block plots and filled contour block plots. The labelled notation (*10^1) indicates that the axes need to be multiplied by 10. On all UDEC plots, the horizontal and vertical axes are in meters. The plot legend includes an indication of the type of output plot, model cycle count, model time and also the contour intervals. In plots with displacement vectors, the scale presented is in meters. The notation 1 E 1 on the scale means that the scale is 1*10 m long. The values of displacement relate to actual displacements in the rock mass in meters. Where plots of unbalanced forces are presented, the x-axis is model time (s) and the y axis is force (kg m s^{-2}).

Chapter 2

Chapter 4

List of Plates

List of Appendices

All appendices are to be found on the disk which is attached to the back cover of Volume 2 of this thesis. The appendices are chapter ordered and the filename corresponds to the appendix number. For the UDEC input files, where the letter '*v*' is used, values are varied for the different model runs.

Chapter 3

3.1 Basic program for calculating the angle of intersection between a joint plane and a UDEC mesh.

Chapter 4

4.1 A FISH function to calculate strain accumulation at gridpoints.

4.2 UDEC input file for a 1 m sandstone rock mass with variable joint spacing. A '*v*' indicates that the block size parameter was varied.

4.3 UDEC input file for a 1 m limestone rock mass with variable joint spacing. A '*v*' indicates that the block size parameter was varied.

4.4 UDEC input file for a 1 m granite rock mass with variable joint spacing. A '*v*' indicates that the block size parameter was varied.

4.5 UDEC input file for a 10 m sandstone rock mass with variable joint spacing. A '*v*' indicates that the block size parameter was varied.

4.6 UDEC input file for a 10 m limestone rock mass with variable joint spacing. A '*v*' indicates that the block size parameter was varied.

4.7 UDEC input file for a 10 m granite rock mass with variable joint spacing. A '*v*' indicates that the block size parameter was varied.

4.8 UDEC input file for a 100 m sandstone rock mass with variable joint spacing. A '*v*' indicates that the block size parameter was varied.

4.9 UDEC input file for a 100 m limestone rock mass with variable joint spacing. A '*v*' indicates that the block size parameter was varied.

4.10 UDEC input file for a 100 m granite rock mass with variable joint spacing. A '*v*' indicates that the block size parameter was varied.

4.11 UDEC input file for a 1000 m sandstone rock mass with variable joint spacing. A '*v*' indicates that the block size parameter was varied.

Chapter 8

Figures

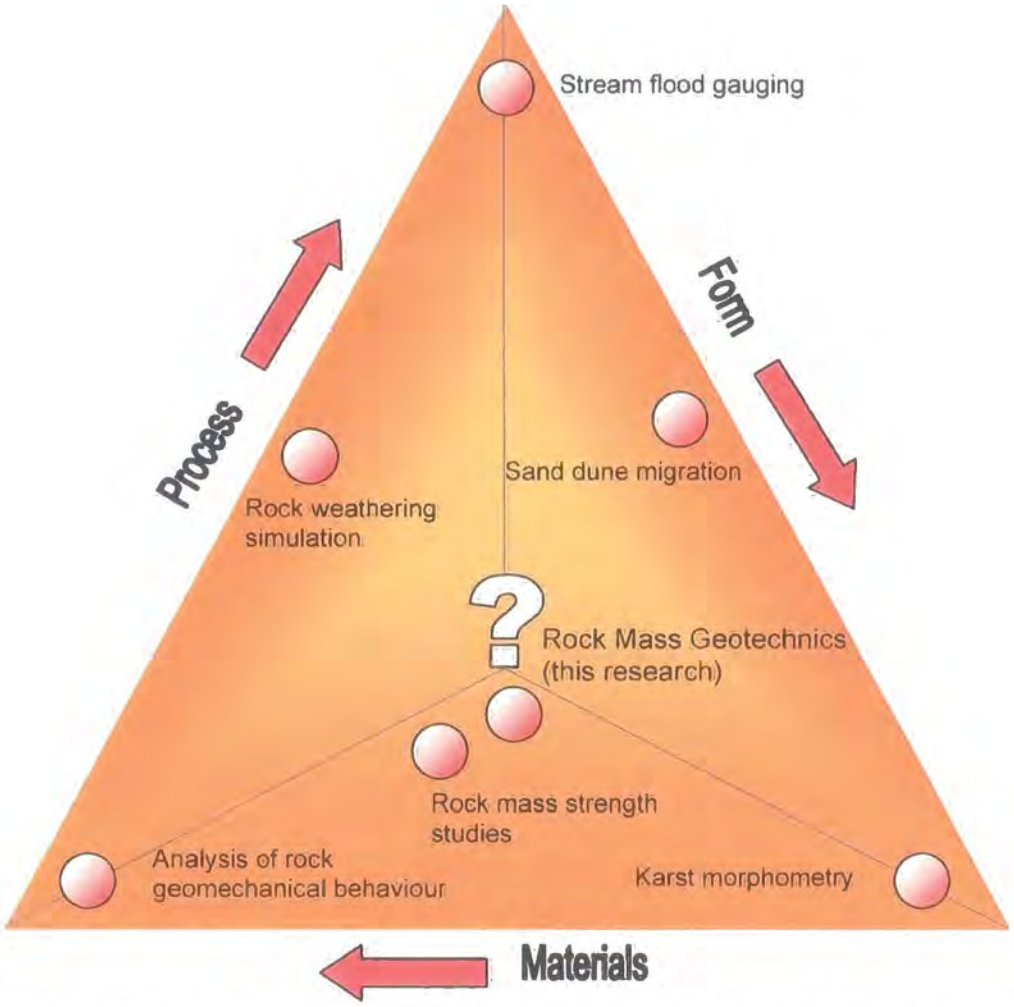

Figure 2.1: Process-Form-Material interaction triangle (after Allison, 1996). The triangle shows where research methodologies lay in relation process, materials and form. An adequate understanding of geomorphological evolution of landforms can only be gained if reference is made to material properties, the shape of the landform and the processes responsible for the evolution of the landform. The current research is embedded in the centre of this relationship utilising geotechnical information, morphometric data and process rates in understanding landform evolution.

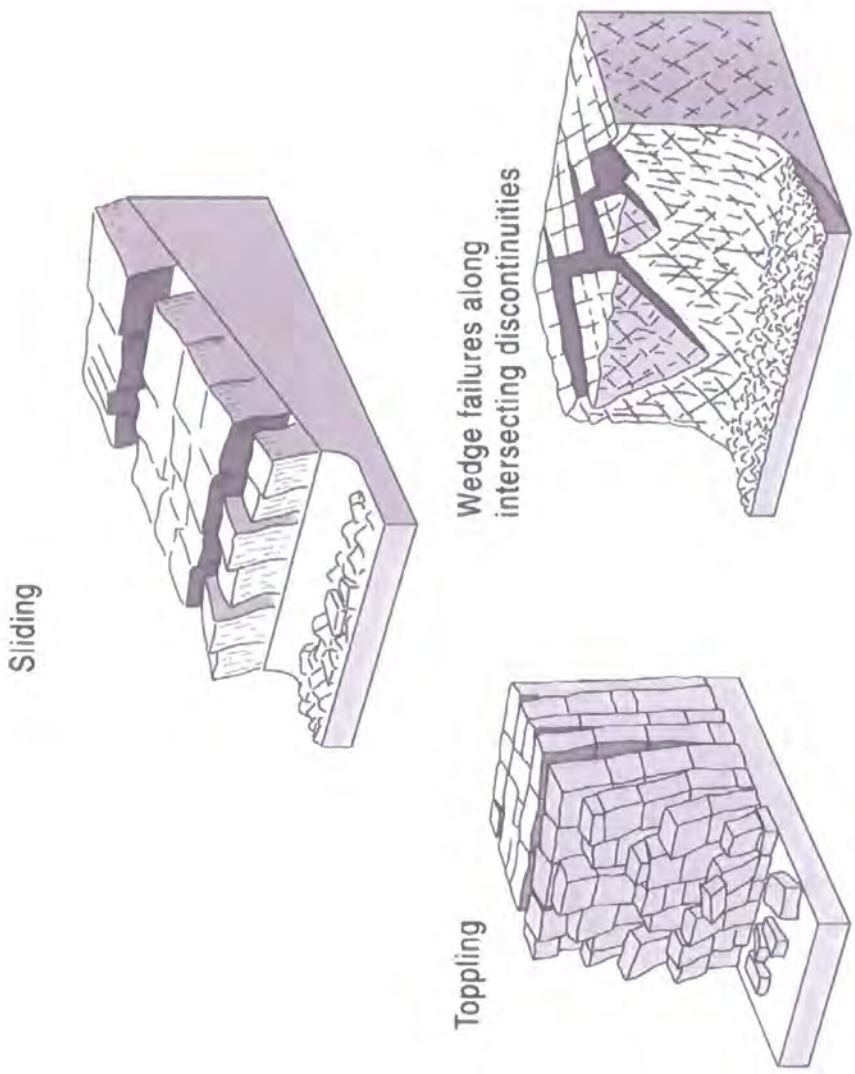

Figure 2.2: Basic failure mechanisms of rock masses under gravitational stress.

Hypothetical scales
(used for theoretical modelling)

Scales in the natural environment

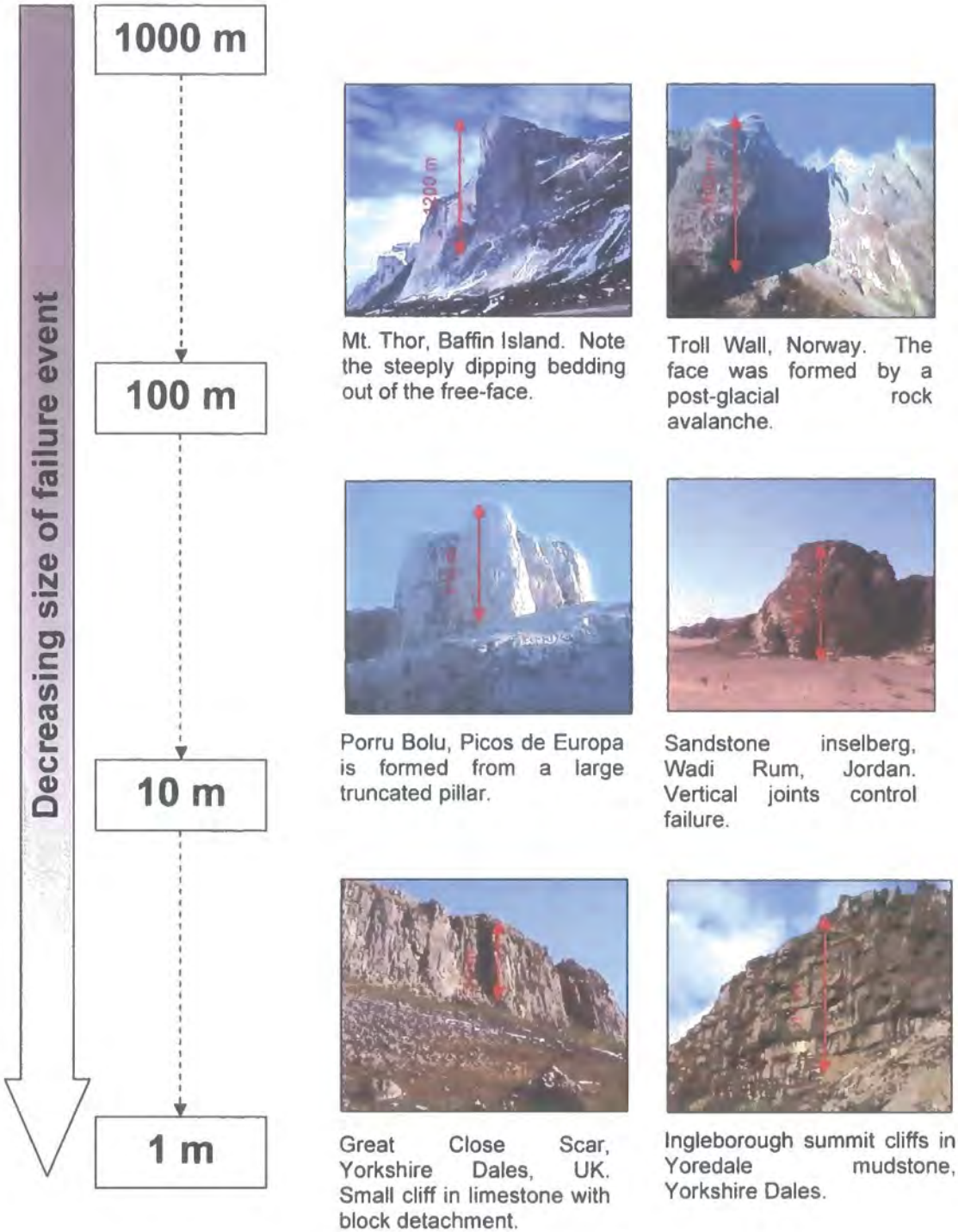

Figure 4.1: Hypothetical slope scales and examples of natural slopes at these scales. The scale boundaries used are a hierarchical framework, with a continuum of slope scales between the boundaries defined here.

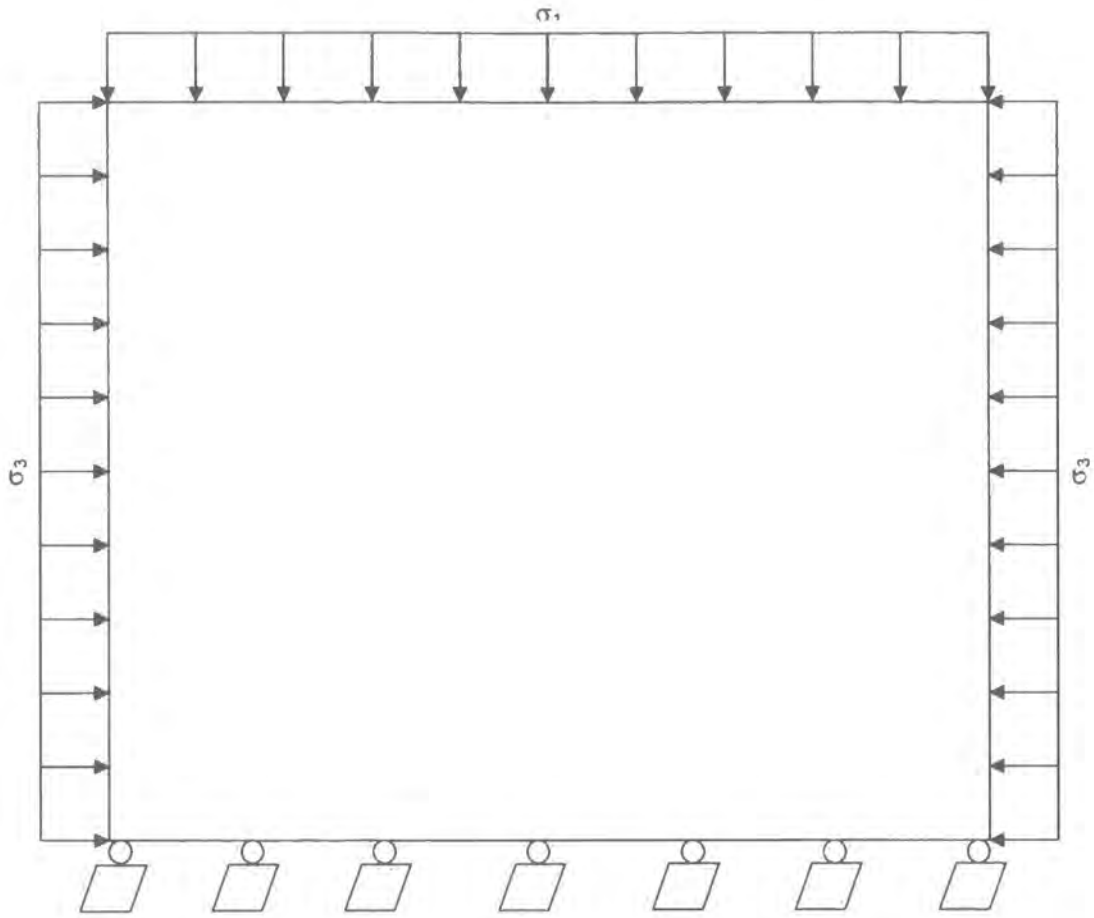

Figure 4.2: Stress boundary conditions imposed on each model. Arrows represent stress boundaries, while the circles / squares indicate a velocity boundary used to fix the model in space.

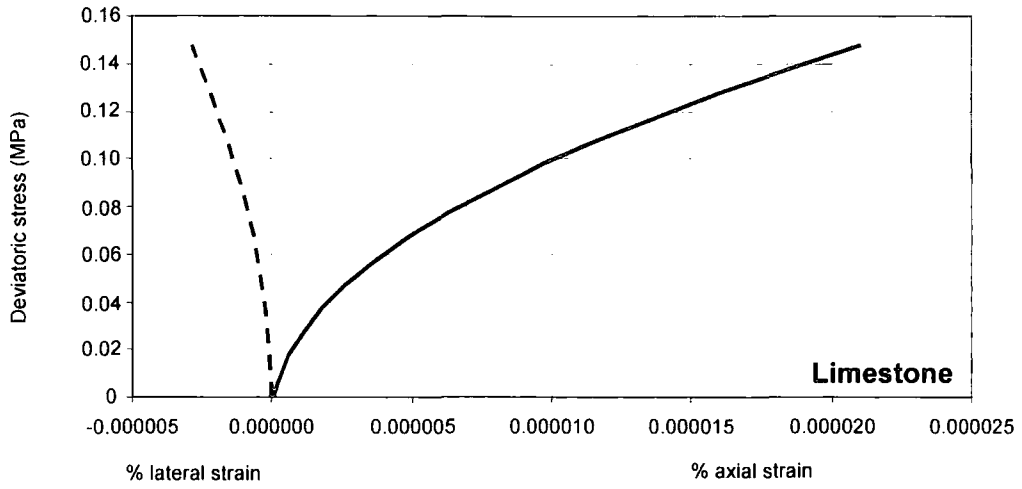

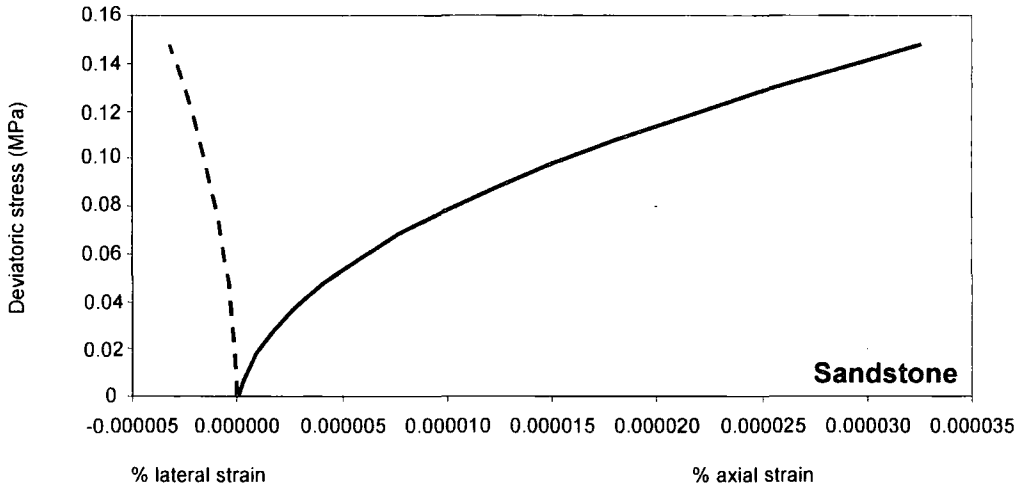

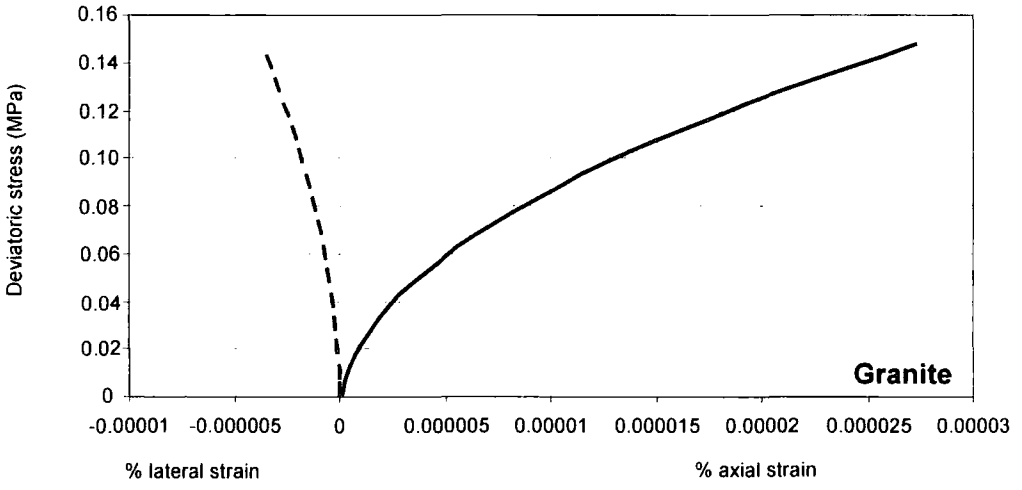

Figure 4.3: Stress-strain response of unjointed 1 m rock masses to simulate the behaviour of intact material.

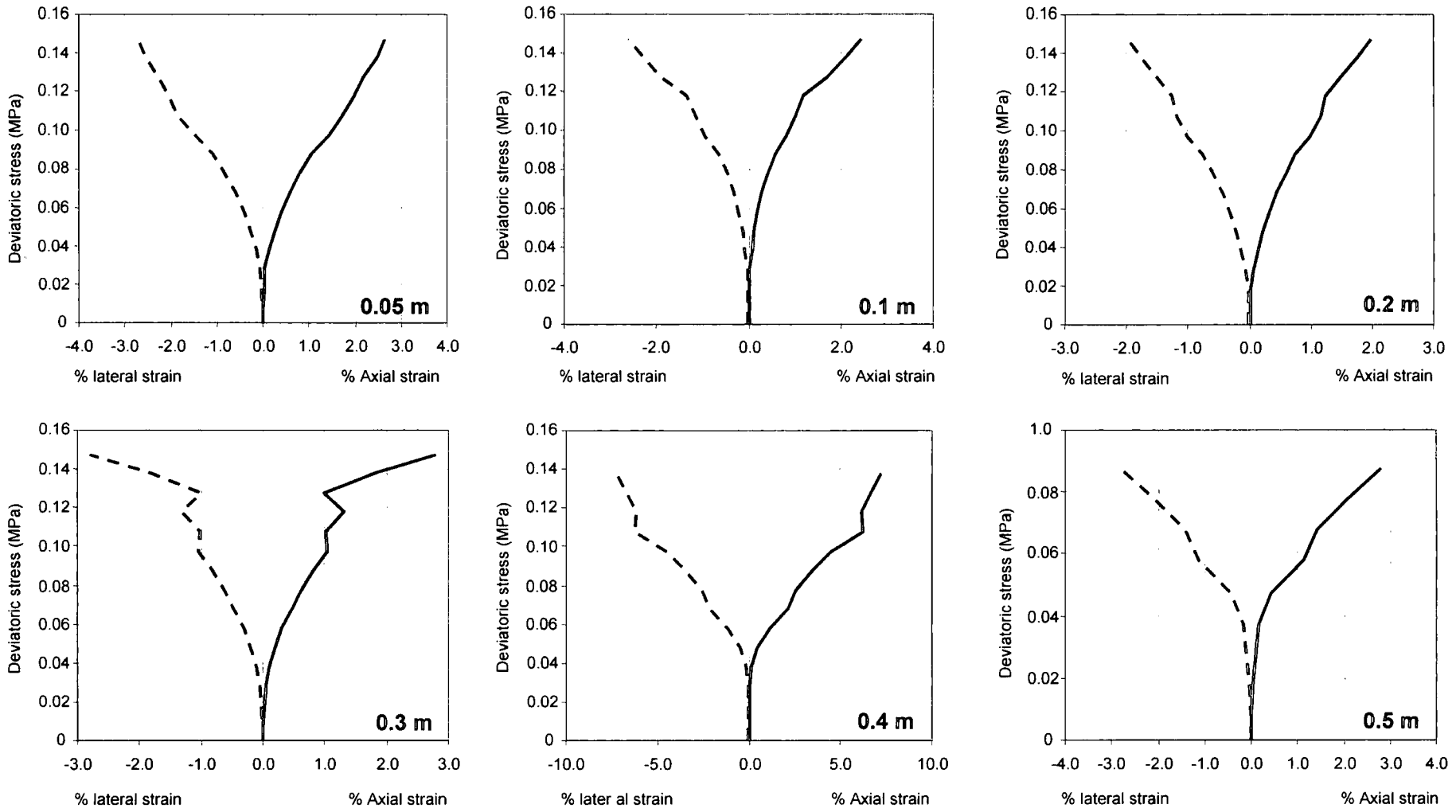

Figure 4.4: Stress-strain response of a 1 m sandstone rock mass with varying block sizes.

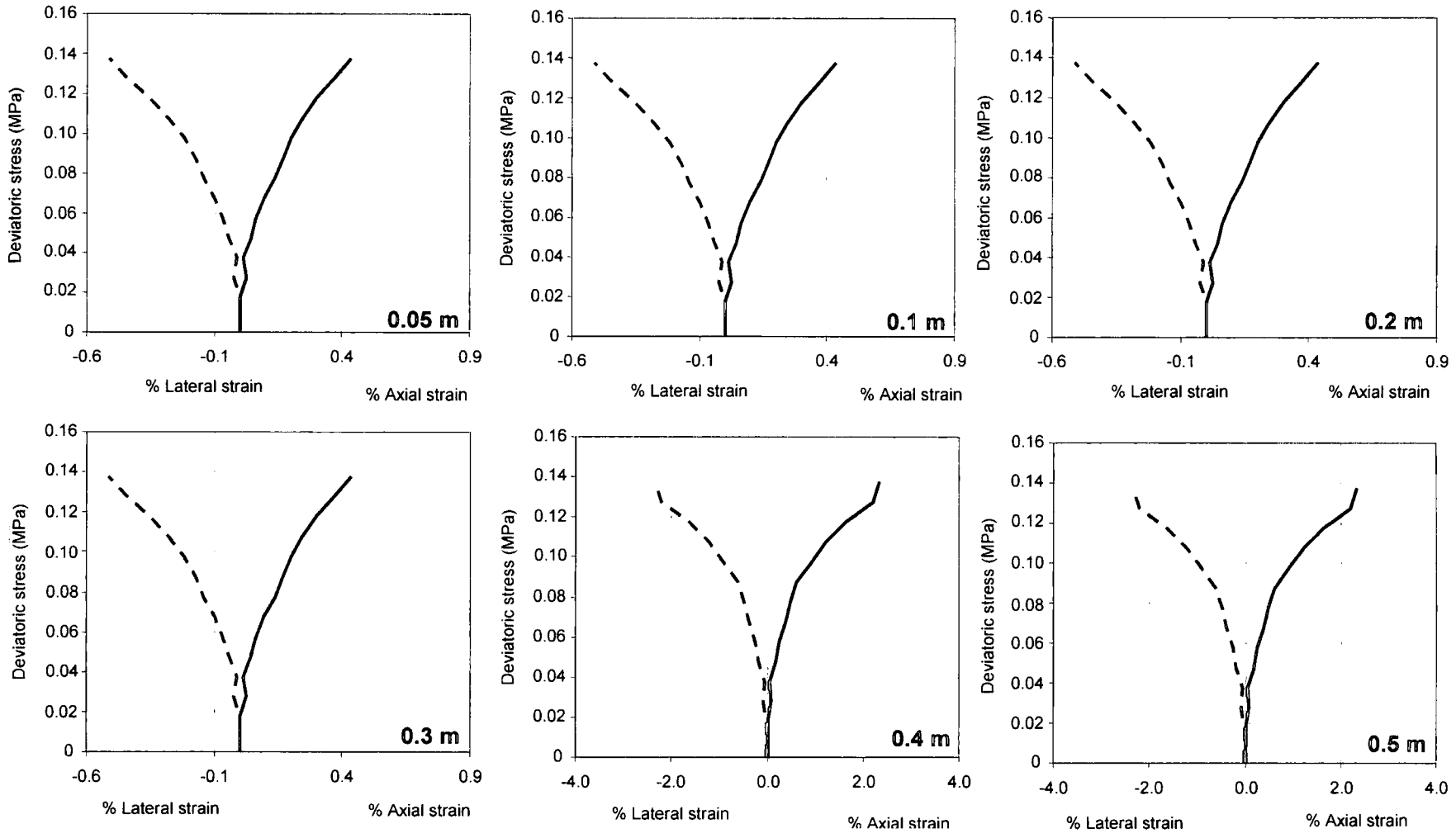

Figure 4.5: Stress-strain response of a 1 m limestone rock mass with varying block sizes.

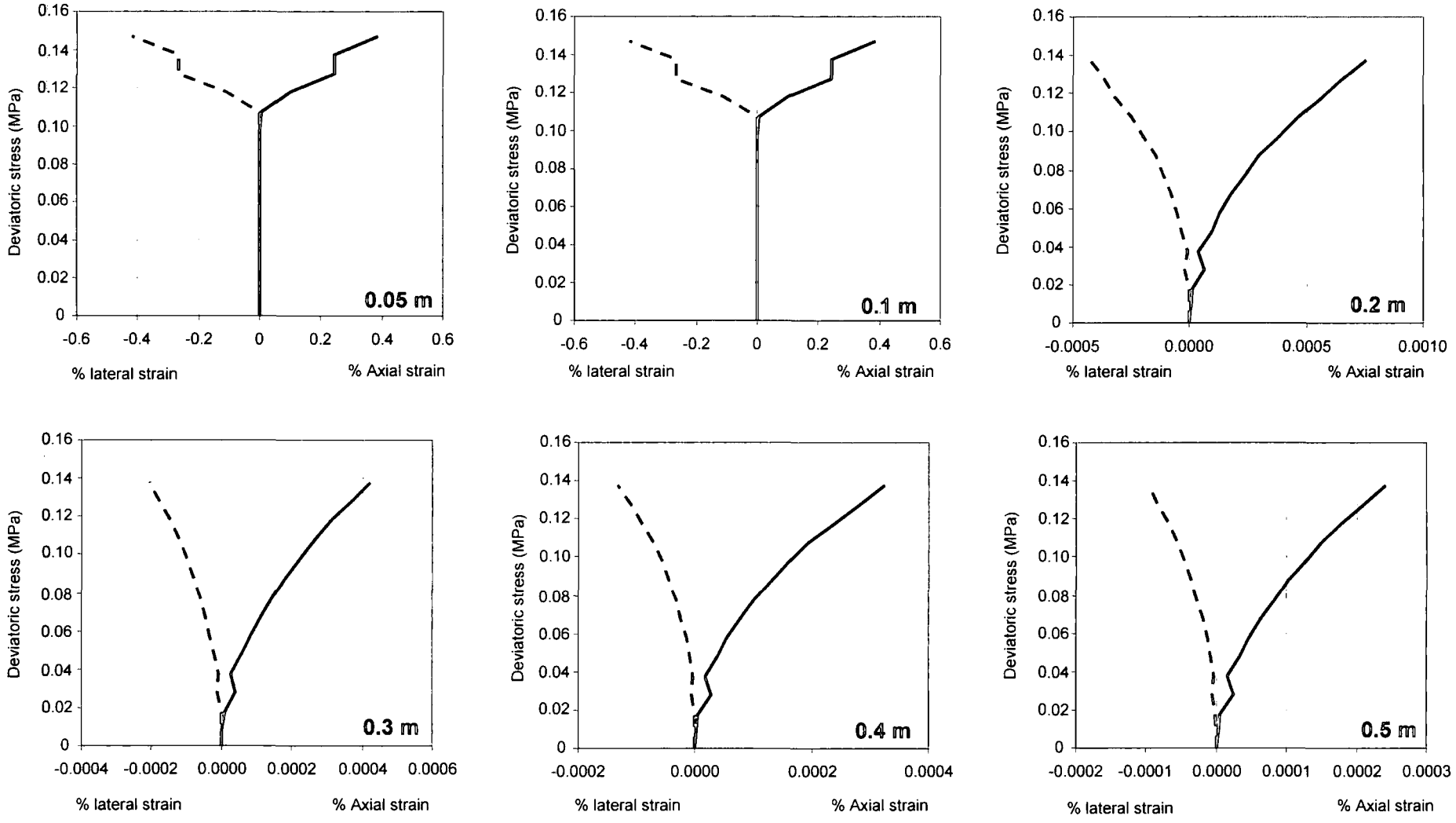

Figure 4.6: Stress-strain response of a 1 m granite rock mass with varying block sizes.

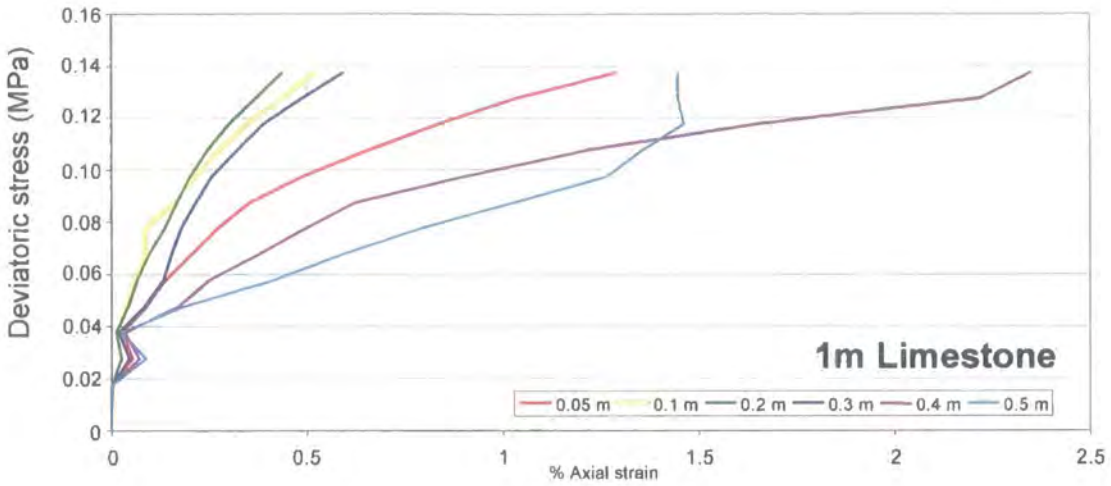

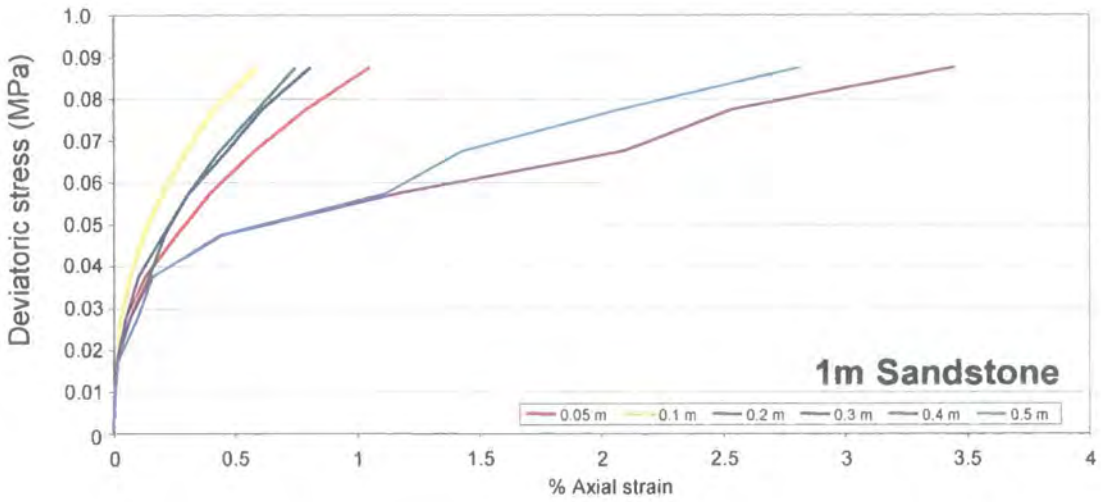

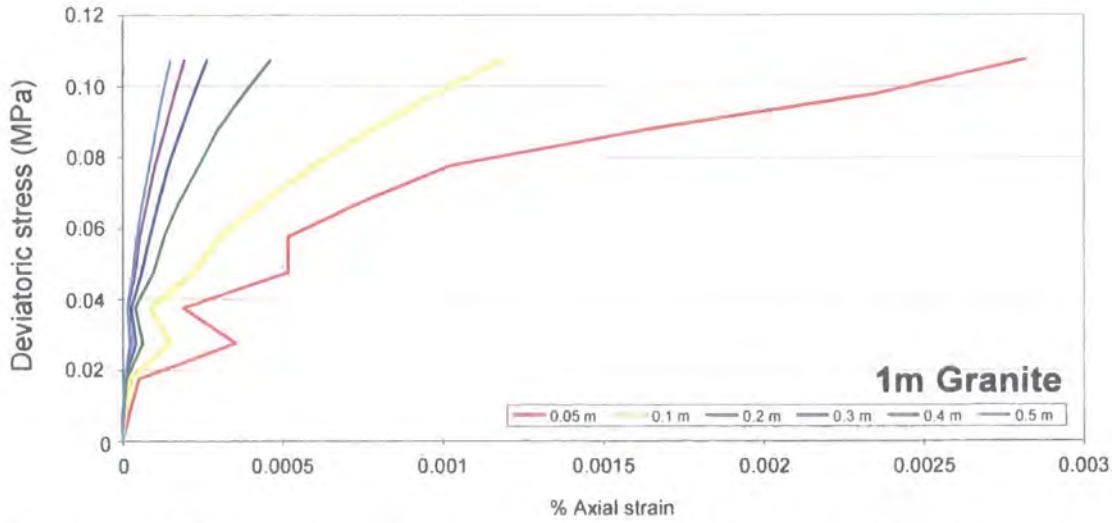

Figure 4.7: Comparative axial strain curves for 1 m rock masses composed of different block sizes.

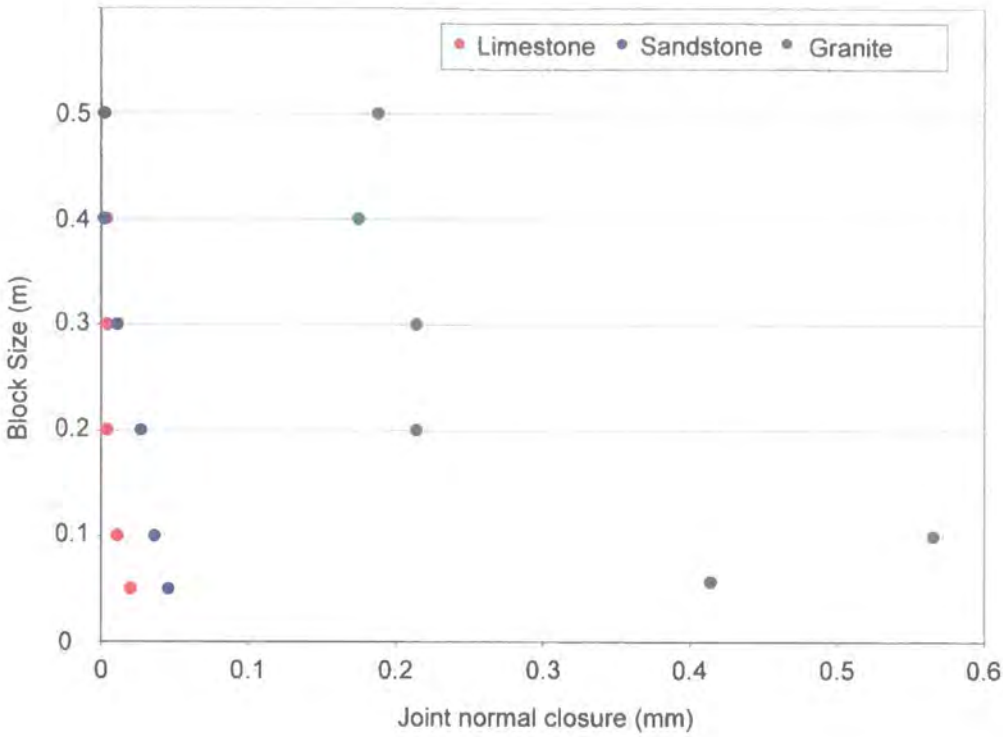

Figure 4.8: Joint normal closure magnitude for 1 m rock masses in limestone, sandstone and granite.

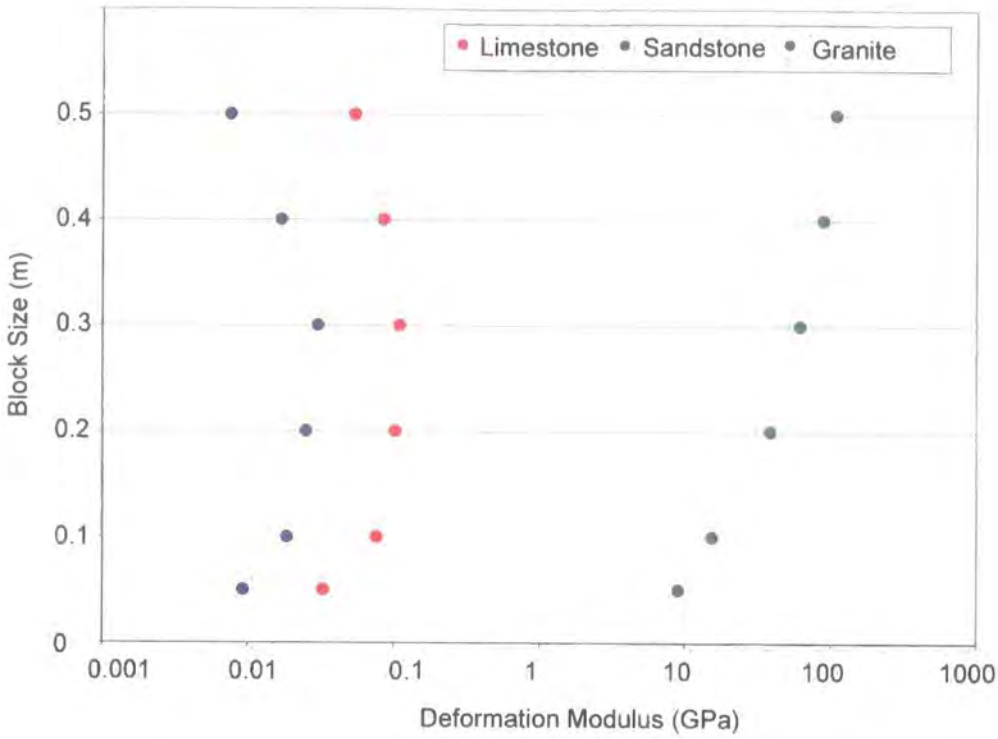

Figure 4.9: Deformation moduli for 1 m rock masses in limestone, sandstone and granite.

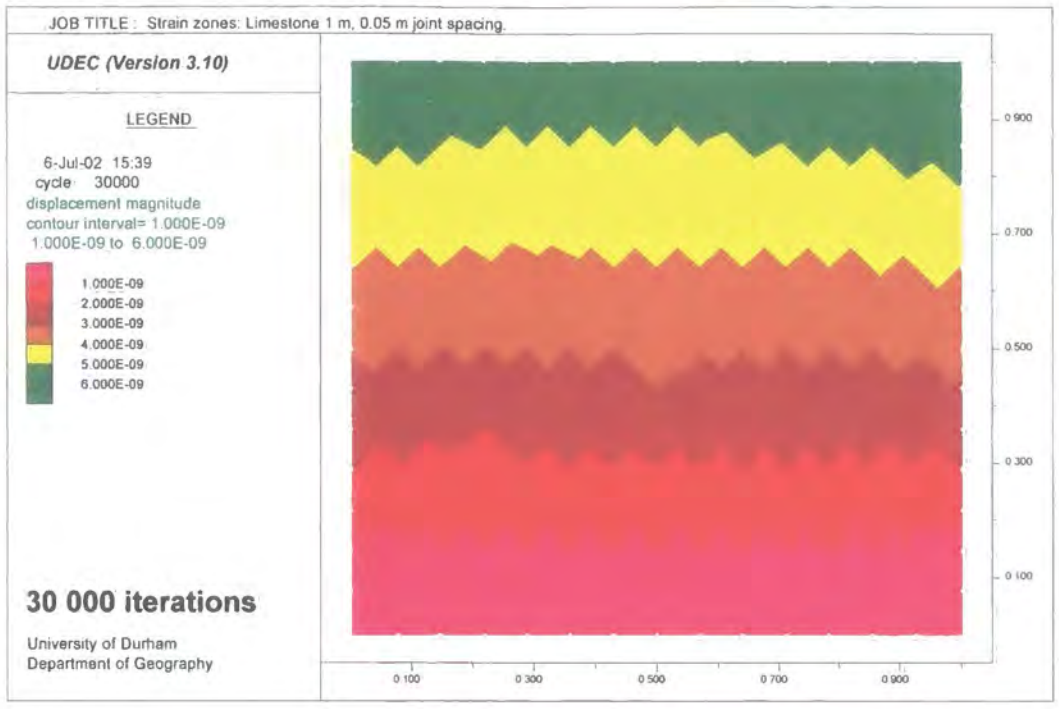

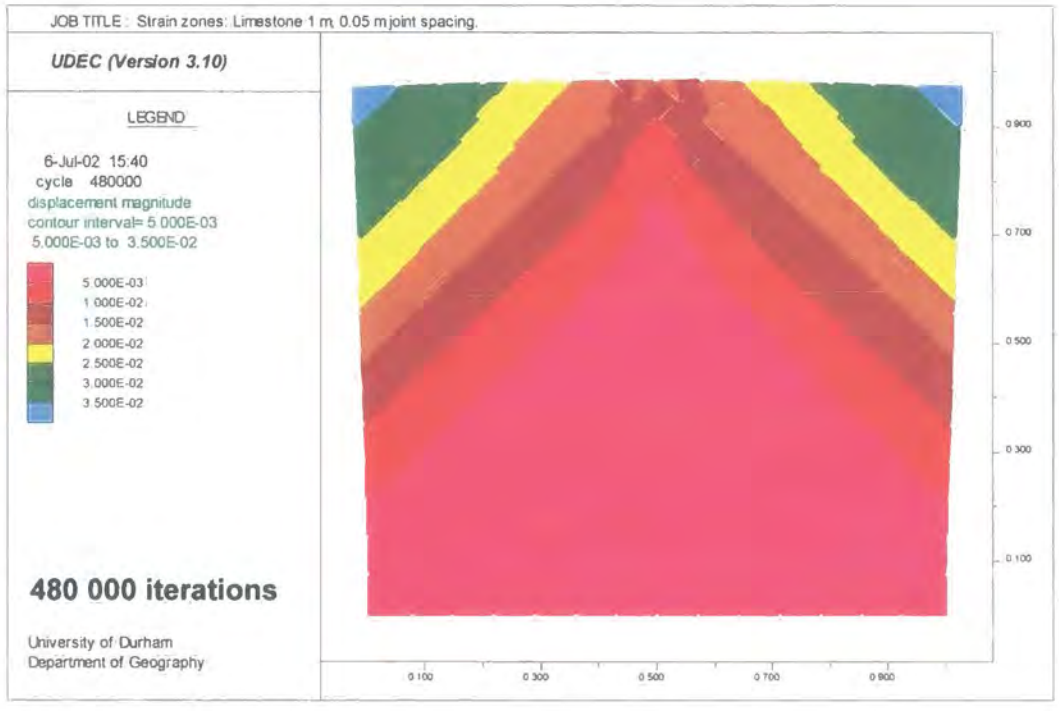

Figure 4.10a: Strain zone development in a 1 m limestone rock mass with 0.05 m block size.

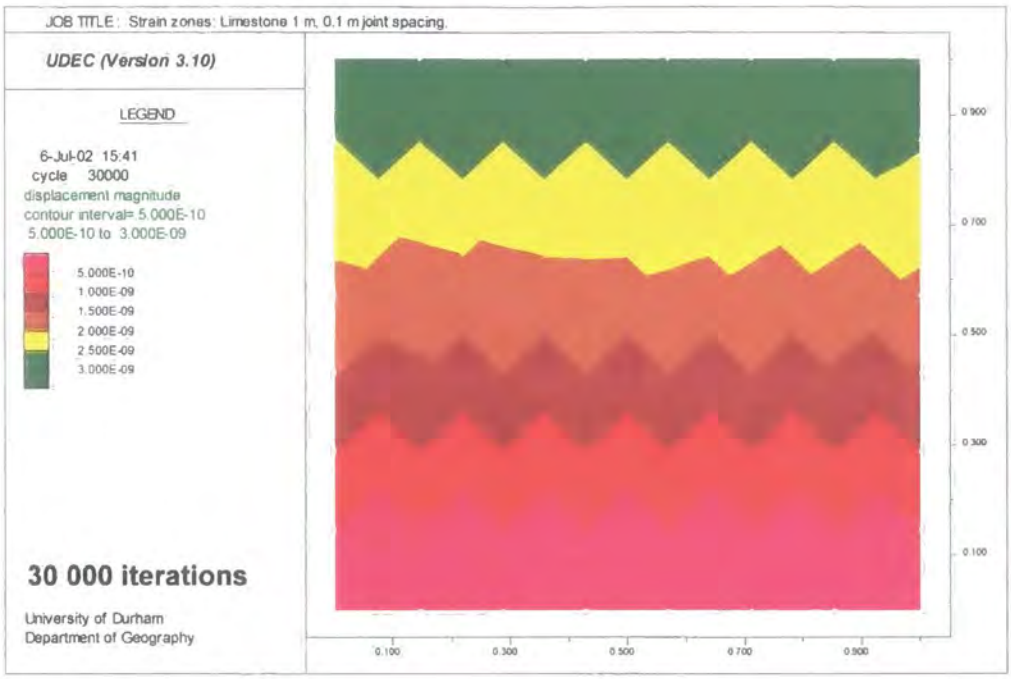

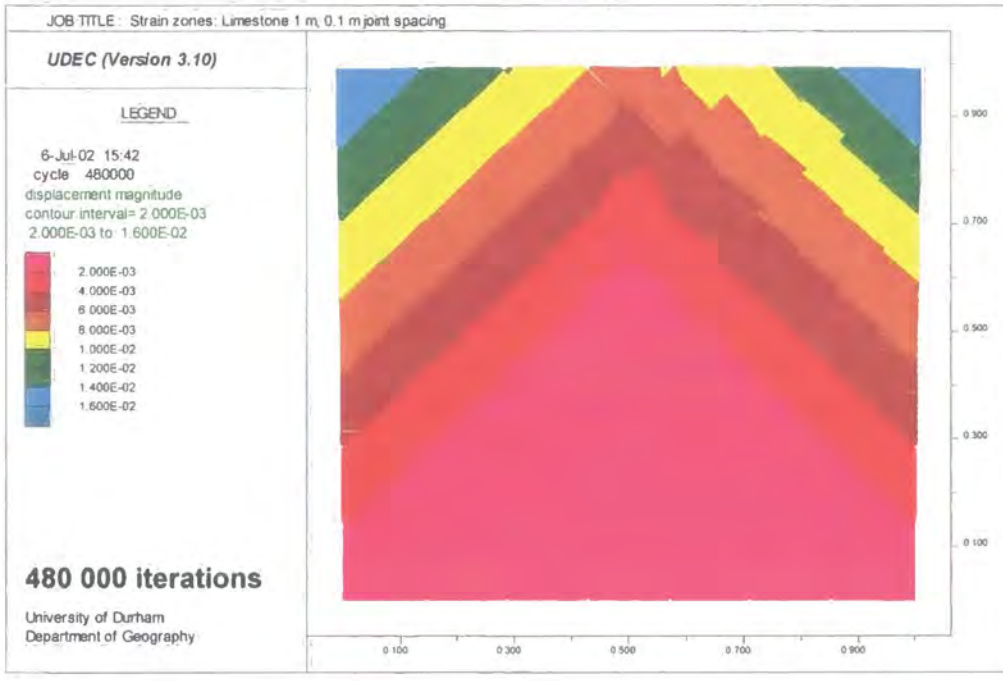

Figure 4.10b: Strain zone development in a 1 m limestone rock mass with 0.1 m block size.

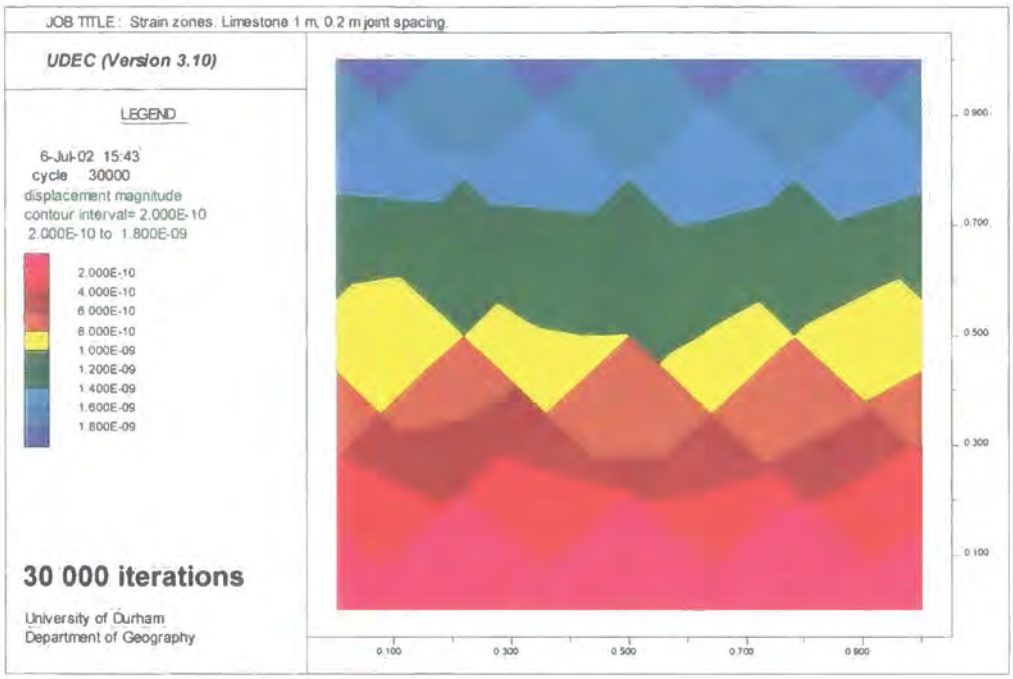

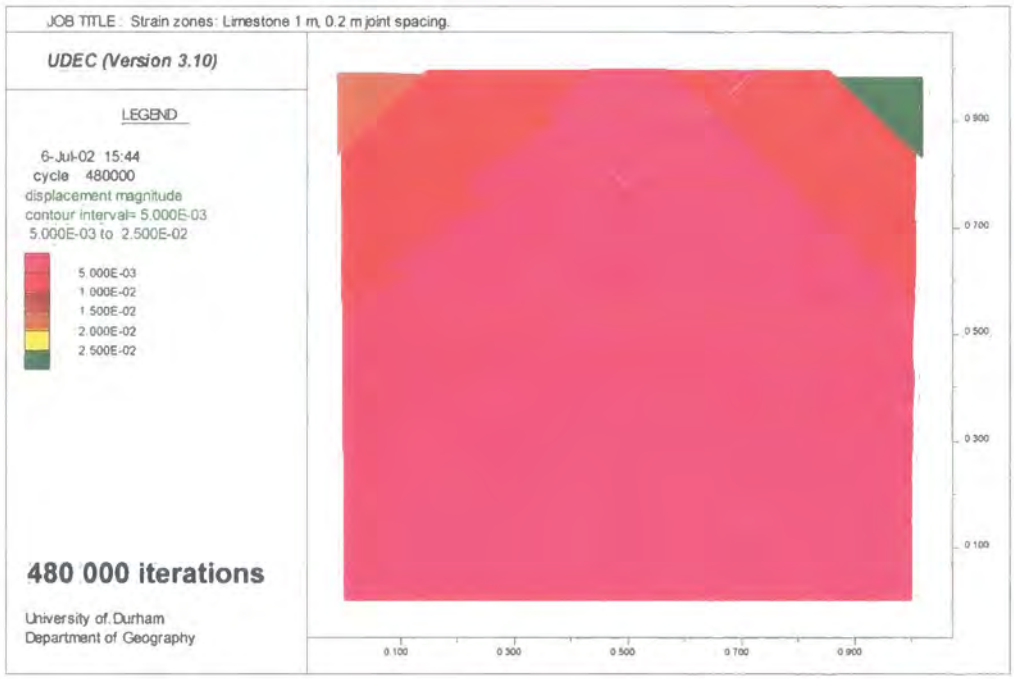

Figure 4.10c: Strain zone development in a 1 m limestone rock mass with 0.2 m block size.

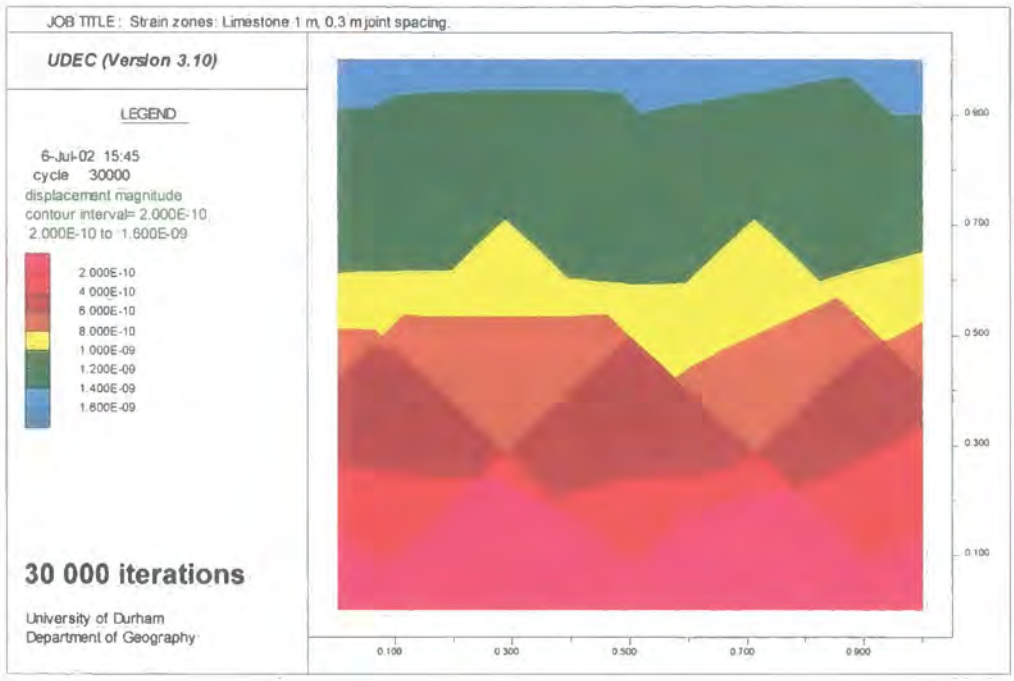

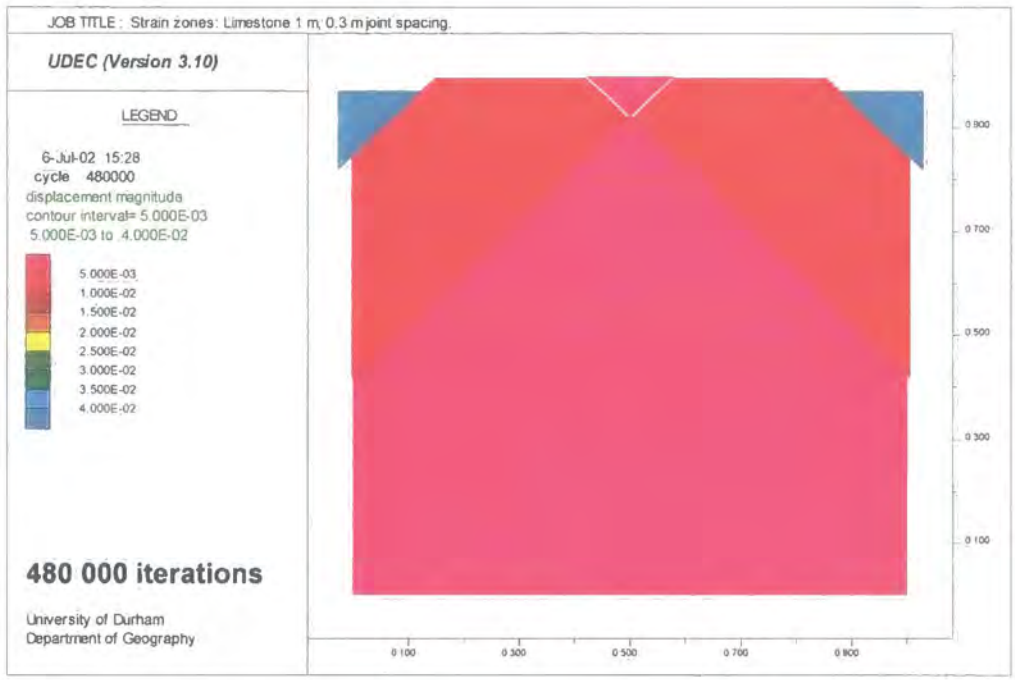

Figure 4.10d: Strain zone development in a 1 m limestone rock mass with 0.3 m block size.

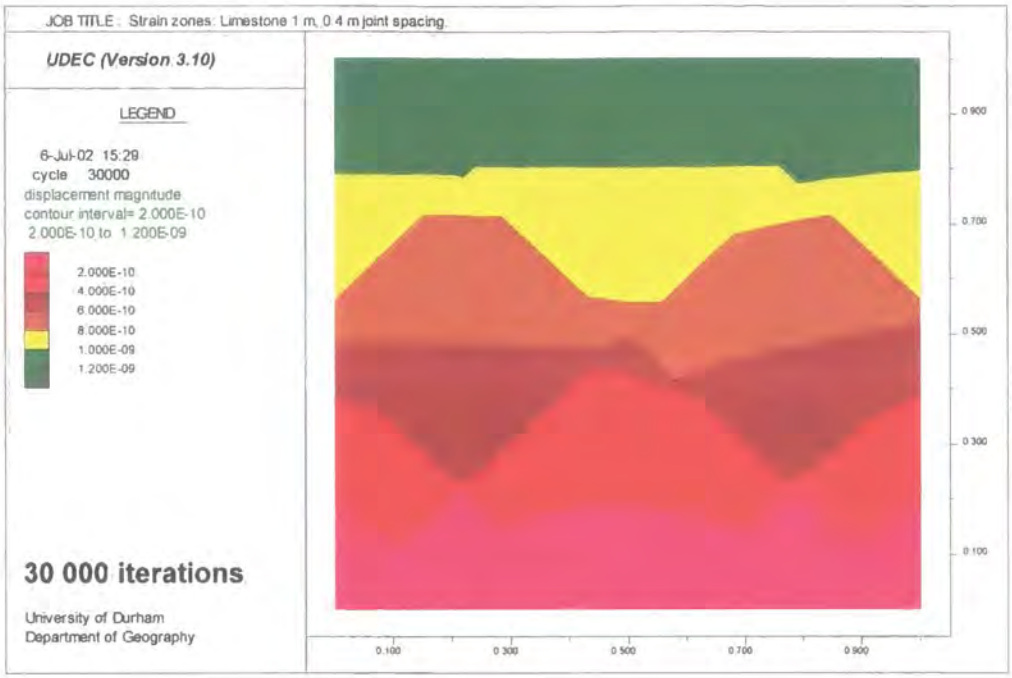

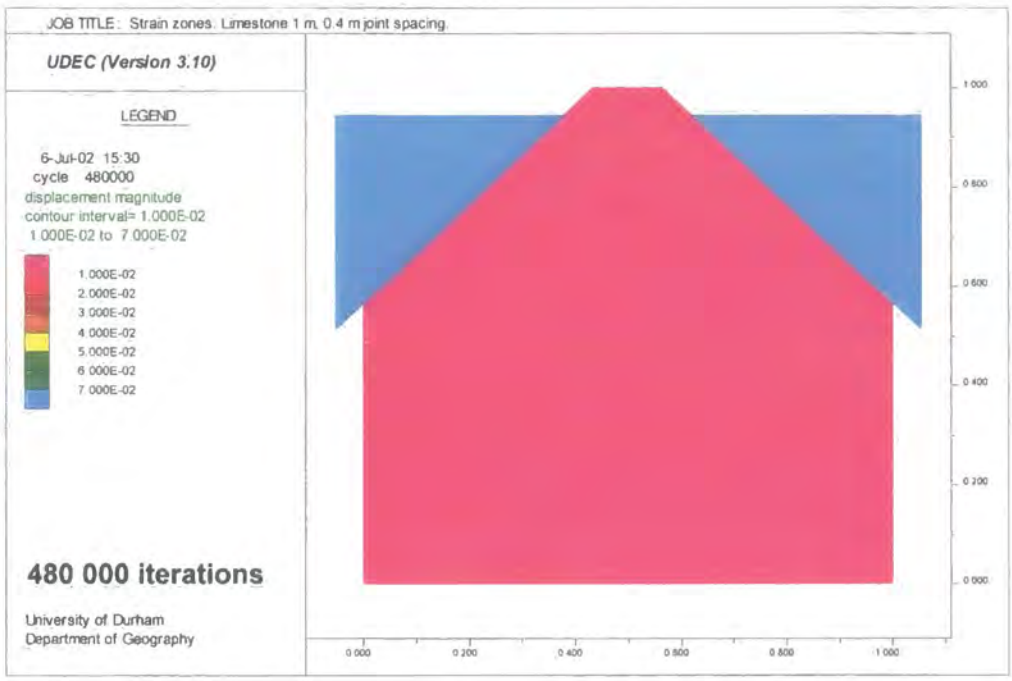

Figure 4.10e: Strain zone development in a 1 m limestone rock mass with 0.4 m block size.

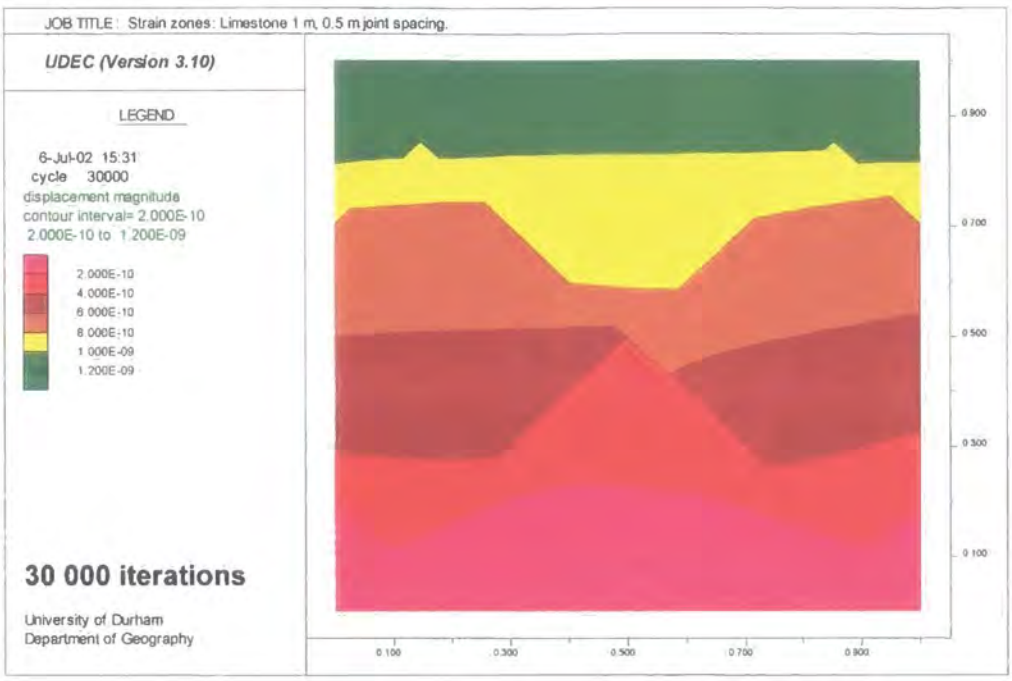

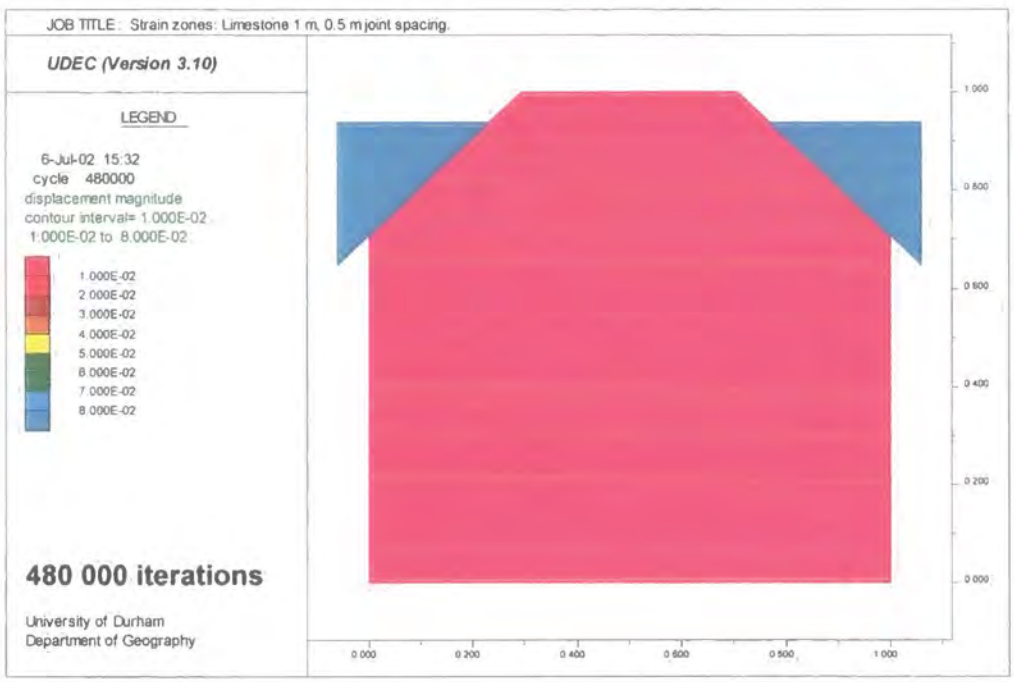

Figure 4.10f: Strain zone development in a 1 m limestone rock mass with 0.5 m block size.

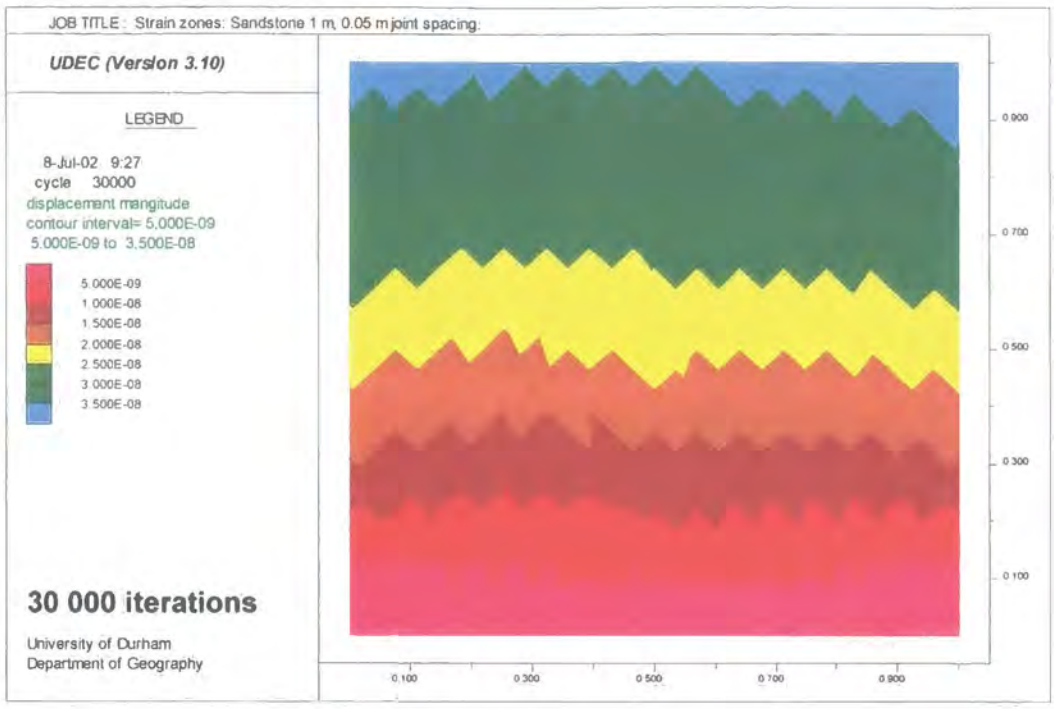

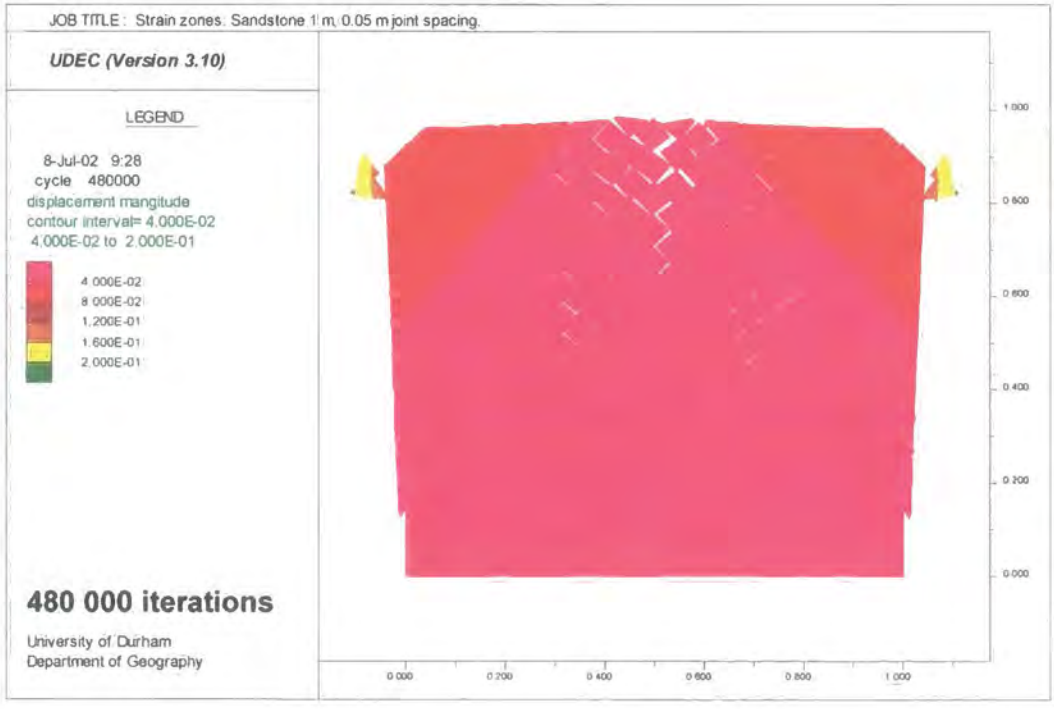

Figure 4.11a: Strain zone development in a 1 m sandstone rock mass with 0.05 m block size.

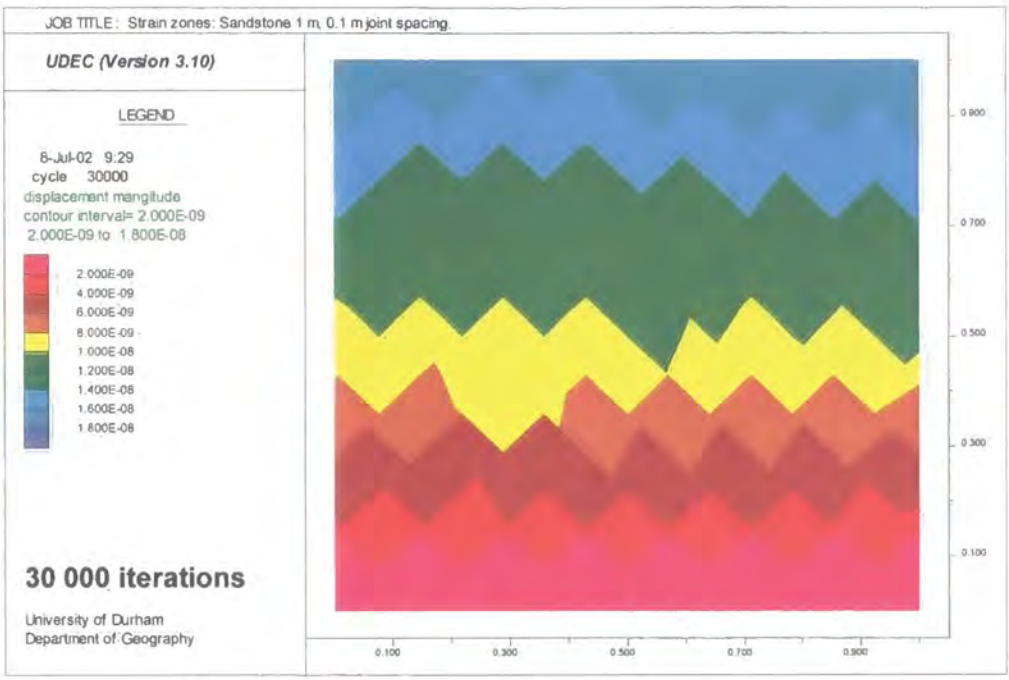

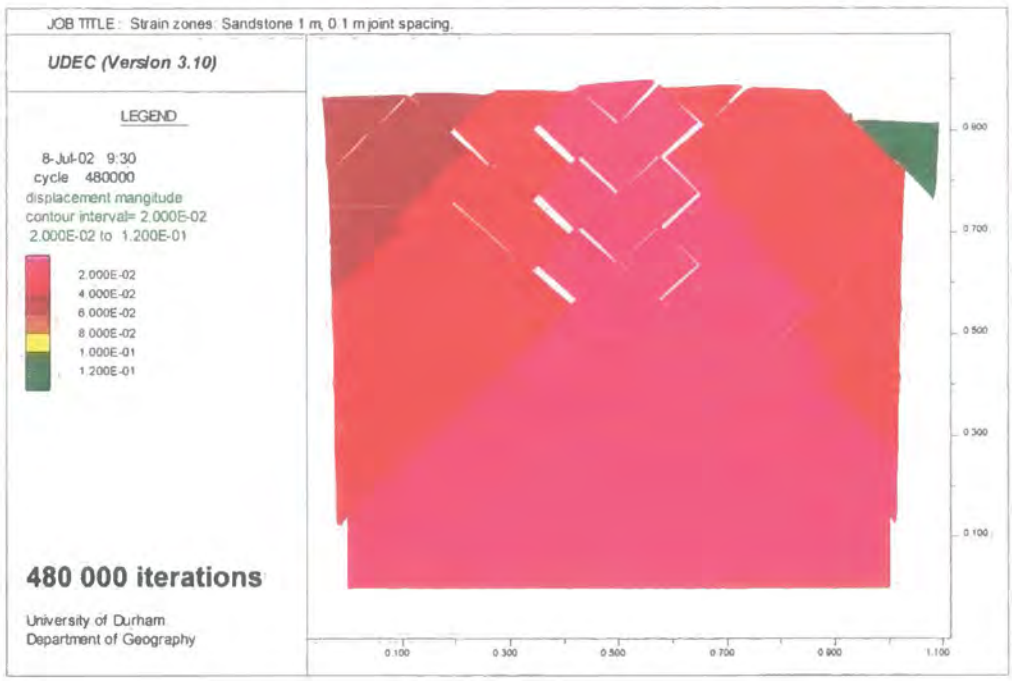

Figure 4.11b: Strain zone development in a 1 m sandstone rock mass with 0.1 m block size.

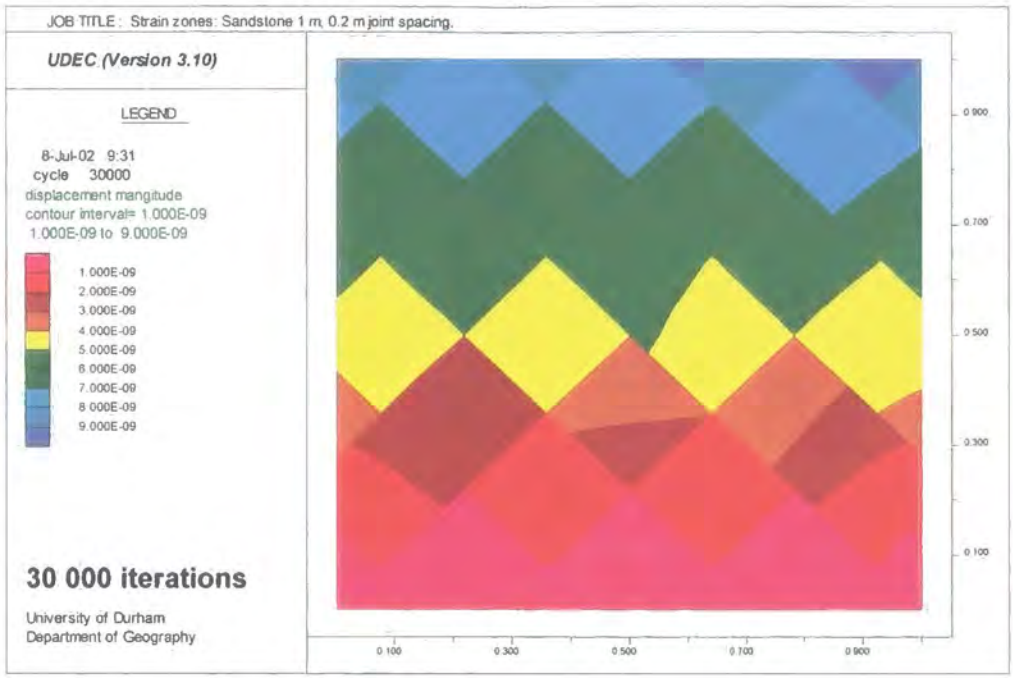

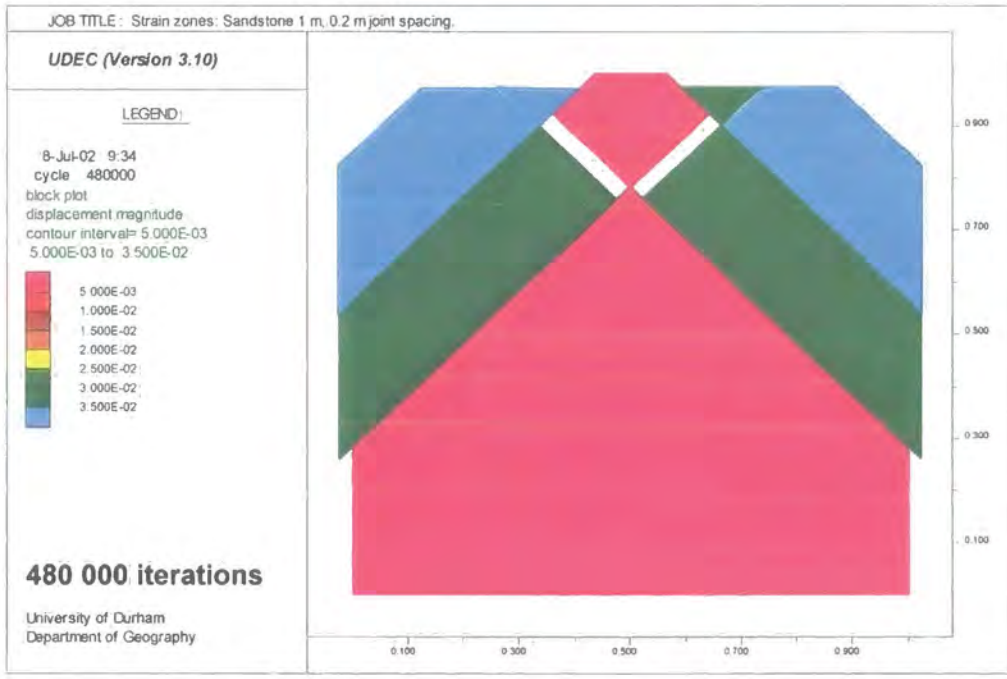

Figure 4.11c: Strain zone development in a 1 m sandstone rock mass with 0.2 m block size.

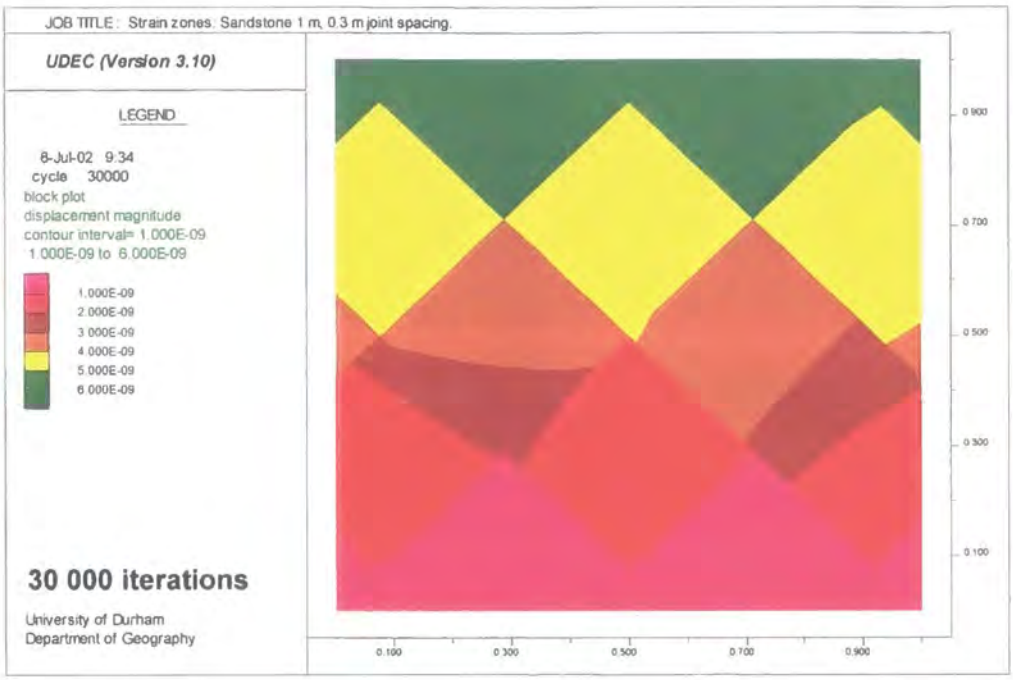

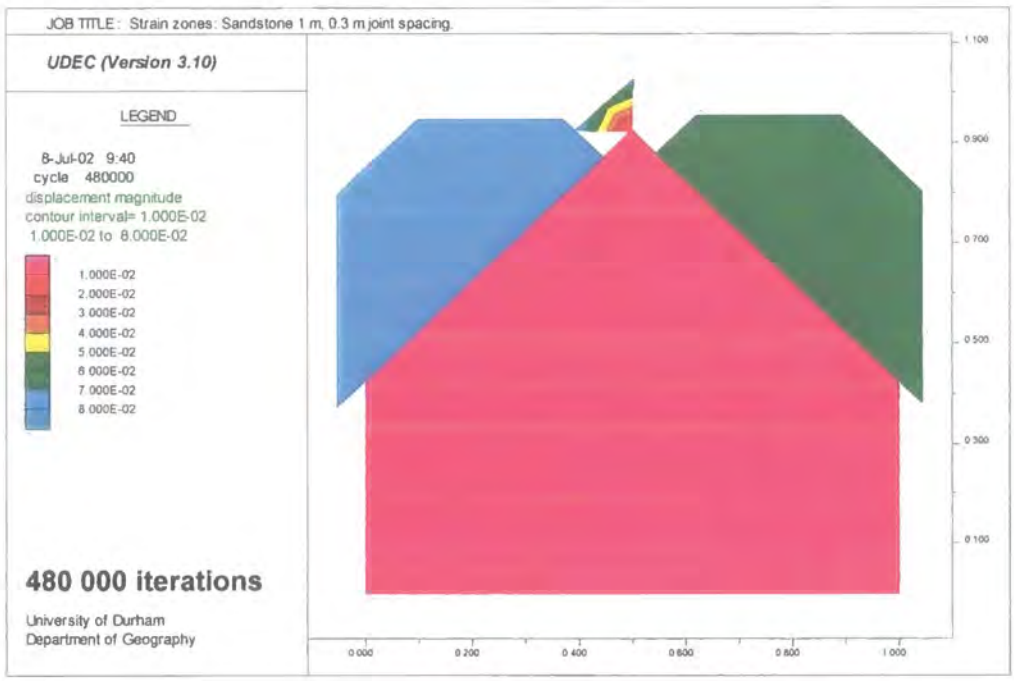

Figure 4.11d: Strain zone development in a 1 m sandstone rock mass with 0.3 m block size.

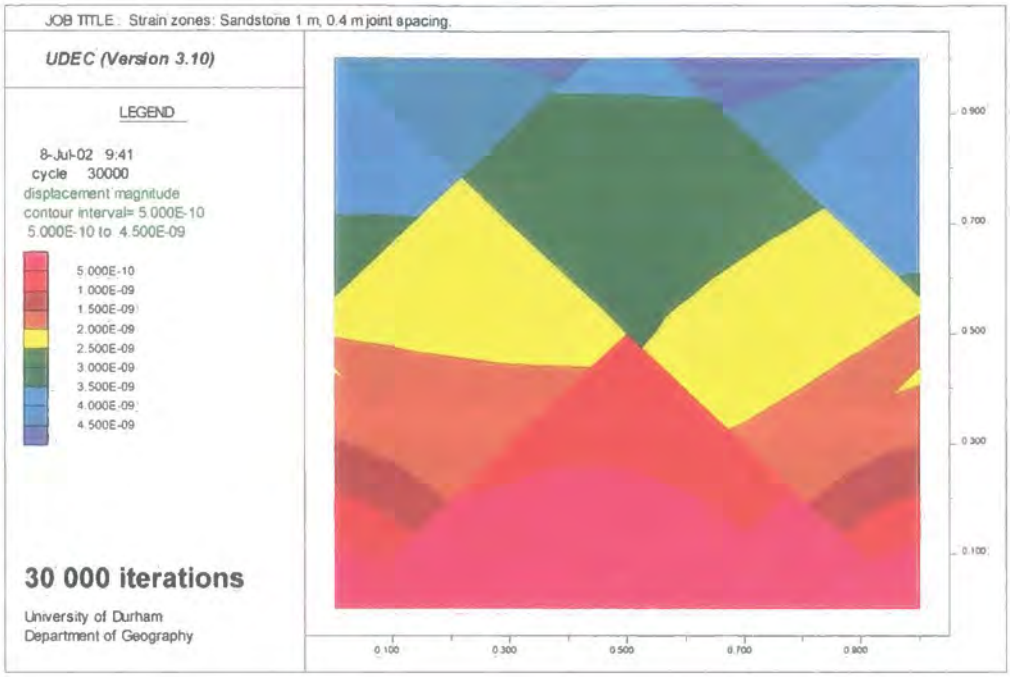

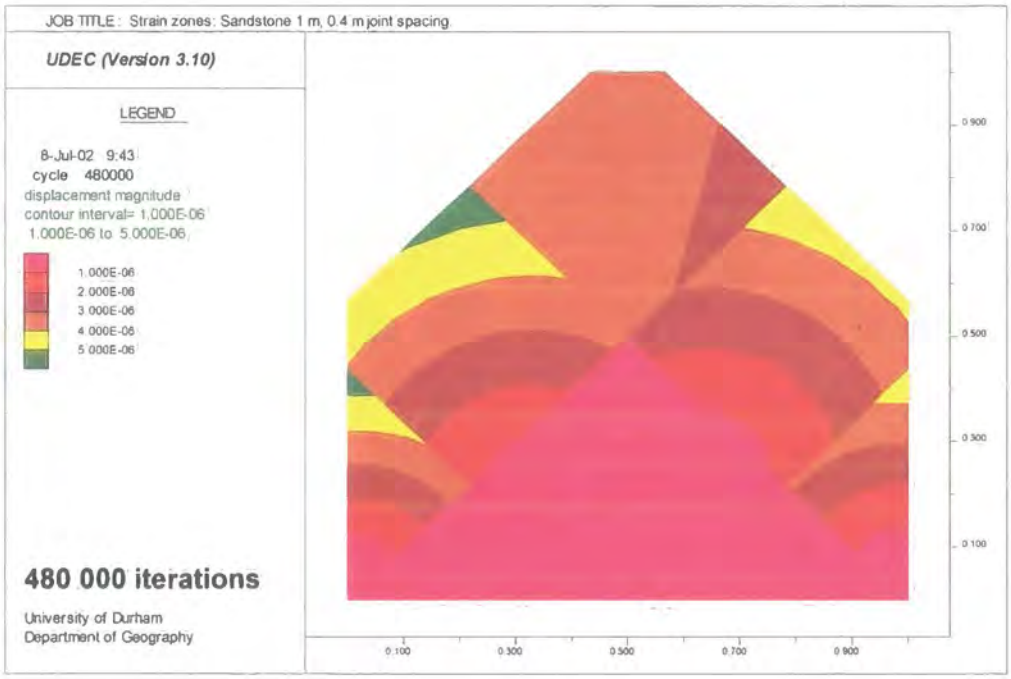

Figure 4.11e: Strain zone development in a 1 m sandstone rock mass with 0.4 m block size.

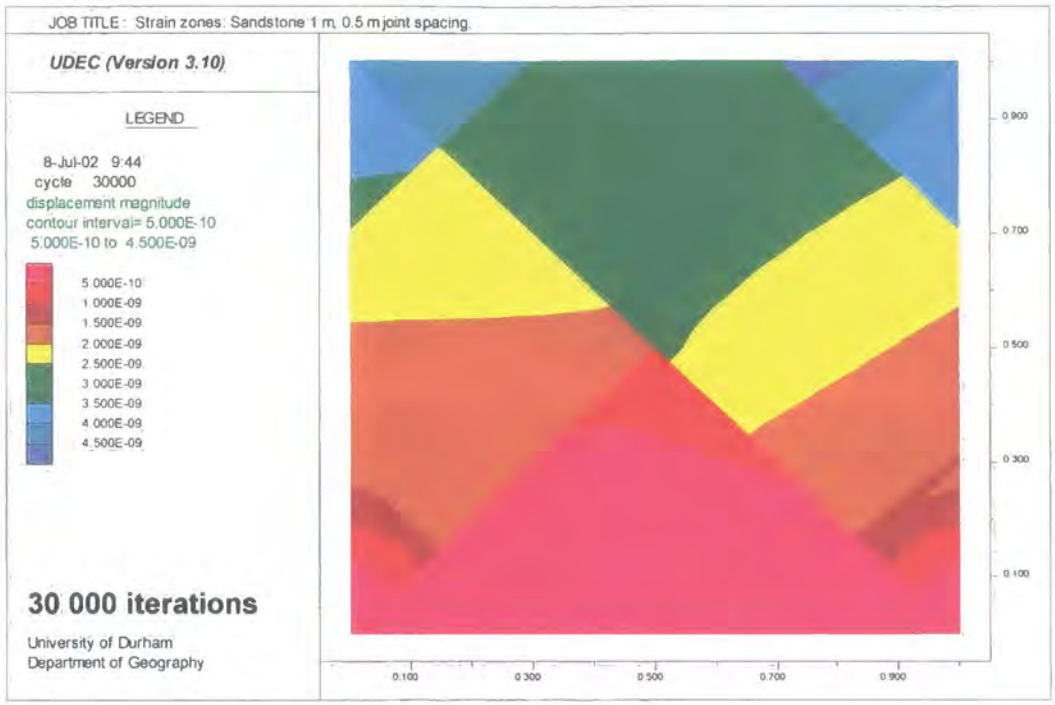

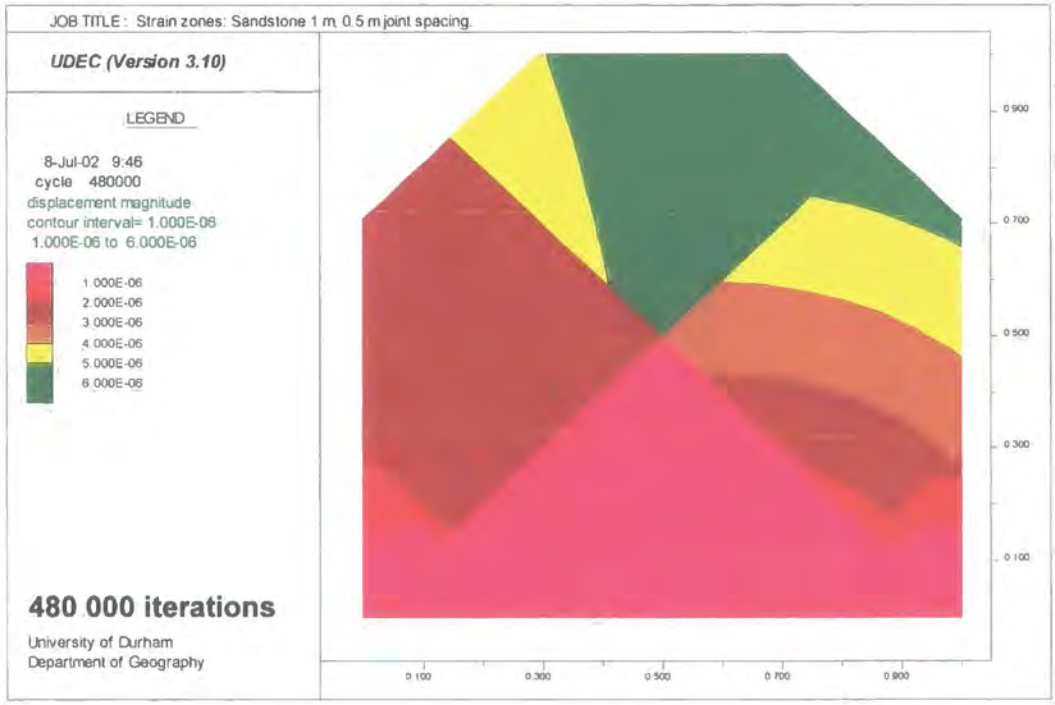

Figure 4.11f: Strain zone development in a 1 m sandstone rock mass with 0.5 m block size.

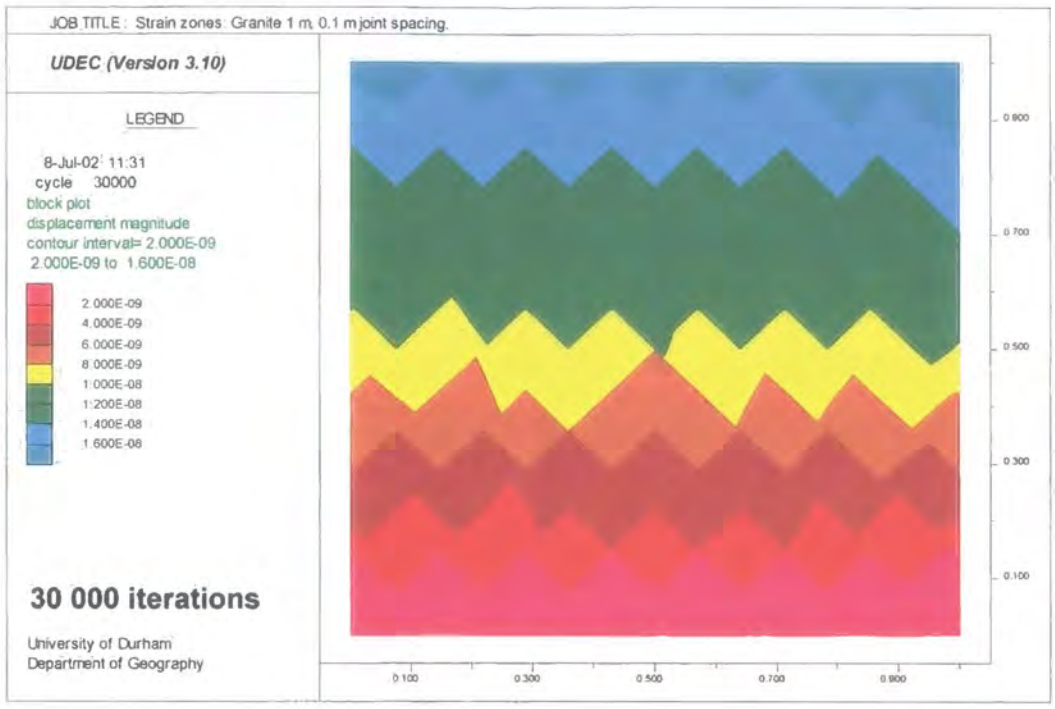

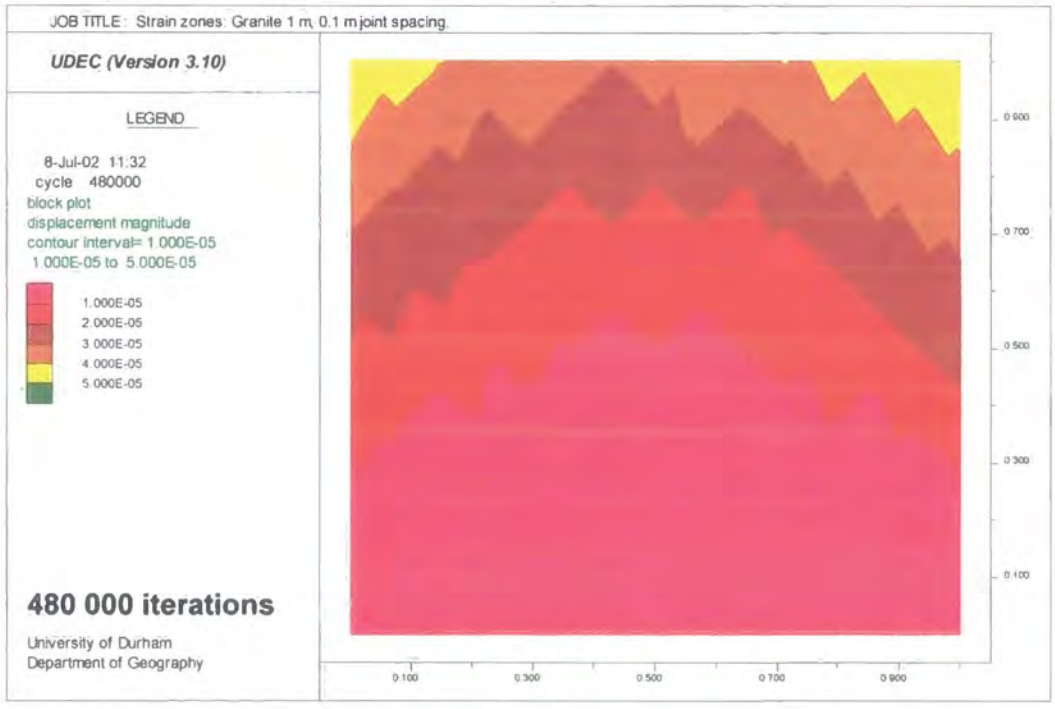

Figure 4.12a: Strain zone development in a 1 m granite rock mass with 0.05 m block size.

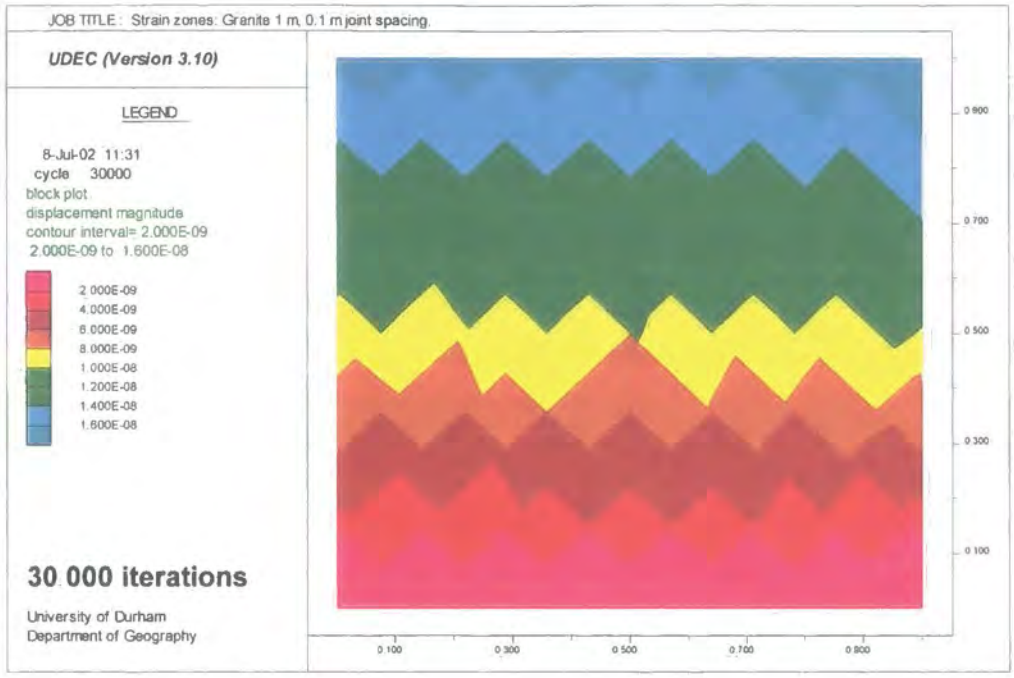

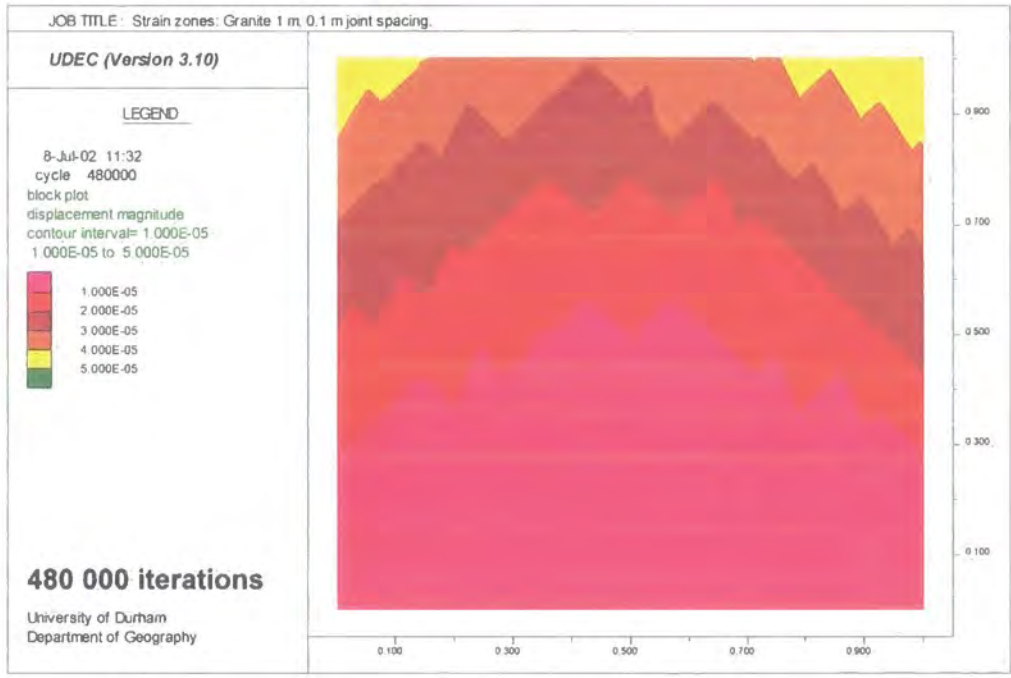

Figure 4.12b: Strain zone development in a 1 m granite rock mass with 0.1 m block size.

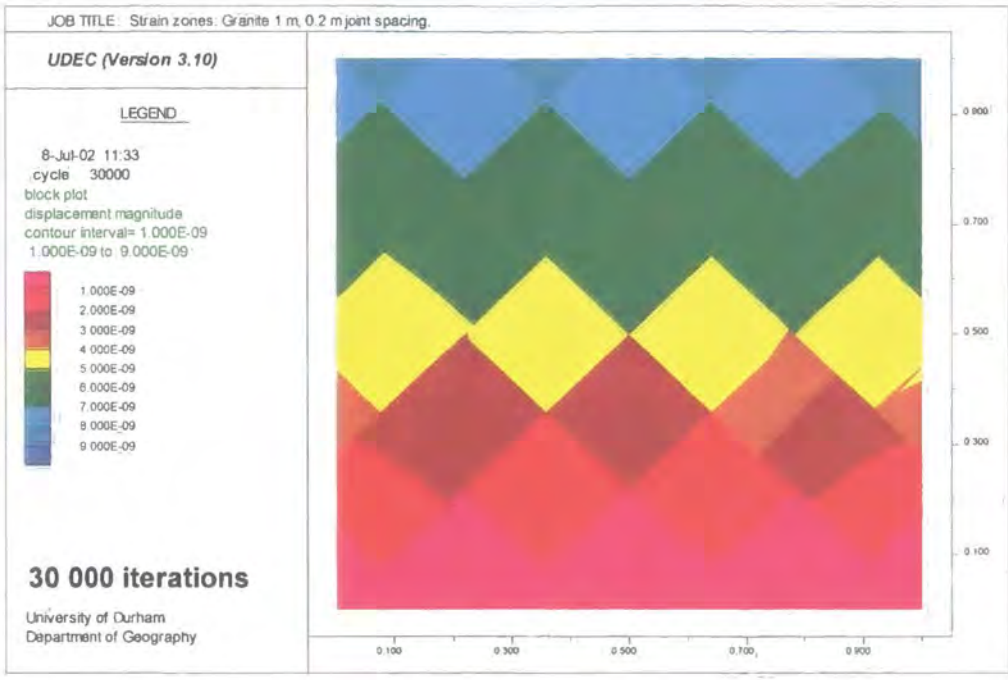

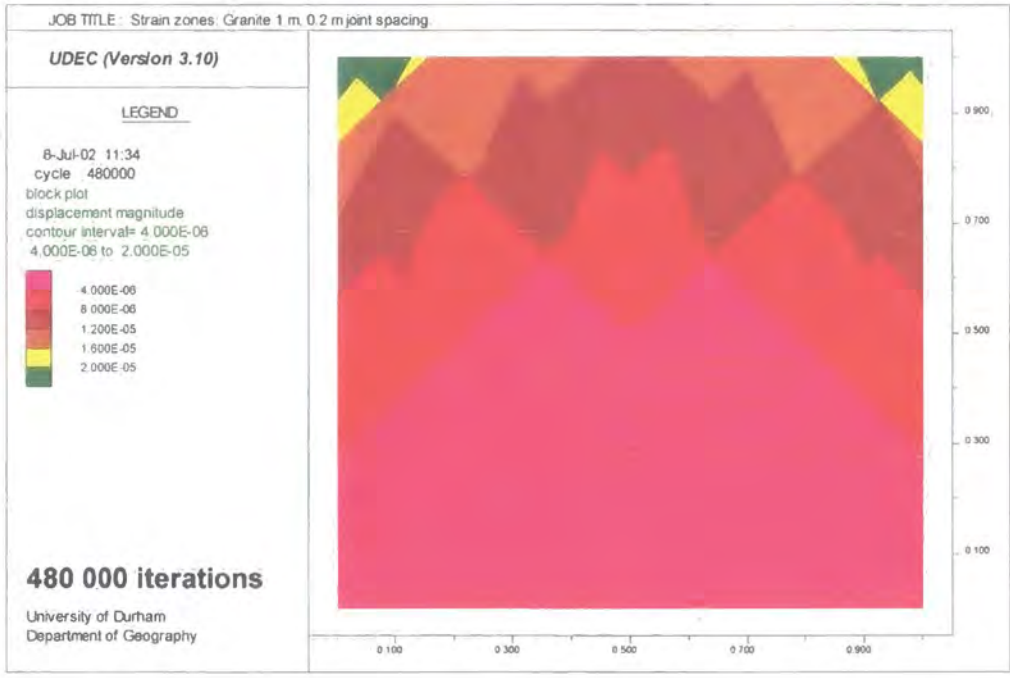

Figure 4.12c: Strain zone development in a 1 m granite rock mass with 0.2 m block size.

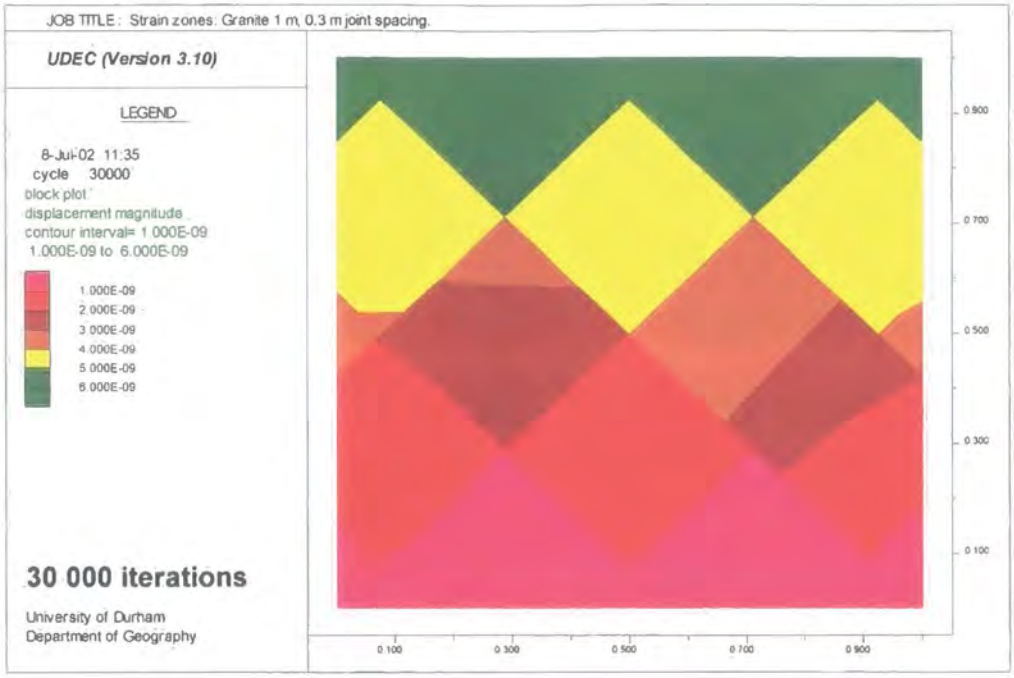

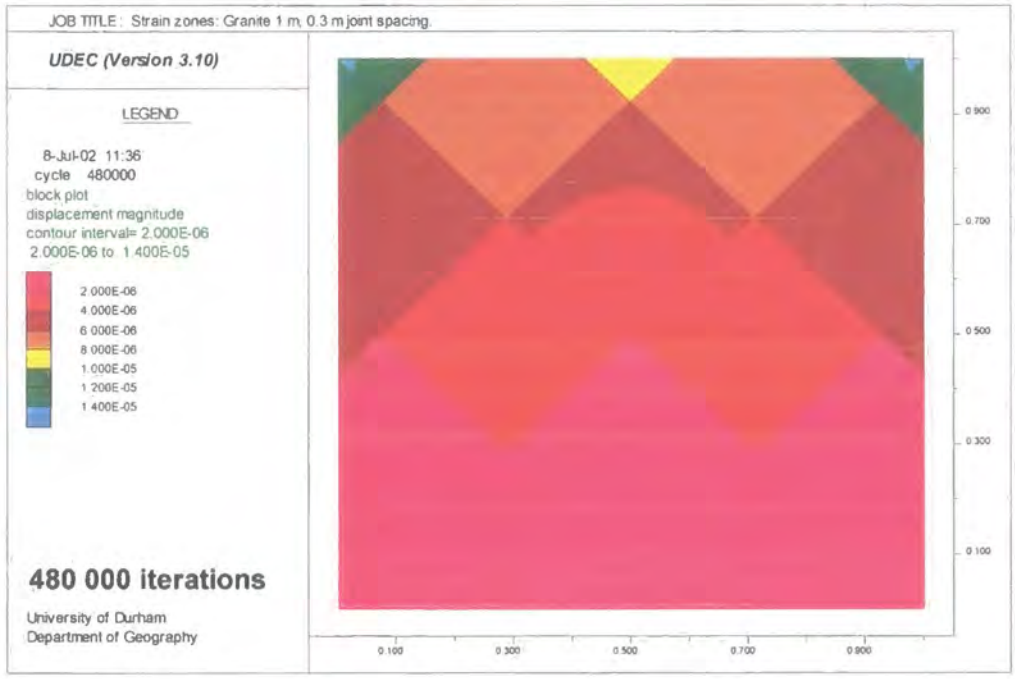

Figure 4.12d: Strain zone development in a 1 m granite rock mass with 0.3 m block size.

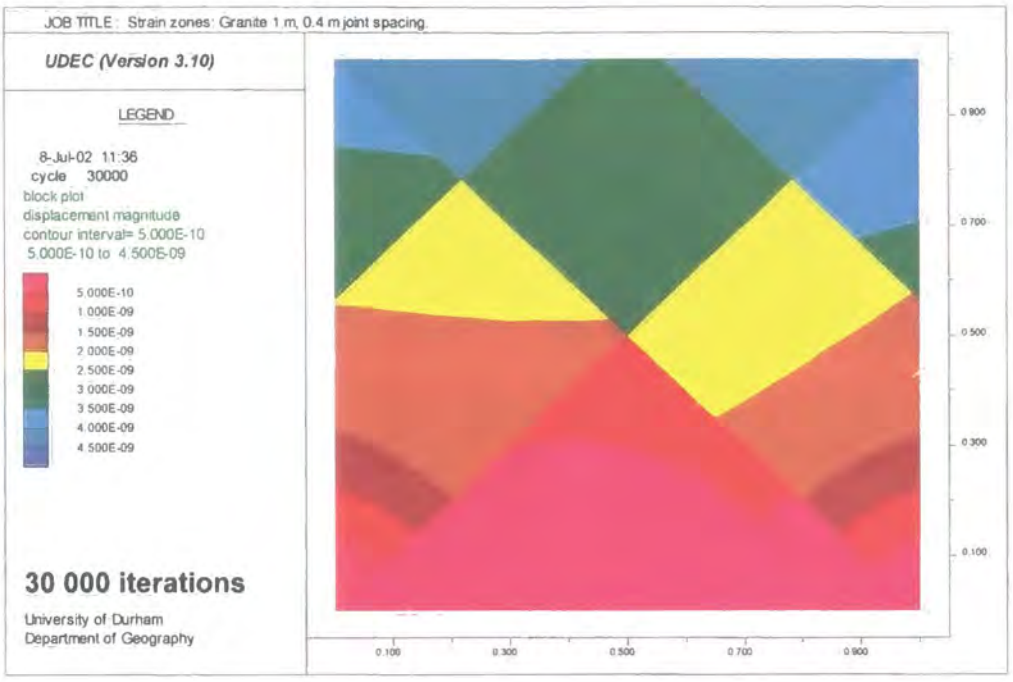

Figure 4.12e: Strain zone development in a 1 m granite rock mass with 0.4 m block size.

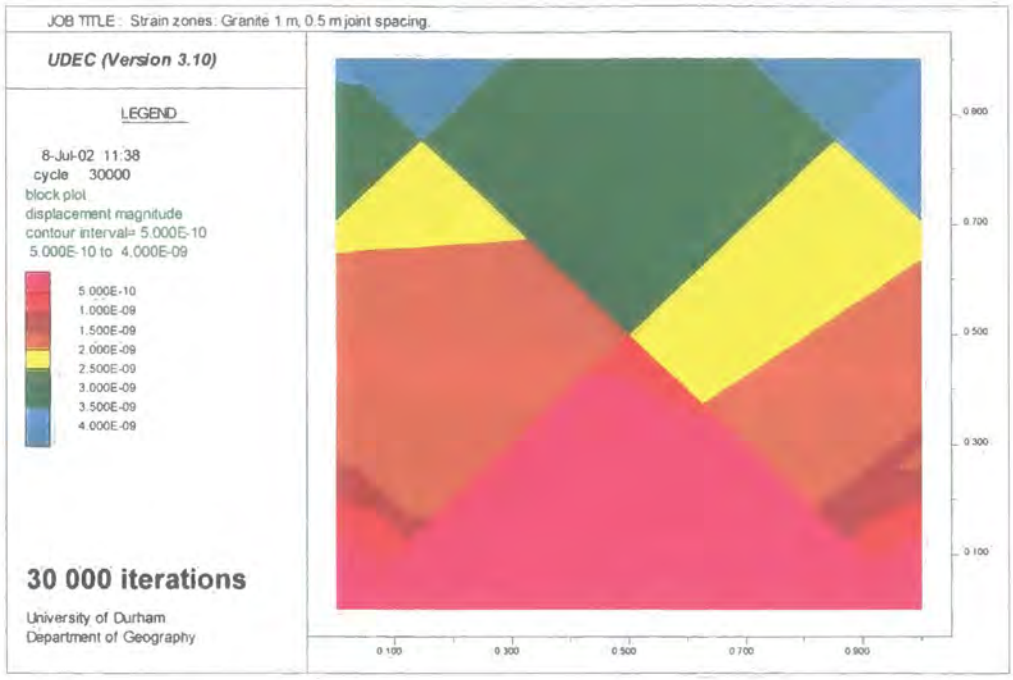

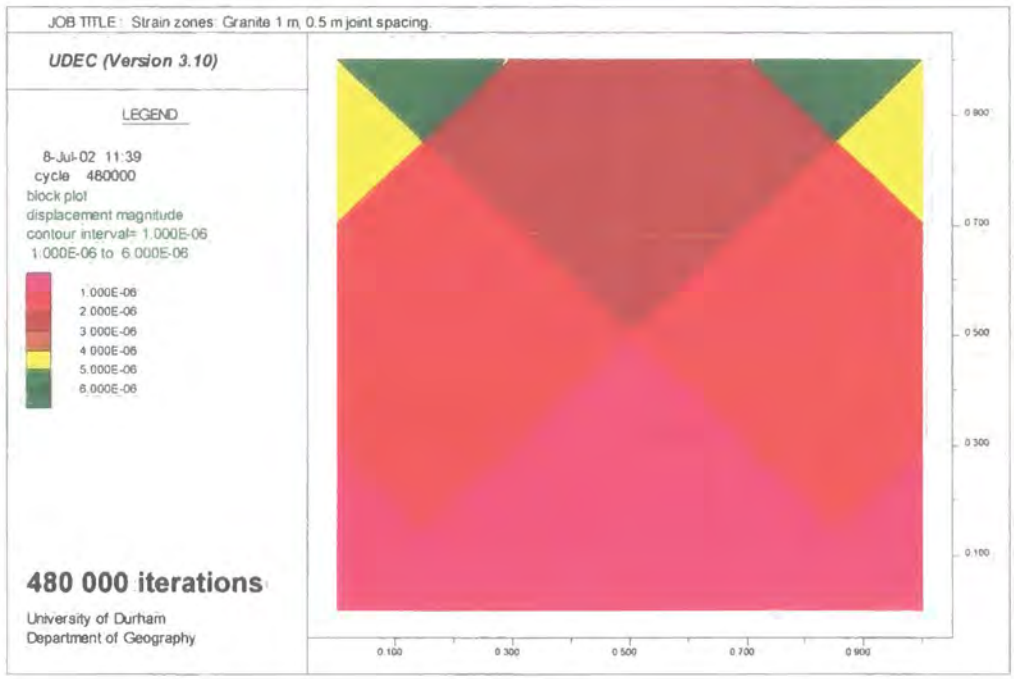

Figure 4.12f: Strain zone development in a 1 m granite rock mass with 0.5 m block size.

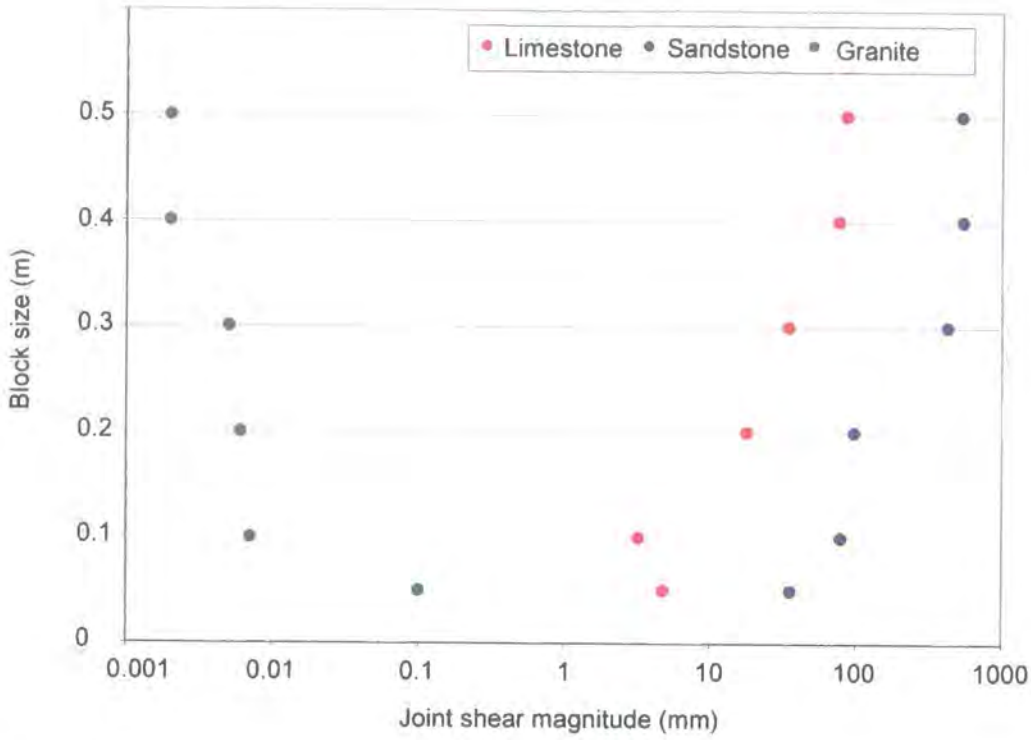

Figure 4.13: Joint shear magnitude for 1 m rock masses in limestone, sandstone and granite.

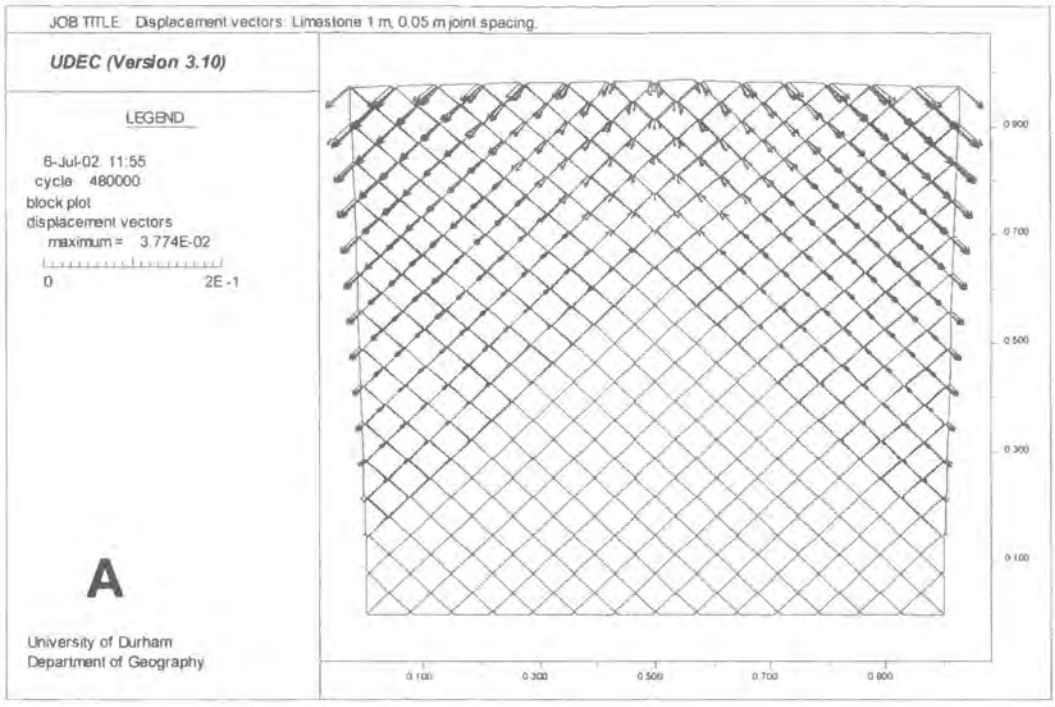

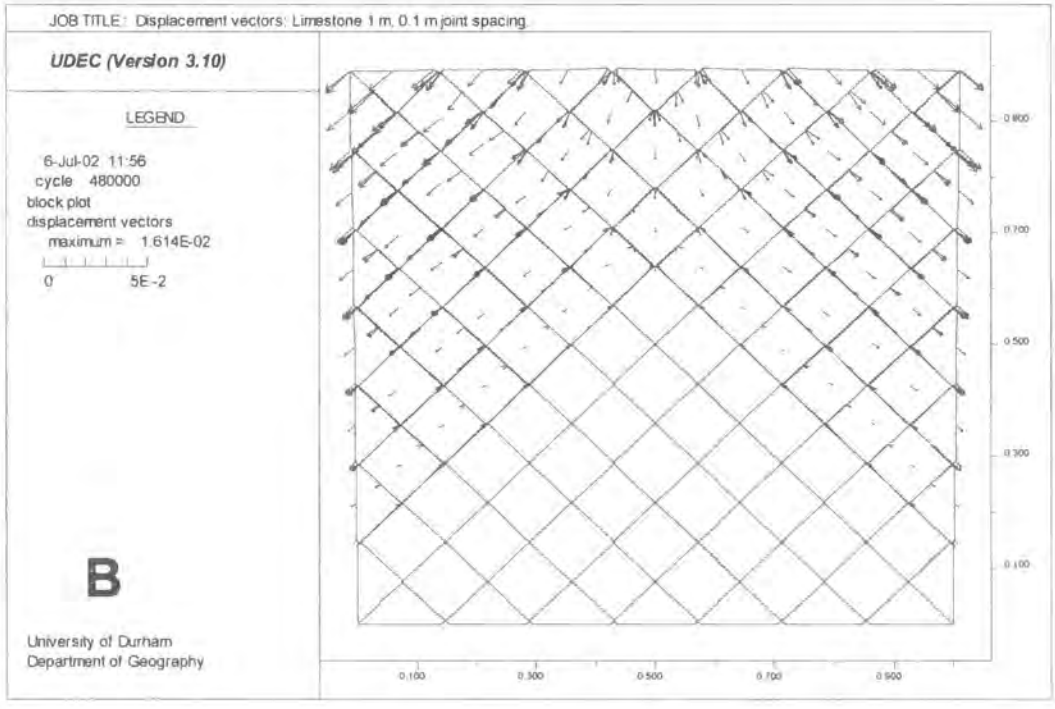

Figure 4.14: Displacement vector plots for a 1m limestone rock mass with 0.05 and 0.1 m block edge length.

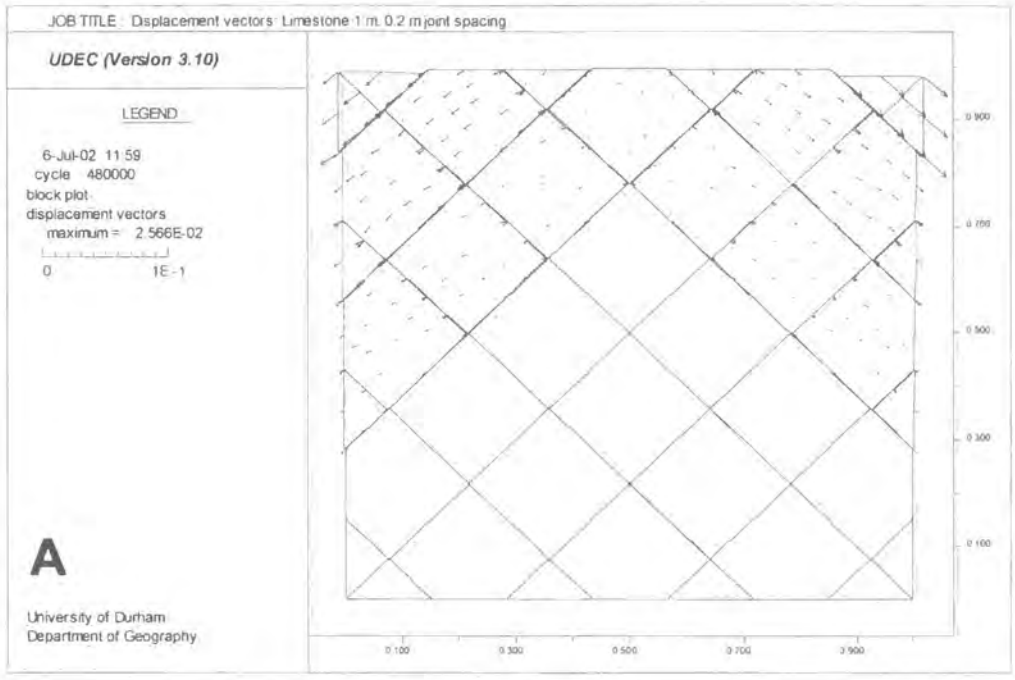

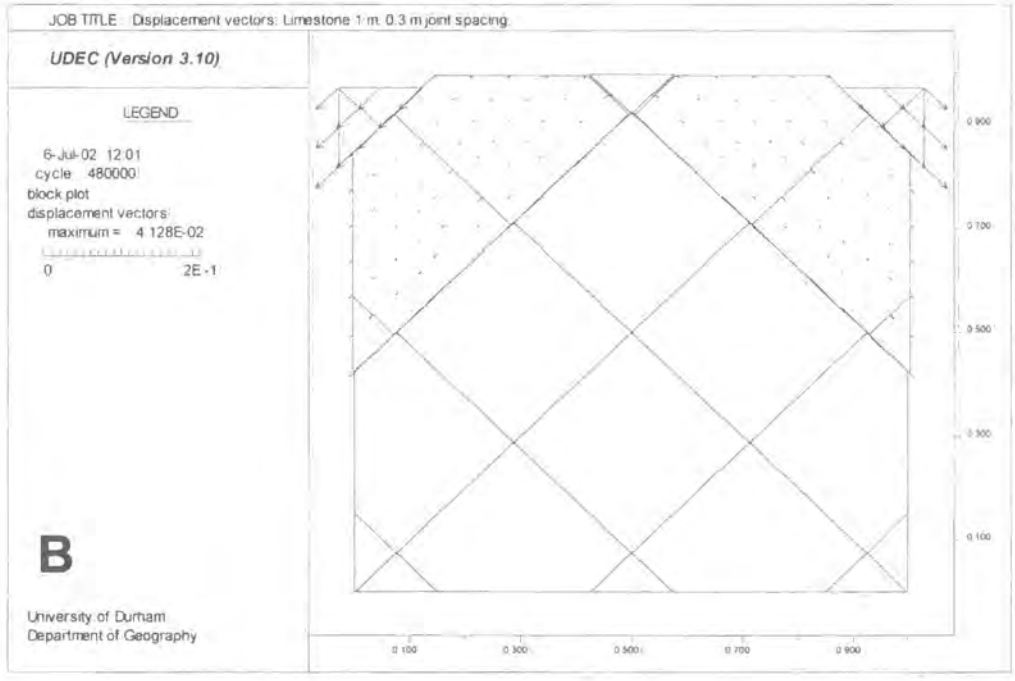

Figure 4.15: Displacement vector plots for a 1m limestone rock mass with 0.2 and 0.3 m block edge length.

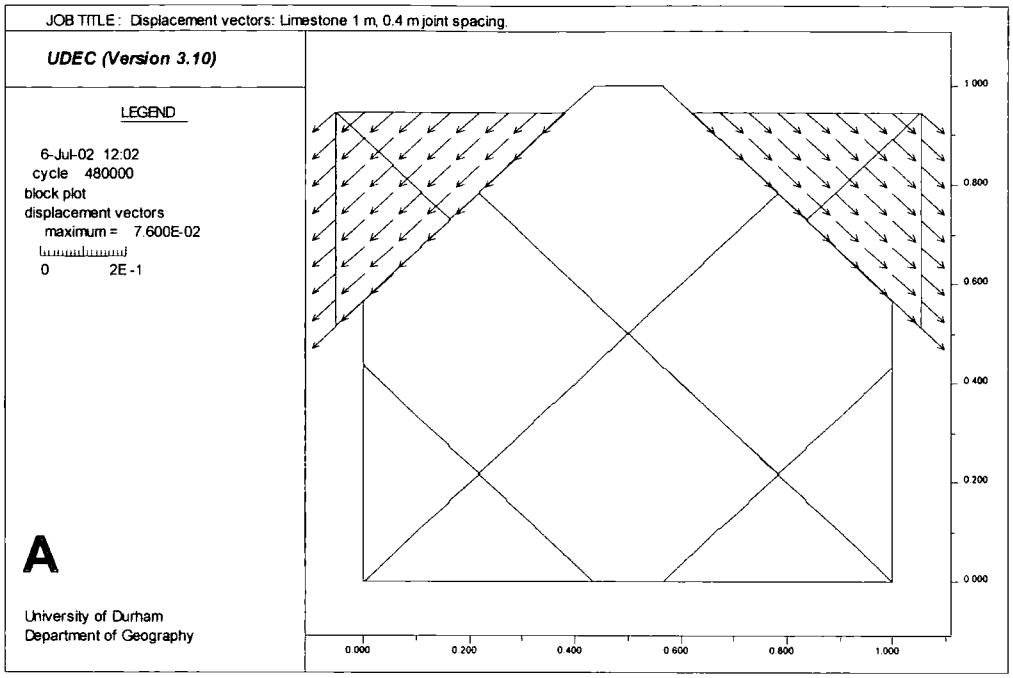

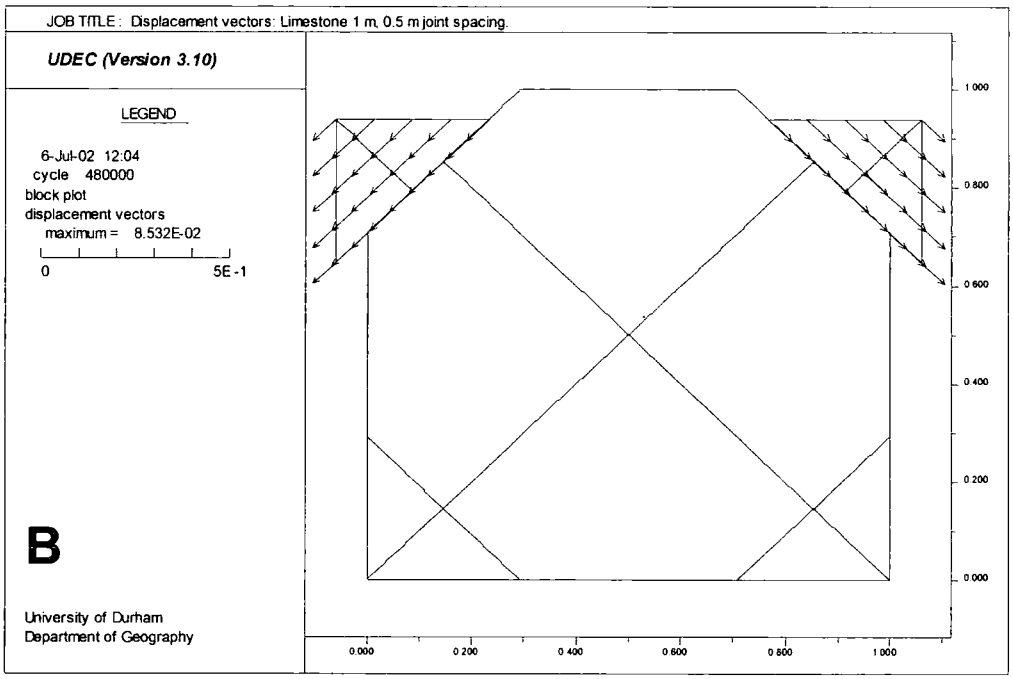

Figure 4.16: Displacement vector plots for a 1m limestone rock mass with 0.4 and 0.5 m block edge length.

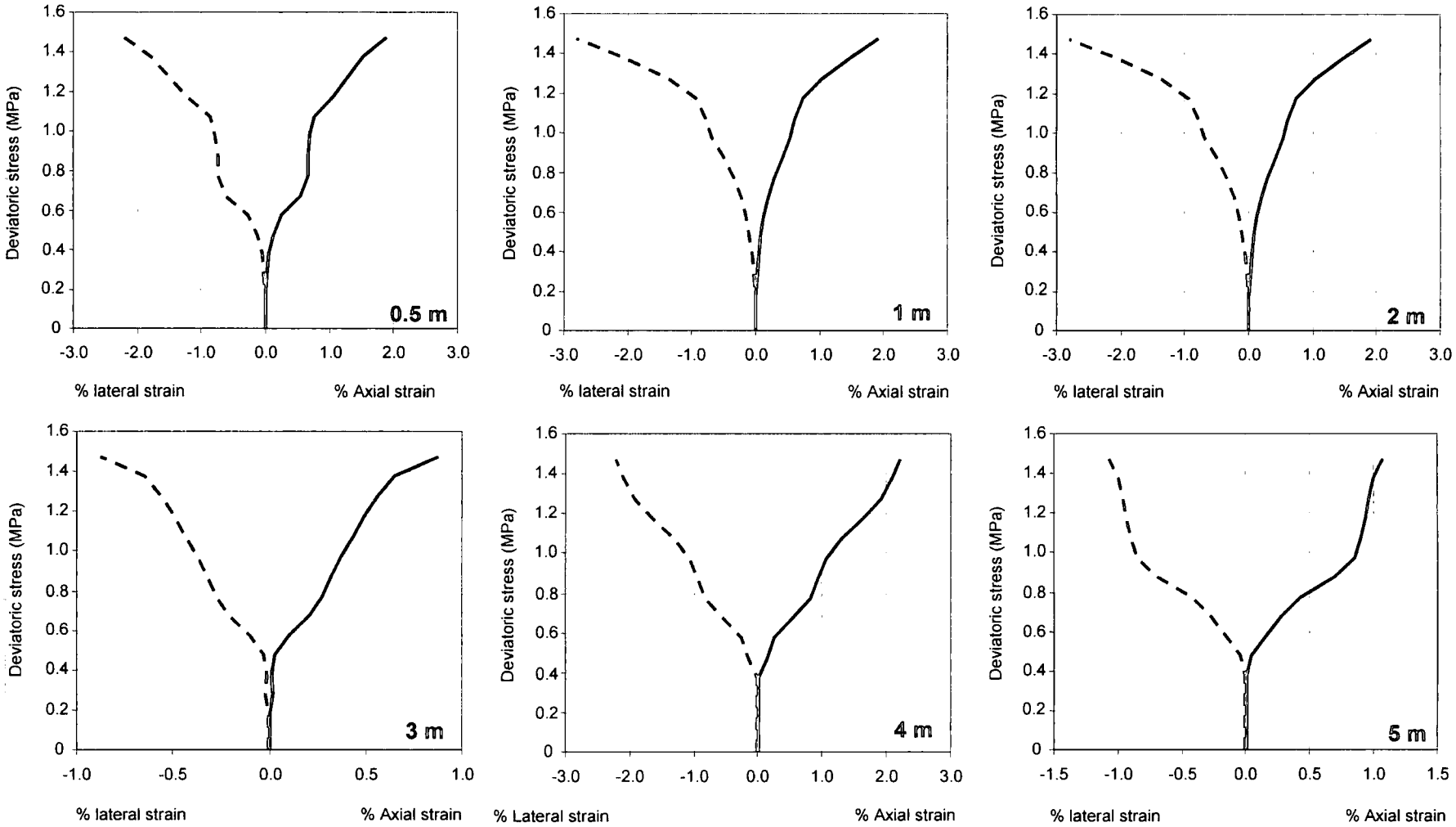

Figure 4.17: Stress-strain in response of a 10 m limestone rock mass with varying block sizes.

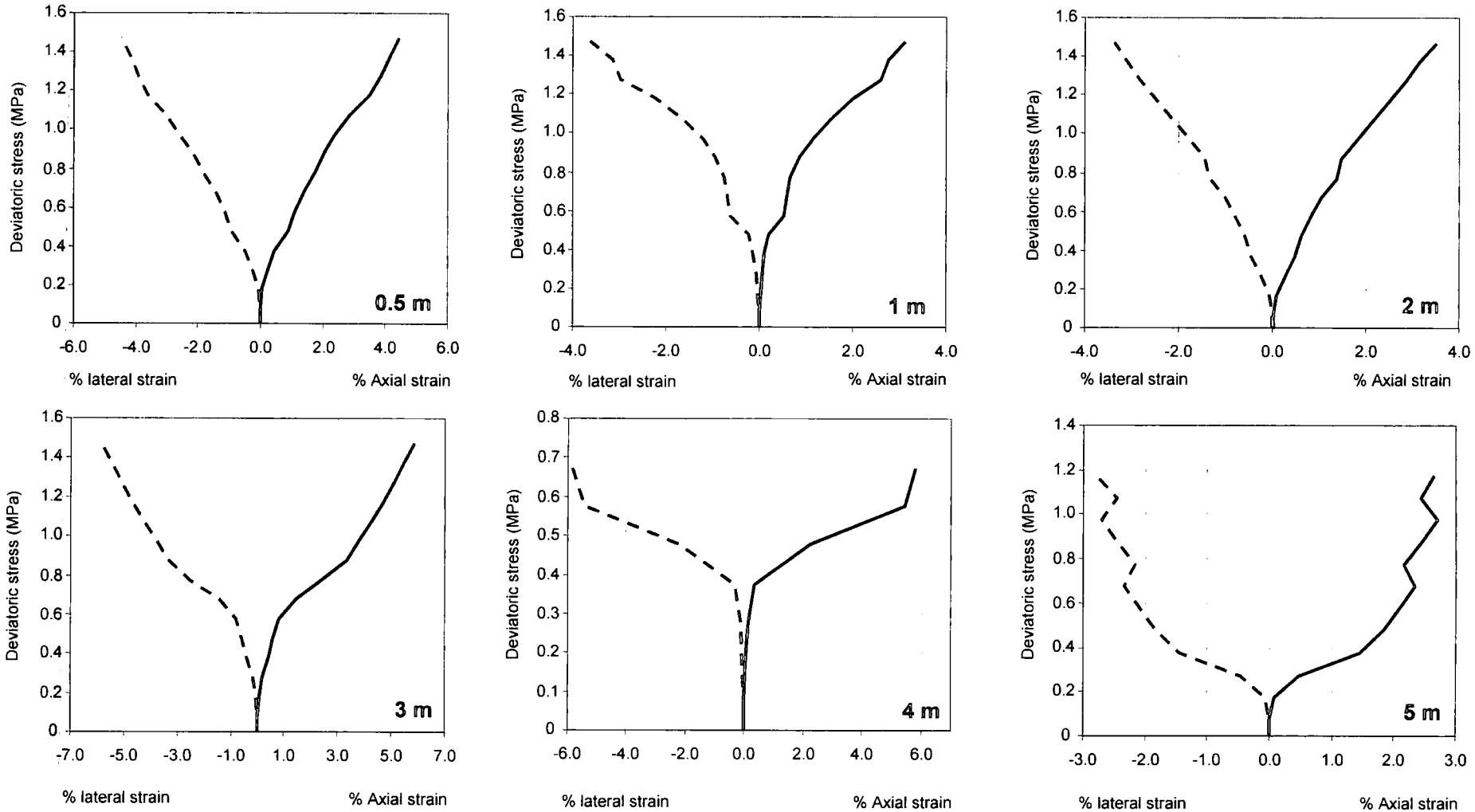

Figure 4.18: Stress-strain response of a 10 m sandstone rock mass with varying block sizes.

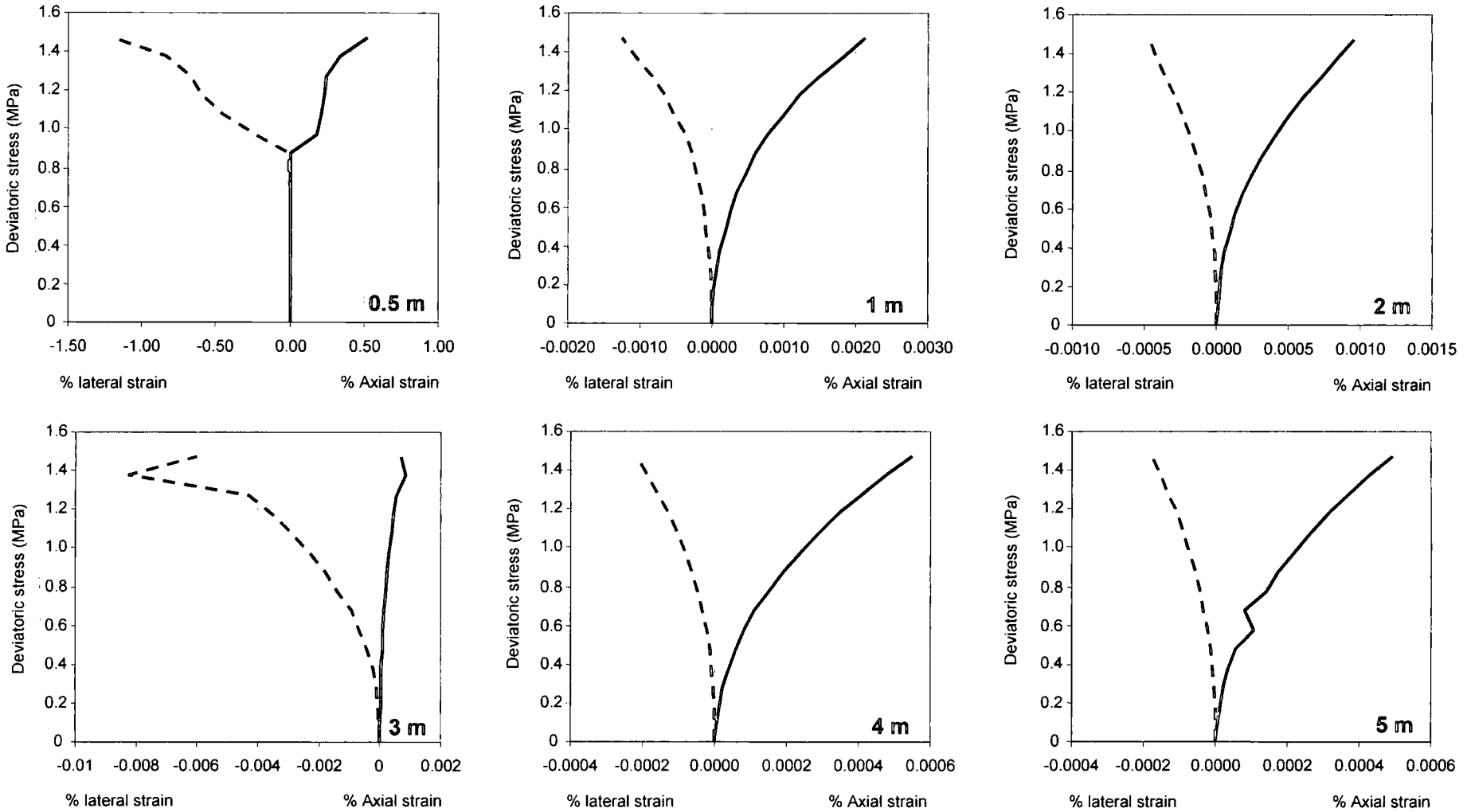

Figure 4.19: Stress-strain response of a 10 m granite rock mass with varying block sizes.

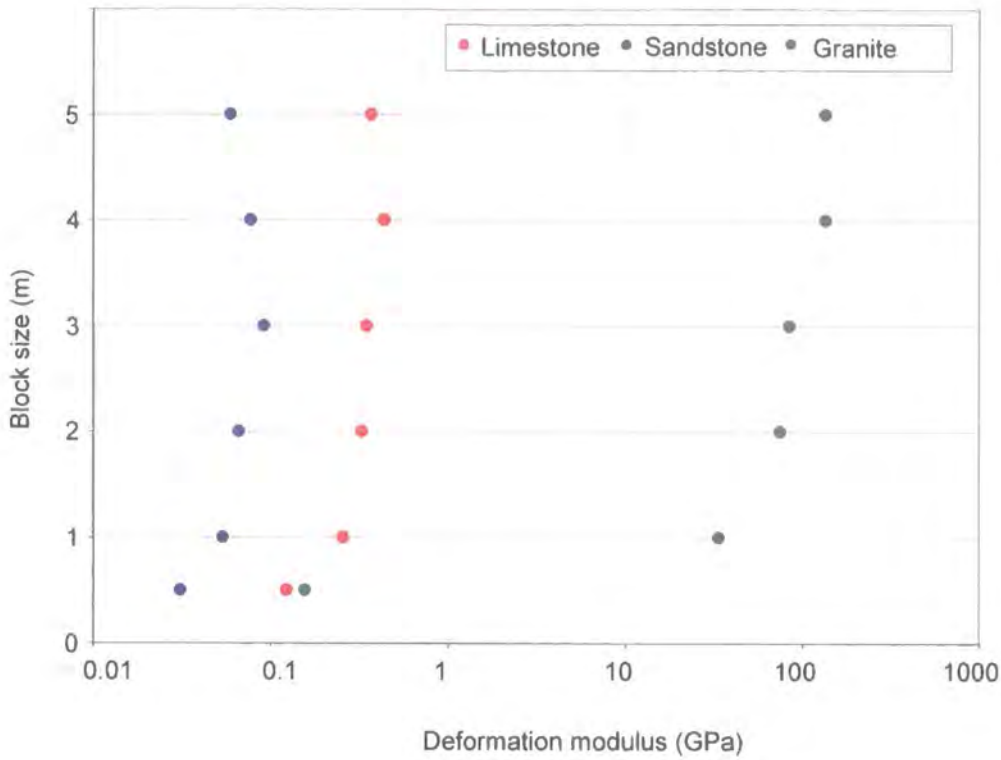

Figure 4.20: Deformation moduli during loading for 10 m limestone, sandstone and granite rock masses.

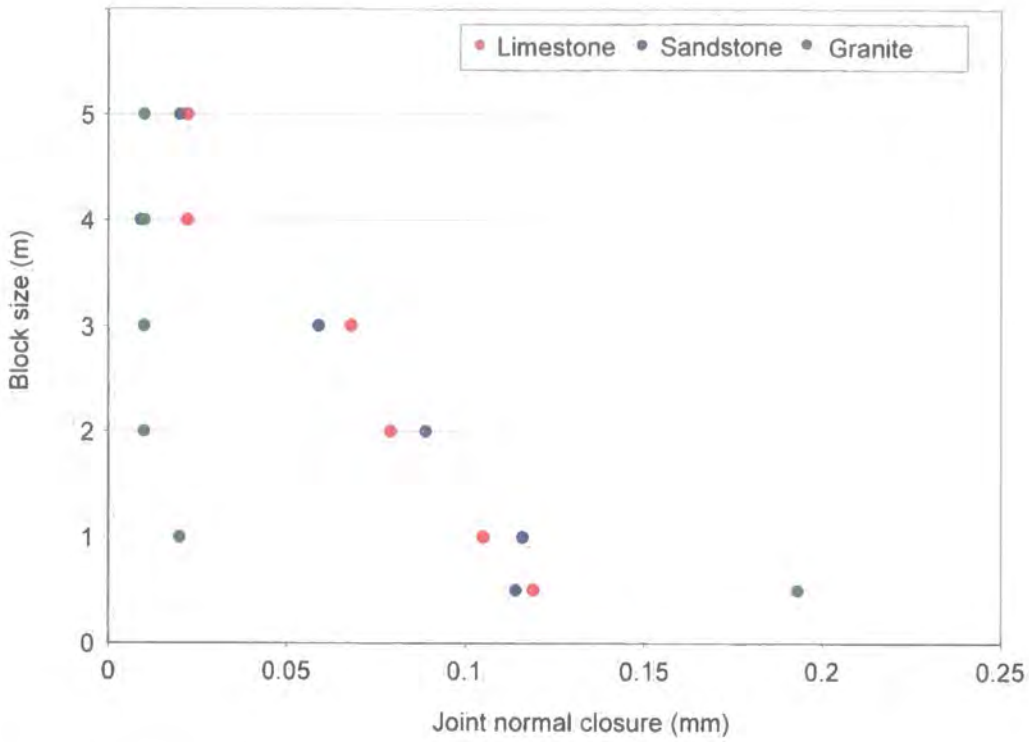

Figure 4.21: Joint normal closure during loading for 10 m limestone, sandstone and granite rock masses.

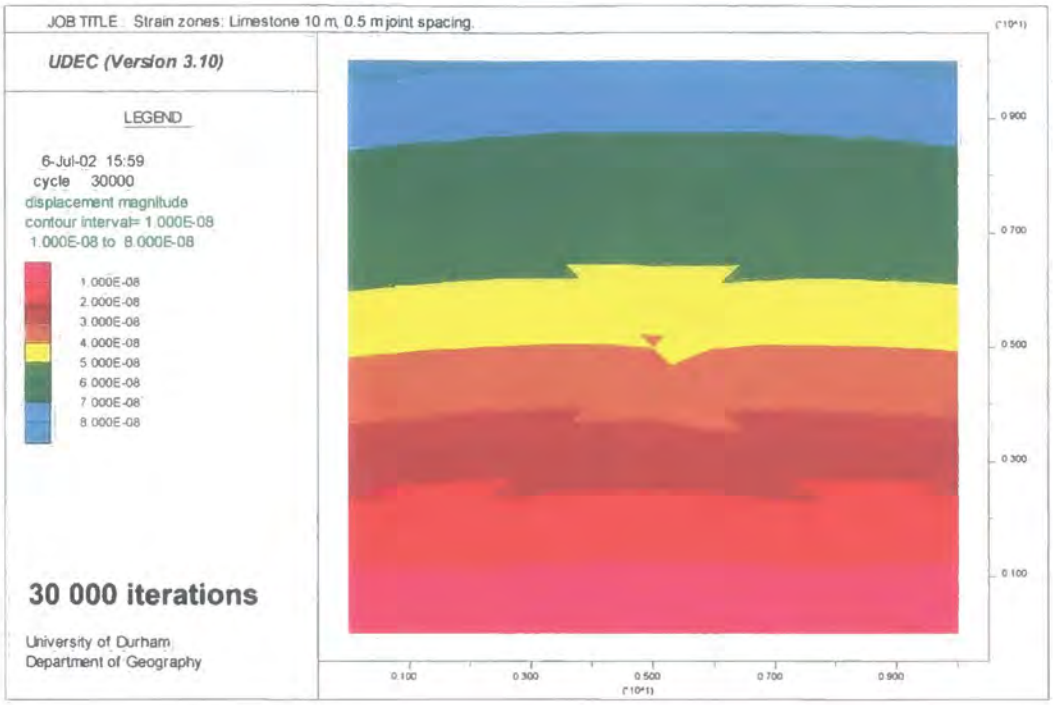

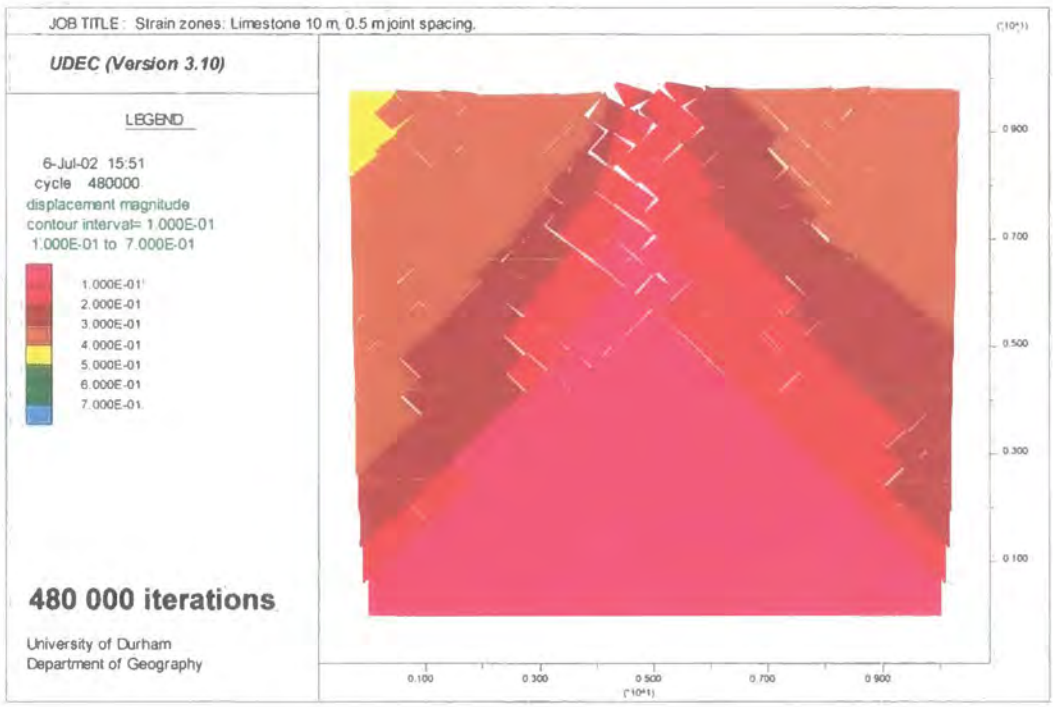

Figure 4.22a: Strain zone development in a 1 m limestone rock mass with 0.5 m block size.

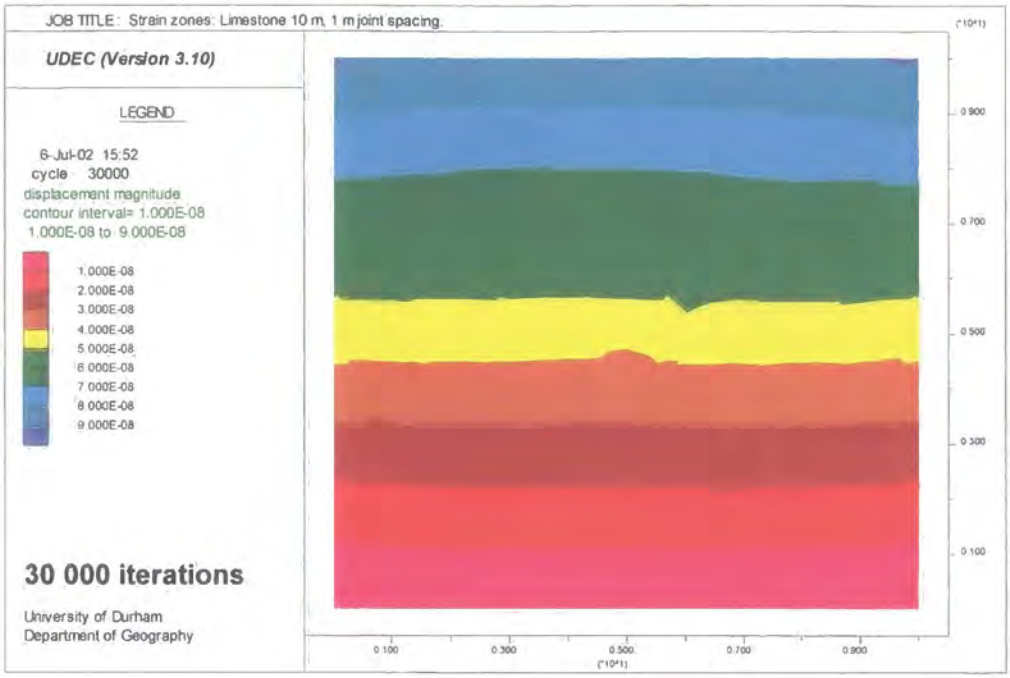

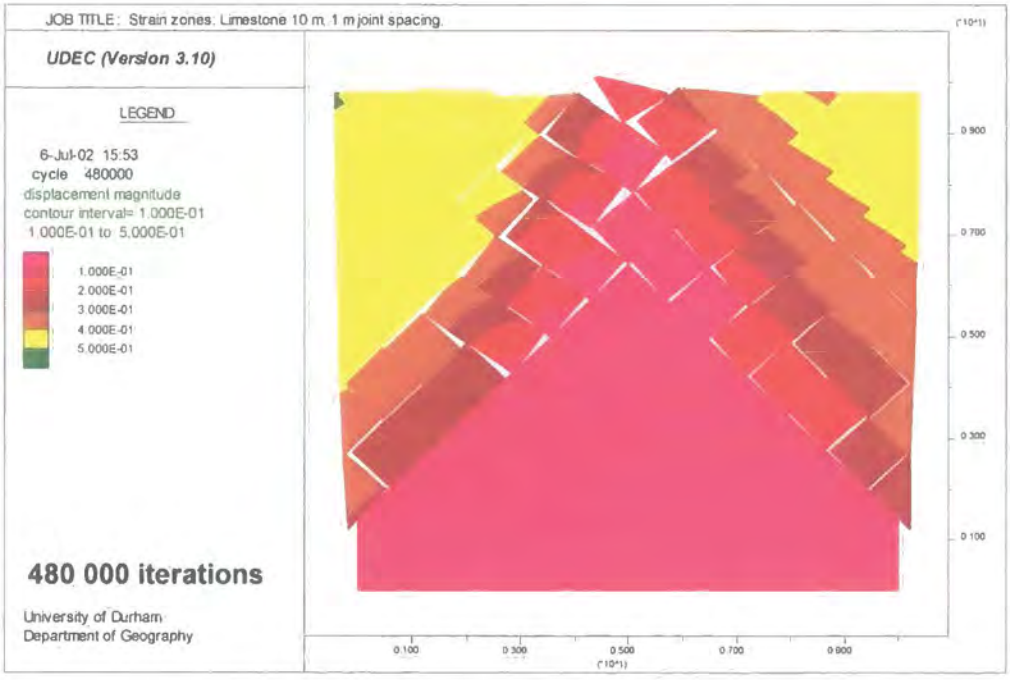

Figure 4.22b: Strain zone development in a 1 m limestone rock mass with 1 m block size.

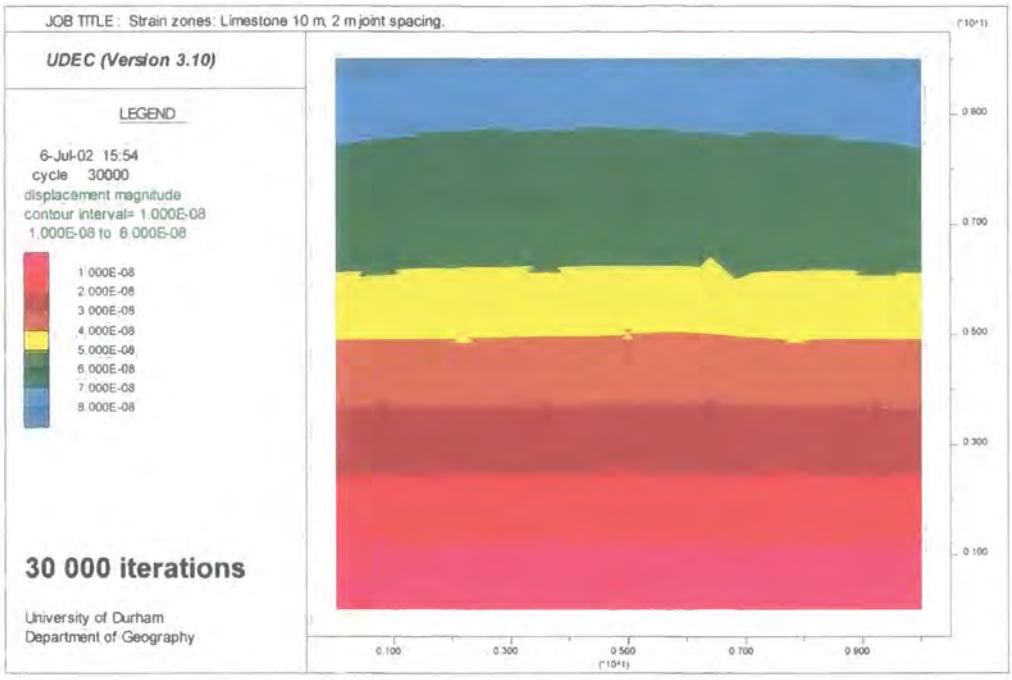

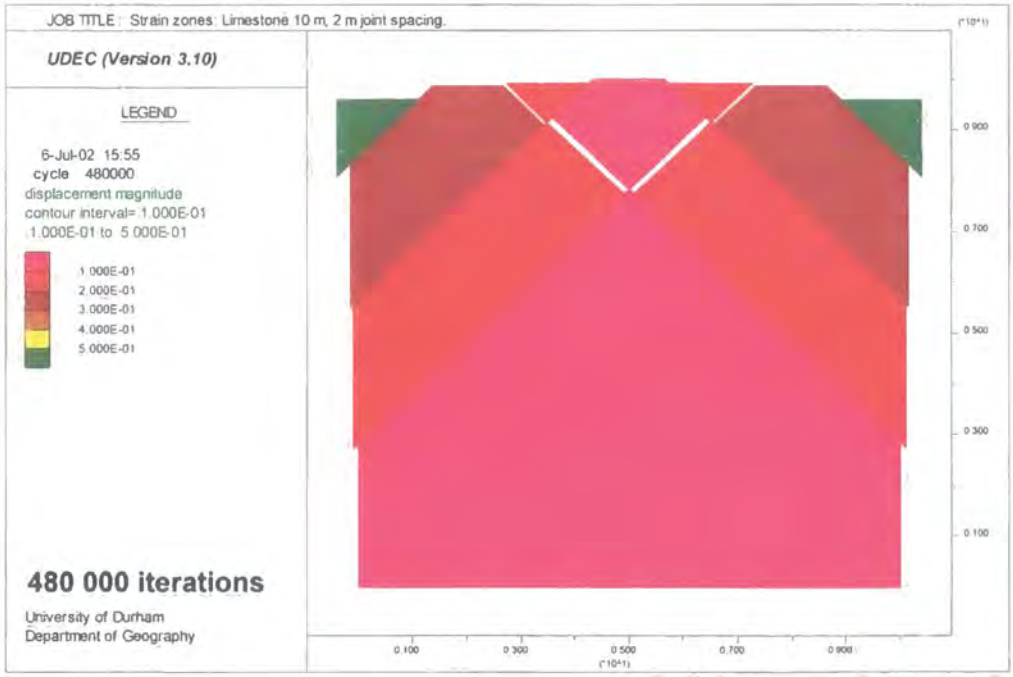

Figure 4.22c: Strain zone development in a 1 m limestone rock mass with 2 m block size.

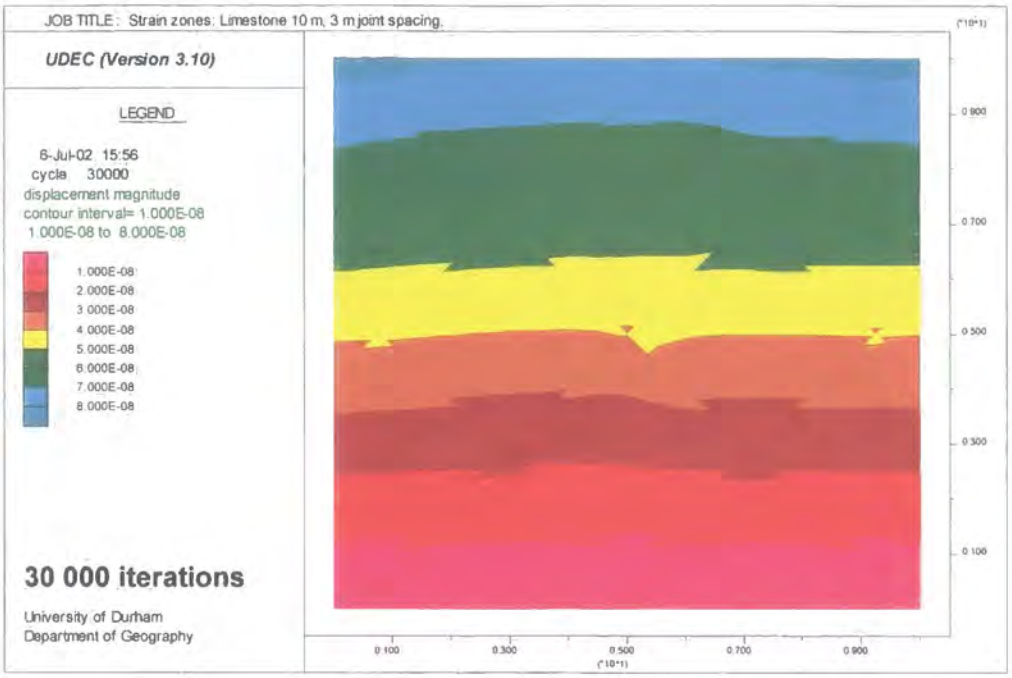

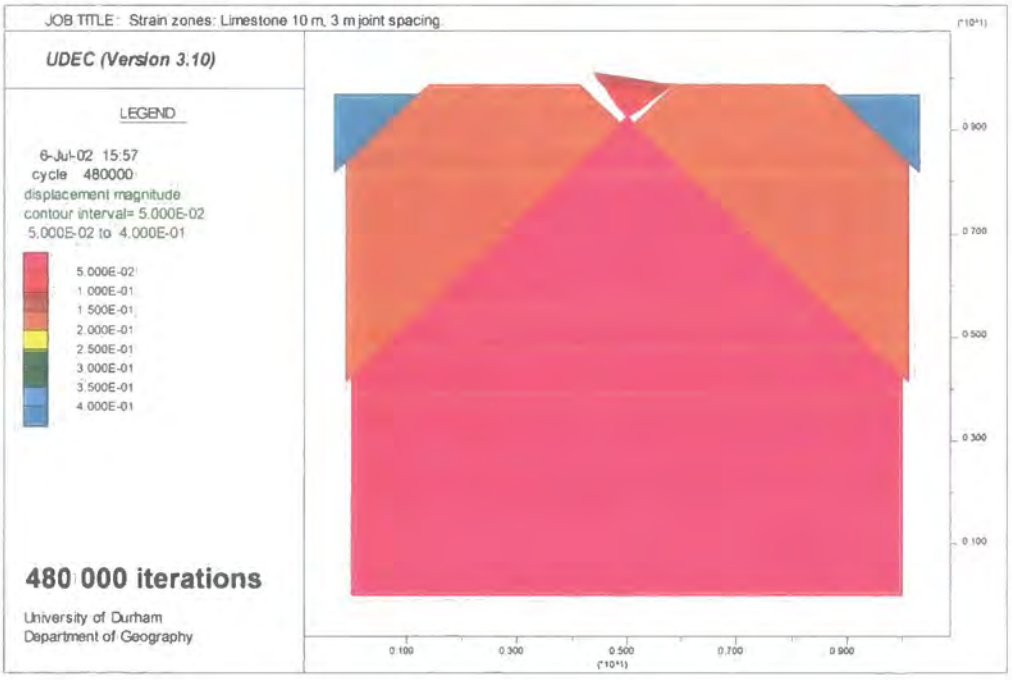

Figure 4.22d: Strain zone development in a 1 m limestone rock mass with 3 m block size.

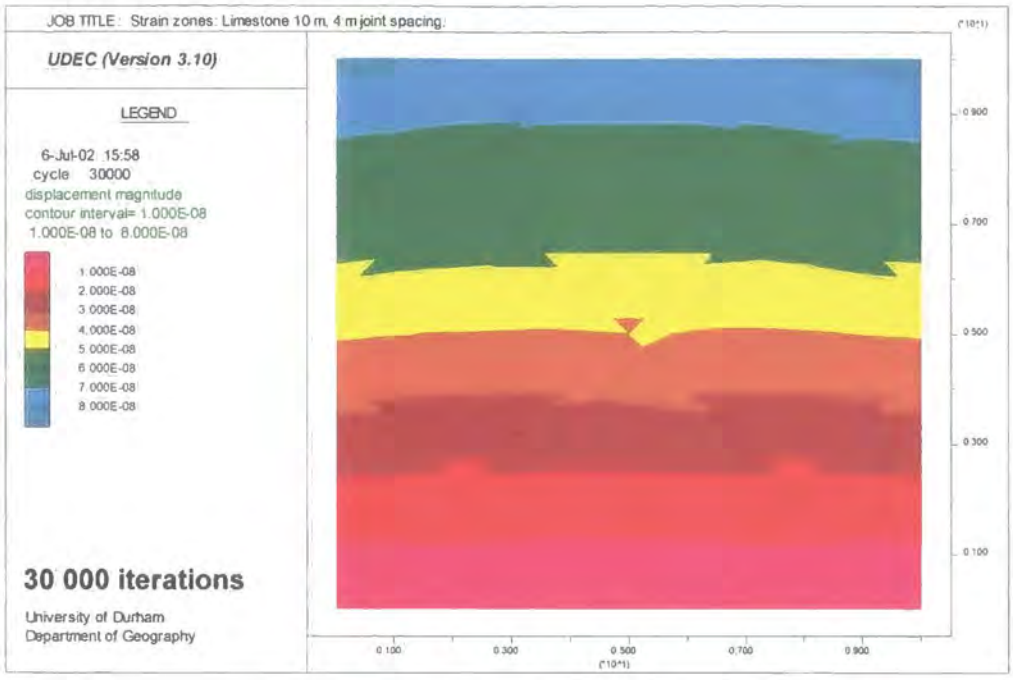

Figure 4.22e: Strain zone development in a 1 m limestone rock mass with 4 m block size.

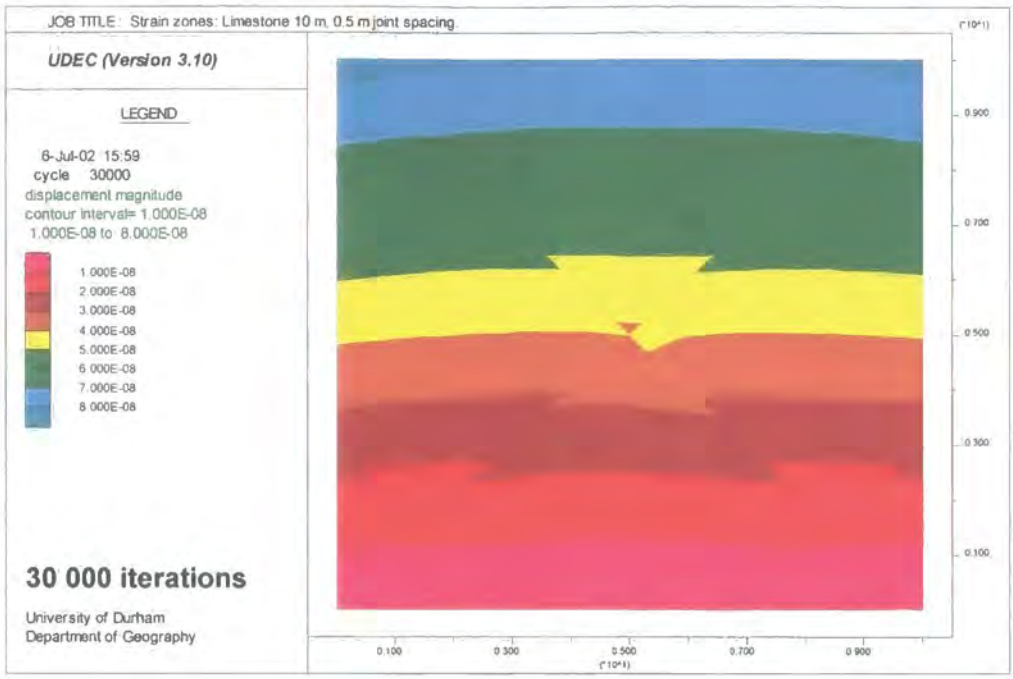

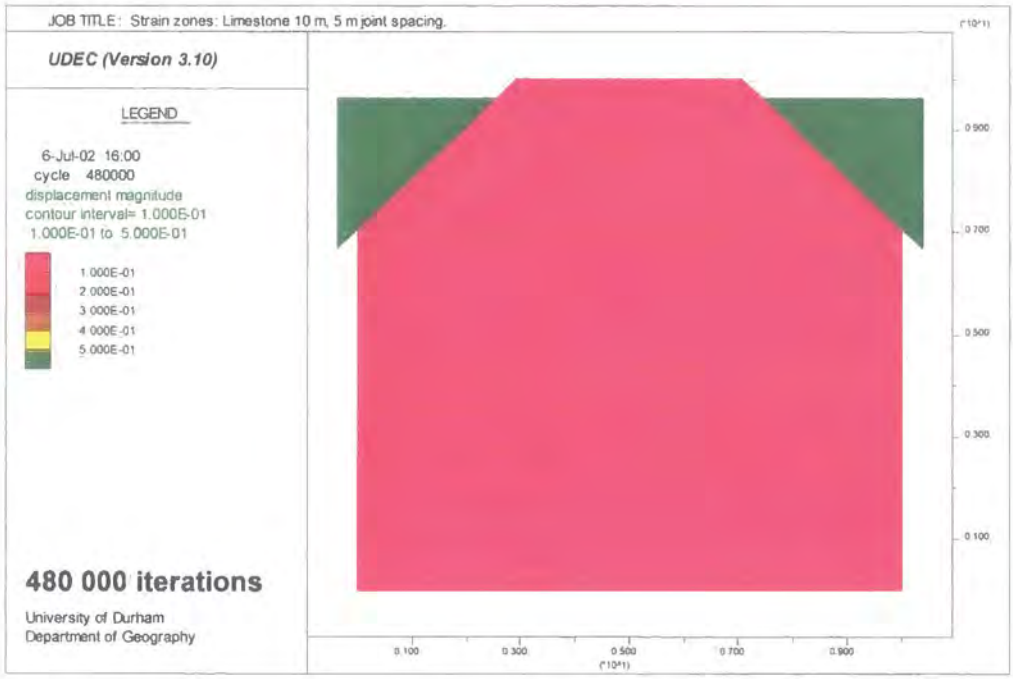

Figure 4.22f: Strain zone development in a 1 m limestone rock mass with 5 m block size.

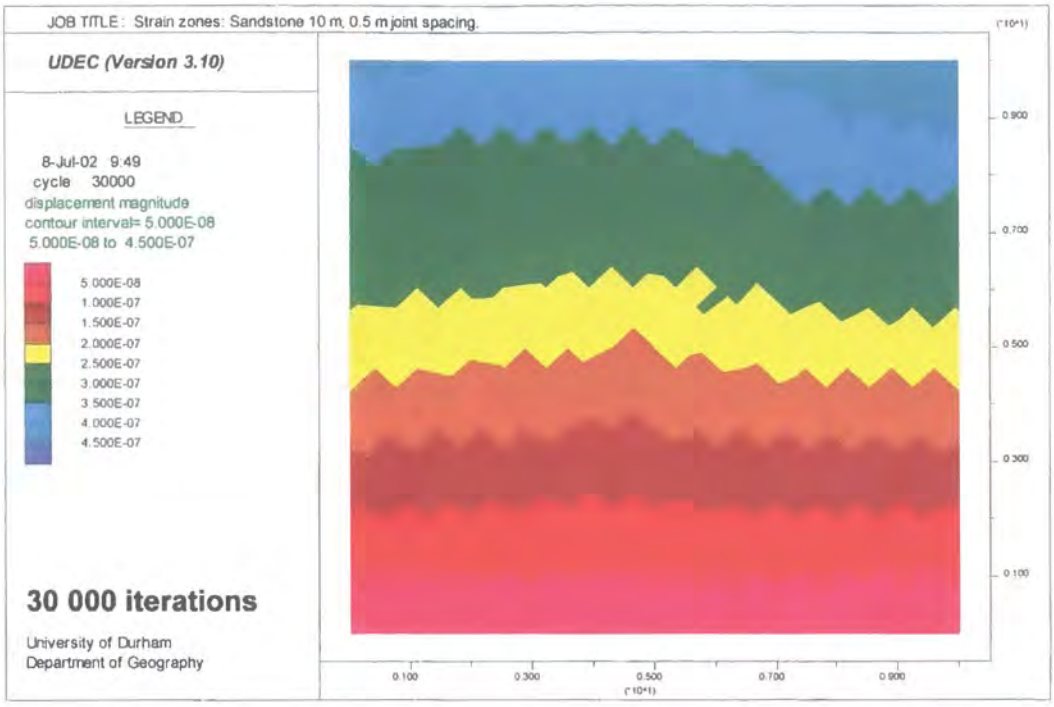

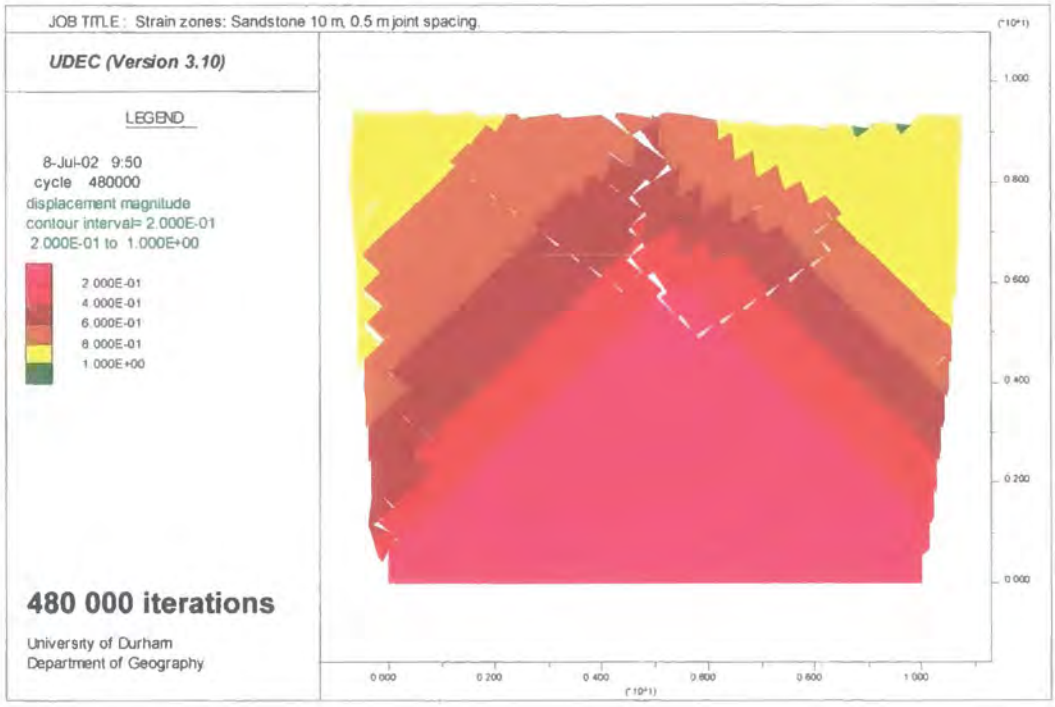

Figure 4.23a: Strain zone development in a 10 m sandstone rock mass with 0.5 m block size.

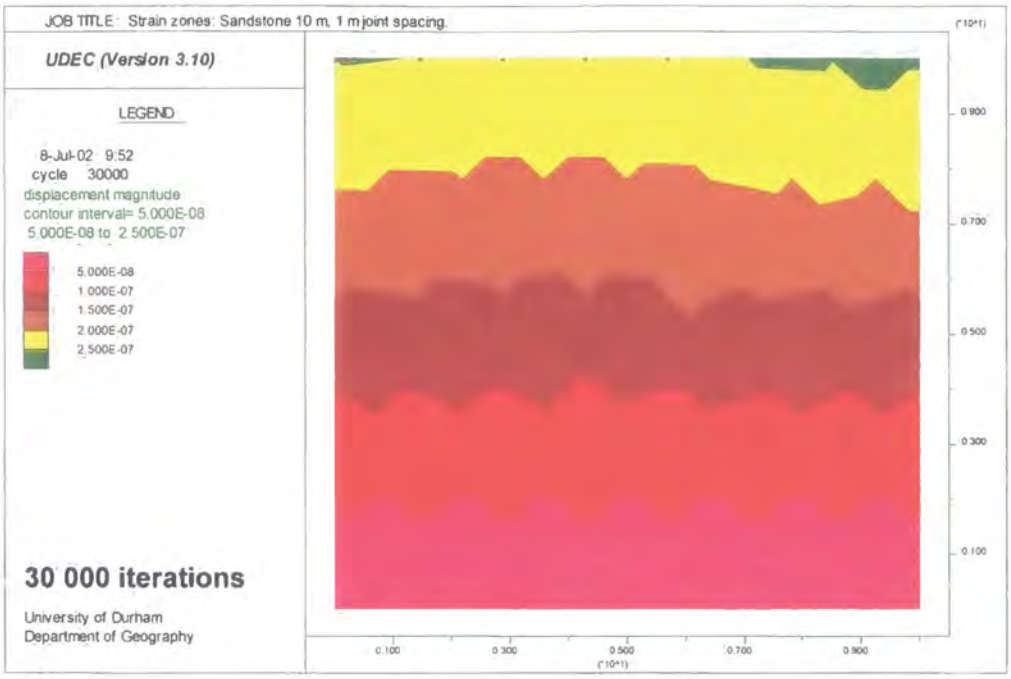

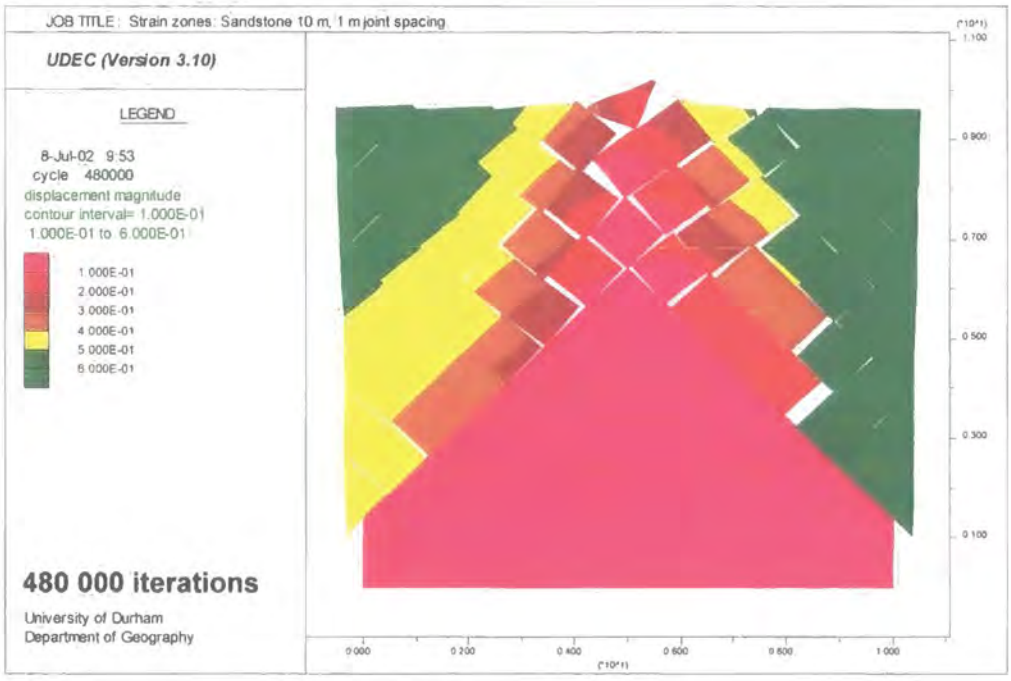

Figure 4.23b: Strain zone development in a 10 m sandstone rock mass with 1 m block size.

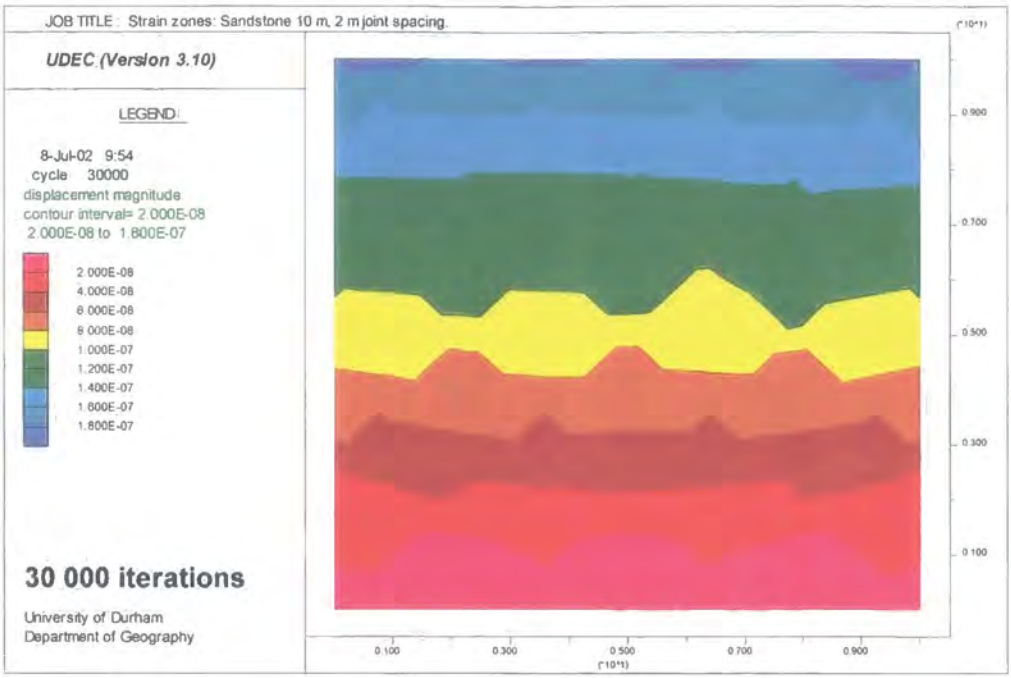

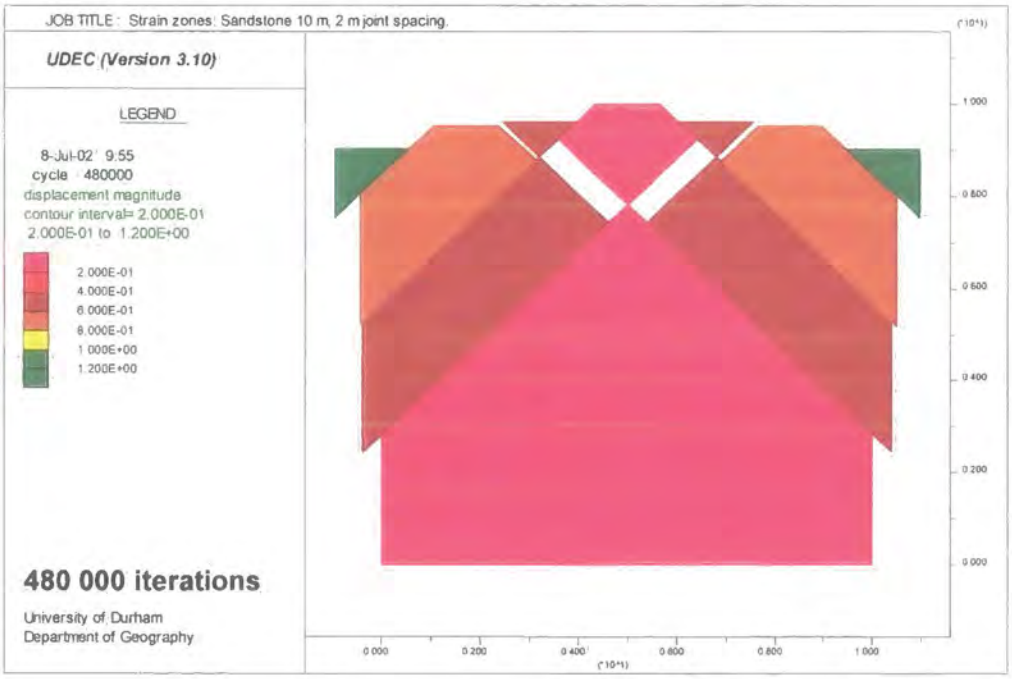

Figure 4.23c: Strain zone development in a 10 m sandstone rock mass with 2 m block size.

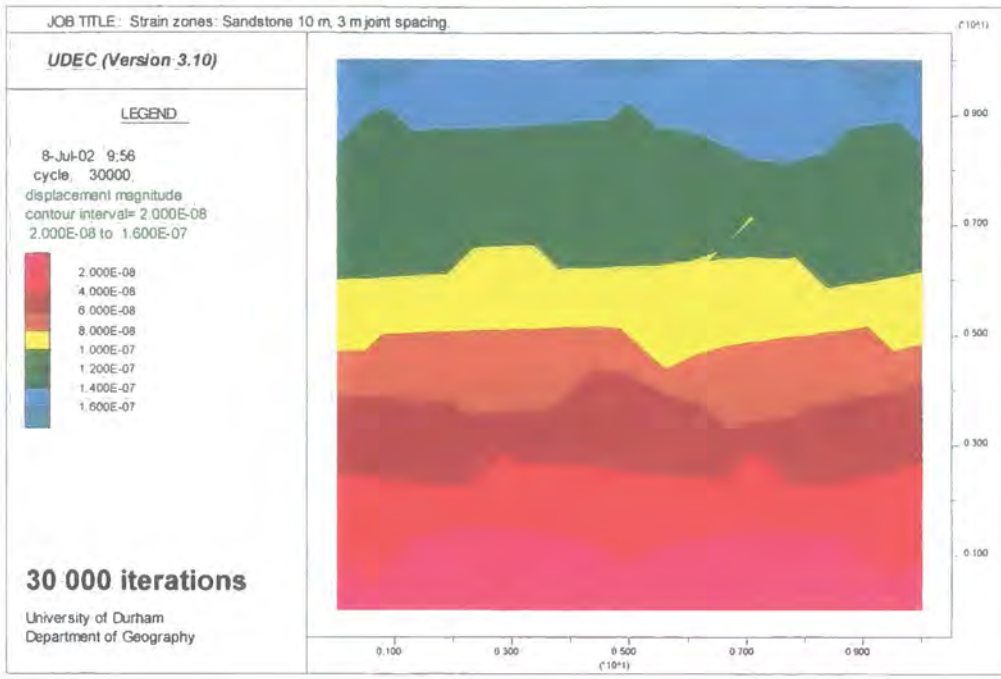

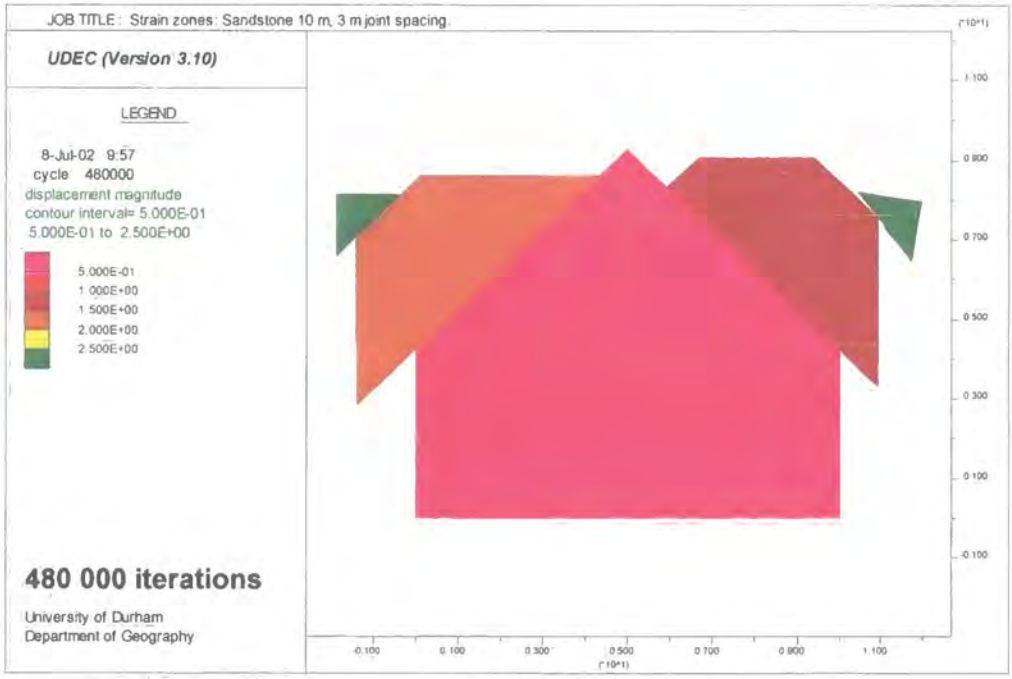

Figure 4.23d: Strain zone development in a 10 m sandstone rock mass with 3 m block size.

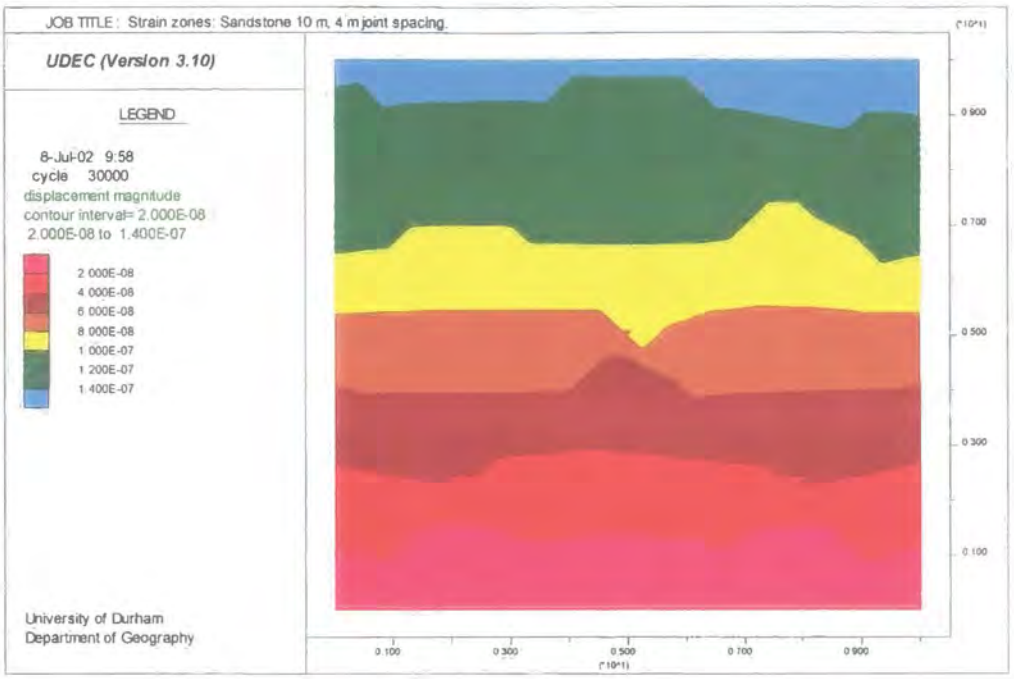

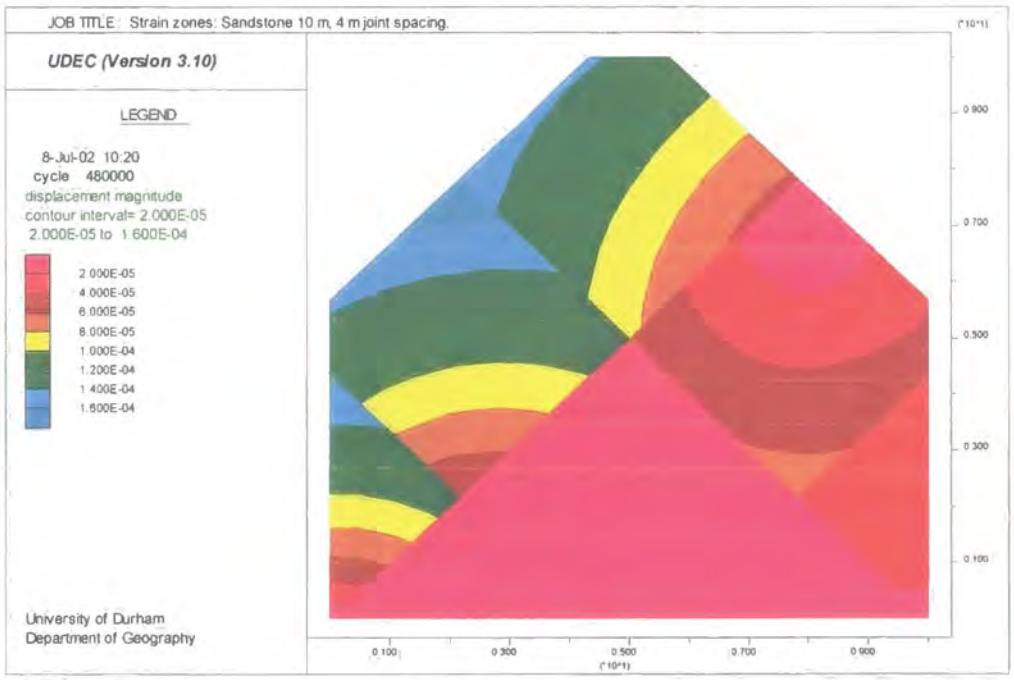

Figure 4.23e: Strain zone development in a 10 m sandstone rock mass with 4 m block size.

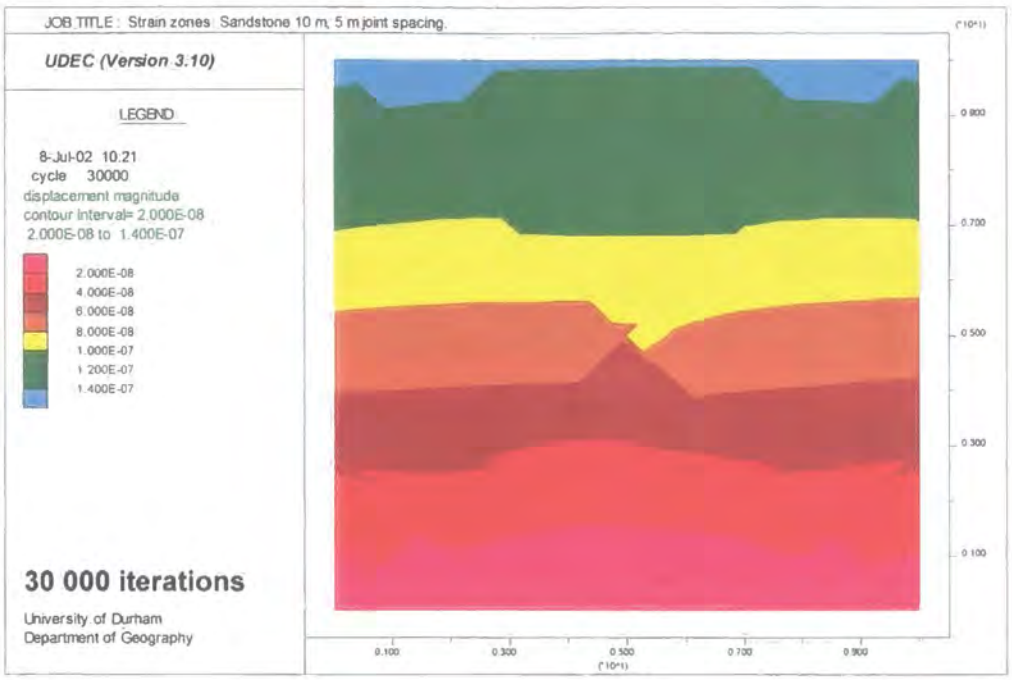

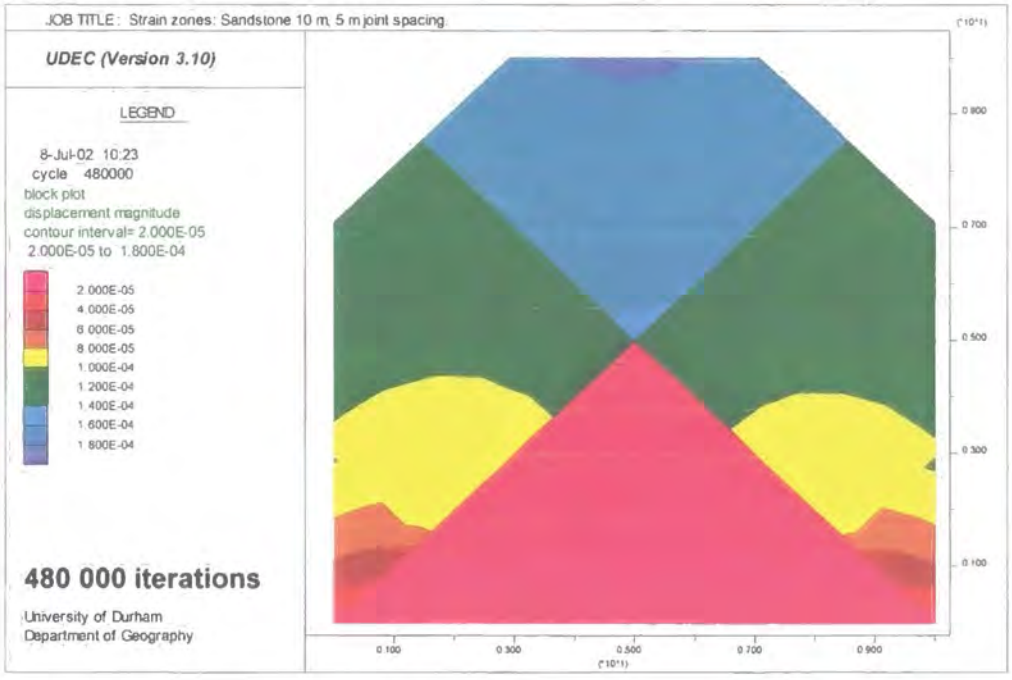

Figure 4.23f: Strain zone development in a 10 m sandstone rock mass with 5 m block size.

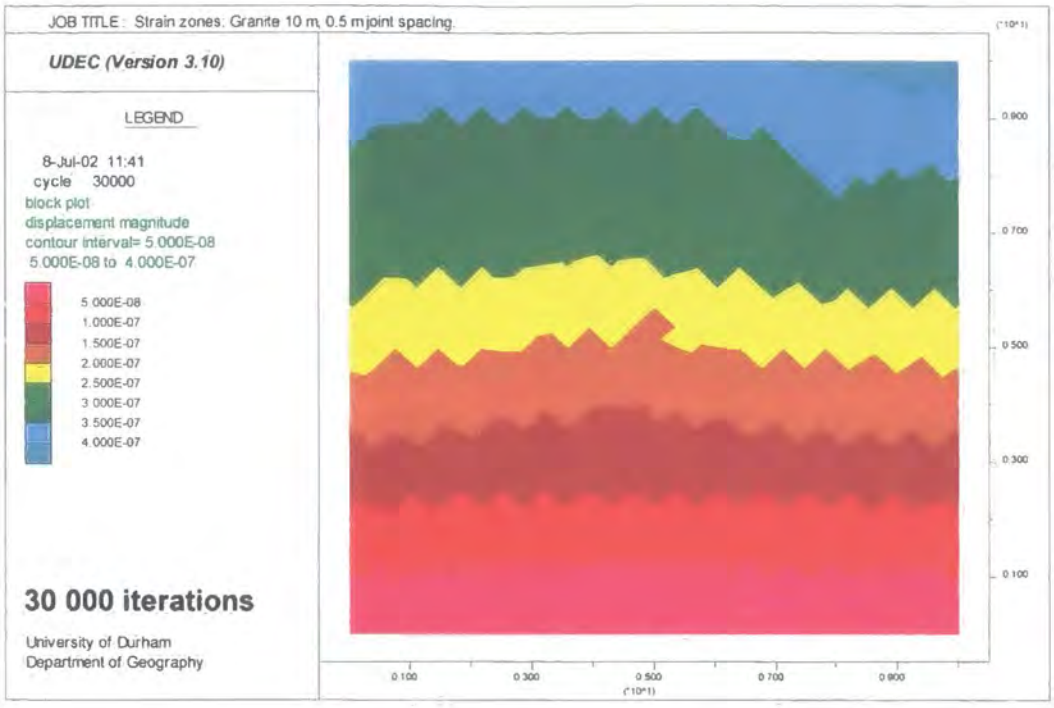

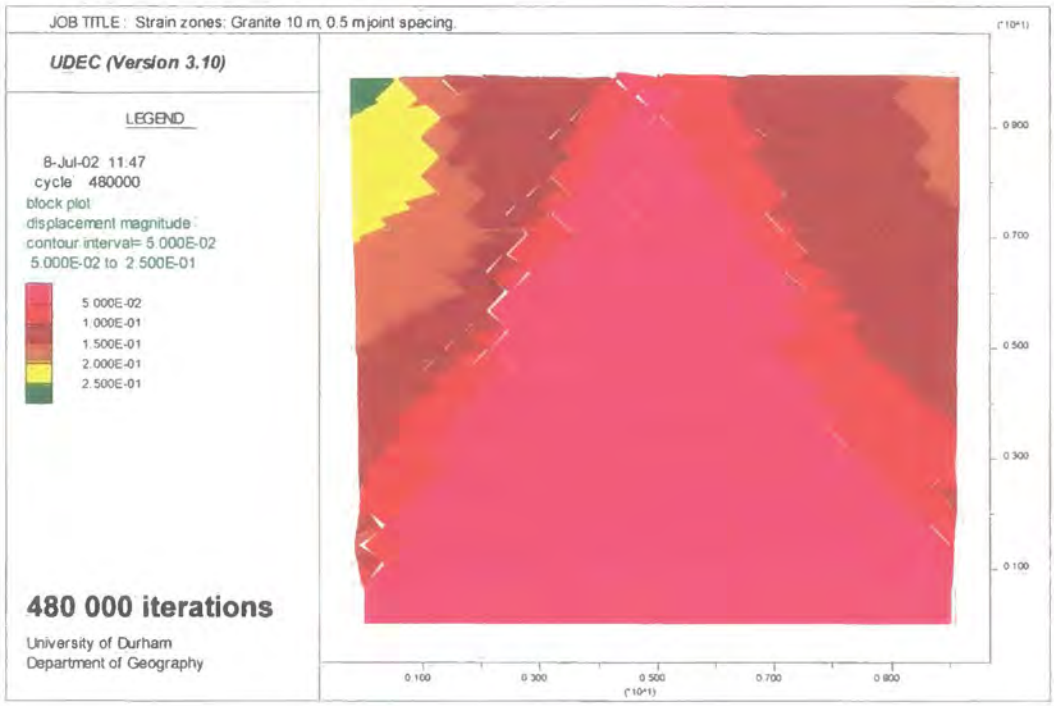

Figure 4.24a: Strain zone development in a 10 m granite rock mass with 0.5 m block size.

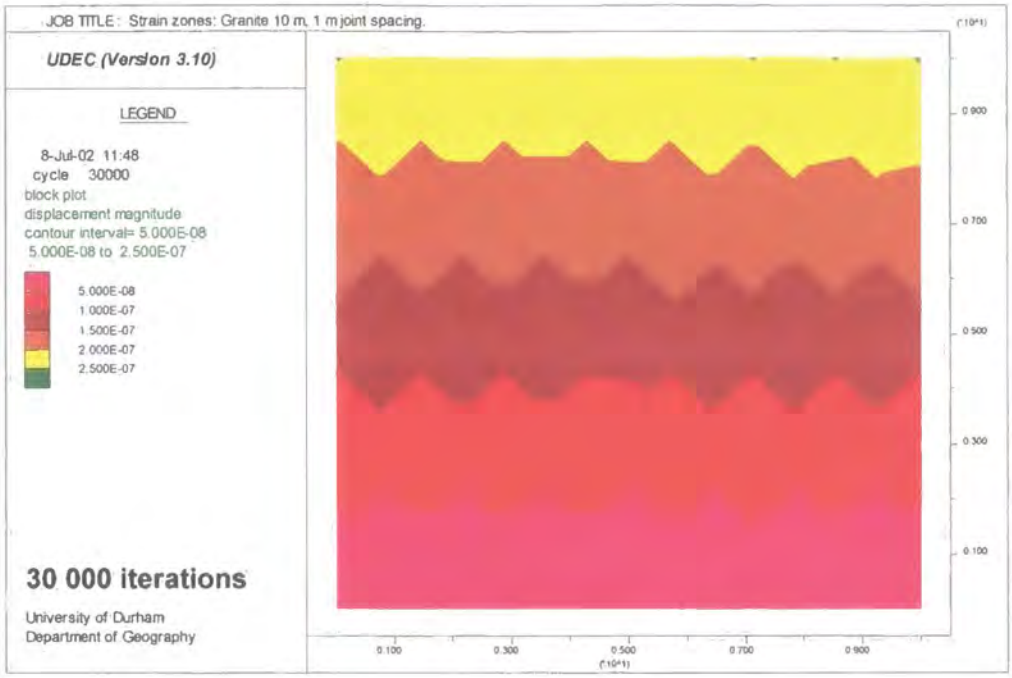

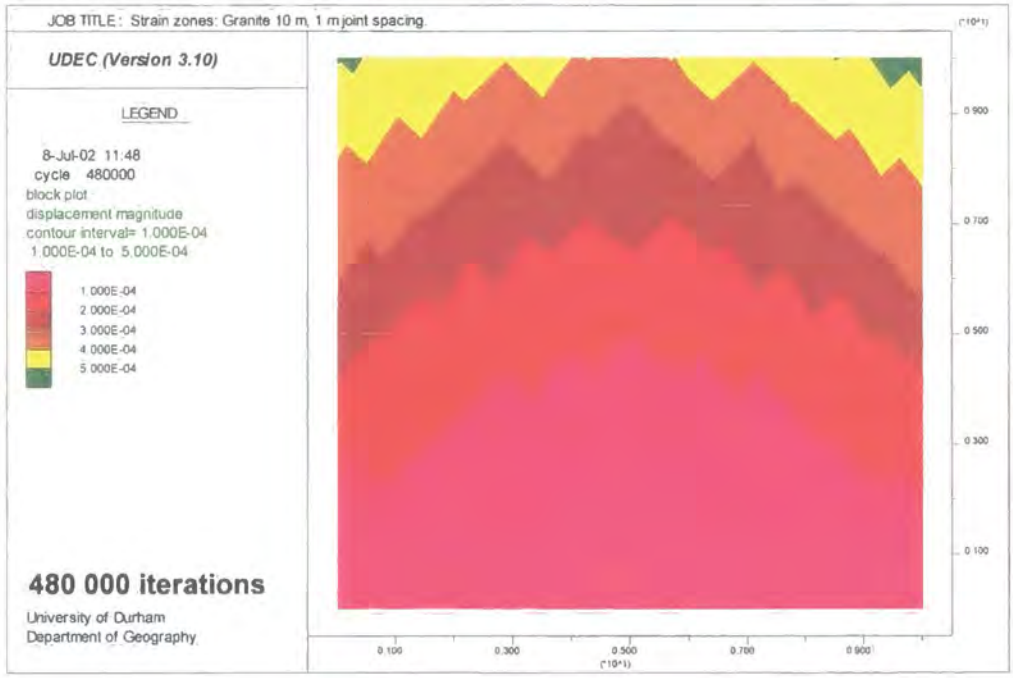

Figure 4.24b: Strain zone development in a 10 m granite rock mass with 1 m block size.

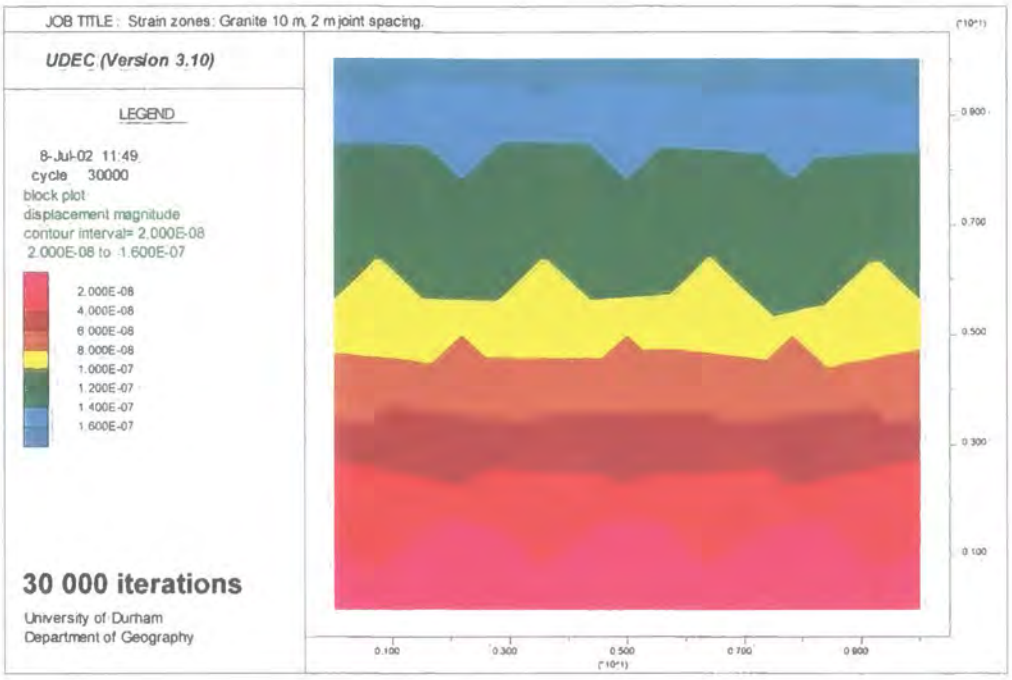

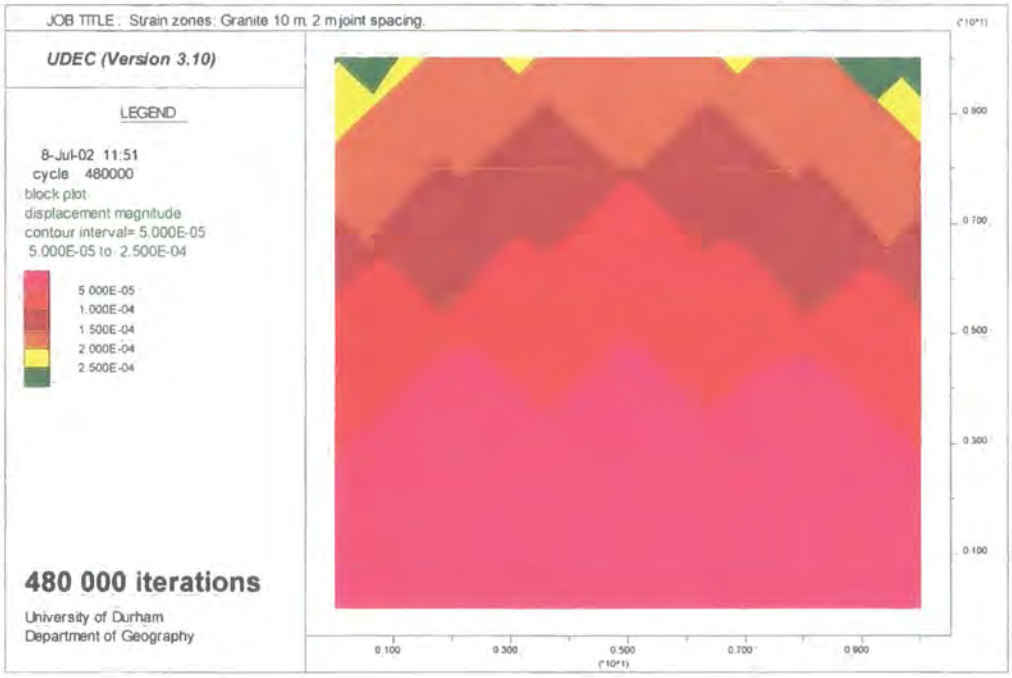

Figure 4.24c: Strain zone development in a 10 m granite rock mass with 2 m block size.

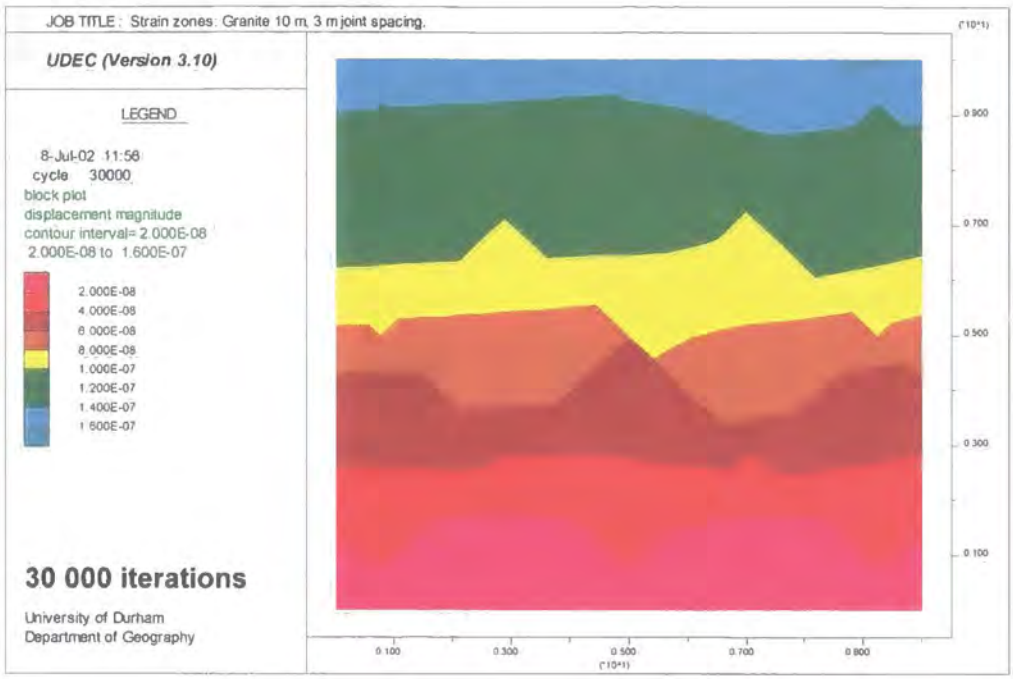

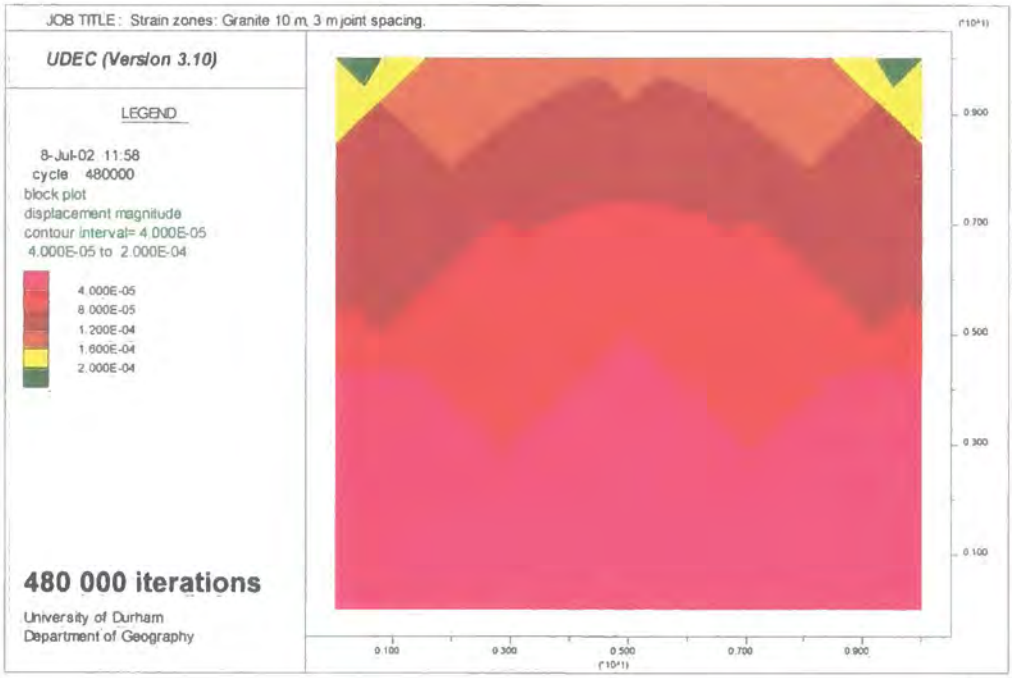

Figure 4.24d: Strain zone development in a 10 m granite rock mass with 3 m block size.

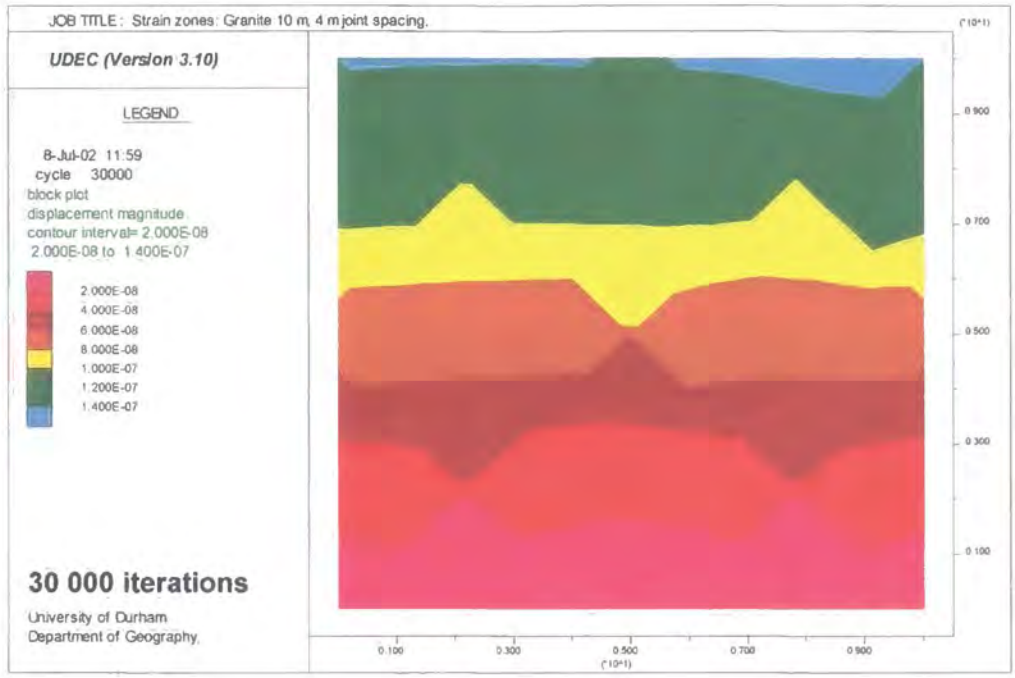

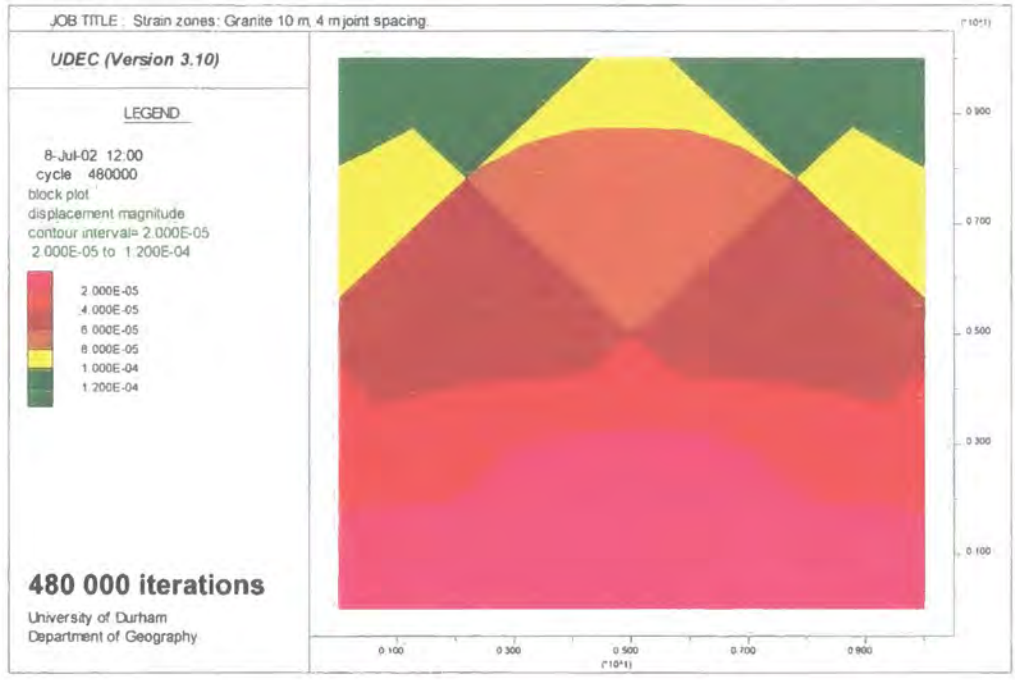

Figure 4.24e: Strain zone development in a 10 m granite rock mass with 4 m block size.

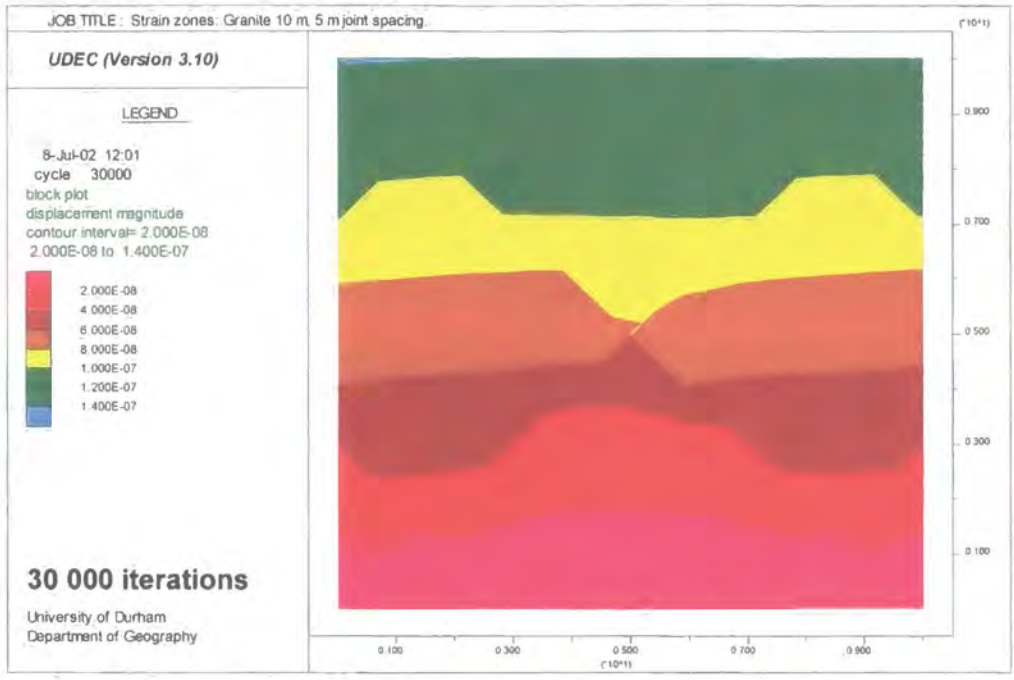

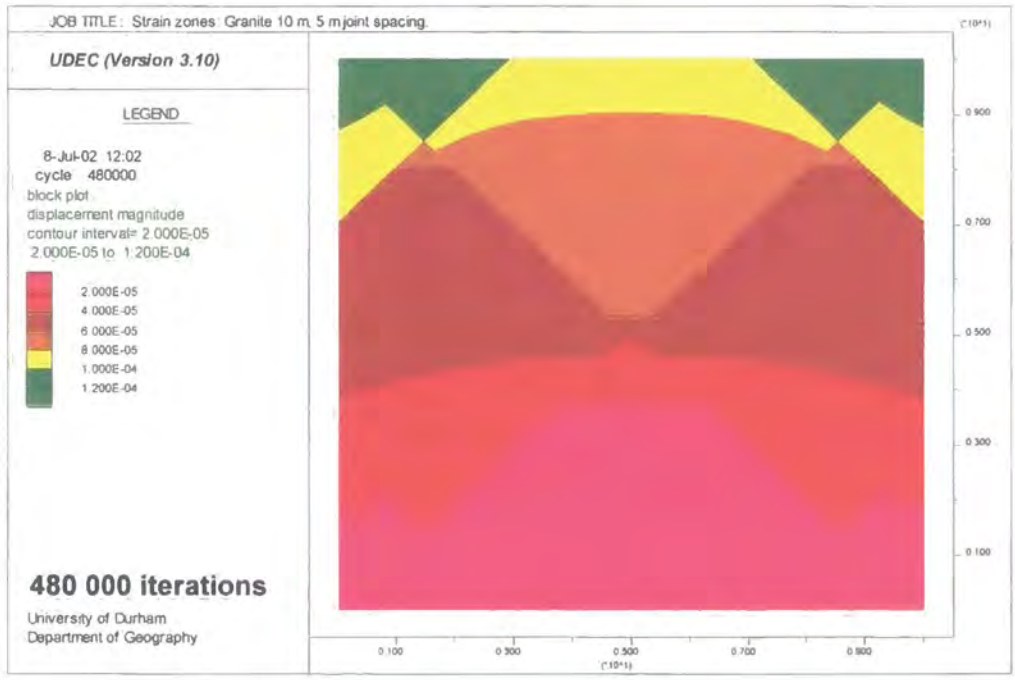

Figure 4.24f: Strain zone development in a 10 m granite rock mass with 5 m block size.

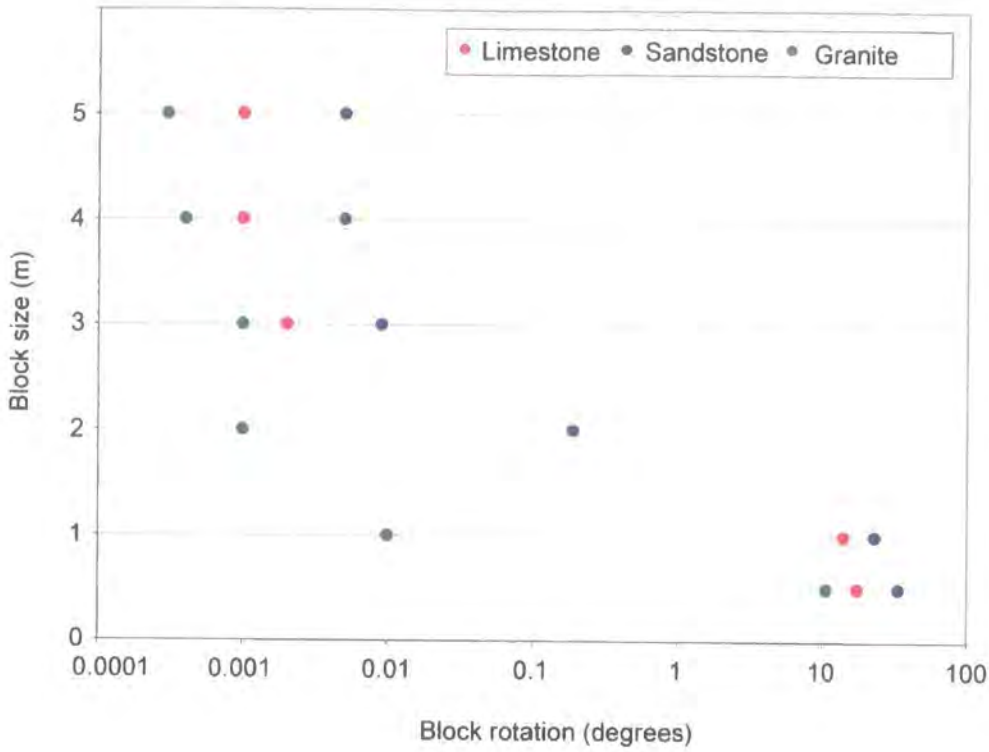

Figure 4.25: Block rotation magnitude for 10 m limestone, sandstone and granite rock masses.

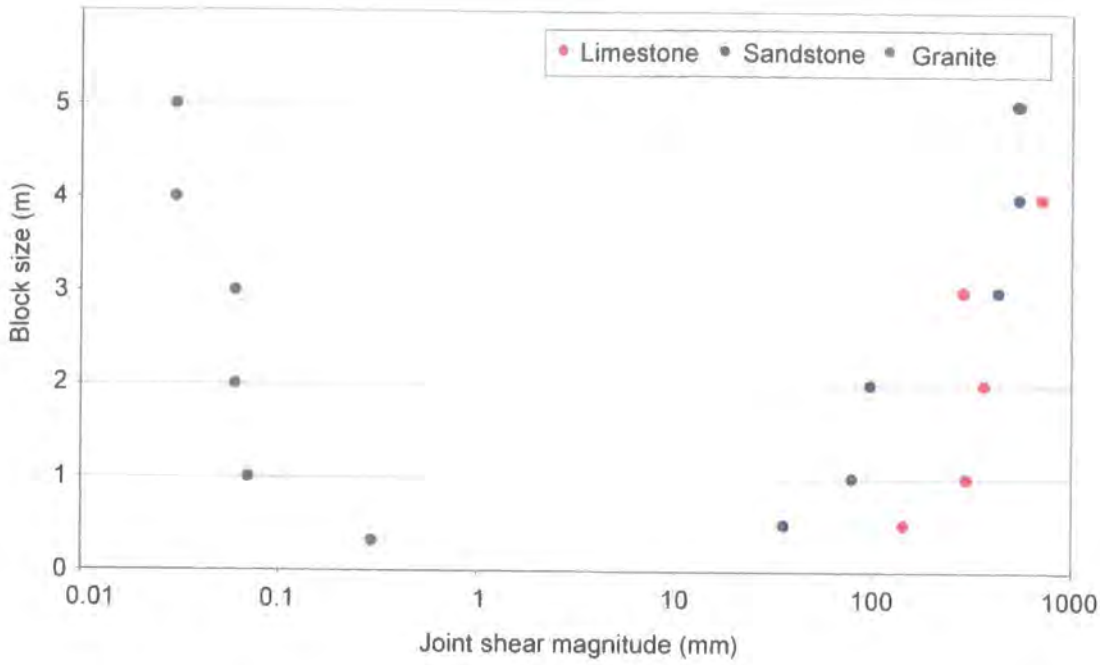

Figure 4.26: Joint shear magnitude during loading for 10 m limestone, sandstone and granite rock masses.

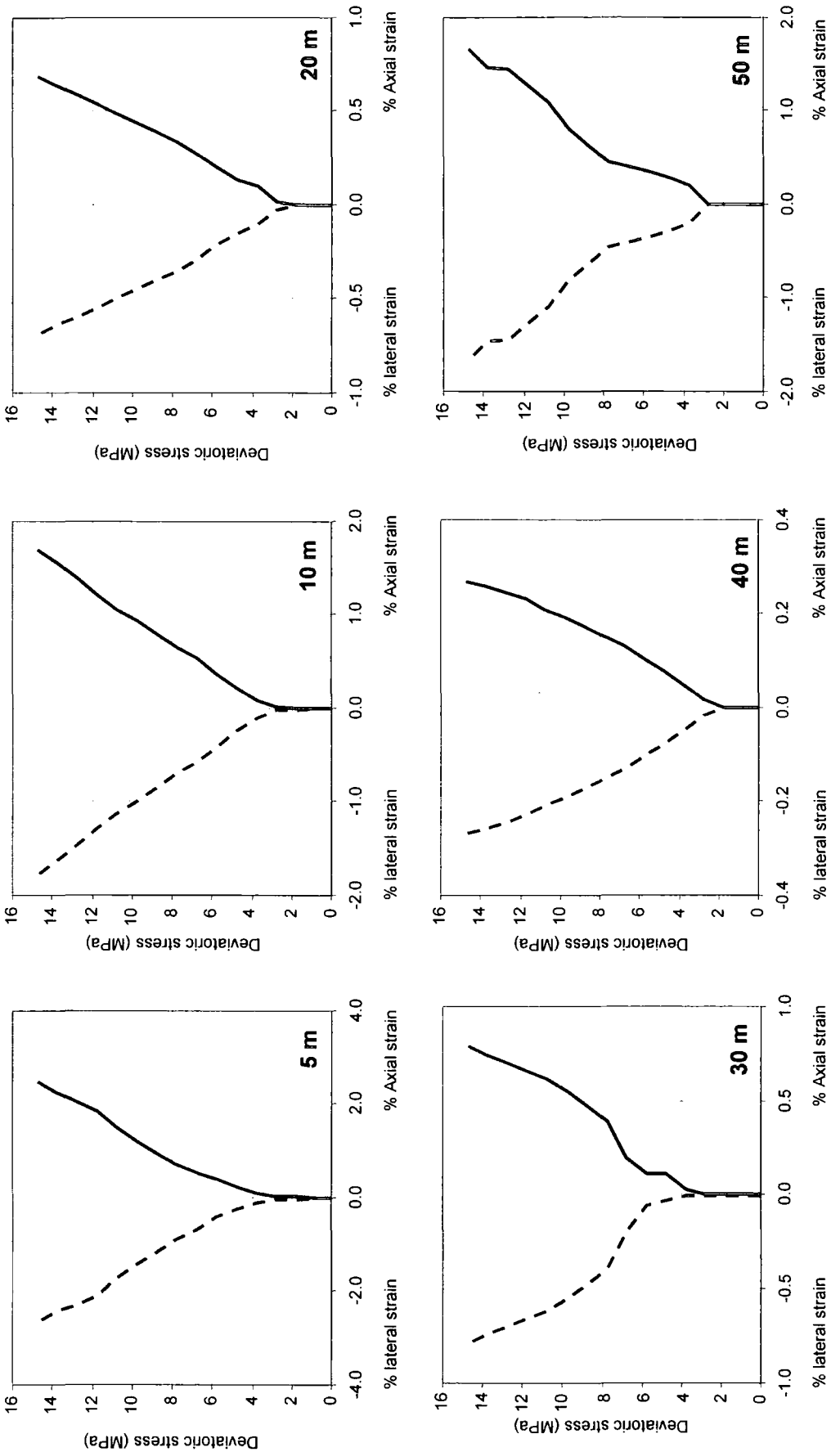

Figure 4.27: Stress-strain response of a 100 m limestone rock mass with varying block sizes.

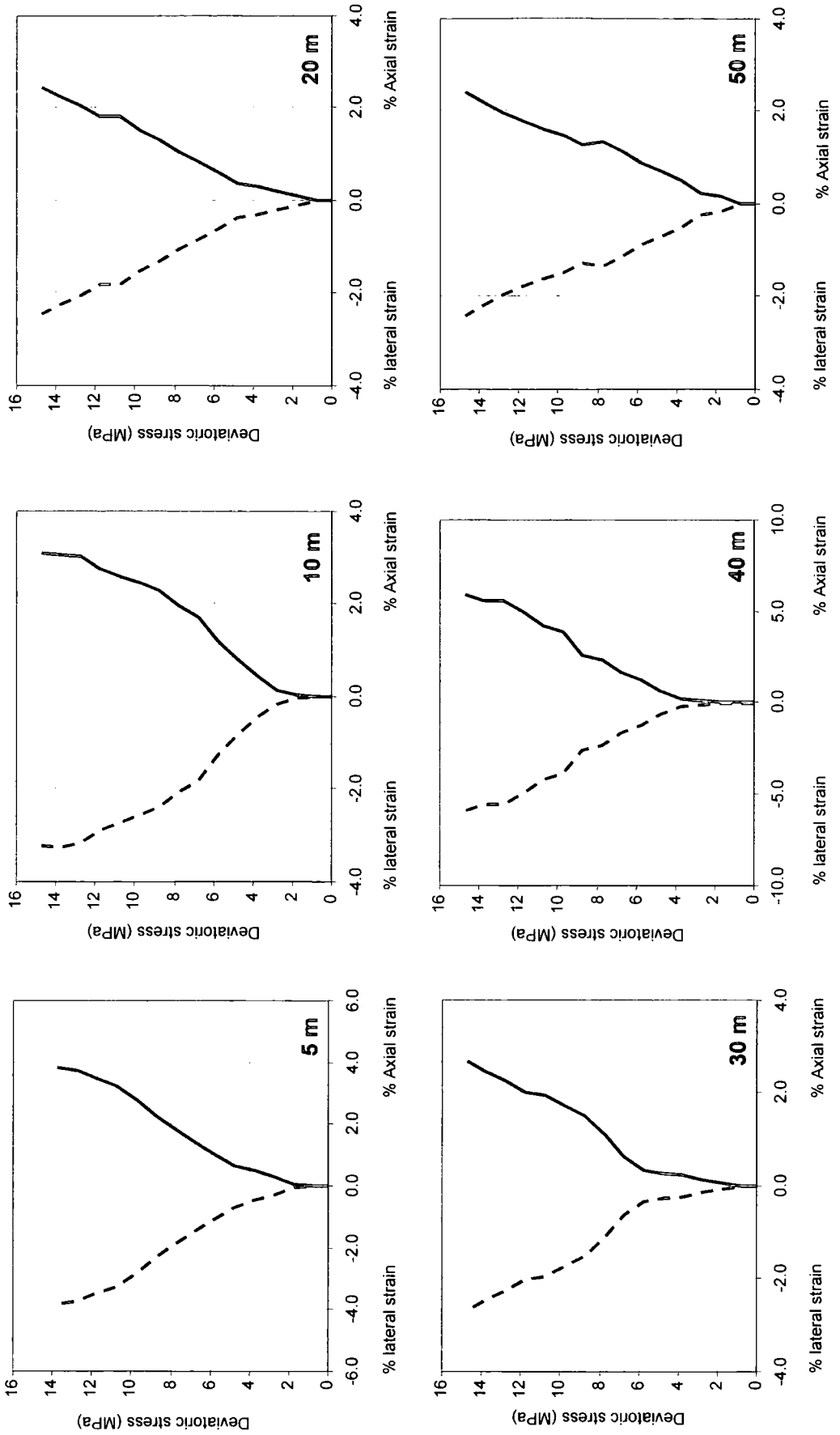

Figure 4.28: Stress-strain response of a 100 m sandstone rock mass with varying block sizes.

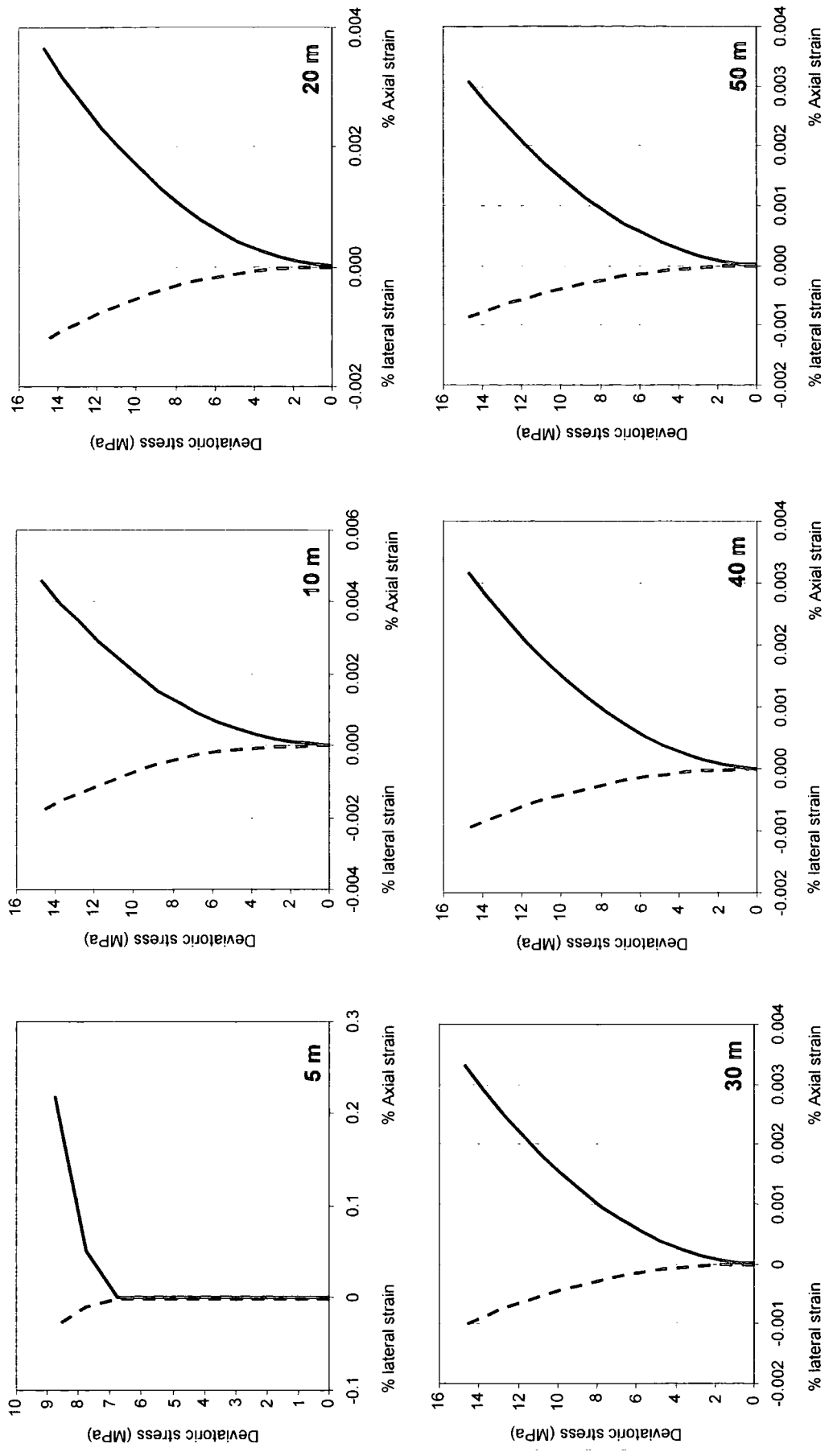

Figure 4.29: Stress-strain response of a 100 m granite rock mass with varying block sizes.

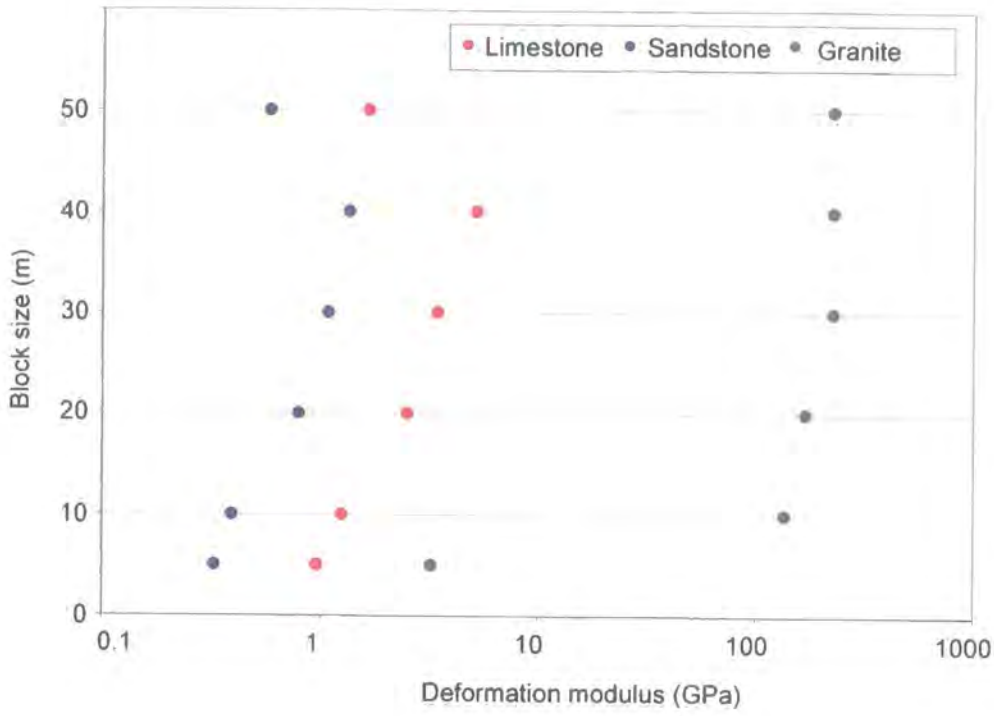

Figure 4.30: Deformation moduli during loading for 100 m limestone, sandstone and granite rock masses.

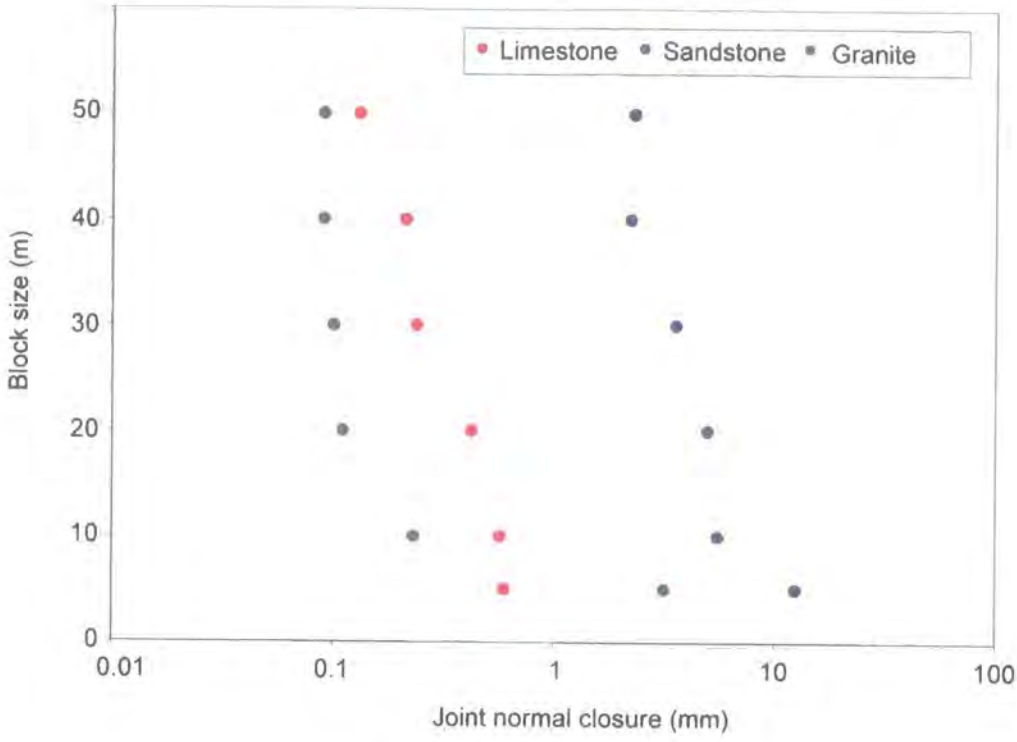

Figure 4.31: Joint normal closure during loading for 100 m limestone, sandstone and granite rock masses.

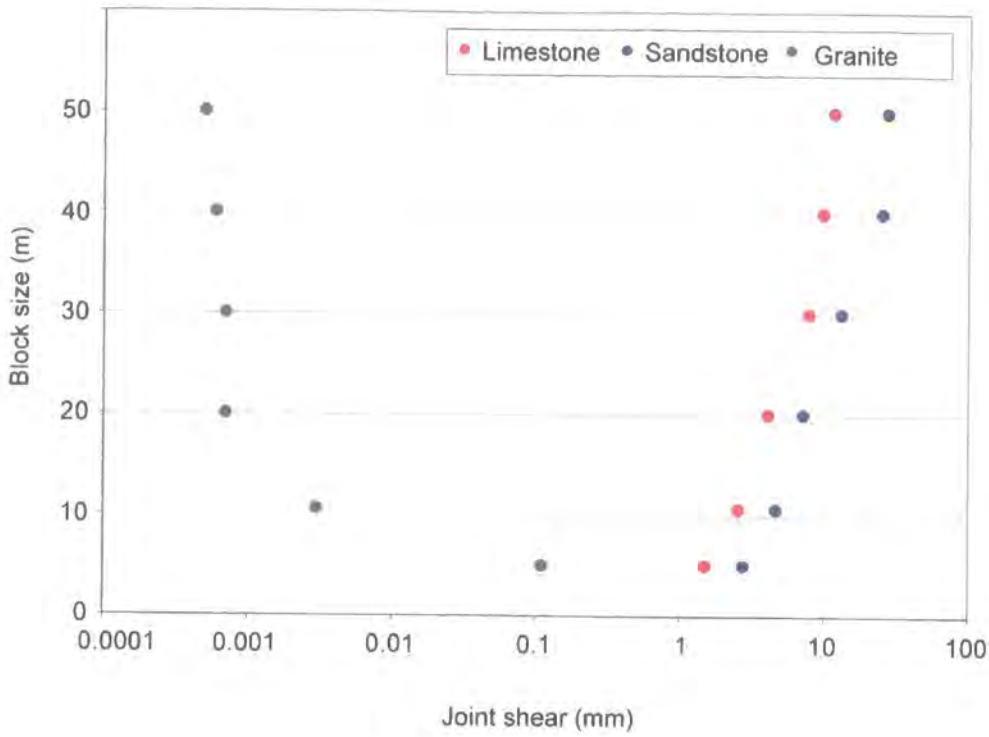

Figure 4.32: Joint shear magnitude during loading for 100 m limestone, sandstone and granite rock masses.

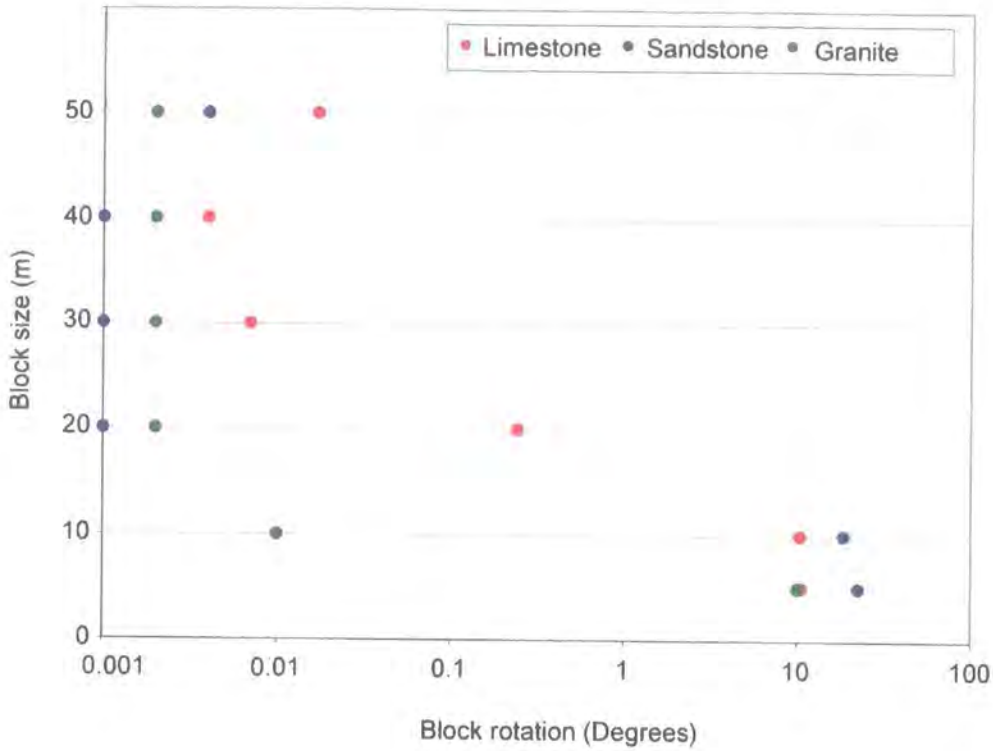

Figure 4.33: Block rotation magnitude for 100 m limestone, sandstone and granite rock masses.

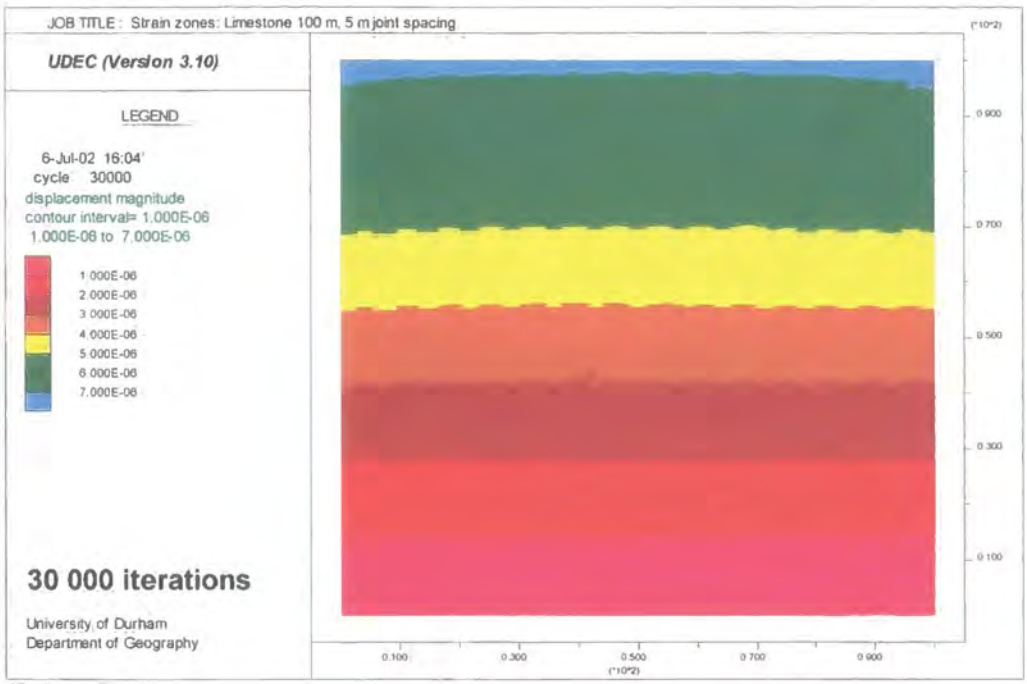

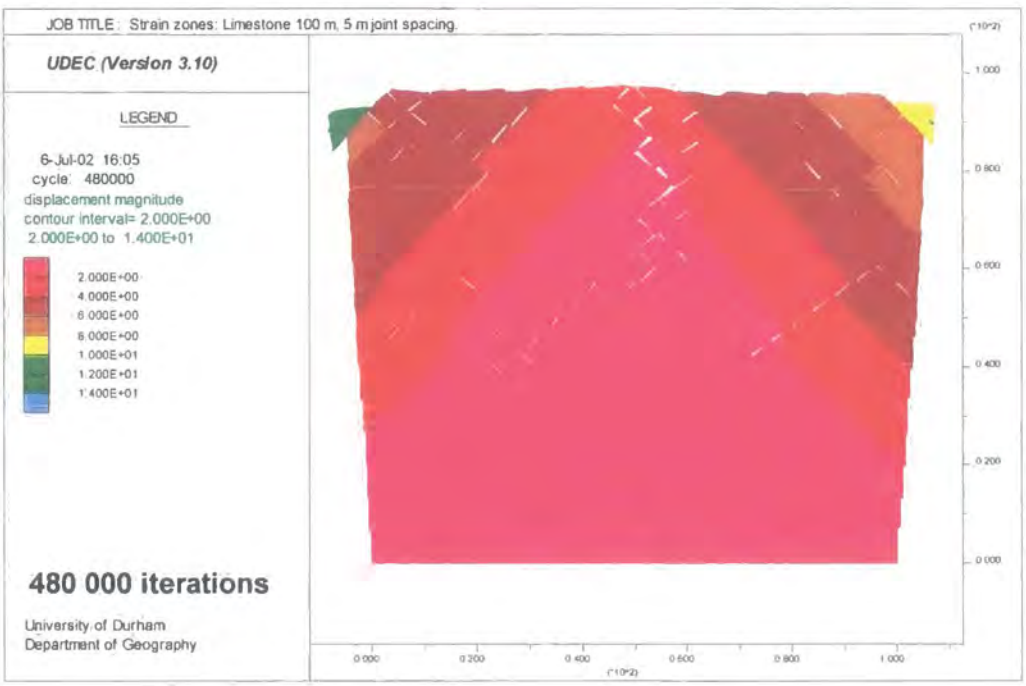

Figure 4.34a: Strain zone development in a 100 m limestone rock mass with 5 m block size.

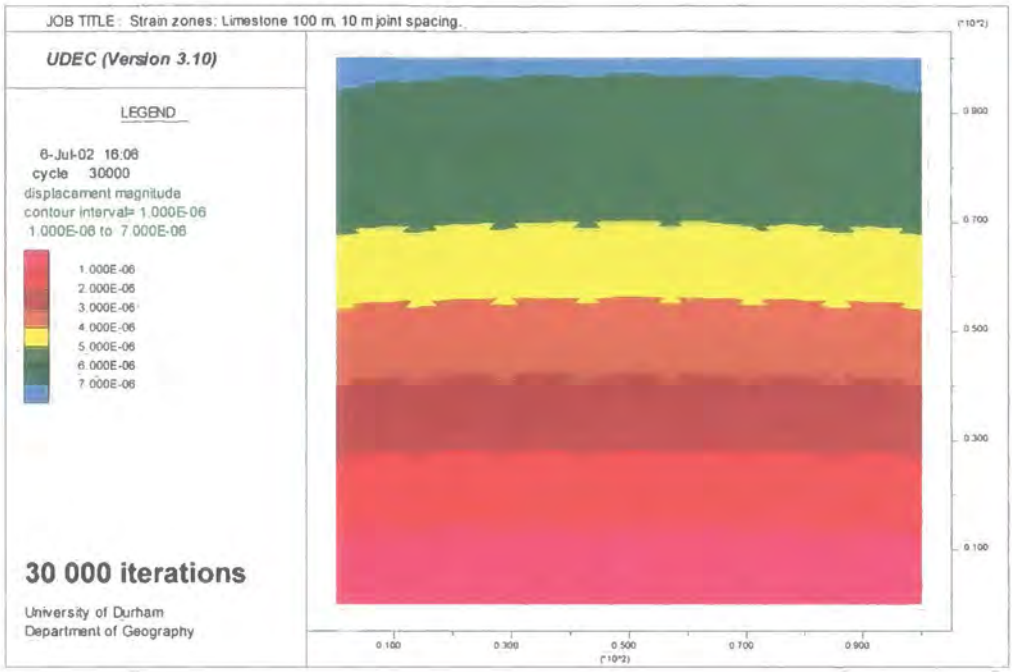

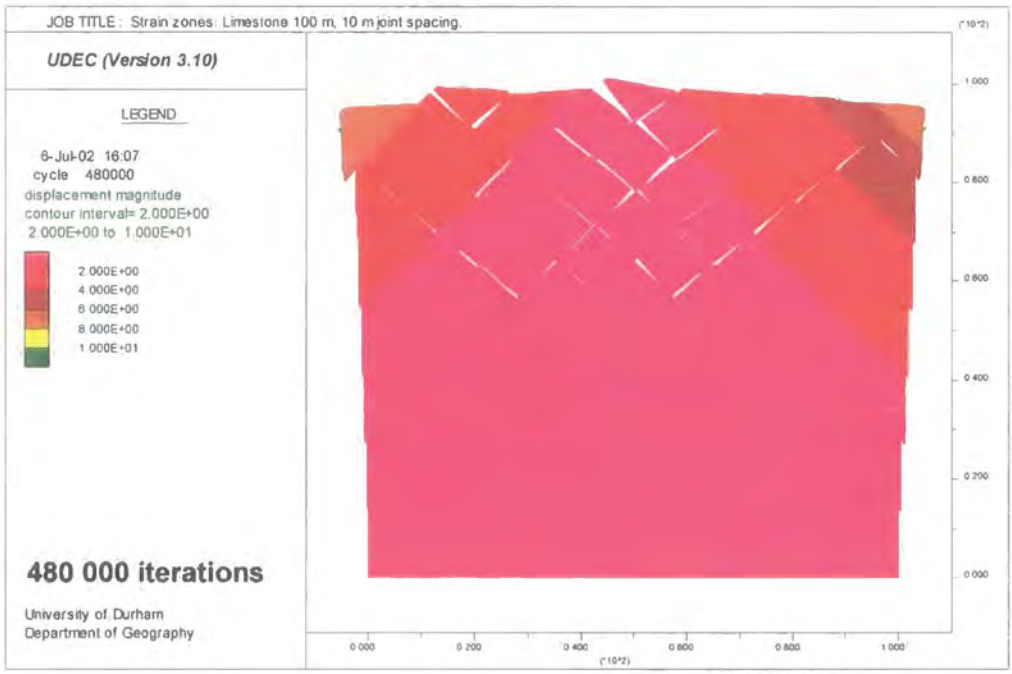

Figure 4.34b: Strain zone development in a 100 m limestone rock mass with 10 m block size.

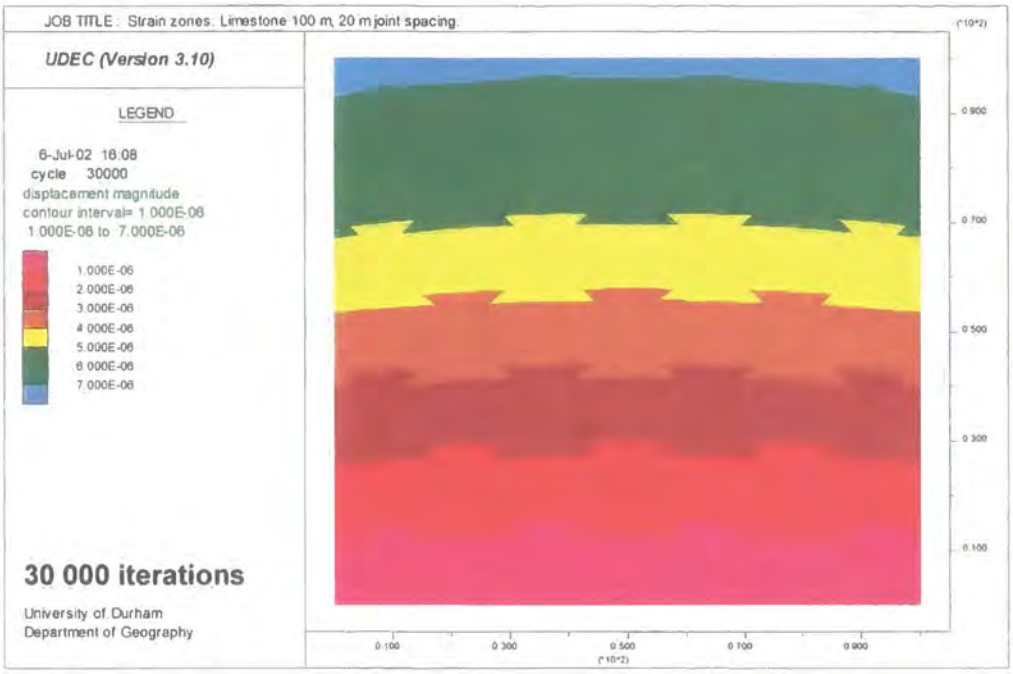

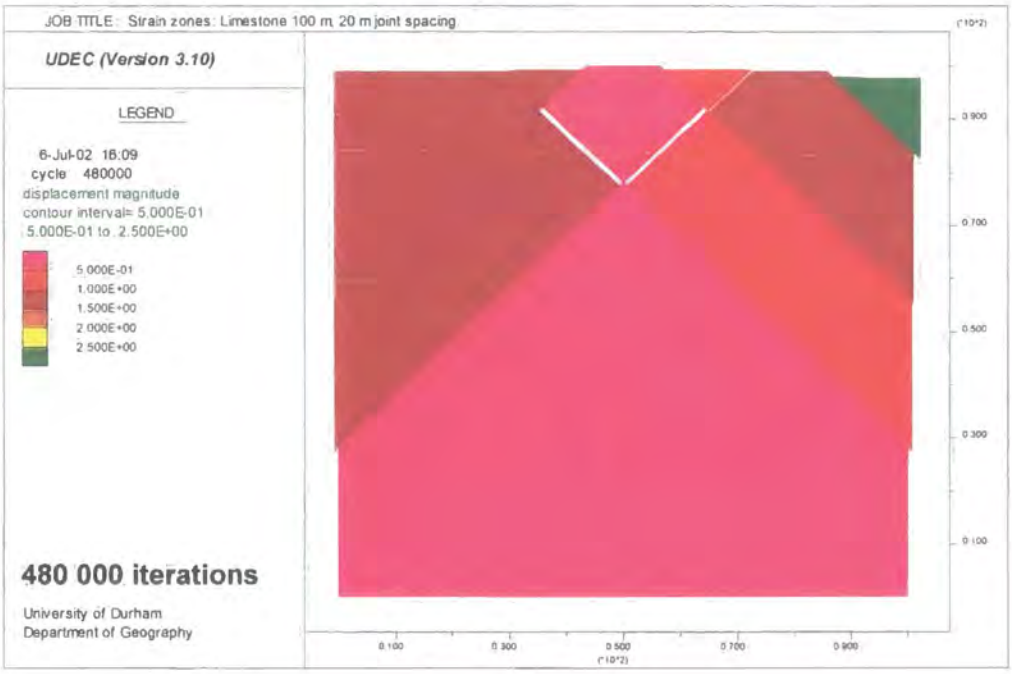

Figure 4.34c: Strain zone development in a 100 m limestone rock mass with 20 m block size.

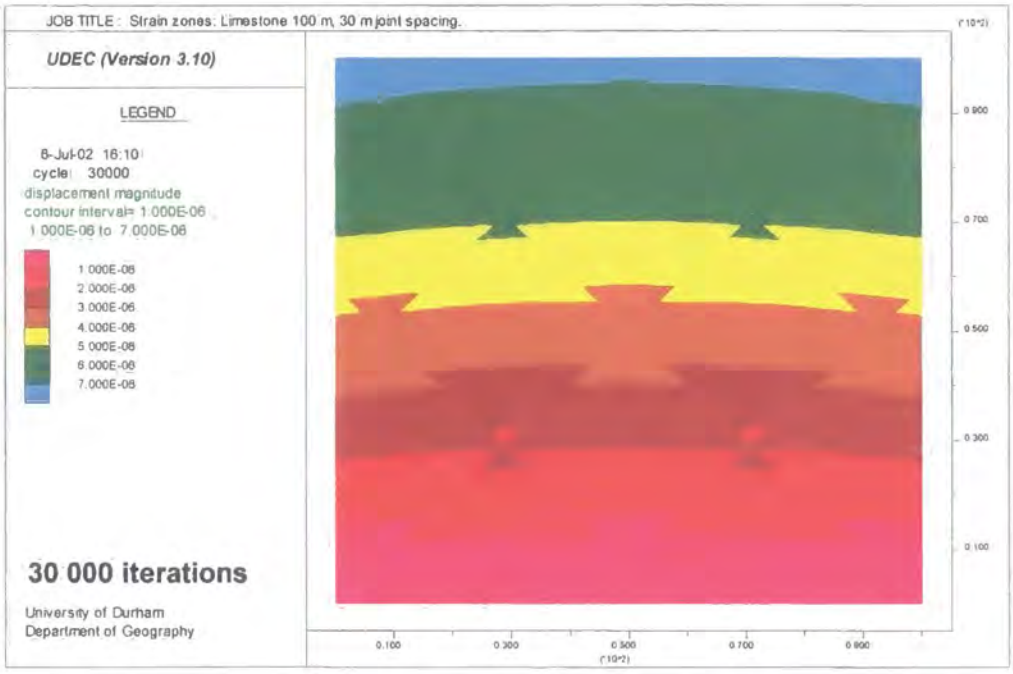

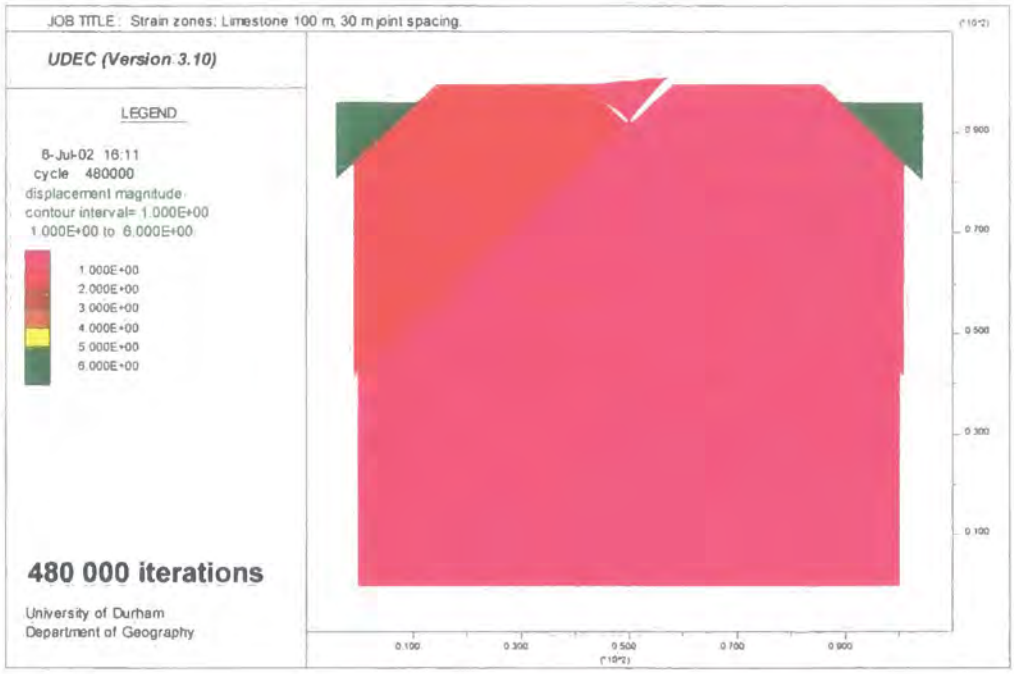

Figure 4.34d: Strain zone development in a 100 m limestone rock mass with 30 m block size.

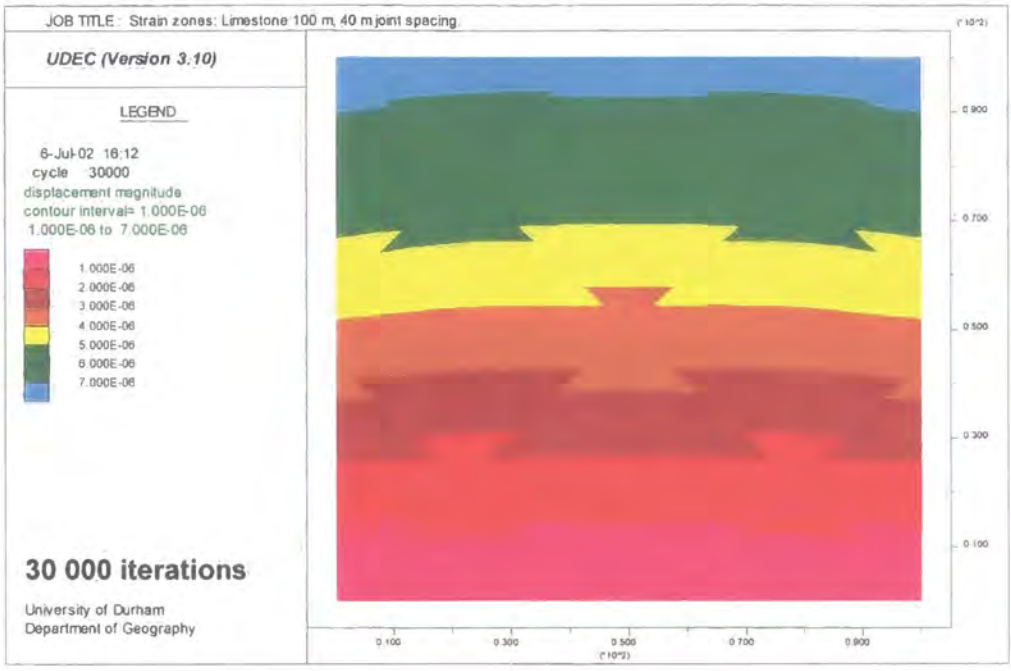

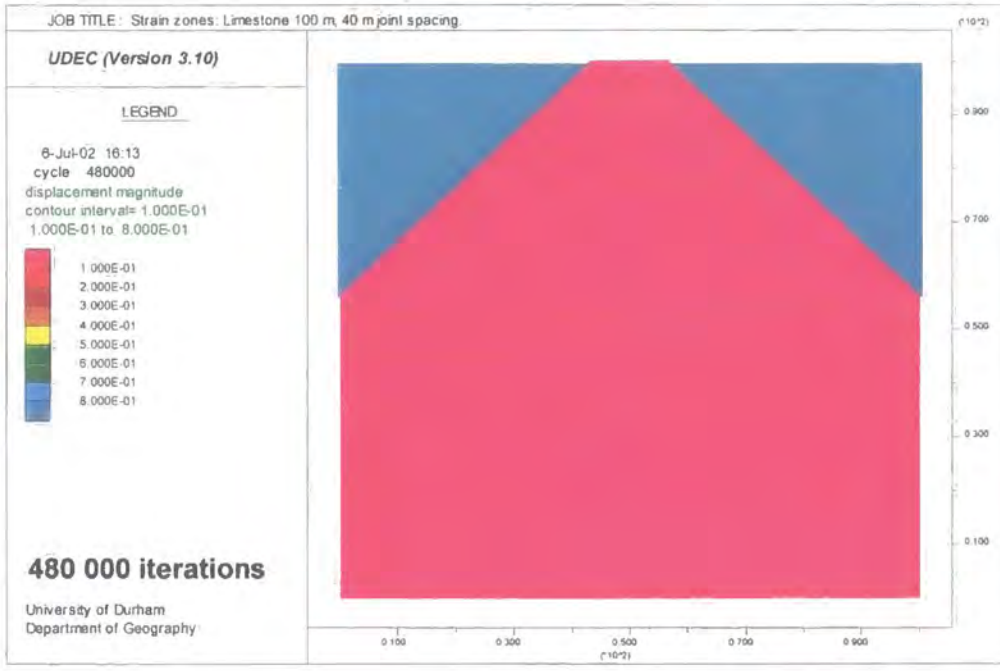

Figure 4.34e: Strain zone development in a 100 m limestone rock mass with 40 m block size.

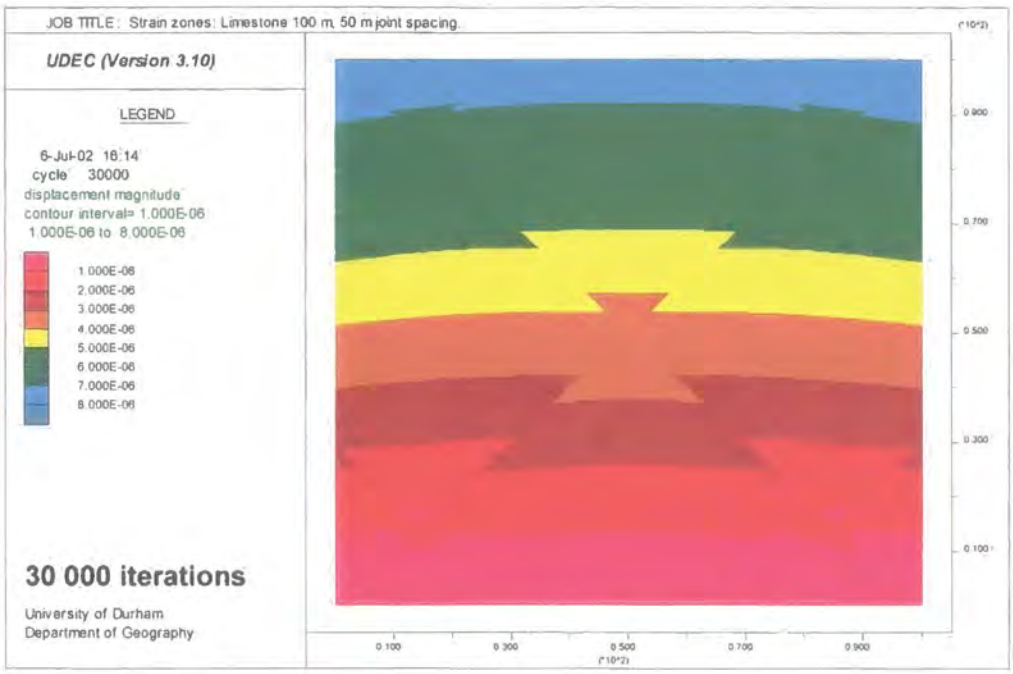

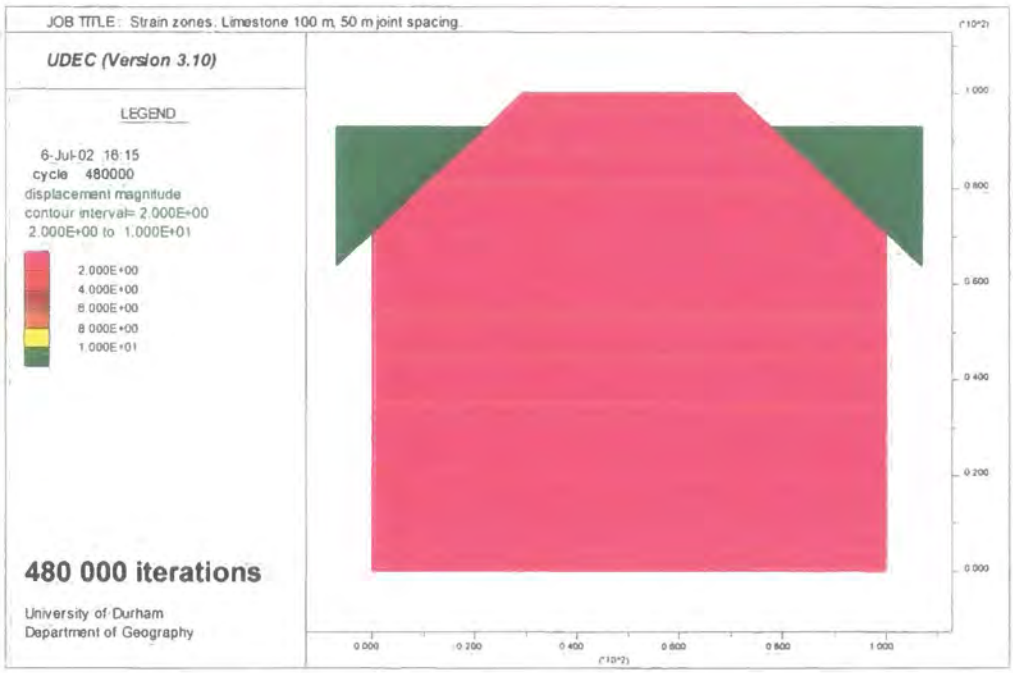

Figure 4.34f: Strain zone development in a 100 m limestone rock mass with 50 m block size.

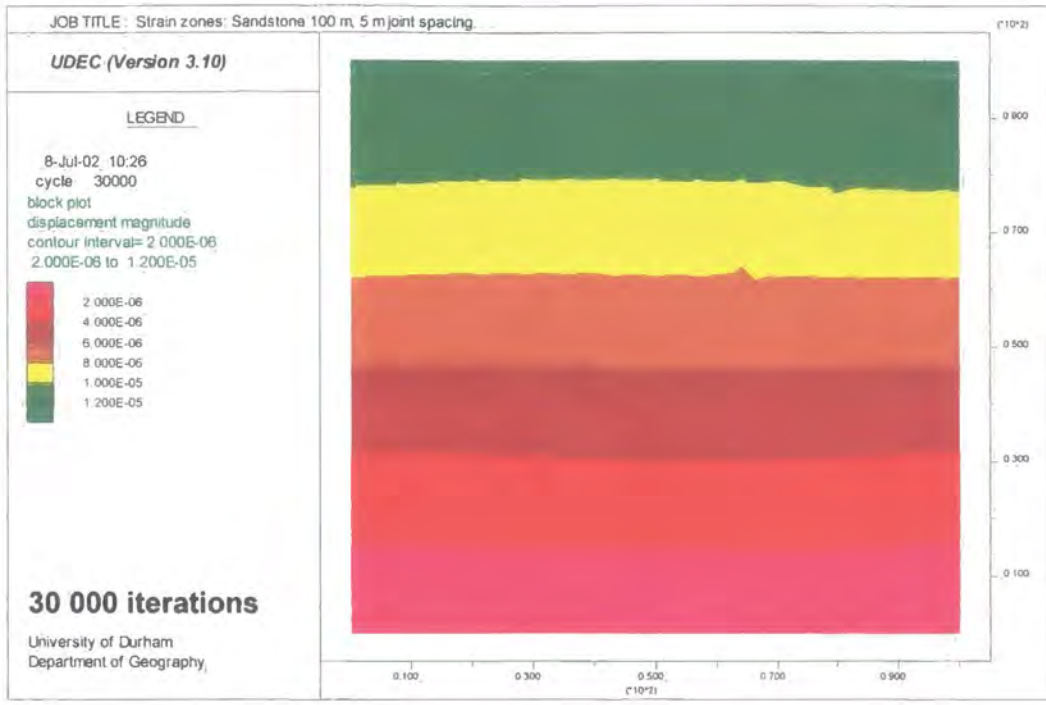

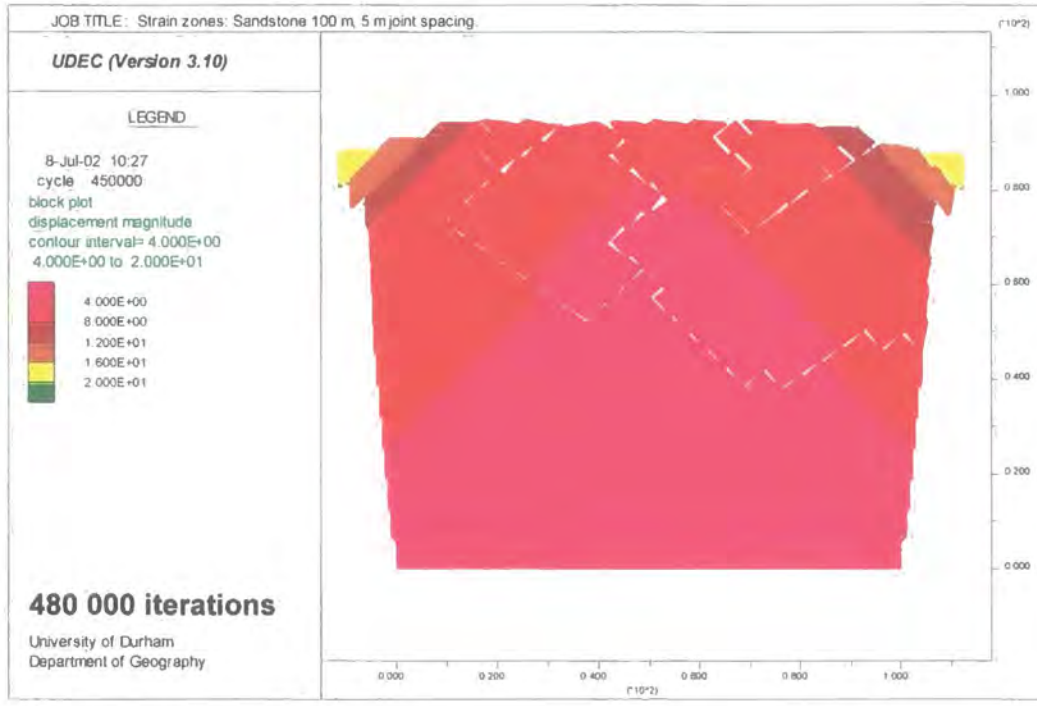

Figure 4.35a: Strain zone development in a 100 m sandstone rock mass with 5 m block size.

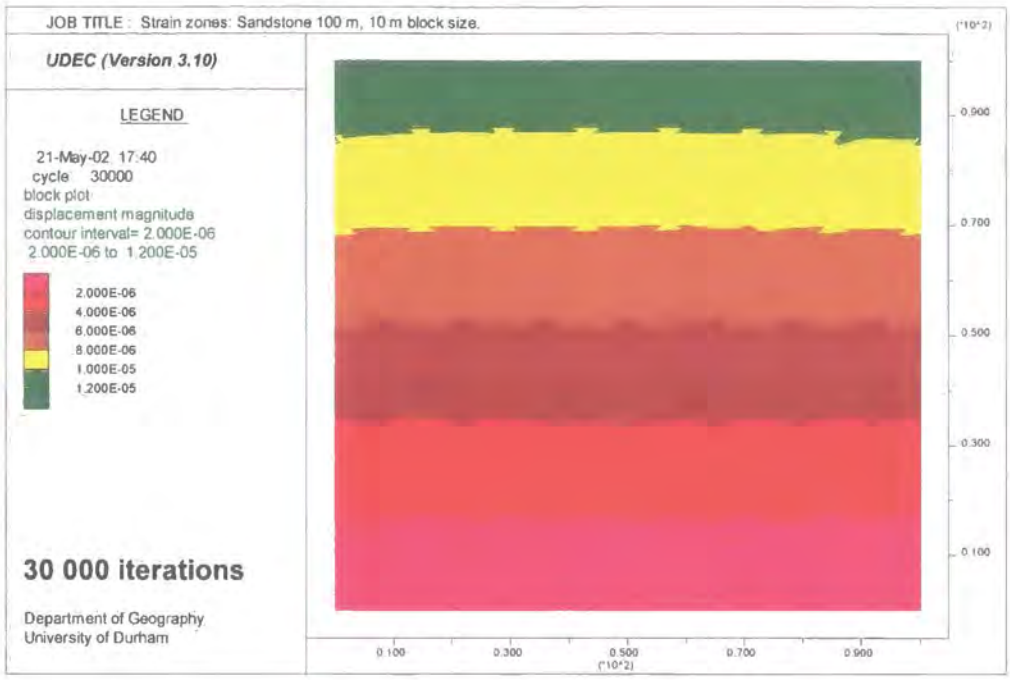

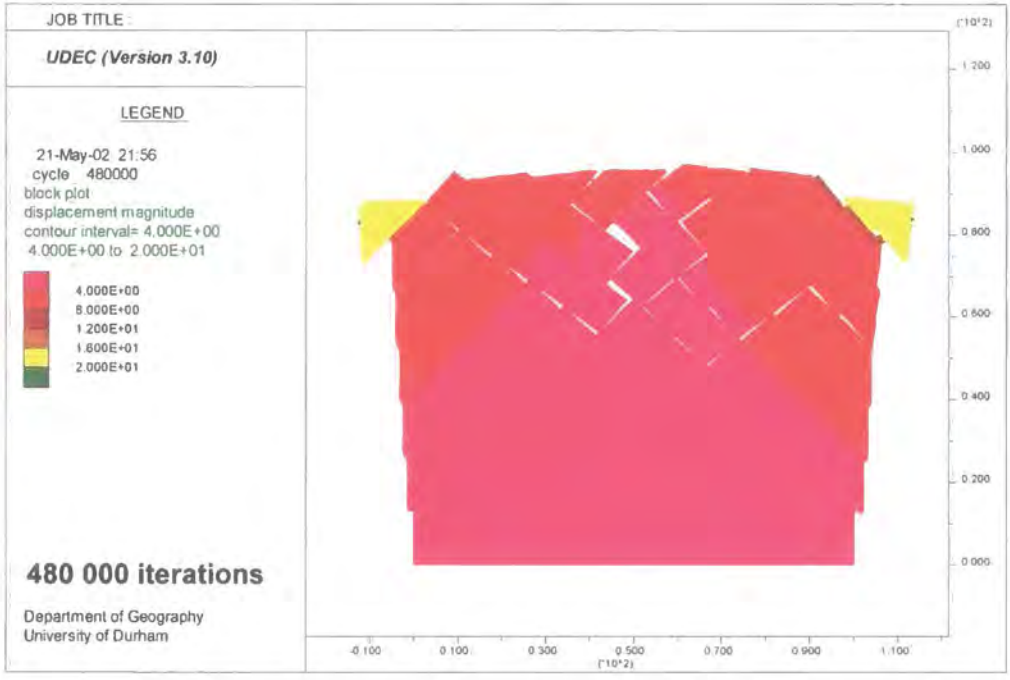

Figure 4.35b: Strain zone development in a 100 m sandstone rock mass with 10 m block size.

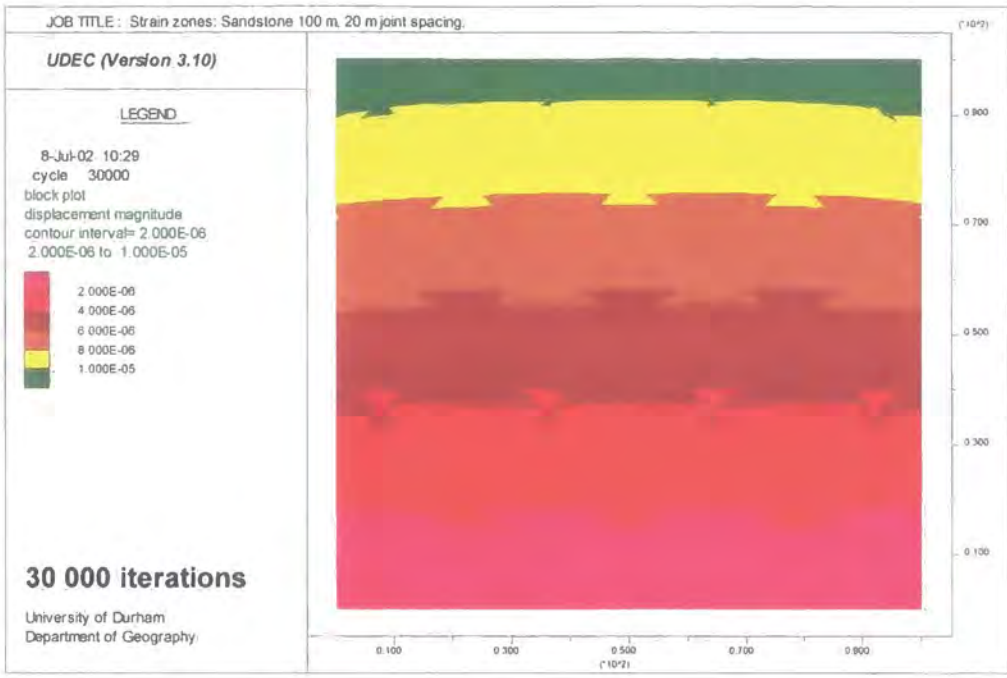

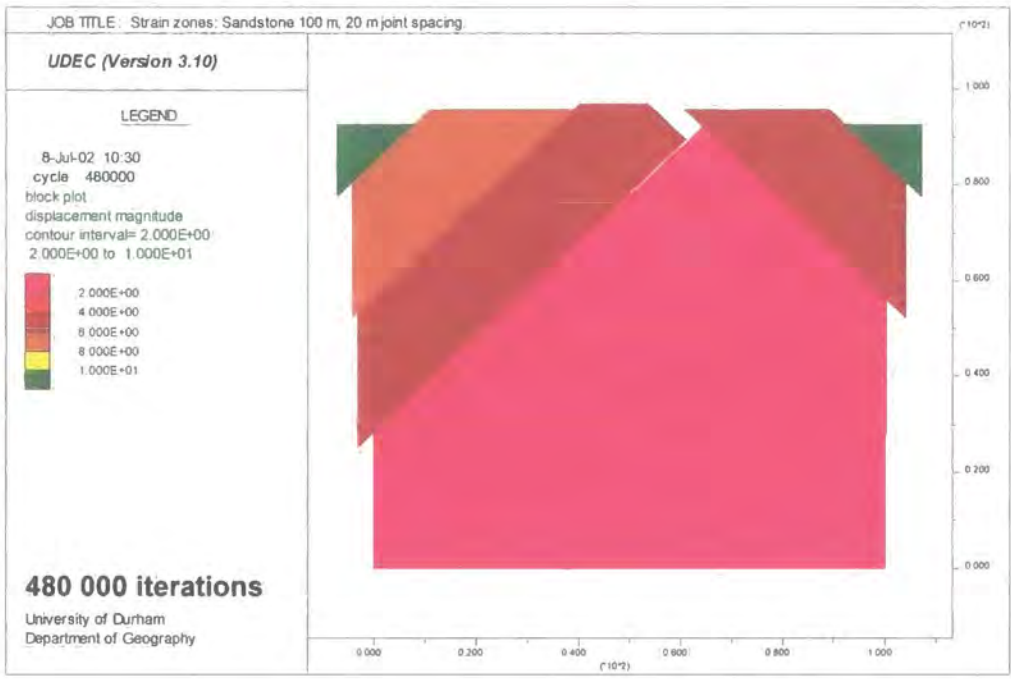

Figure 4.35c: Strain zone development in a 100 m sandstone rock mass with 20 m block size.

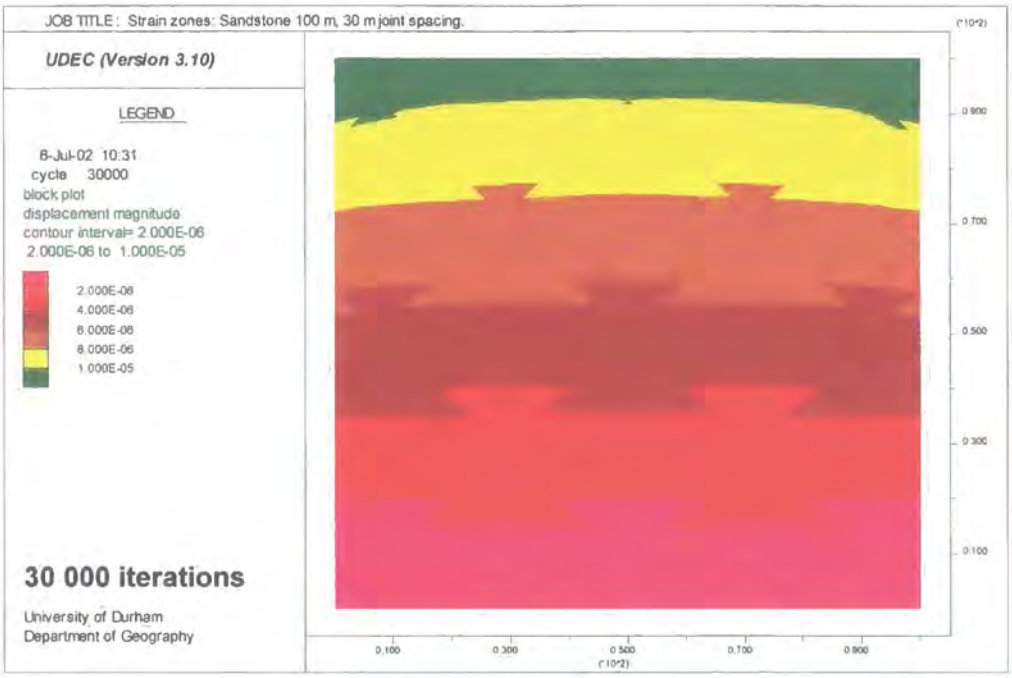

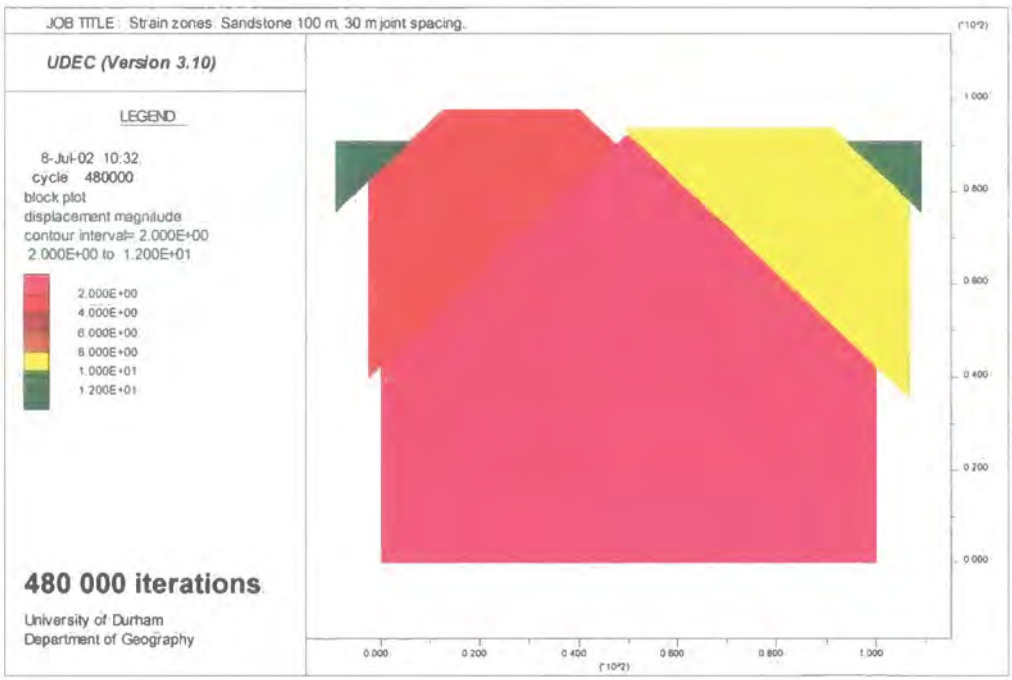

Figure 4.35d: Strain zone development in a 100 m sandstone rock mass with 30 m block size.

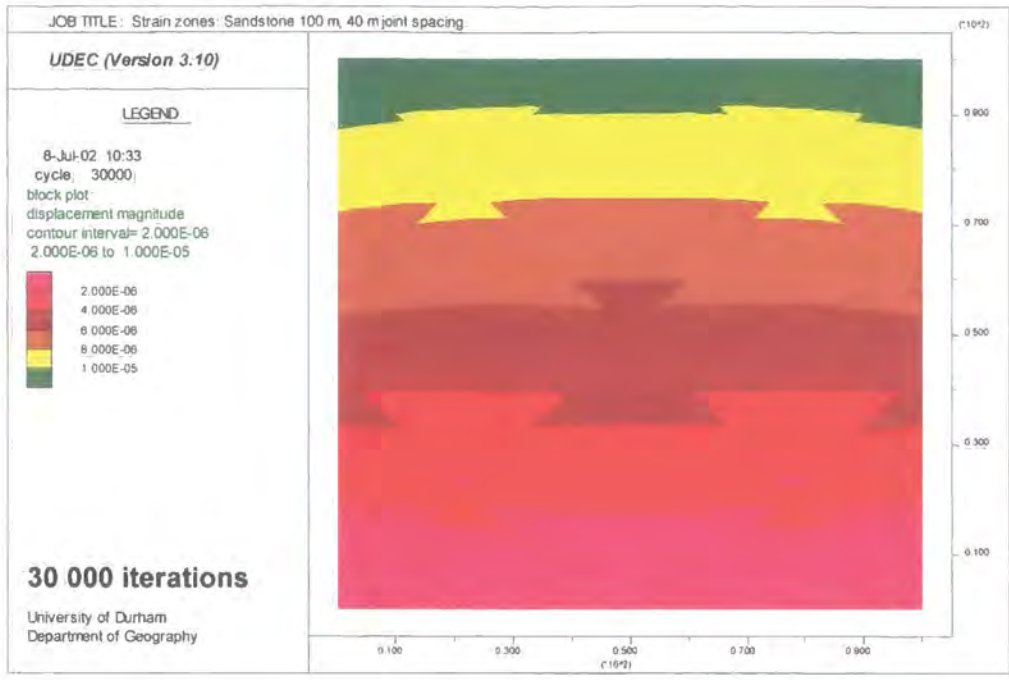

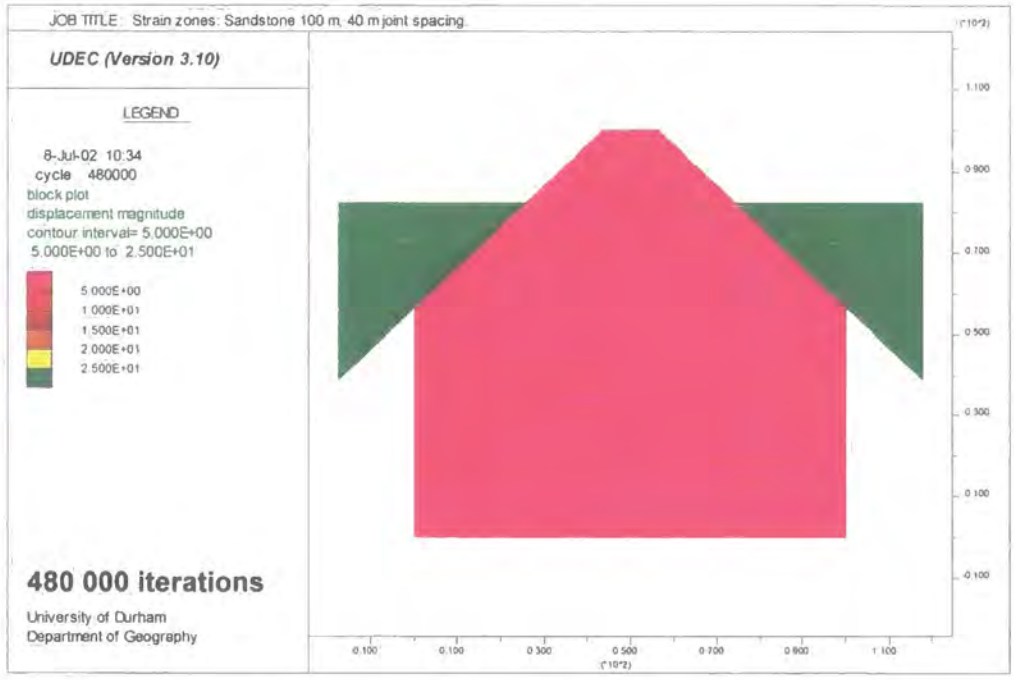

Figure 4.35e: Strain zone development in a 100 m sandstone rock mass with 40 m block size.

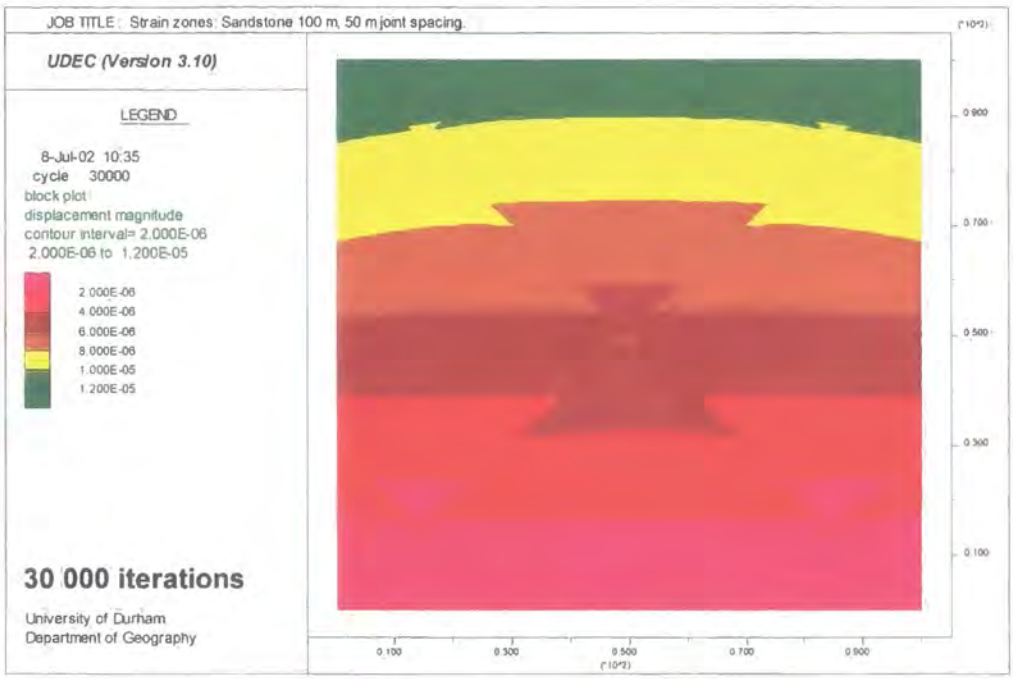

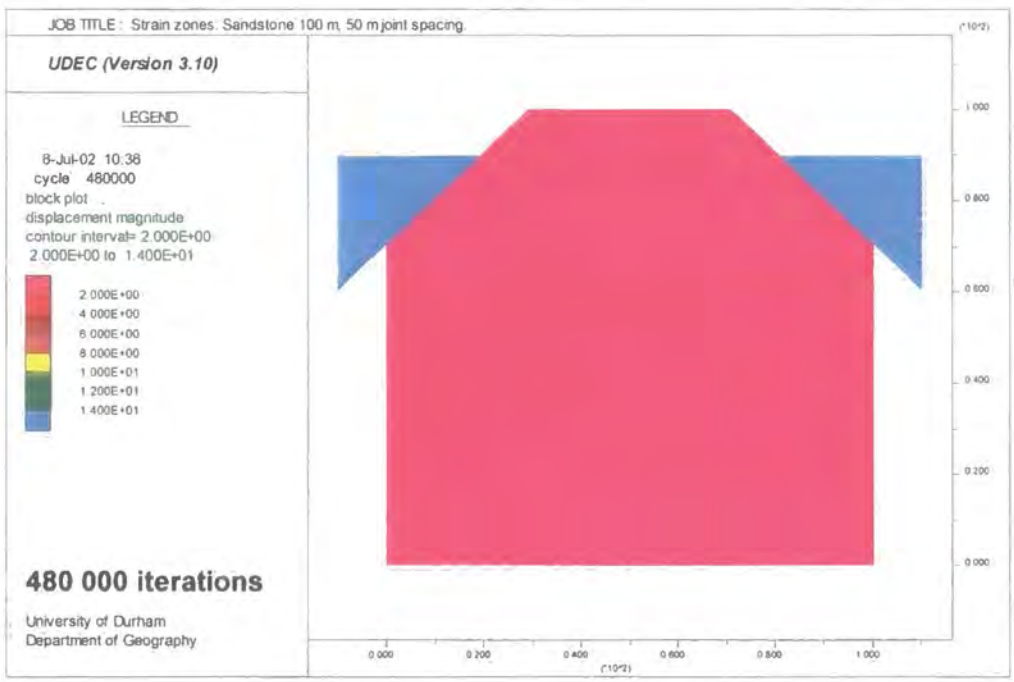

Figure 4.35f: Strain zone development in a 100 m sandstone rock mass with 50 m block size.

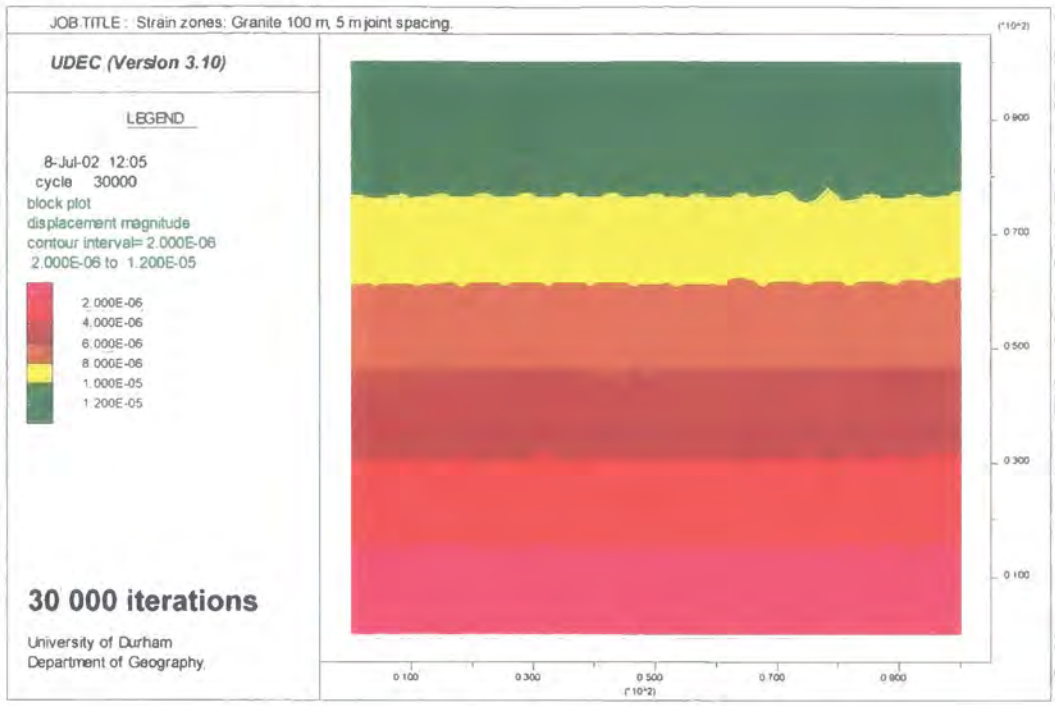

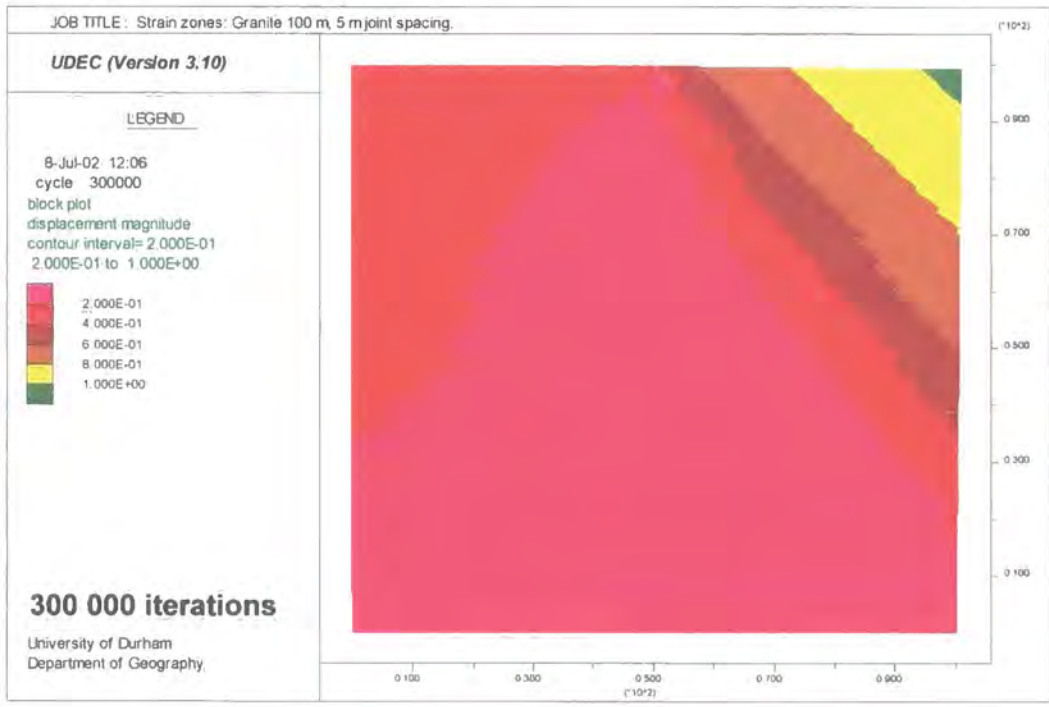

Figure 4.36a: Strain zone development in a 100 m granite rock mass with 5 m block size.

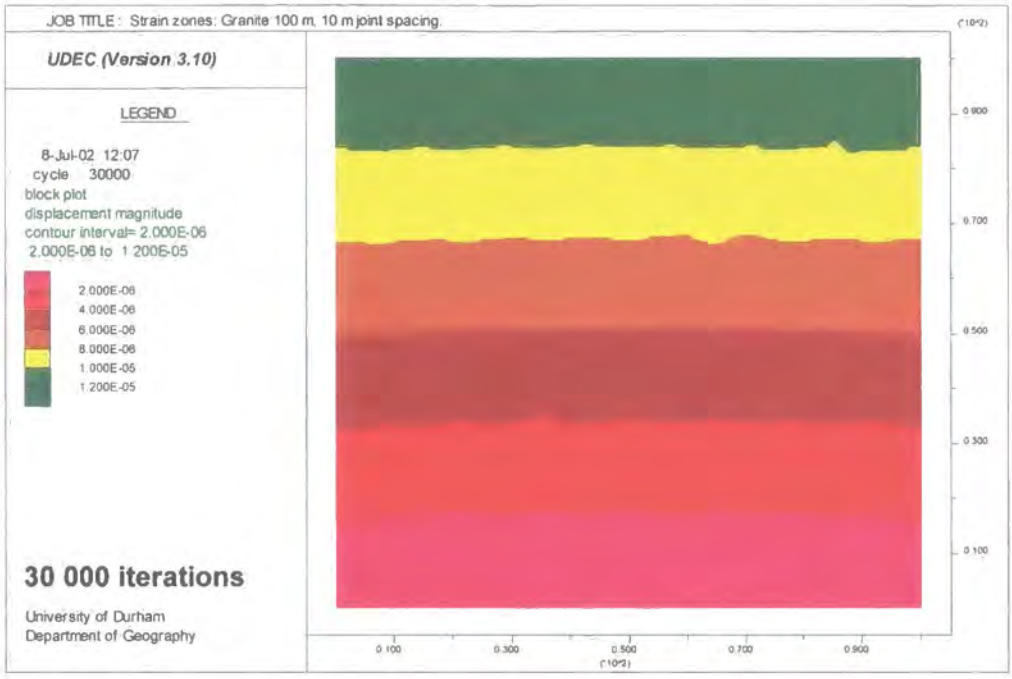

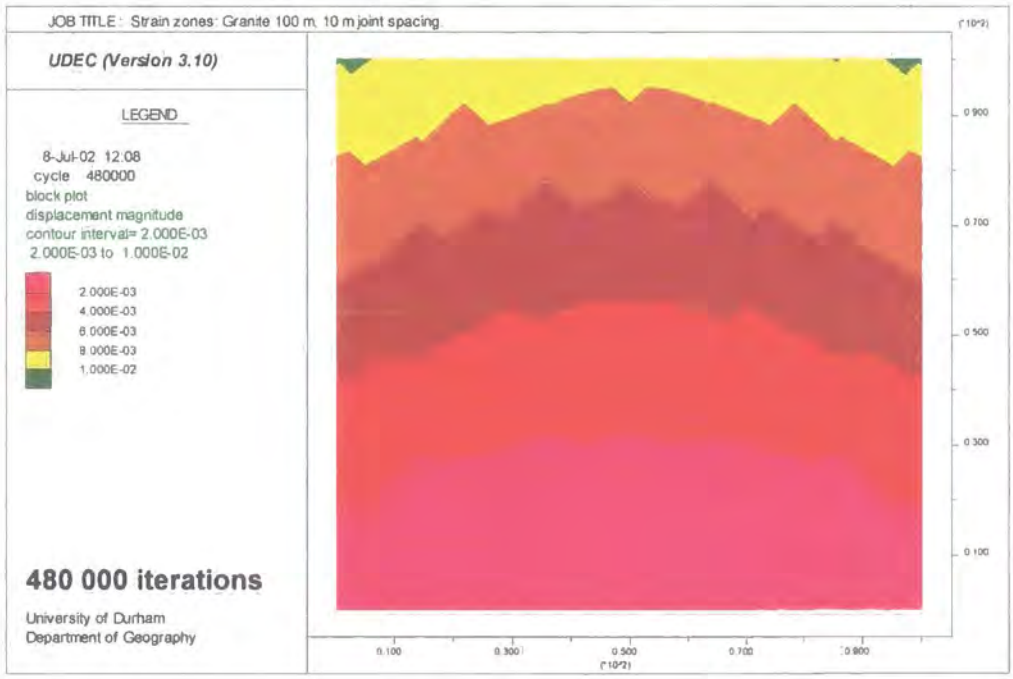

Figure 4.36b: Strain zone development in a 100 m granite rock mass with 10 m block size.

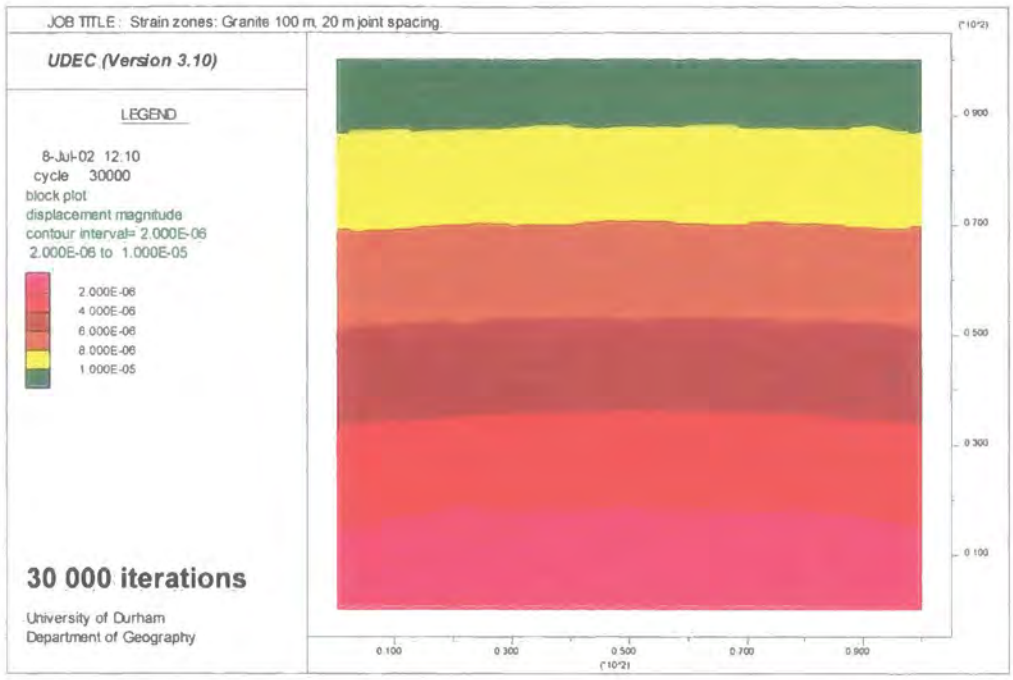

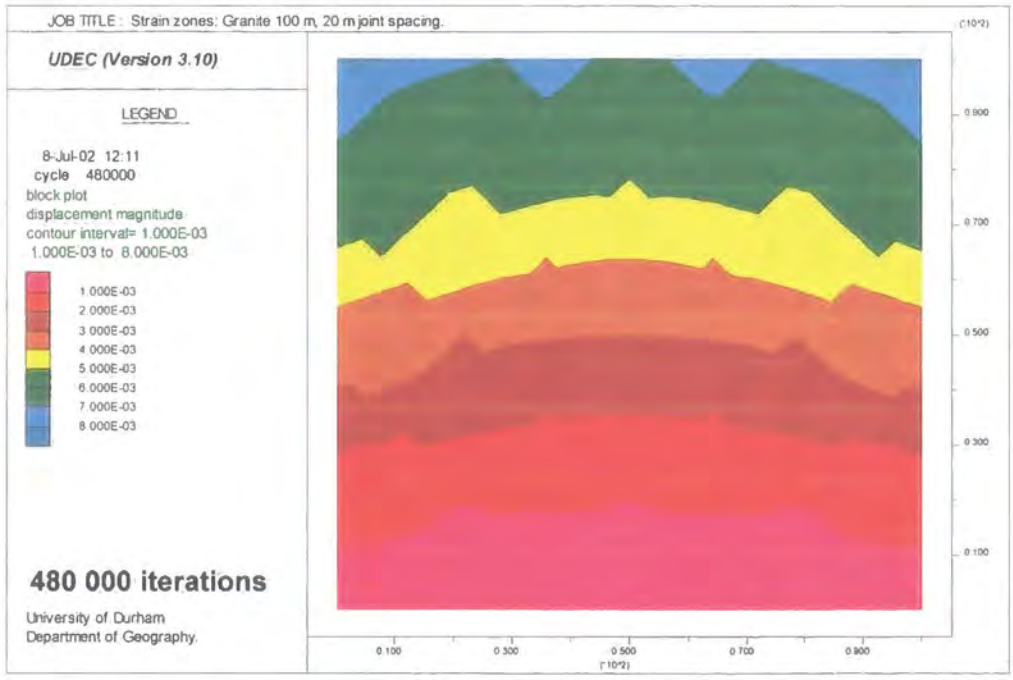

Figure 4.36c: Strain zone development in a 100 m granite rock mass with 20 m block size.

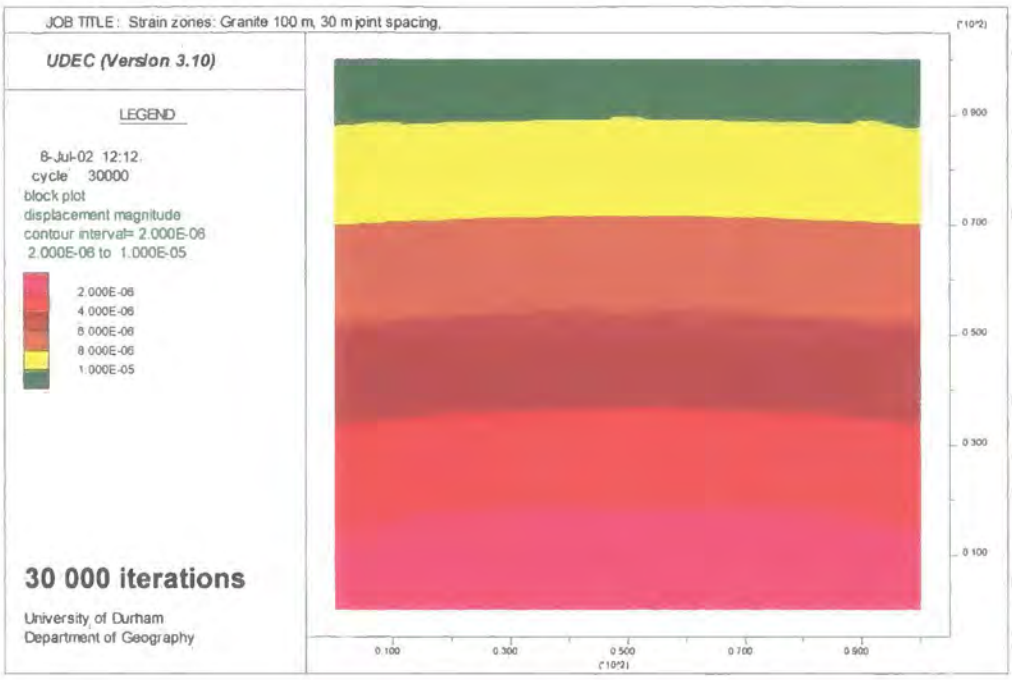

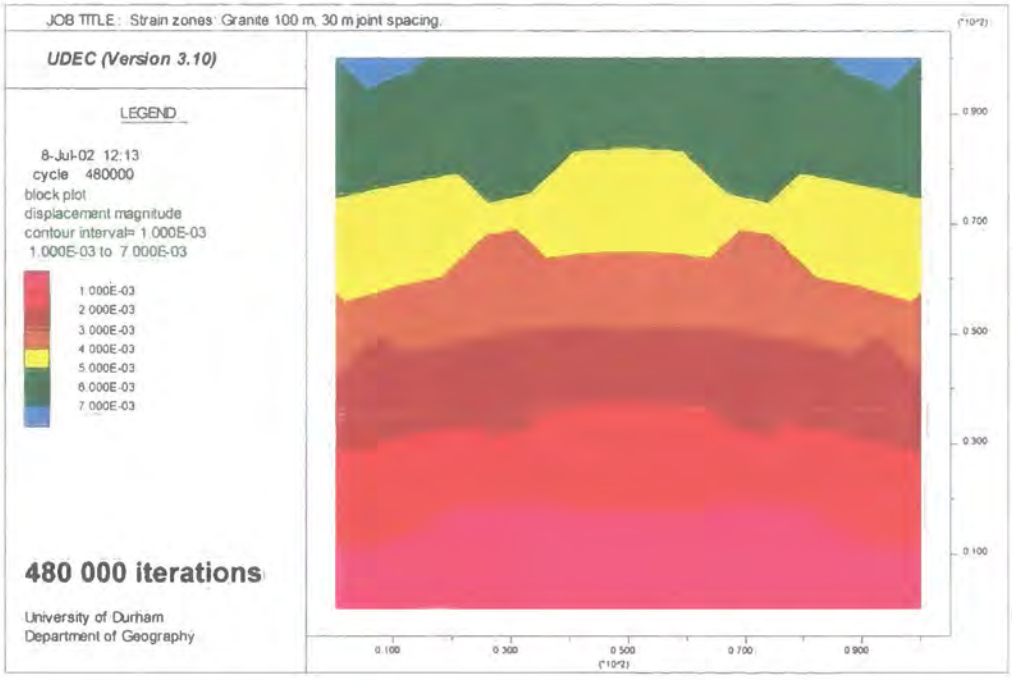

Figure 4.36d: Strain zone development in a 100 m granite rock mass with 30 m block size.

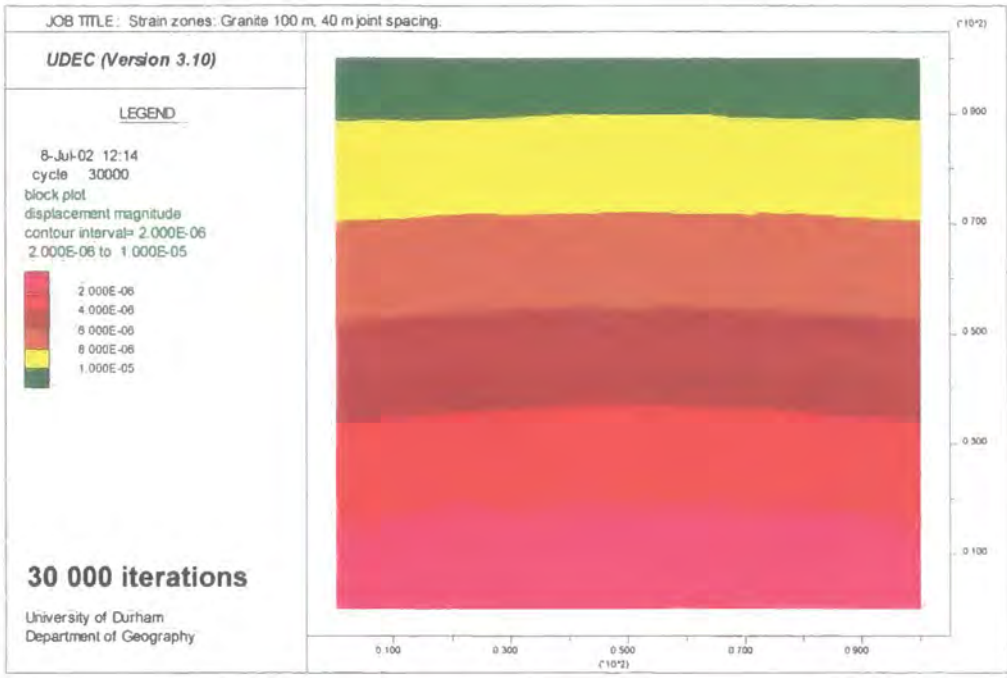

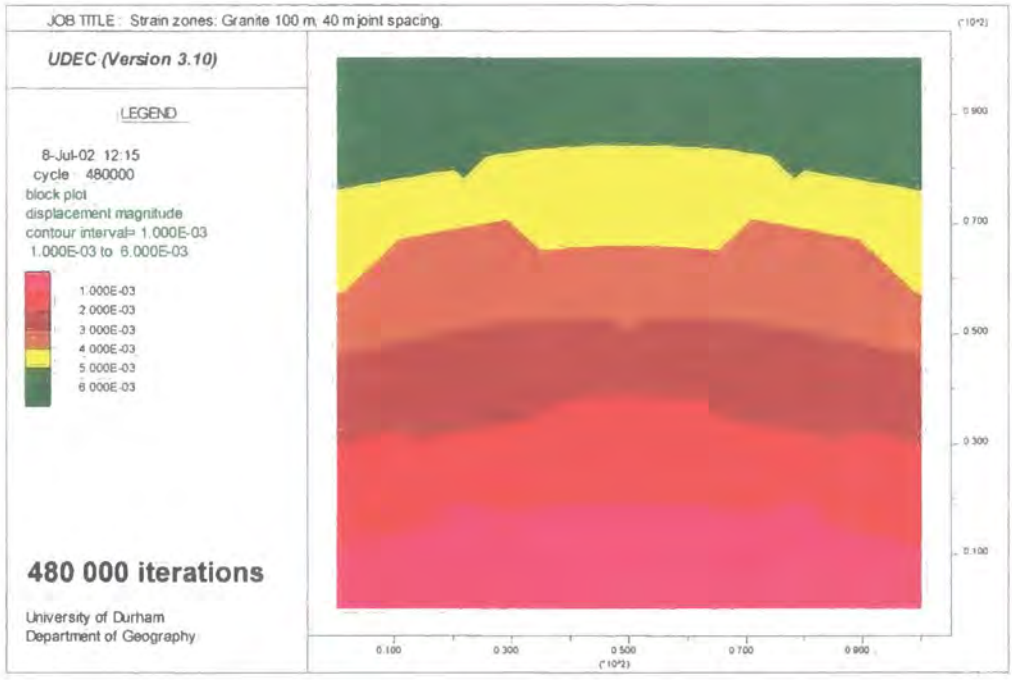

Figure 4.36e: Strain zone development in a 100 m granite rock mass with 40 m block size.

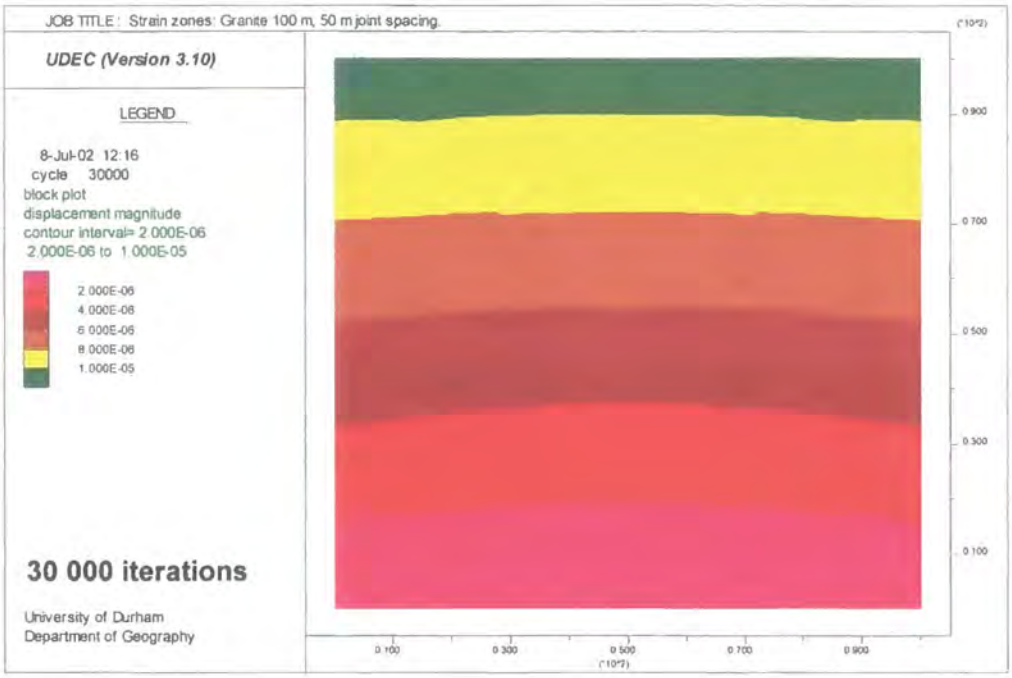

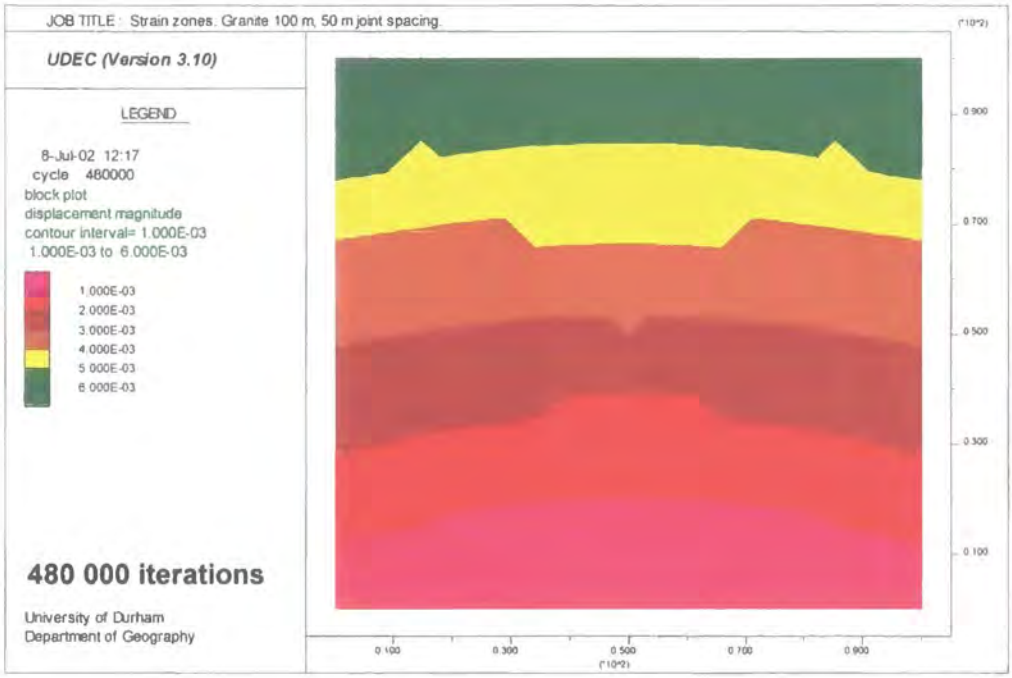

Figure 4.36f: Strain zone development in a 100 m granite rock mass with 50 m block size.

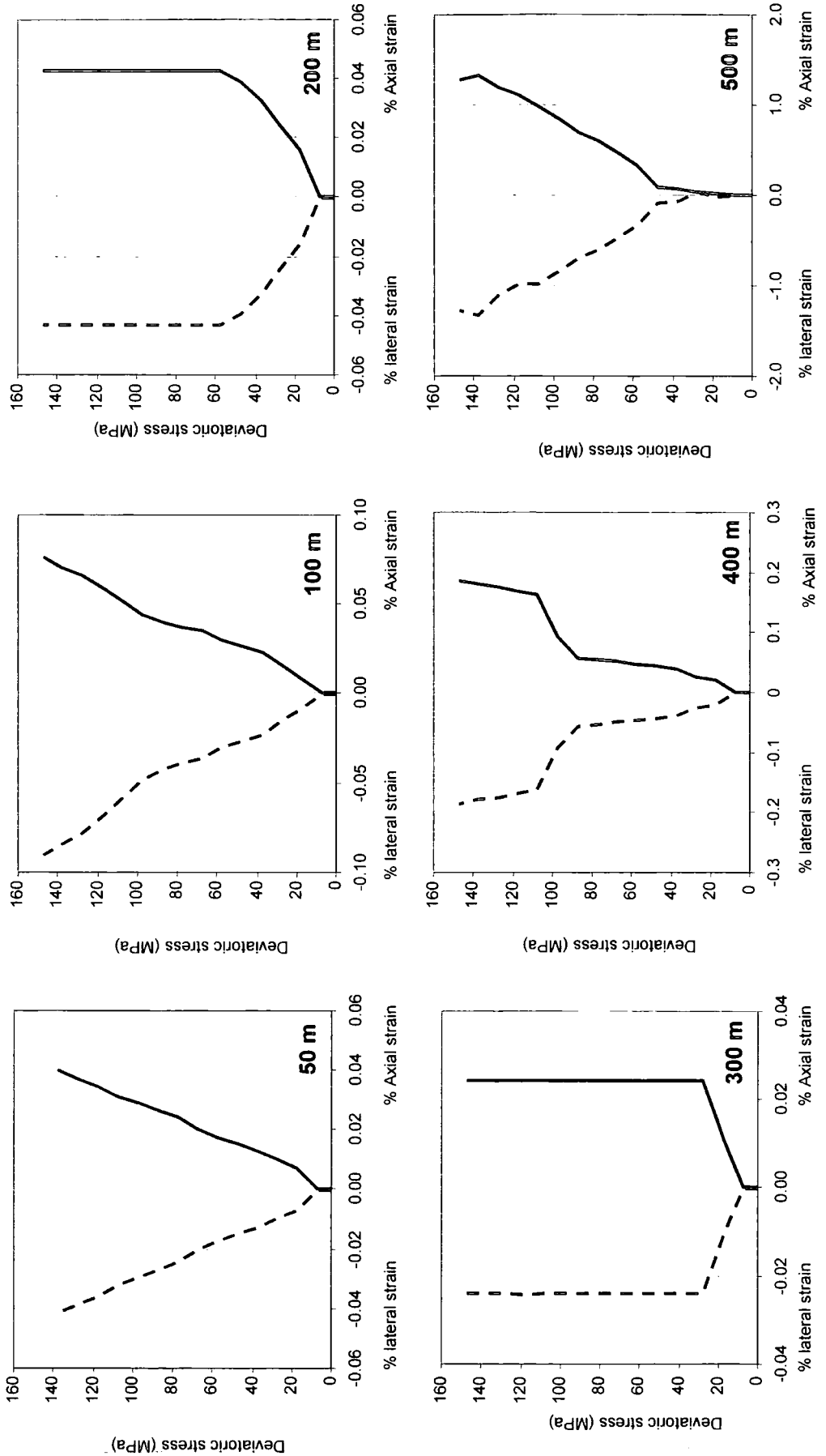

Figure 4.37: Stress-strain response of a 1000 m limestone rock mass with varying block sizes.

Figure 4.38: Stress-strain response of a 1000 m sandstone rock mass with varying block sizes.

Figure 4.39: Stress-strain response of a 1000 m granite rock mass with varying block sizes.

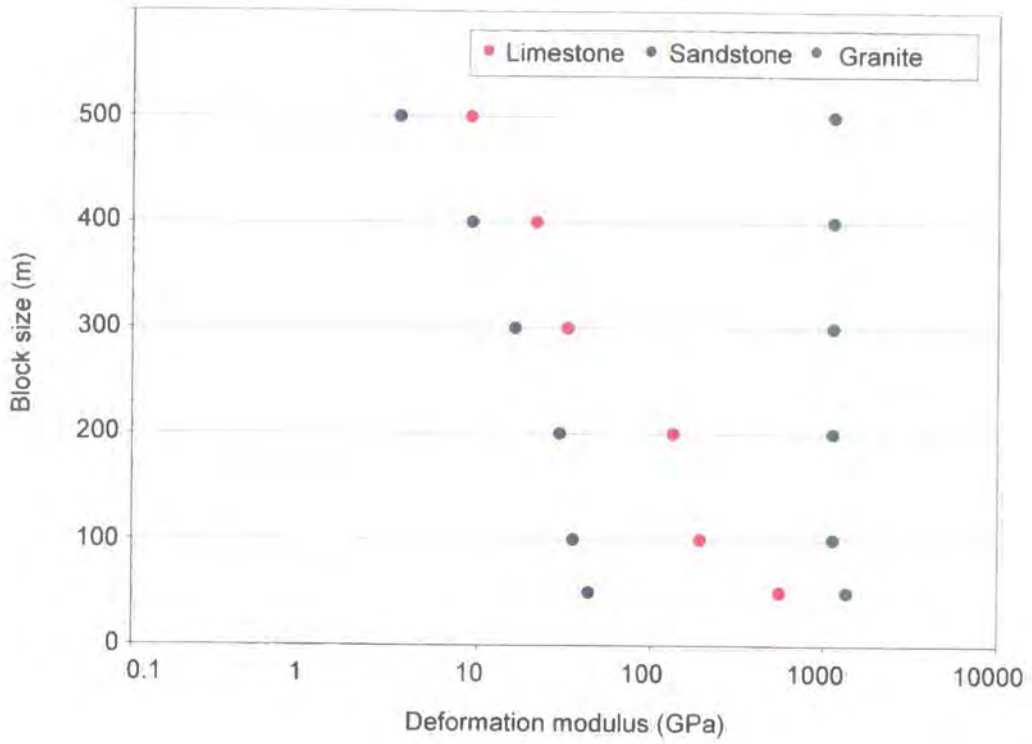

Figure 4.40: Deformation moduli for 1000 m limestone, sandstone and granite rock masses.

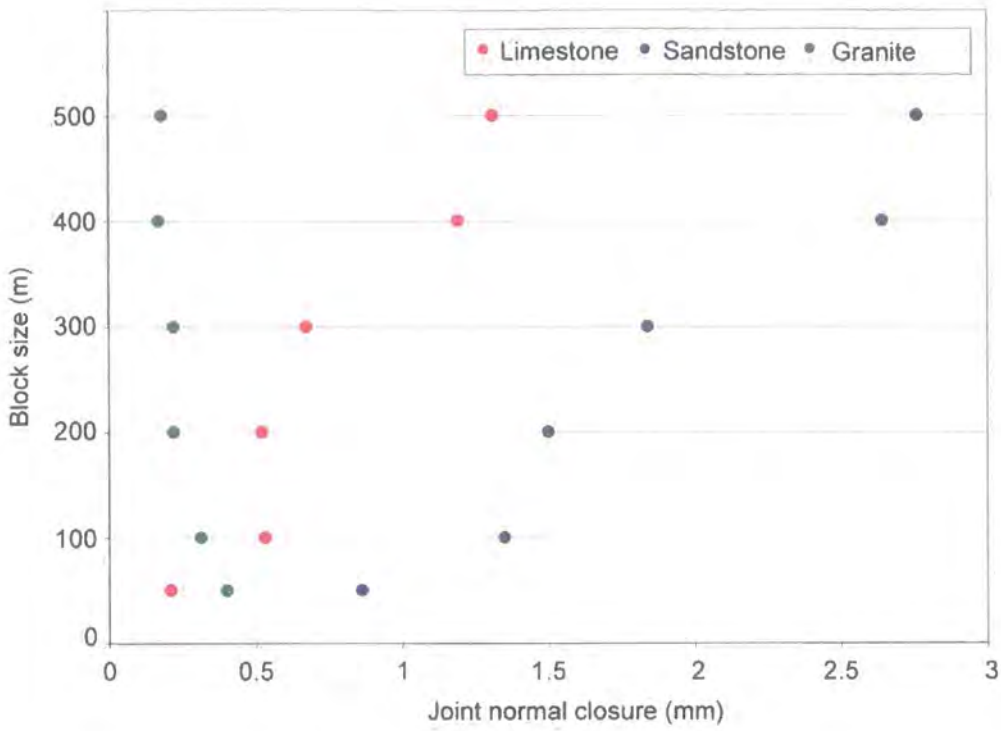

Figure 4.41: Joint normal closure for 1000 m limestone, sandstone and granite rock masses.

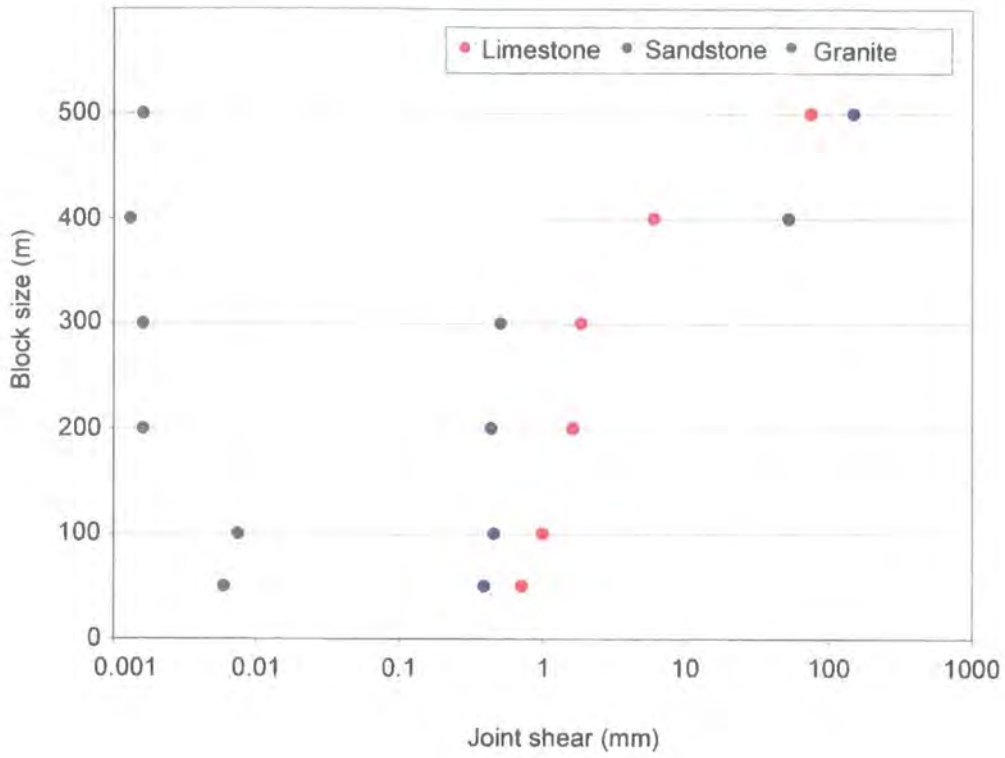

Figure 4.42: Joint shear displacement for 1000 m limestone, sandstone and granite rock masses.

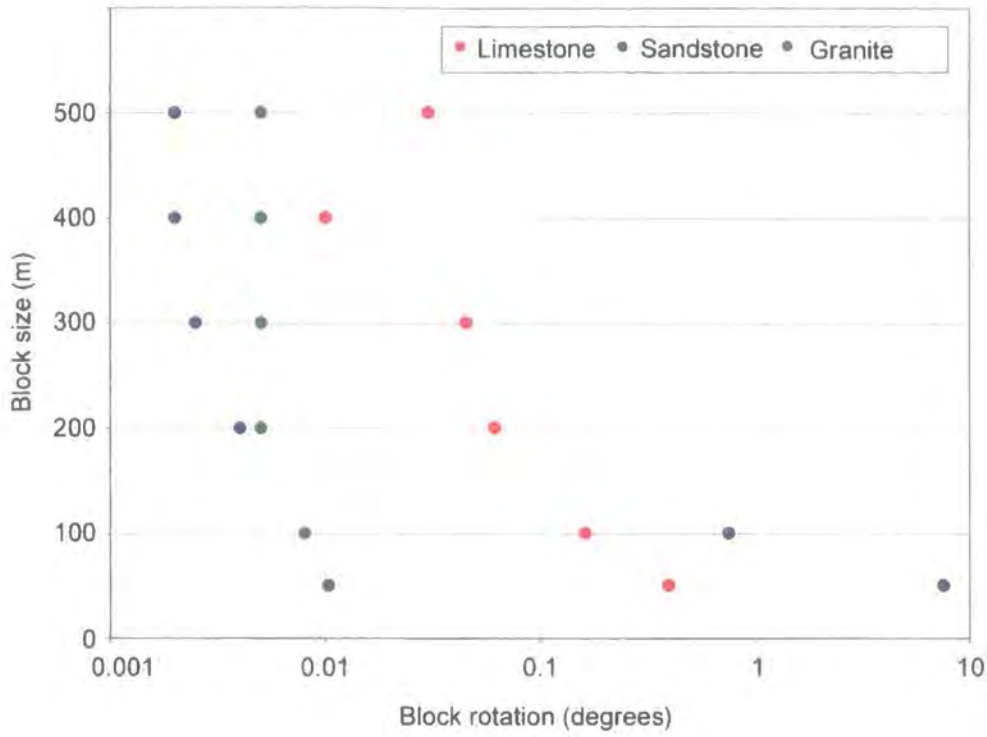

Figure 4.43: Block rotation magnitudes for 1000 m limestone, sandstone and granite rock masses.

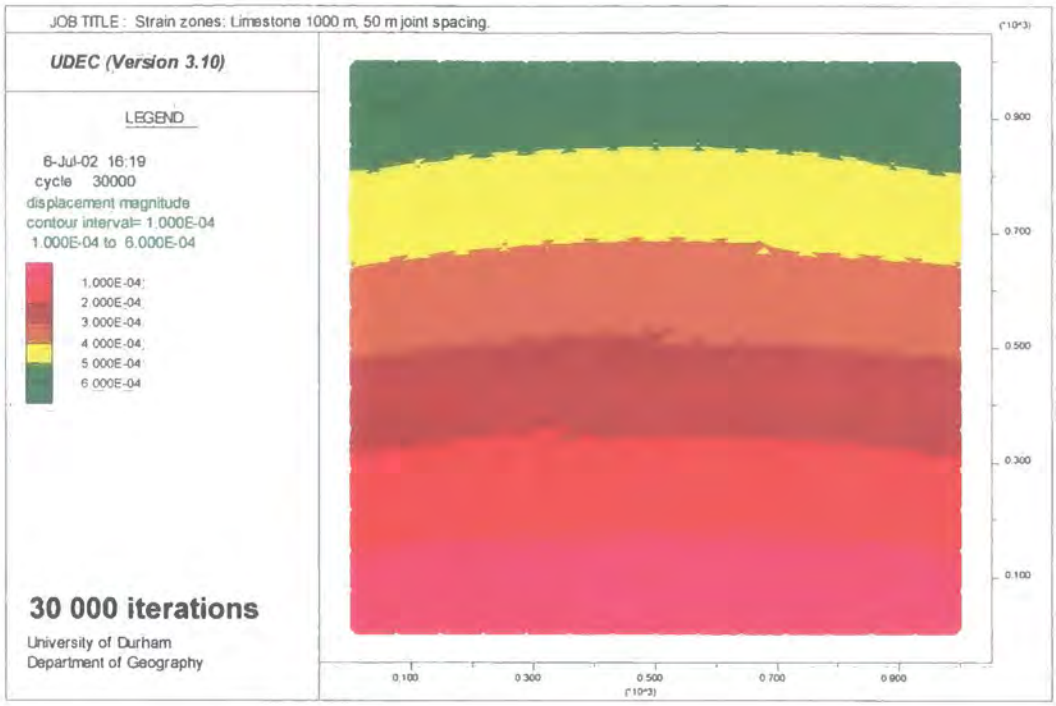

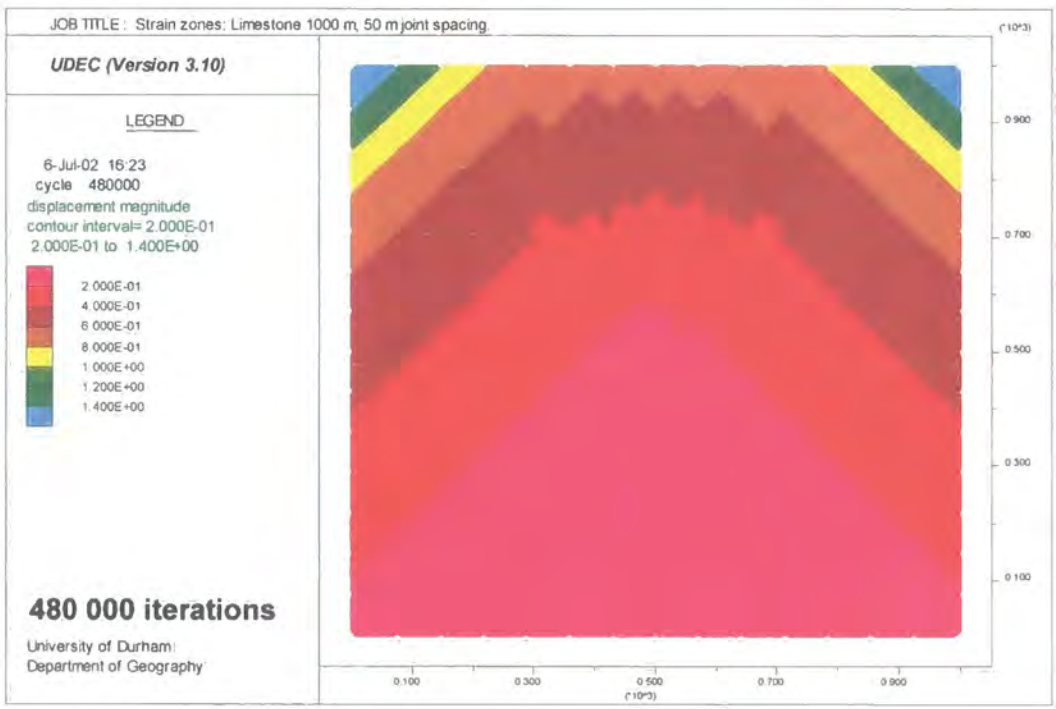

Figure 4.44a: Strain zone development in a 1000 m limestone rock mass with 50 m block size.

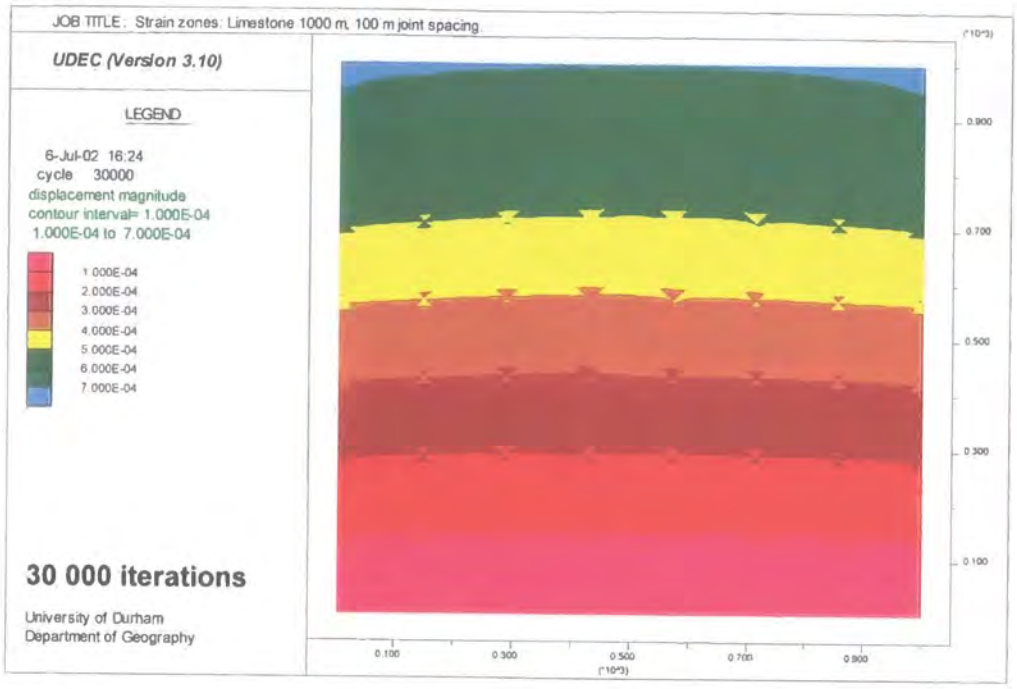

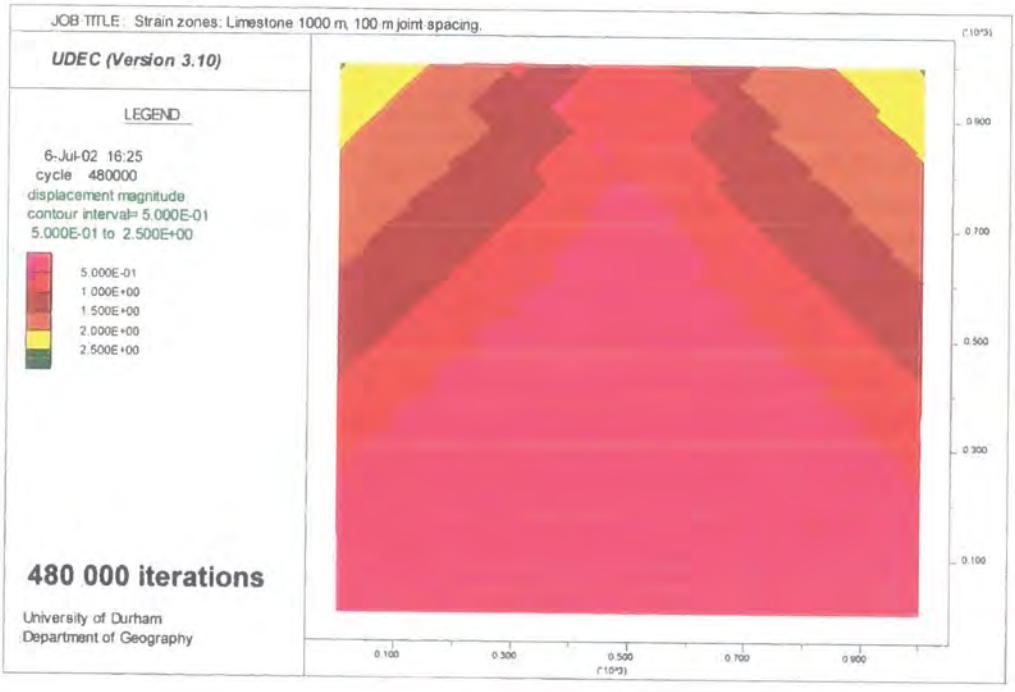

Figure 4.44b: Strain zone development in a 1000 m limestone rock mass with 100 m block size.

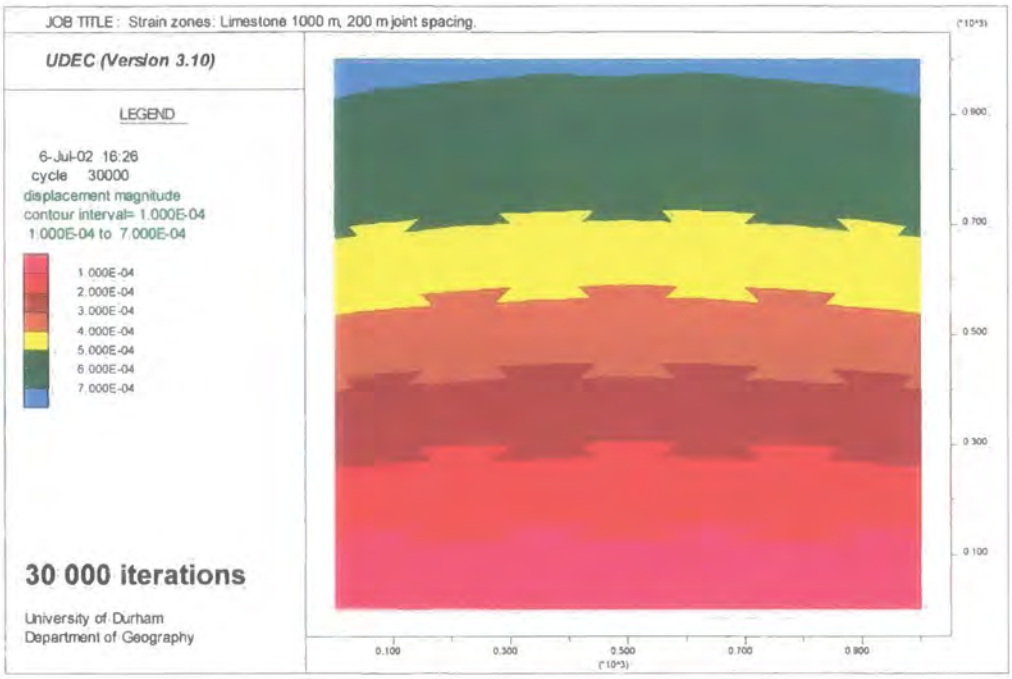

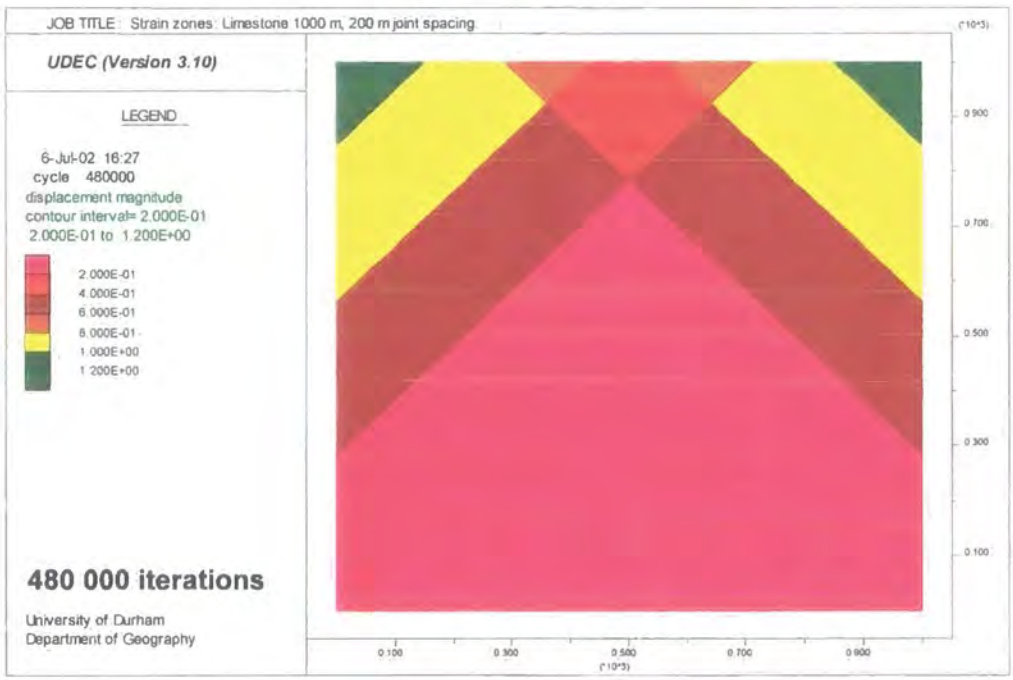

Figure 4.44c: Strain zone development in a 1000 m limestone rock mass with 200 m block size.

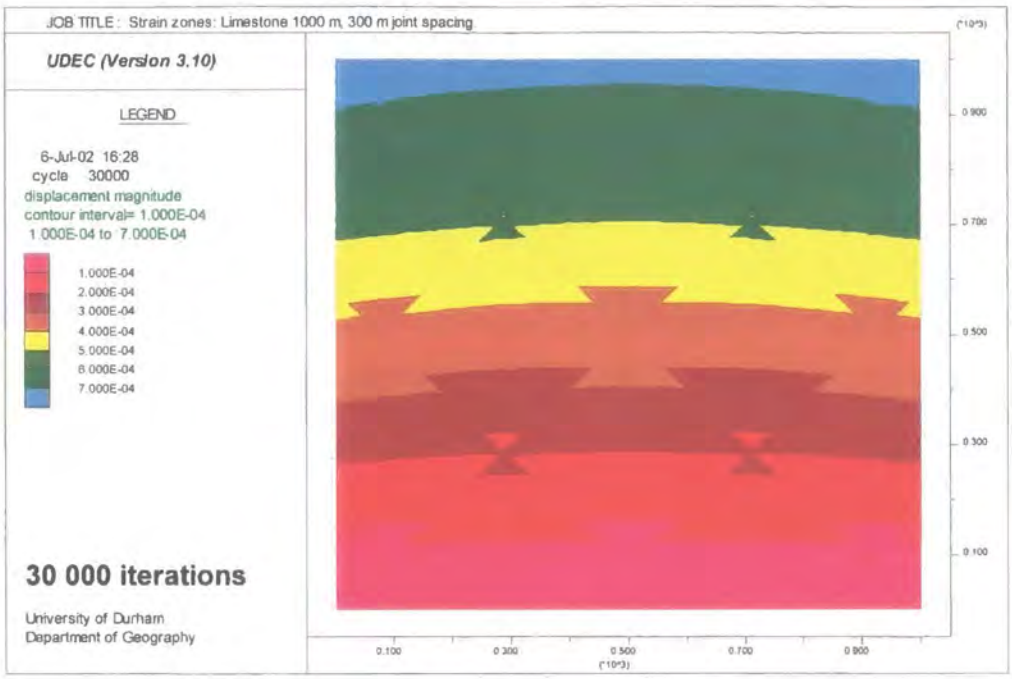

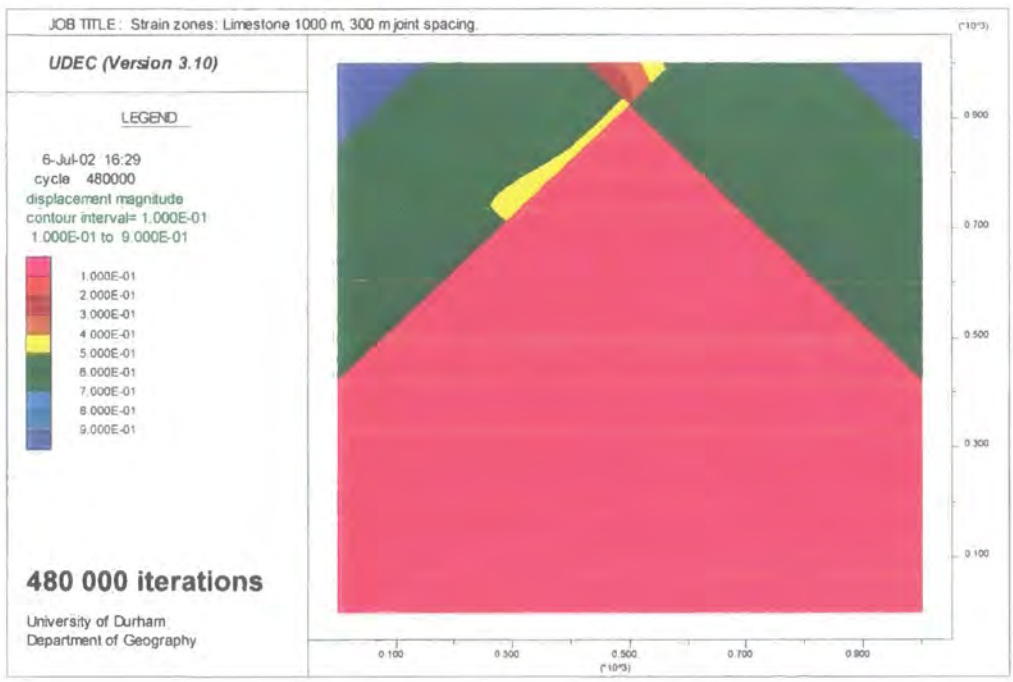

Figure 4.44d: Strain zone development in a 1000 m limestone rock mass with 300 m block size.

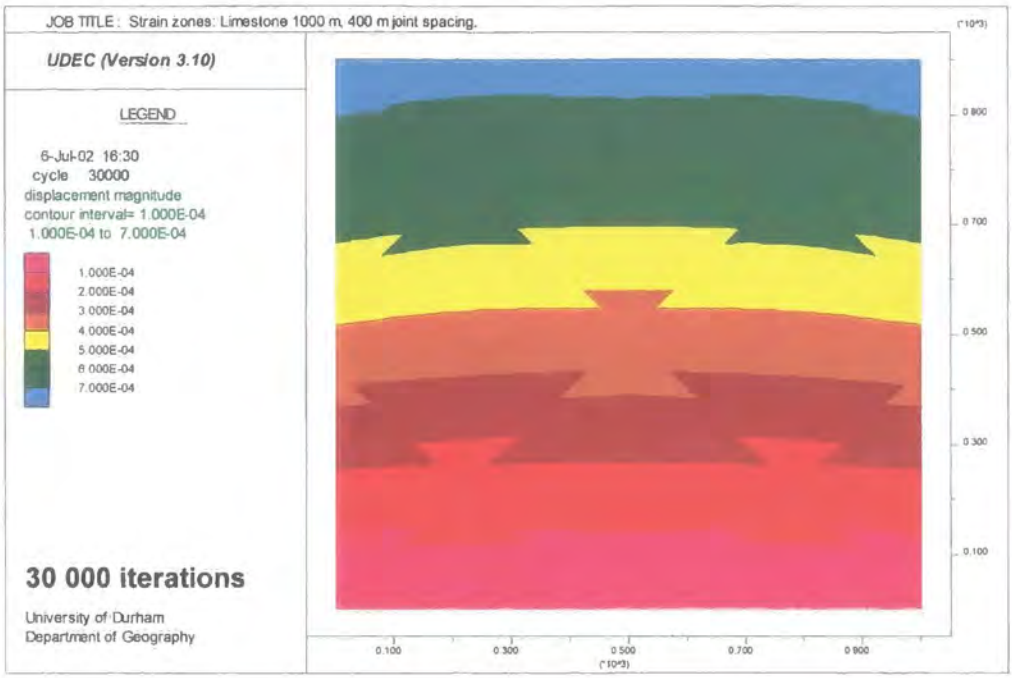

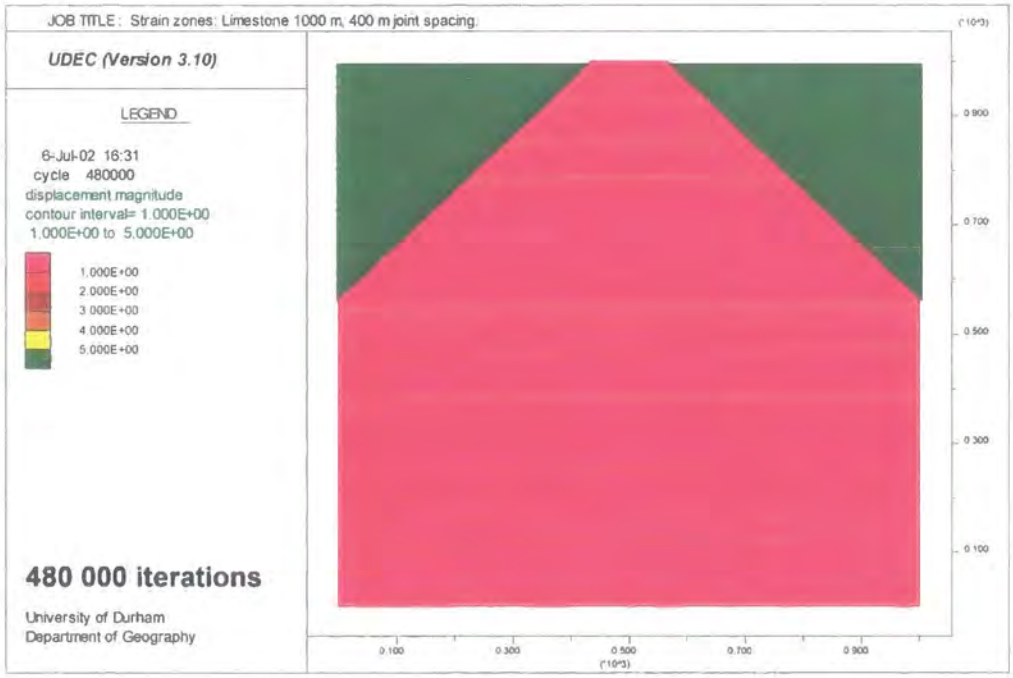

Figure 4.44e: Strain zone development in a 1000 m limestone rock mass with 400 m block size.

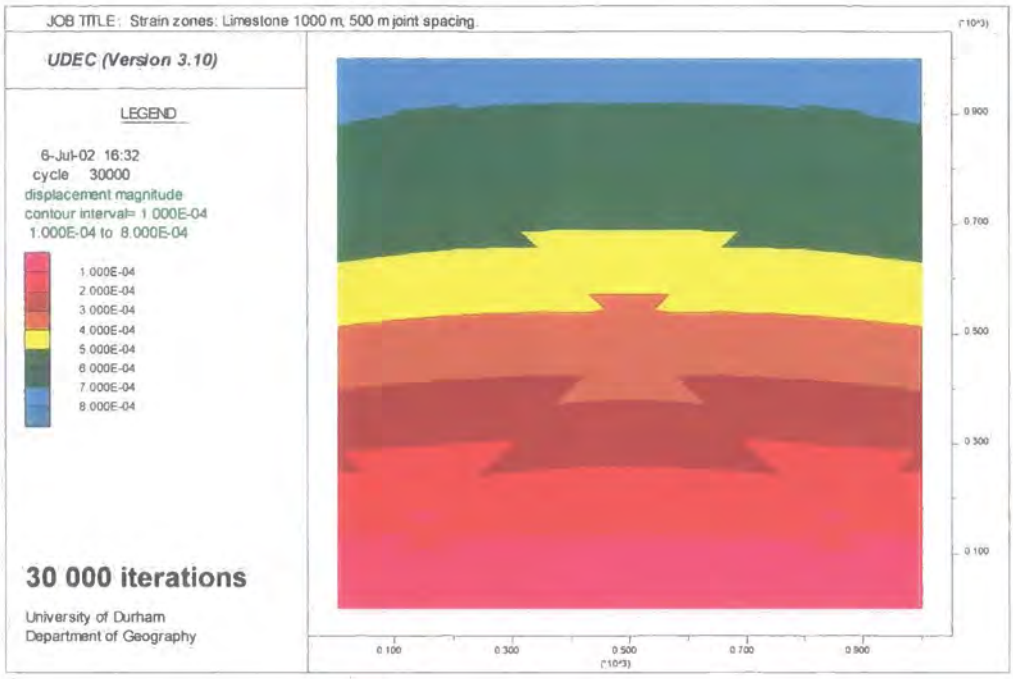

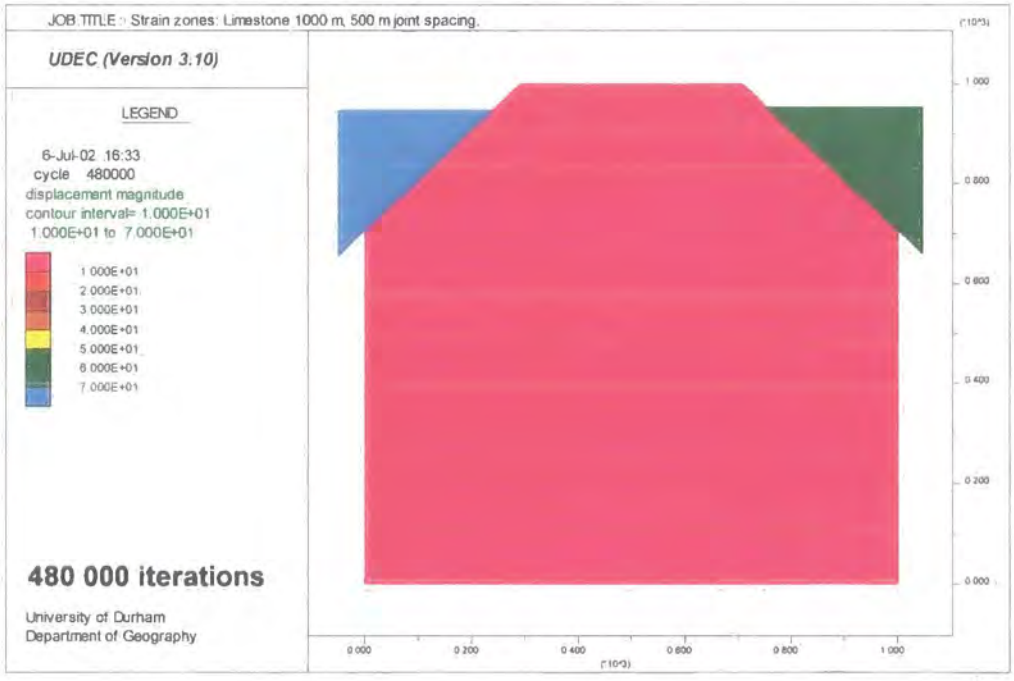

Figure 4.44f: Strain zone development in a 1000 m limestone rock mass with 500 m block size.

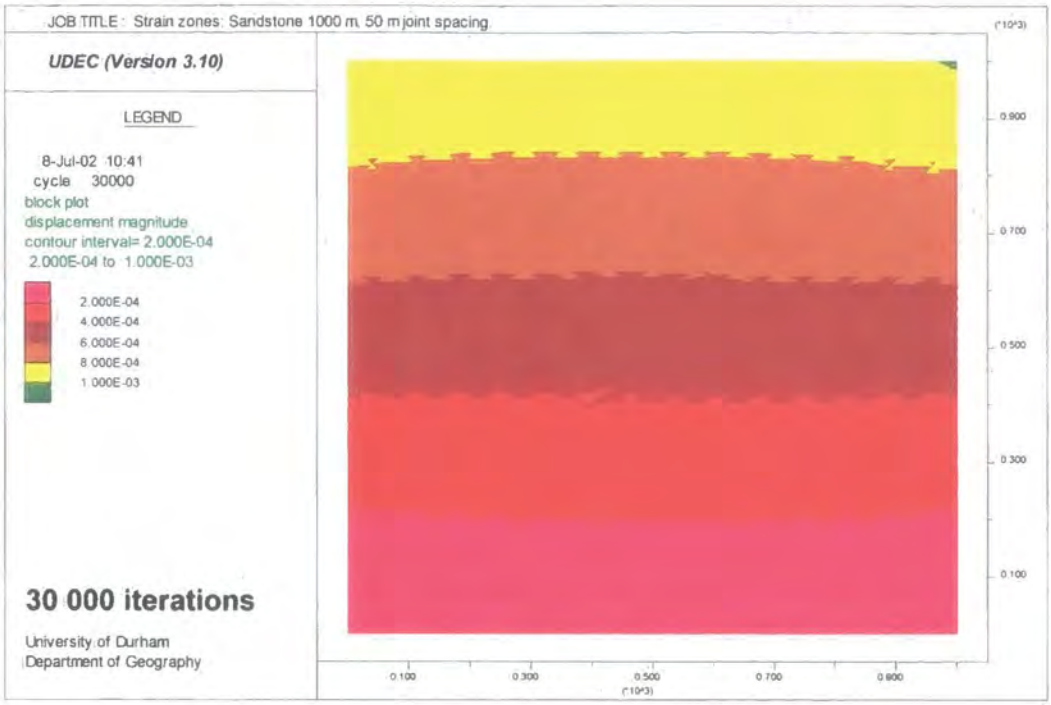

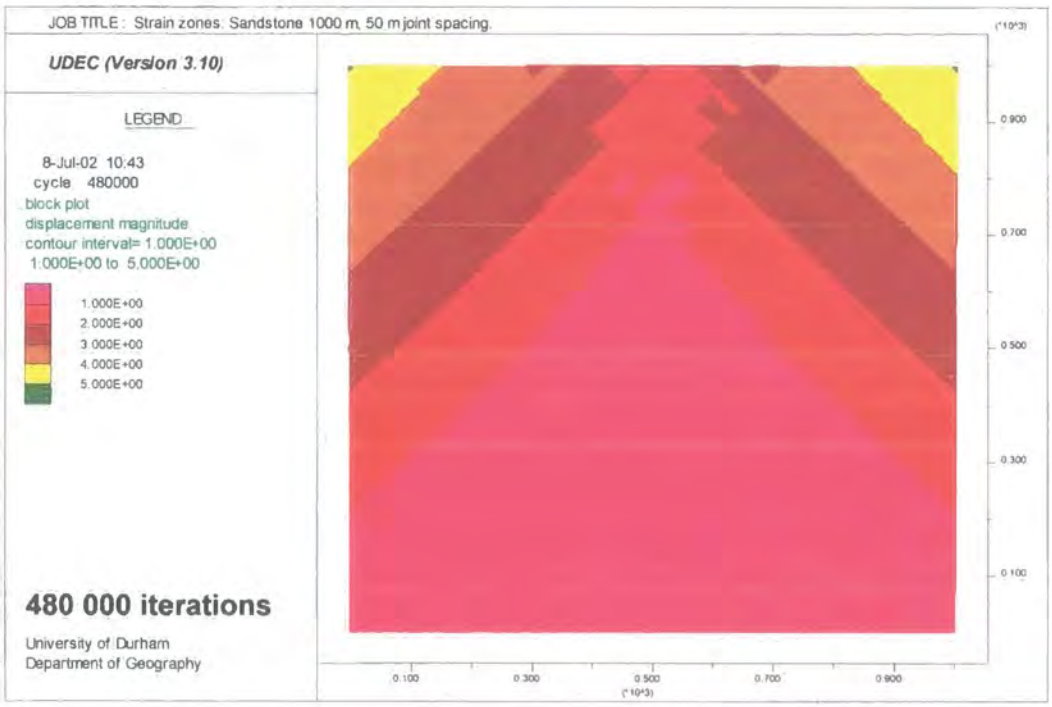

Figure 4.45a: Strain zone development in a 1000 m sandstone rock mass with 50 m block size.

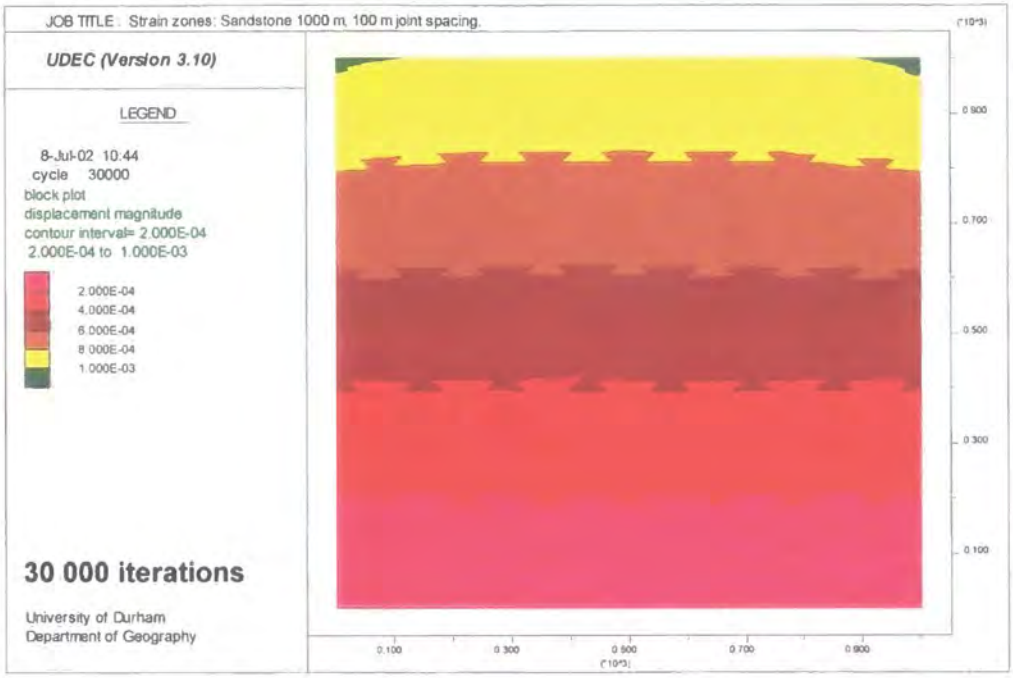

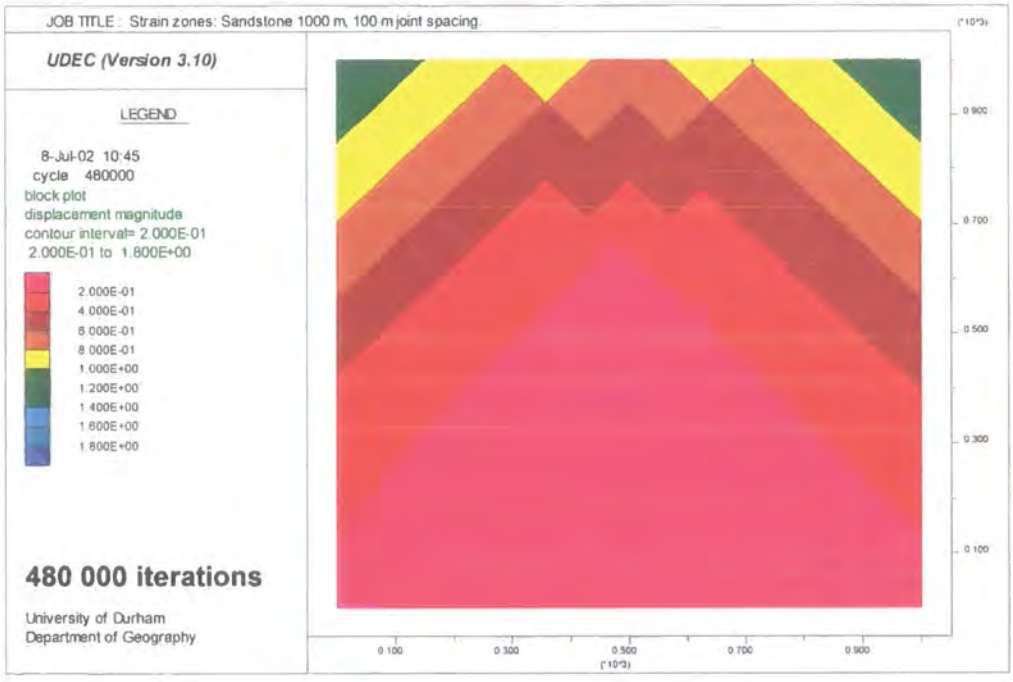

Figure 4.45b: Strain zone development in a 1000 m sandstone rock mass with 100 m block size.

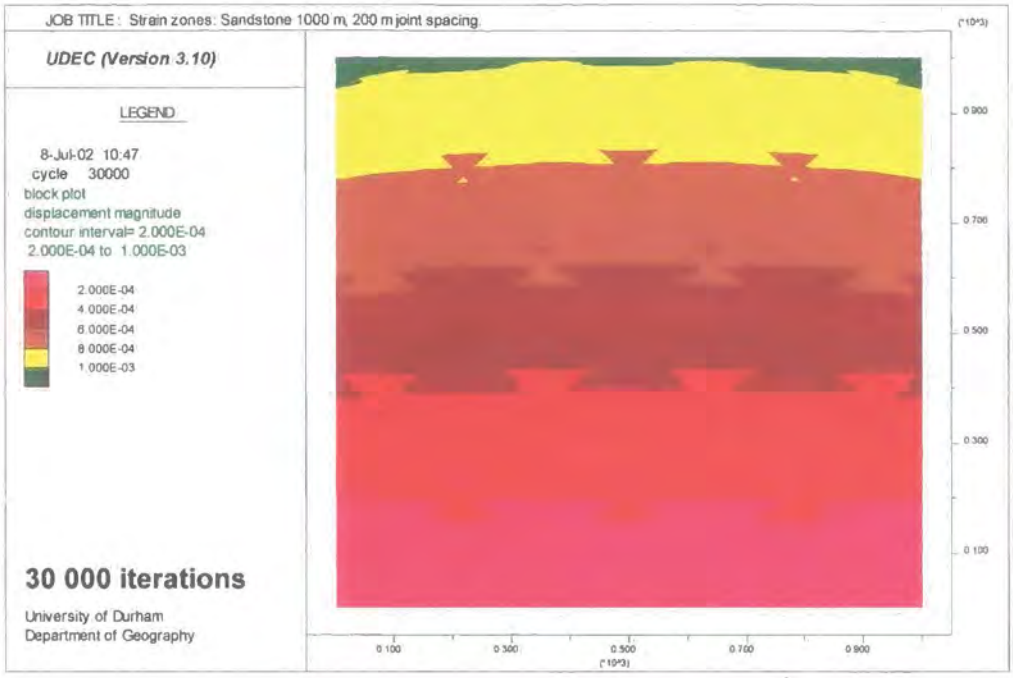

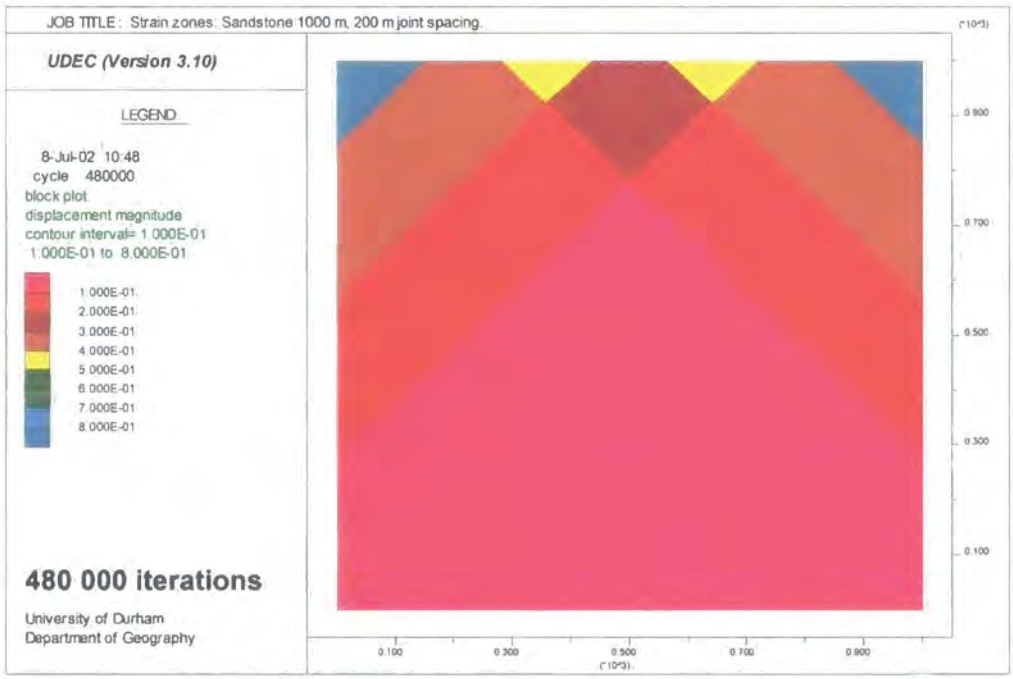

Figure 4.45c: Strain zone development in a 1000 m sandstone rock mass with 50 m block size.

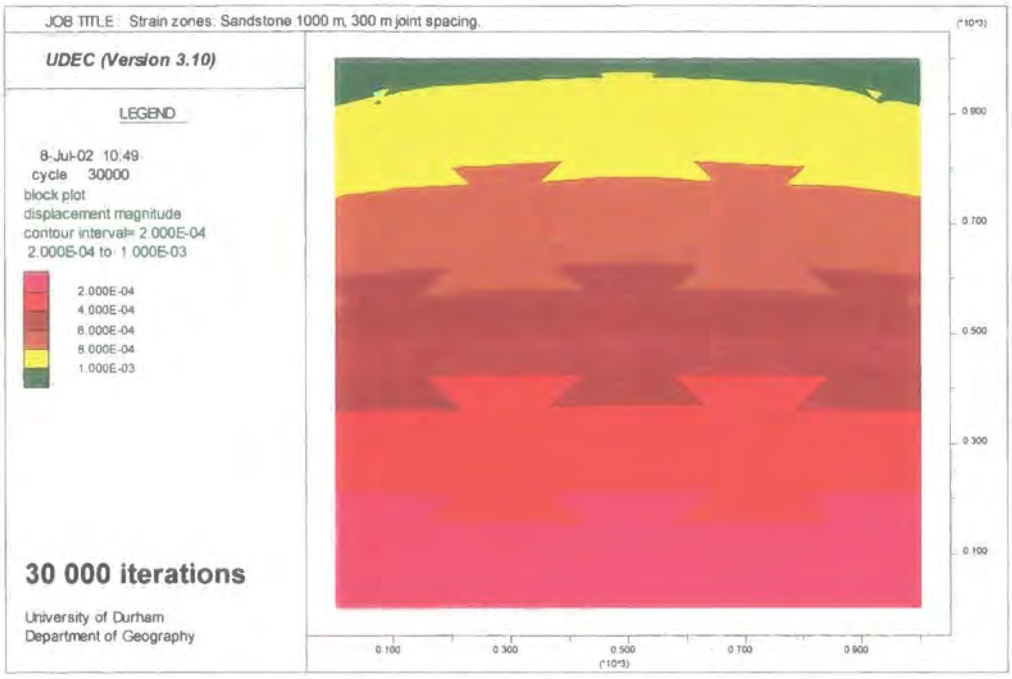

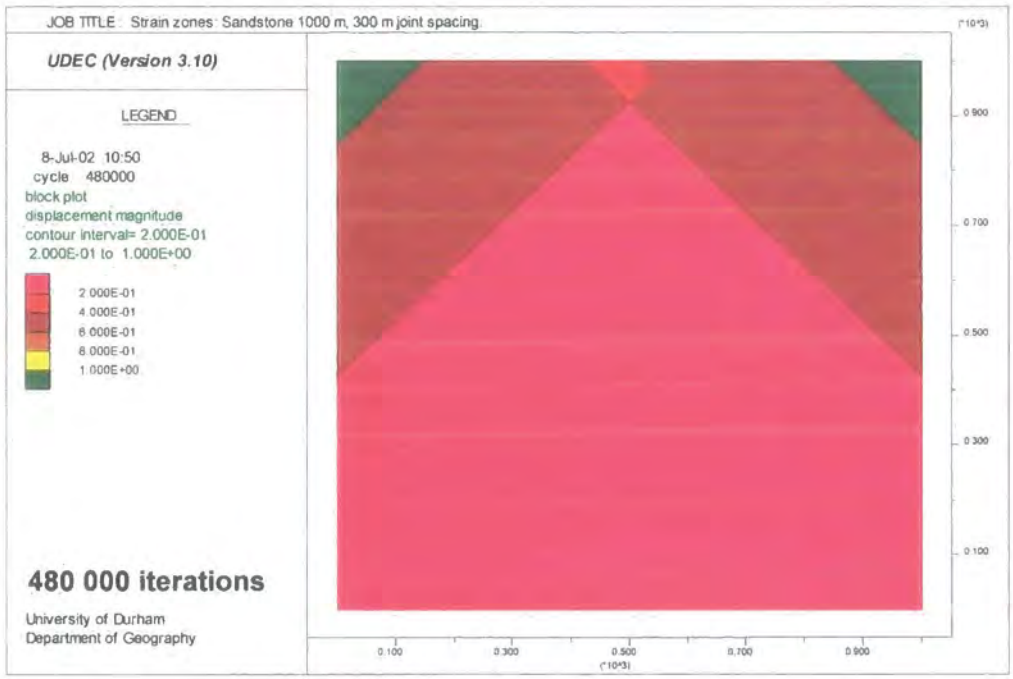

Figure 4.45d: Strain zone development in a 1000 m sandstone rock mass with 300 m block size.

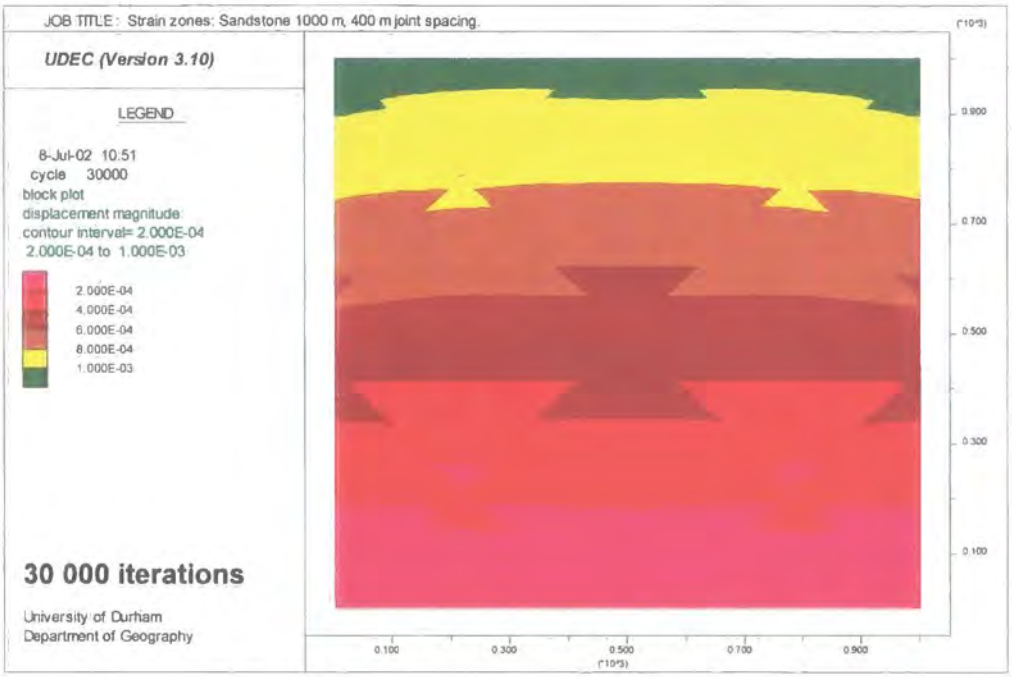

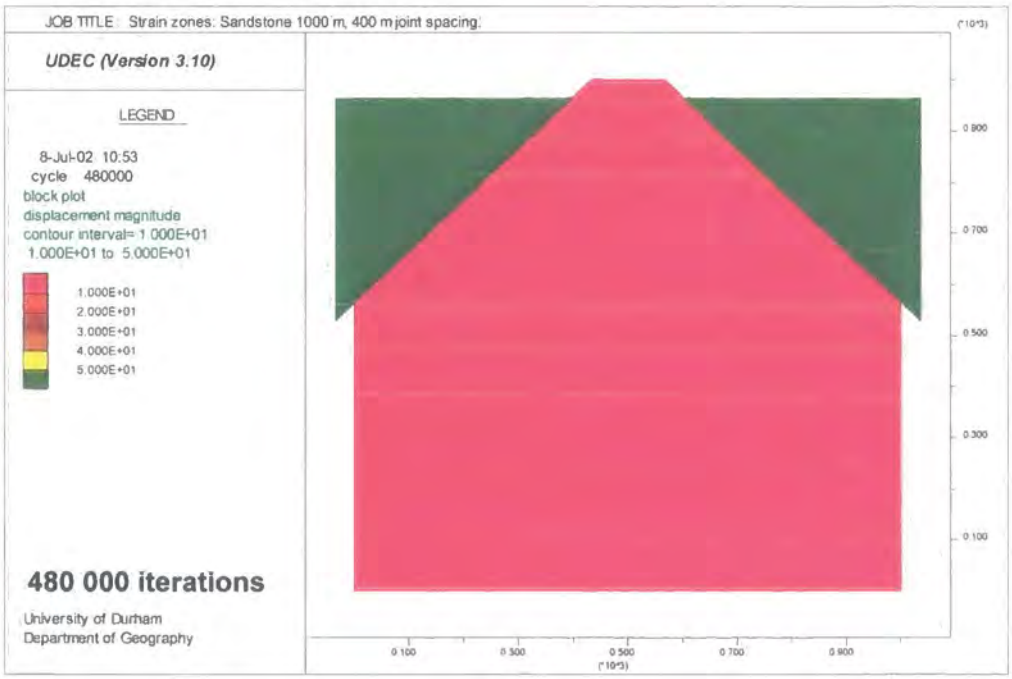

Figure 4.45e: Strain zone development in a 1000 m sandstone rock mass with 400 m block size.

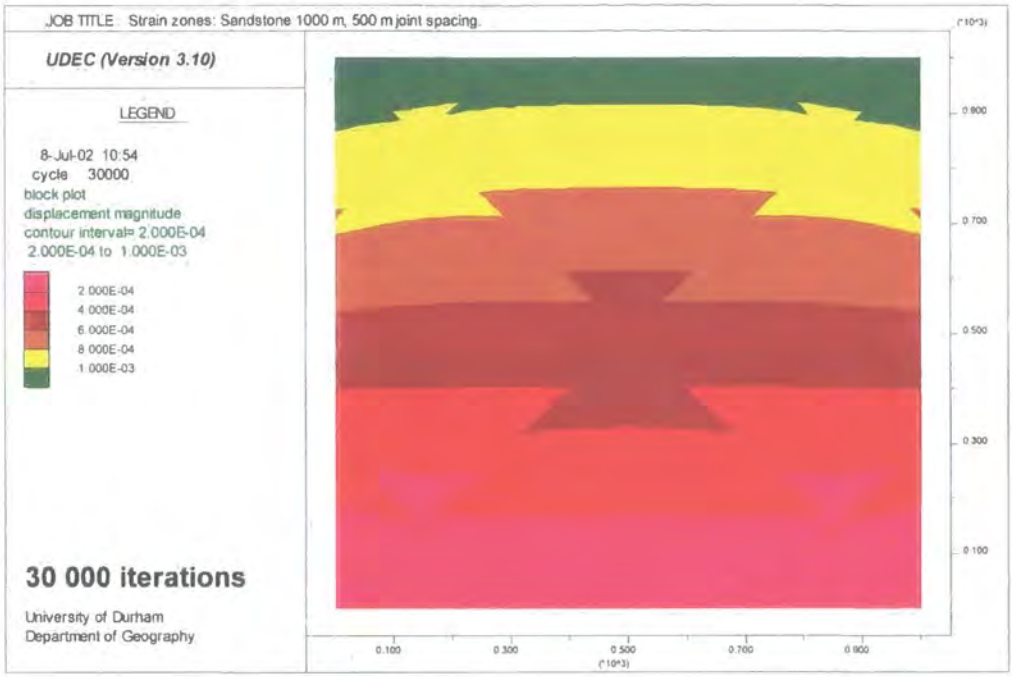

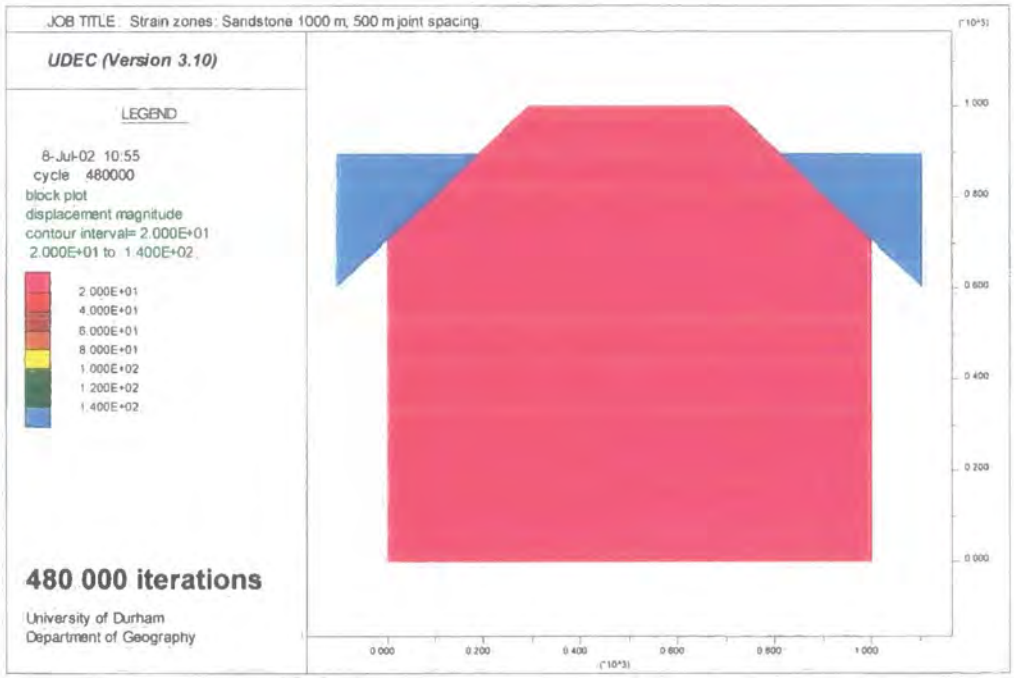

Figure 4.45f: Strain zone development in a 1000 m sandstone rock mass with 500 m block size.

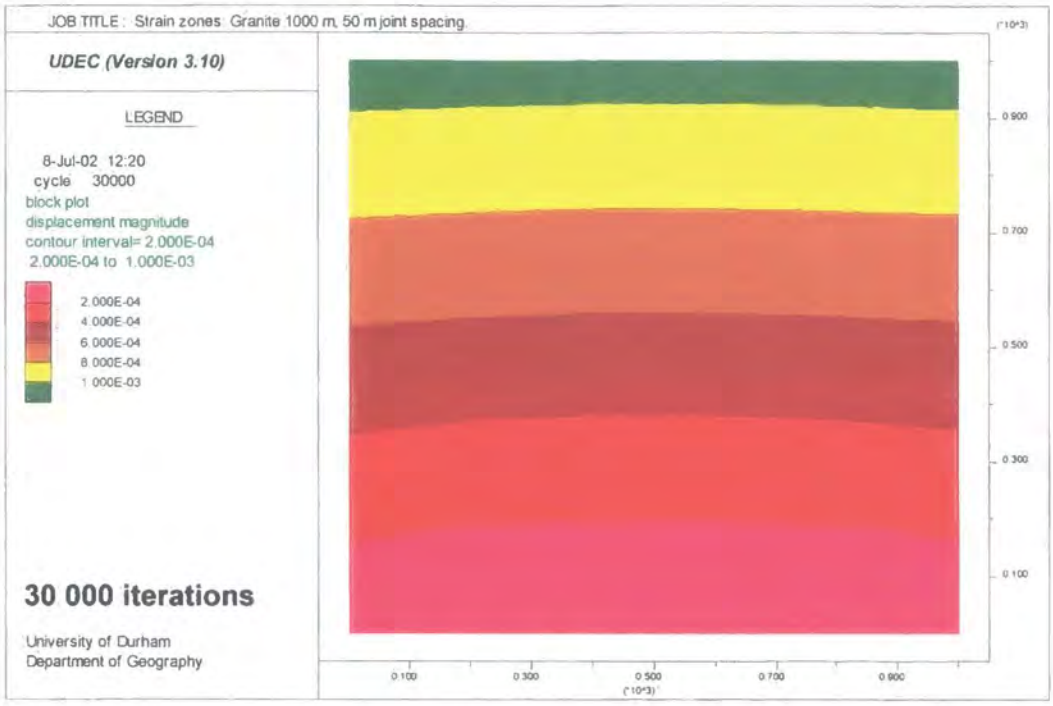

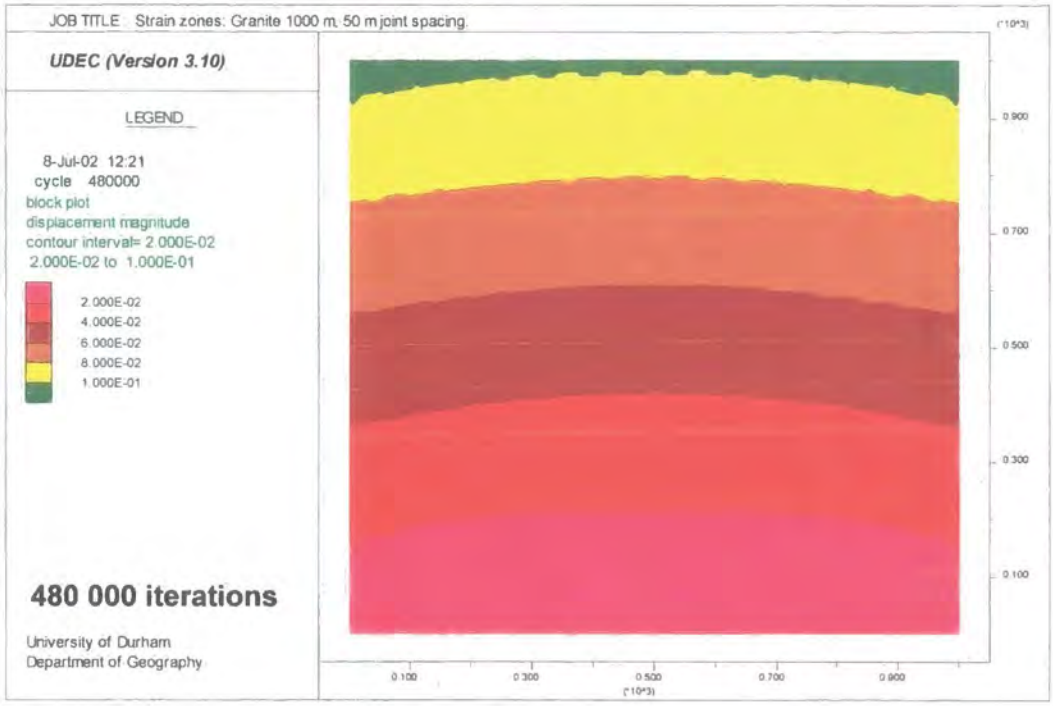

Figure 4.46a: Strain zone development in a 1000 m granite rock mass with 50 m block size.

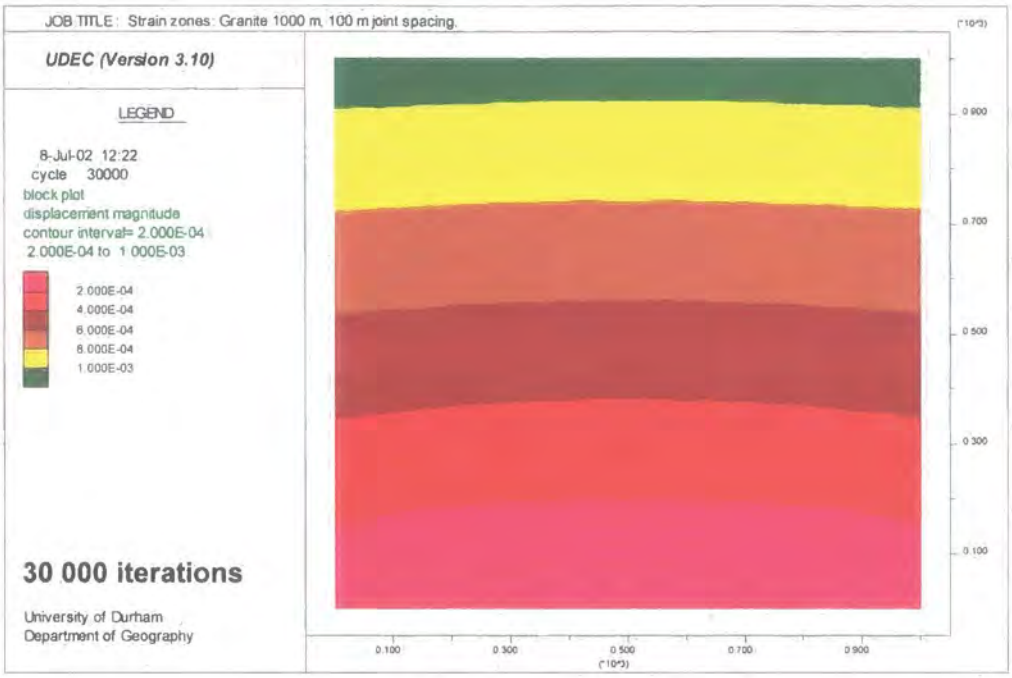

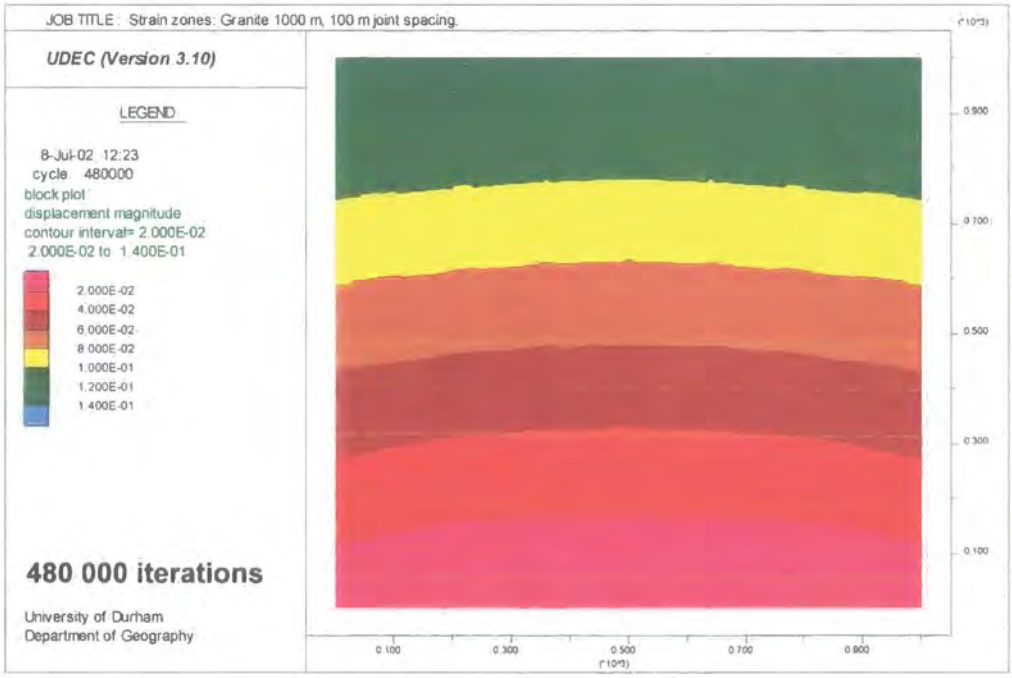

Figure 4.46b: Strain zone development in a 1000 m granite rock mass with 100 m block size.

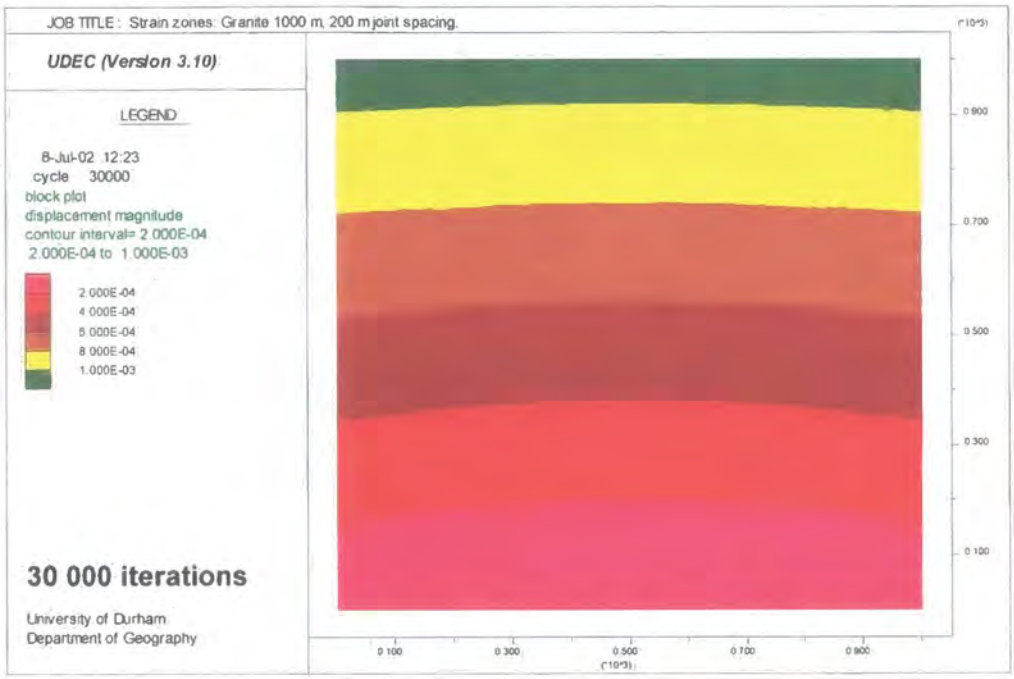

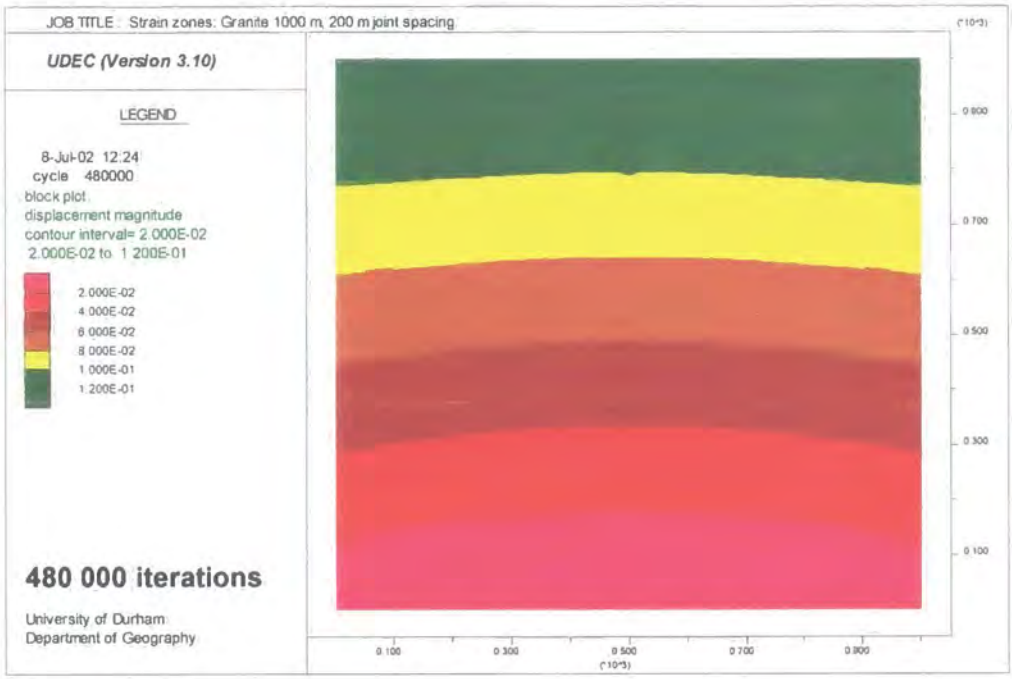

Figure 4.46c: Strain zone development in a 1000 m granite rock mass with 200 m block size.

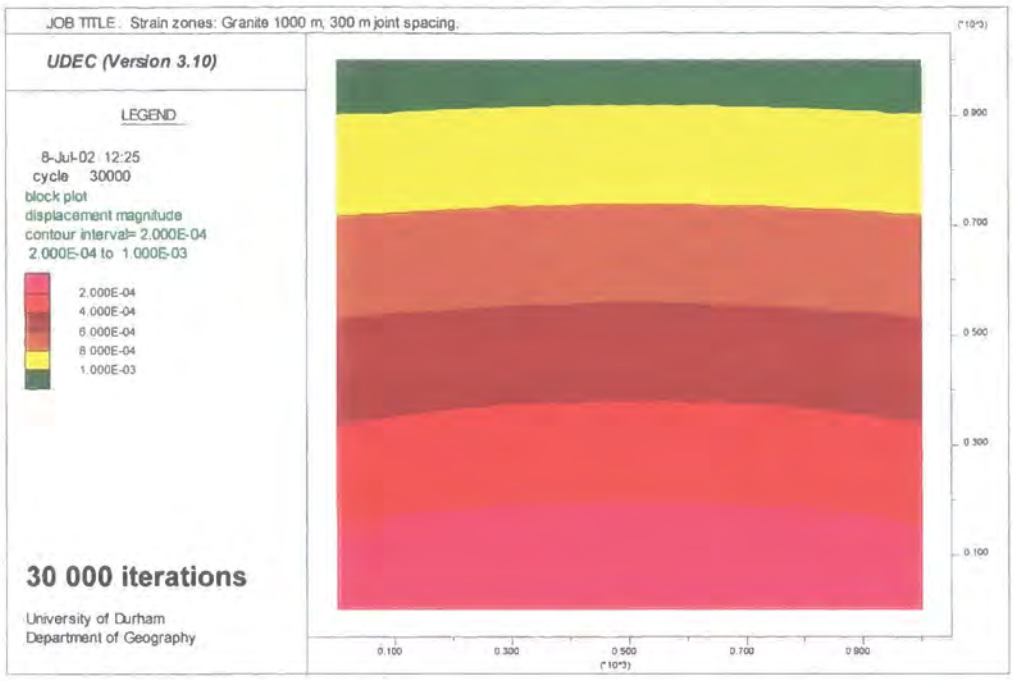

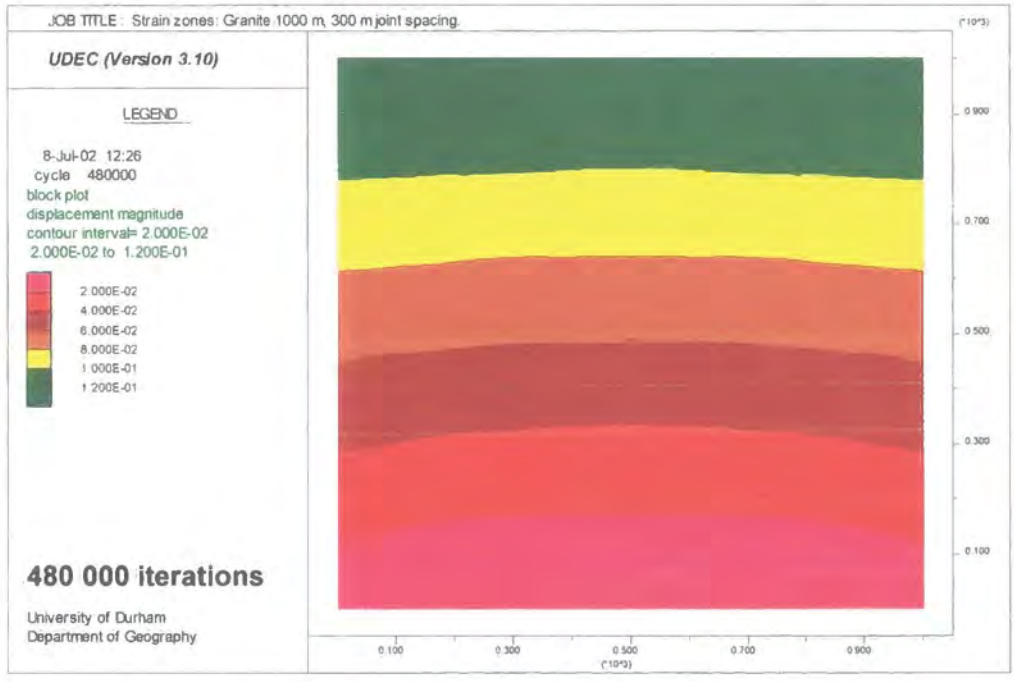

Figure 4.46d: Strain zone development in a 1000 m granite rock mass with 300 m block size.

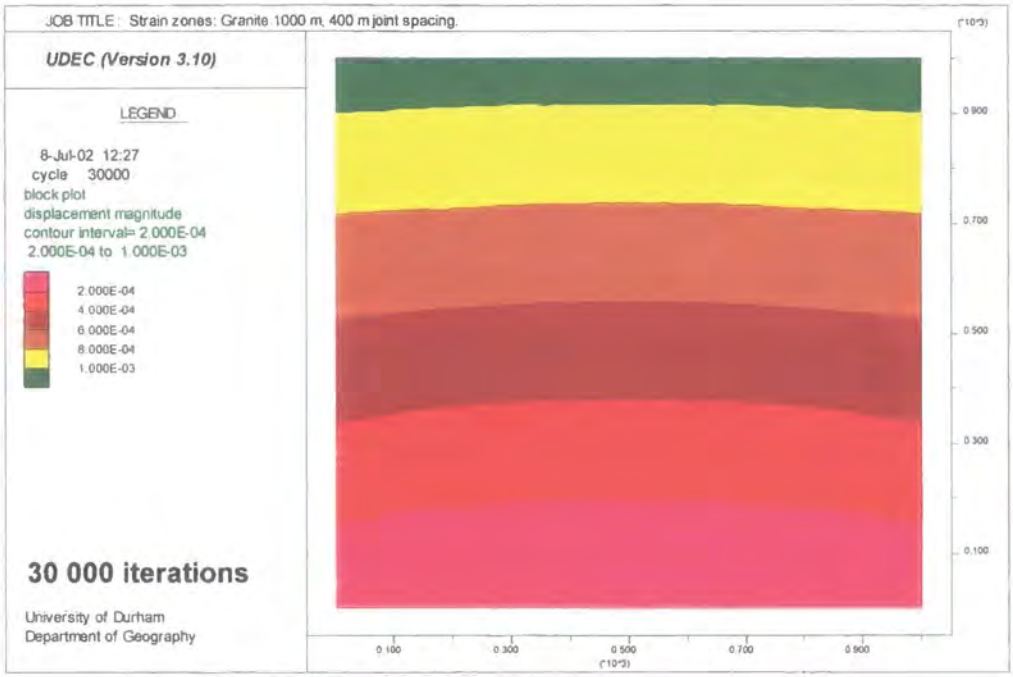

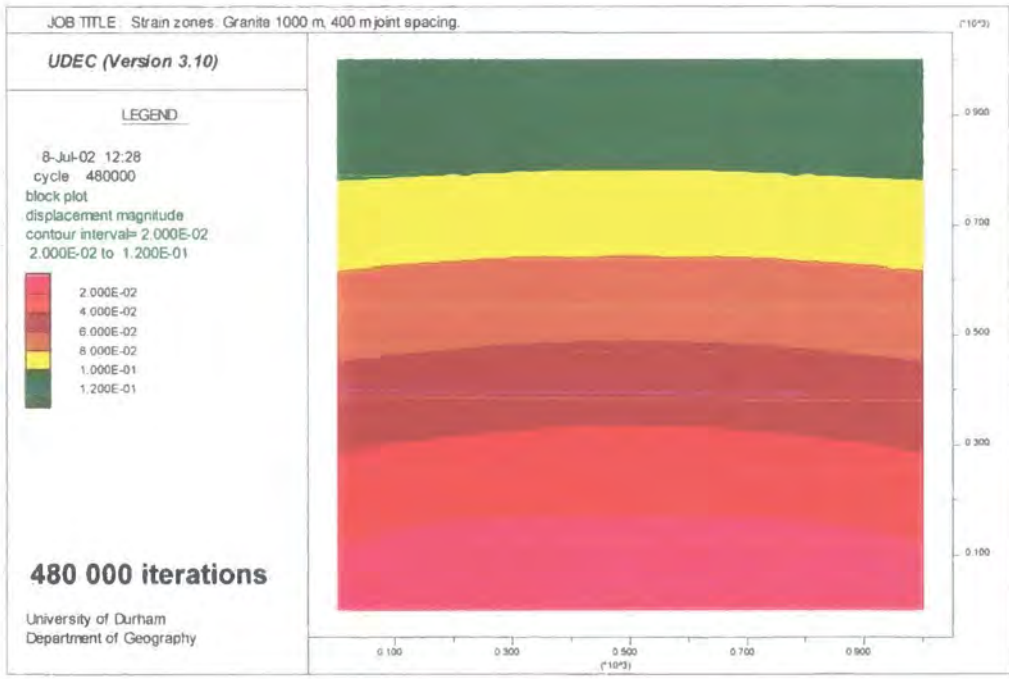

Figure 4.46e: Strain zone development in a 1000 m granite rock mass with 400 m block size.

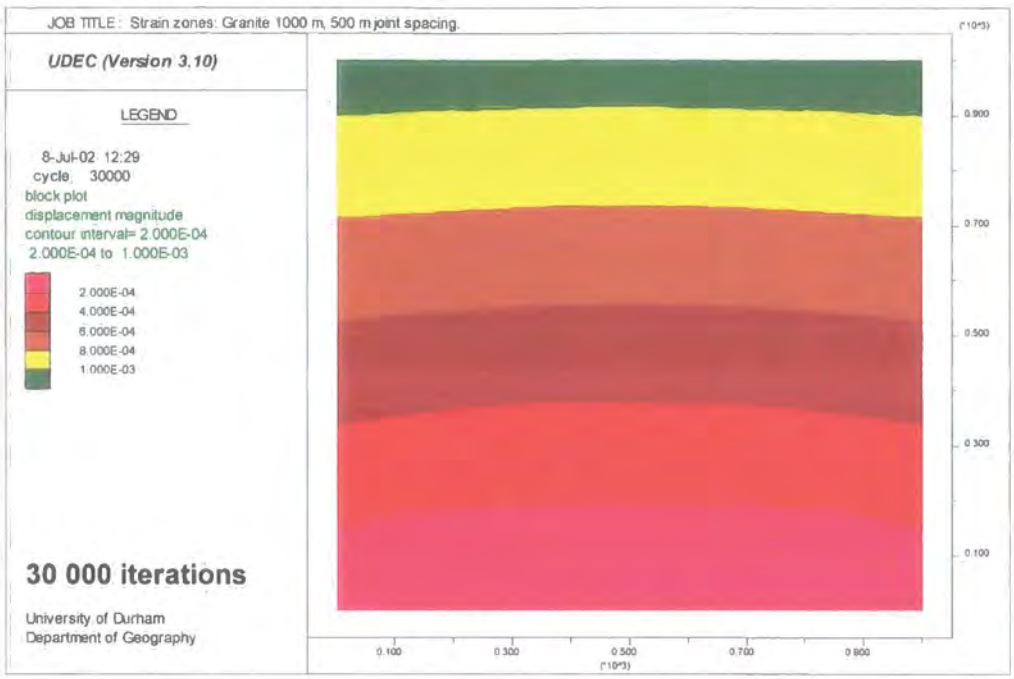

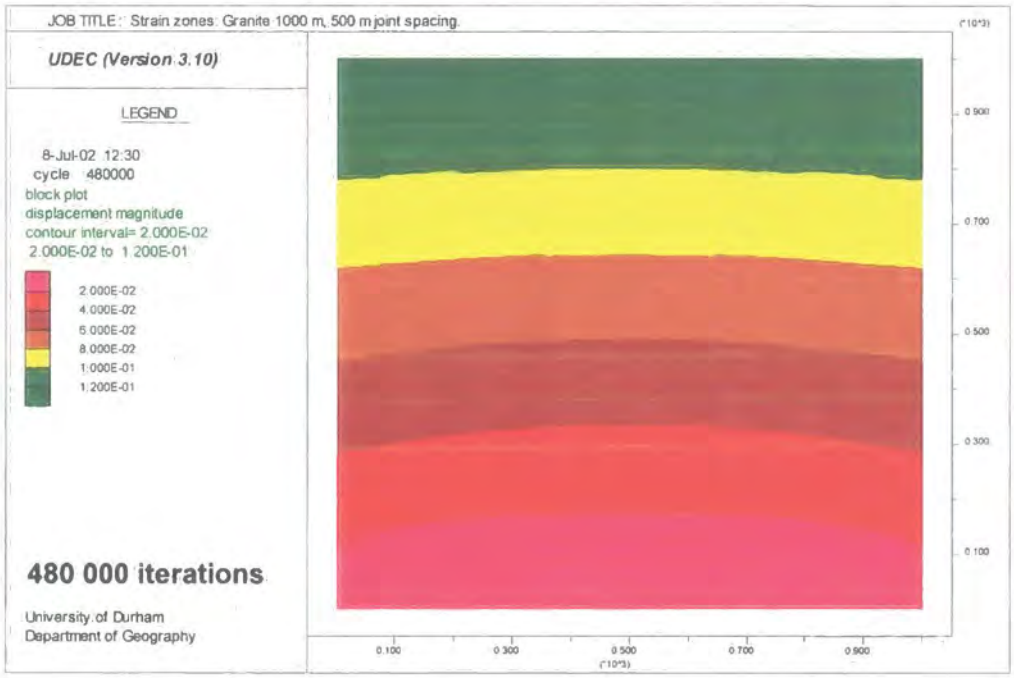

Figure 4.46f: Strain zone development in a 1000 m granite rock mass with 500 m block size.

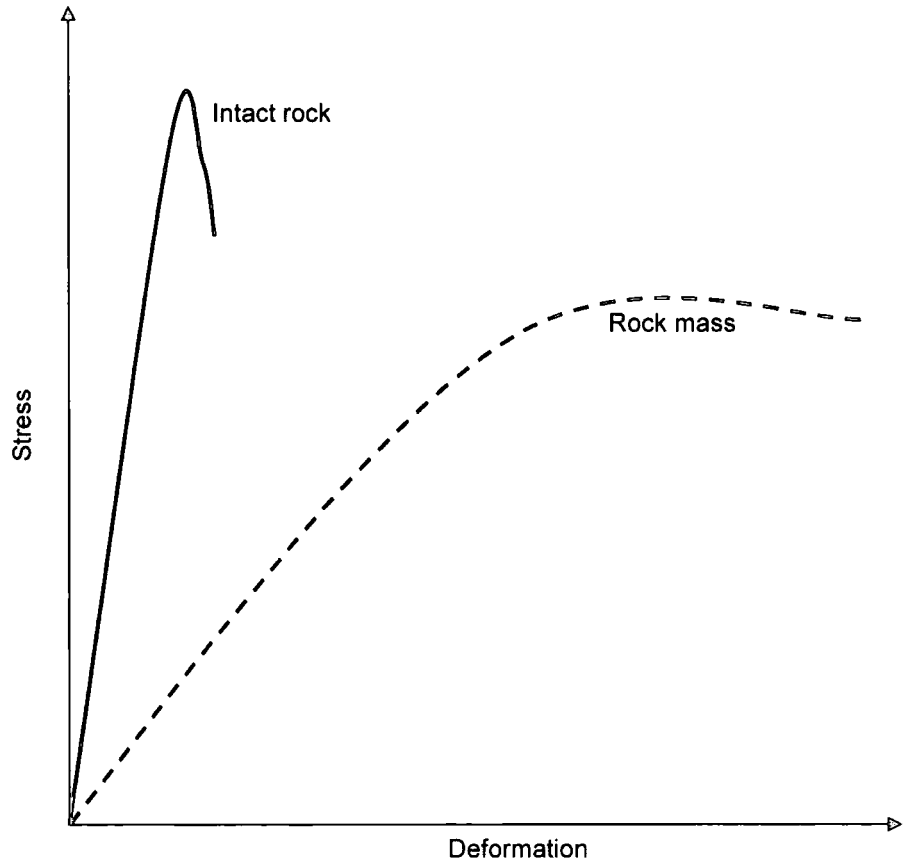

Figure 4.47: The stress-strain response of a rock mass compared to that commonly seen for intact rock.

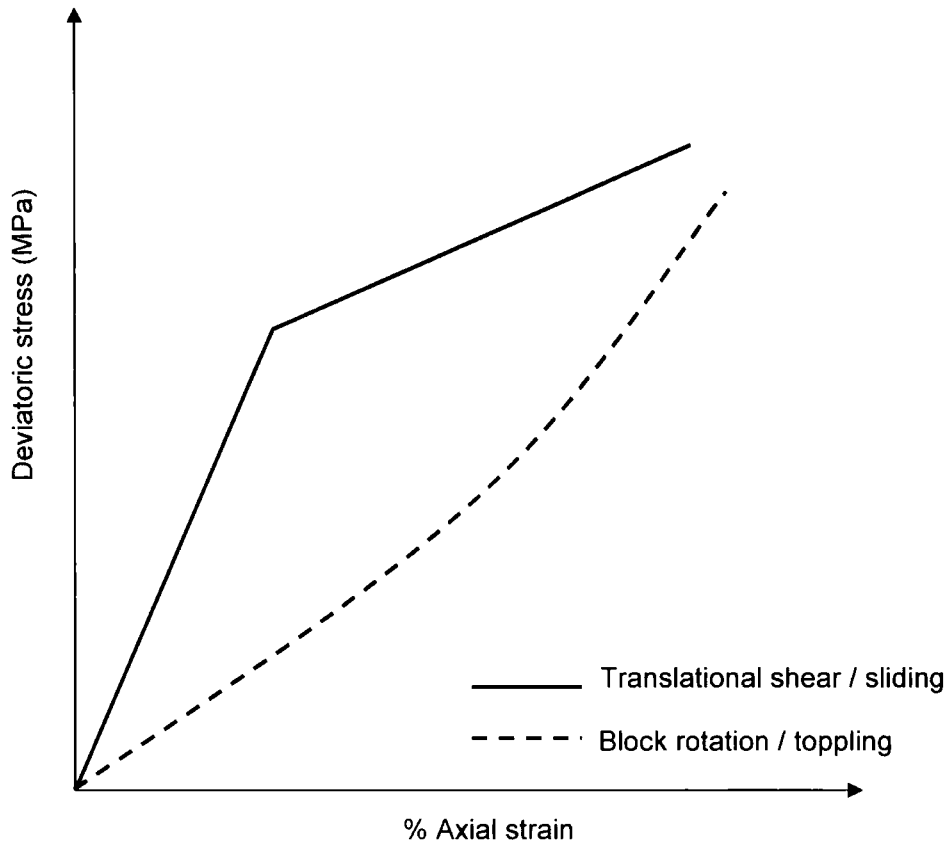

Figure 4.48: Summary stress-strain response of the two failure mechanisms which develop due to block size effects in the simulated rock masses.

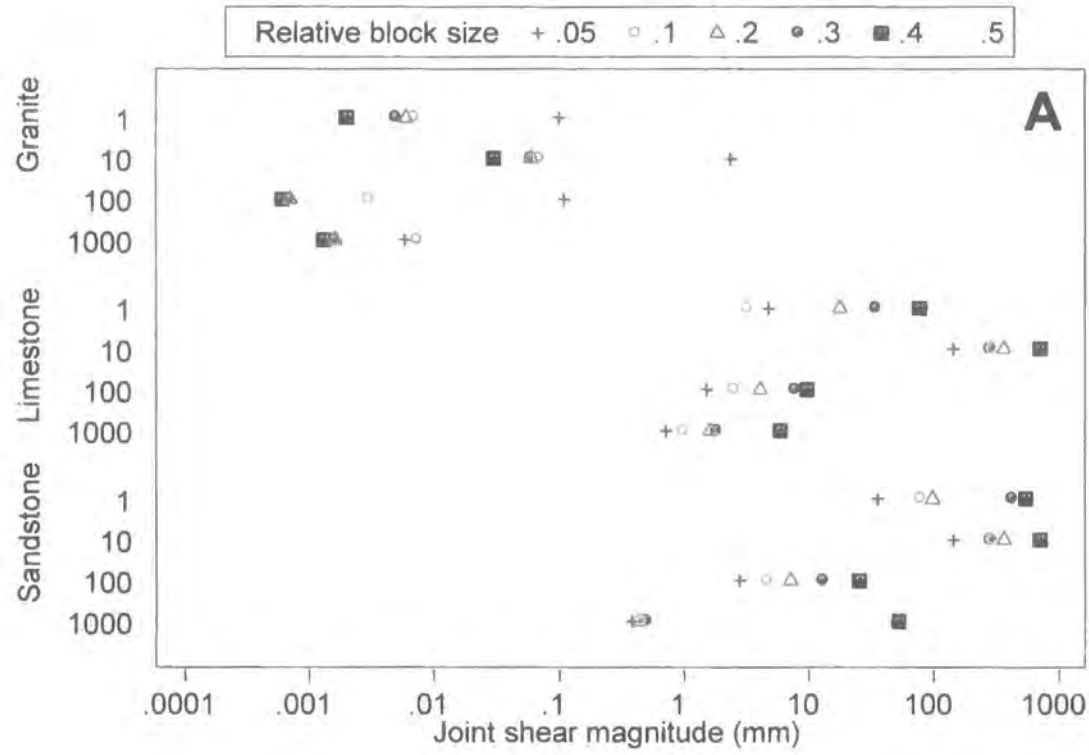

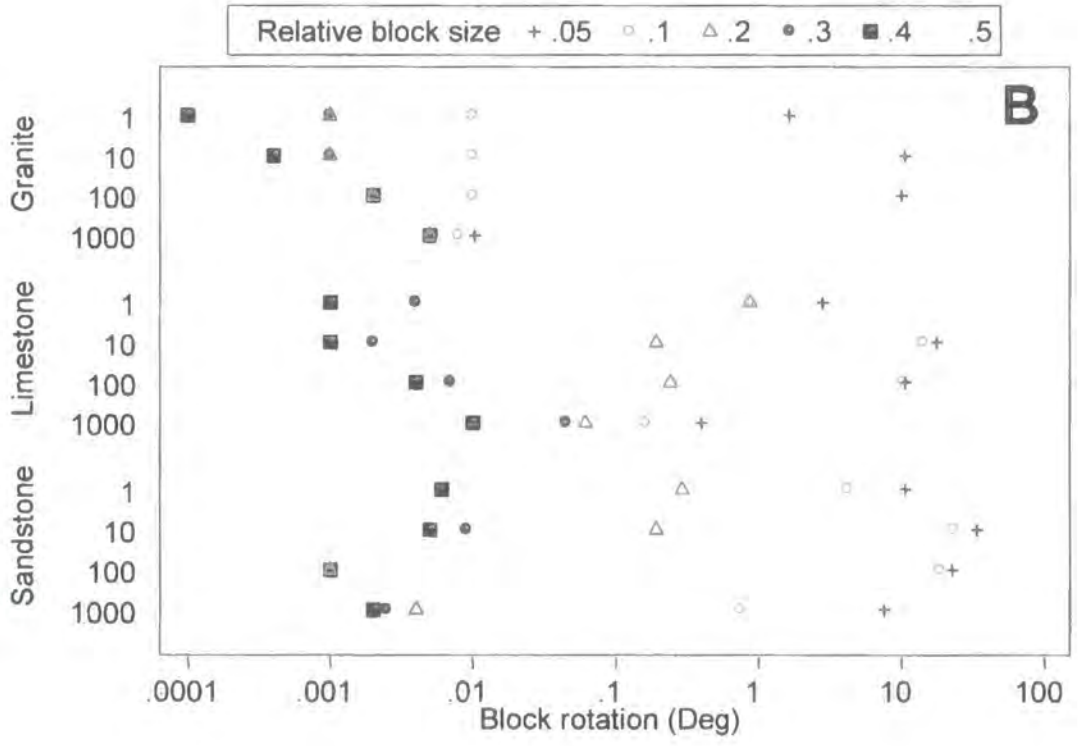

Figure 4.49: Comparison of joint shear magnitude for all scales and all lithologies (a). Block rotation magnitude for all scales and lithologies (b).

Simulated rock mass	Proposed slope form	Deformation / failure mode	Identifying characteristics	Rock mass characteristics	Failure mode	Examples
		Translational shear	High vertical cliffs enhanced by brittle failure.	Widely spaced joints, minimal joint normal closure, high stiffness, low shear strength.	Shear failure along persistent shear surfaces. Wide joint spacing limits depth of deformation	The Vaiont Dam failure, 1963. Large planar / translational slide.
		Translational shear with secondary rotation	Near vertical cliffs, with lower angle free-face.	Medium spaced joints, average joint normal closure, stiffness and shear strength.	Shear and rotation of blocks. Transition from brittle to more time-dependent deformation	Siwalik Hills, Nepal. Sliding and toppling structure. (Tamrakar, *et al.*, 2002).
		Rotation and gradual deformation of slope with minimal shear	Relatively low angle slope profile with concave-convex profile	Closely spaced joints, high degree of joint normal closure, low stiffness, but high shear strength limits shear failure.	Rotation and ductile, time-dependent deformation of the rock mass. Deep-seated deformation pattern.	Ben Lomond, Tasmania (Caine, 1980).

Figure 4.50: Link between theoretical modelling and slope form.

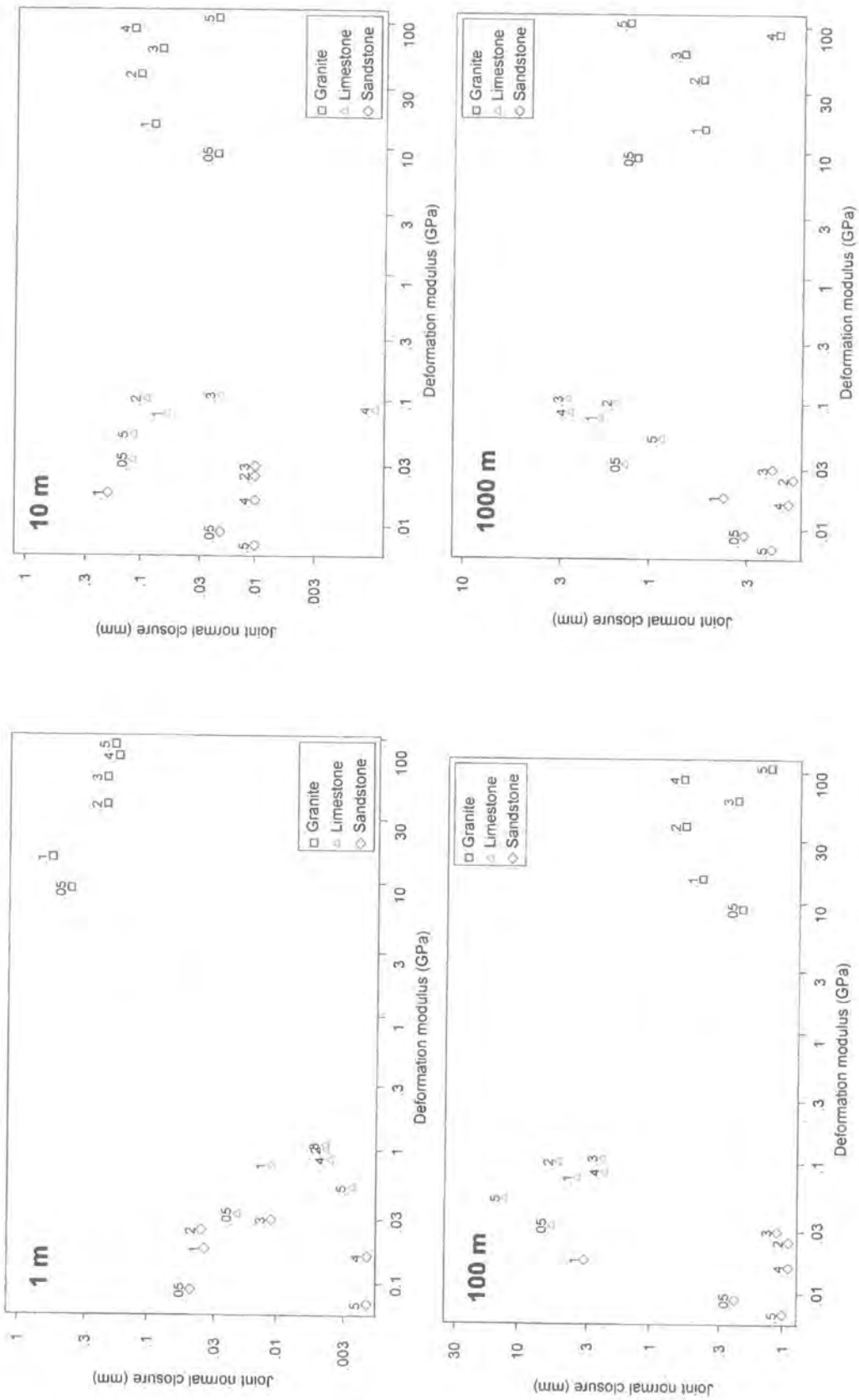

Figure 4.51: Comparison of joint normal closure and deformation modulus for all block sizes and lithologies at a range of outcrop scales.

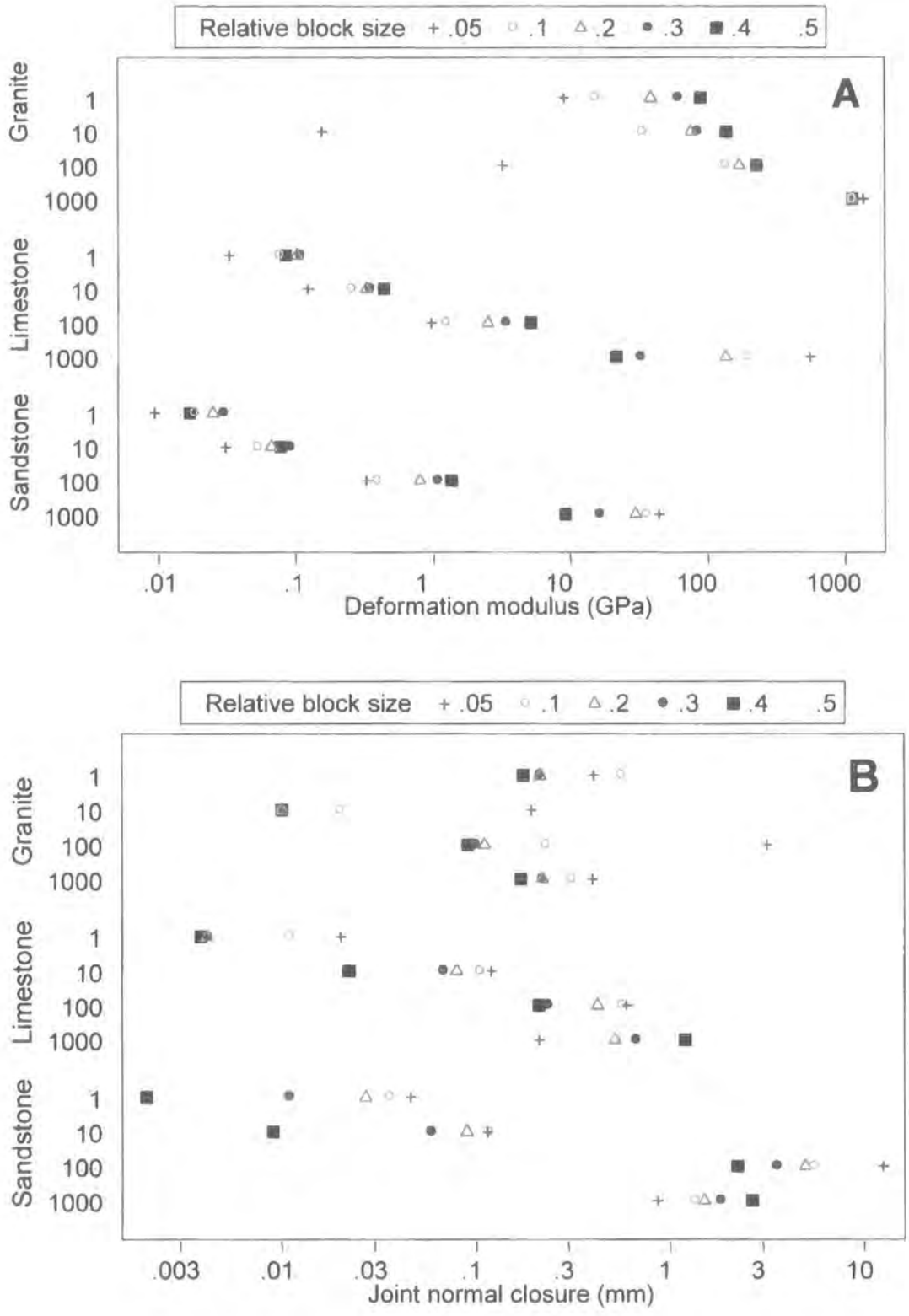

Figure 4.52: Comparison of deformation moduli for all scales and all lithologies (a) and comparison of joint normal closure magnitude for all scales and lithologies (b).

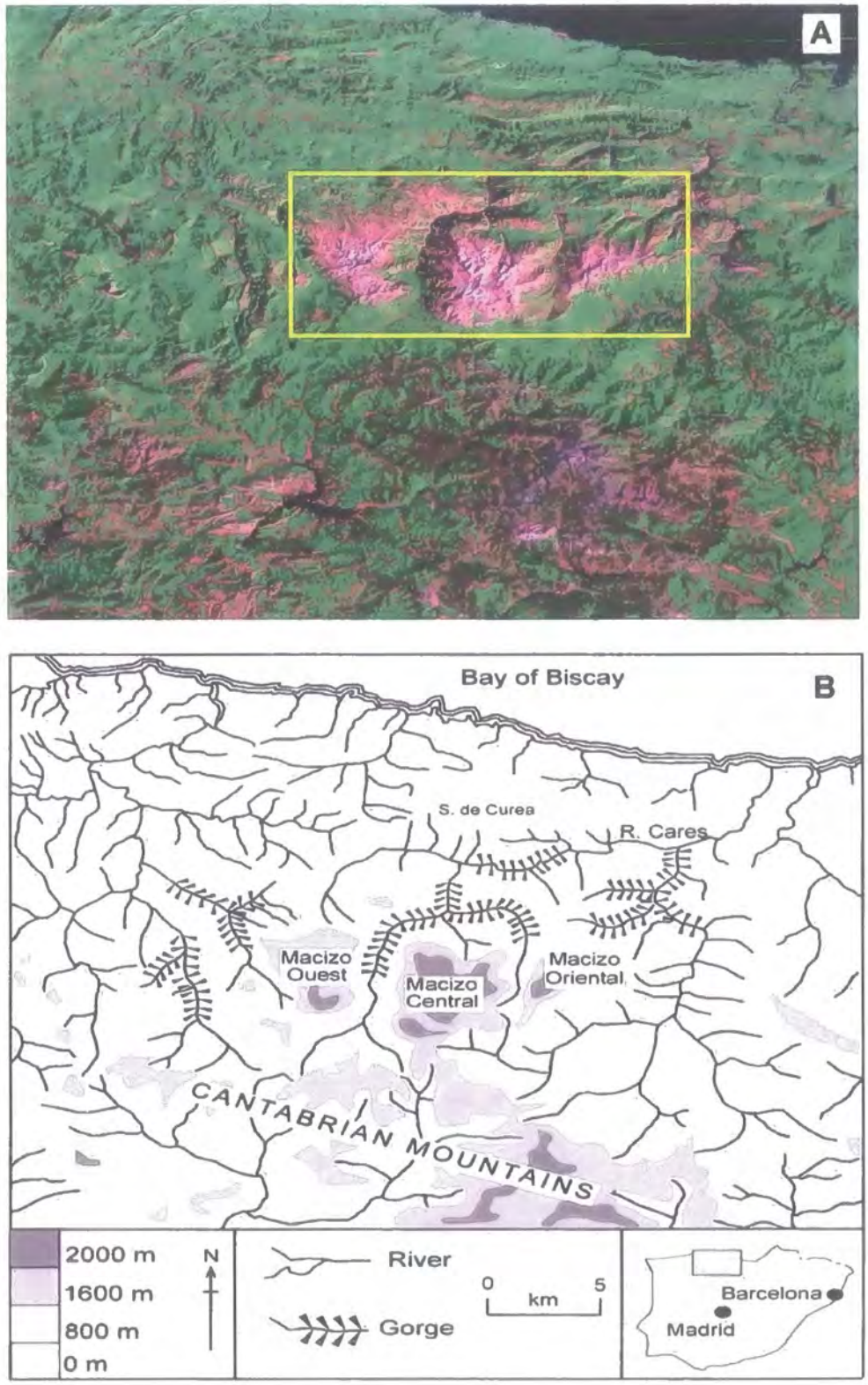

Figure 5.1: (A) Regional topographic and structural situation of the Picos de Europa and relation to the Elsa Nappe Unit (Earthetc, 2004). (B) Topography of the Picos de Europa, northern Spain (Adapted from Smart,1986).

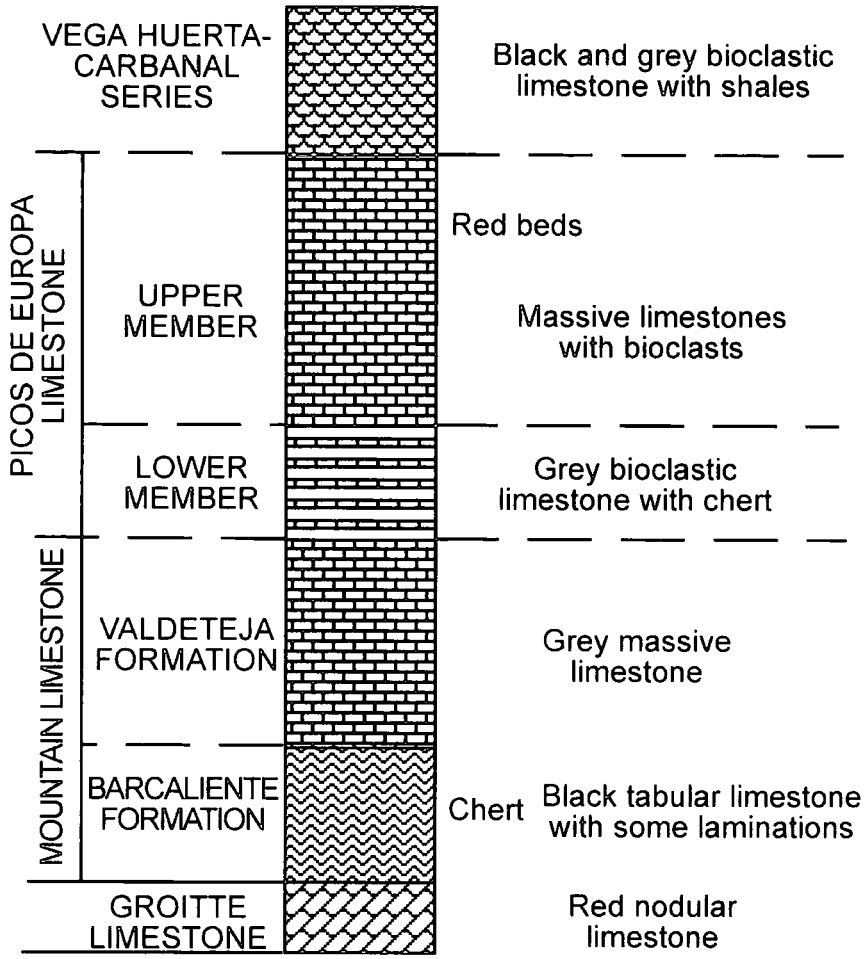

Figure 5.2: The main geological successions found in the Picos de Europa (Adapted from Smart, 1986).

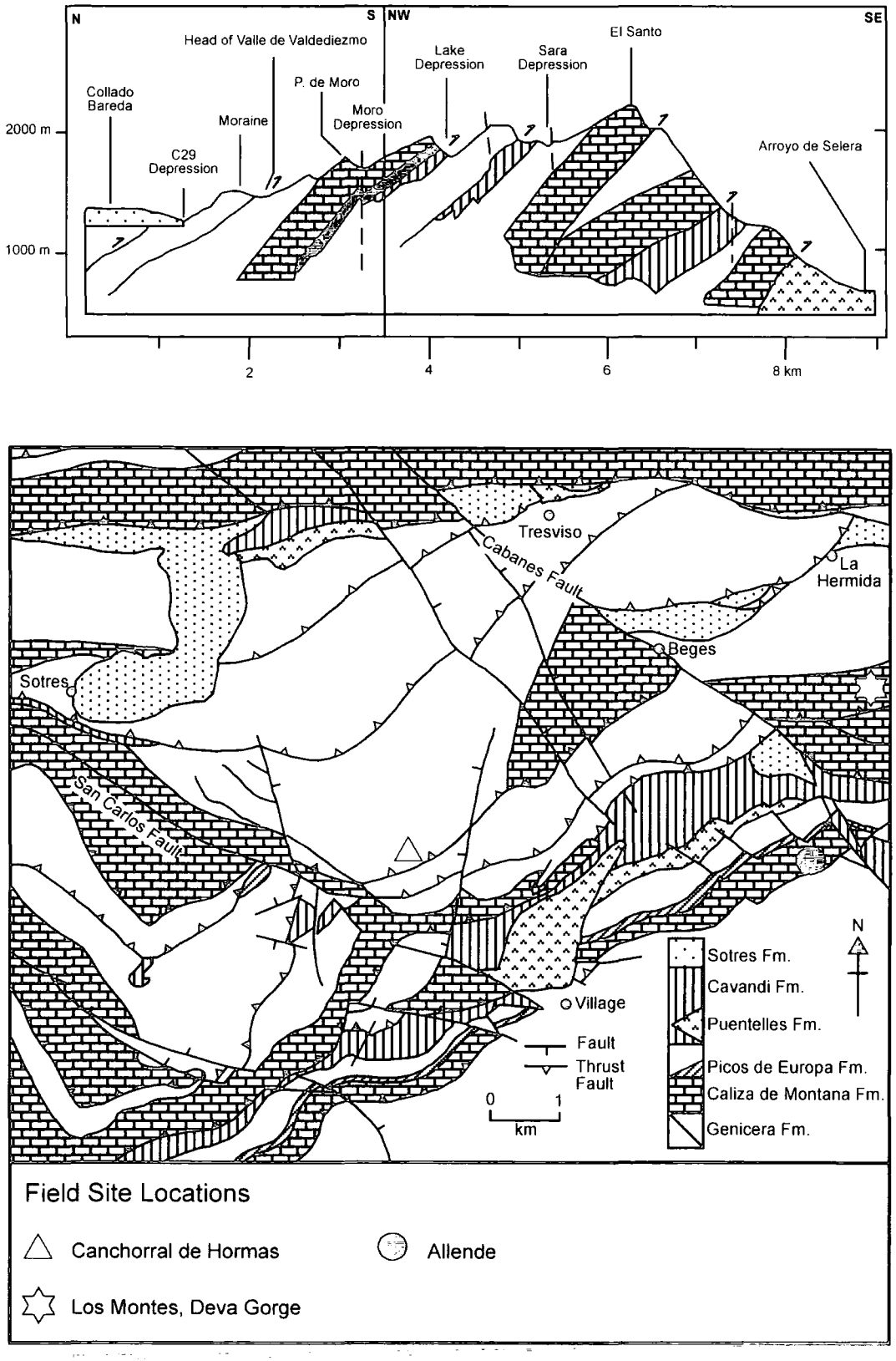

Figure 5.3: Geological setting of the Andara region of the Eastern Massif of the Picos de Europa. This area encompasses the sites Canchorral de Hormas, Deva Gorge and Allende (Adapted from Smart, 1986).

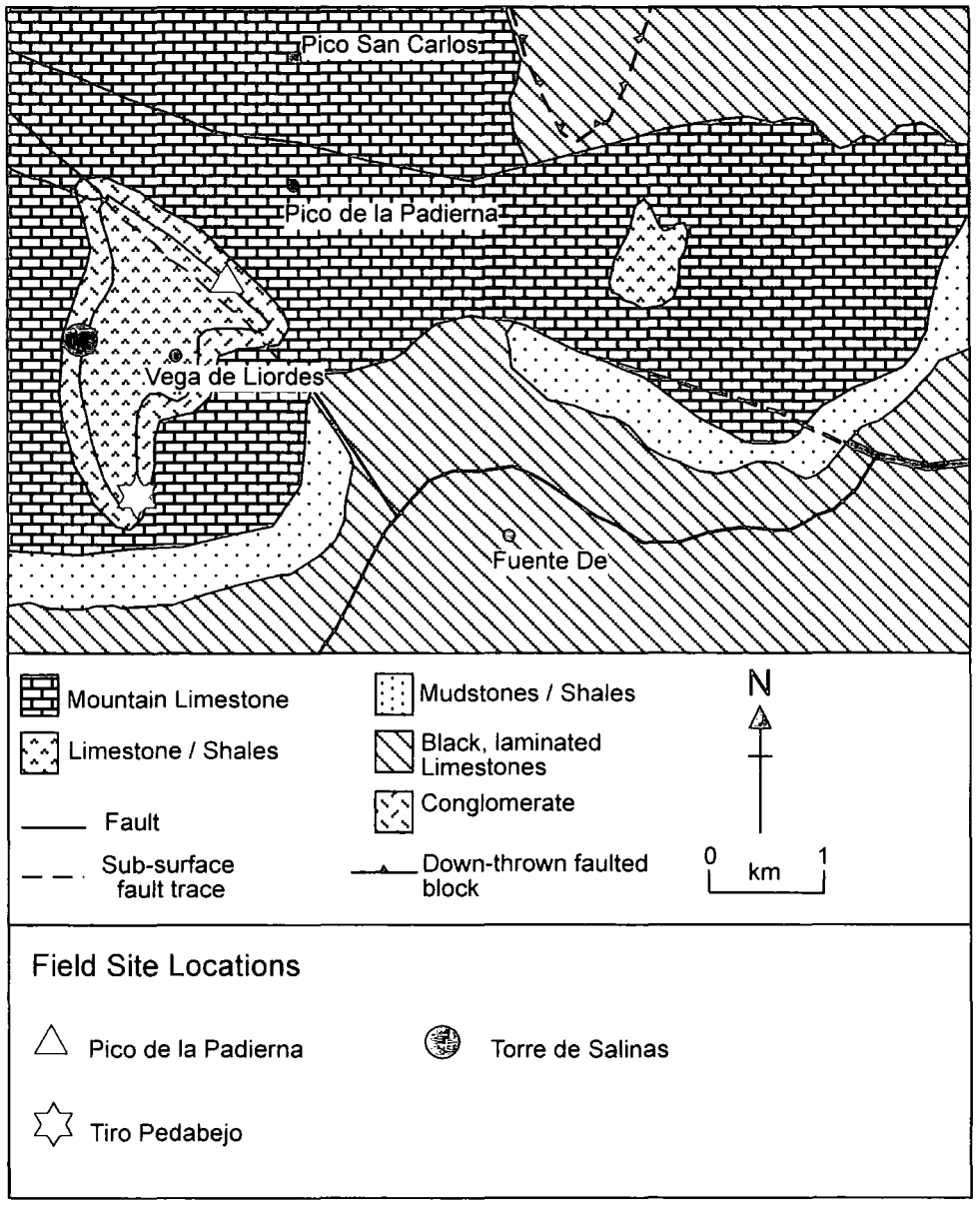

Figure 5.4: General geological setting of the Vega de Liordes, which encompasses the sites Pico de la Padierna, Tiro Pedabejo and Torre de Salinas.

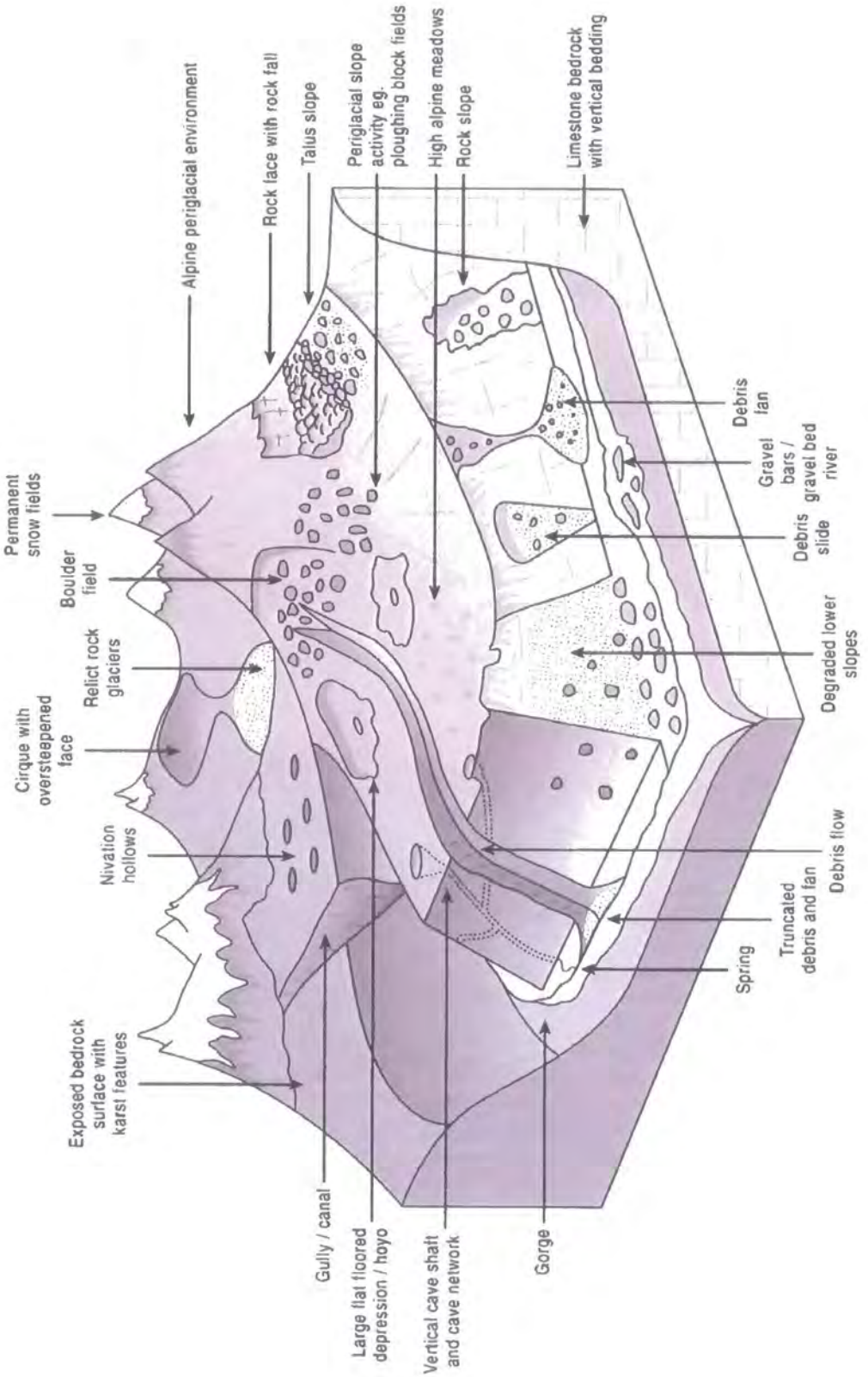

Figure 5.5: Landscape component model depicting the most important landscape elements and linkages in the Picos de Europa mountains (Source: Author).

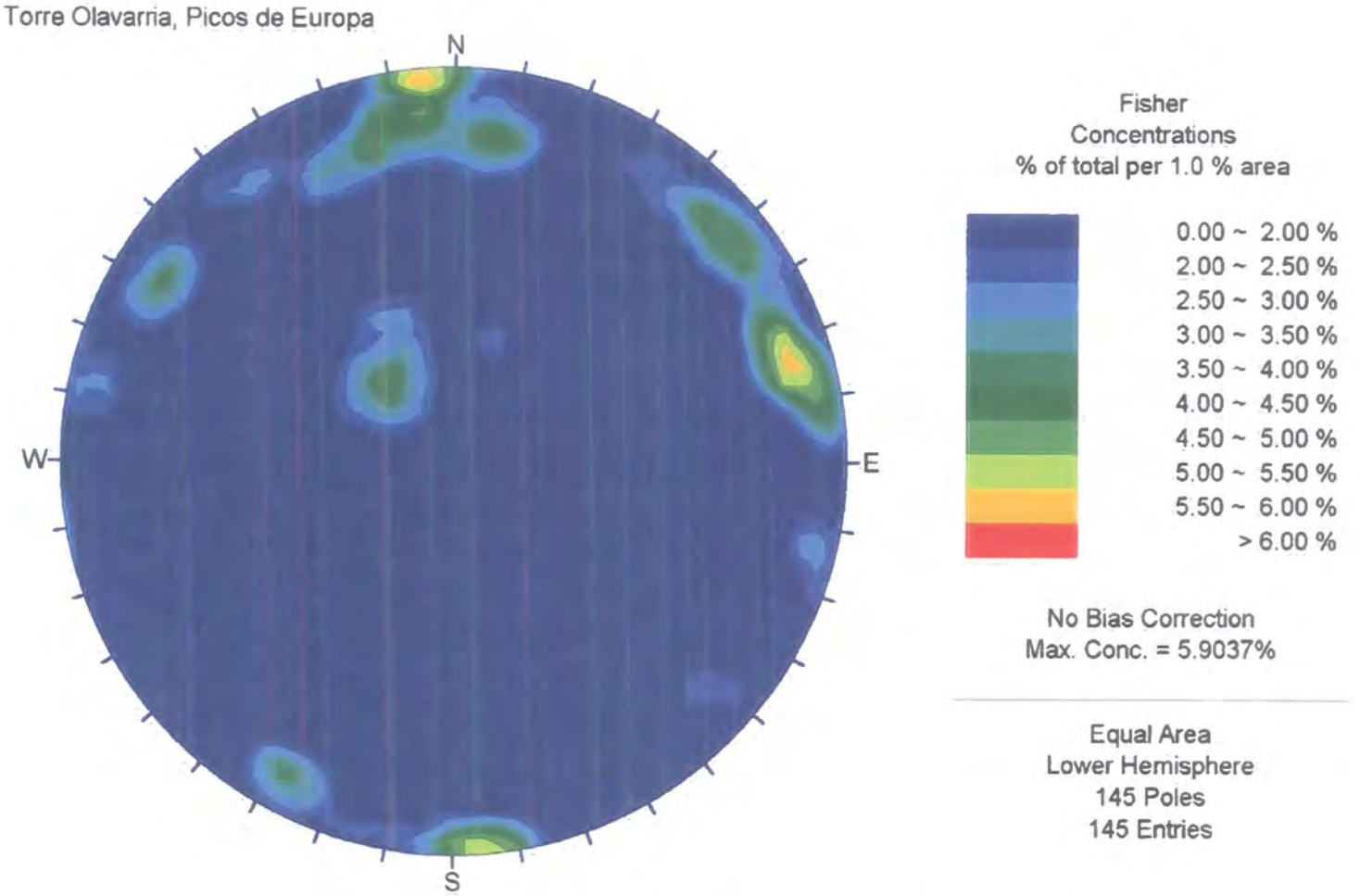

Figure 5.6: Contoured polar projection of the discontinuities at Torre Olavarría, Picos de Europa, northern Spain.

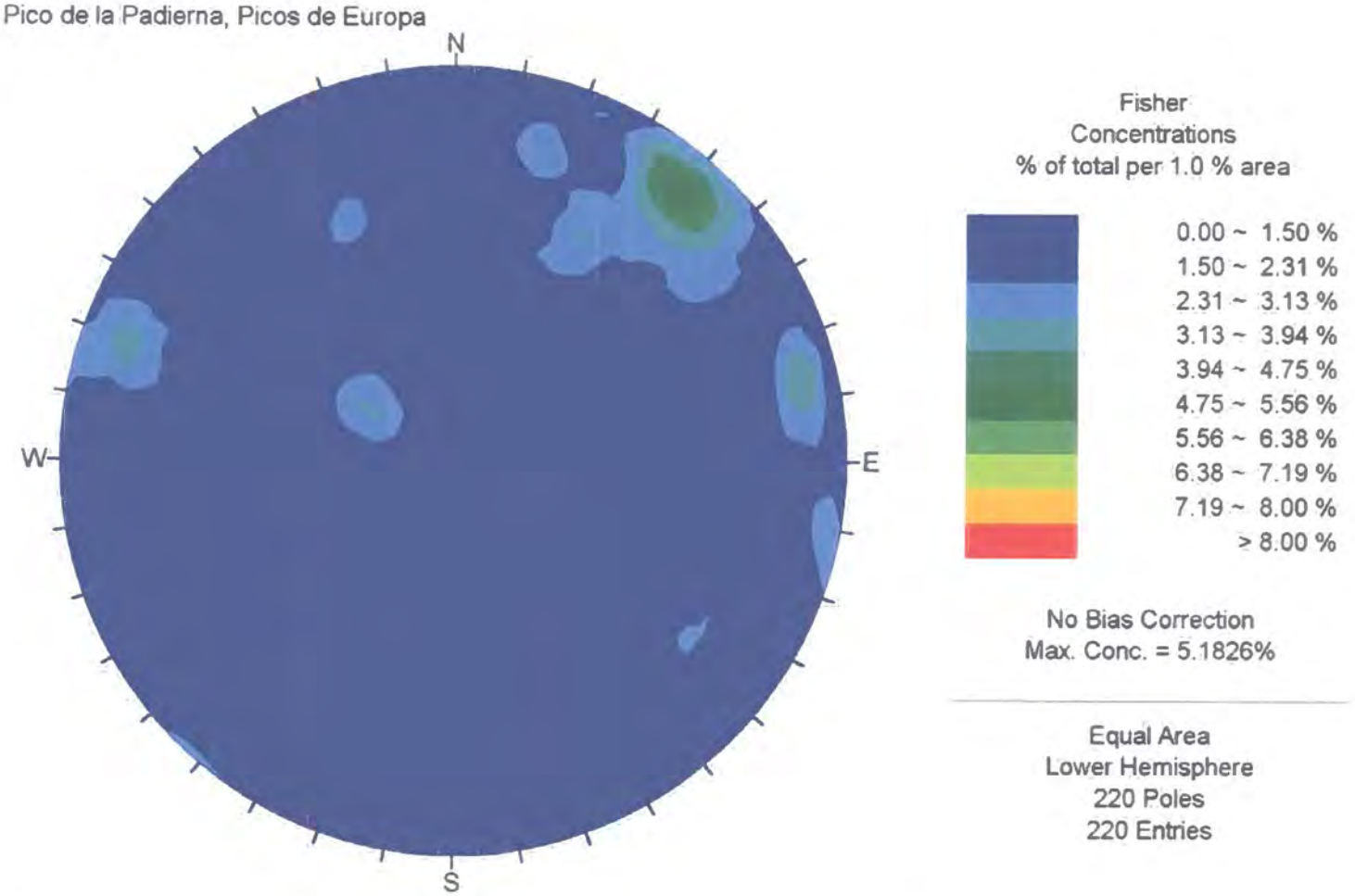

Figure 5.7: Contoured polar projection for the discontinuities at Pico de la Padierna, Picos de Europa, northern Spain.

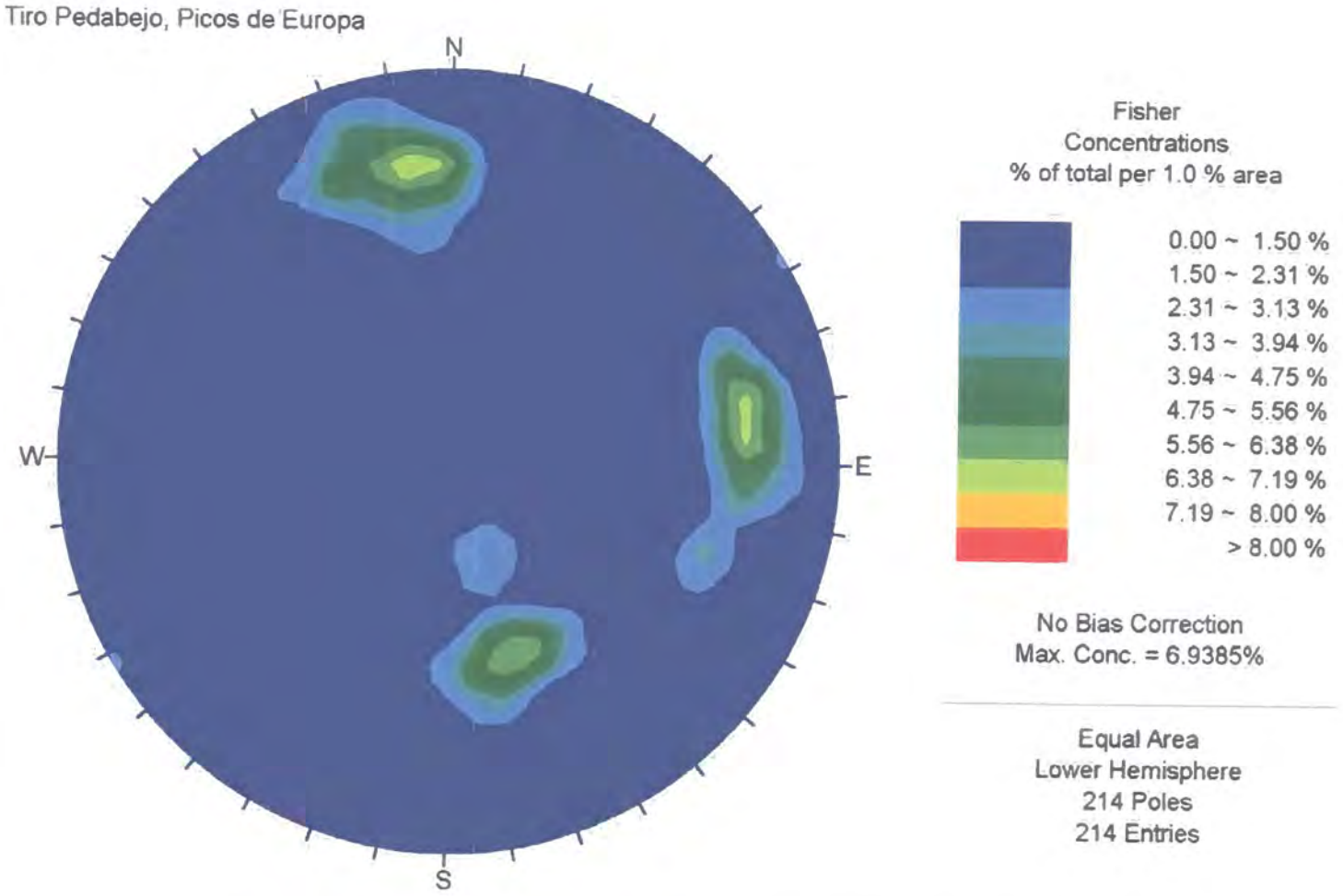

Figure 5.8: Contoured polar projection of the discontinuities at Tiro Pedabejo, Picos de Europa, northern Spain.

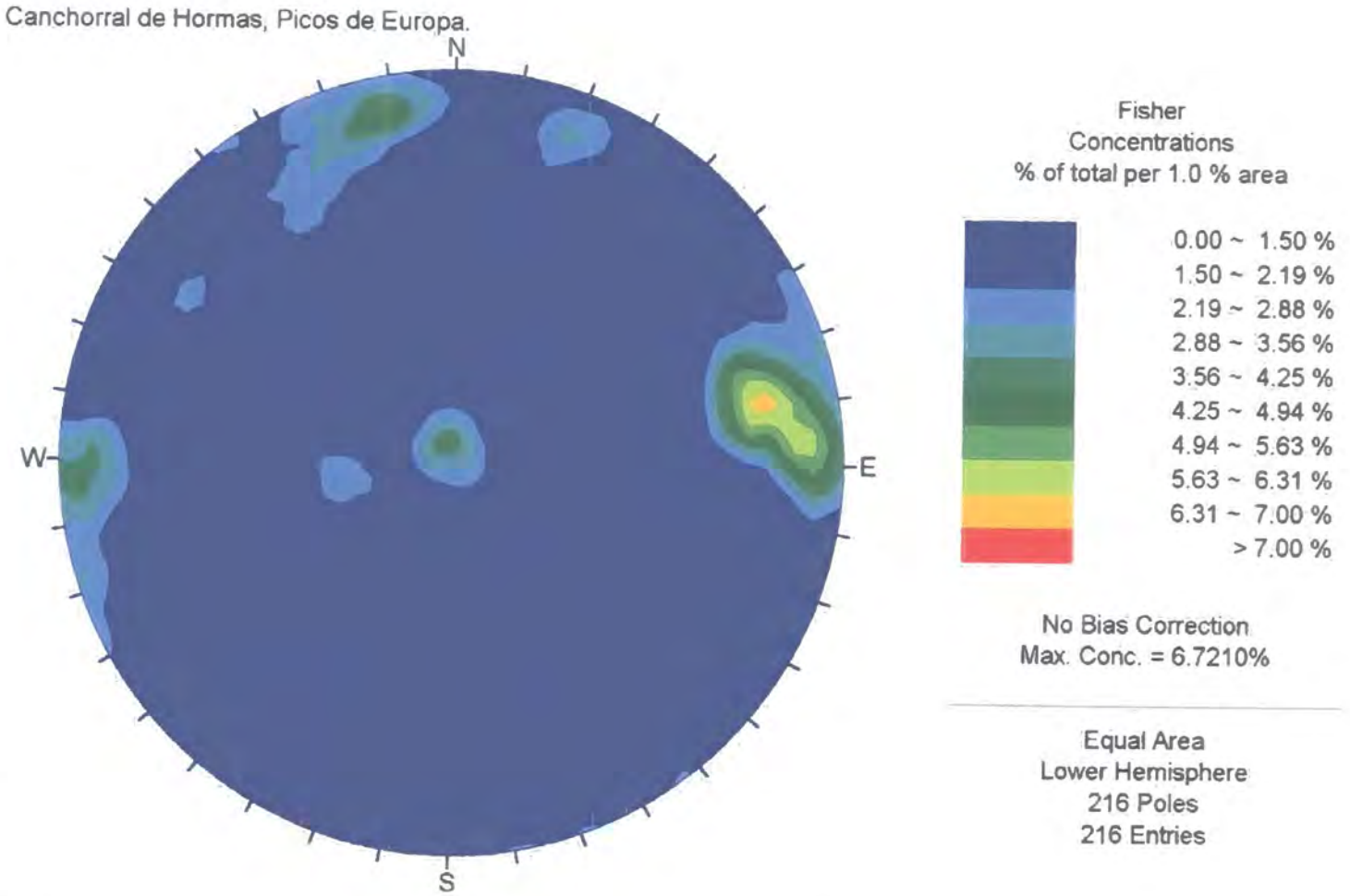

Figure 5.9: Contoured polar projections for the discontinuities at Canchorral de Hormas, Picos de Europa, northern Spain.

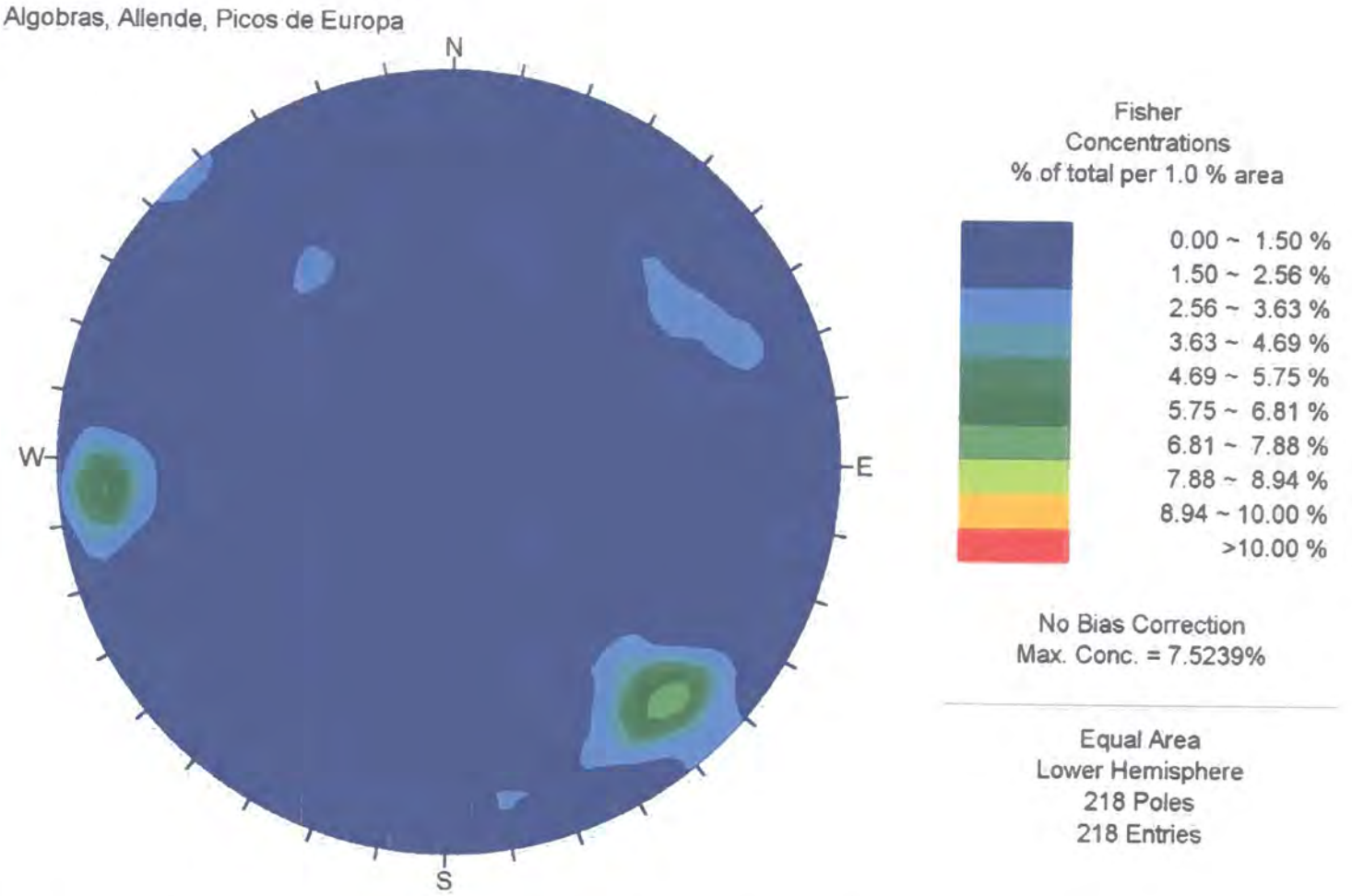

Figure 5.10: Contoured polar projection of the discontinuities at Algobras, Allende, Picos de Europa, northern Spain.

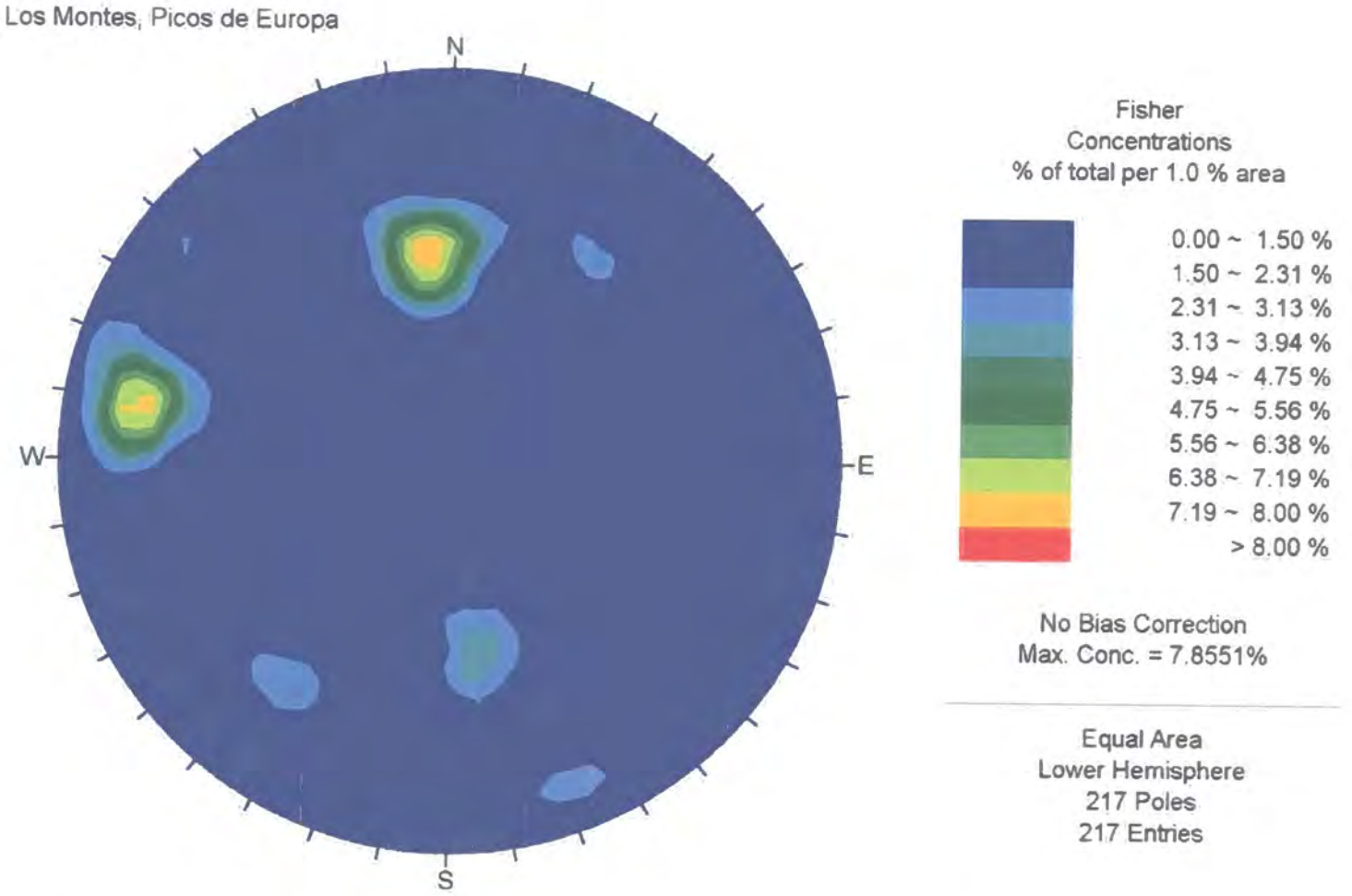

Figure 5.11: Contoured polar projection of the discontinuities at Los Montes, Picos de Europa, northern Spain.

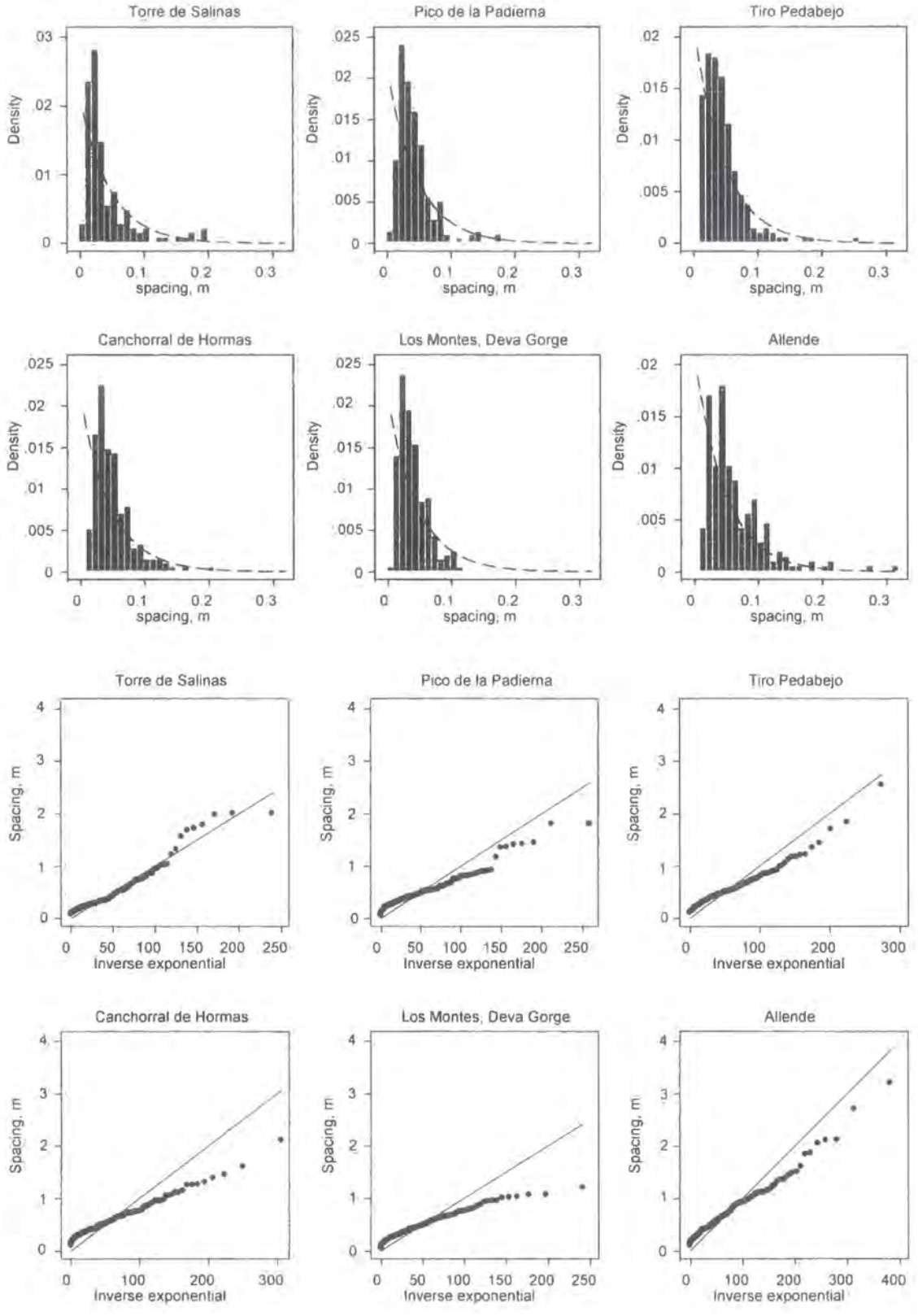

Figure 5.12: Histograms and quantile plots of joint spacing with a fitted exponential distribution.

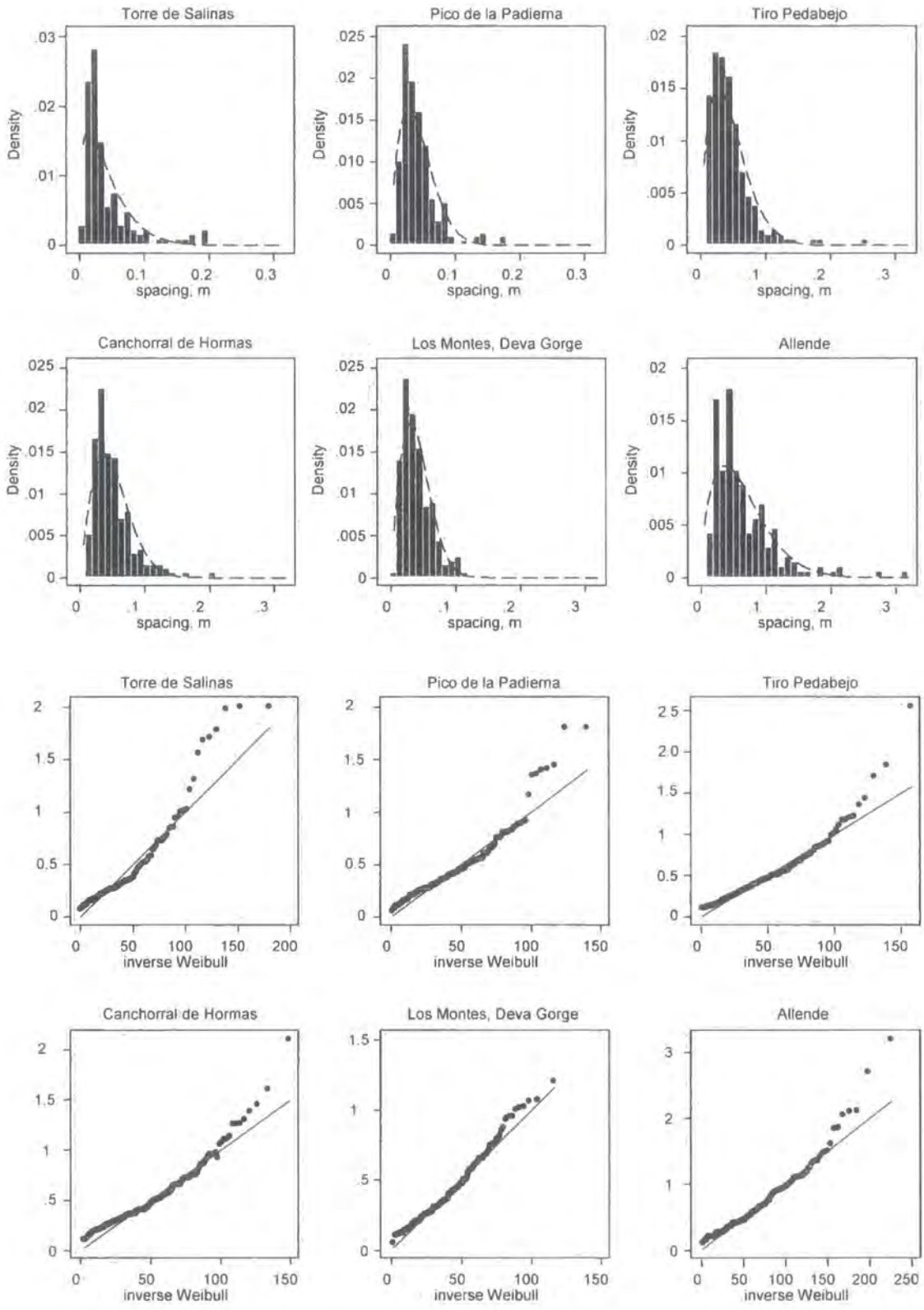

Figure 5.13: Histograms and quantile plots of joint spacing with compared with an ideal Weibull distribution.

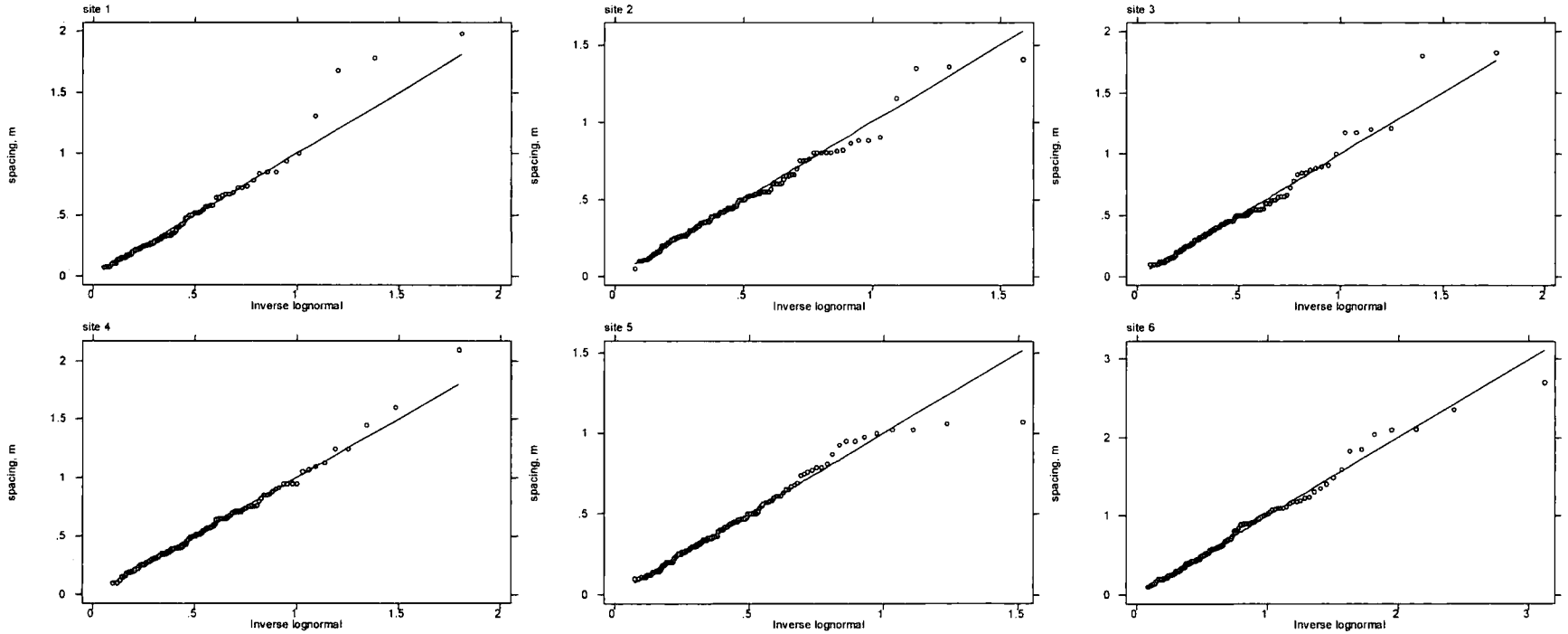

Figure 5.14: Aggregated joint spacing data from all sites in the Picos de Europa show an approximately lognormal distribution. The solid line represents an ideal lognormal distribution and the symbols the actual joint spacing data. Bedding data is excluded.

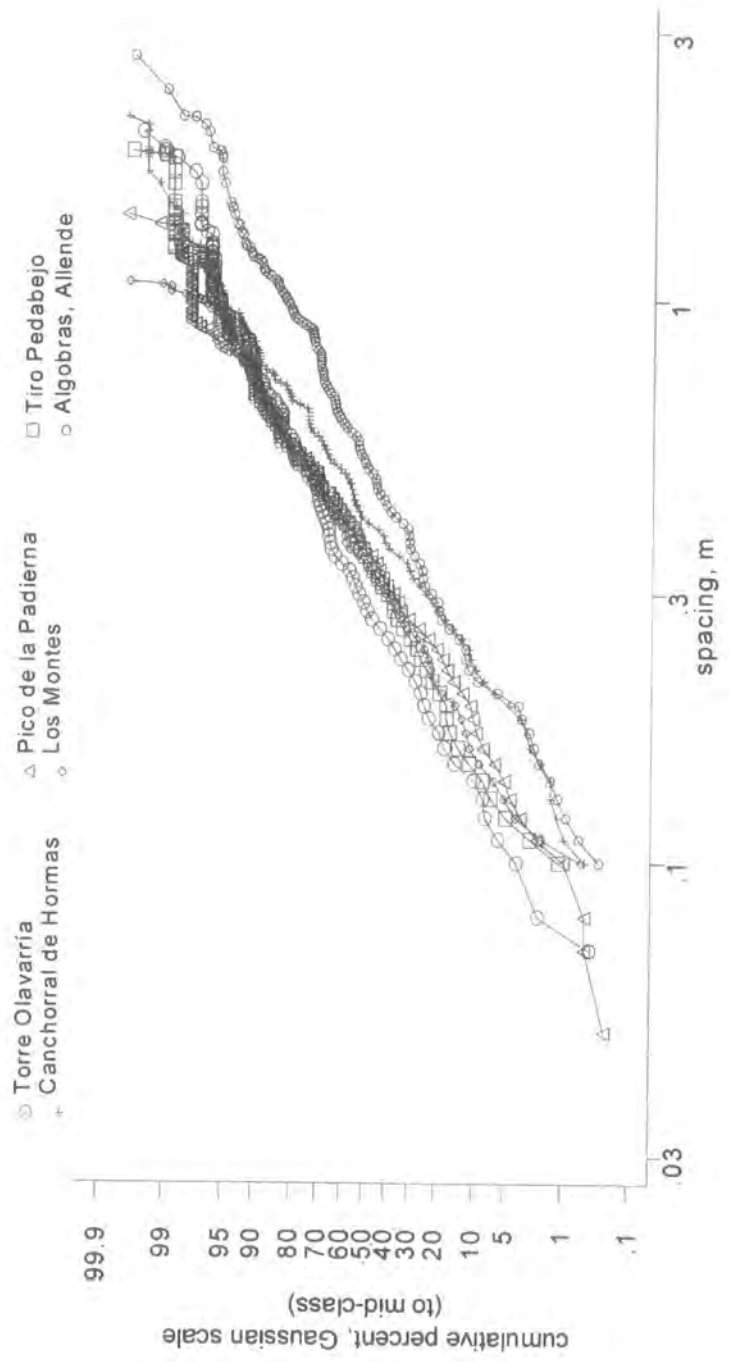

Figure 5.15: Cumulative probability distribution functions of joint spacing for each site investigated in the Picos de Europa. Joint spacing is plotted

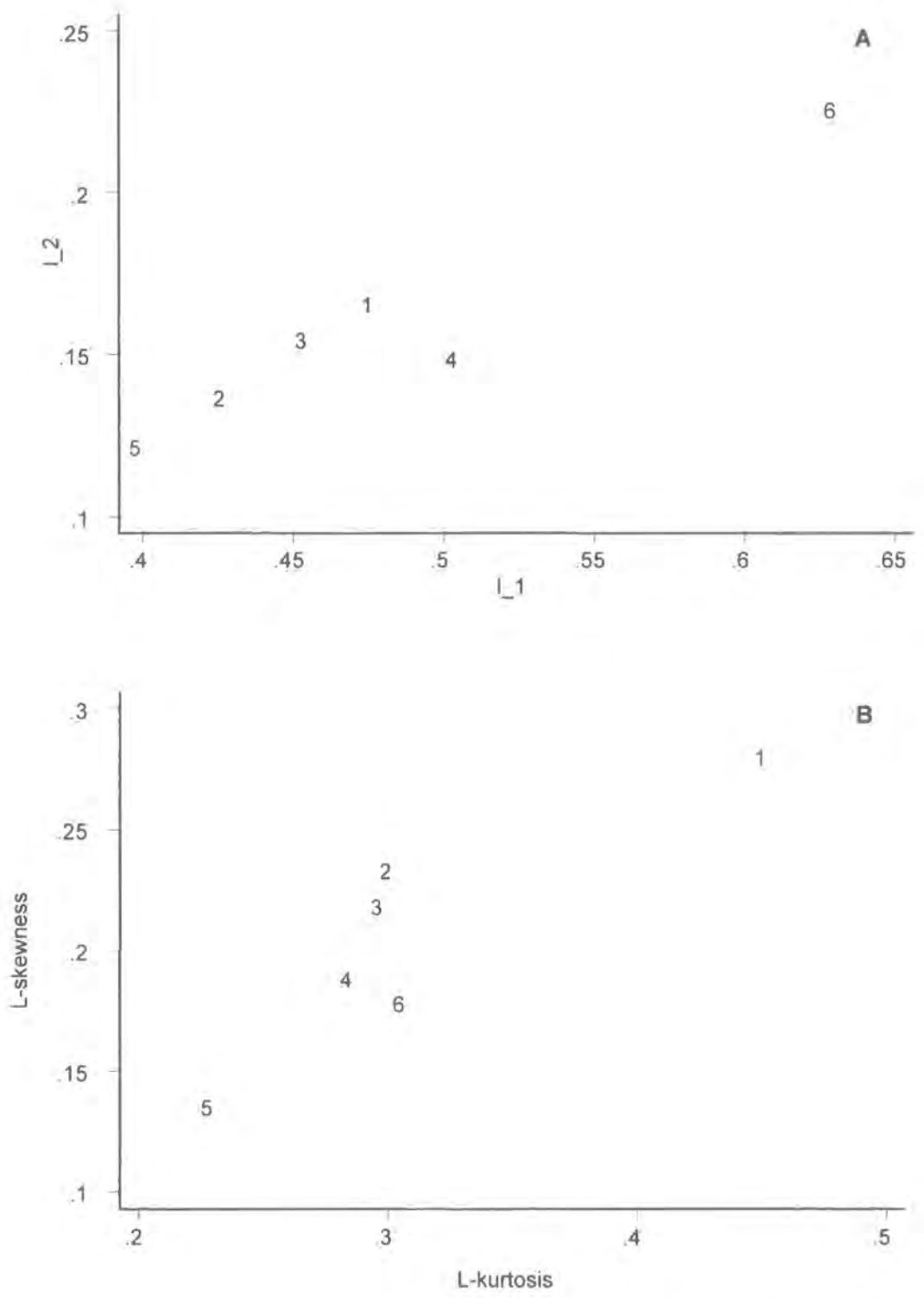

Figure 5.16: L-moments for joint spacing for sites in the Picos de Europa. Figure 5.16a plots the first two L-moments and Figure 5.16b plots measure of skewness and kurtosis. The key to the graph is given as

1 = Torre de Salinas, 2 = Pico de la Padierna, 3 = Tiro Pedabejo, 4 = Canchorral de Hormas, 5 = Los Montes (Deva Gorge) 6 = Allende.

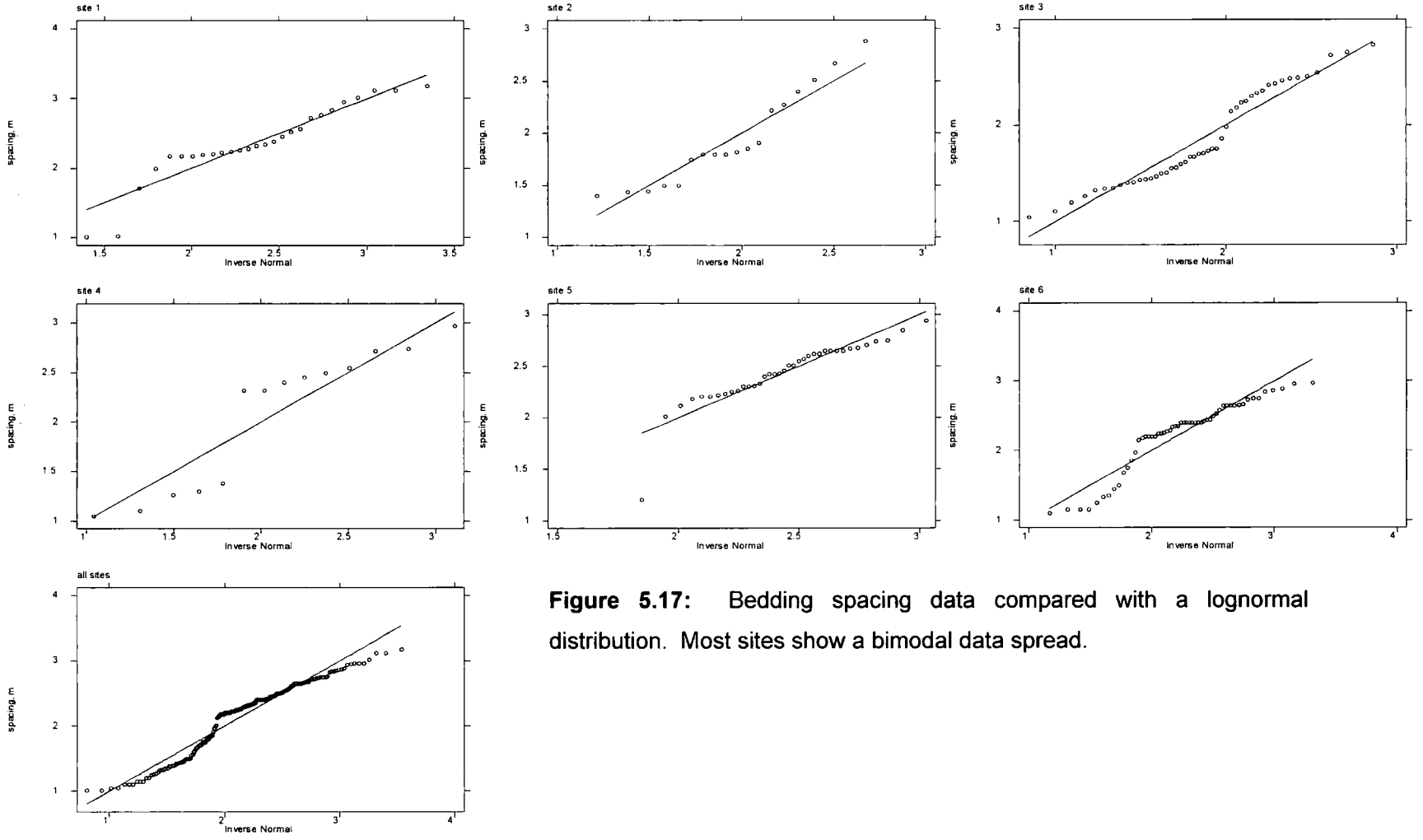

Figure 5.17: Bedding spacing data compared with a lognormal distribution. Most sites show a bimodal data spread.

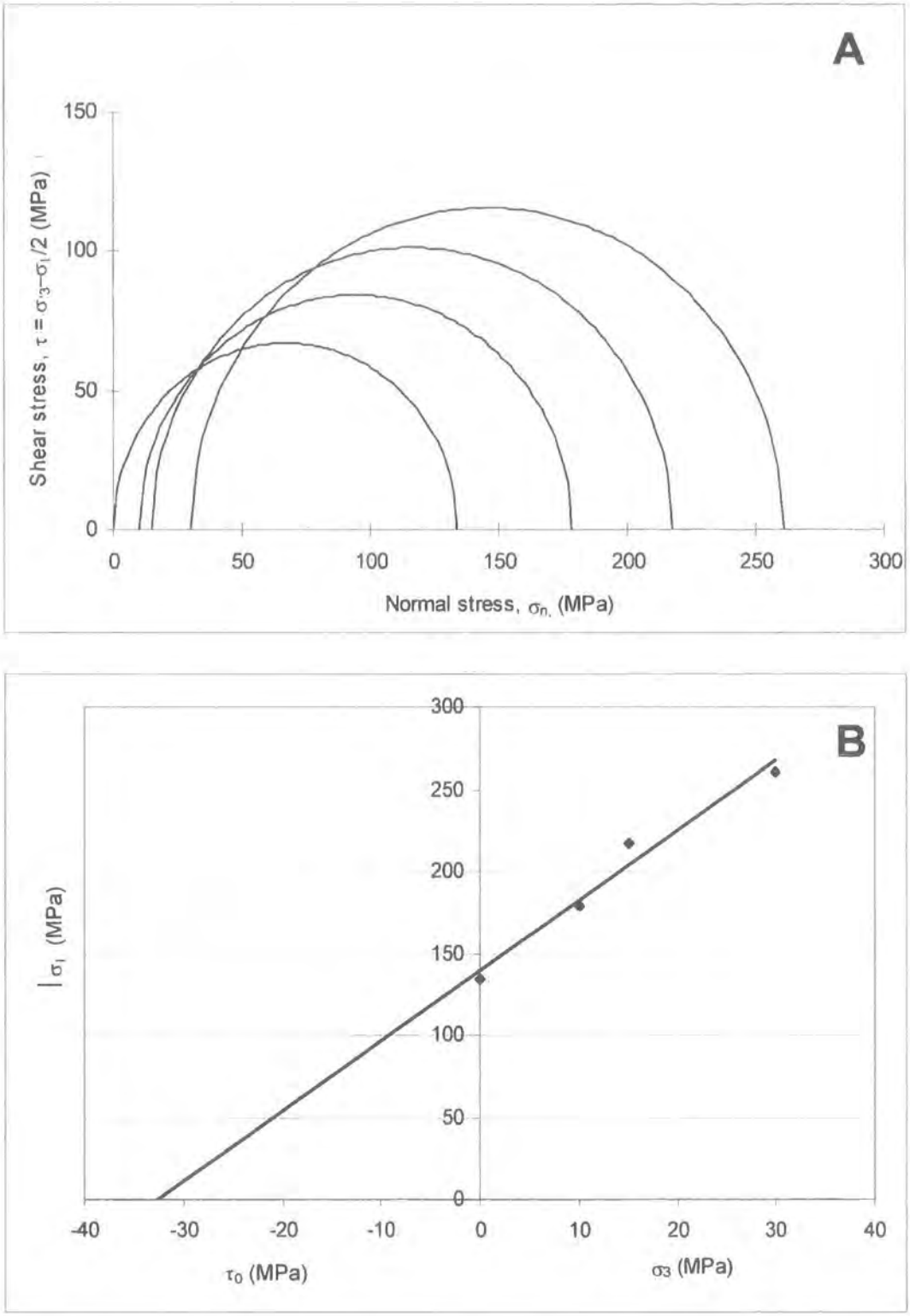

Figure 5.18: Mohr's circles (A) and sigma 1 / sigma 3 stress space with fitted Mohr-Coulomb failure envelope (B) for Pico de la Padierna, Picos de Europa.

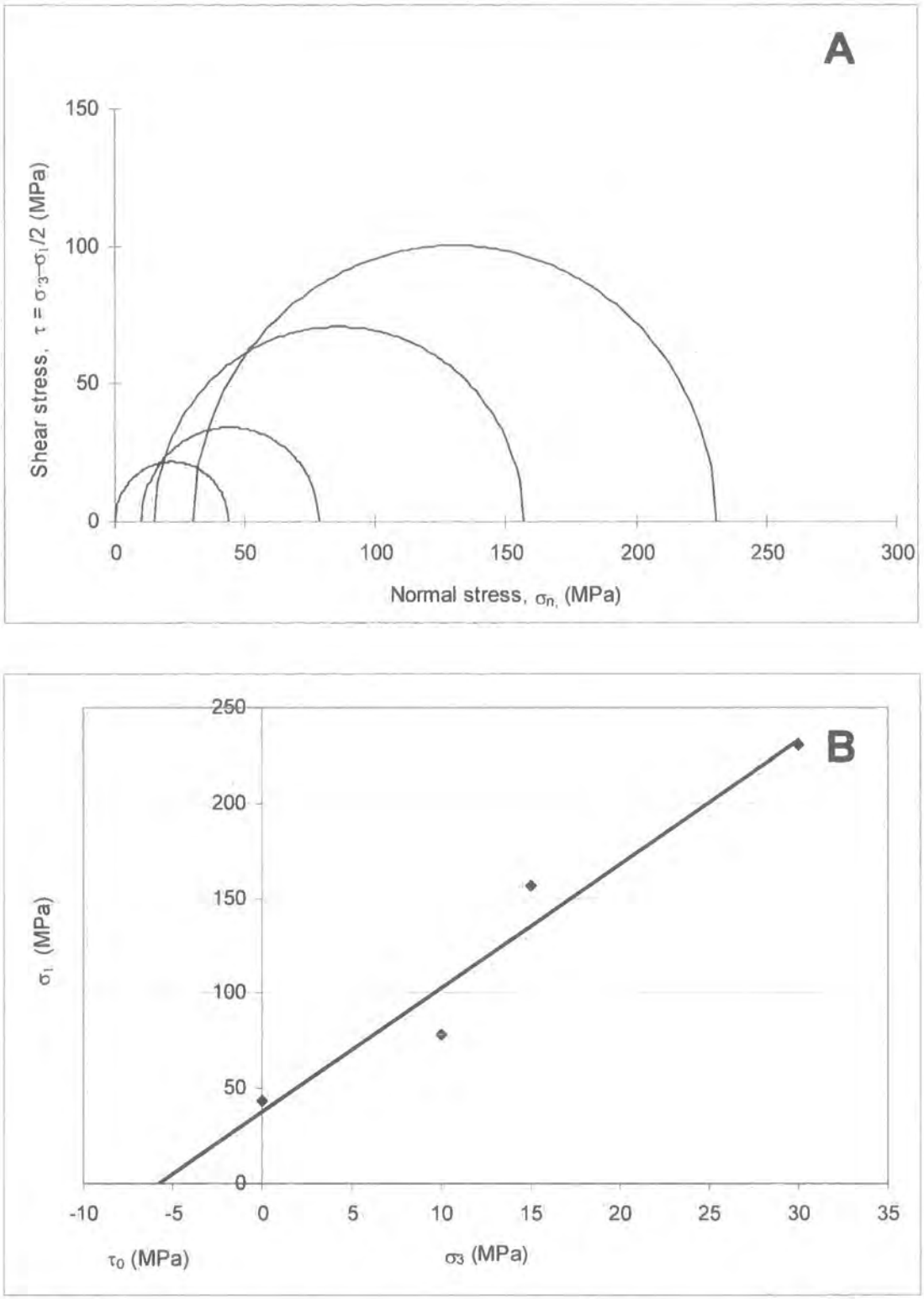

Figure 5.19: Mohr's circles (A) and sigma 1 / sigma 3 stress space with fitted Mohr-Coulomb failure envelope (B) for Tiro Pedabejo, Picos de Europa.

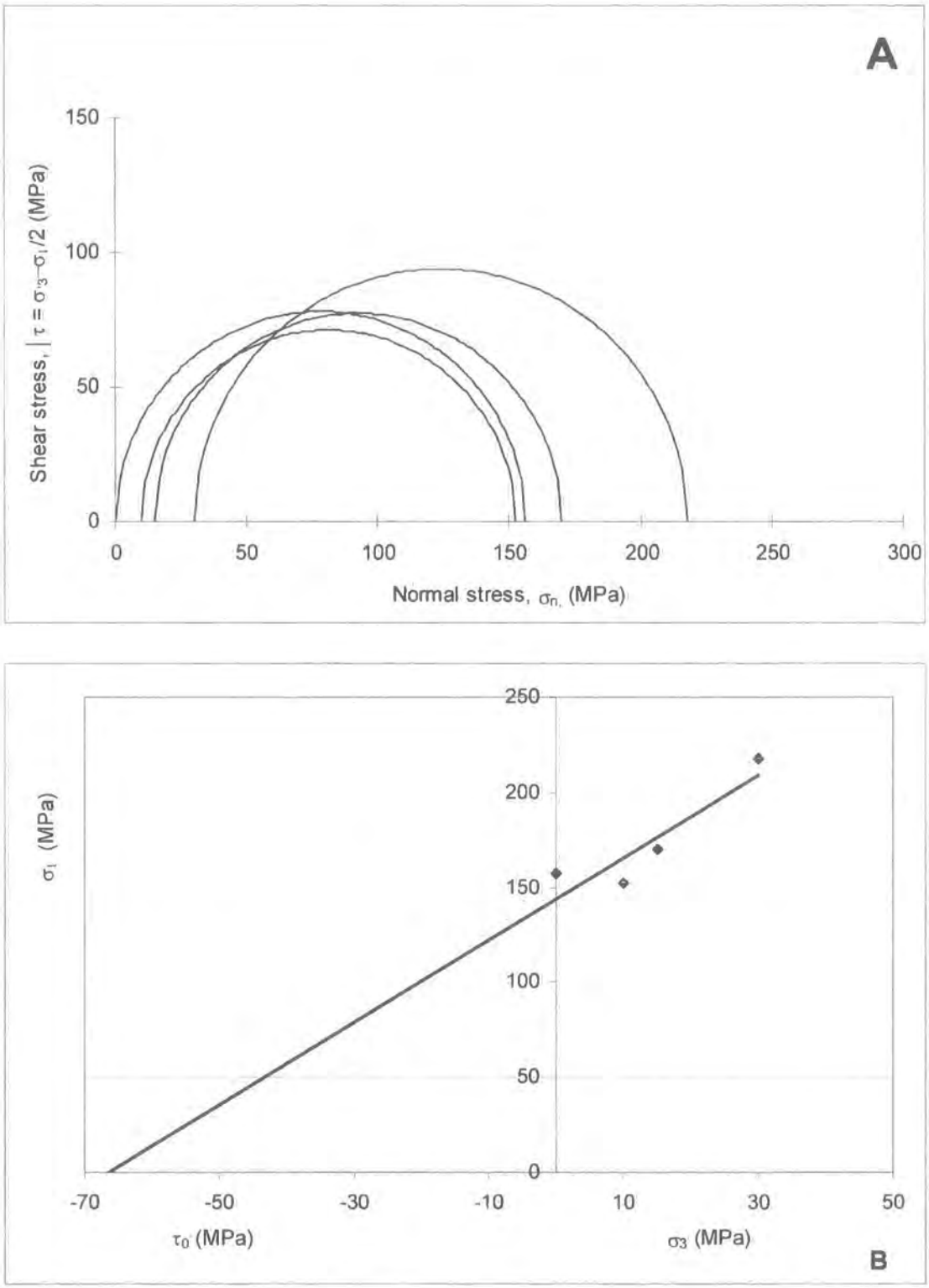

Figure 5.20: Mohr's circles (A) and sigma 1 / sigma 3 stress space with fitted Mohr-Coulomb failure envelope (B) for Canchorral de Hormas, Picos de Europa.

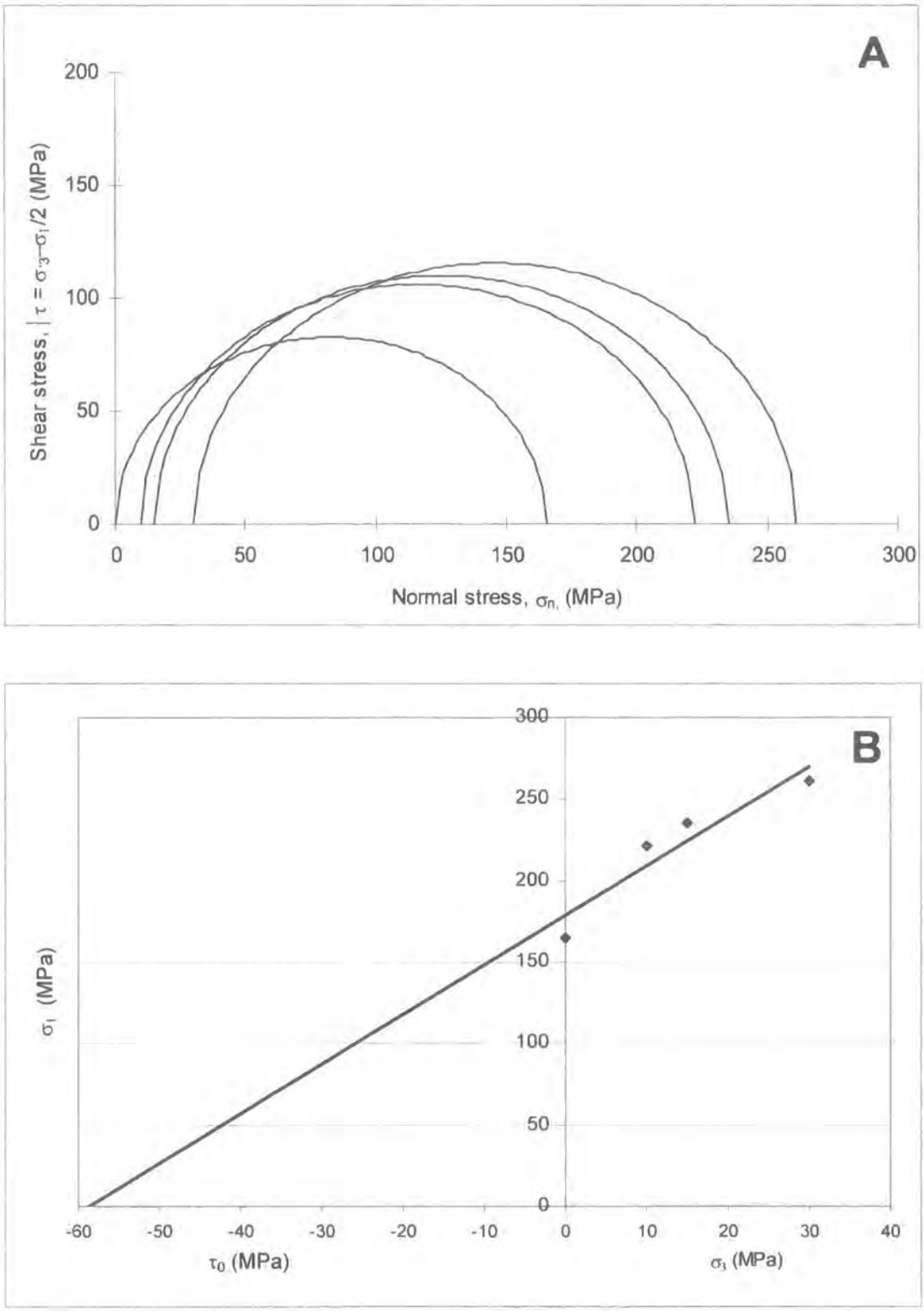

Figure 5.21: Mohr's circles (A) and sigma 1 / sigma 3 stress space with fitted Mohr-Coulomb failure envelope (B) for Deva Gorge limestones, Picos de Europa.

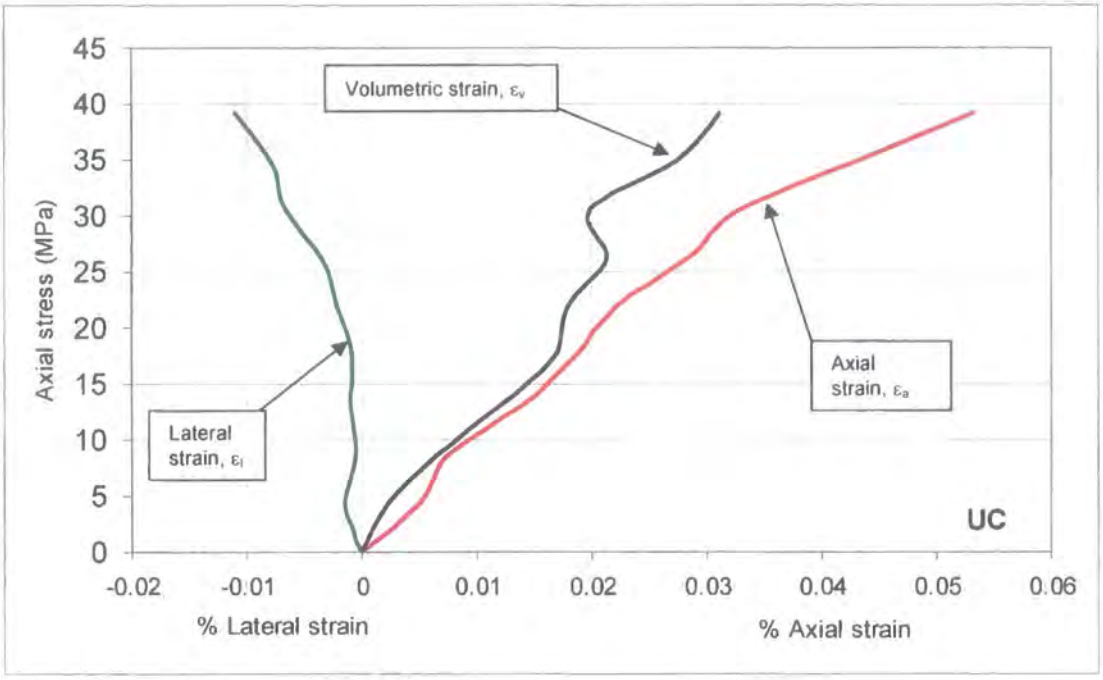

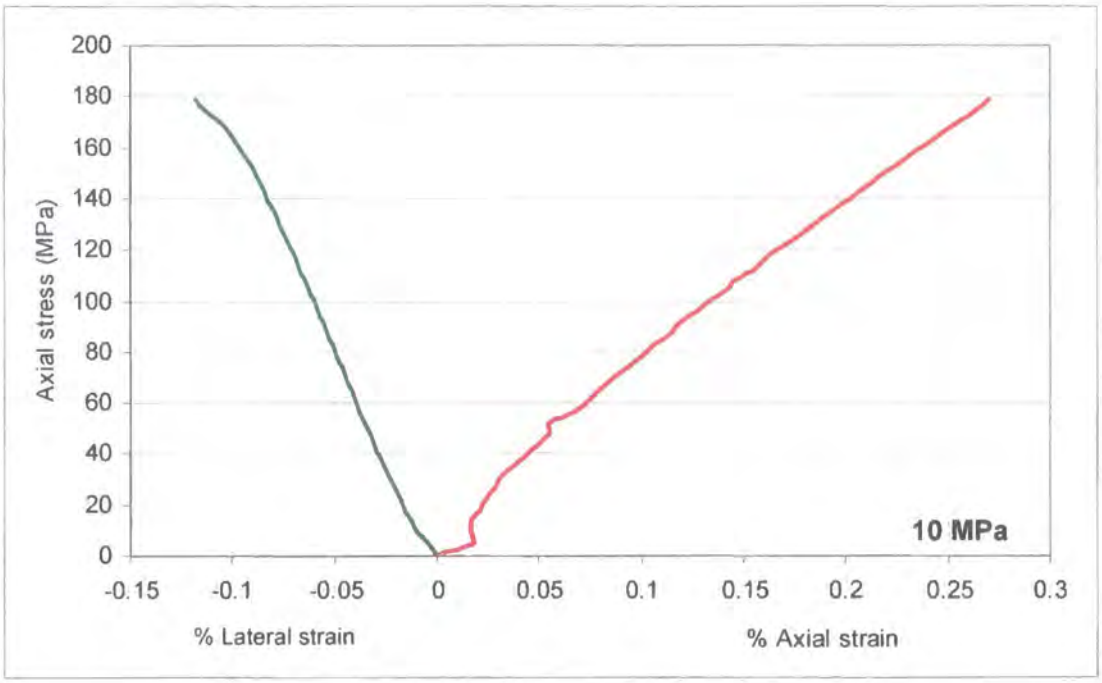

Figure 5.22: Axial (red line), lateral (green line) and volumetric (black line) stress-strain curves for Pico de la Padierna limestones for specimens tested at 0 (UC), 10 and MPa confining pressures. Lateral and axial strains for 15MPa confining pressure were unavailable due to strain gauge failure.

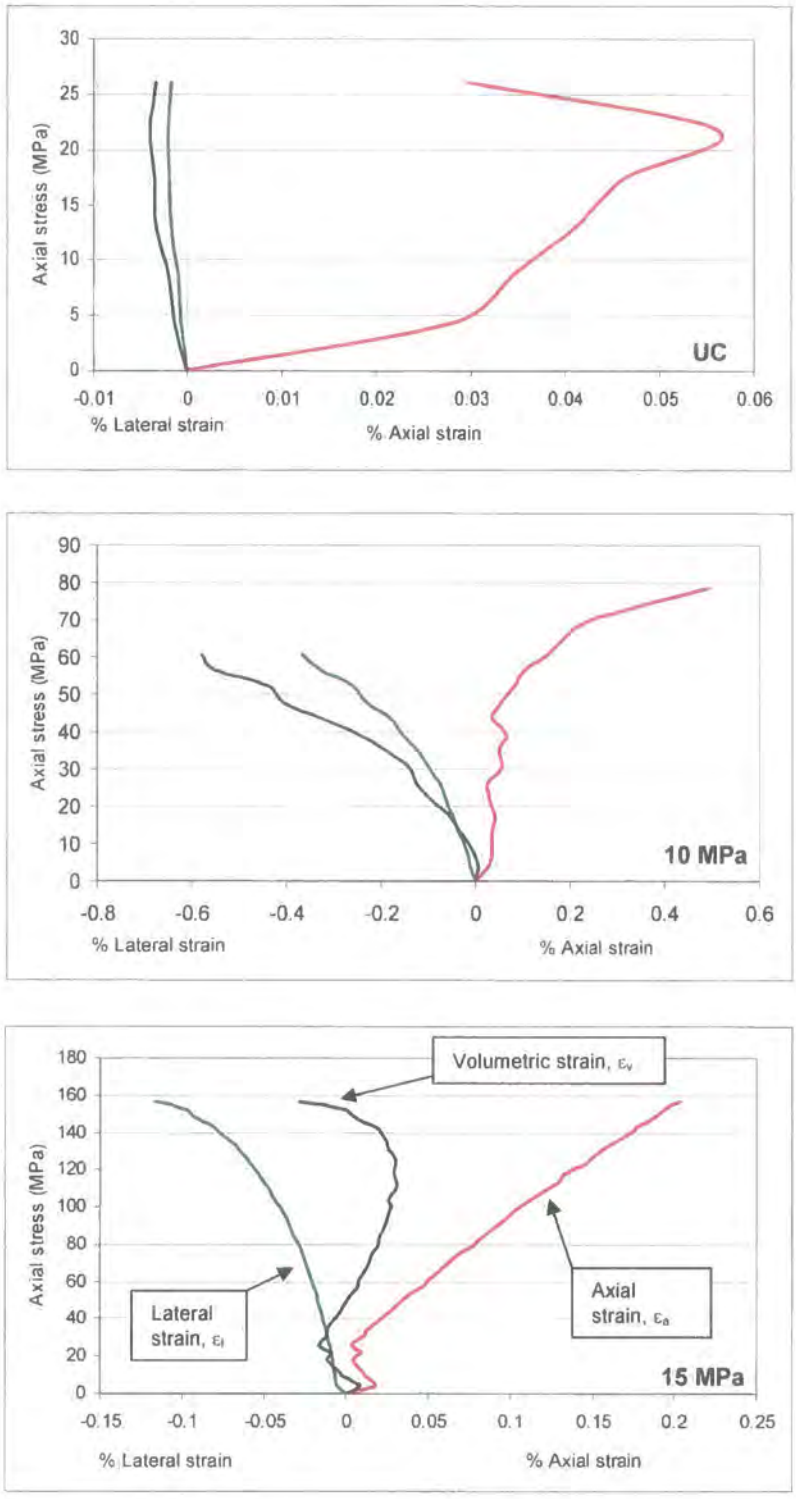

Figure 5.23: Axial (red line), lateral (green line) and volumetric (black line) stress-strain curves for Tiro Pedabejo limestones for specimens tested at 0 (UC), 10 and 15 MPa confining pressures.

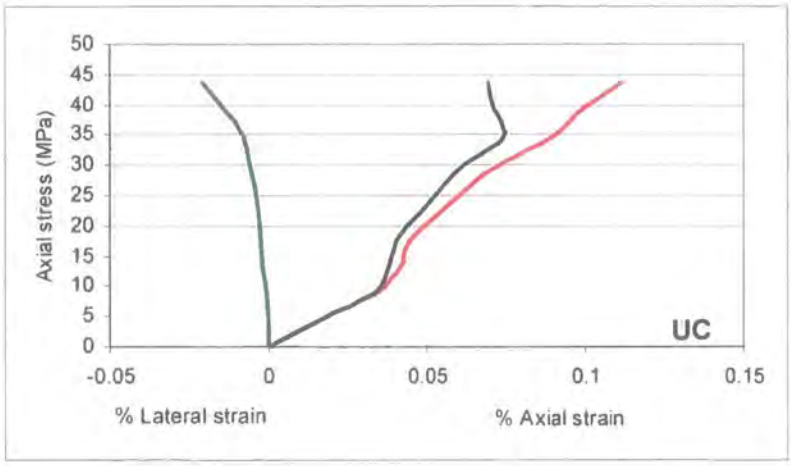

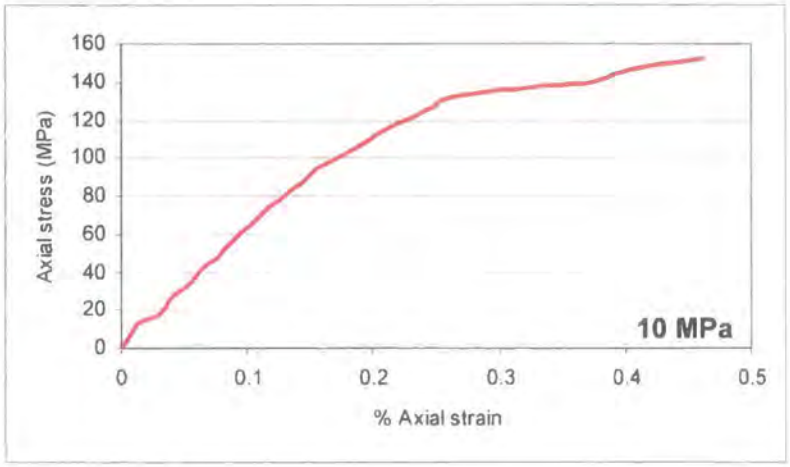

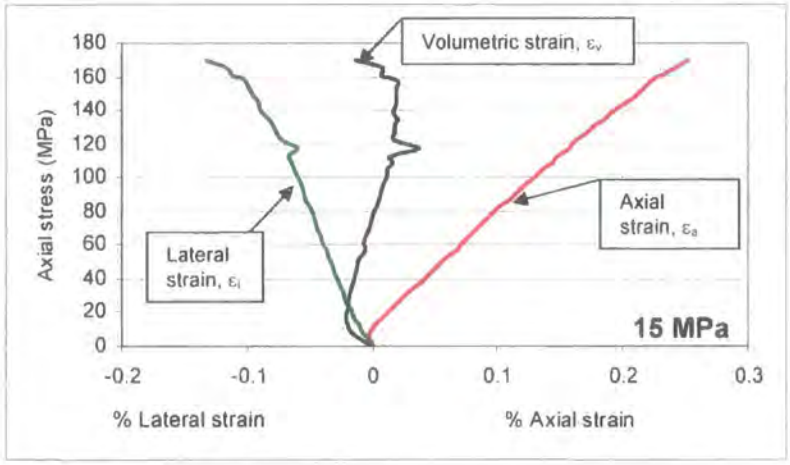

Figure 5.24: Axial (red line), lateral (green line) and volumetric (black line) stress-strain curves for Canchorral de Hormas limestones for specimens tested at 0 (UC), 10 and 15 MPa confining pressures. Lateral strain for 10 MPa confining pressure was unavailable due to strain gauge failure.

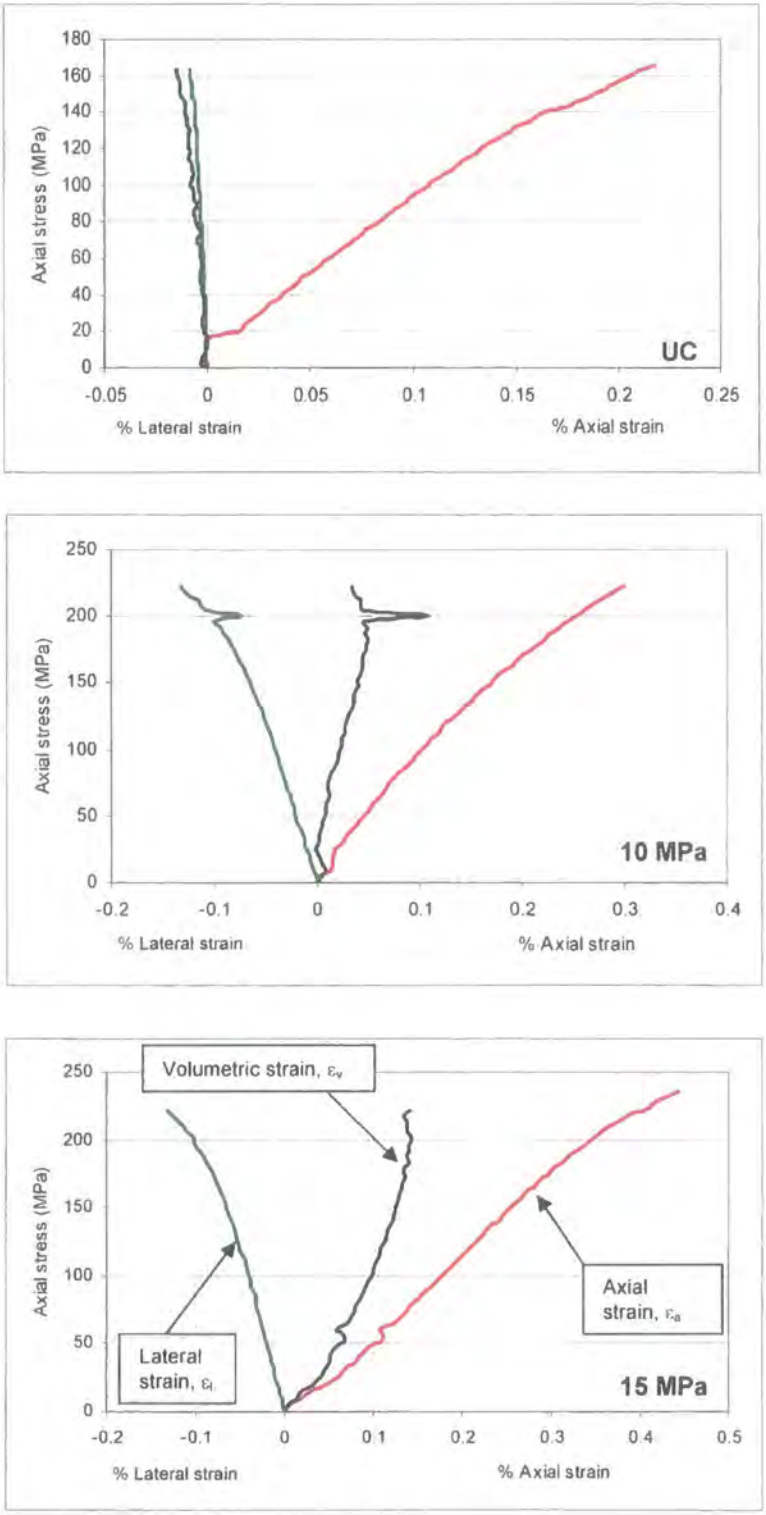

Figure 5.25: Axial, lateral and volumetric stress-strain curves for Deva Gorge limestones for specimens tested at 0 (UC), 10 and 15 MPa confining pressures.

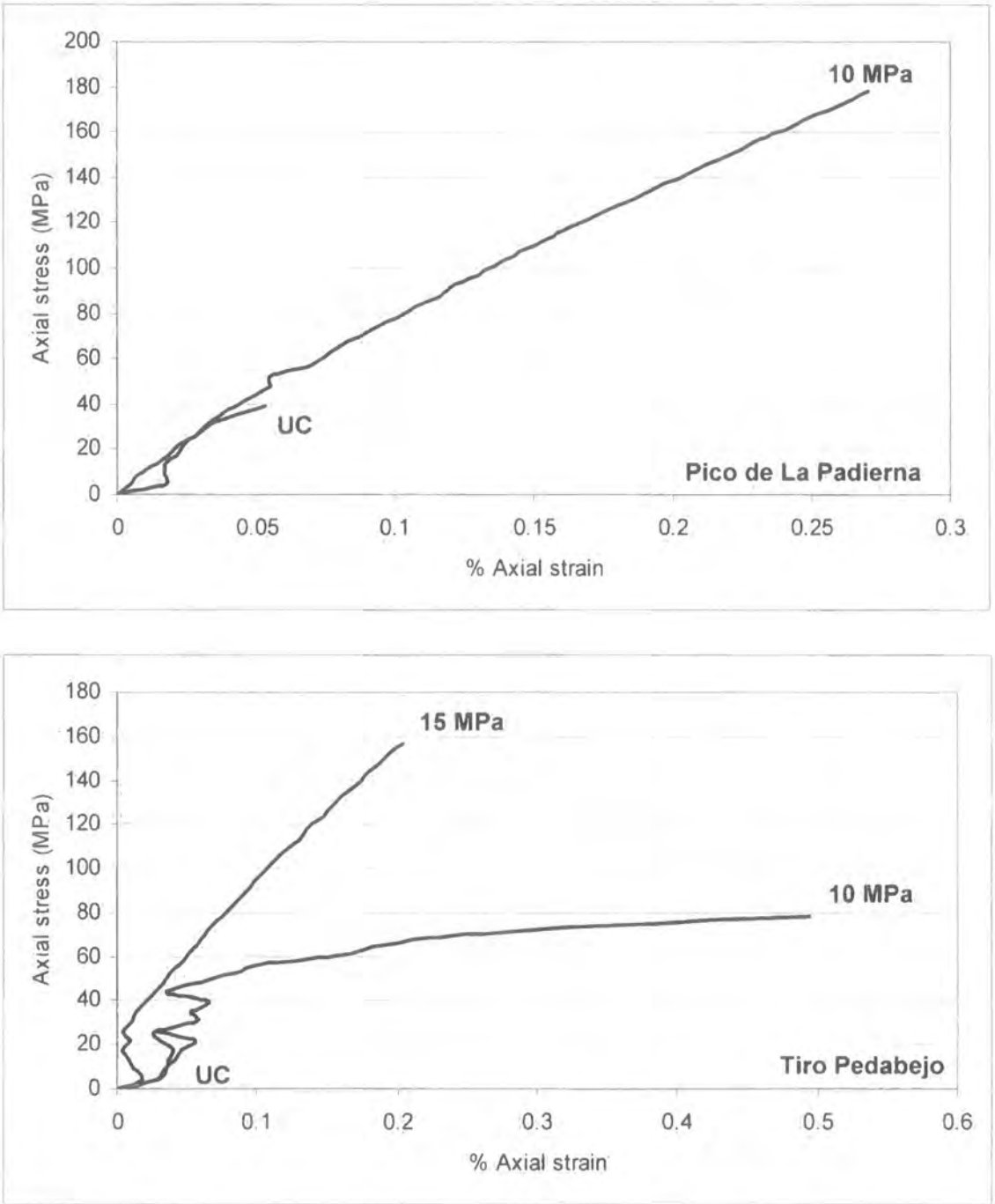

Figure 5.26: Comparative axial strain curves for Pico de la Padierna and Tiro Pedabejo at 0 (UC), 10 and 15 MPa confining pressures.

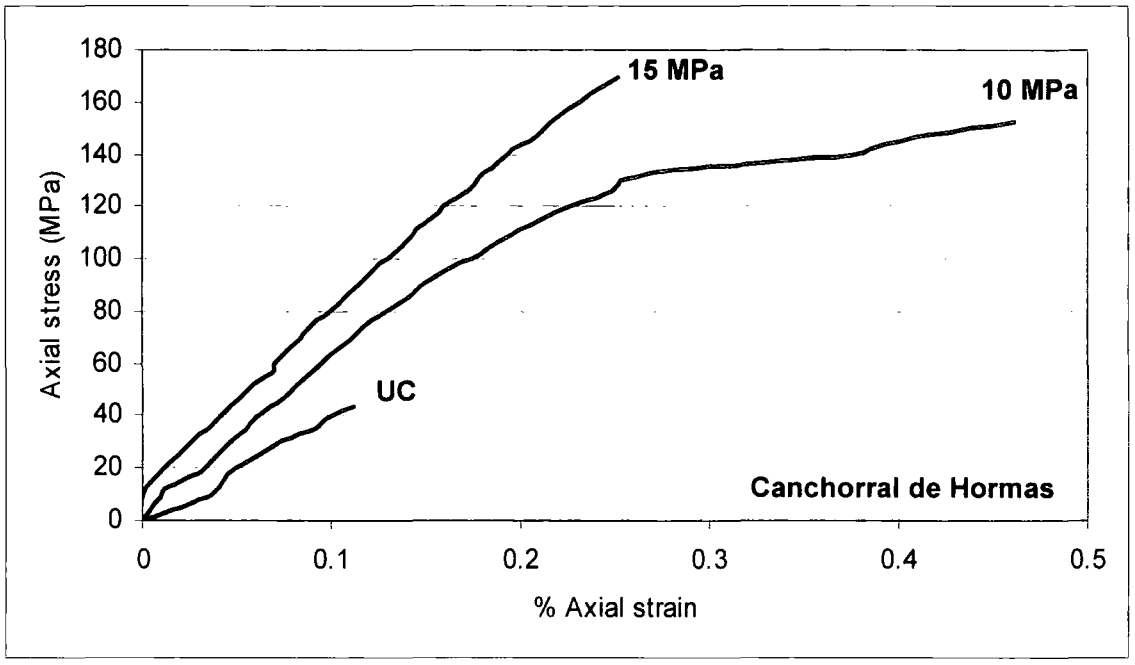

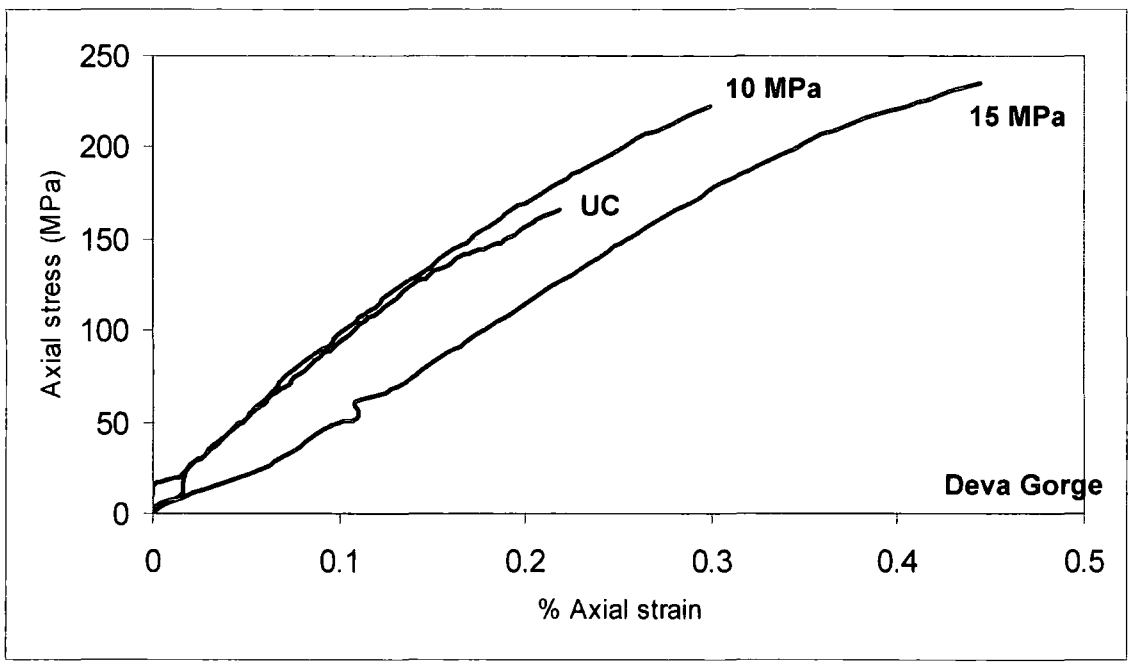

Figure 5.27: Comparative axial strain curves Canchorral de Hormas and Deva Gorge limestones at 0 (UC), 10 and 15 MPa confining pressures.

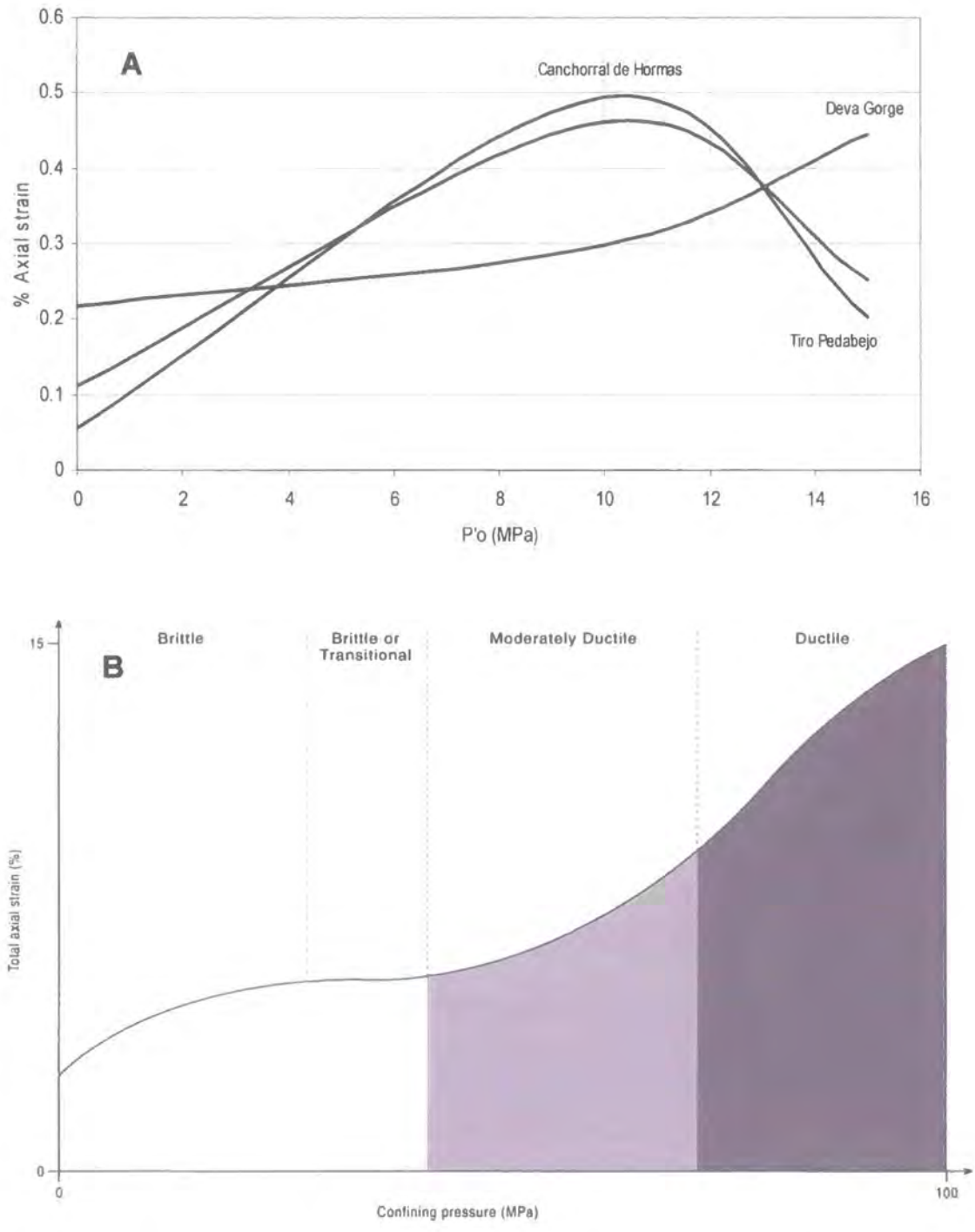

Figure 5.28: (A) Axial strain plotted against Confining pressure, P'o (MPa) to help determine whether the limestones are deforming in a very brittle, brittle, transitional or ductile manner. (B) Idealised strain response of limestone under increasing P'o (After Donath *et al.*, 1971)

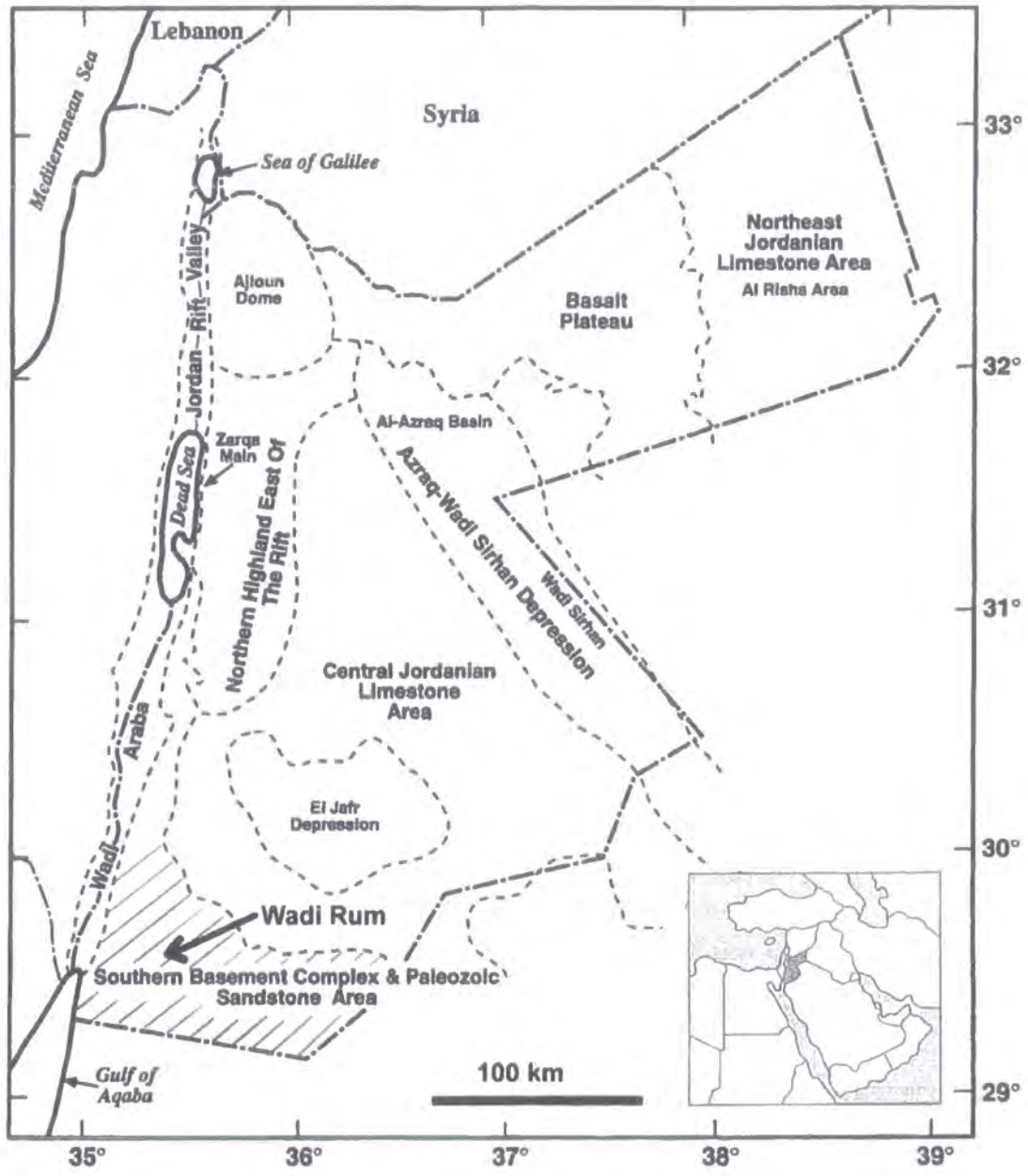

Figure 6.1: Location of Al-Quwayra and Wadi Rum, southern Jordan (Adapted from Bender, 1975).

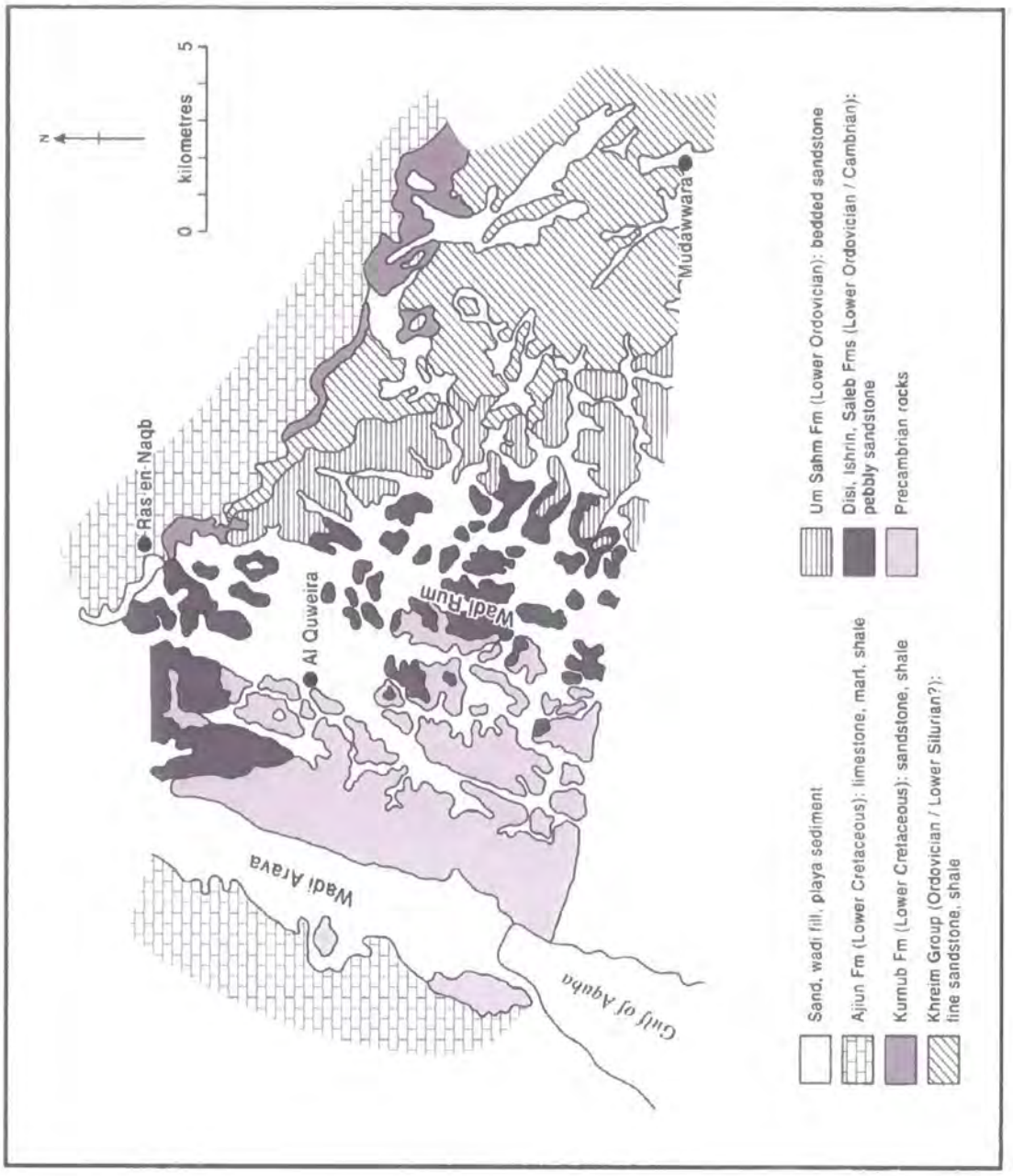

Figure 6.2: Broad geological setting of the Wadi Rum–Al-Quwayra area (Adapted from Osborn, 1985).

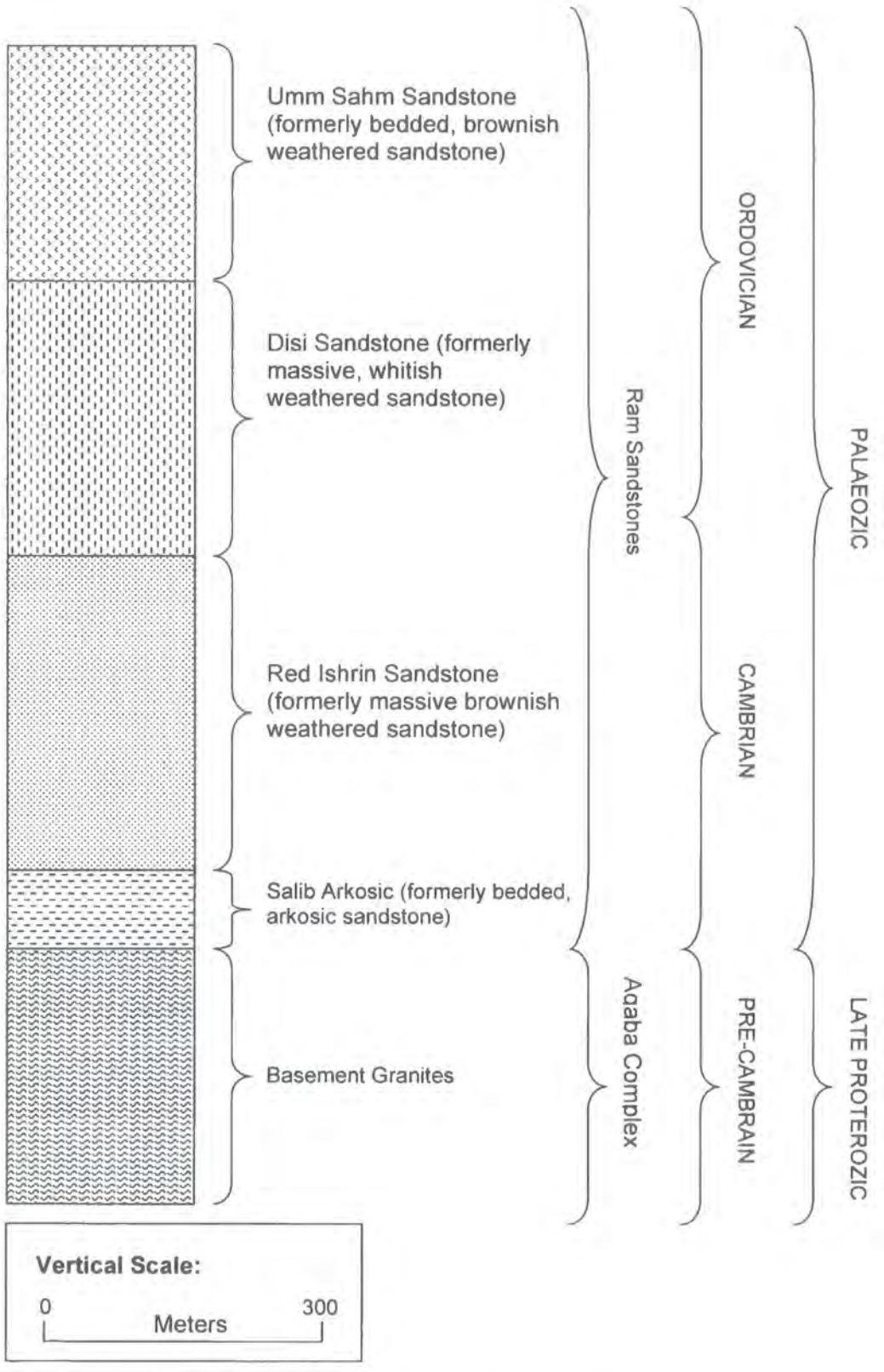

Figure 6.3: Generalised geological section of the Wadi Rum-Al Quwayra region of southern Jordan (After Bender, 1975)

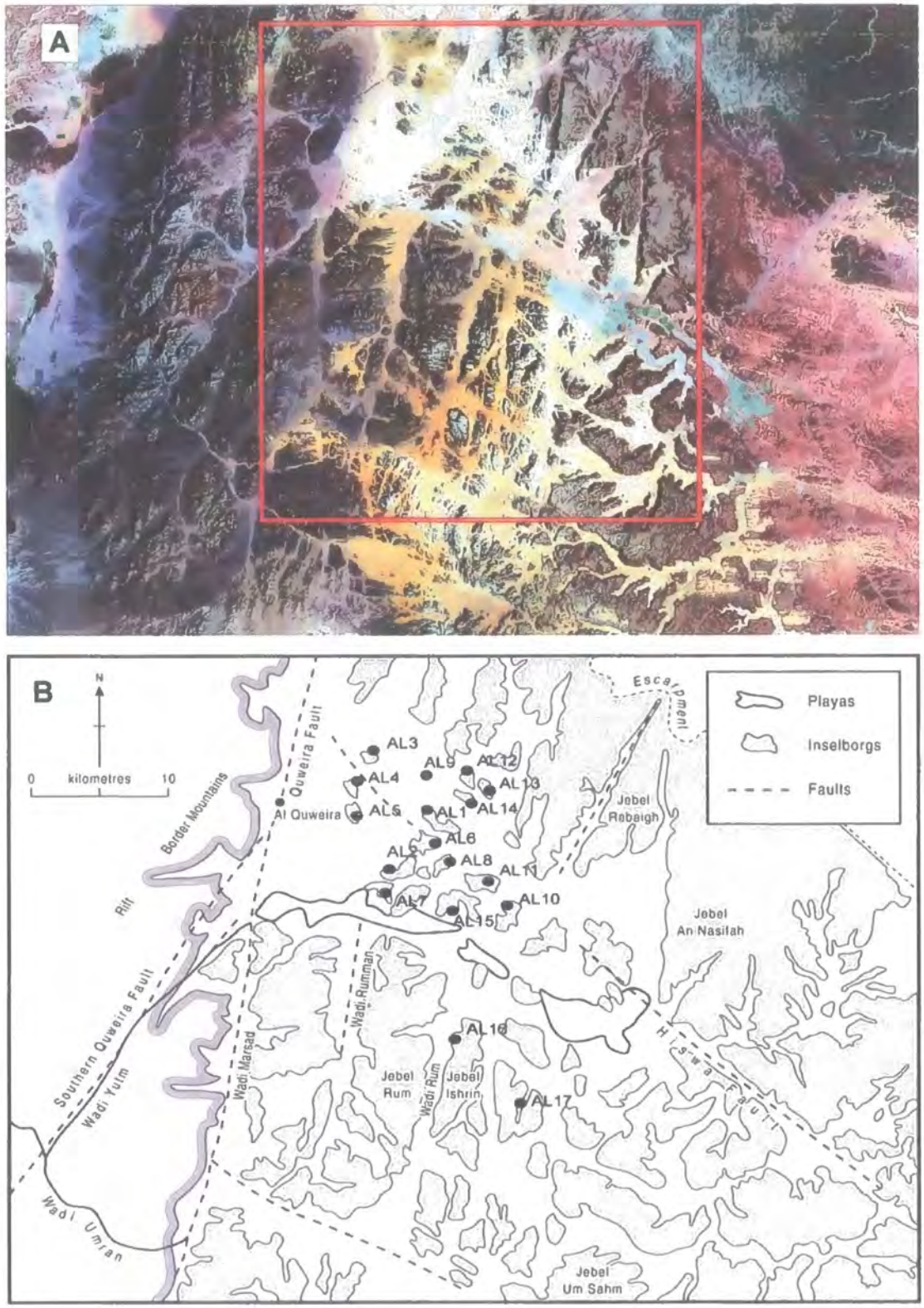

Figure 6.4: (A) Earthsat/NASA mosaic of Wadi Rum (Earthetc, 2004) and (B) map showing the extent of the sandstone inselbergs and field sites within the Al Quwayra Wadi Rum study area (Adapted from Osborn and Duford, 1981). The red box shows the extent of map (B).

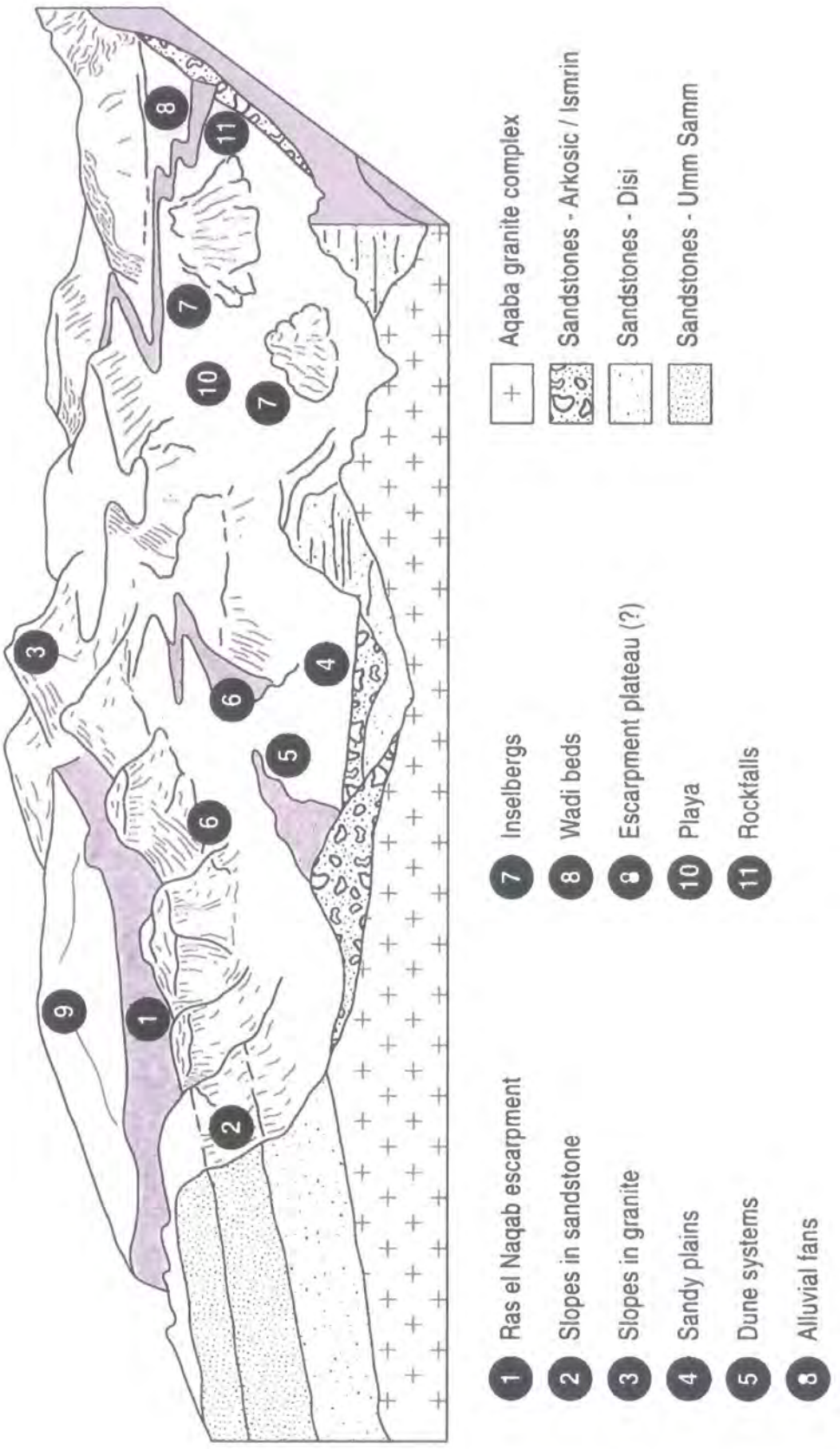

Figure 6.5: Landscape component model showing the important geomorphic features in the Al Quwayra Wadi Rum study area.

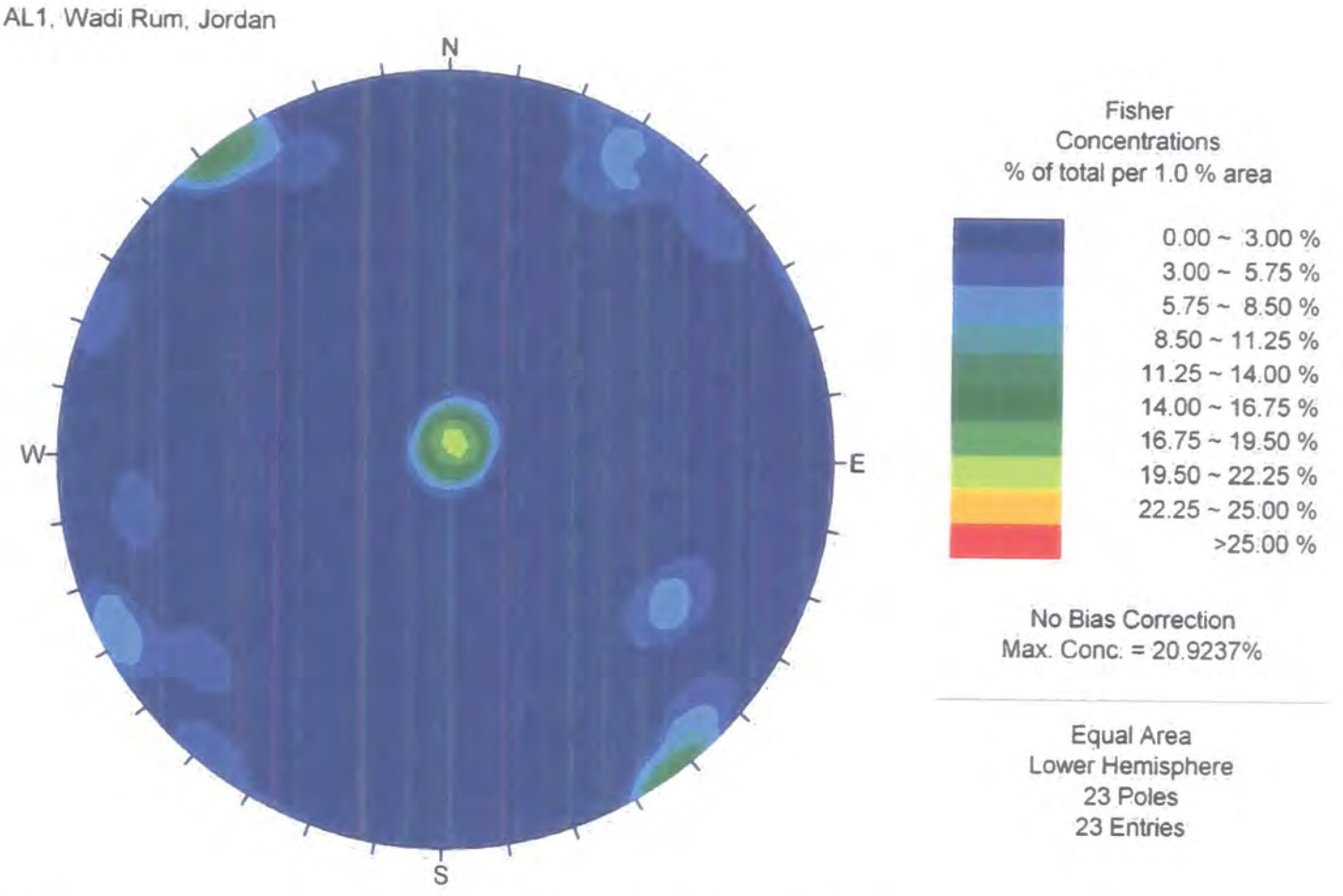

Figure 6.6: Contoured polar projection of the discontinuities at AL1, Wadi Rum, Jordan.

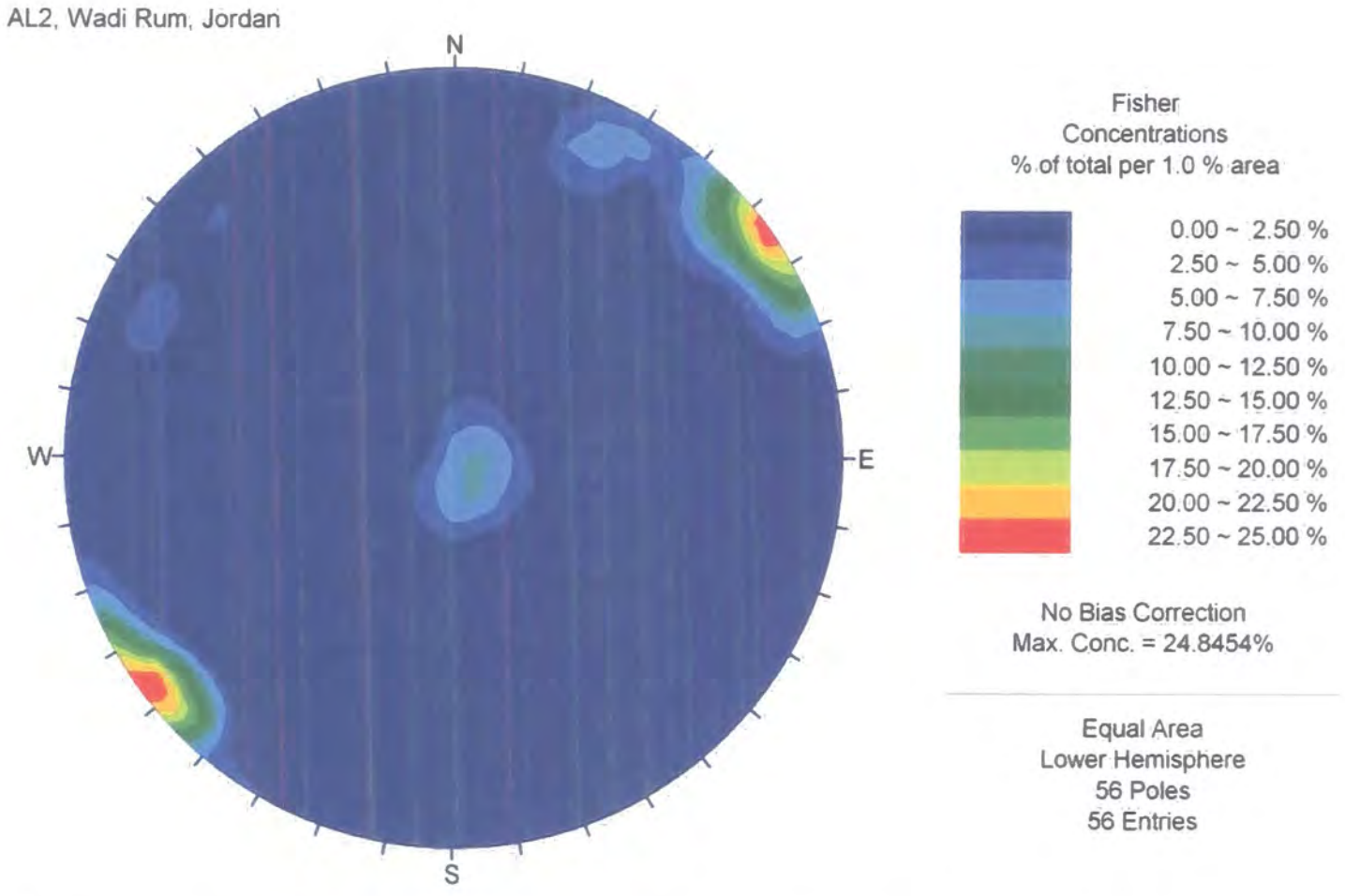

Figure 6.7: Contoured polar projection of the discontinuities at AL2, Wadi Rum, Jordan.

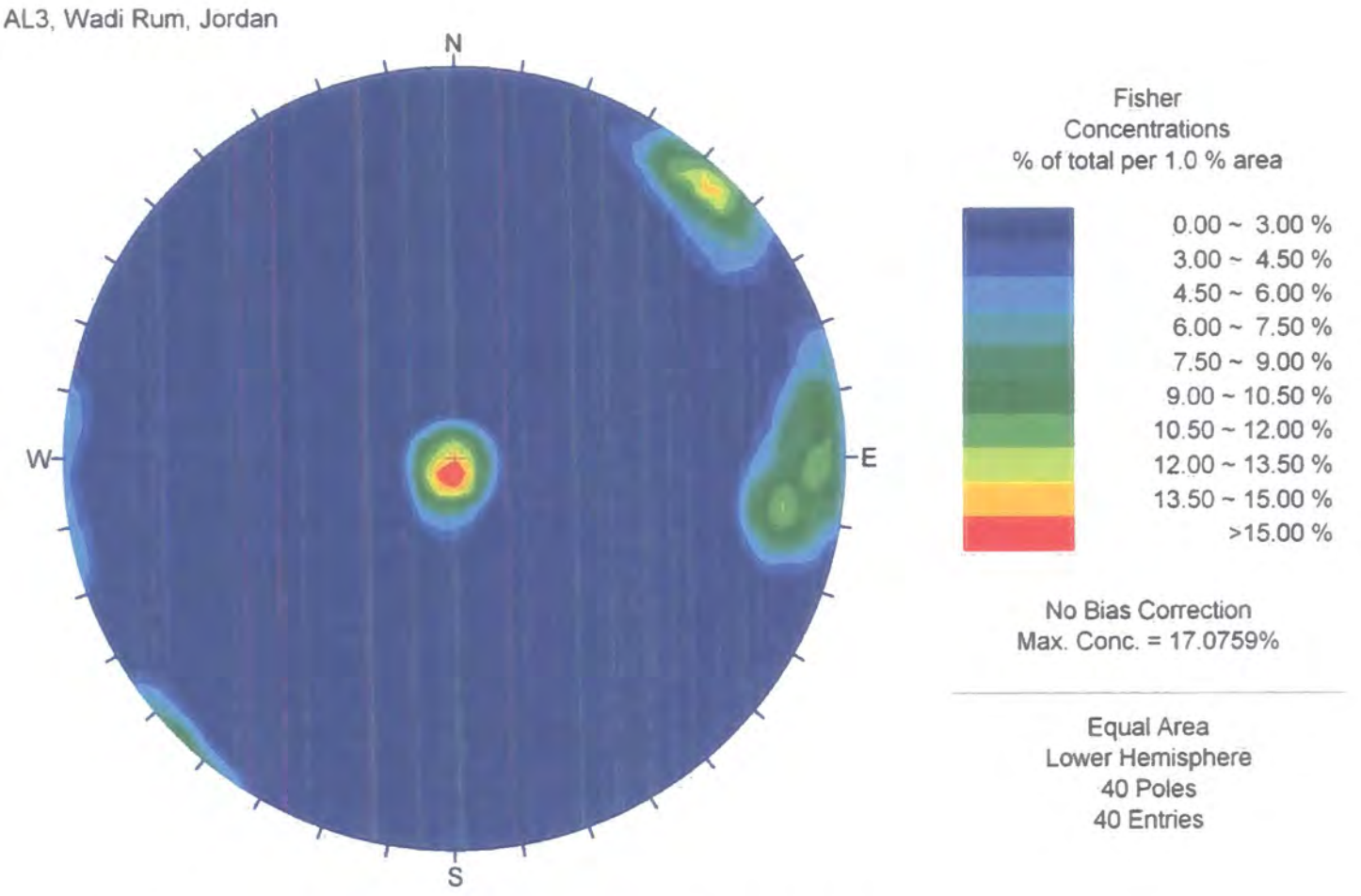

Figure 6.8: Contoured polar projection of the discontinuities at AL3, Wadi Rum, Jordan.

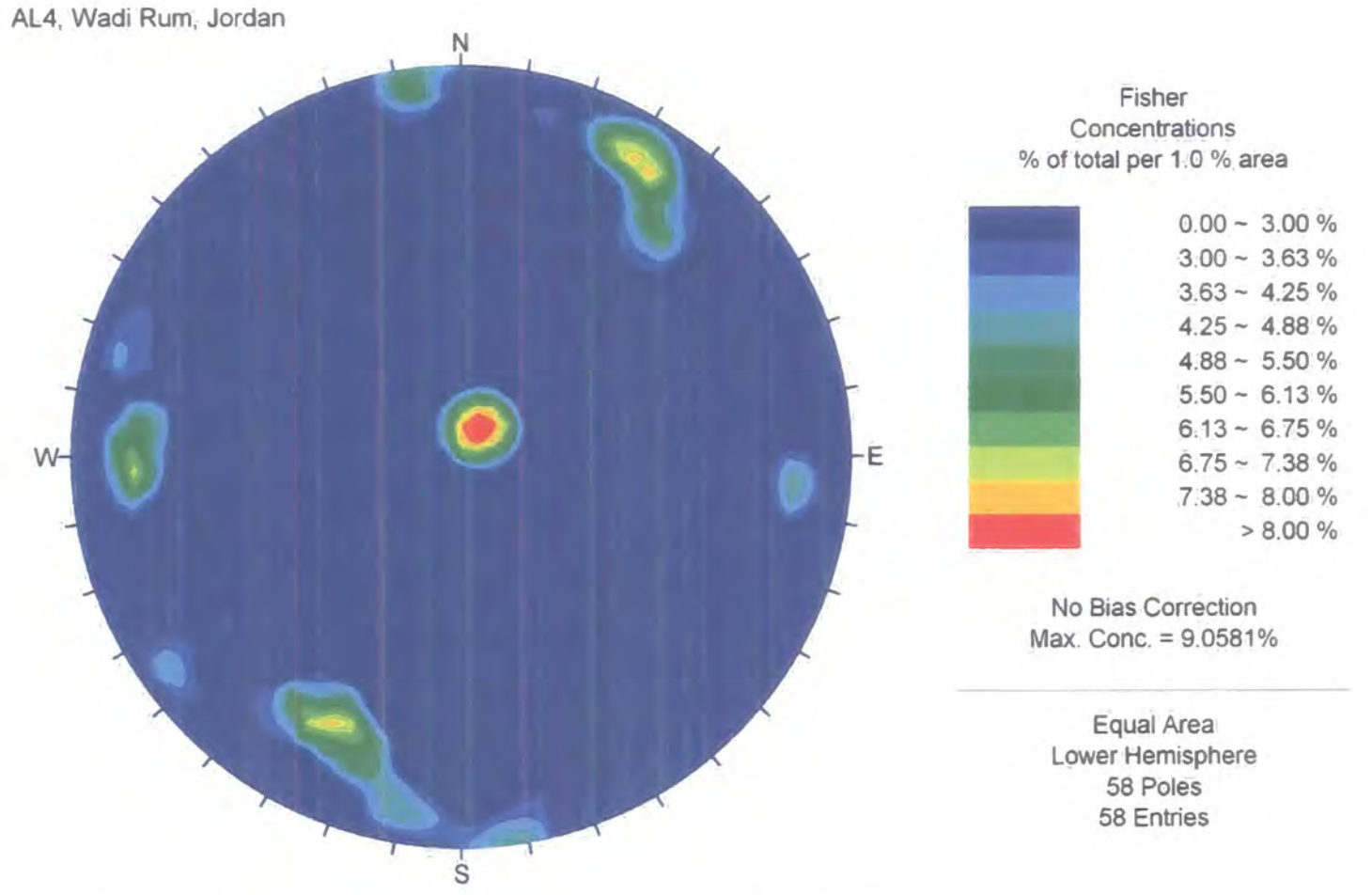

Figure 6.9: Contoured polar projection of the discontinuities at AL4, Wadi Rum, Jordan.

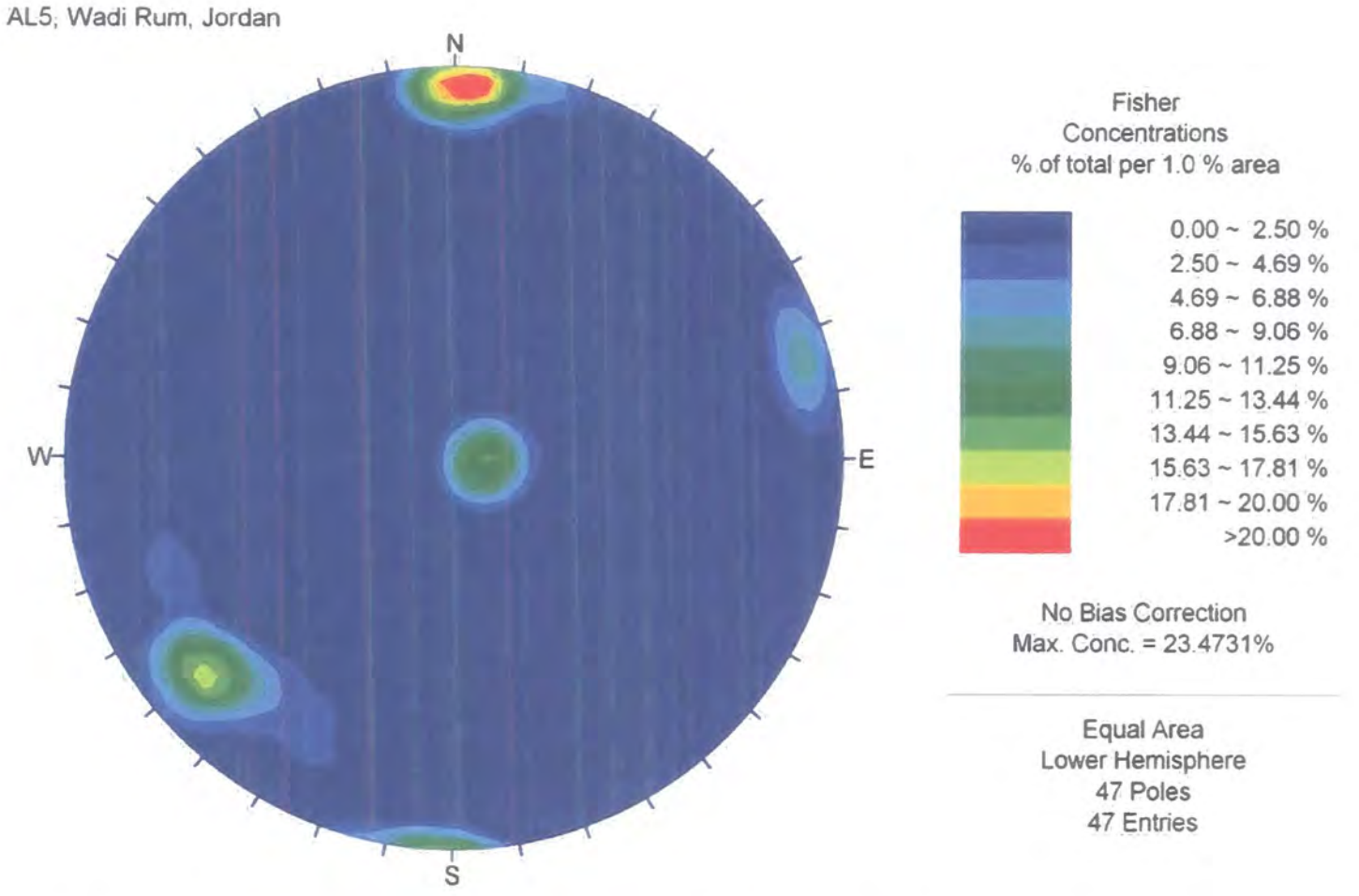

Figure 6.10: Contoured polar projection of the discontinuities at AL5, Wadi Rum, Jordan.

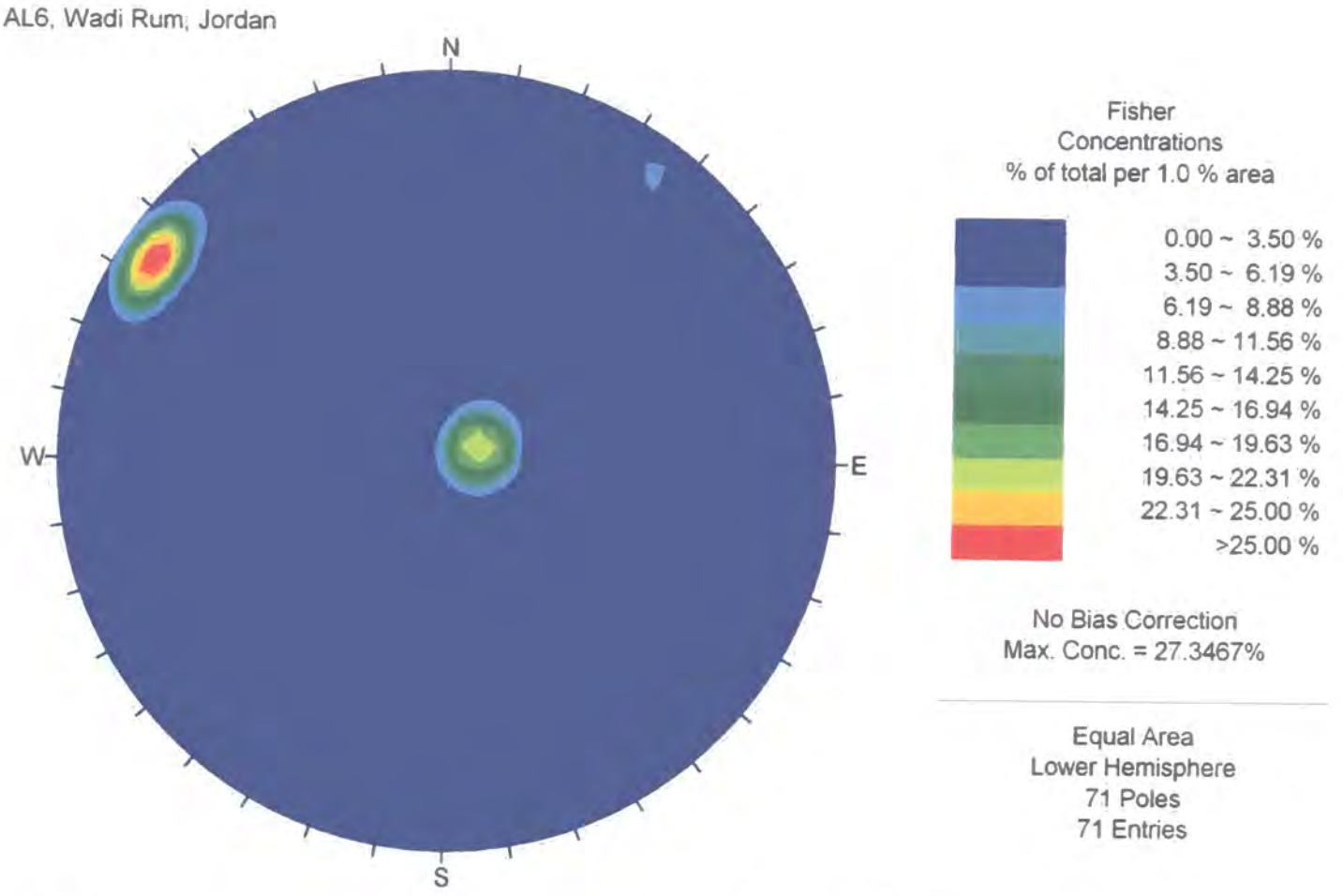

Figure 6.11: Contoured polar projection of the discontinuities at AL6, Wadi Rum, Jordan.

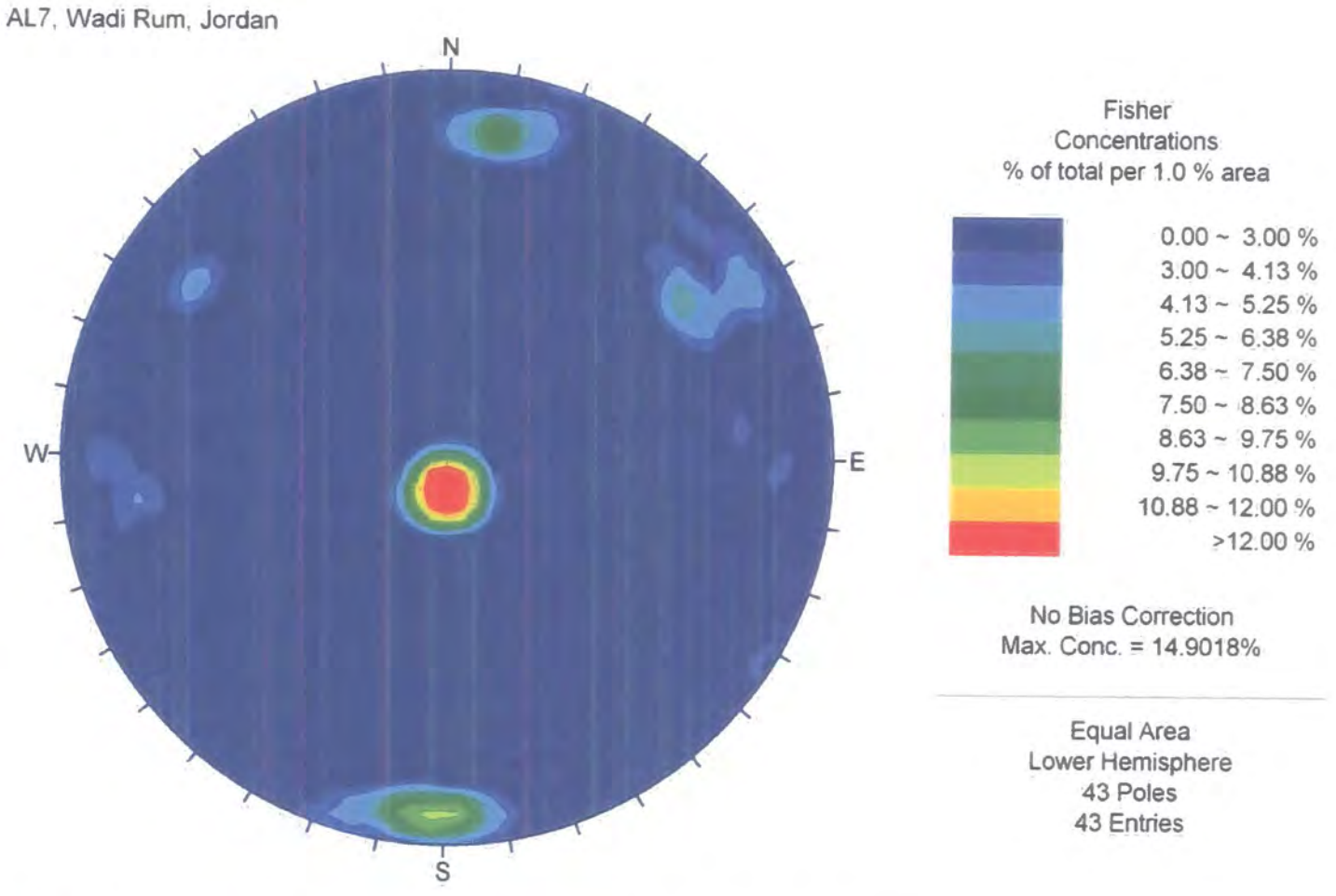

Figure 6.12: Contoured polar projection of the discontinuities at AL7, Wadi Rum, Jordan.

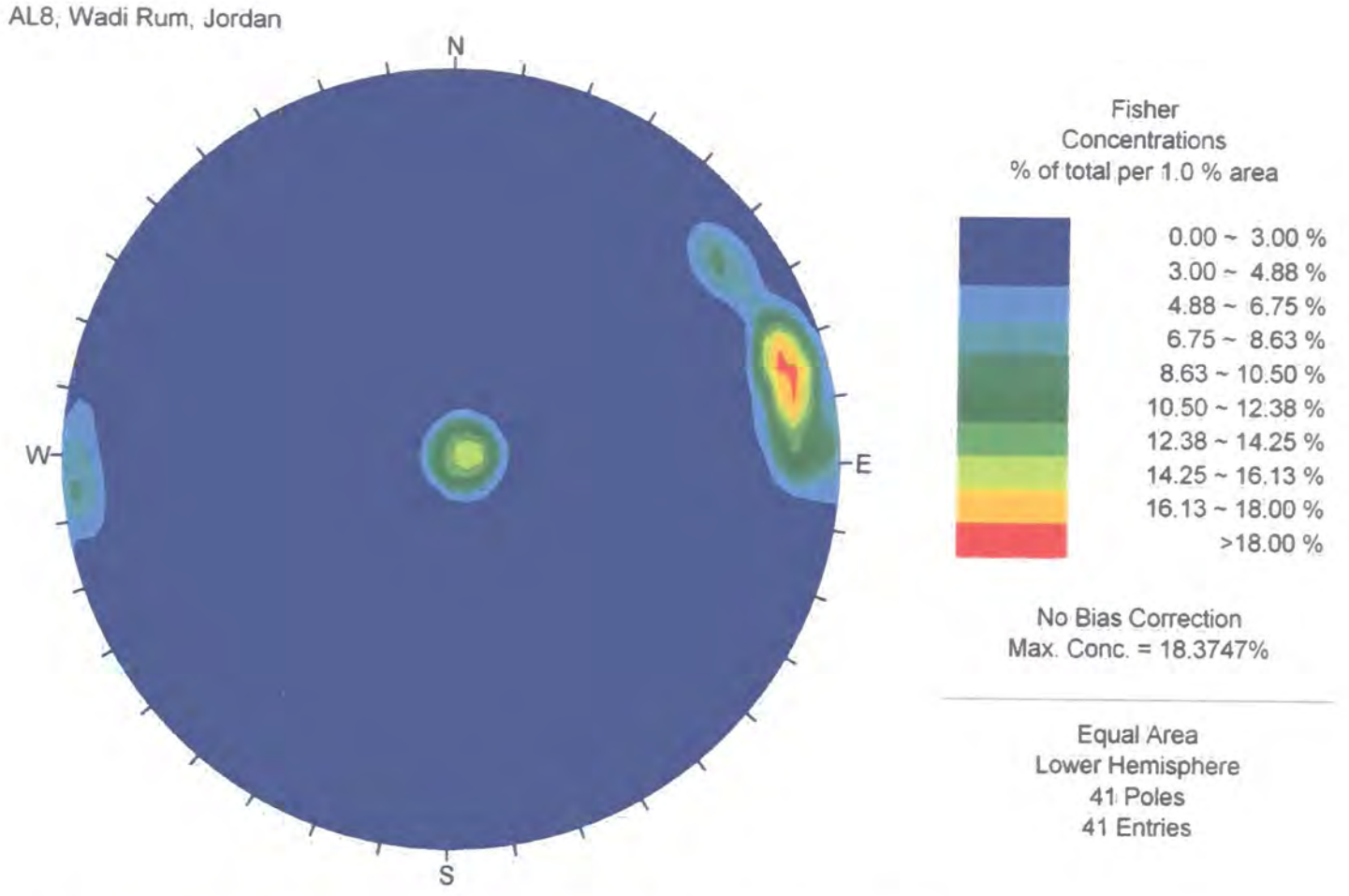

Figure 6.13: Contoured polar projection of the discontinuities at AL8, Wadi Rum, Jordan.

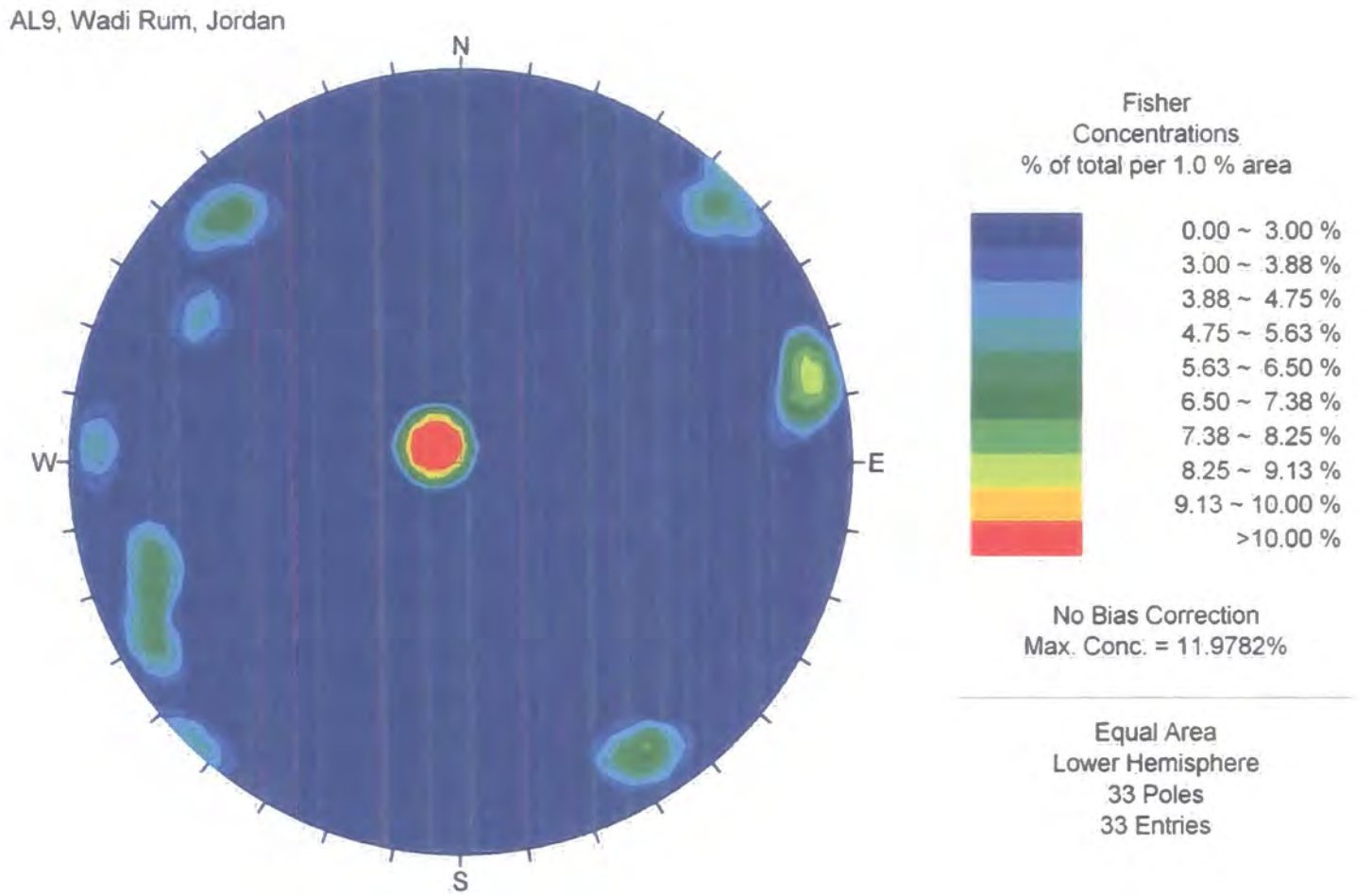

Figure 6.14: Contoured polar projection of the discontinuities at AL9, Wadi Rum, Jordan.

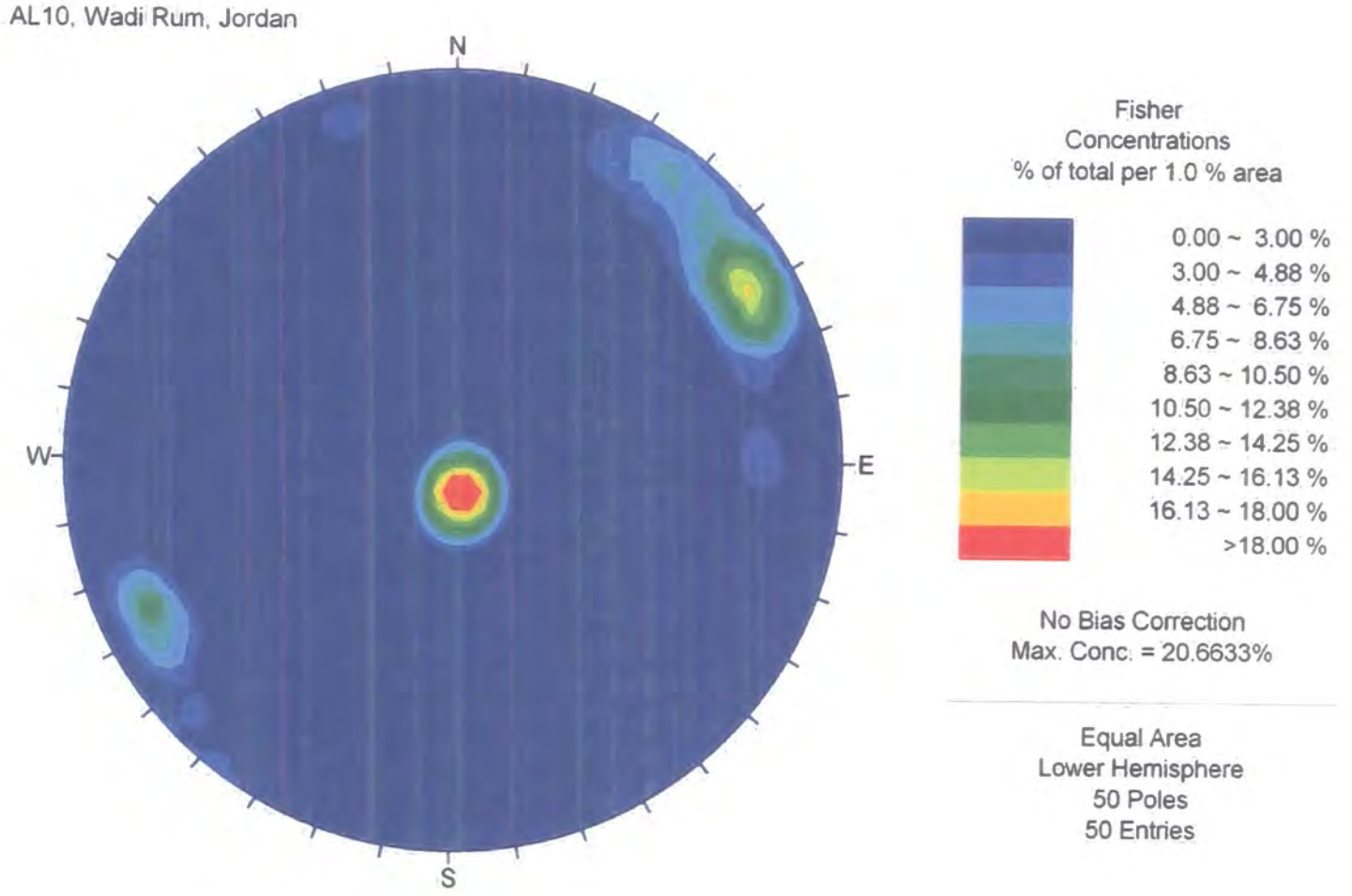

Figure 6.15: Contoured polar projection of the discontinuities at AL10, Wadi Rum, Jordan.

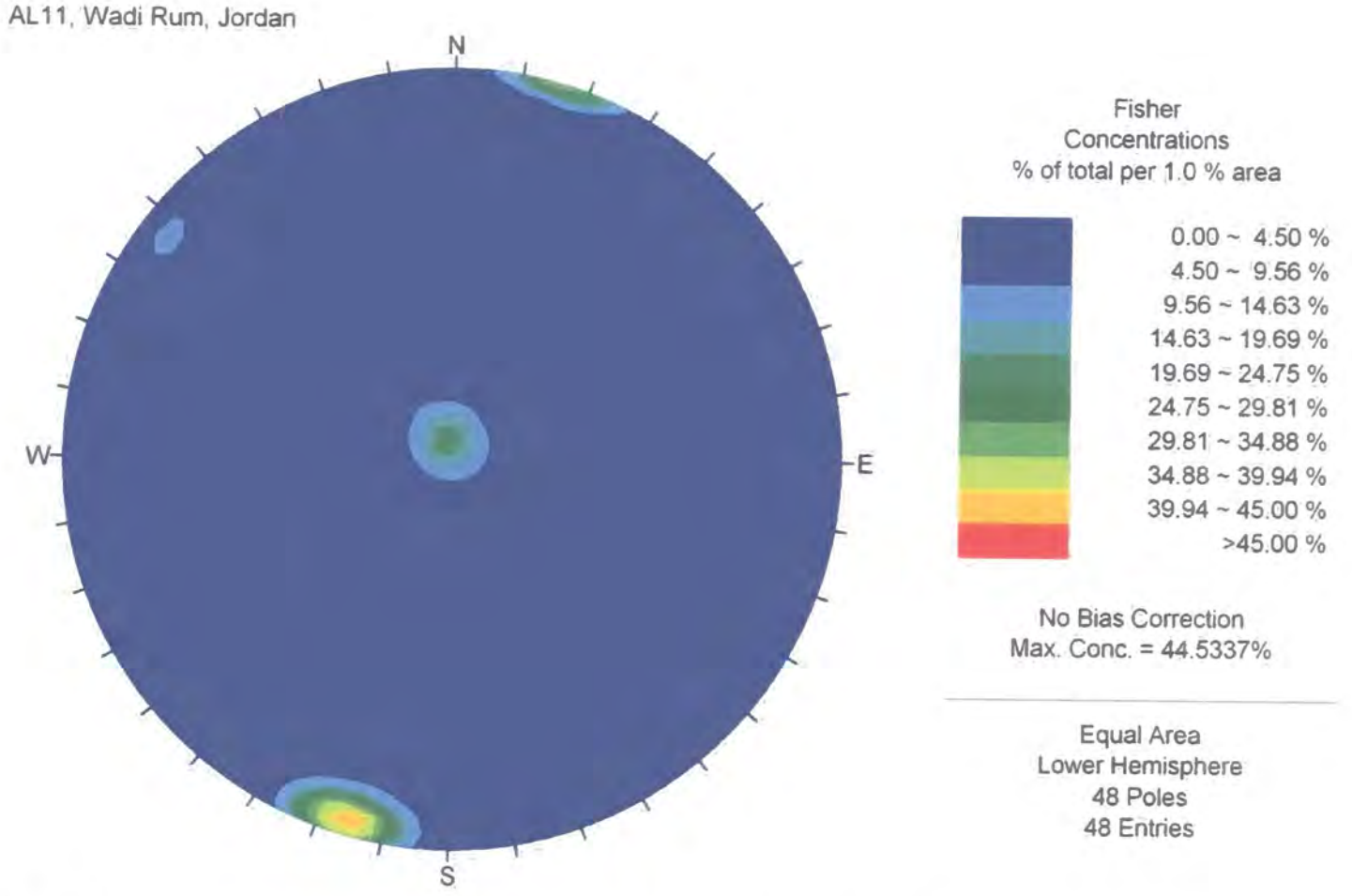

Figure 6.16: Contoured polar projection of the discontinuities at AL11, Wadi Rum, Jordan.

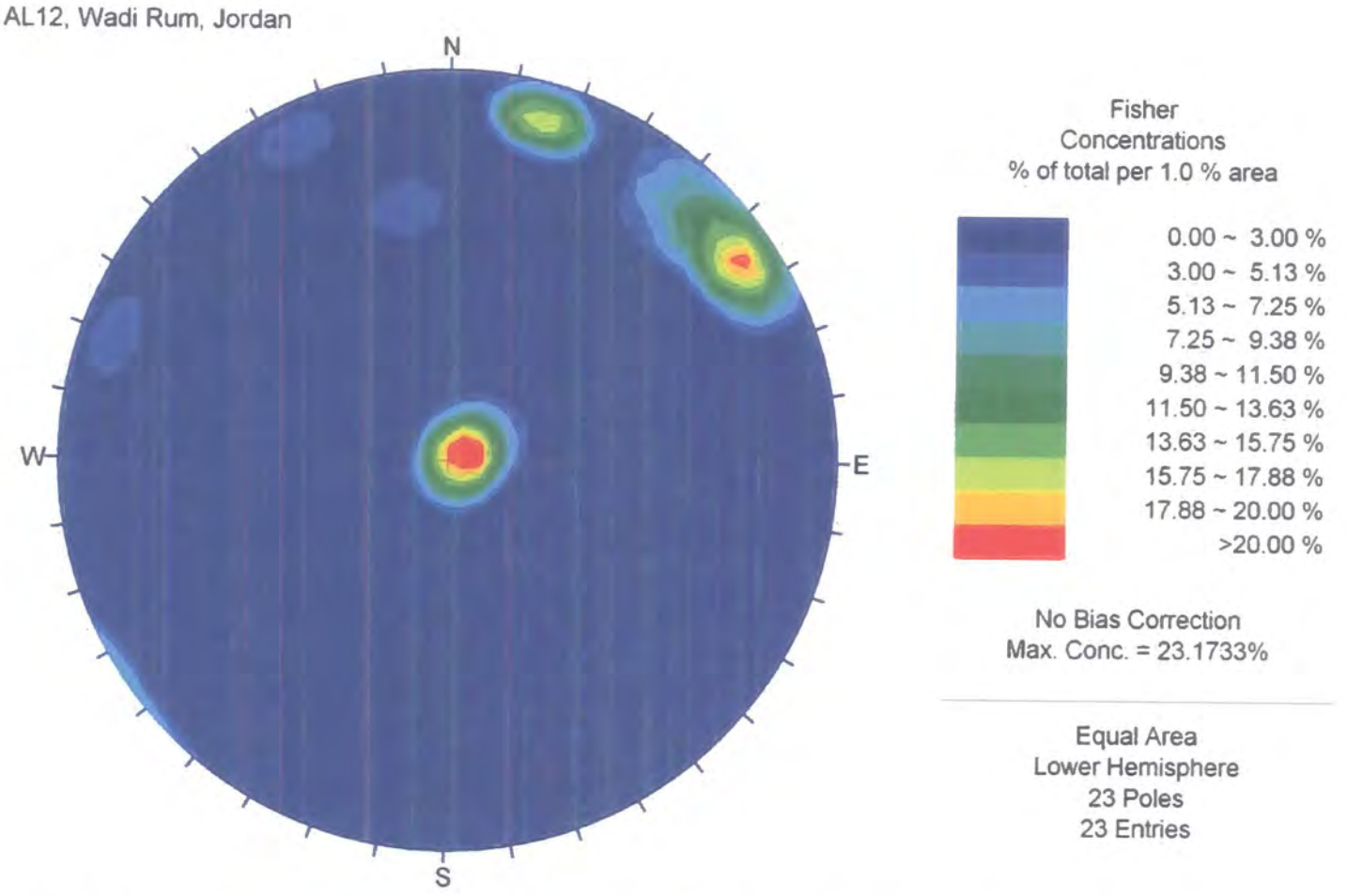

Figure 6.17: Contoured polar projection of the discontinuities at AL12, Wadi Rum, Jordan.

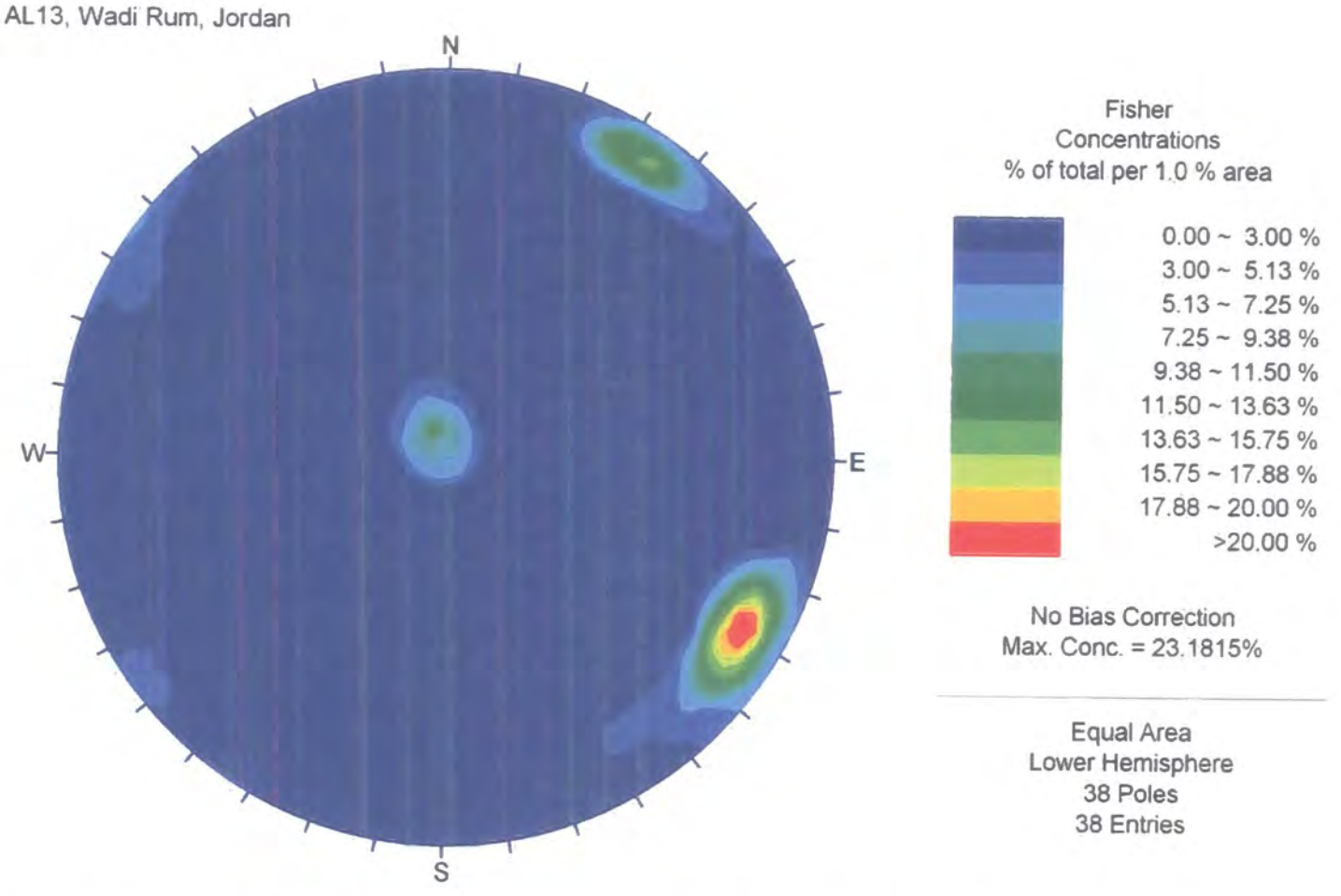

Figure 6.18: Contoured polar projection of the discontinuities at AL13, Wadi Rum, Jordan.

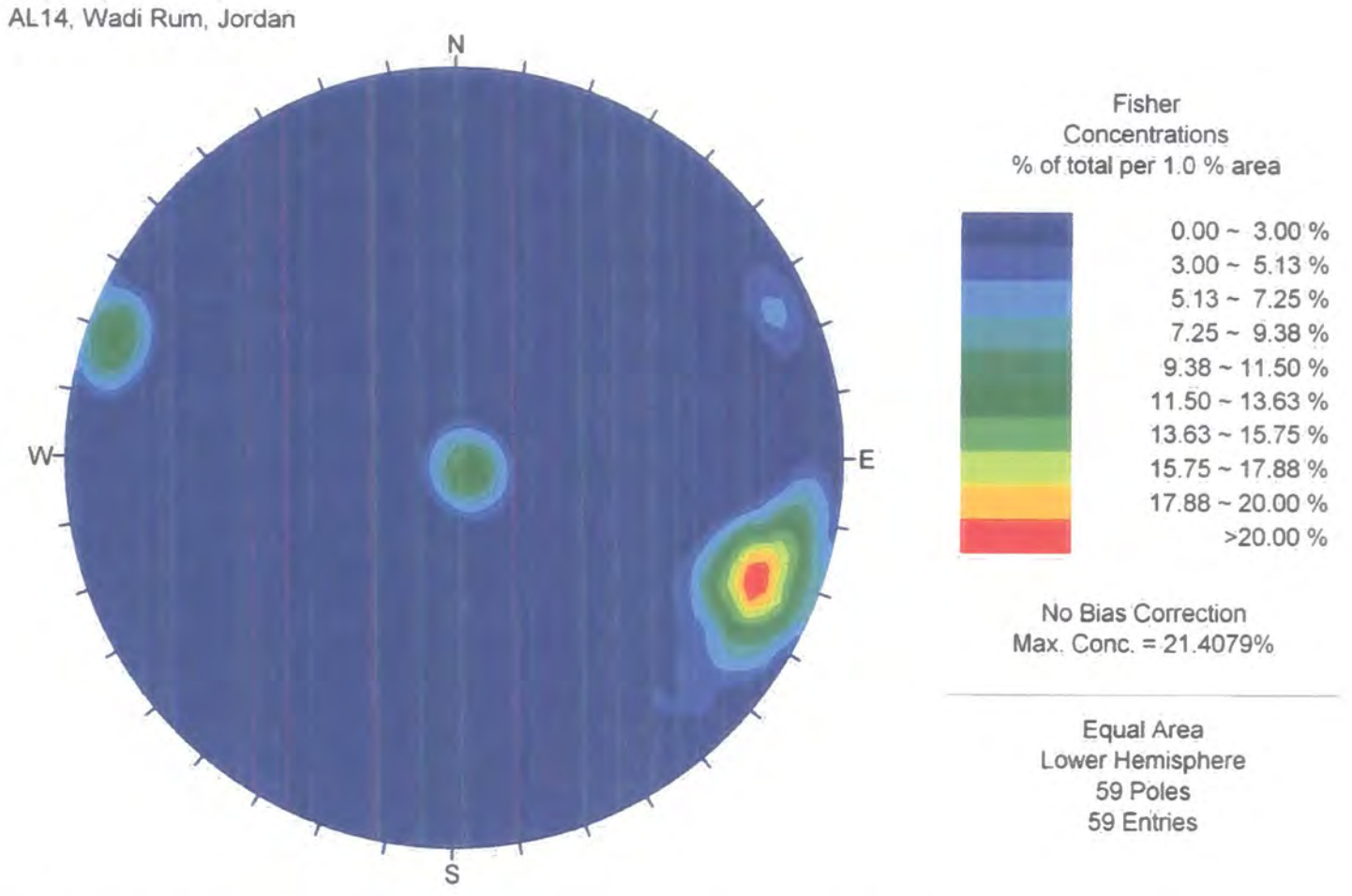

Figure 6.19: Contoured polar projection of the discontinuities at AL14, Wadi Rum, Jordan.

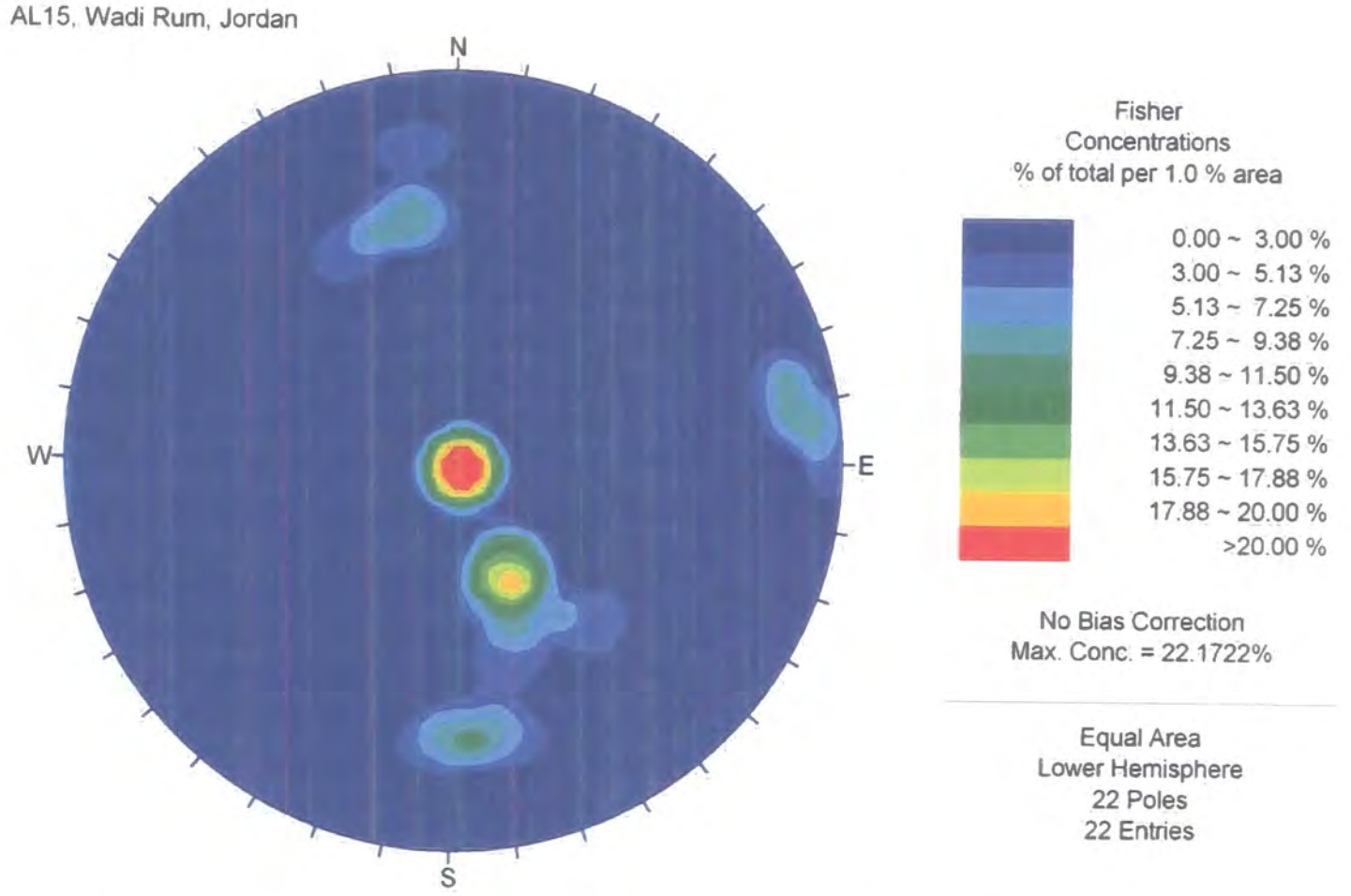

Figure 6.20: Contoured polar projection of the discontinuities at AL15, Wadi Rum, Jordan.

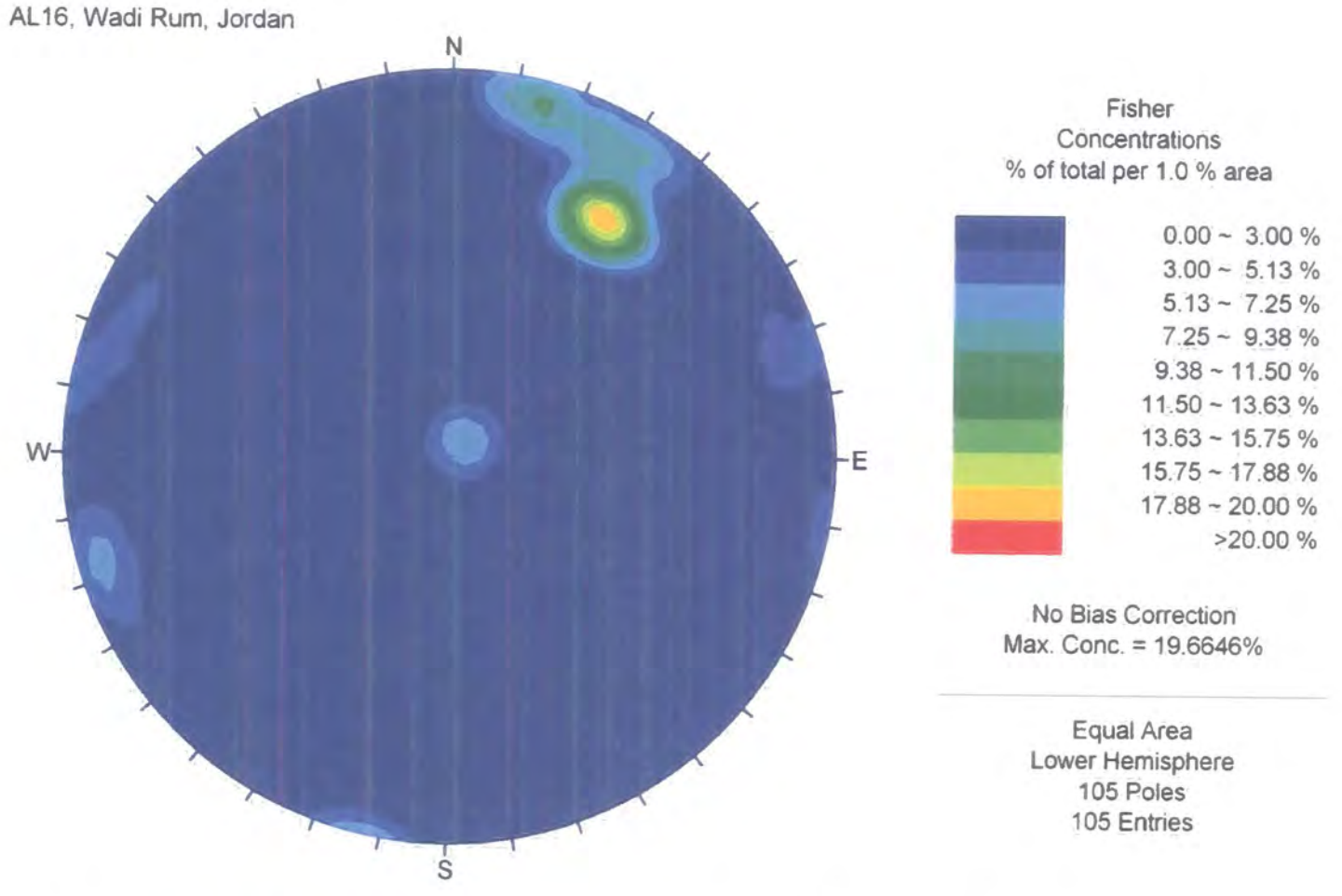

Figure 6.21: Contoured polar projection of the discontinuities at AL16, Wadi Rum, Jordan.

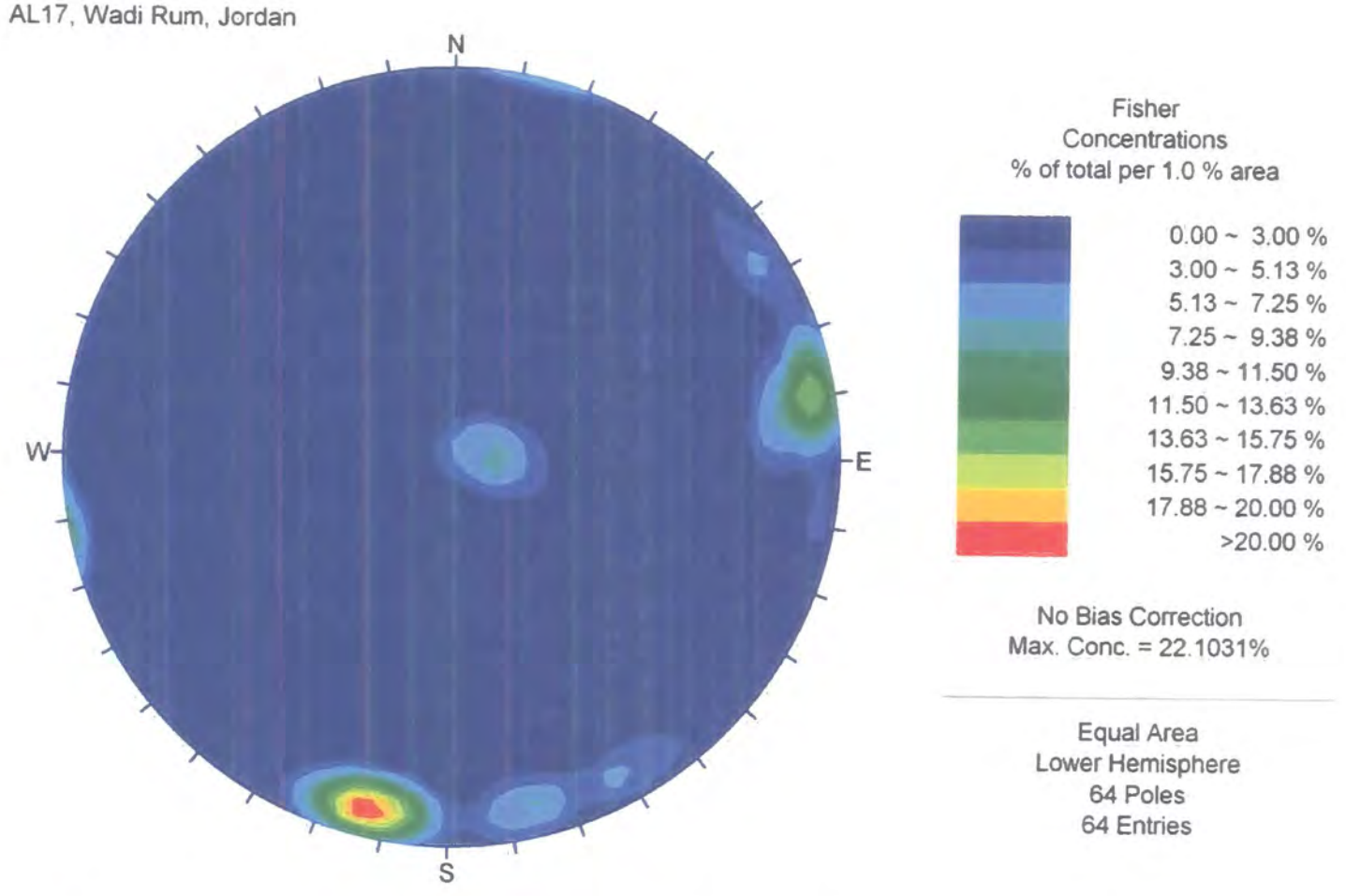

Figure 6.22: Contoured polar projection of the discontinuities at AL17, Wadi Rum, Jordan.

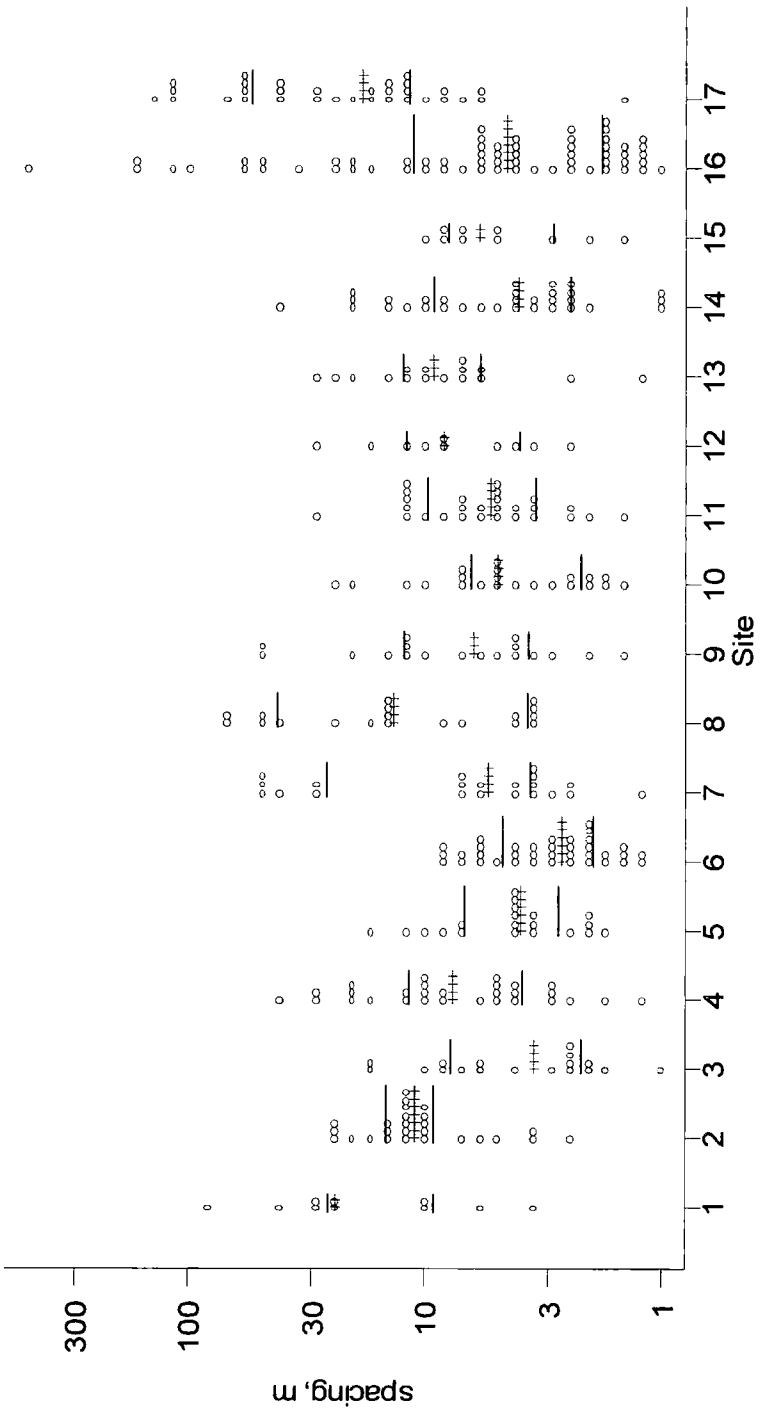

Figure 6.23: Dotplots of lumped joint spacing data for all sites examined in the Al-Quwayra–Wadi Rum region of southern Jordan. The upper bars through the plot represent the upper quartile, mid bars the median and lower bars the lower quartiles.

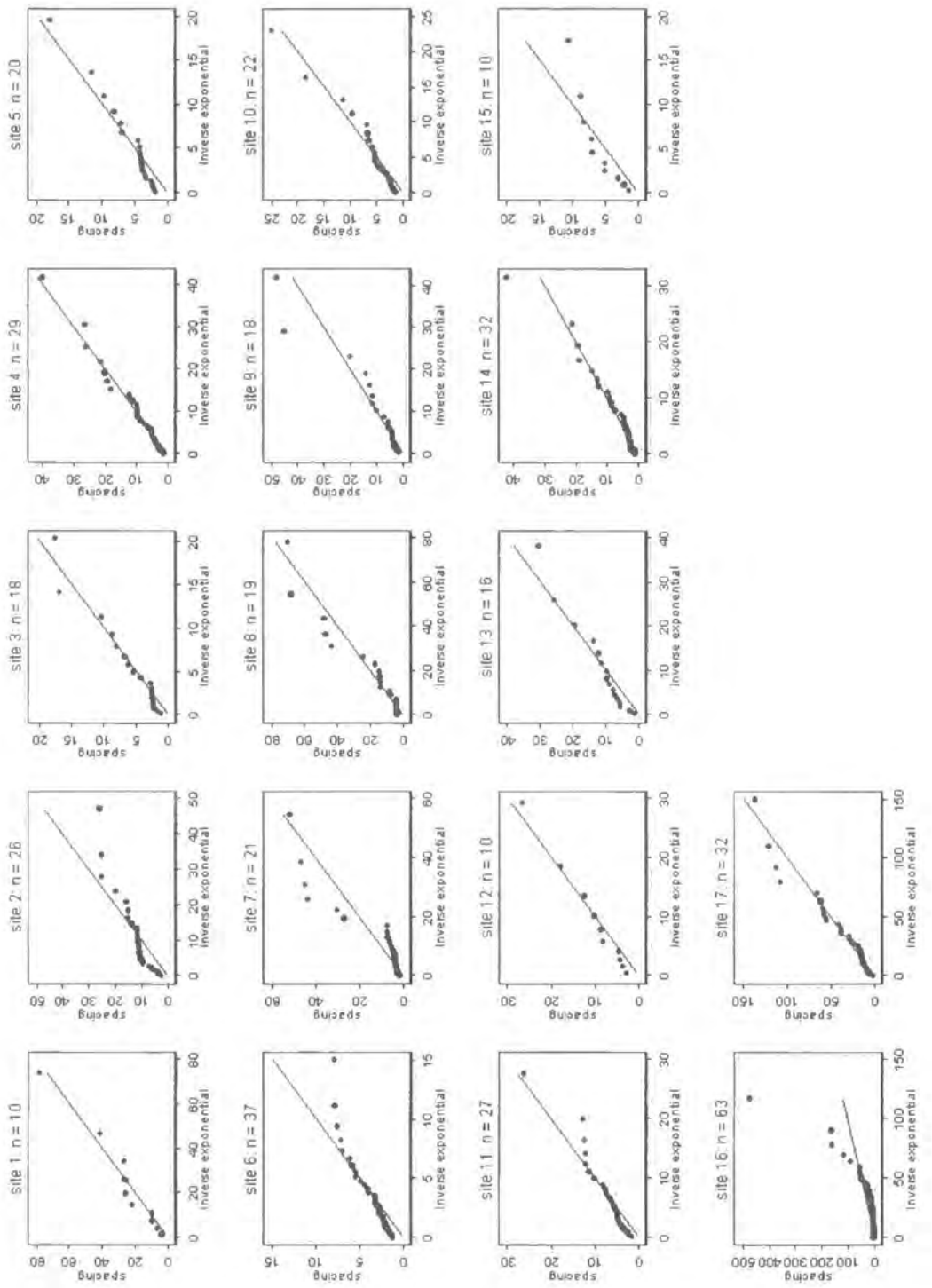

Figure 6.24: Quantiles of joint spacing compared with an ideal exponential distribution for all sites in the Al Quwayra-Wadi Rum region, Jordan.

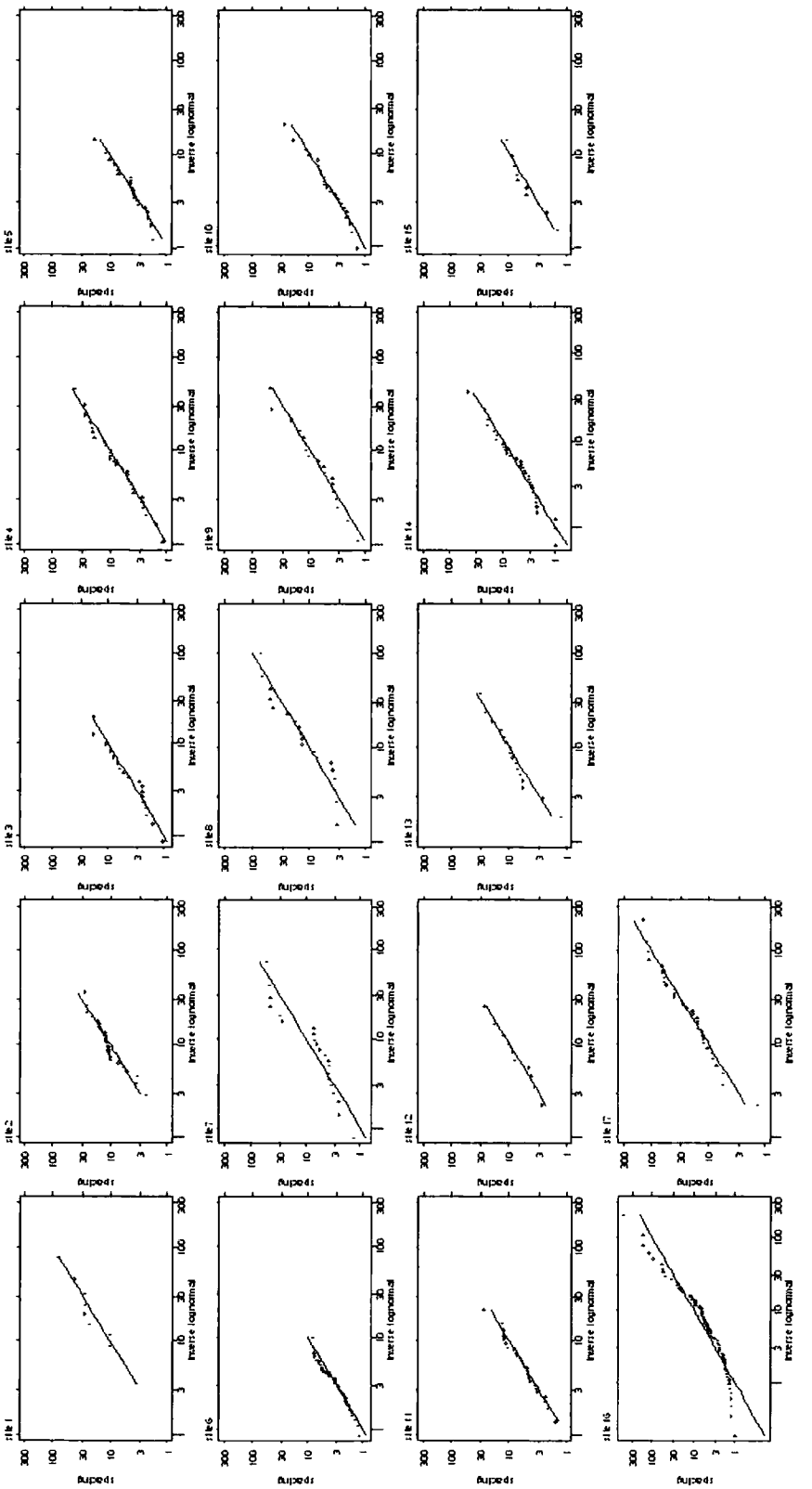

Figure 6.25: Log normal distributions of lumped discontinuity data for all sites in the Al-Quwayra and Wadi Rum areas of Jordan. The solid line represents an ideal lognormal distribution, with a spread of data points around this.

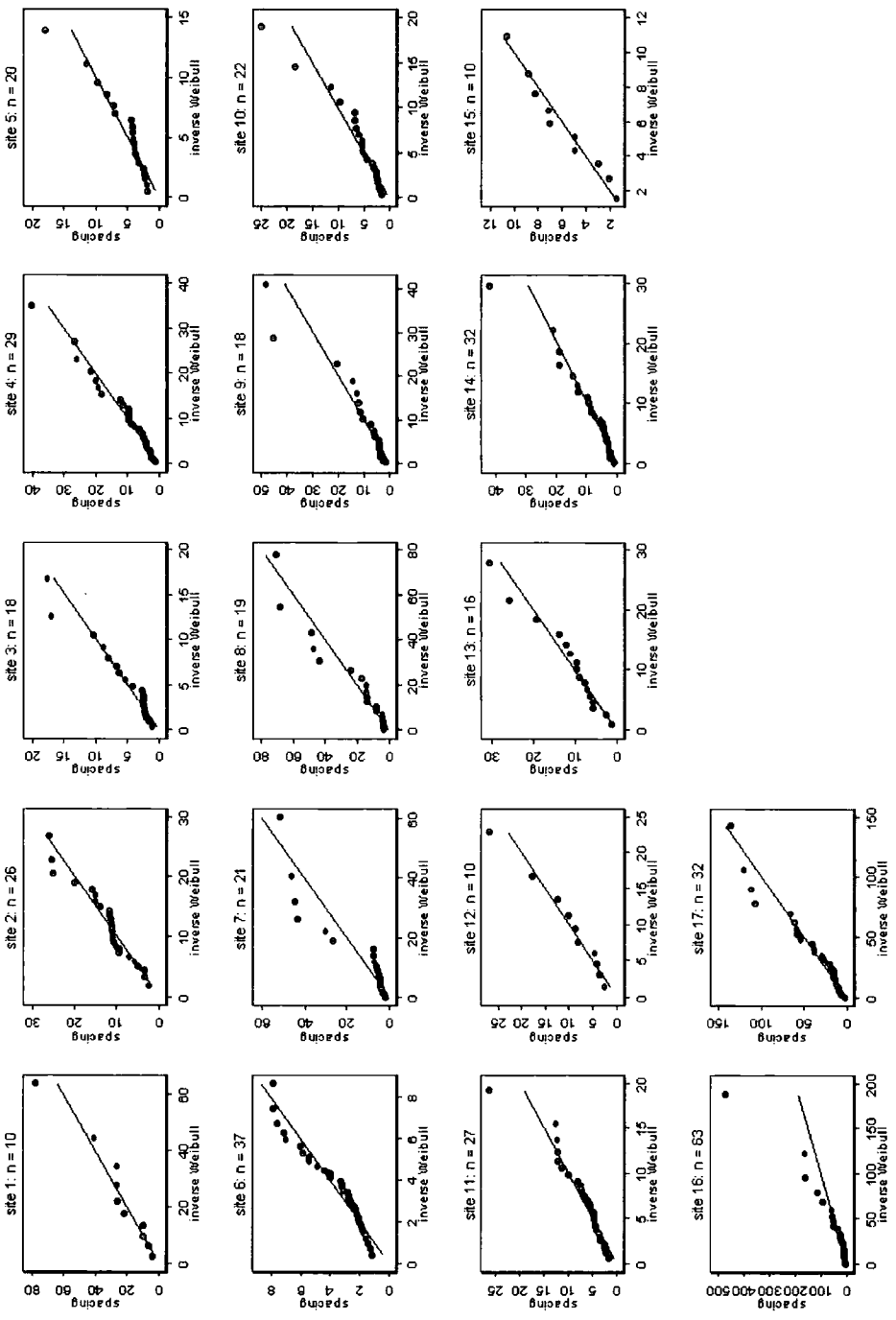

Figure 6.26: Quantiles of joint spacing compared with fitted Weibull distributions for all sites in the Al Quwayra-Wadi Rum region, Jordan.

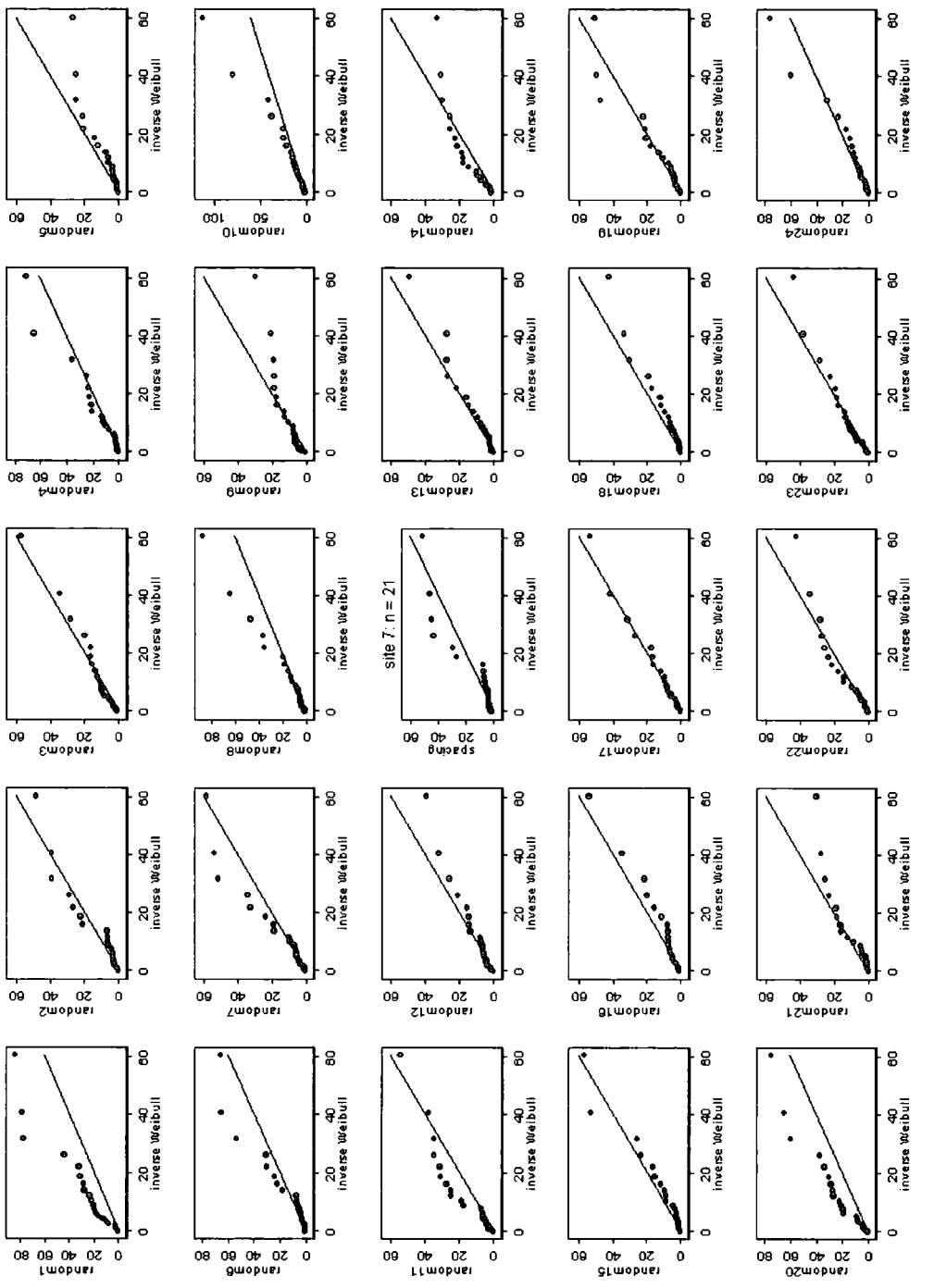

Figure 6.27: AL7 compared with randomly generated Weibull distributions given the same population mean. Note that although the parameters are randomly generated, scatter exists in the tails of the distributions.

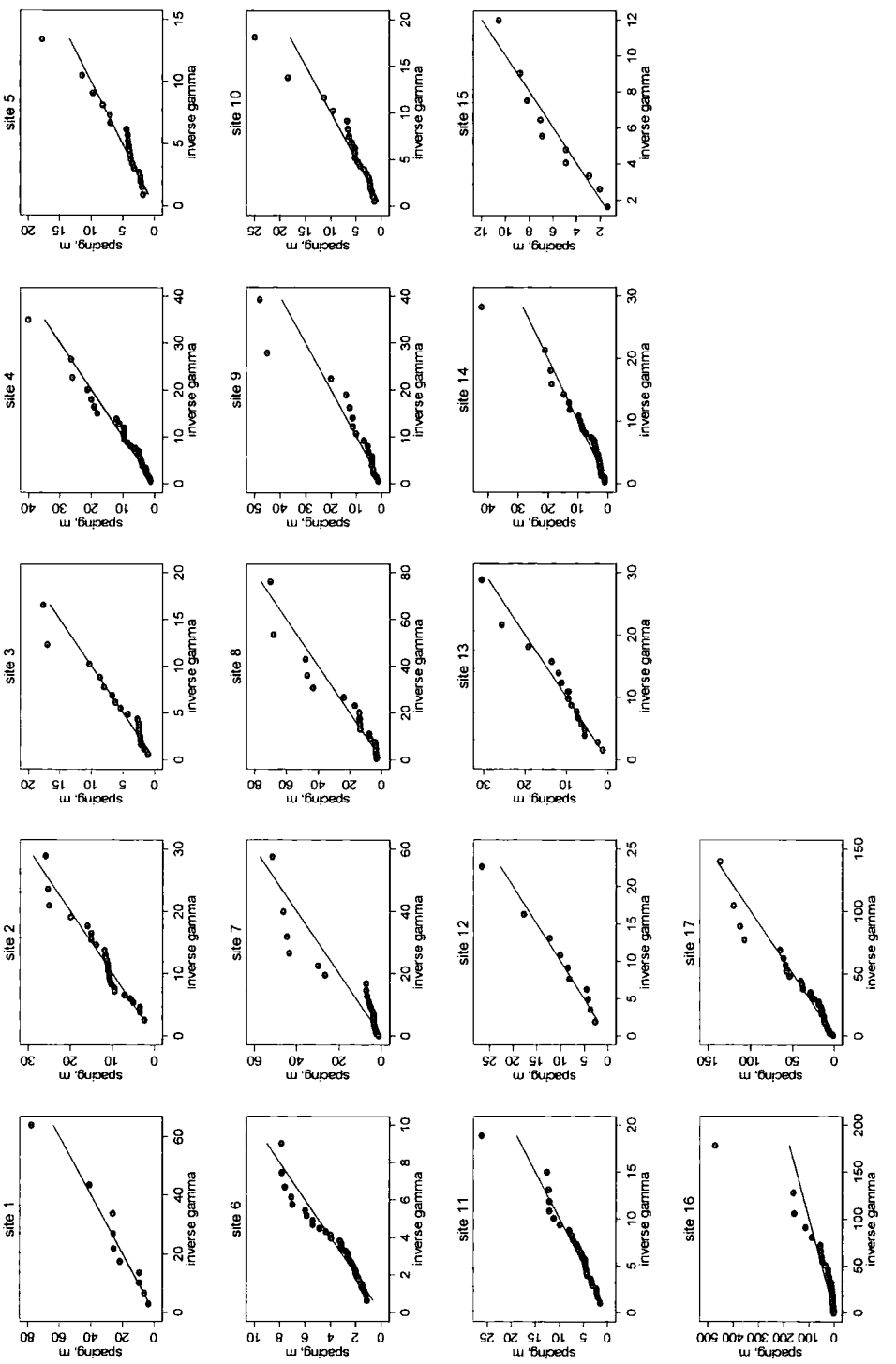

Figure 6.28: Quantiles of joint spacing compared with a gamma distribution for all sites in the Al Quwayra-Wadi Rum region, Jordan.

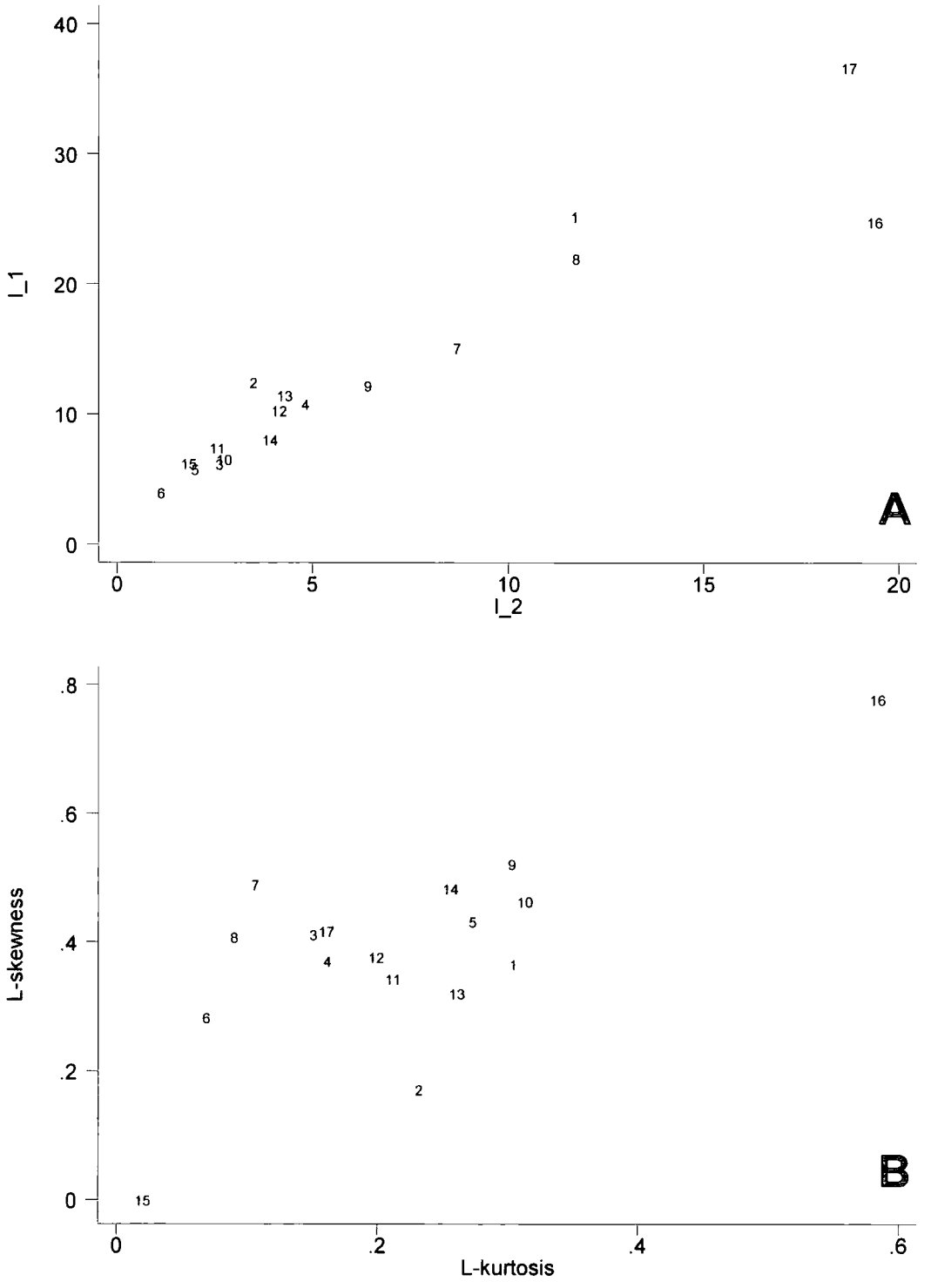

Figure 6.29: Summary L-moments for aggregated joint spacing for all sites. The first two L-moments are shown in (a) and the second two in (b).

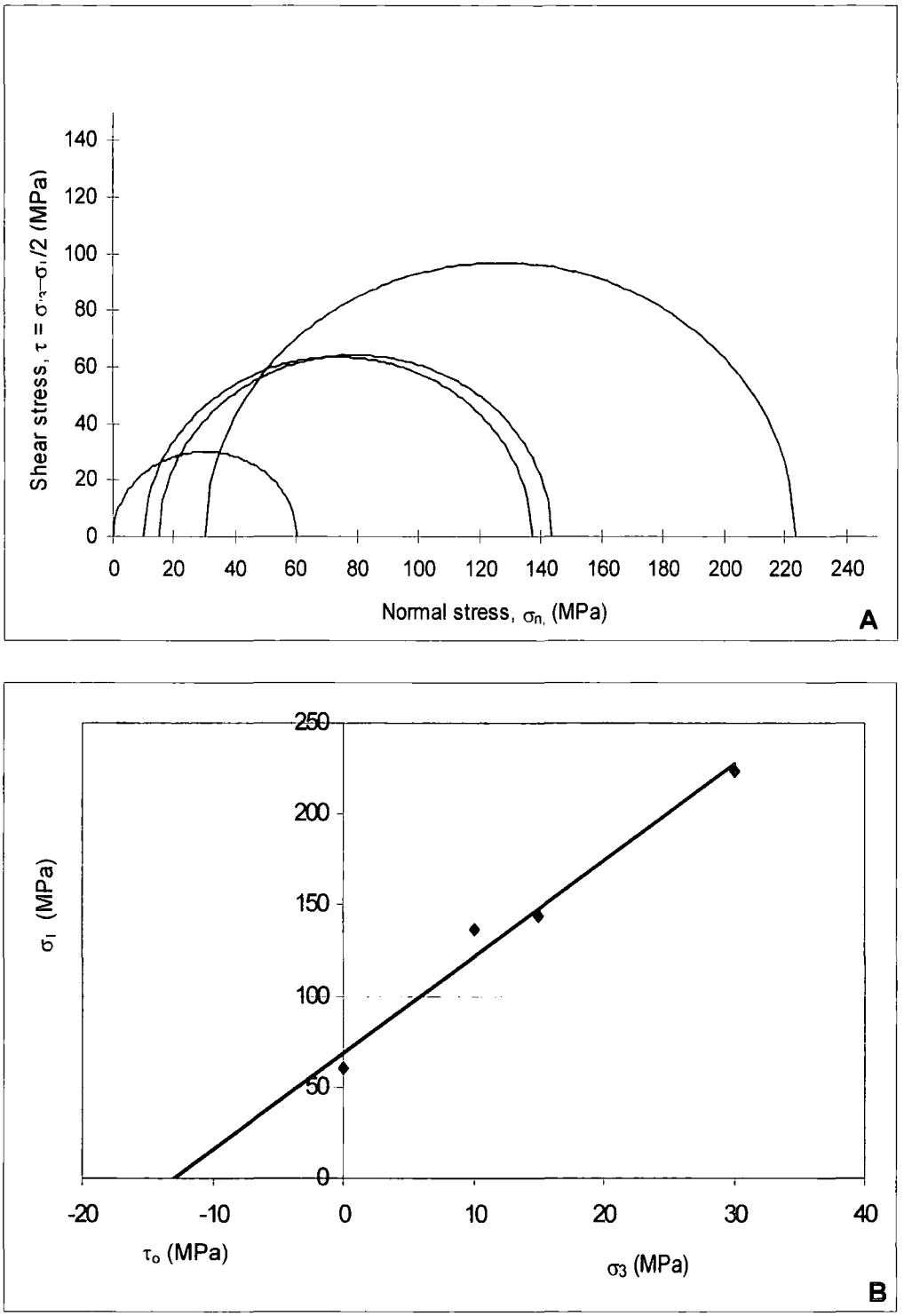

Figure 6.30: Mohr's circles (A) and sigma 1 / sigma 3 stress space with fitted Mohr-Coulomb failure envelope (B) for Red Ishrin Sandstone, Jordan.

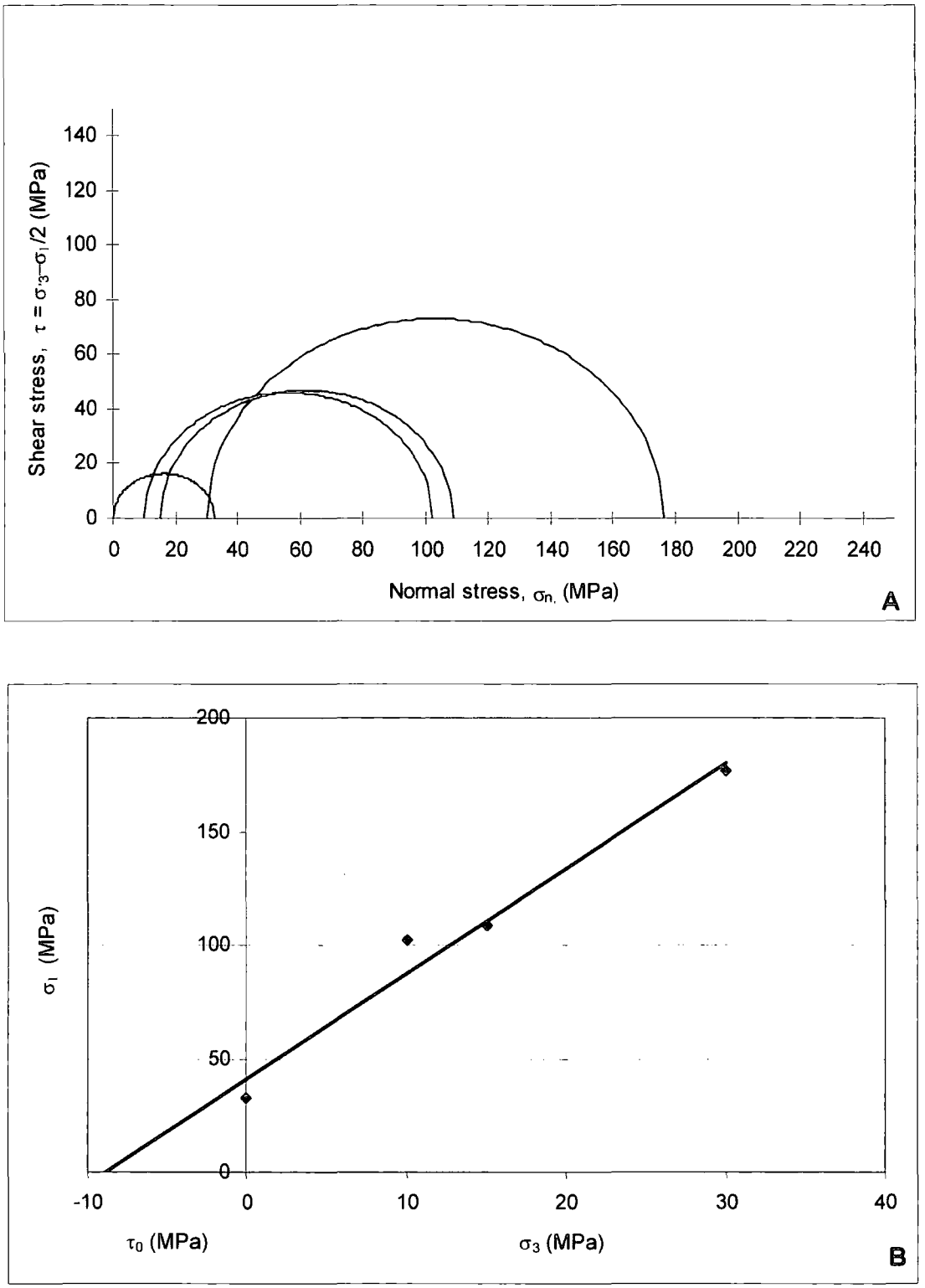

Figure 6.31: Mohr's circles (A) and sigma 1 / sigma 3 stress space with fitted Mohr-Coulomb failure envelope (B) for Disi Sandstone, Jordan.

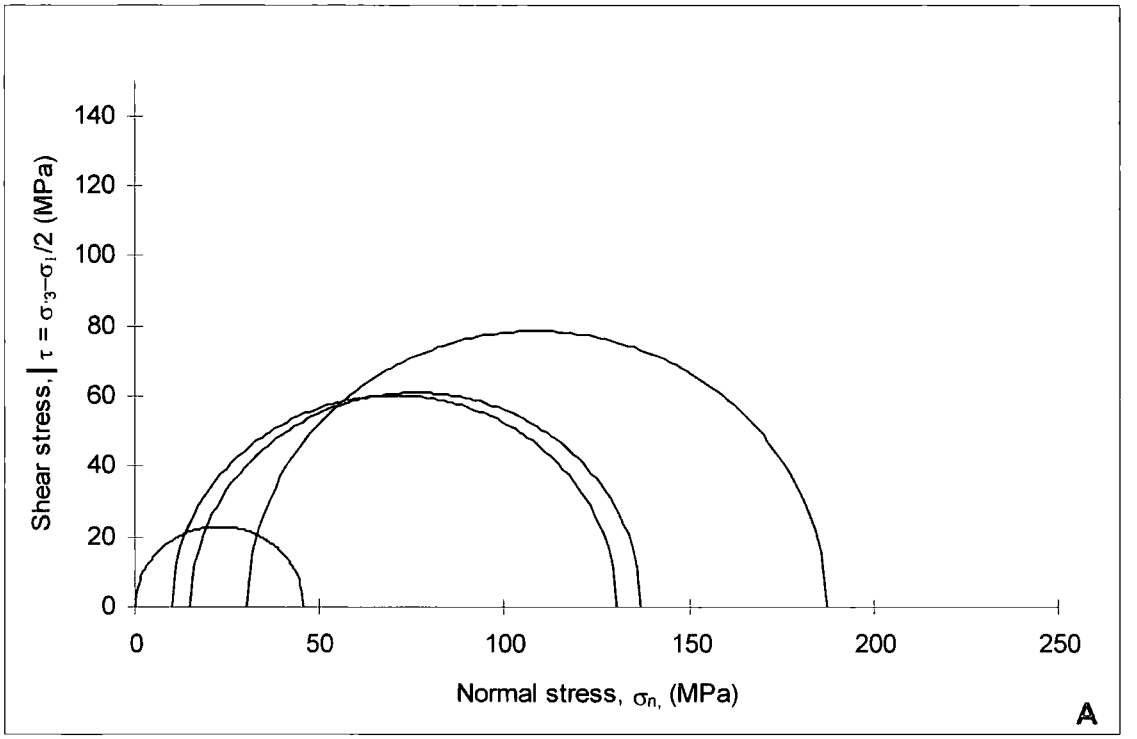

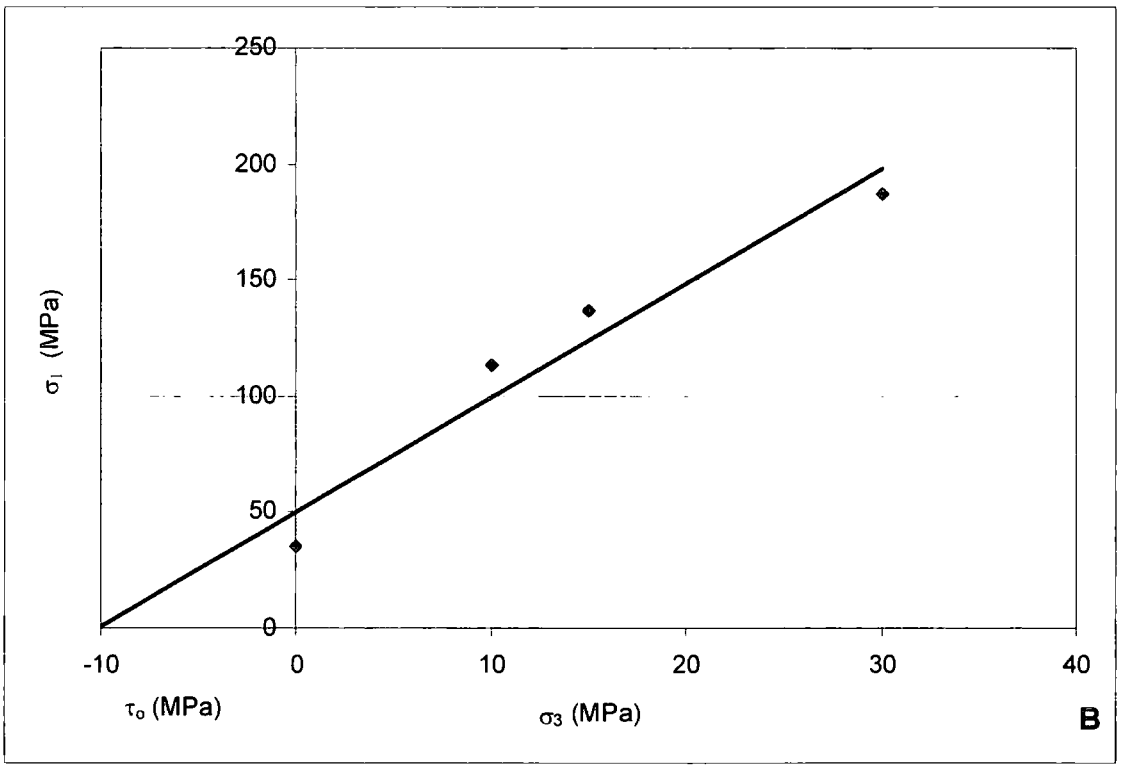

Figure 6.32: Mohr's circles (A) and sigma 1 / sigma 3 stress space with fitted Mohr-Coulomb failure envelope (B) for Salib Arkosic Sandstone, Jordan.

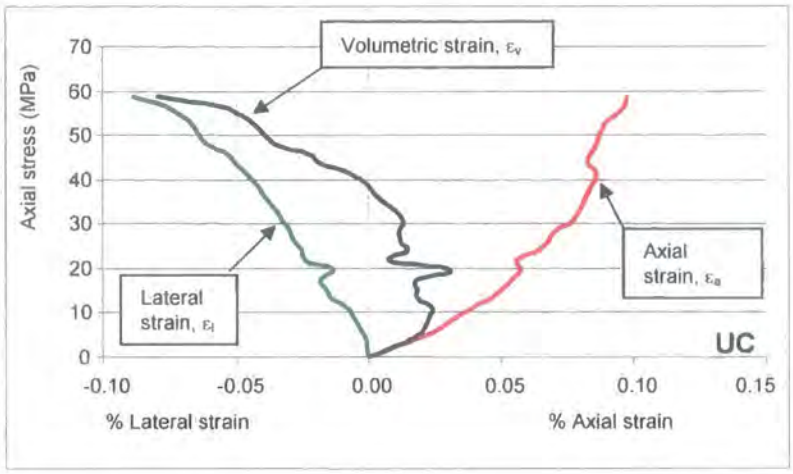

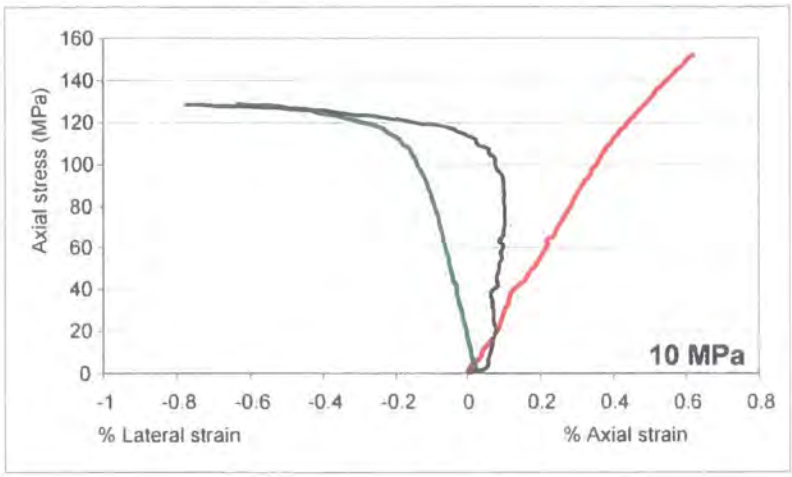

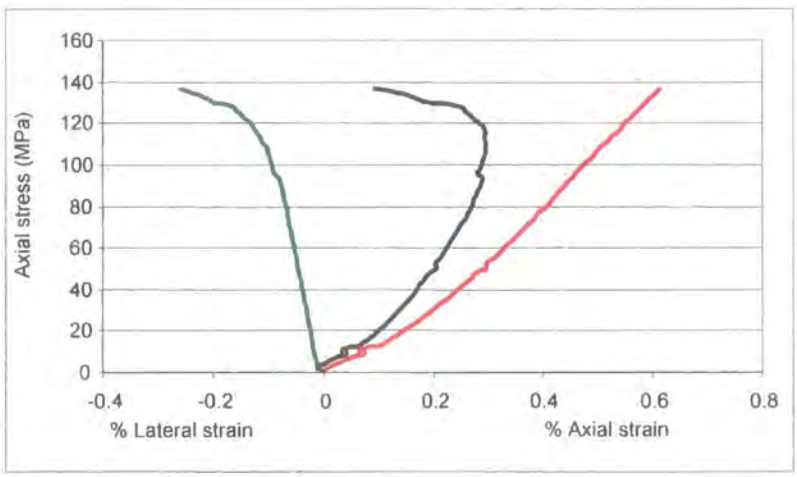

Figure 6.33: Axial (red line), lateral (green line) and volumetric (black line) stress-strain curves for Red Ishrin sandstones for specimens tested at 0 (UC), 10 and 15 MPa confining pressures.

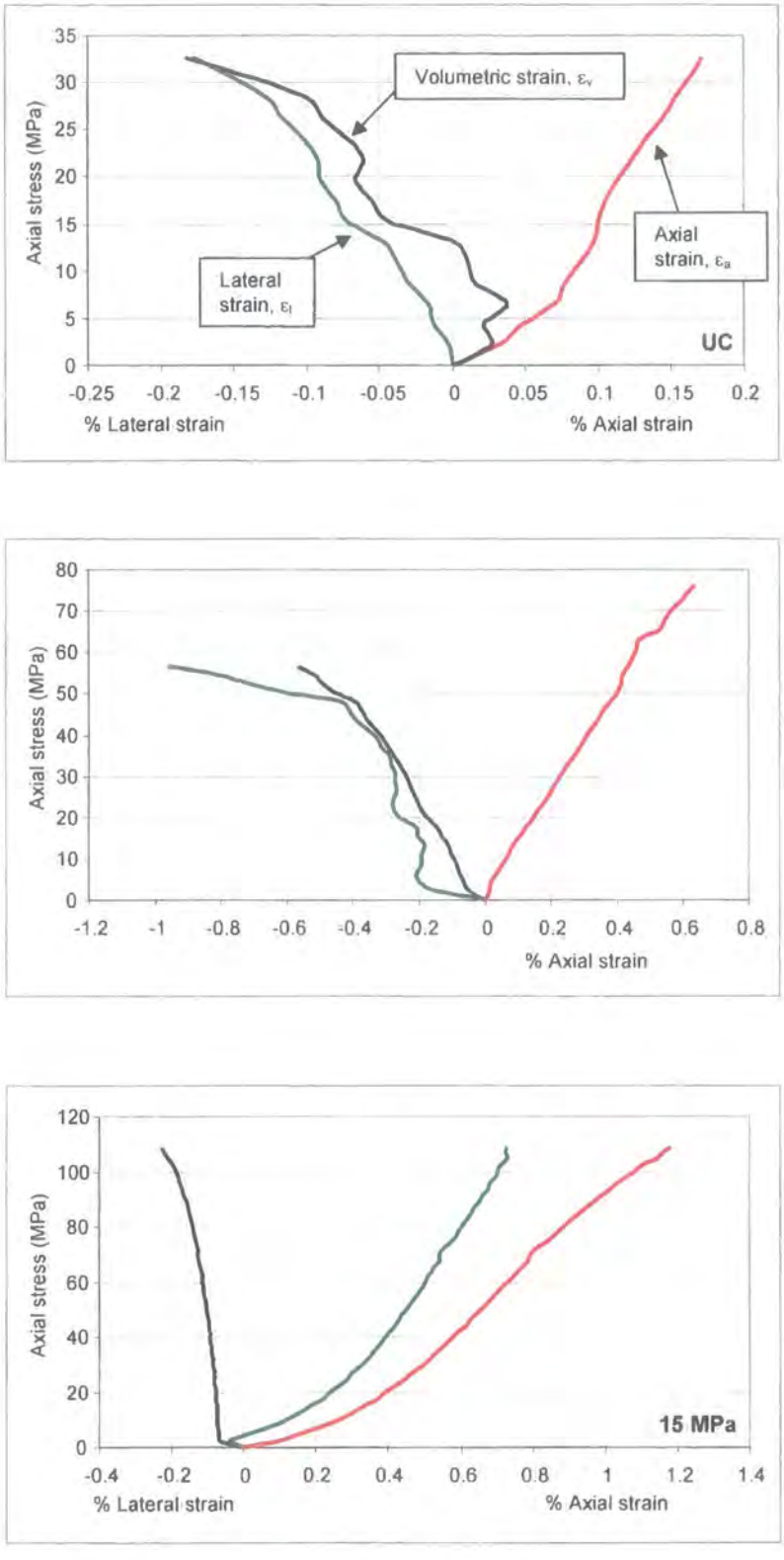

Figure 6.34: Axial (red line), lateral (green line) and volumetric (black line) stress-strain curves for Disi sandstones for specimens tested at 0 (UC), 10 and 15 MPa confining pressures.

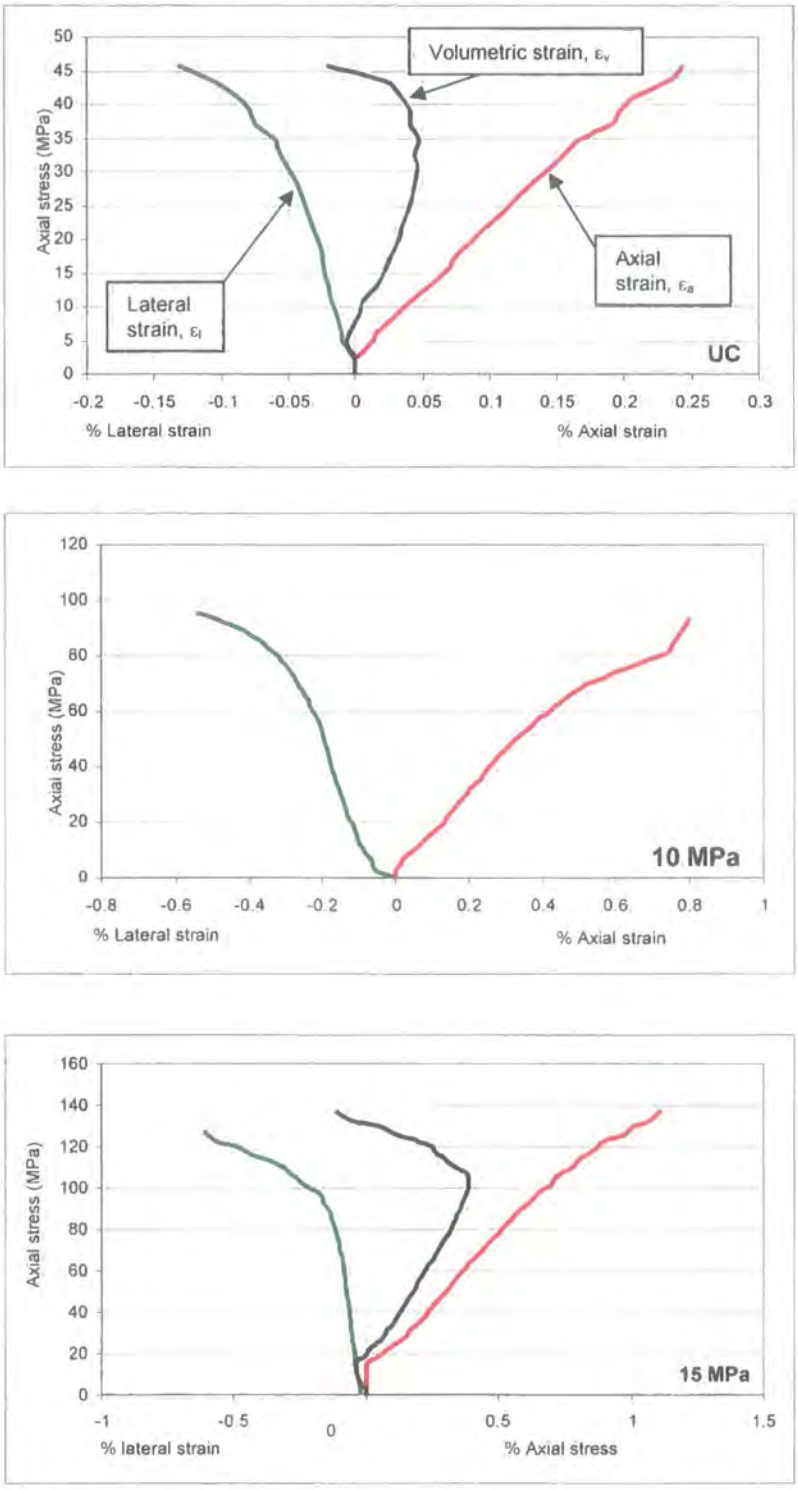

Figure 6.35: Axial, lateral and volumetric stress-strain curves for Salib Arkosic sandstone for specimens tested at 0 (UC), 10 and 15 MPa confining pressures. The volumetric curve is not included on the 10 MPa graph as it is identical to the lateral strain curve, representing data error.

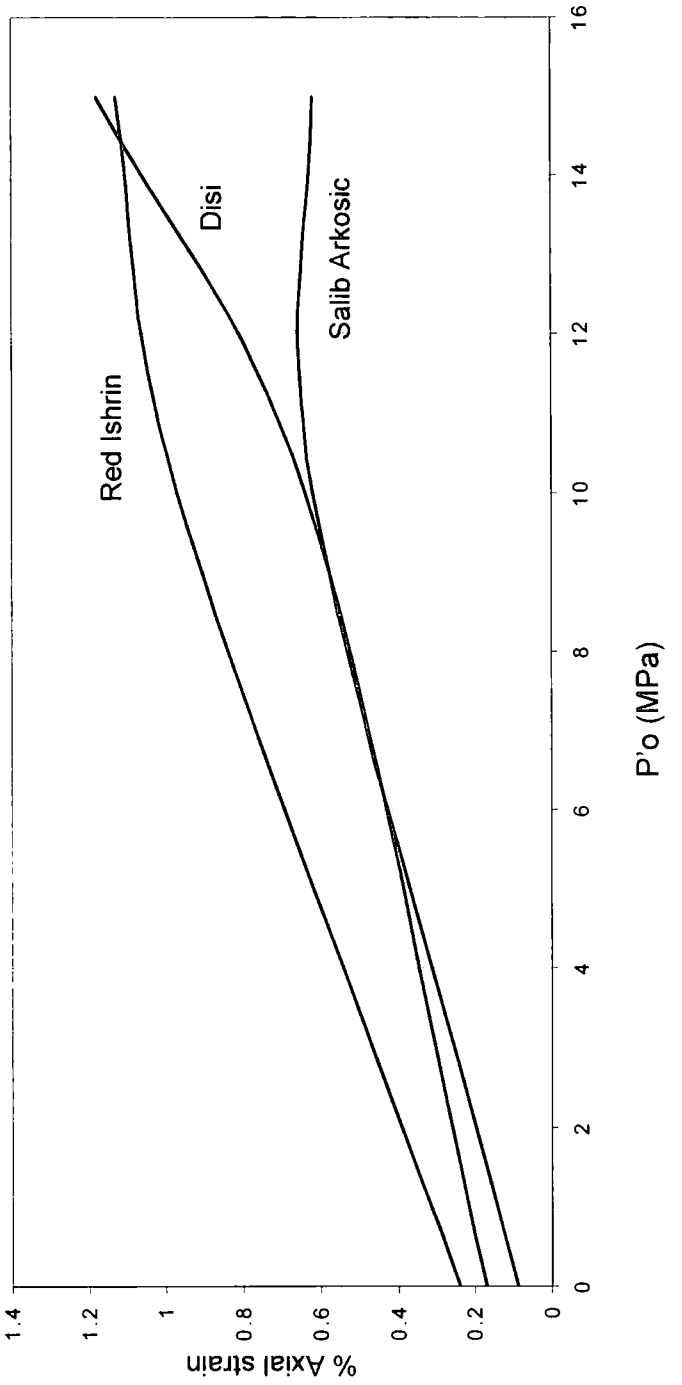

Figure 6.36: Axial strain plotted against Confining pressure, P'o (MPa) to help determine whether the sandstones are deforming in a very brittle, brittle, transitional or ductile manner.

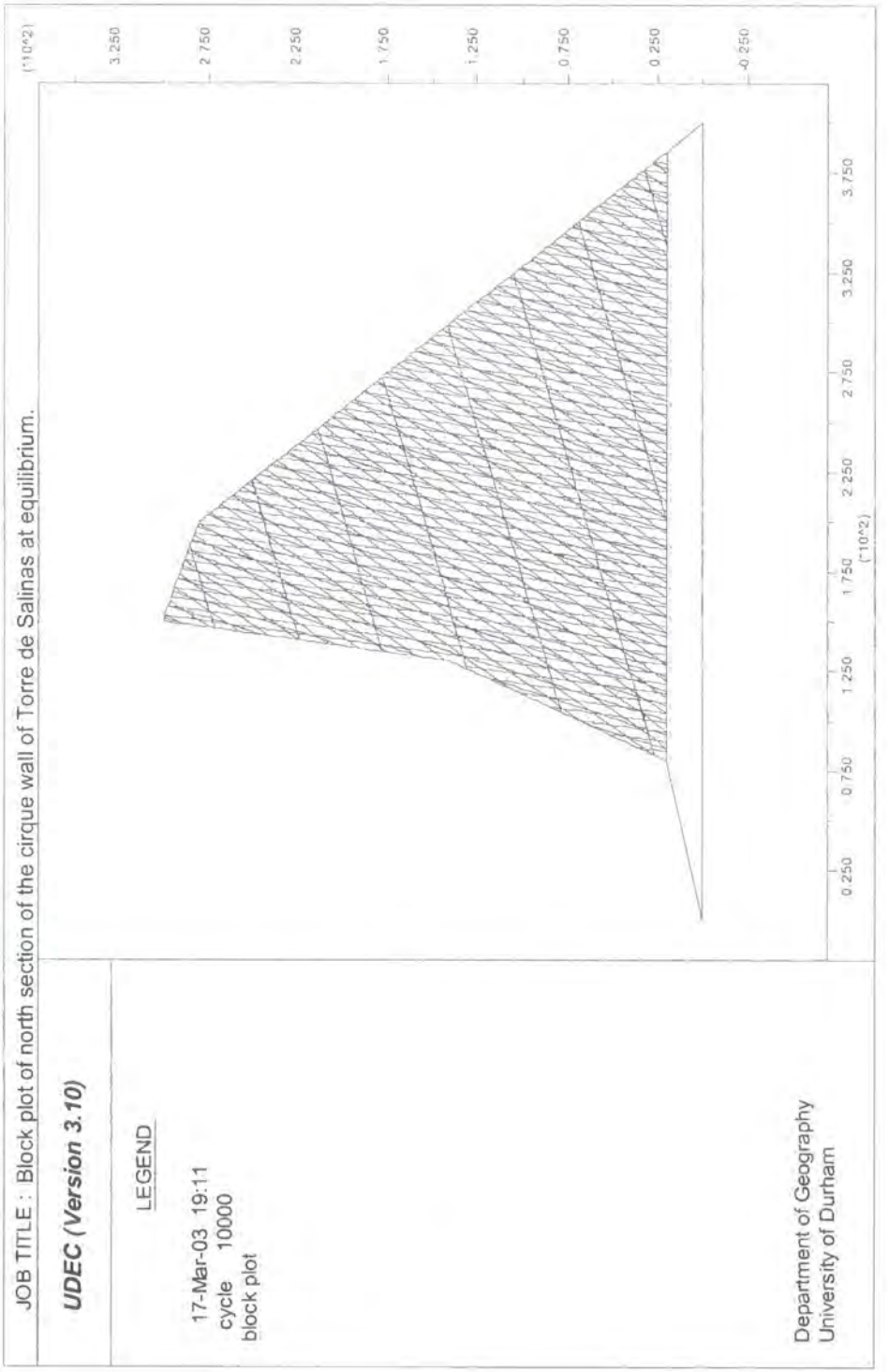

Figure 7.1: Block plot of the north section of the cirque wall of Torre de Salinas, Picos de Europa at equilibrium.

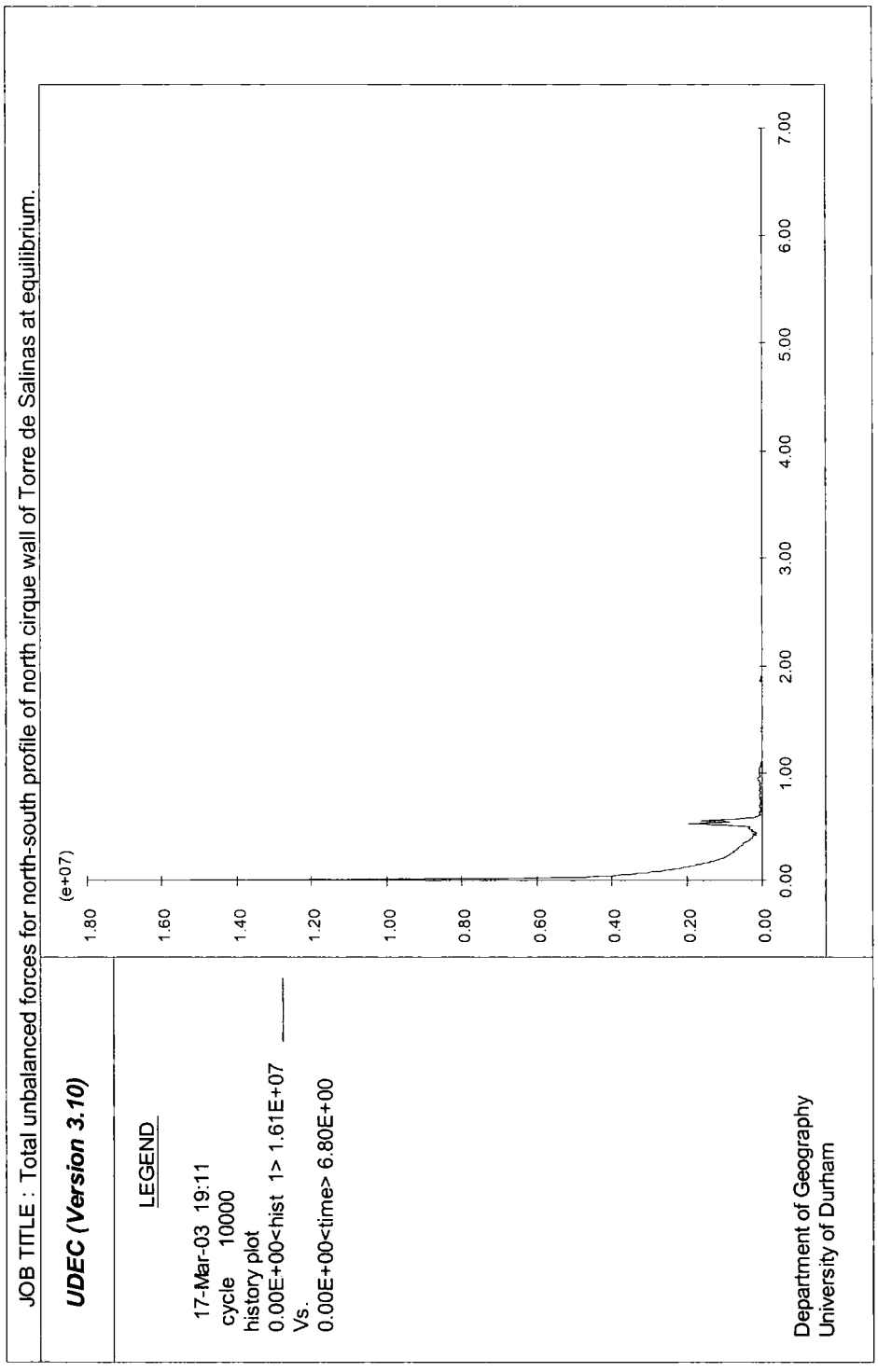

Figure 7.2: Total unbalanced forces for the north-south profile of the northern cirque wall of Torre de Salinas at equilibrium.

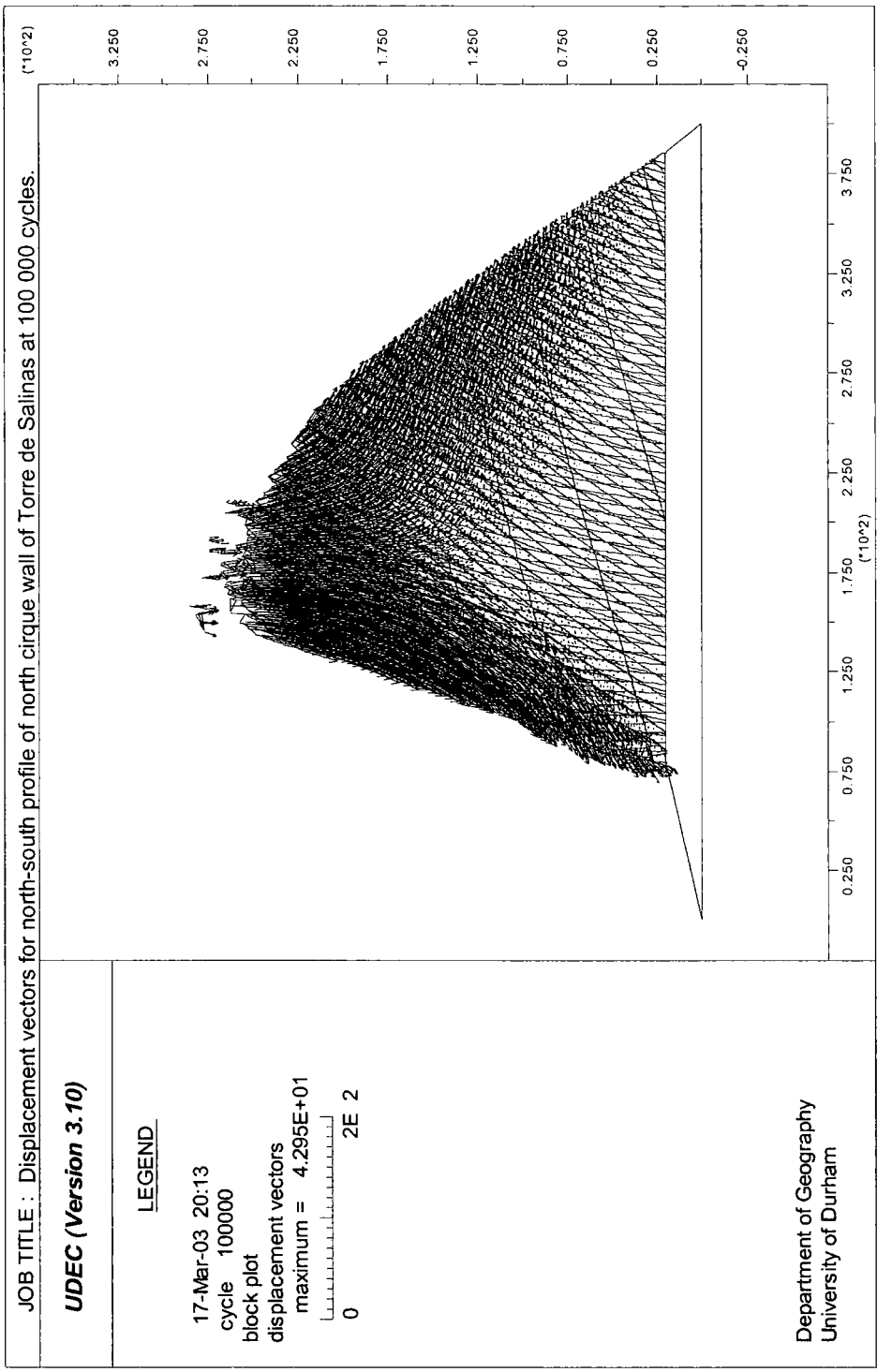

Figure 7.3a: Displacement vectors for the north-south profile of the northern cirque wall of Torre de Salinas at 100 000 cycles.

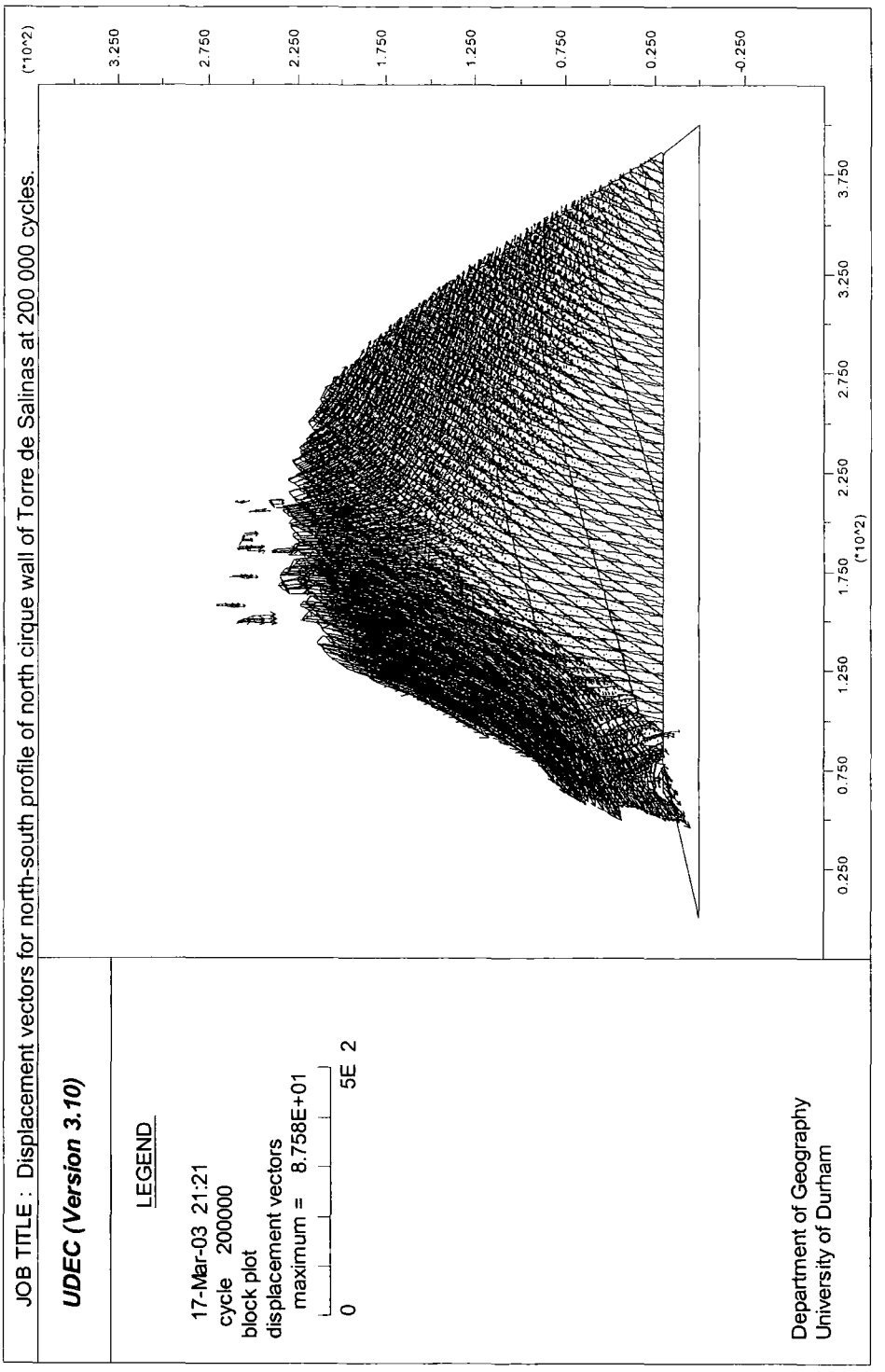

Figure 7.3b: Displacement vectors for the north-south profile of the northern cirque wall of Torre de Salinas at 200 000 cycles.

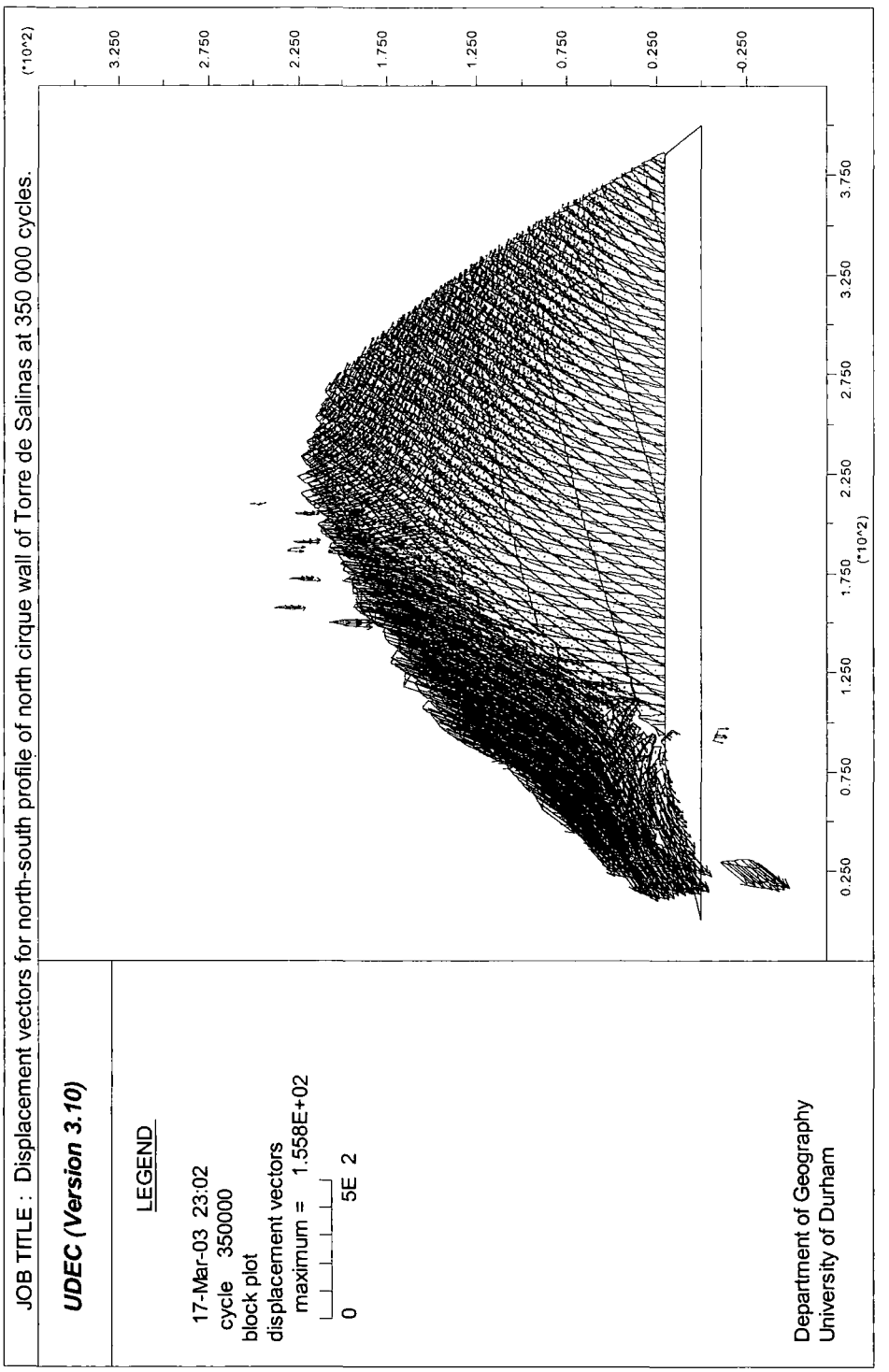

Figure 7.3c: Displacement vectors for the north-south profile of the northern cirque wall of Torre de Salinas at 300 000 cycles.

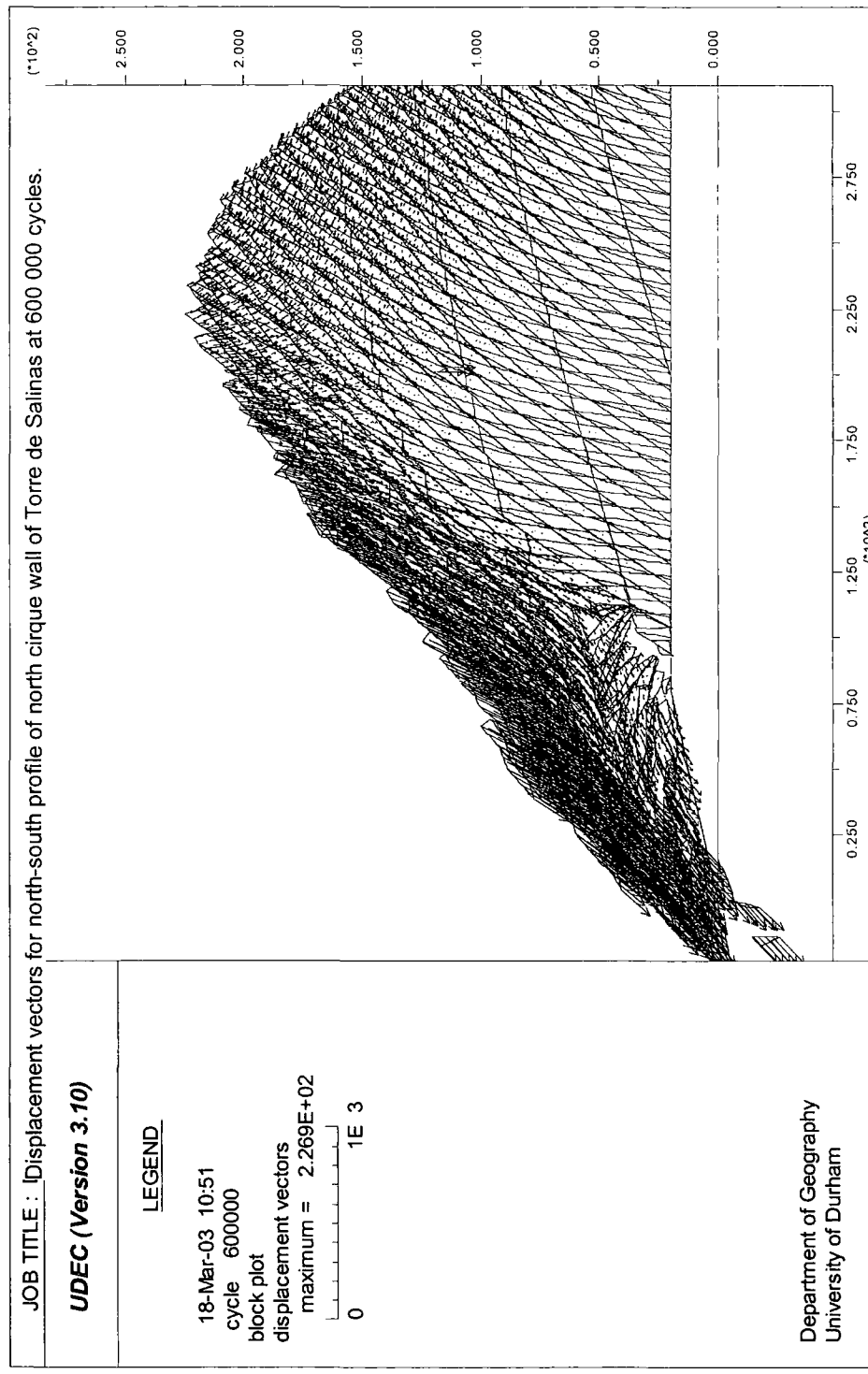

Figure 7.3d: Displacement vectors for the north-south profile of the northern cirque wall of Torre de Salinas at 600 000 cycles.

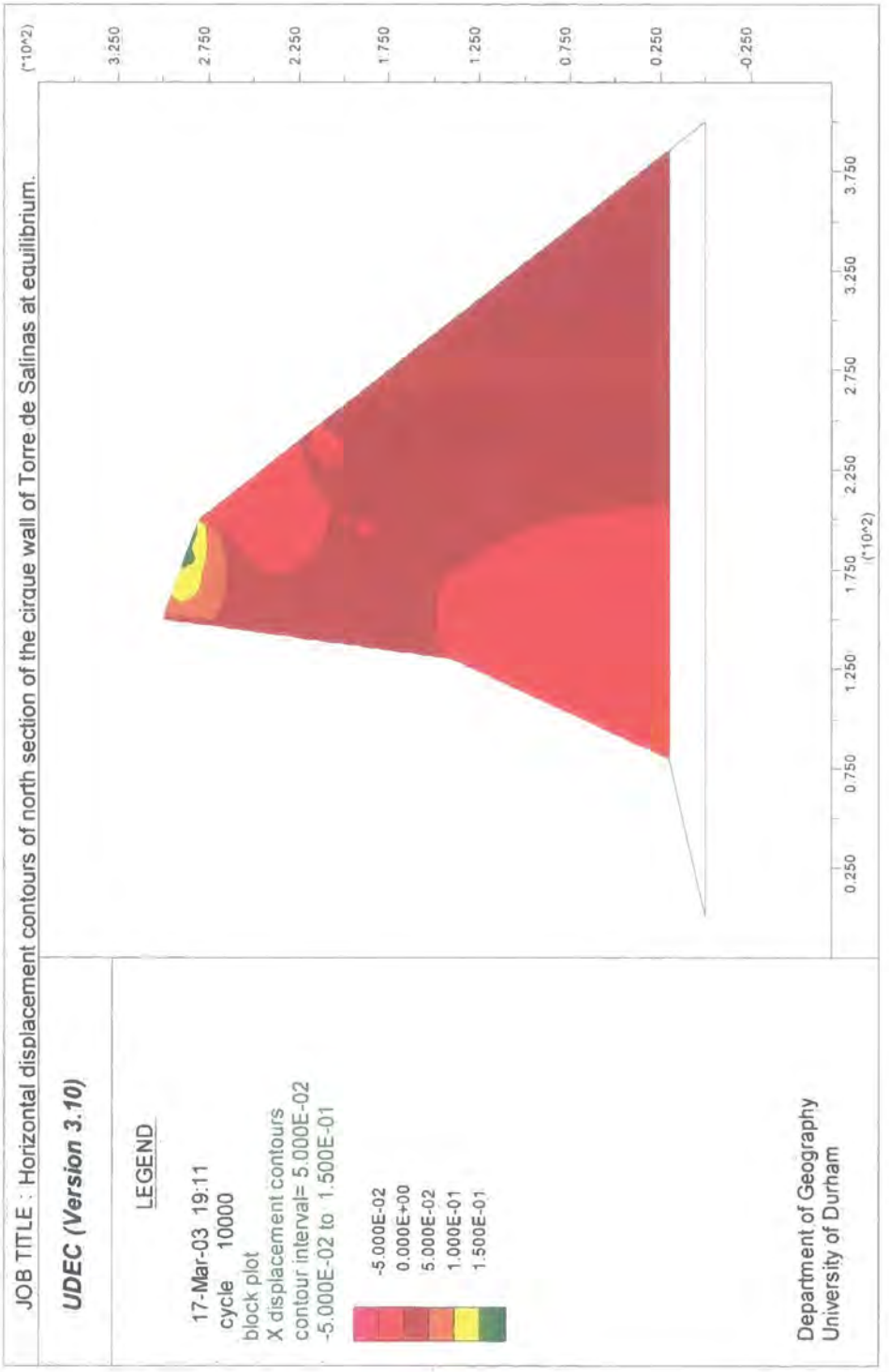

Figure 7.4a: Horizontal displacement contours of the north section of the cirque wall of Torre de Salinas at equilibrium.

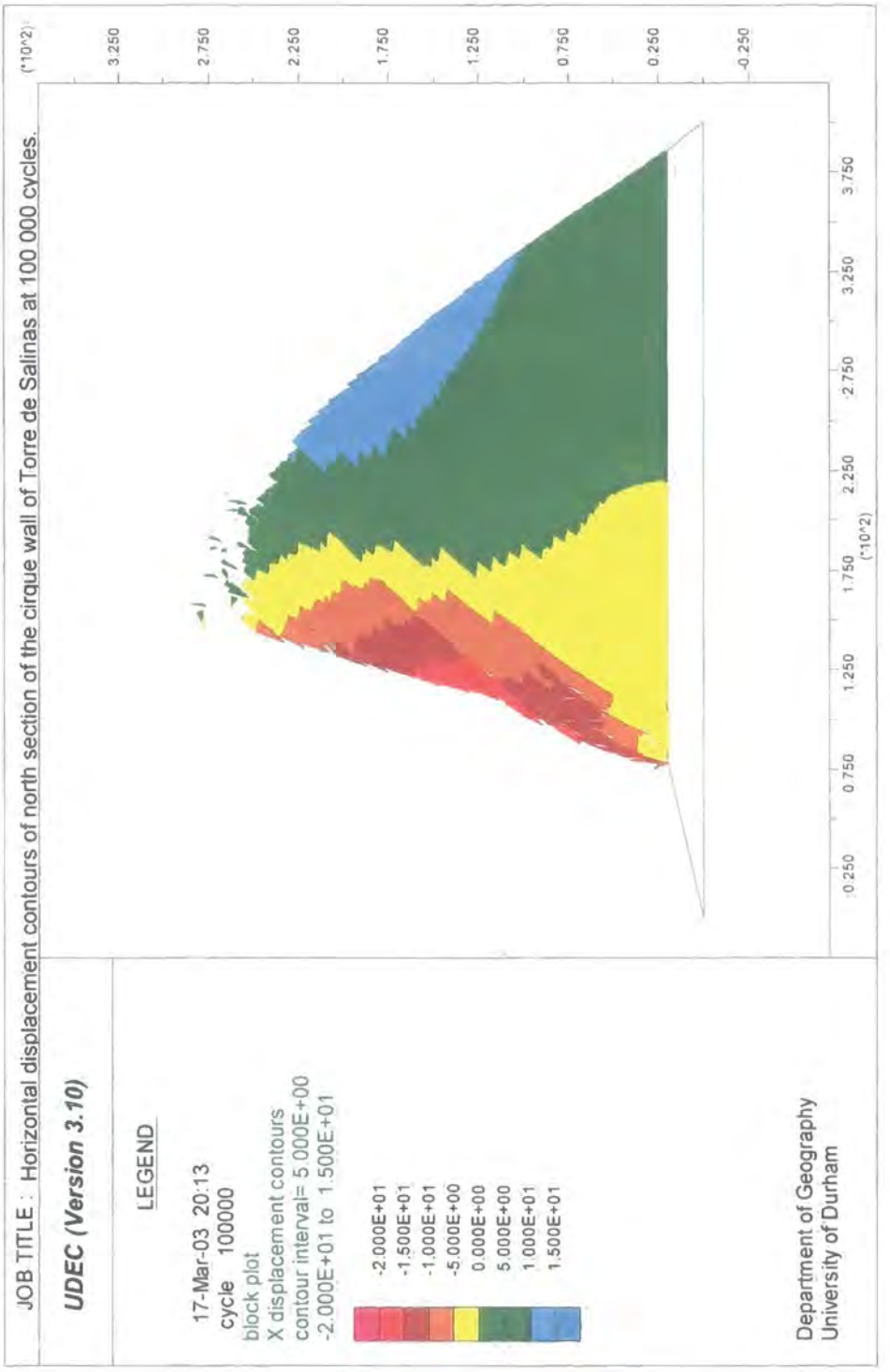

Figure 7.4b: Horizontal displacement contours of the north section of the cirque wall of Torre de Salinas at 100 000 cycles.

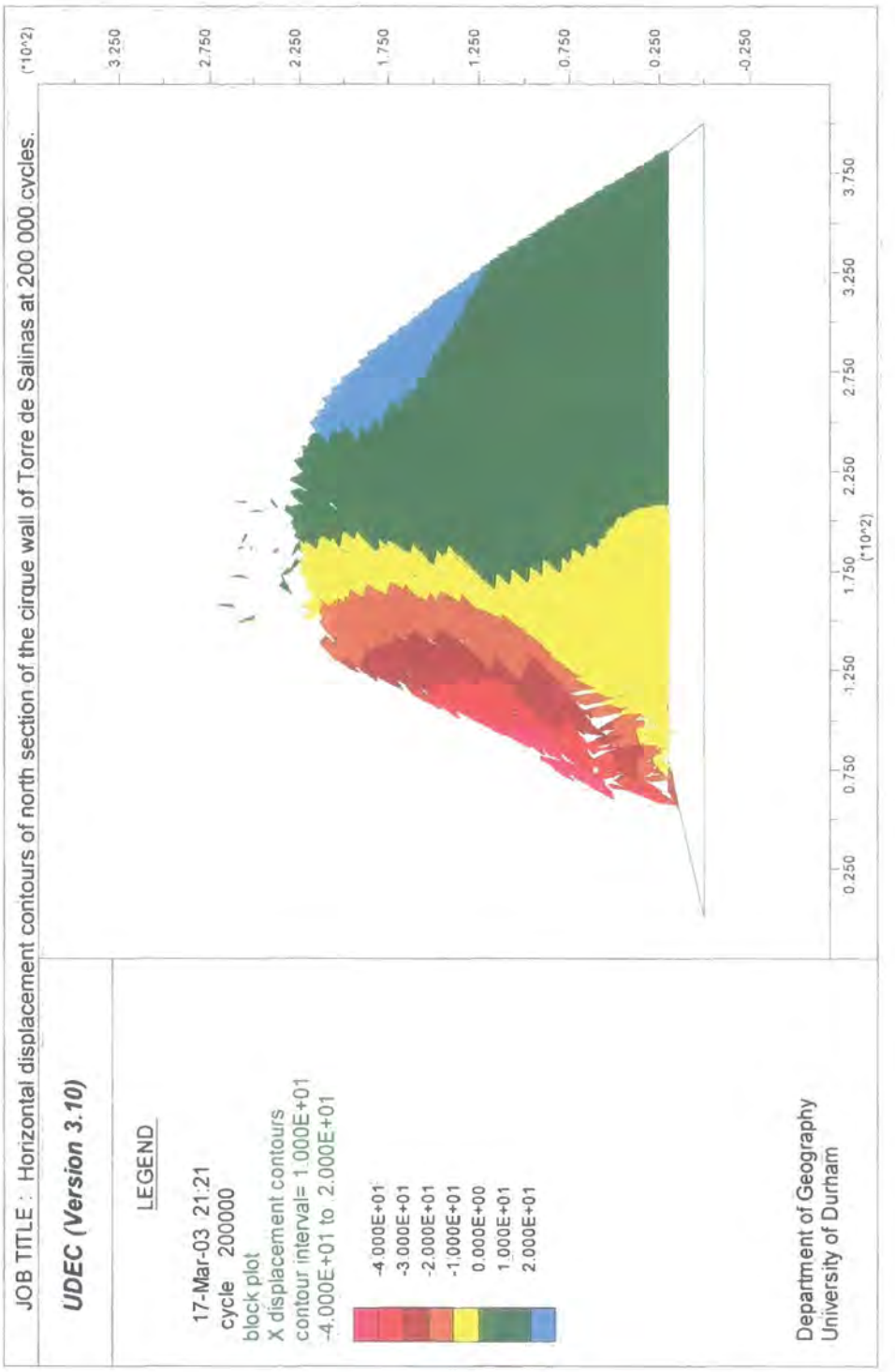

Figure 7.4c: Horizontal displacement contours of the north section of the cirque wall of Torre de Salinas at 200 000 cycles.

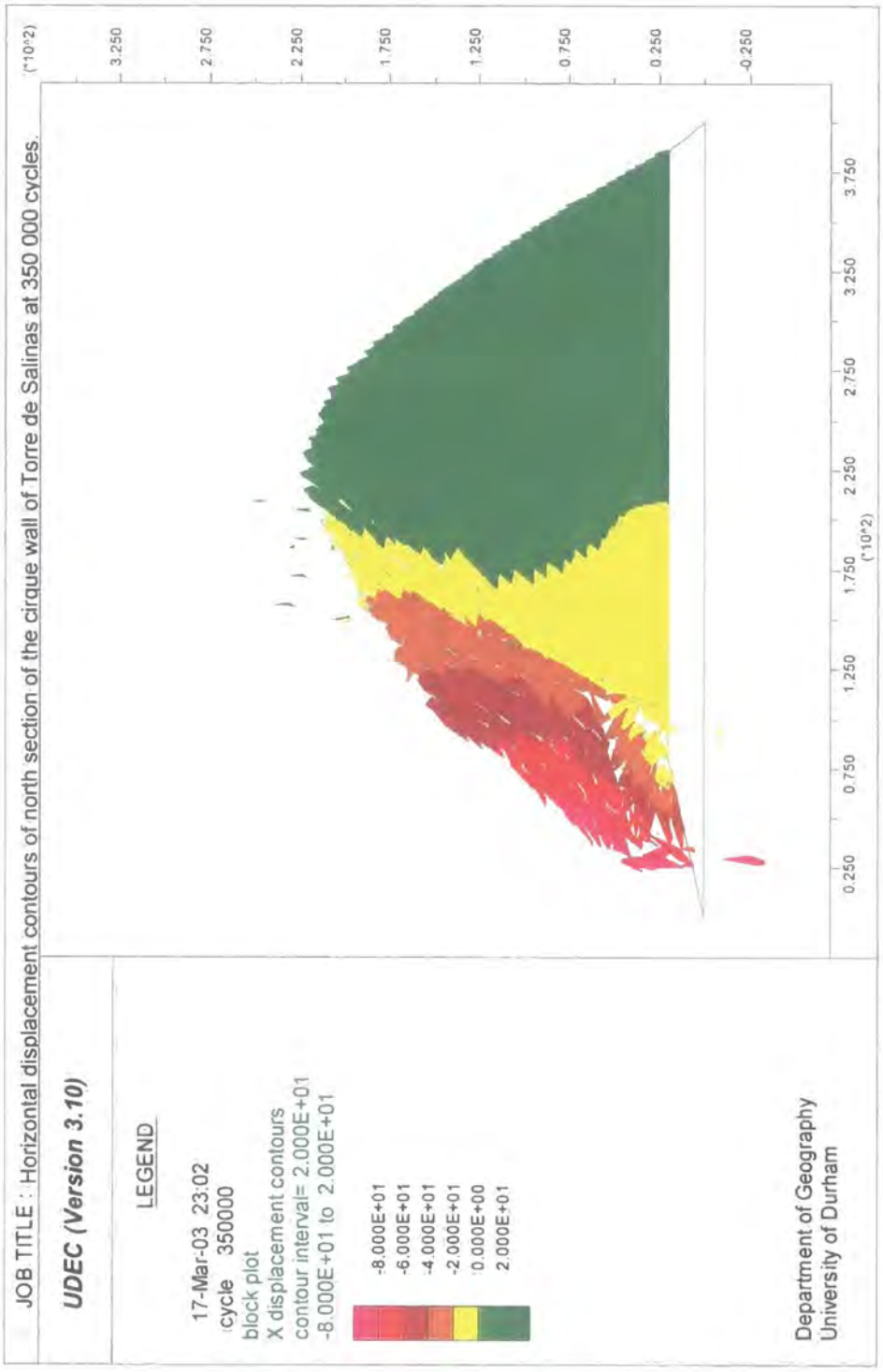

Figure 7.4d: Horizontal displacement contours of the north section of the cirque wall of Torre de Salinas at 350 000 cycles.

Figure 7.4e: Horizontal displacement contours of the north section of the cirque wall of Torre de Salinas at 600 000 cycles.

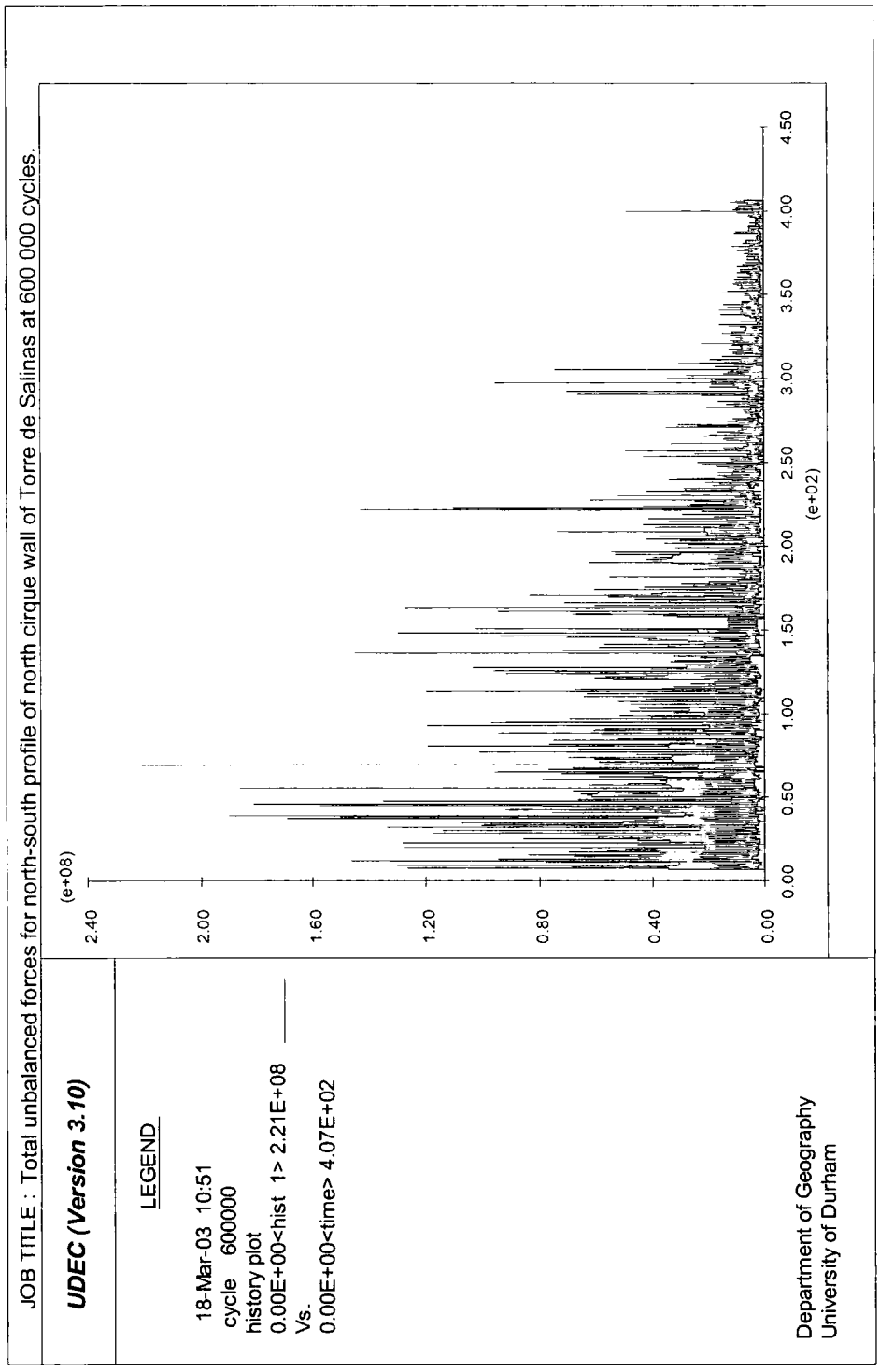

Figure 7.5: Total unbalanced forces for the north-south profile of the northern cirque wall of Torre de Salinas at 600 000 cycles.

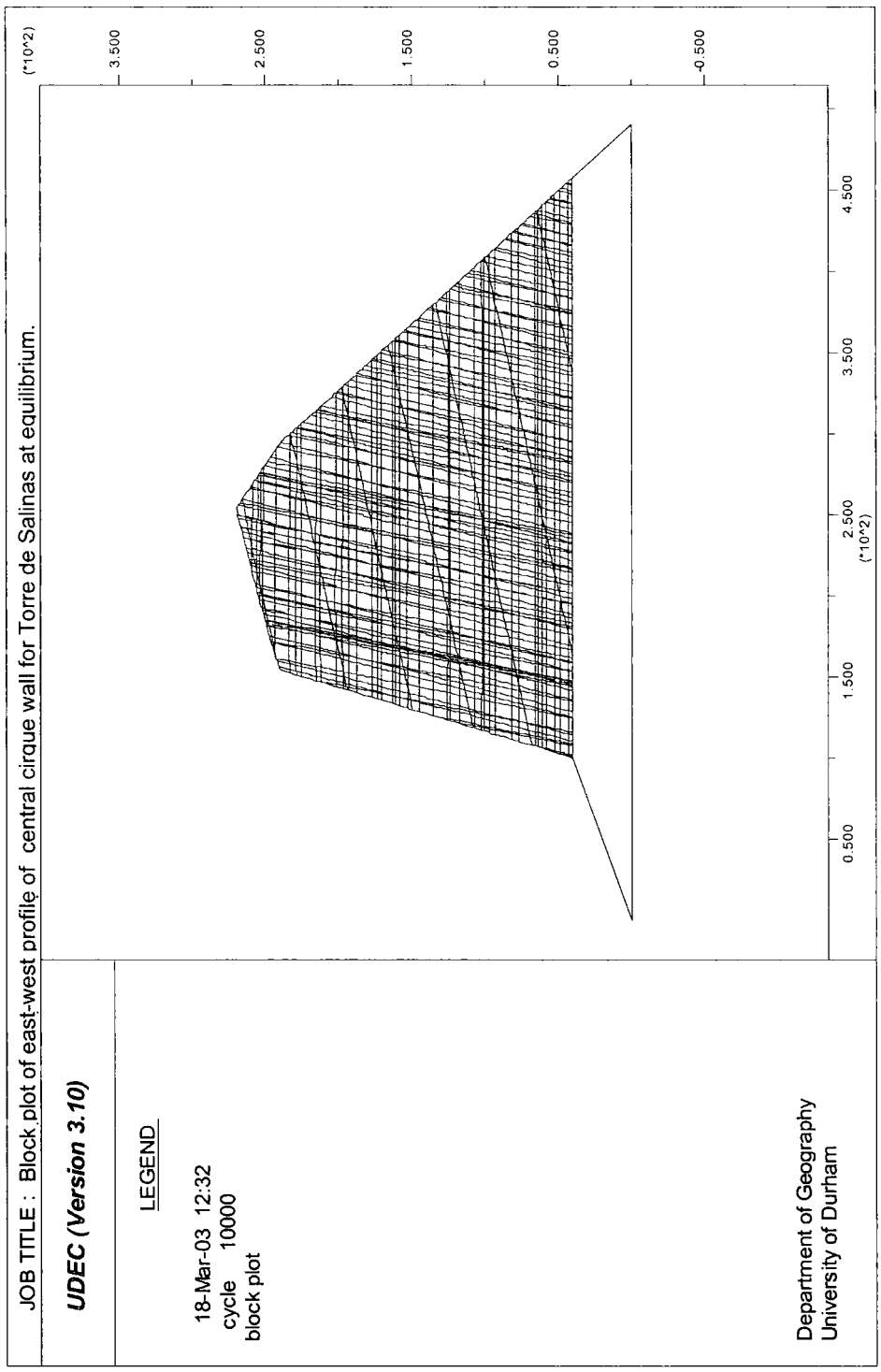

Figure 7.6a: Block plot of the east-west profile of the central cirque headwall for Torre de Salinas, Picos de Europa, at equilibrium.

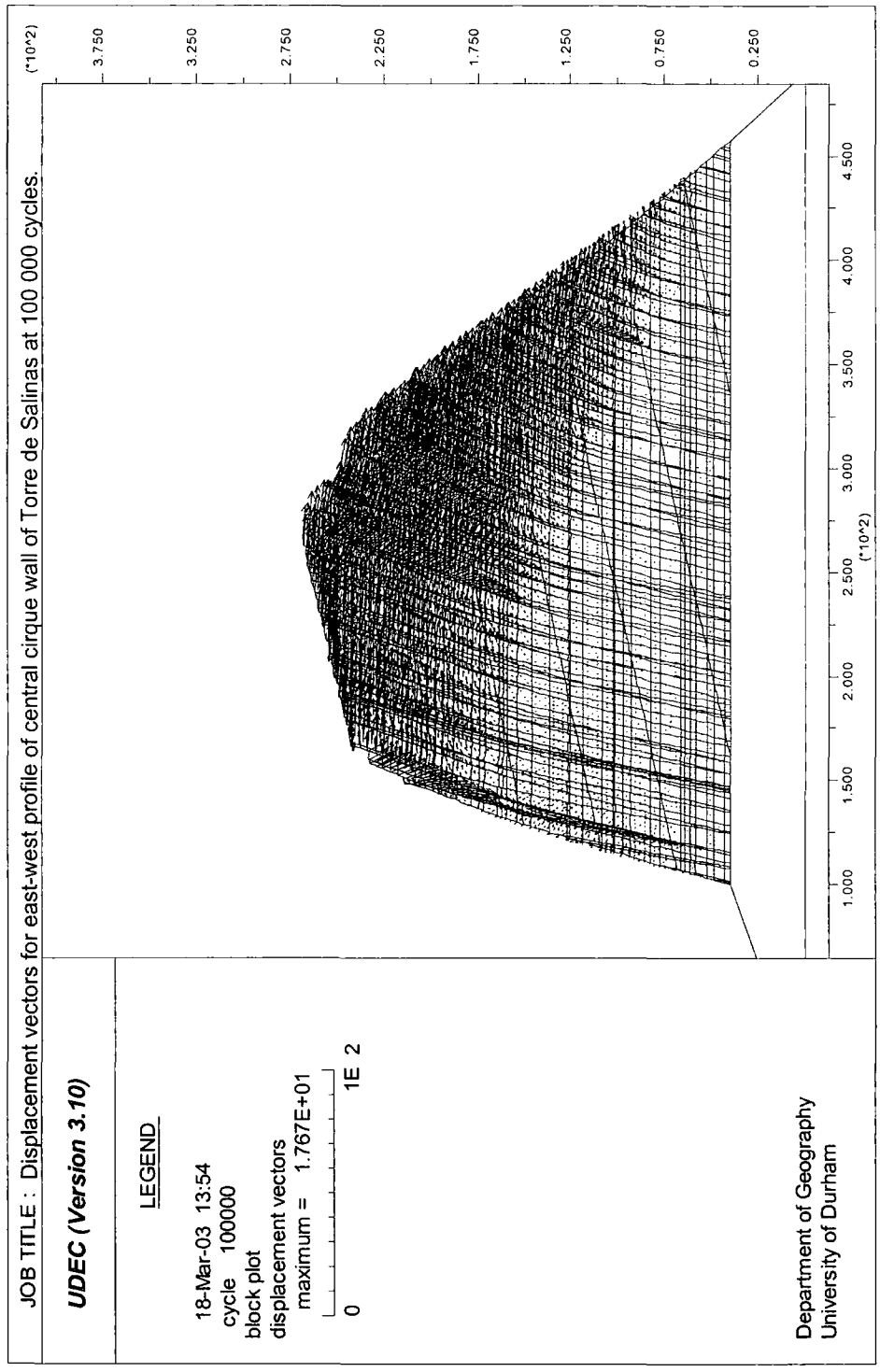

Figure 7.6b: Displacement vectors for the east-west profile of the central cirque wall of Torre de Salinas at 100 000 cycles.

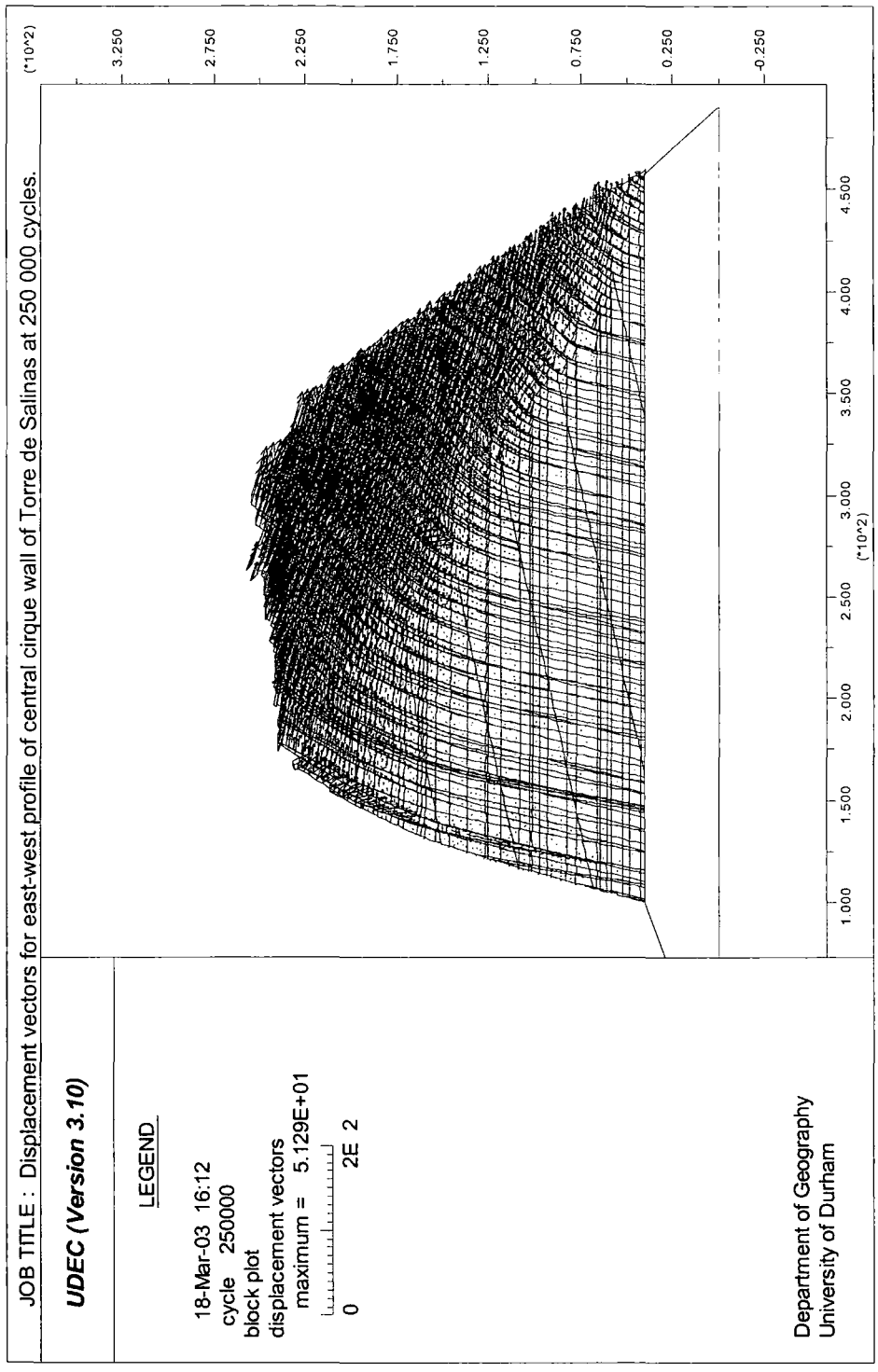

Figure 7.6c: Displacement vectors for the east-west profile of the central cirque wall of Torre de Salinas at 250 000 cycles.

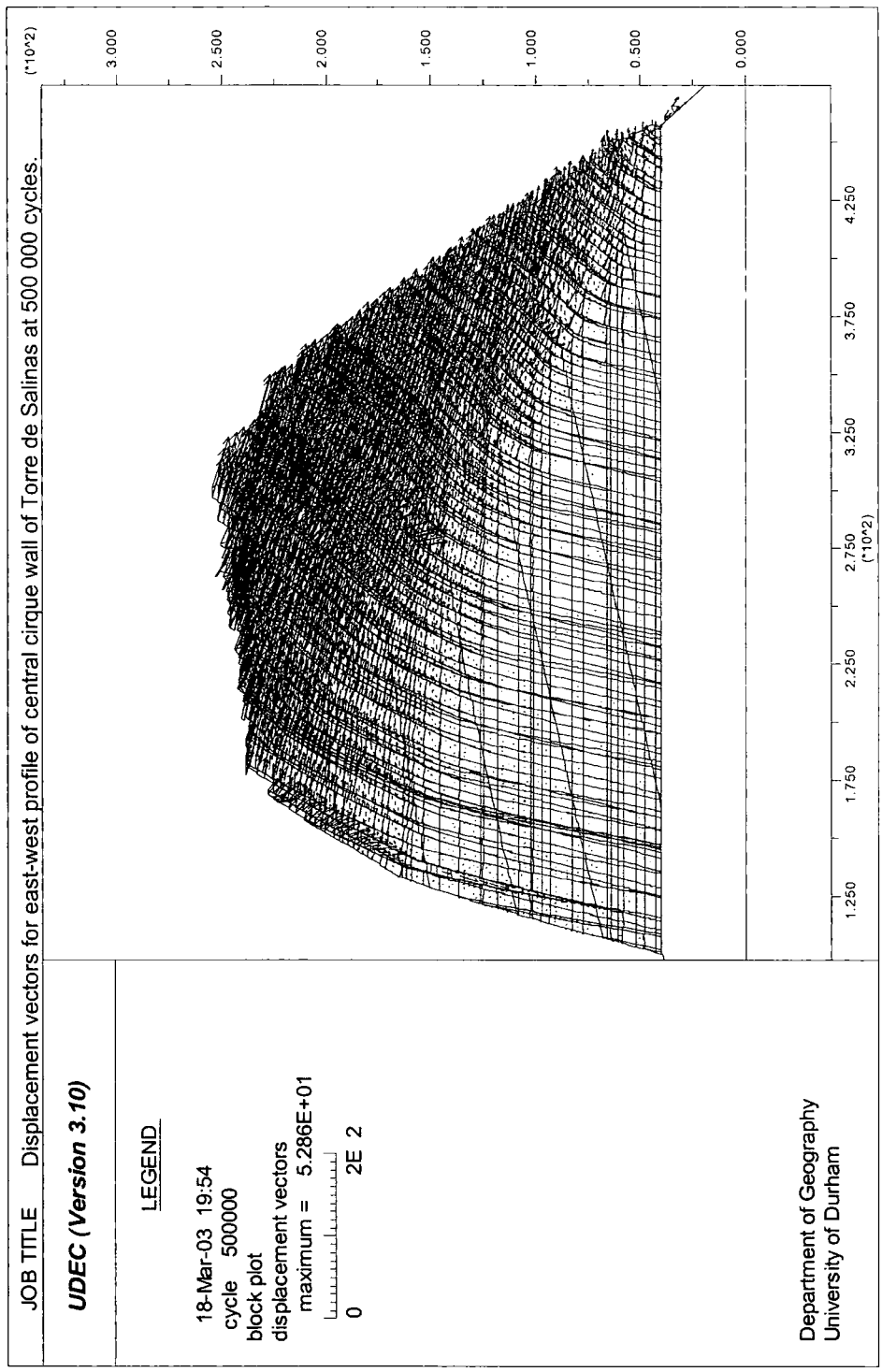

Figure 7.6d: Displacement vectors for the east-west profile of the central cirque wall of Torre de Salinas at 500 000 cycles.

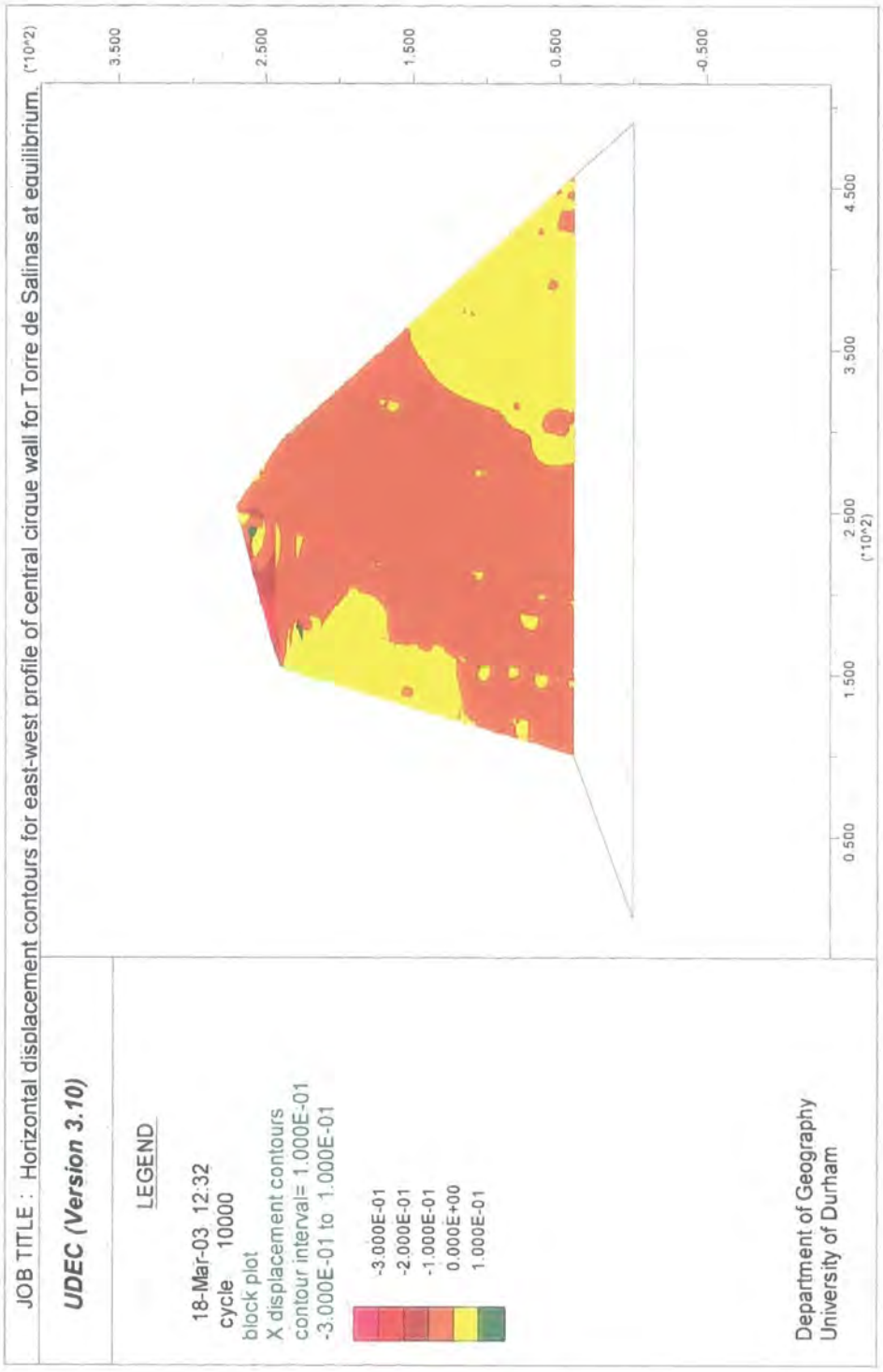

Figure 7.7a: Horizontal displacement contours for the east-west profile of the cirque headwall for Torre de Salinas at equilibrium.

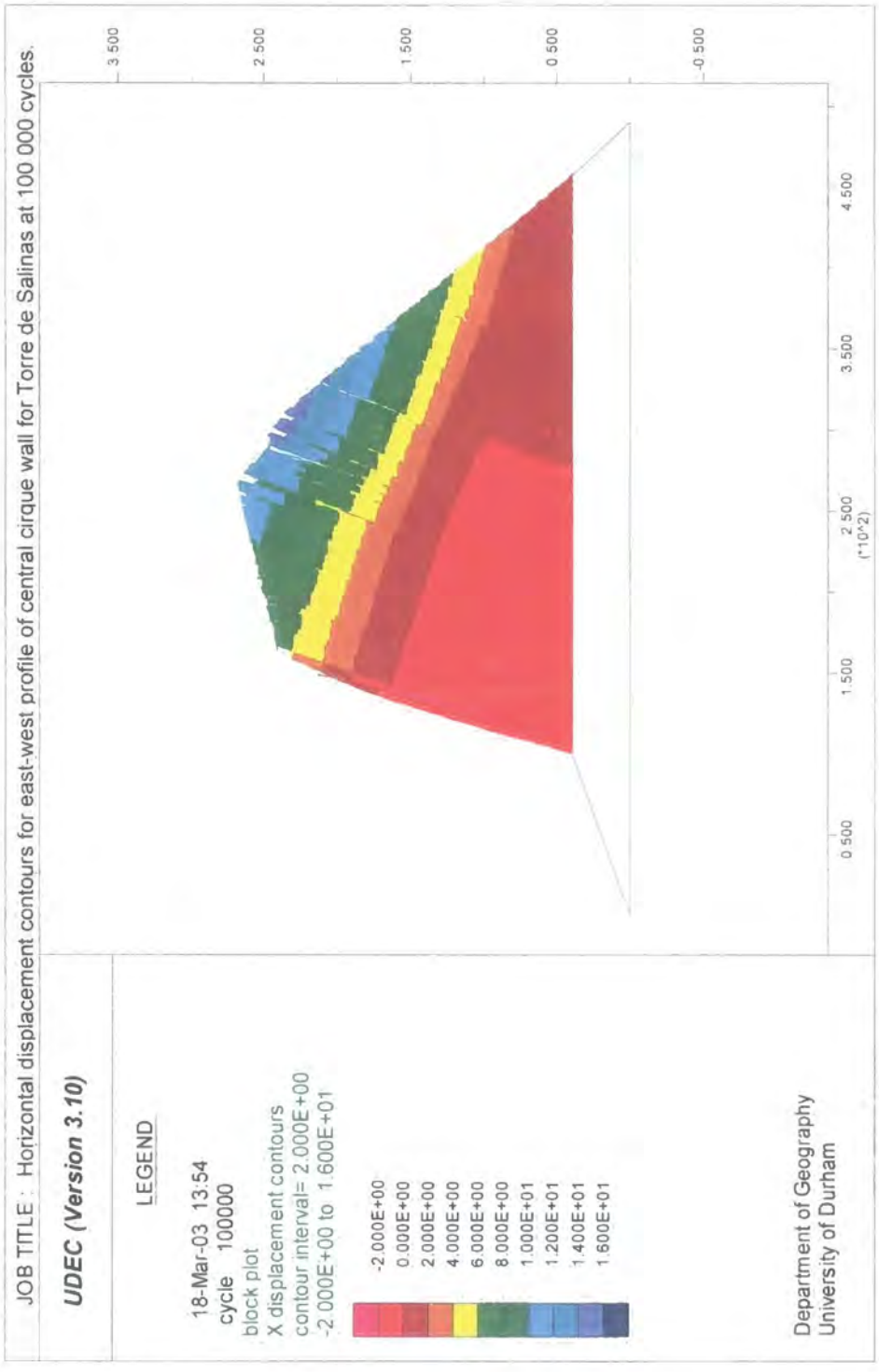

Figure 7.7b: Horizontal displacement contours for the east-west profile of the cirque headwall for Torre de Salinas 100 000 cycles.

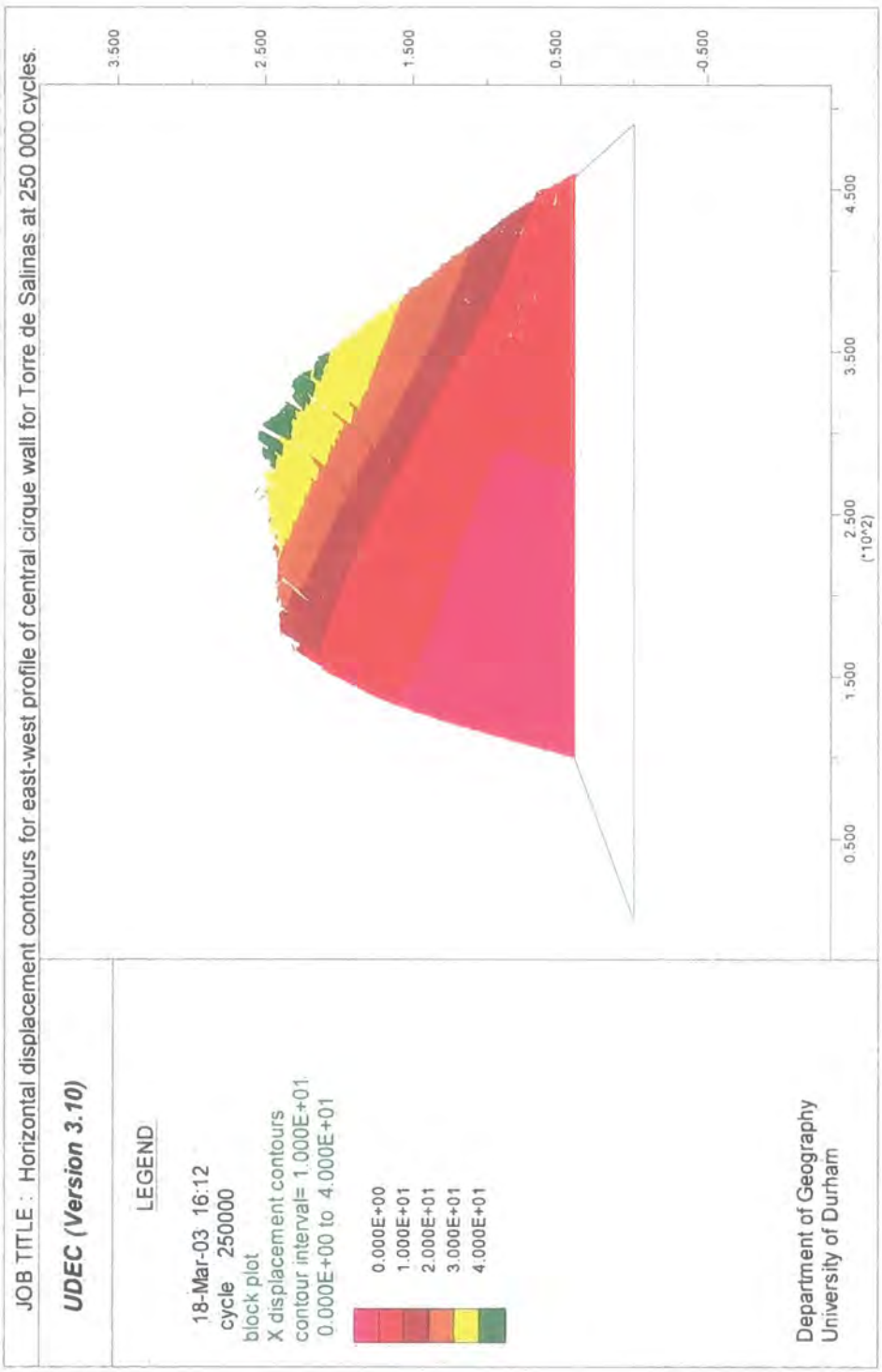

Figure 7.7c: Horizontal displacement contours for the east-west profile of the cirque headwall for Torre de Salinas 250 000 cycles.

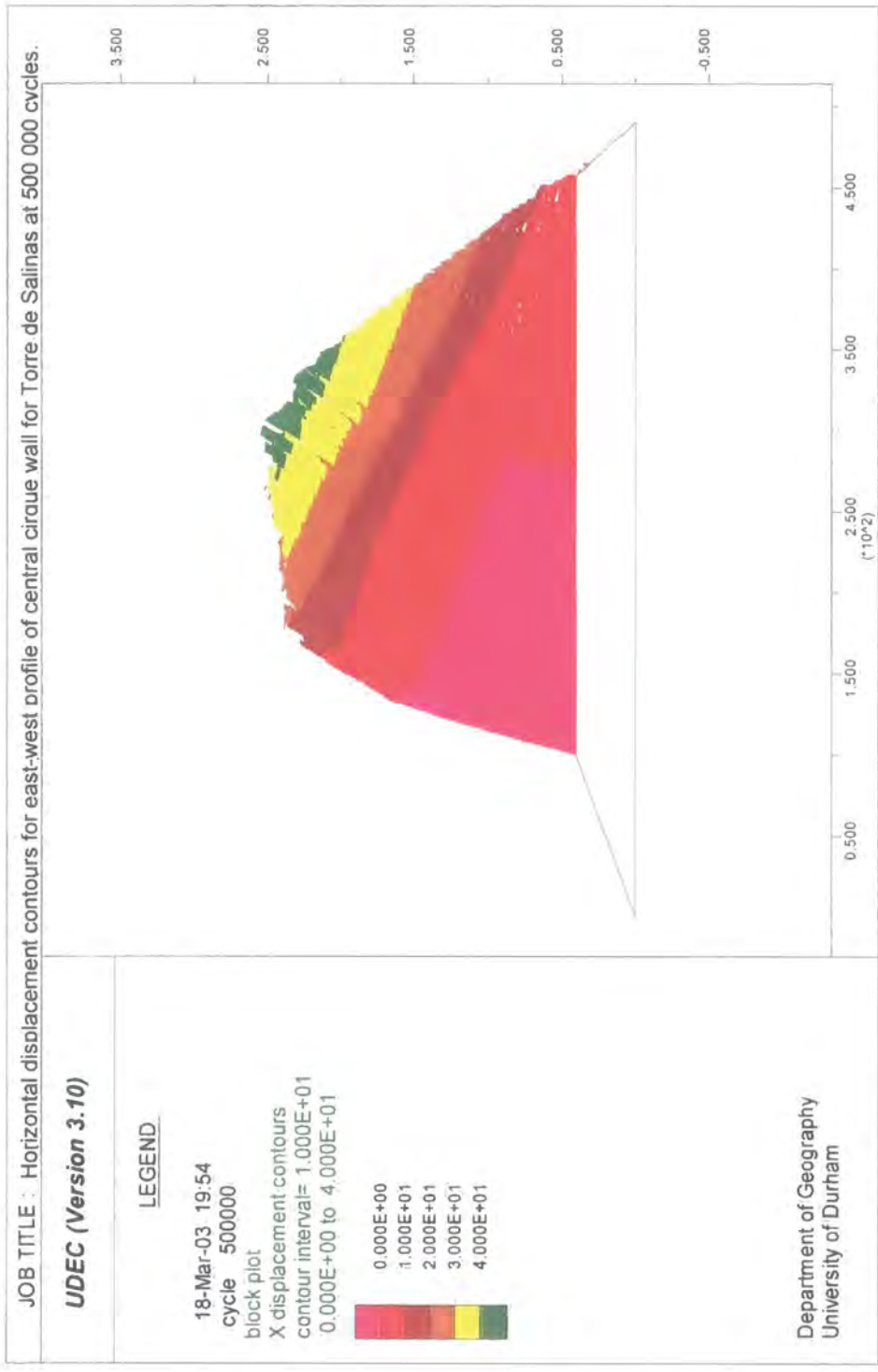

Figure 7.7d: Horizontal displacement contours for the east-west profile of the cirque headwall for Torre de Salinas 500 000 cycles.

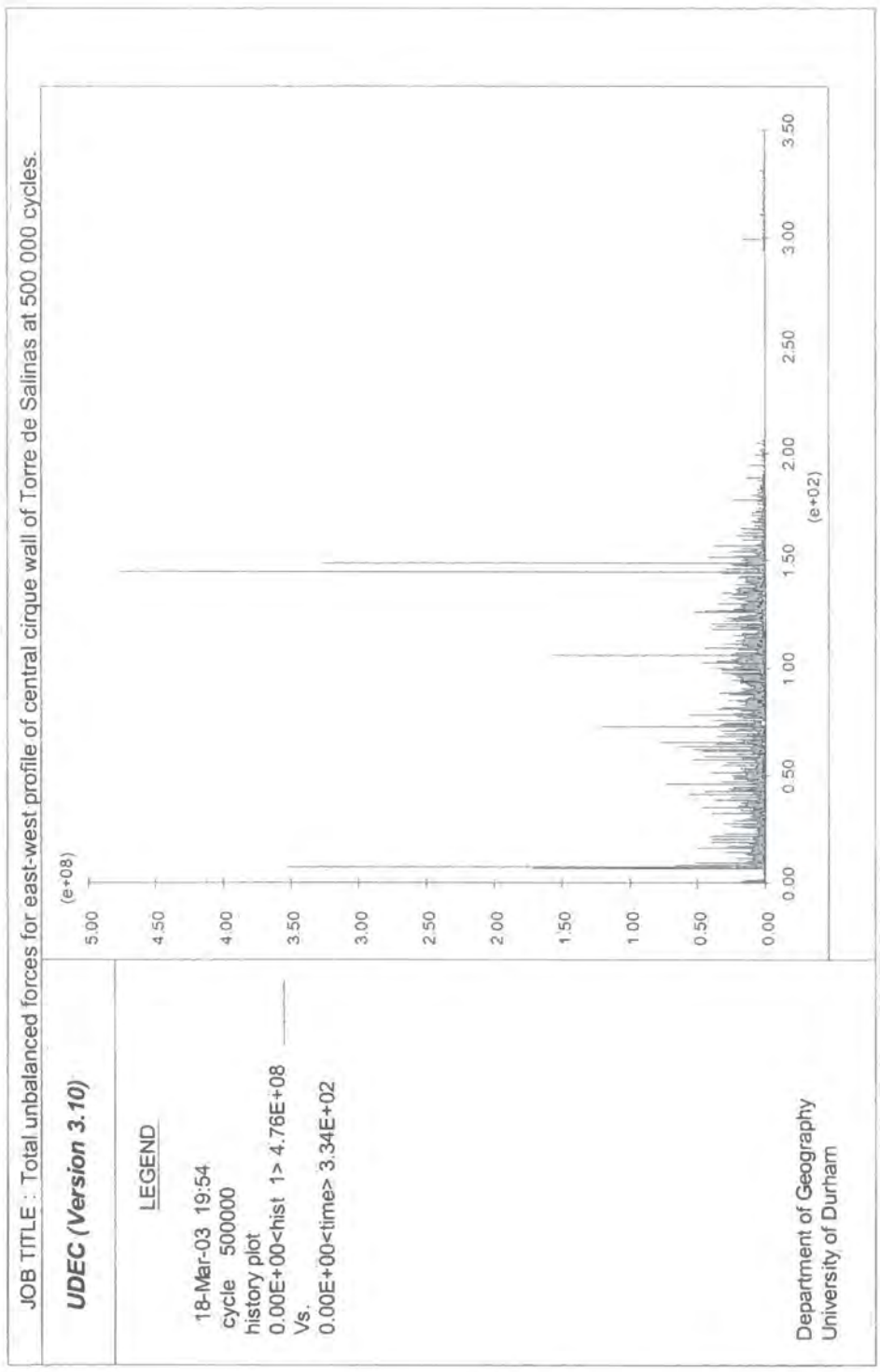

Figure 7.8: Total unbalanced forces for the east-west profile of the central cirque wall of Torre de Salinas at 500 000 cycles.

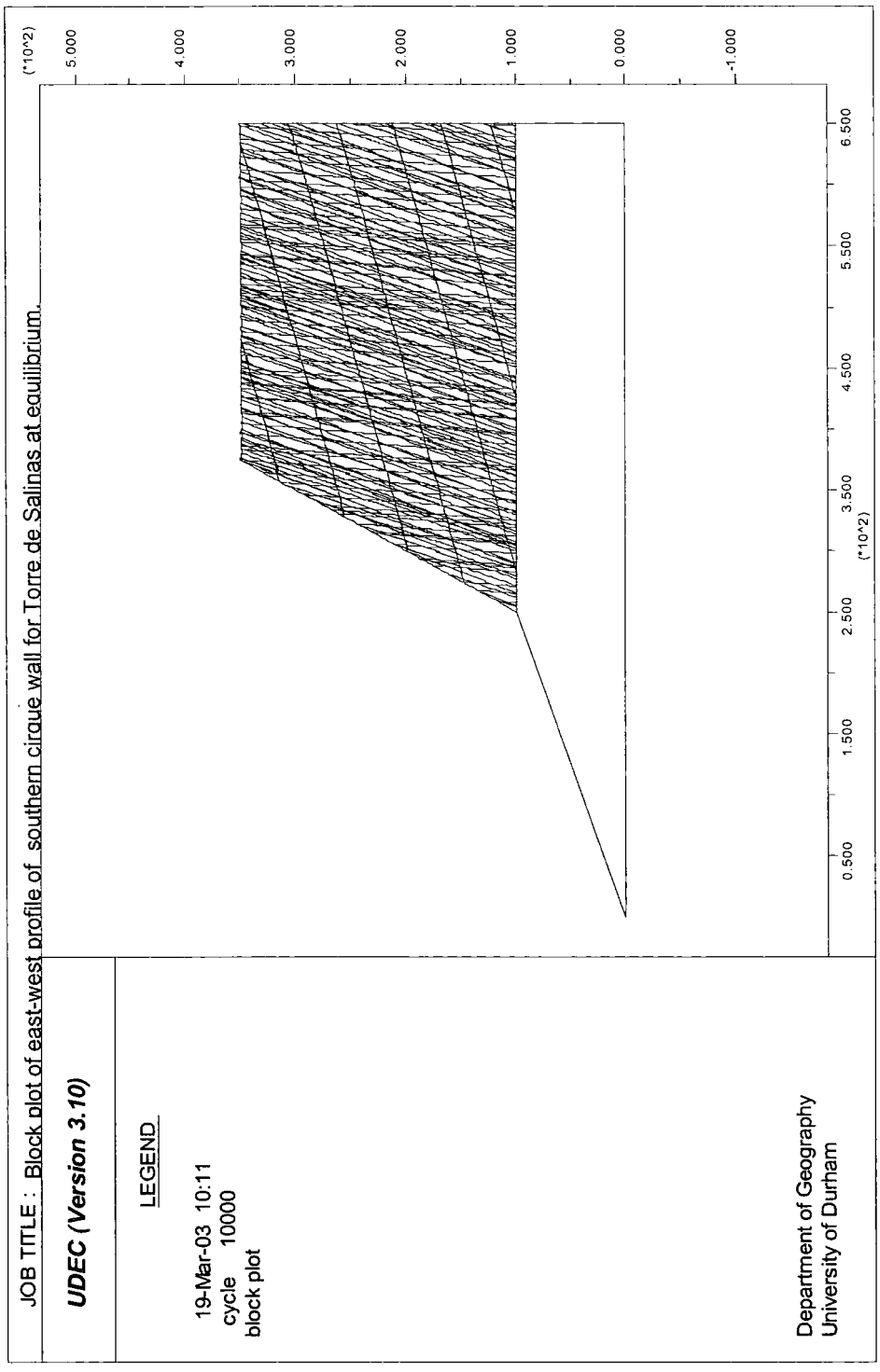

Figure 7.9a: Block plot of the east-west profile of the southern cirque headwall for Torre de Salinas, Picos de Europa, at equilibrium.

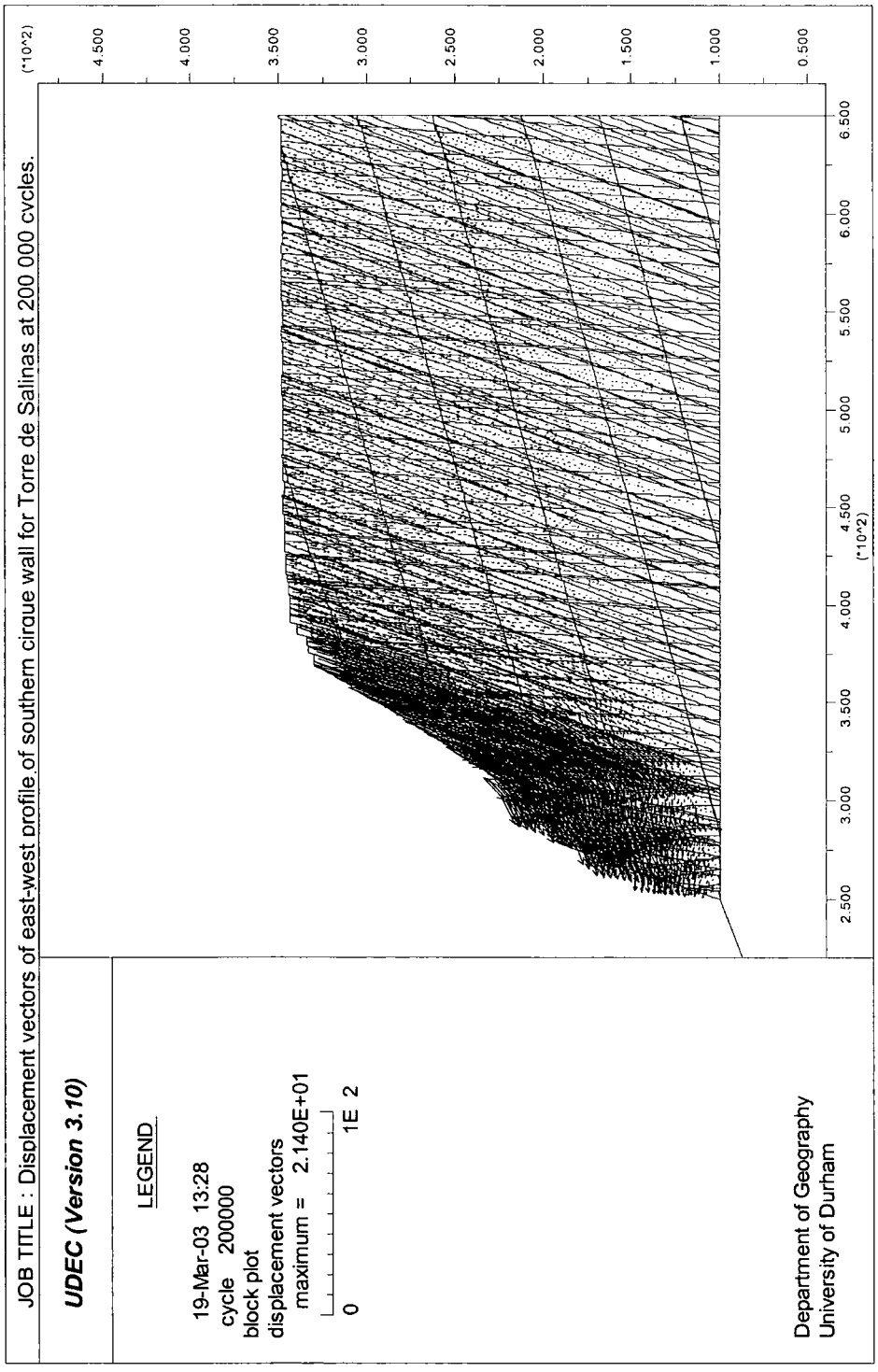

Figure 7.9b: Displacement vectors of the east-west profile of the southern cirque headwall for Torre de Salinas, Picos de Europa, at 200 000 cycles.

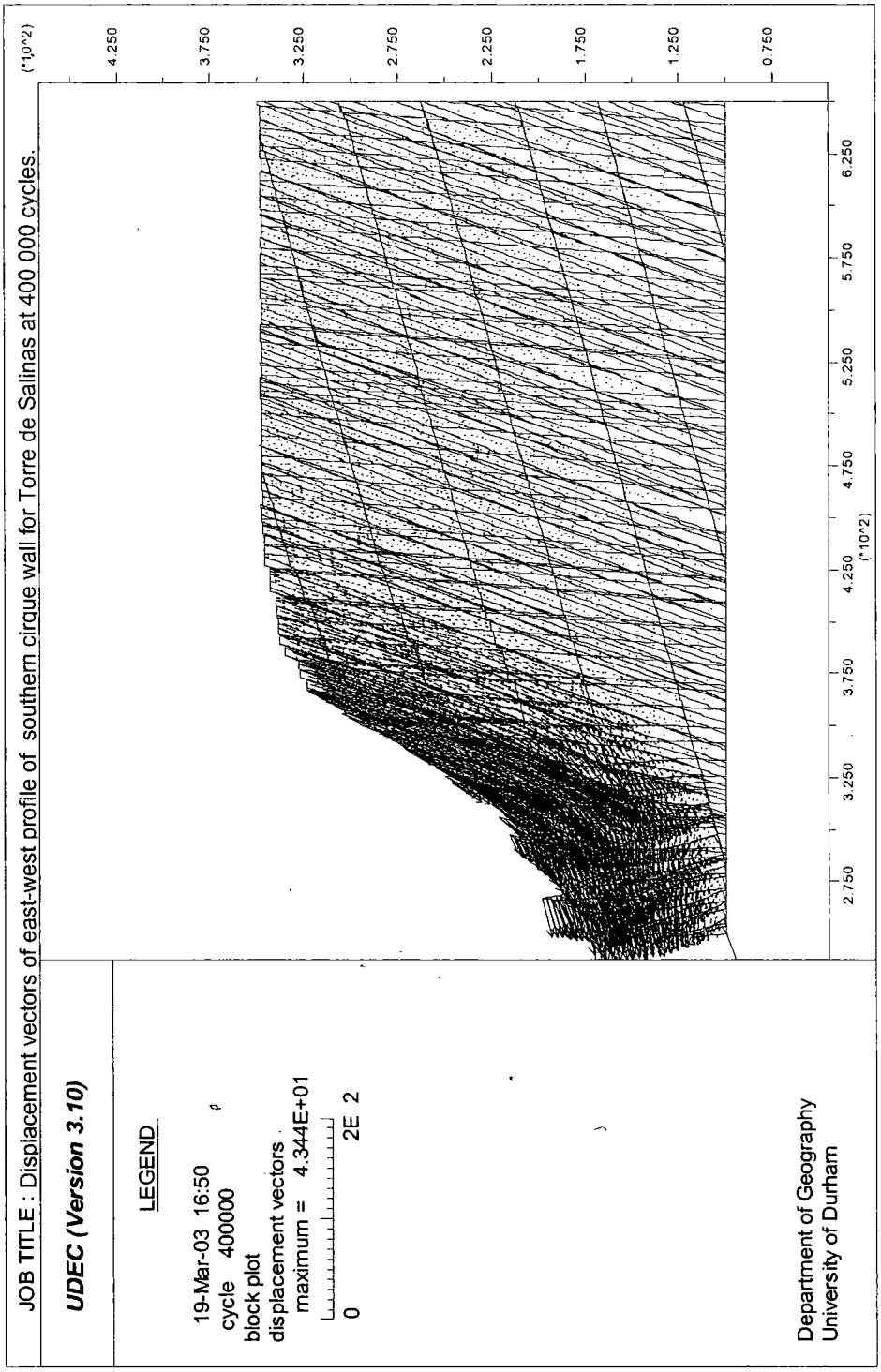

Figure 7.9c: Displacement vectors of the east-west profile of the southern cirque headwall for Torre de Salinas, Picos de Europa, at 400 000 cycles.

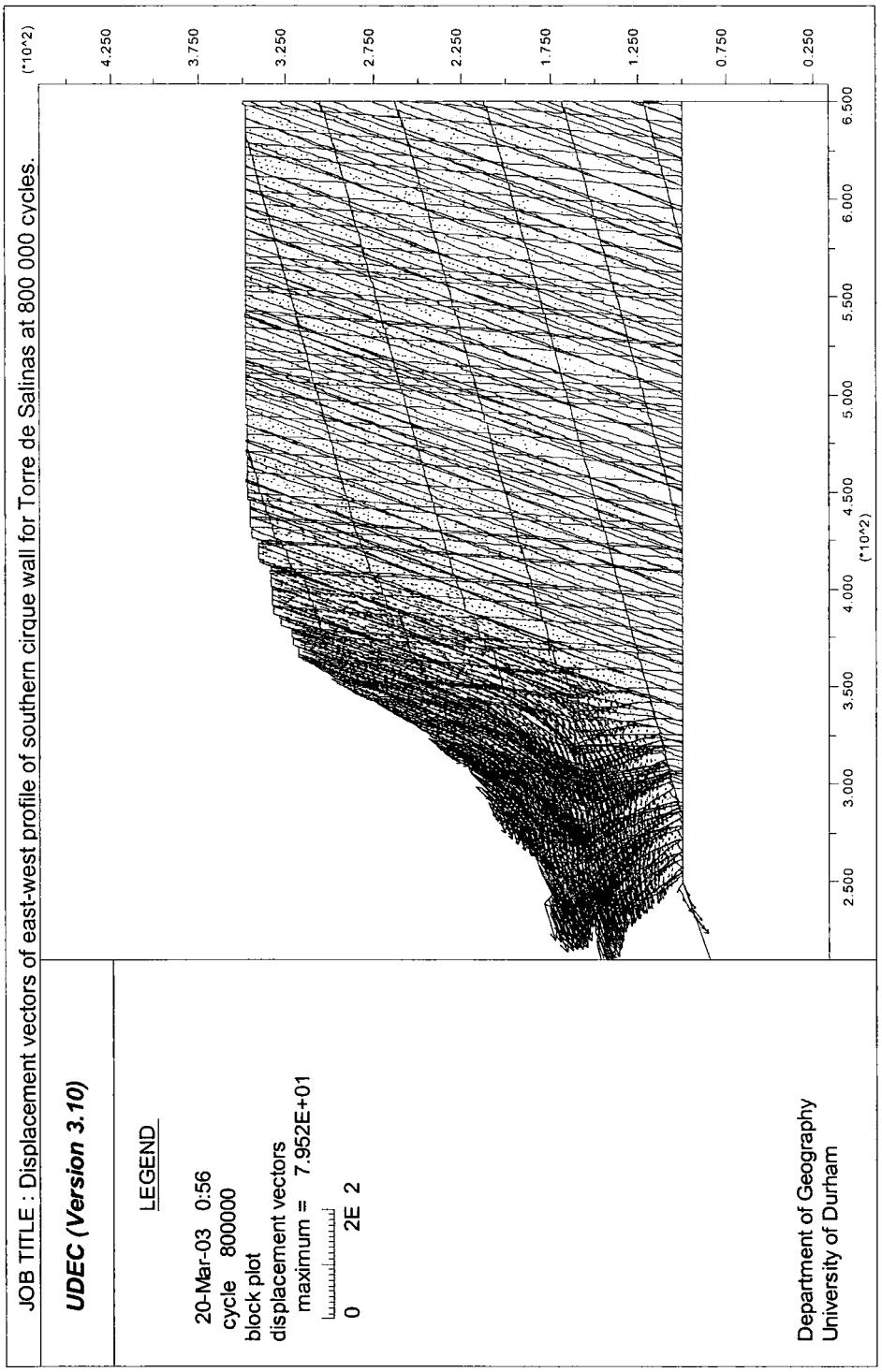

Figure 7.9d: Displacement vectors of the east-west profile of the southern cirque headwall for Torre de Salinas, Picos de Europa, at 800 000 cycles.

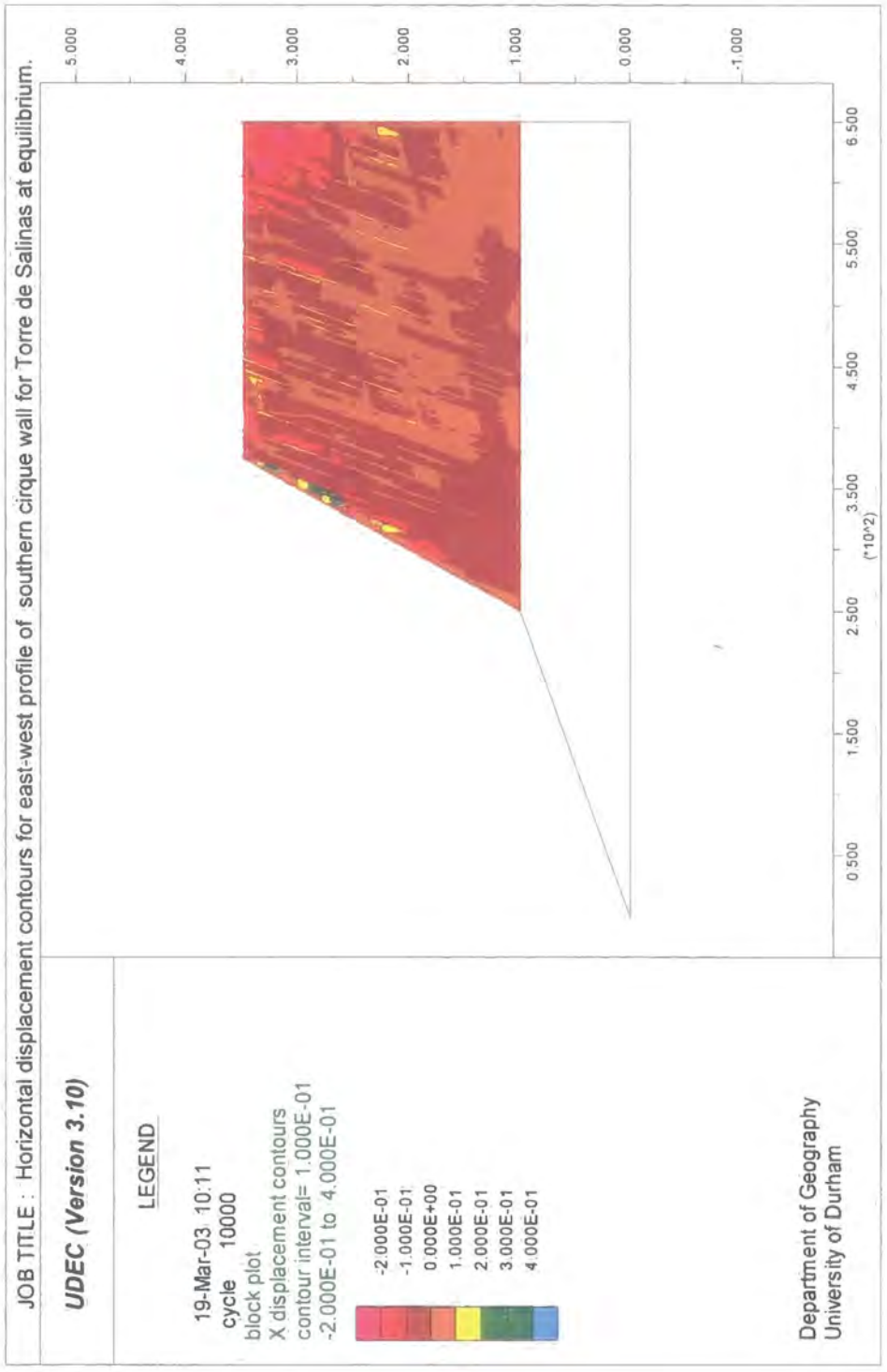

Figure 7.10a: Horizontal displacement contours for the east-west profile of the southern cirque headwall for Torre de Salinas at equilibrium.

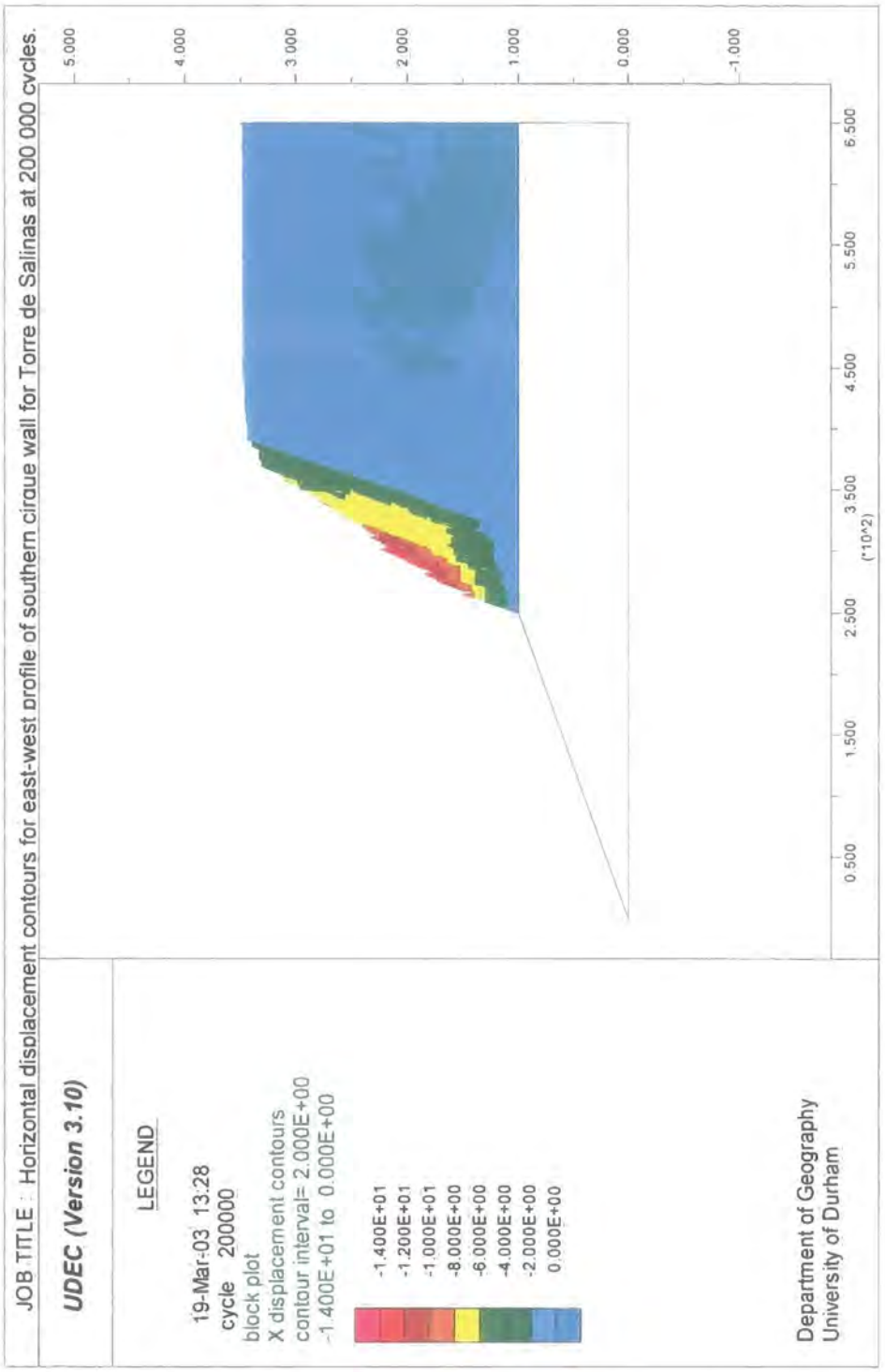

Figure 7.10b: Horizontal displacement contours for the east-west profile of the southern cirque headwall for Torre de Salinas at 200 000 cycles.

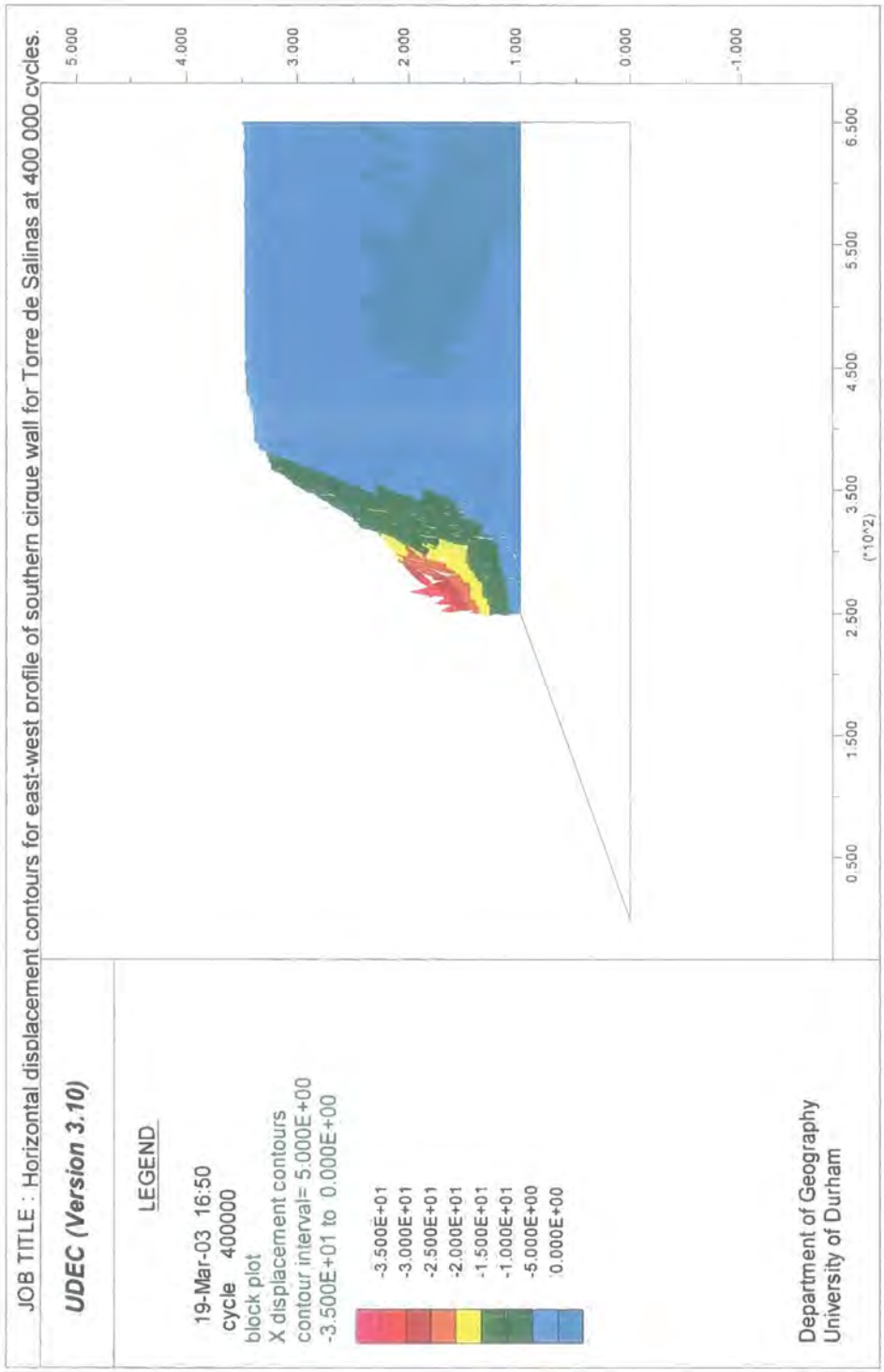

Figure 7.10c: Horizontal displacement contours for the east-west profile of the southern cirque headwall for Torre de Salinas at 400 000 cycles.

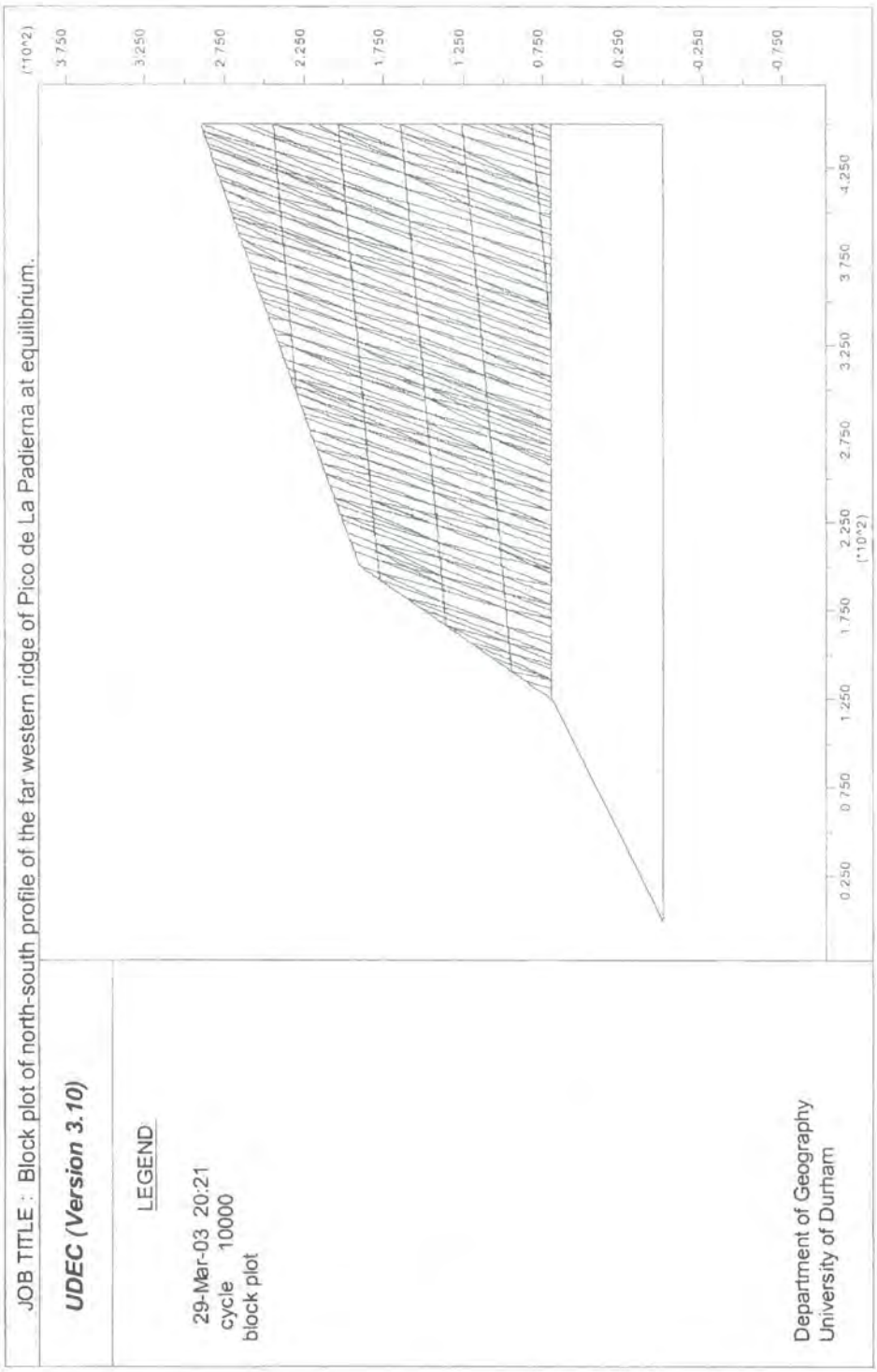

Figure 7.11a: Block plot of the north-south profile of the far western section for the ridge of Pico de La Padierna at equilibrium.

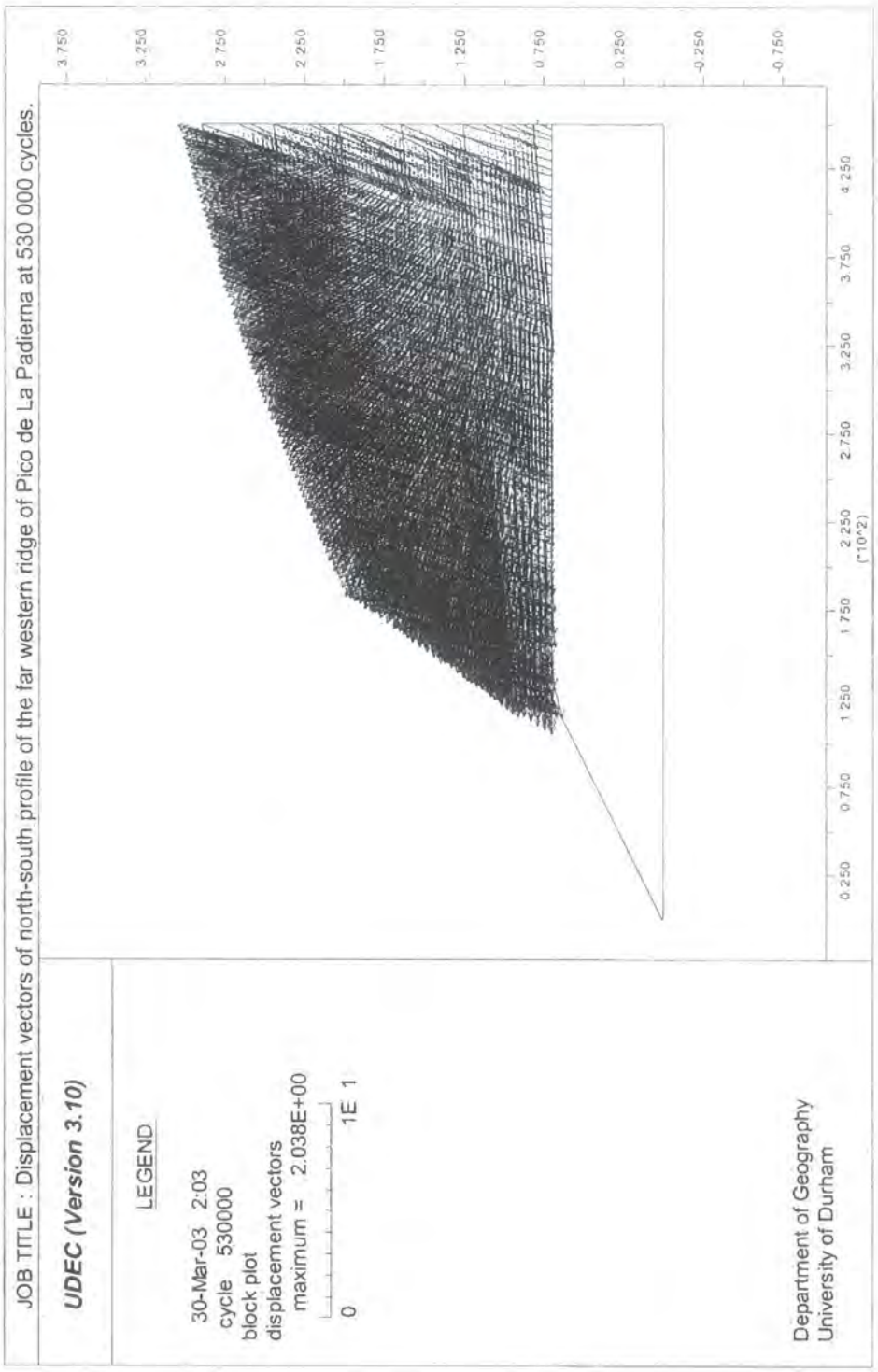

Figure 7.11b: Displacement vectors of the north-south profile of the far western section for the ridge of Pico de La Padierna at 530 000 cycles.

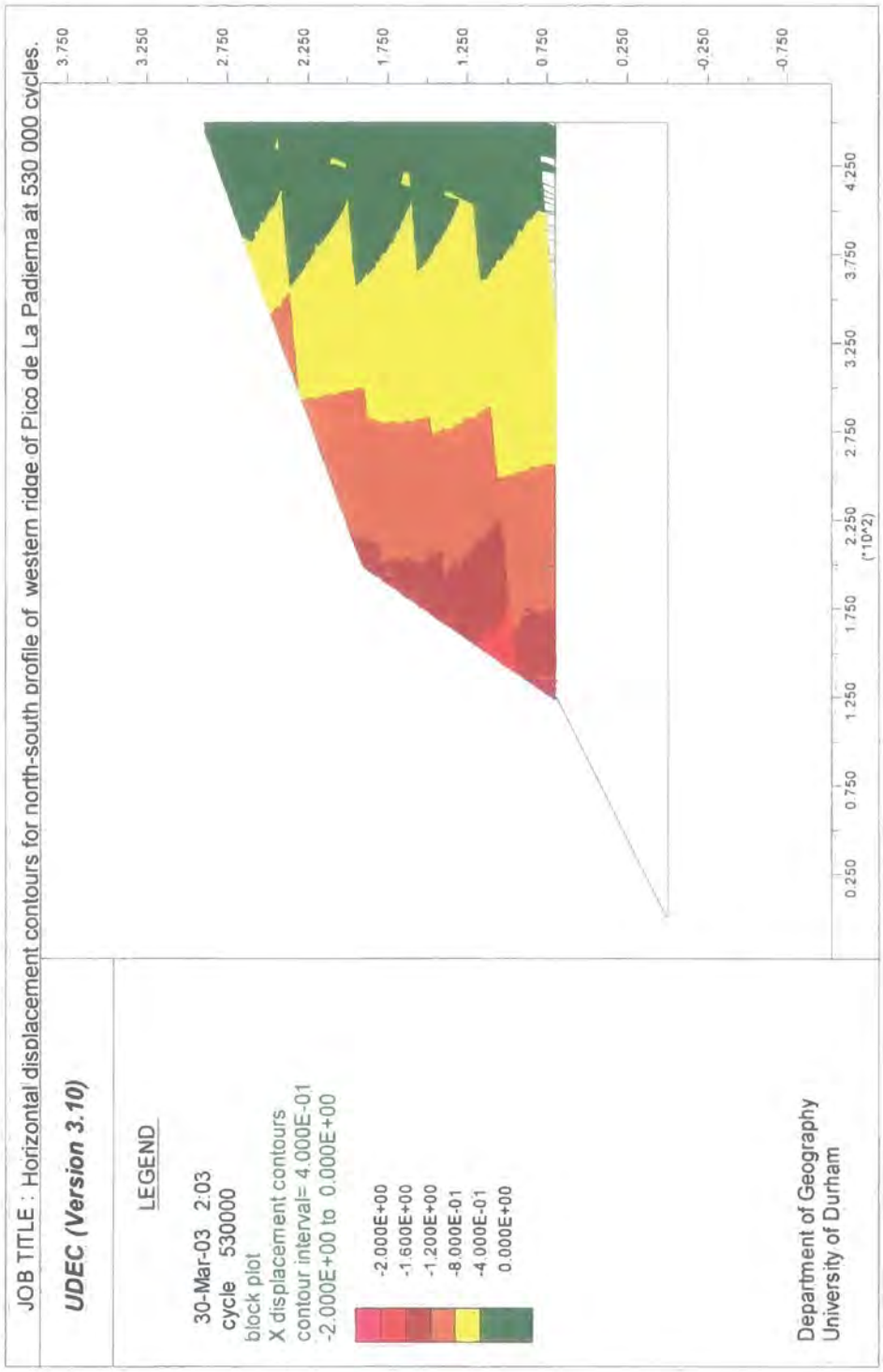

Figure 7.12: Horizontal displacement contours for the north-south profile of the far western section of the ridge of Pico de La Padierna at 530 000 cycles.

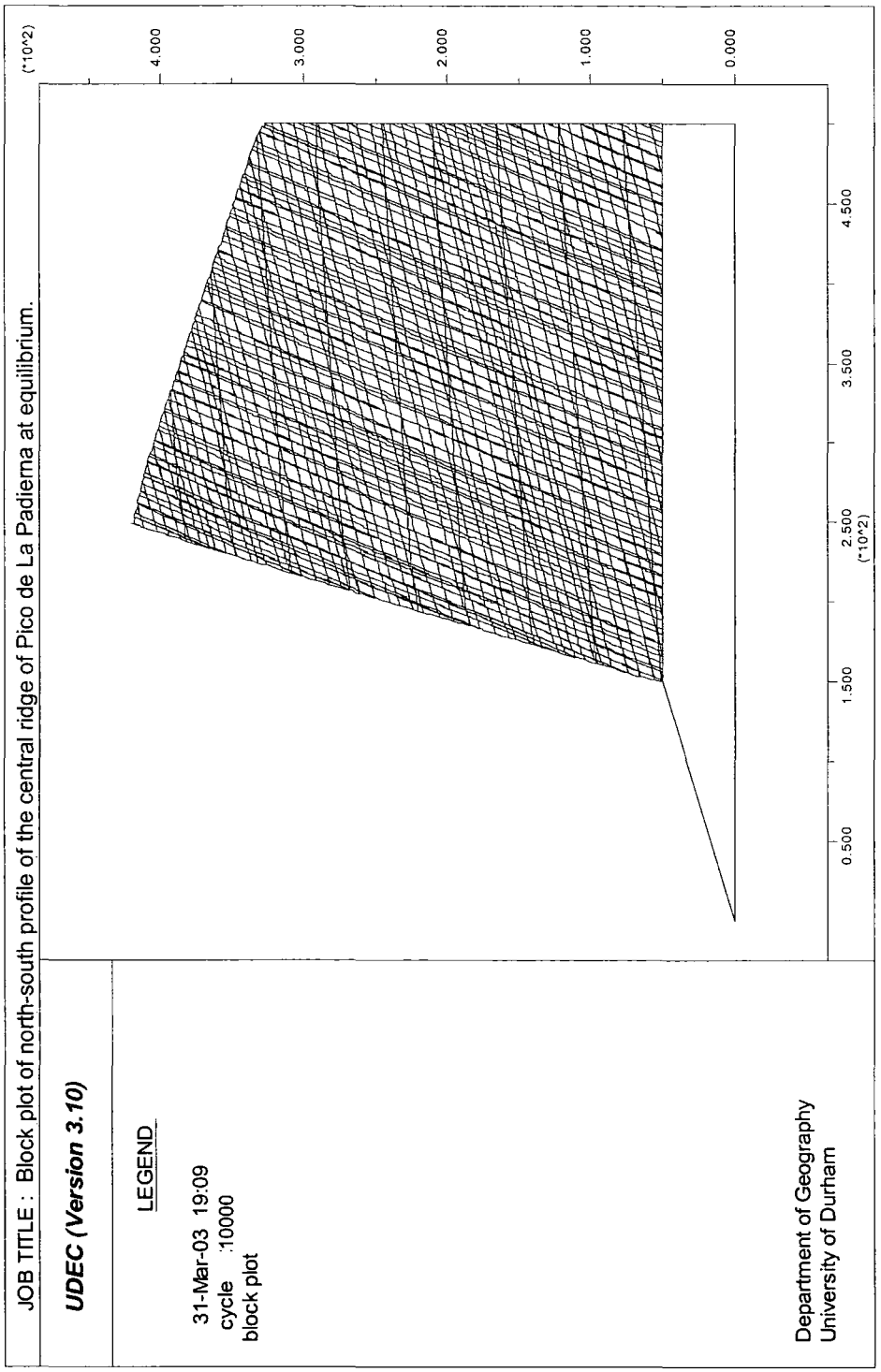

Figure 7.13a: Block plot of the north-south profile of the central ridge of Pico de La Padierna at equilibrium.

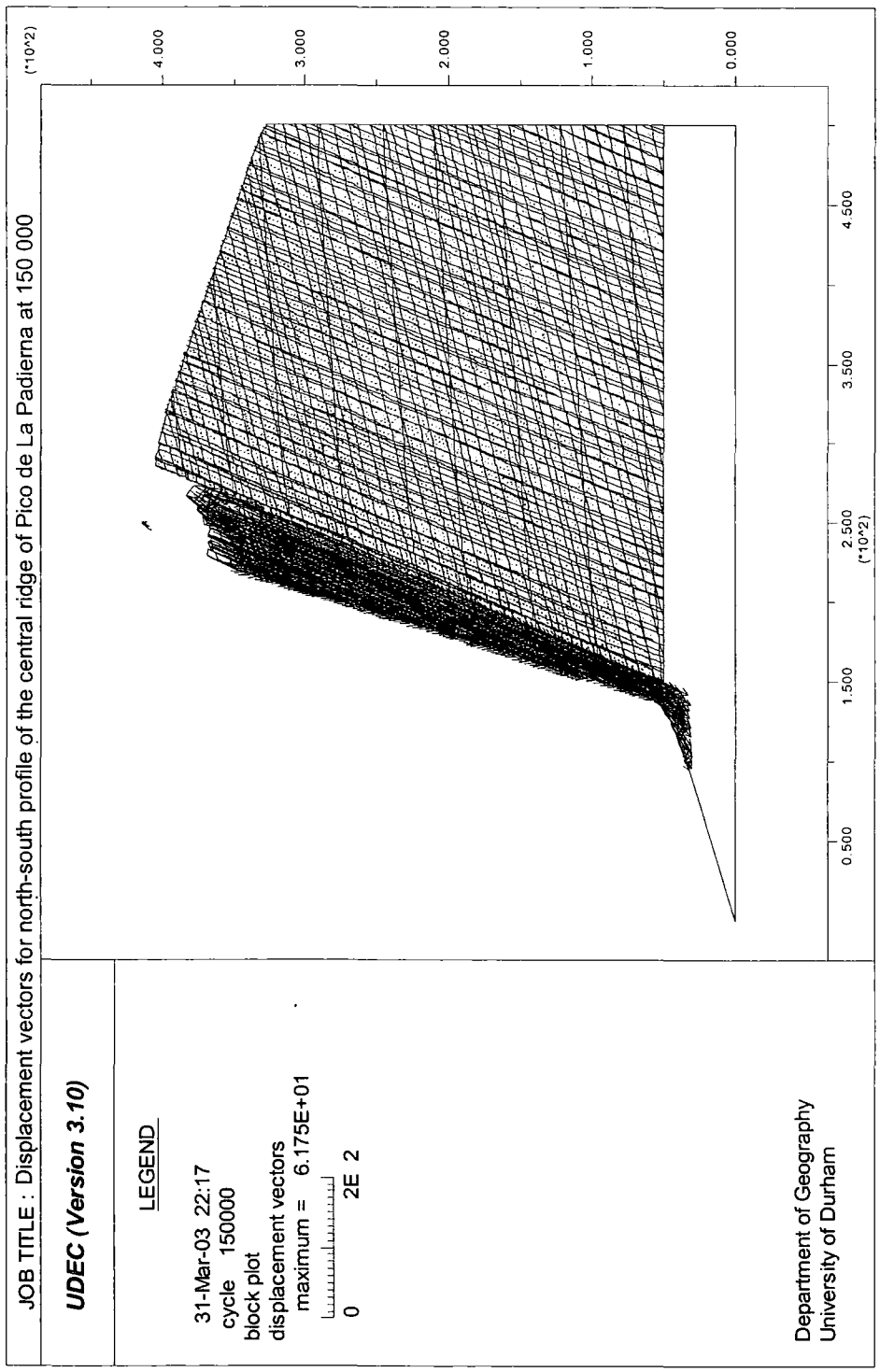

Figure 7.13b: Displacement vectors for the north-south profile of the central ridge of Pico de La Padierna at 150 000 cycles.

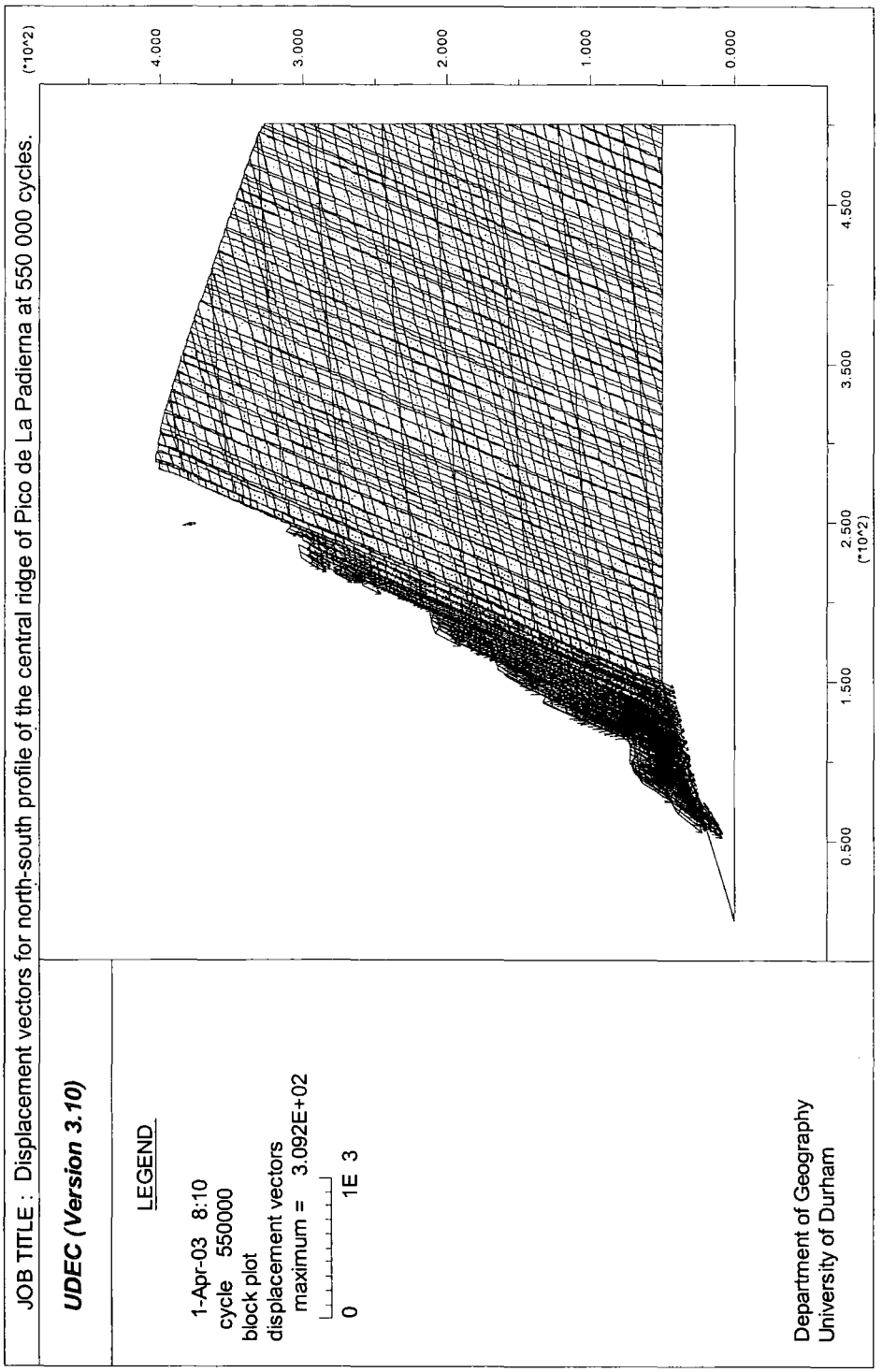

Figure 7.13c: Displacement vectors for the north-south profile of the central ridge of Pico de La Padierna at 550 000 cycles.

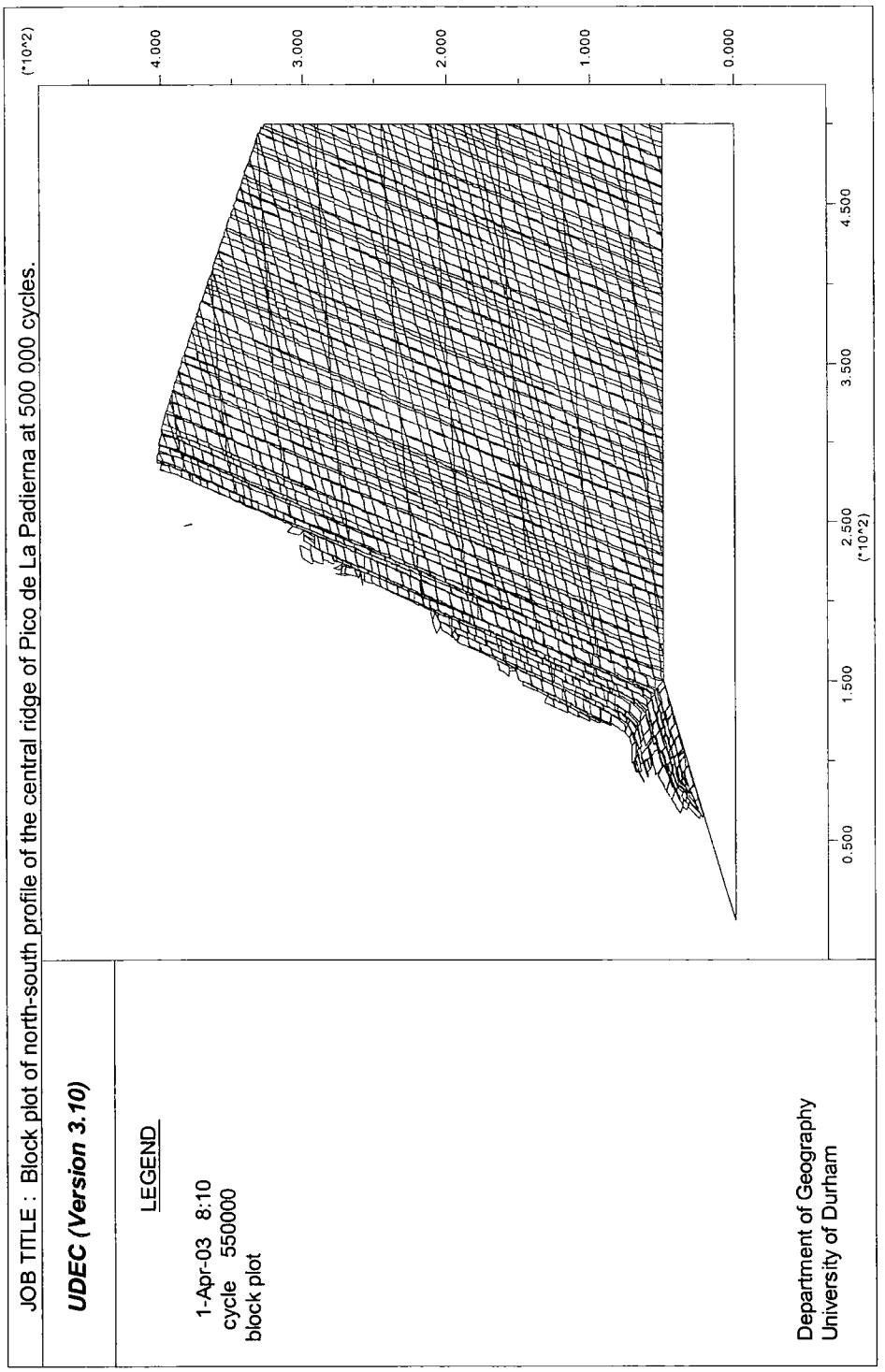

Figure 7.14: Block plot of the north-south profile of the central ridge of Pico de La Padierna at 500 000 cycles.

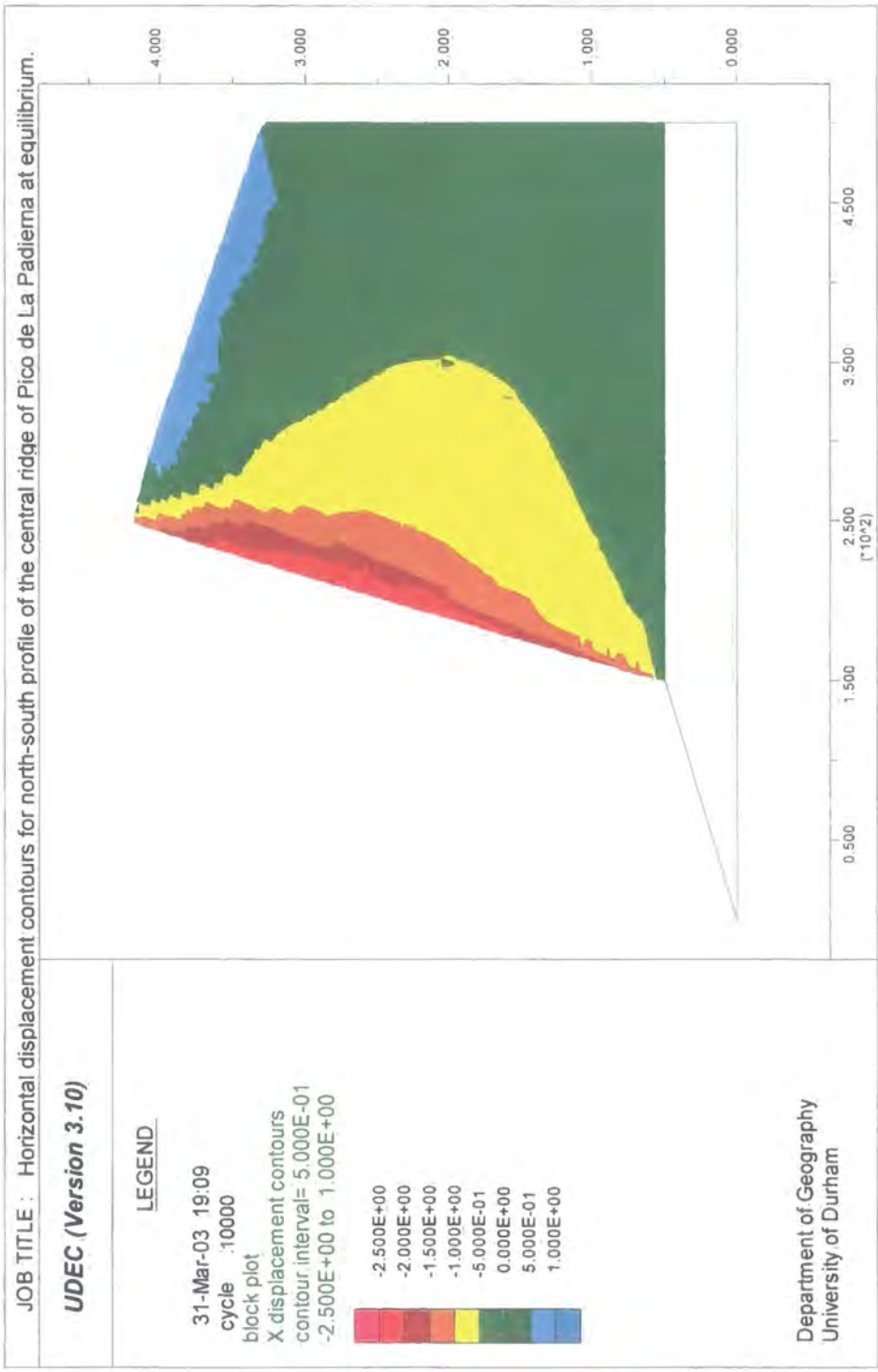

Figure 7.15a: Horizontal displacement contours for the north-south profile of the central ridge of Pico de La Padierna at equilibrium.

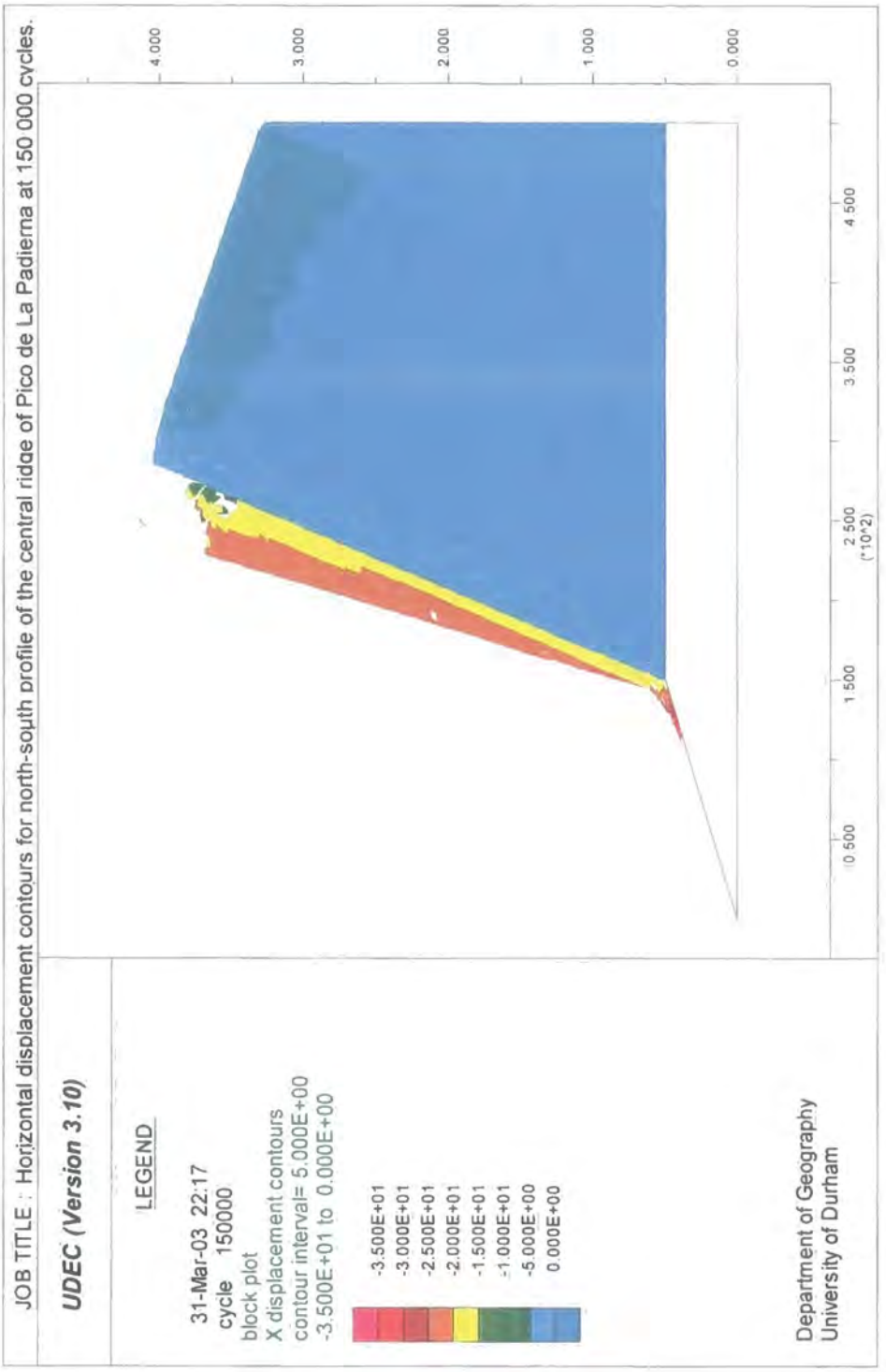

Figure 7.15b: Horizontal displacement contours for the north-south profile of the central ridge of Pico de La Padierna at 150 000 cycles.

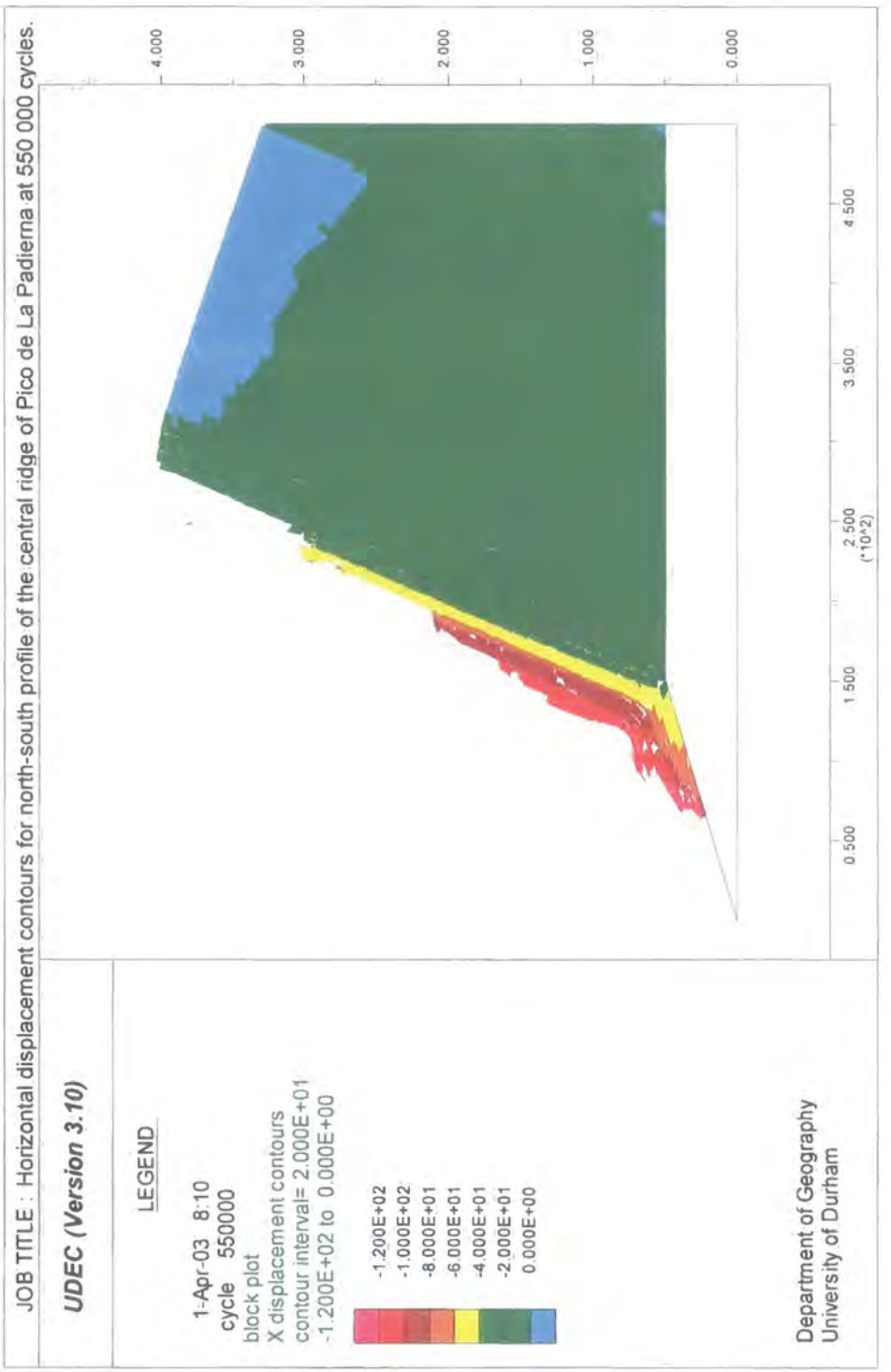

Figure 7.15c: Horizontal displacement contours for the north-south profile of the central ridge of Pico de La Padierna at 550 000 cycles.

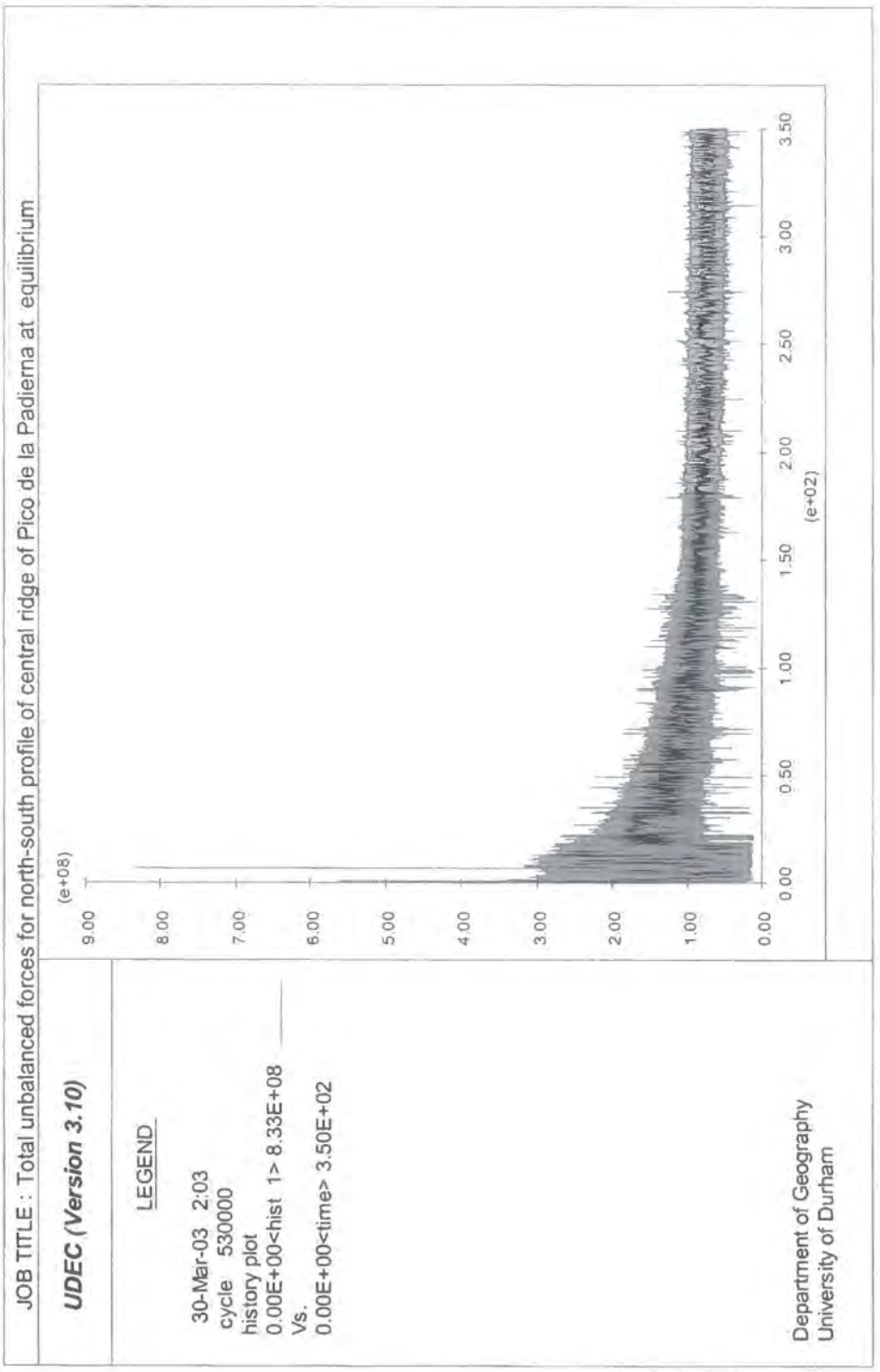

Figure 7.16: Total unbalanced forces for the north-south profile of Pico de la Padierna at equilibrium.

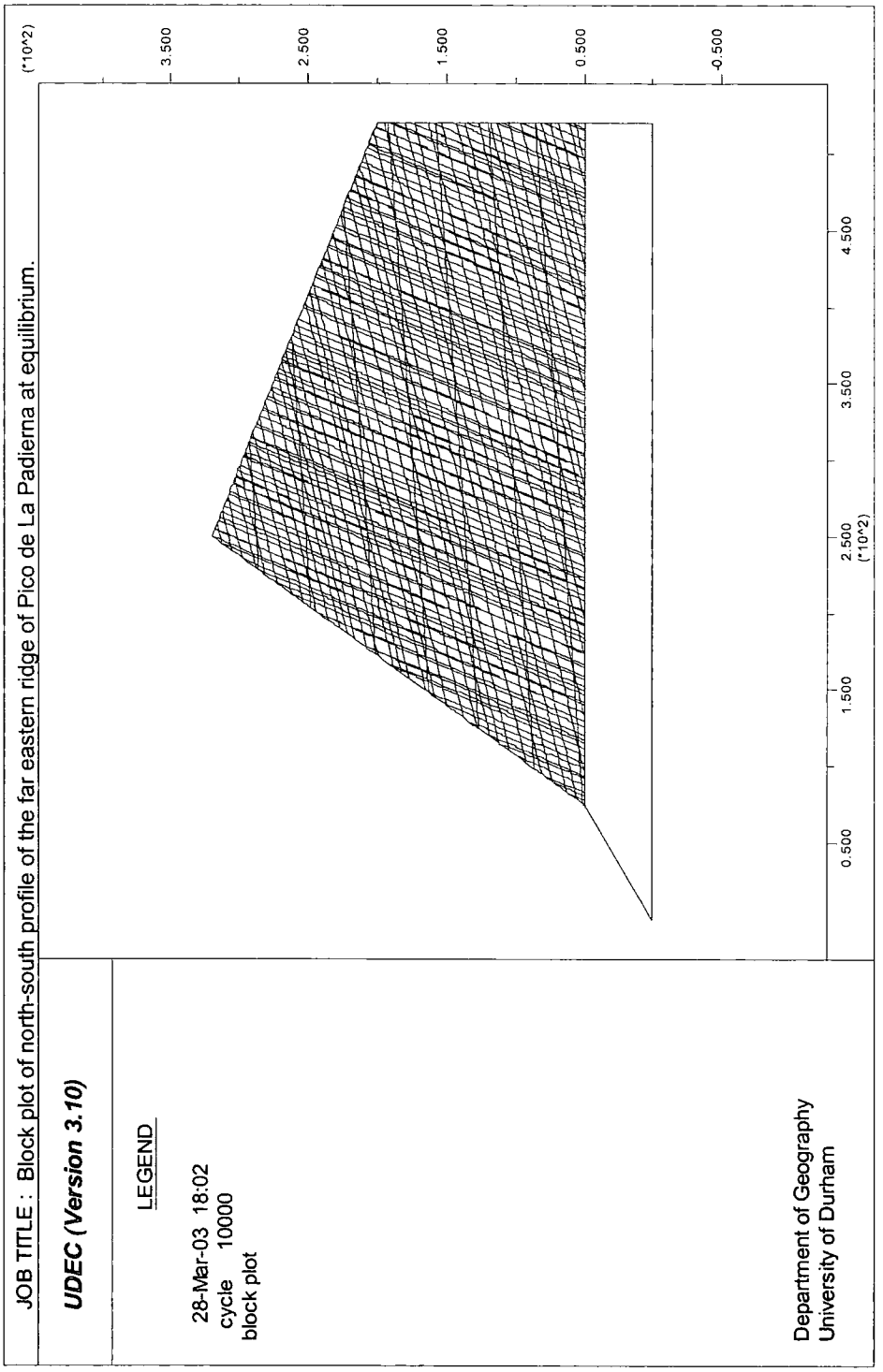

Figure 7.17a: Block plot of the north-south profile of the far eastern section for the ridge of Pico de La Padierna at equilibrium.

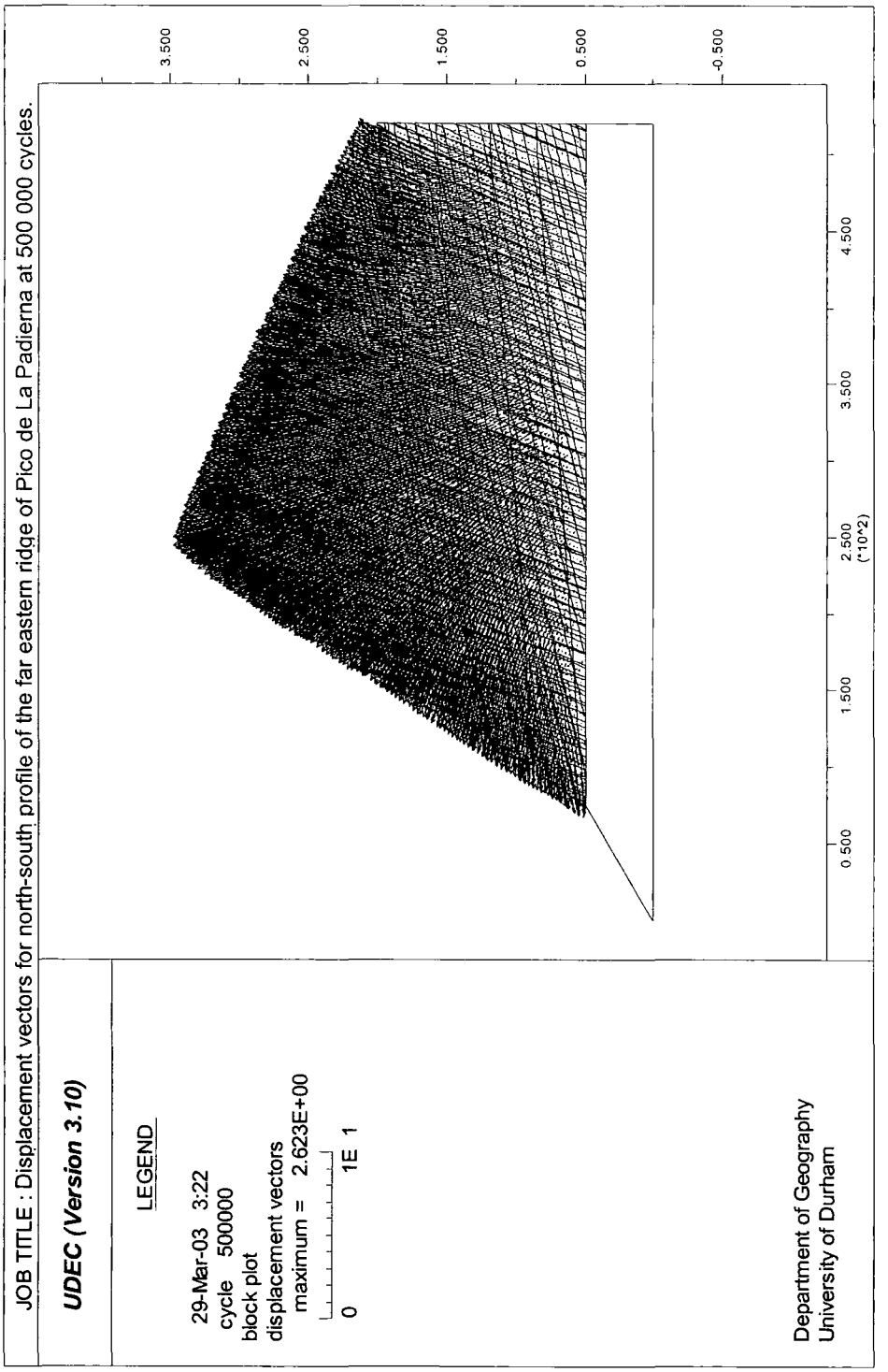

Figure 7.17b: Displacement vectors for the north-south profile of the far eastern section for the ridge of Pico de La Padierna at 500 000 cycles.

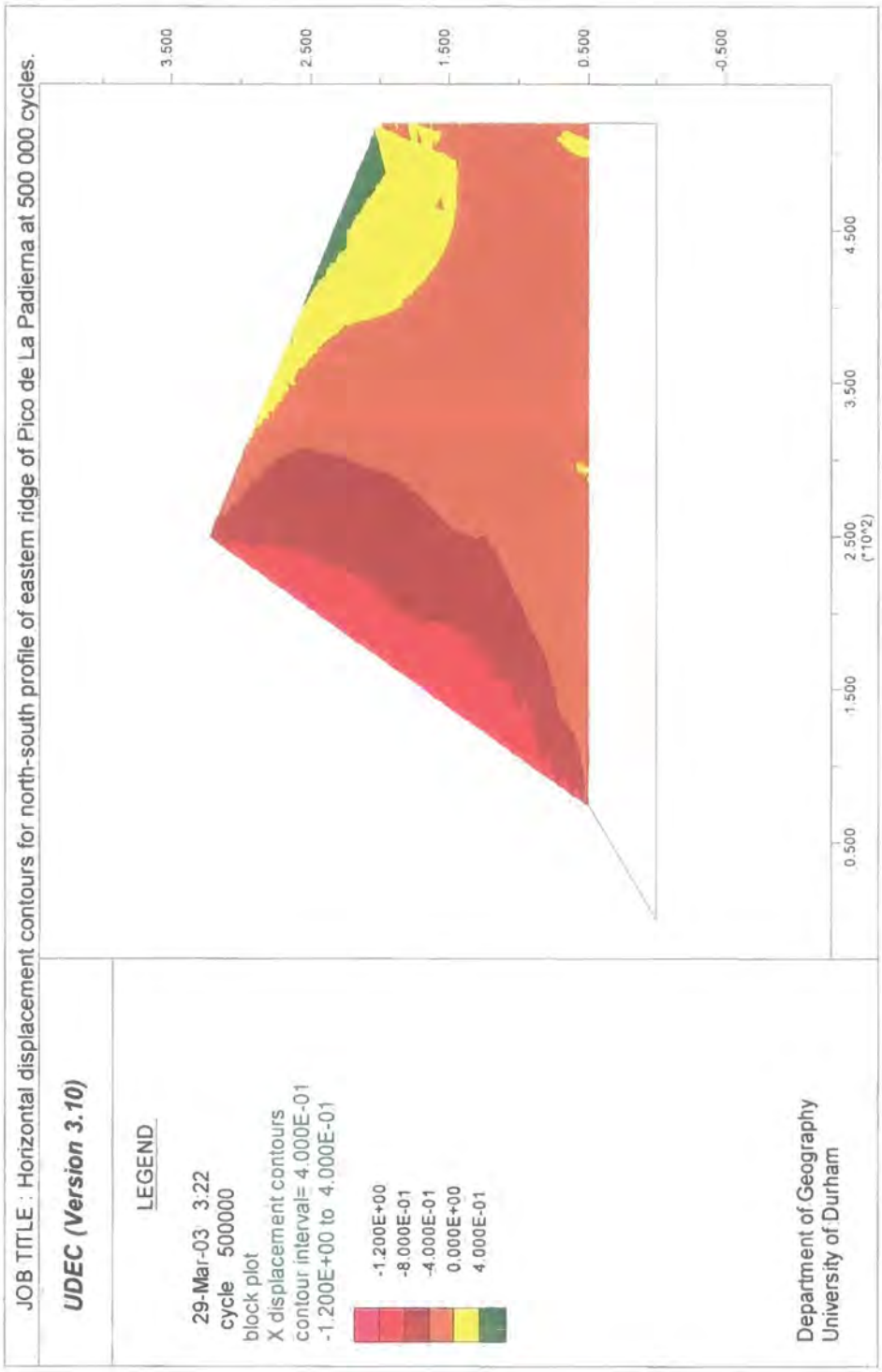

Figure 7.18: Horizontal displacement contours of the north-south profile of the far eastern section for the ridge of Pico de La Padierna at 500 000 cycles.

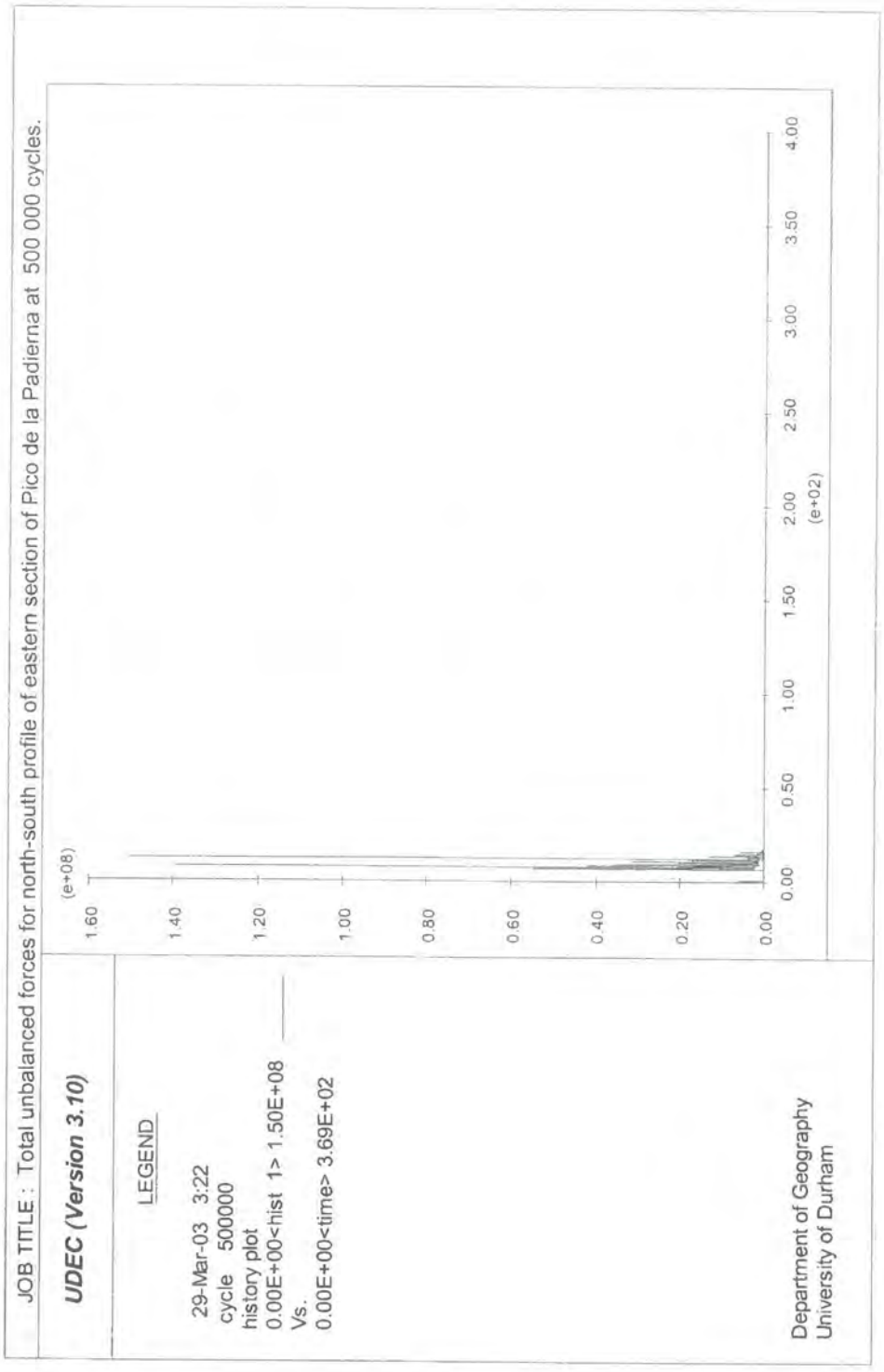

Figure 7.19: Total unbalanced forces for the north-south of the eastern section of Pico de la Padierna at 500 000 cycles.

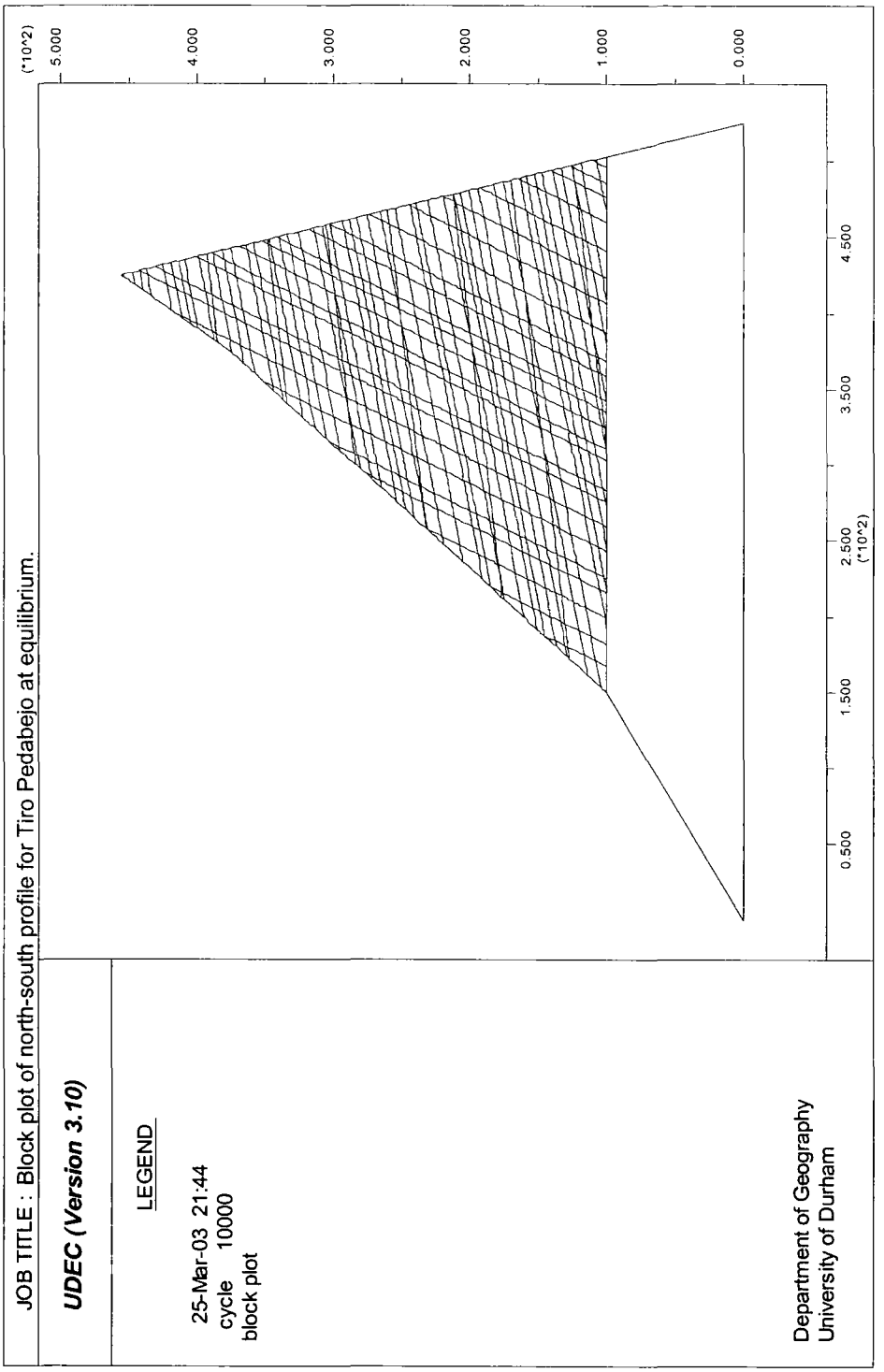

Figure 7.20a: Block plot of the north-south profile for Tiro Pedabejo, Picos de Europa, at equilibrium.

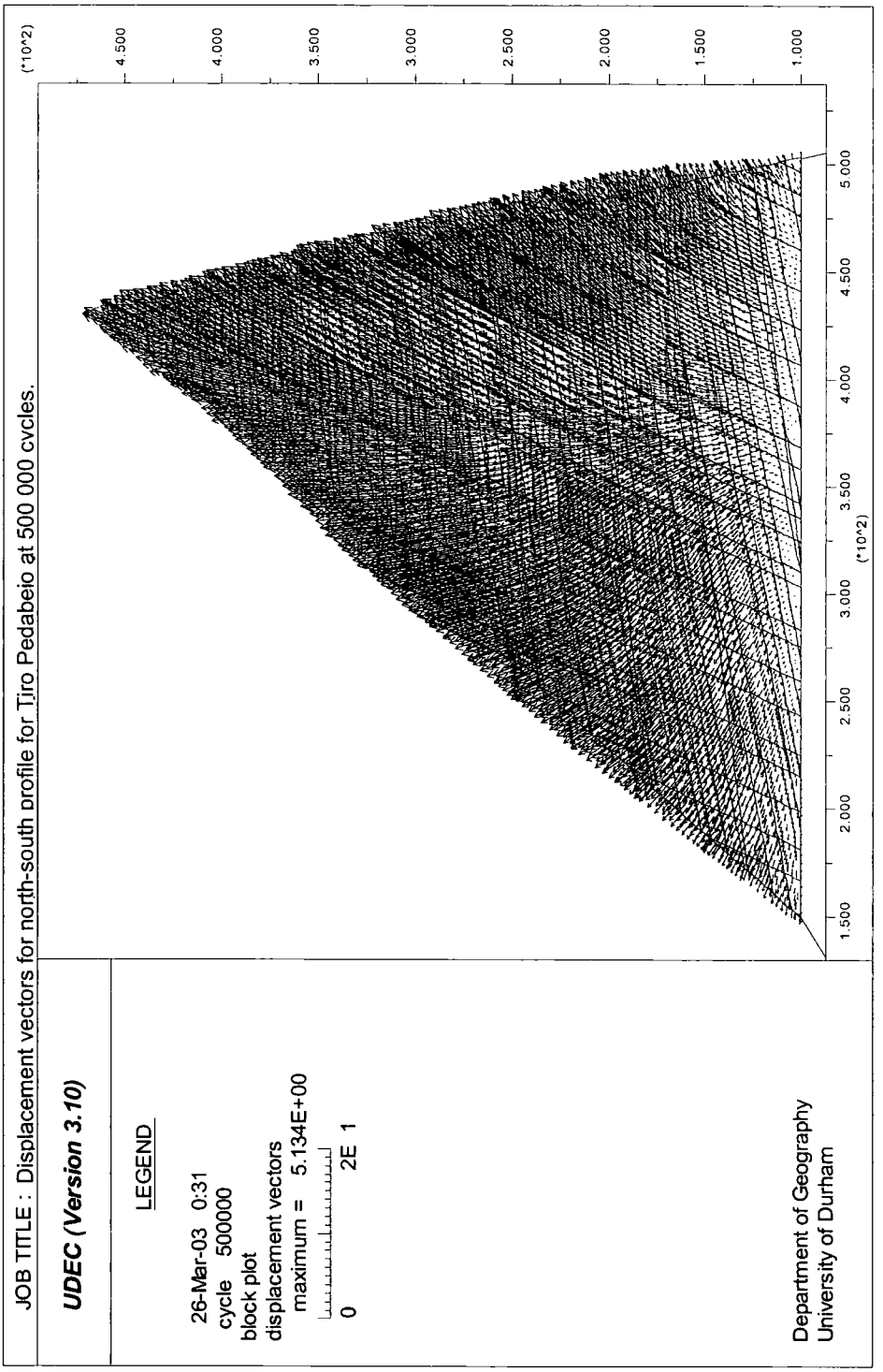

Figure 7.20b: Displacement vectors for the north-south profile for Tiro Pedabejo, Picos de Europa, at 500 000 cycles.

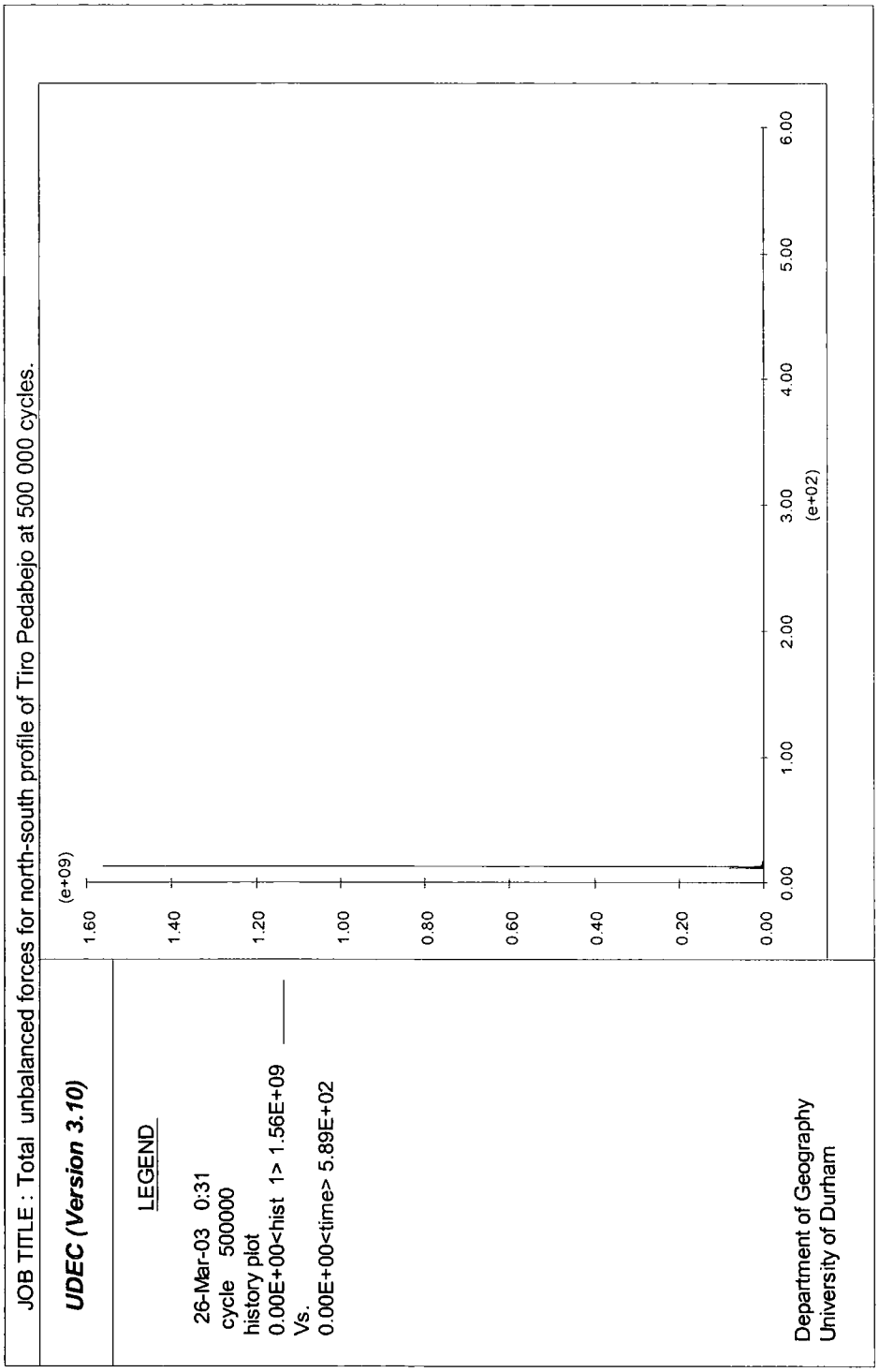

Figure 7.21: Total unbalanced forces for the north-south profile of Tiro Pedabejo at 500 000 cycles.

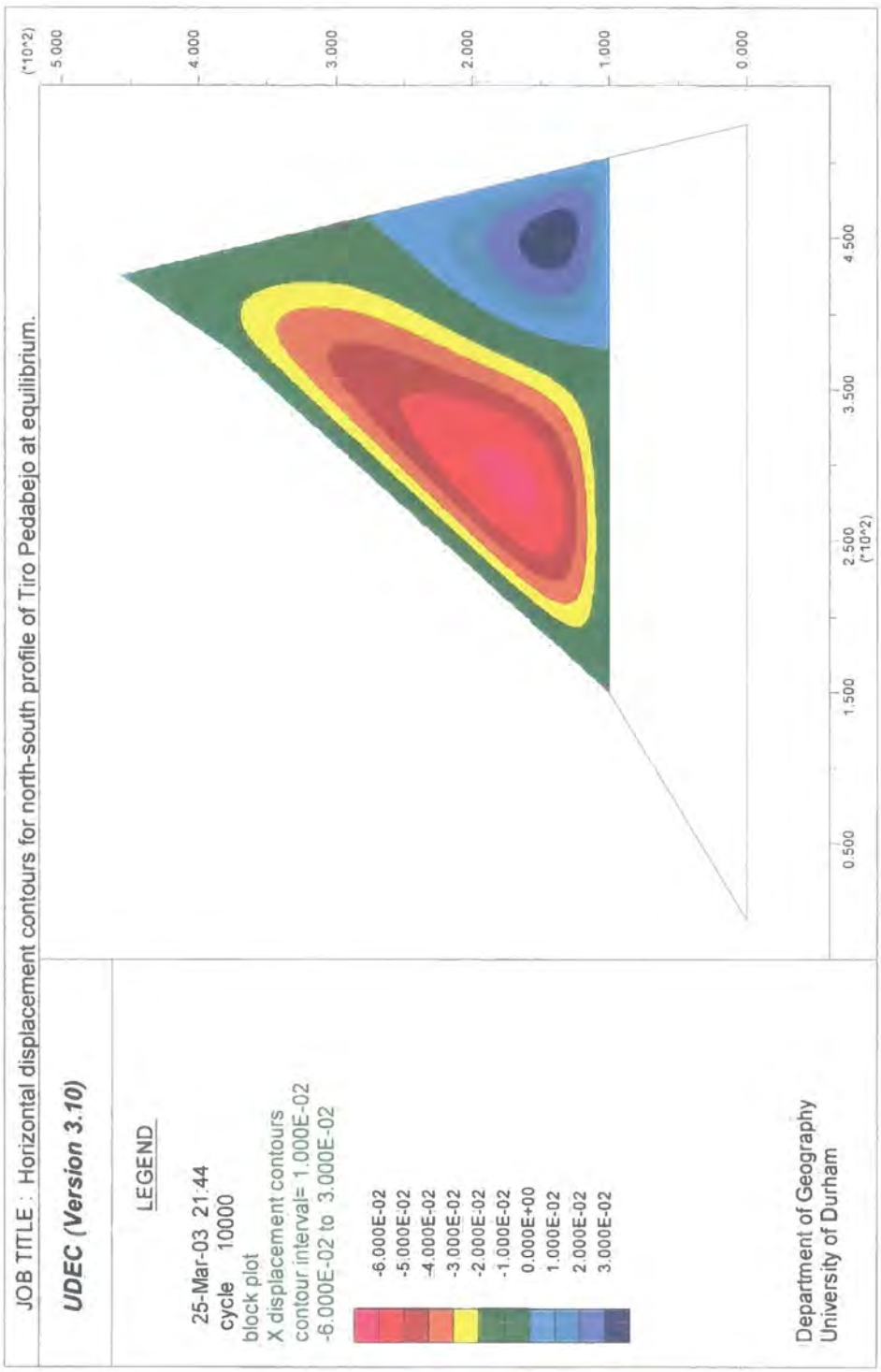

Figure 7.22a: Horizontal displacement contours for the north-south profile of Tiro Pedabejo at equilibrium.

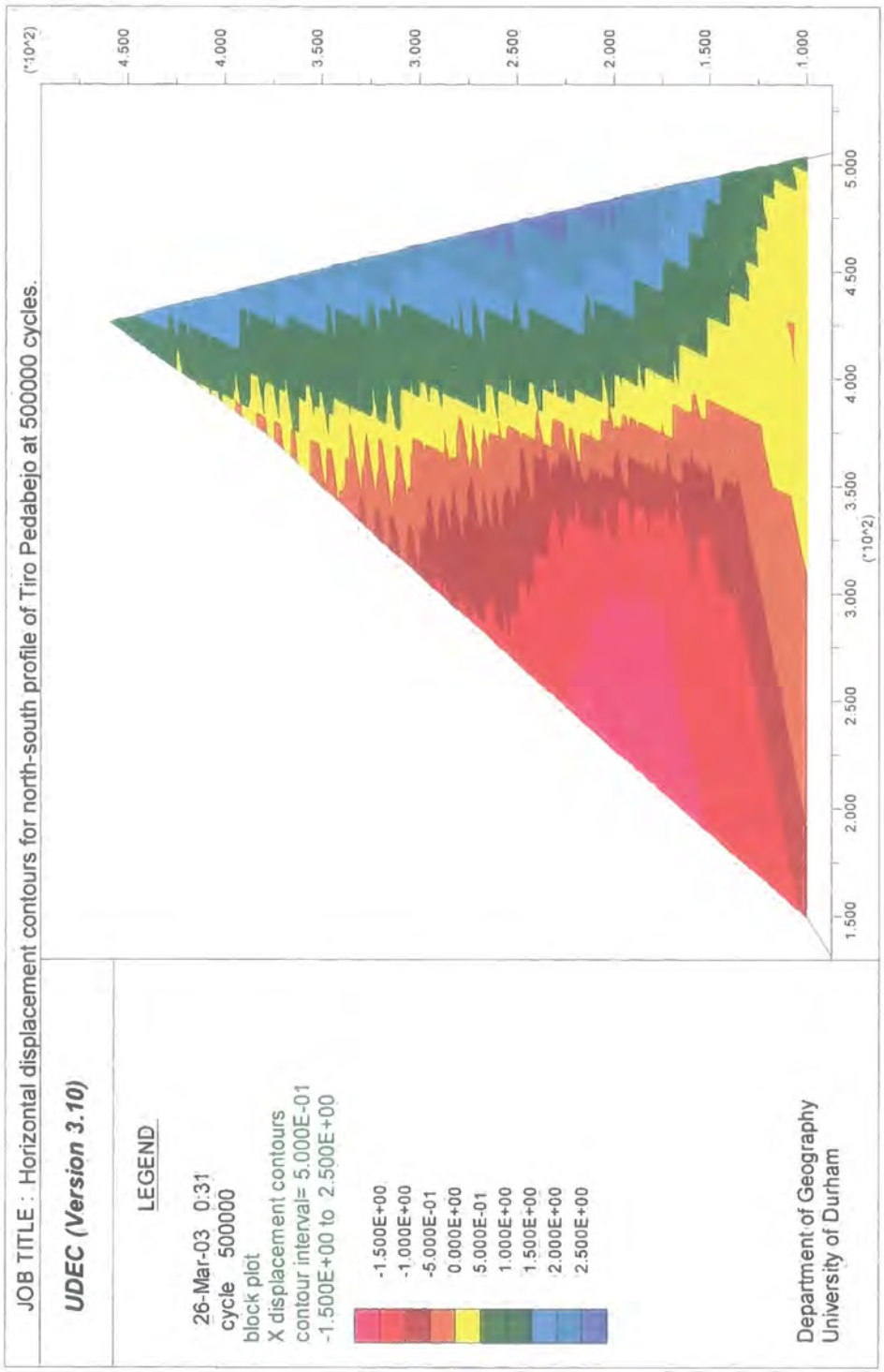

Figure 7.22b: Horizontal displacement contours for the north-south profile of Tiro Pedabejo at 500 000 cycles.

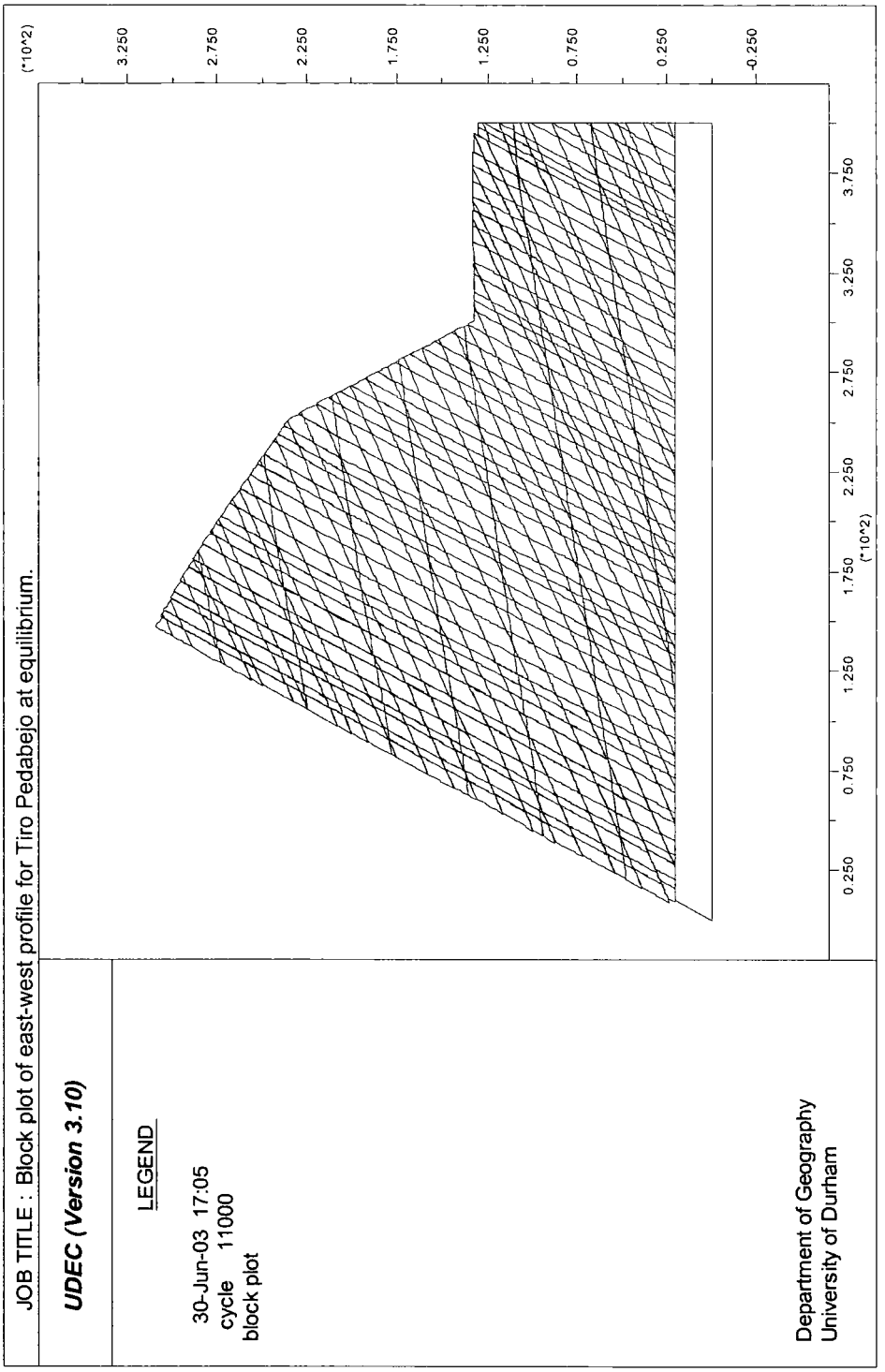

Figure 7.23a: Block plot of the east-west profile for Tiro Pedabejo, Picos de Europa, at equilibrium.

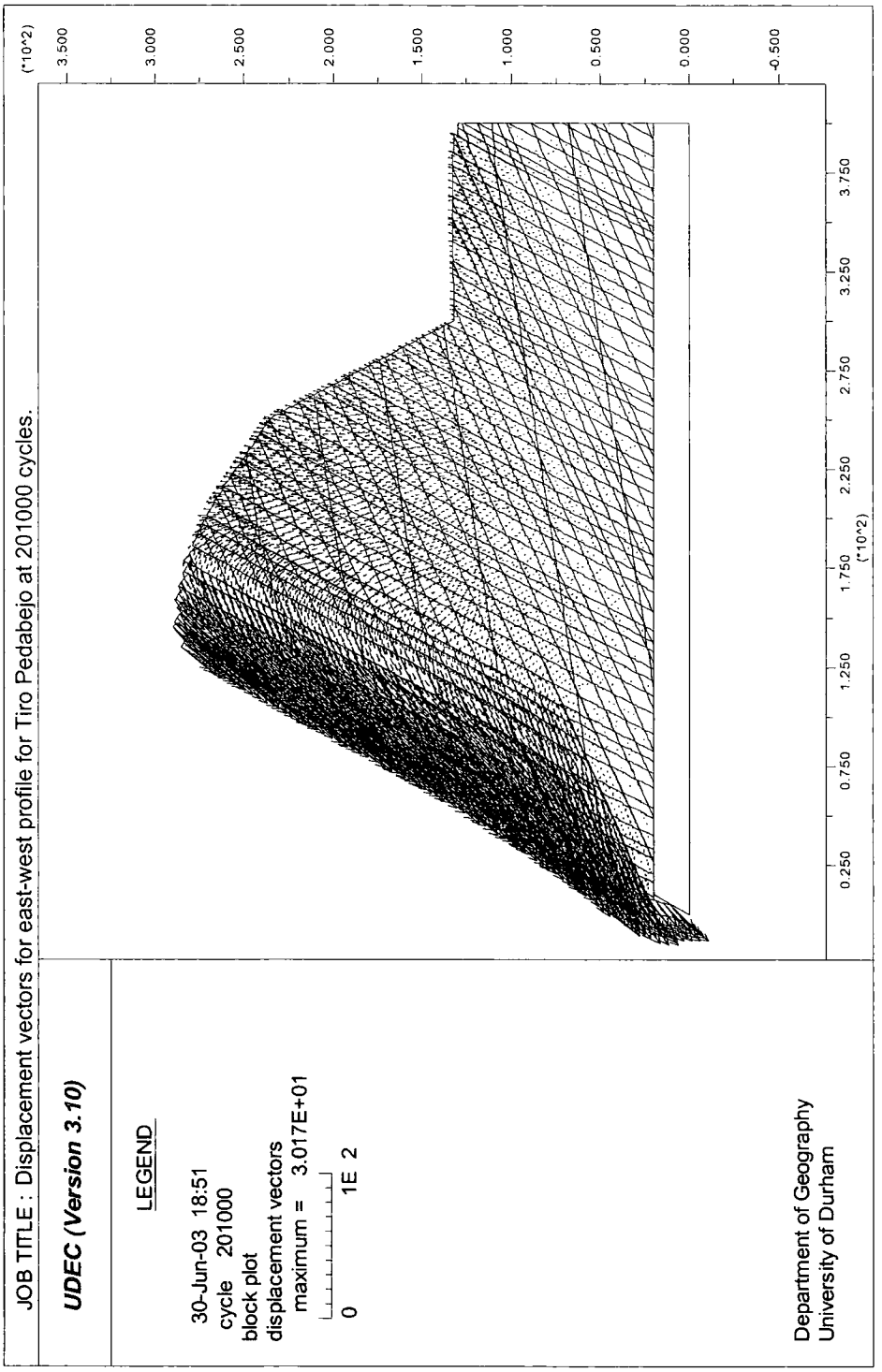

Figure 7.23b: Displacement vectors for the north-south profile for Tiro Pedabejo, Picos de Europa, at 201 000 cycles.

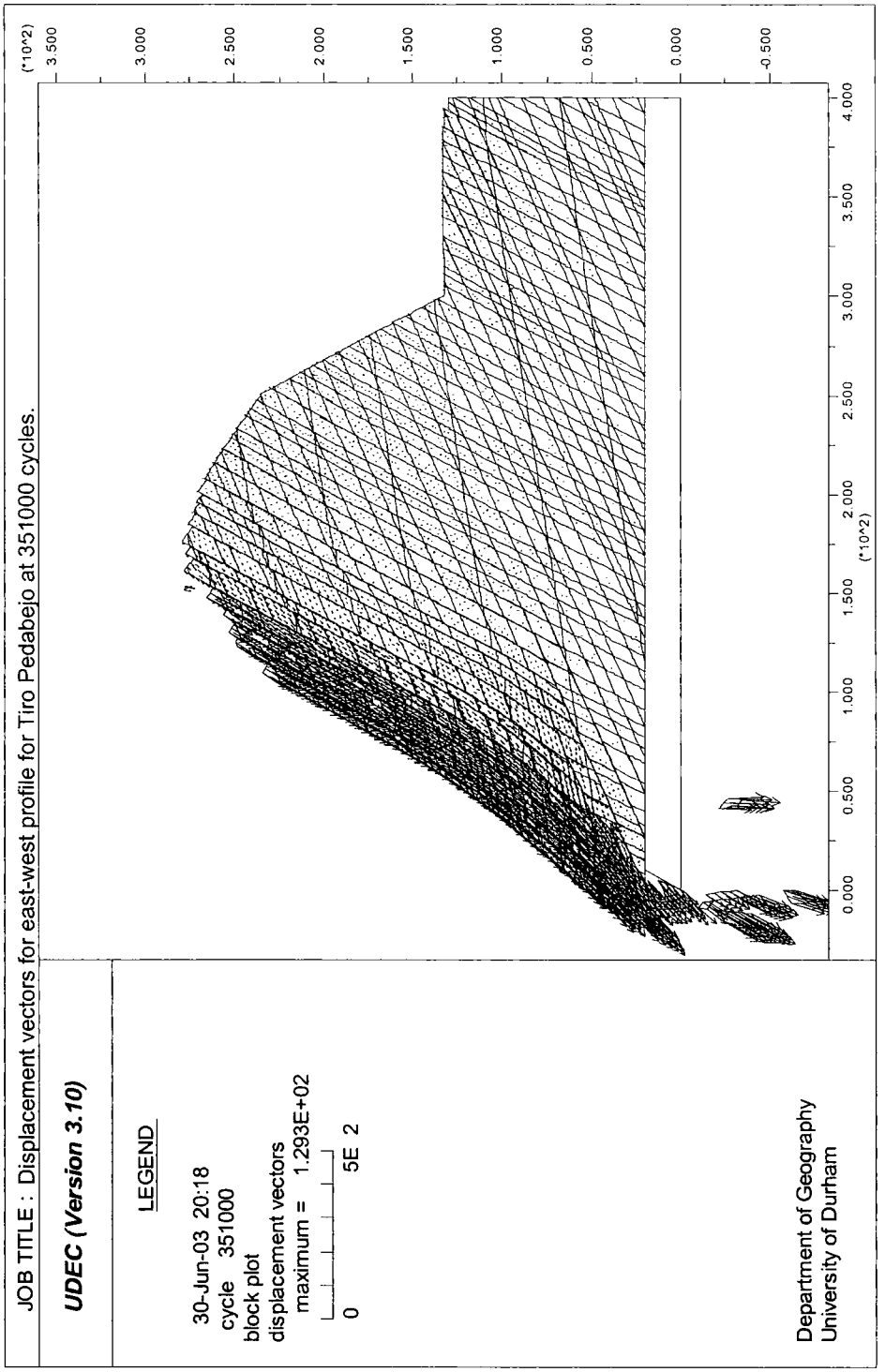

Figure 7.23c: Displacement vectors for the north-south profile for Tiro Pedabejo, Picos de Europa, at 351 000 cycles.

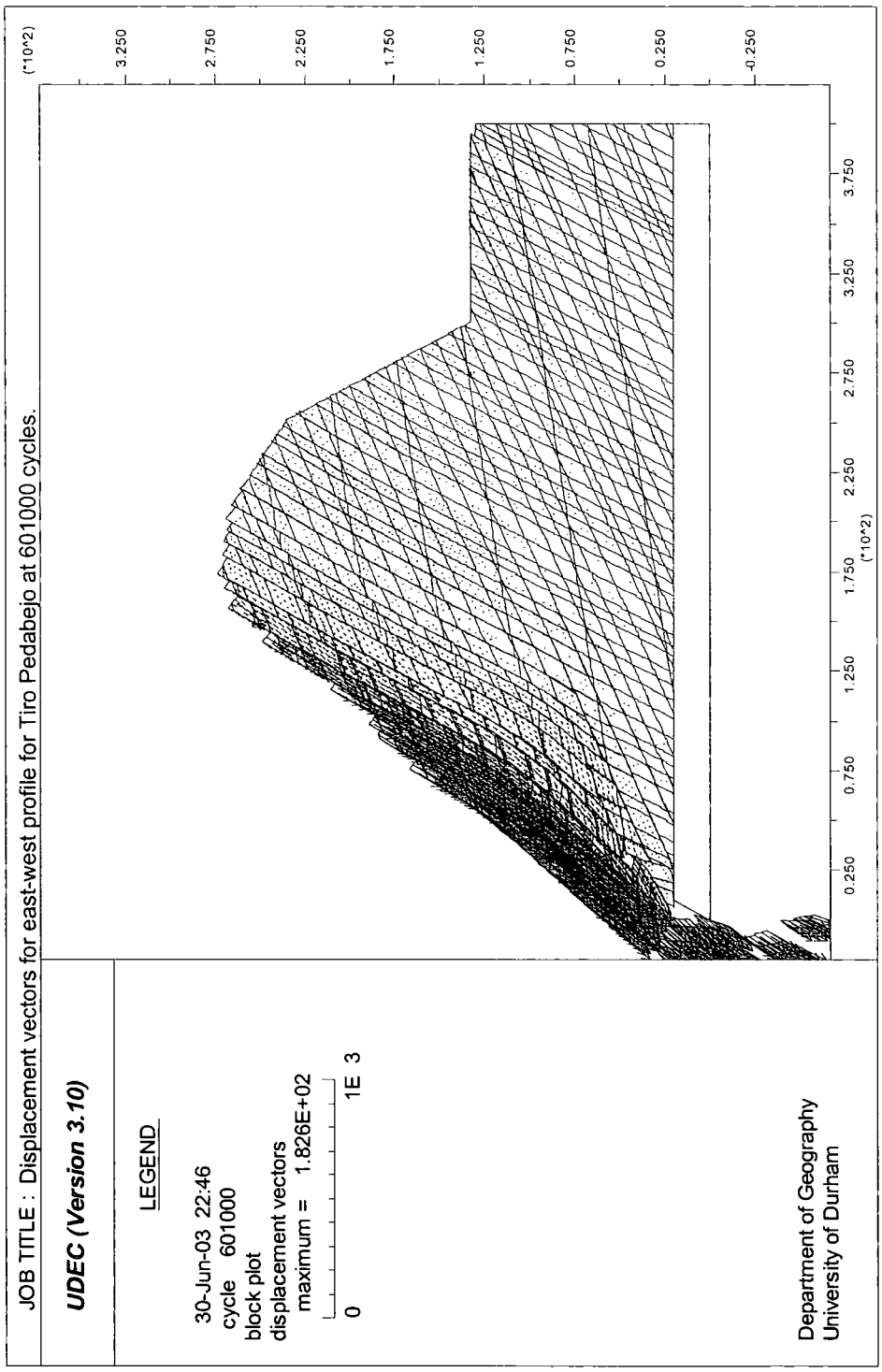

Figure 7.23d: Displacement vectors for the north-south profile for Tiro Pedabejo, Picos de Europa, at 601 000 cycles.

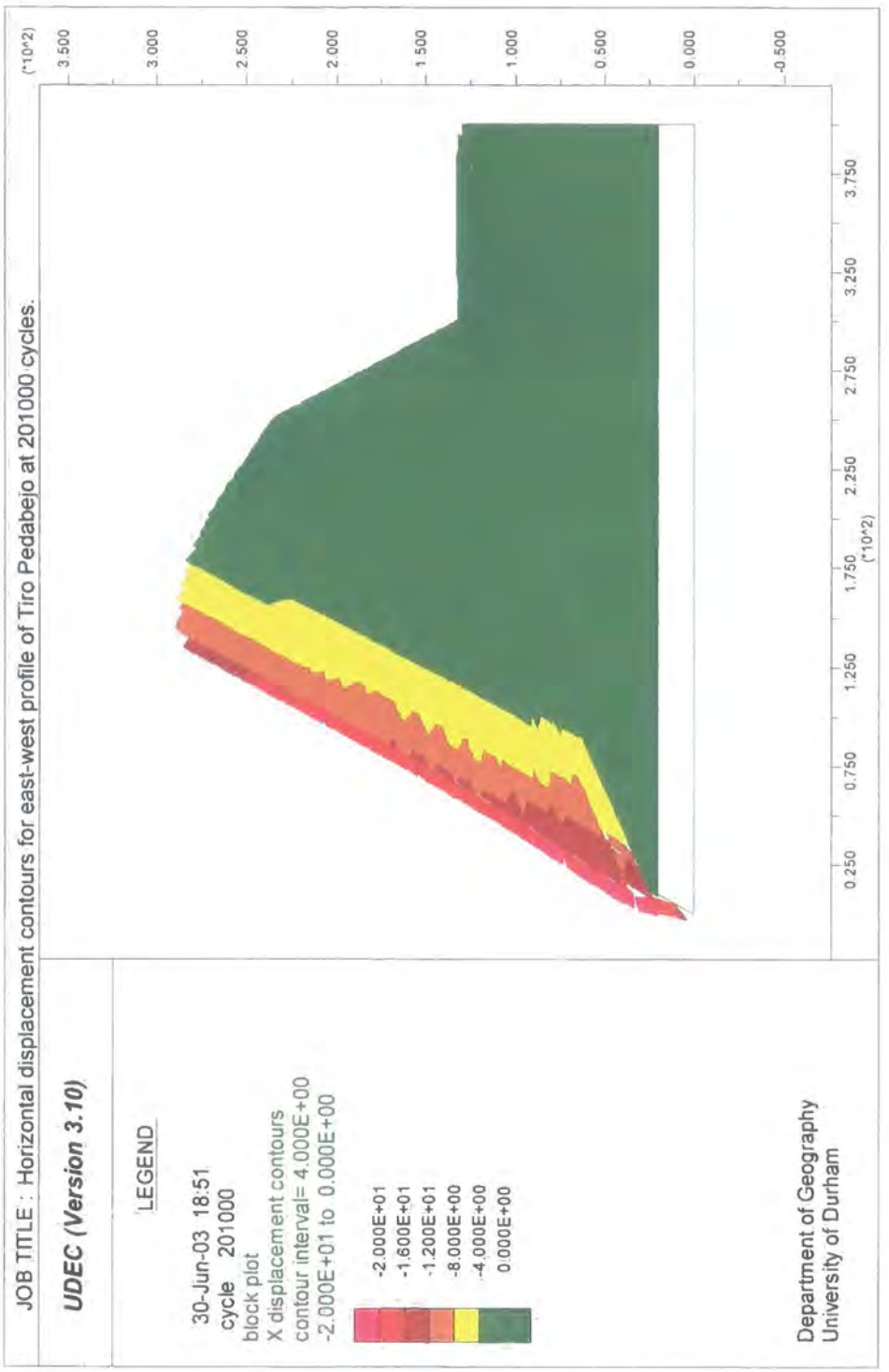

Figure 7.24a: Horizontal displacement contours for the east-west profile of Tiro Pedabejo at 201 000 cycles.

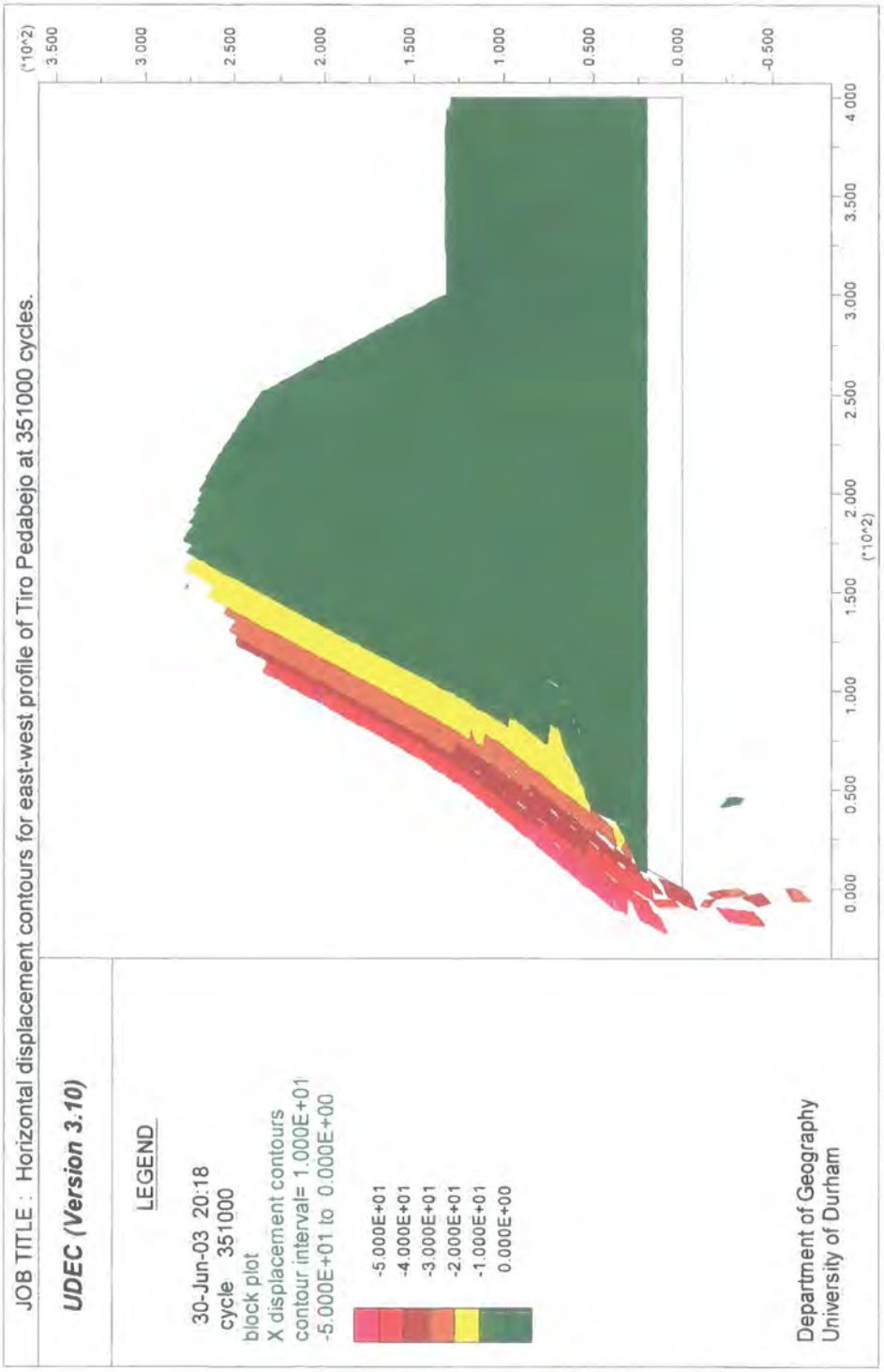

Figure 7.24b: Horizontal displacement contours for the east-west profile of Tiro Pedabejo at 351 000 cycles.

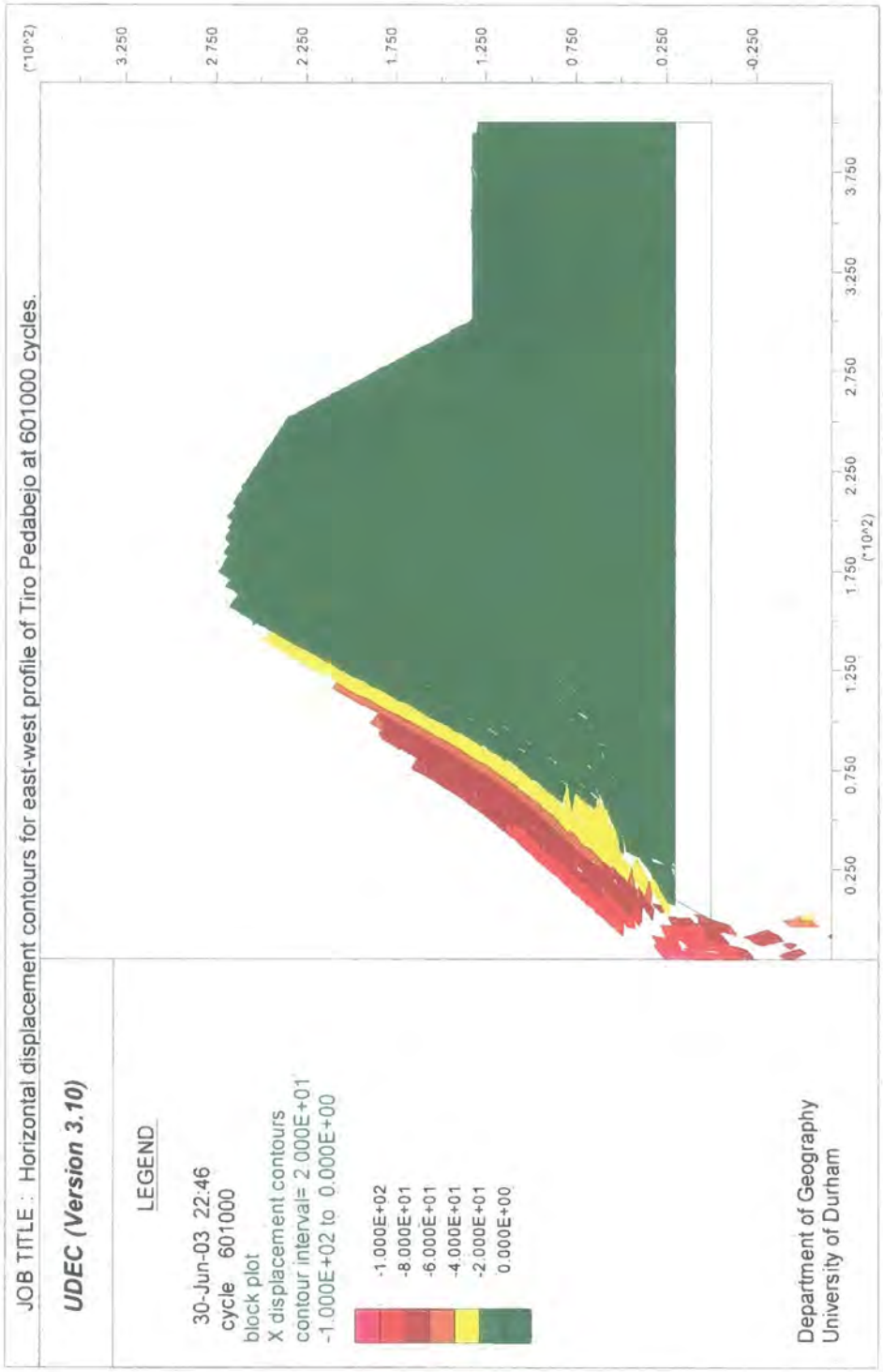

Figure 7.24c: Horizontal displacement contours for the east-west profile of Tiro Pedabejo at 601 000 cycles.

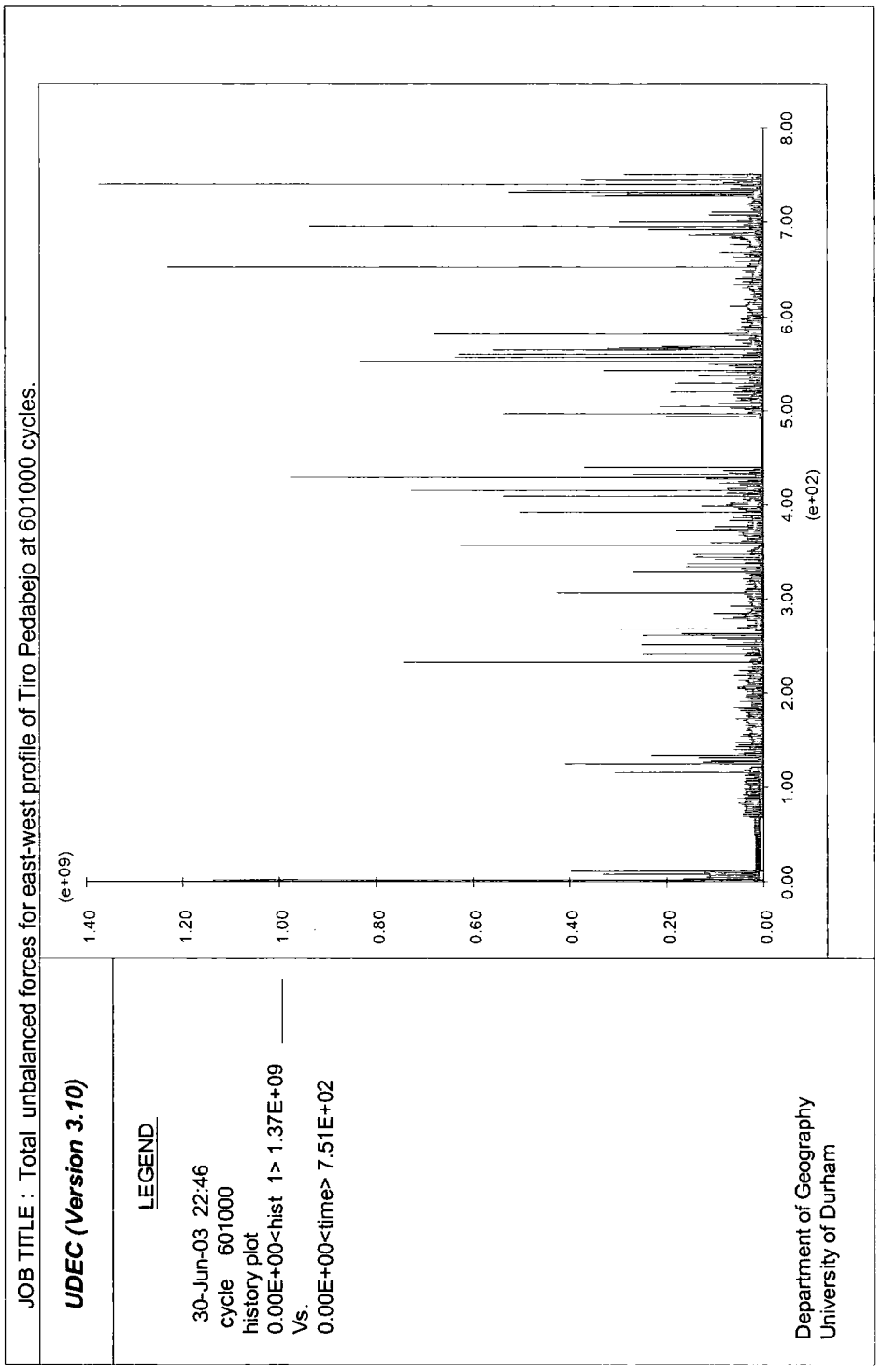

Figure 7.25: Total unbalanced forces for the north-south profile of Tiro Pedabejo at 601 000 cycles.

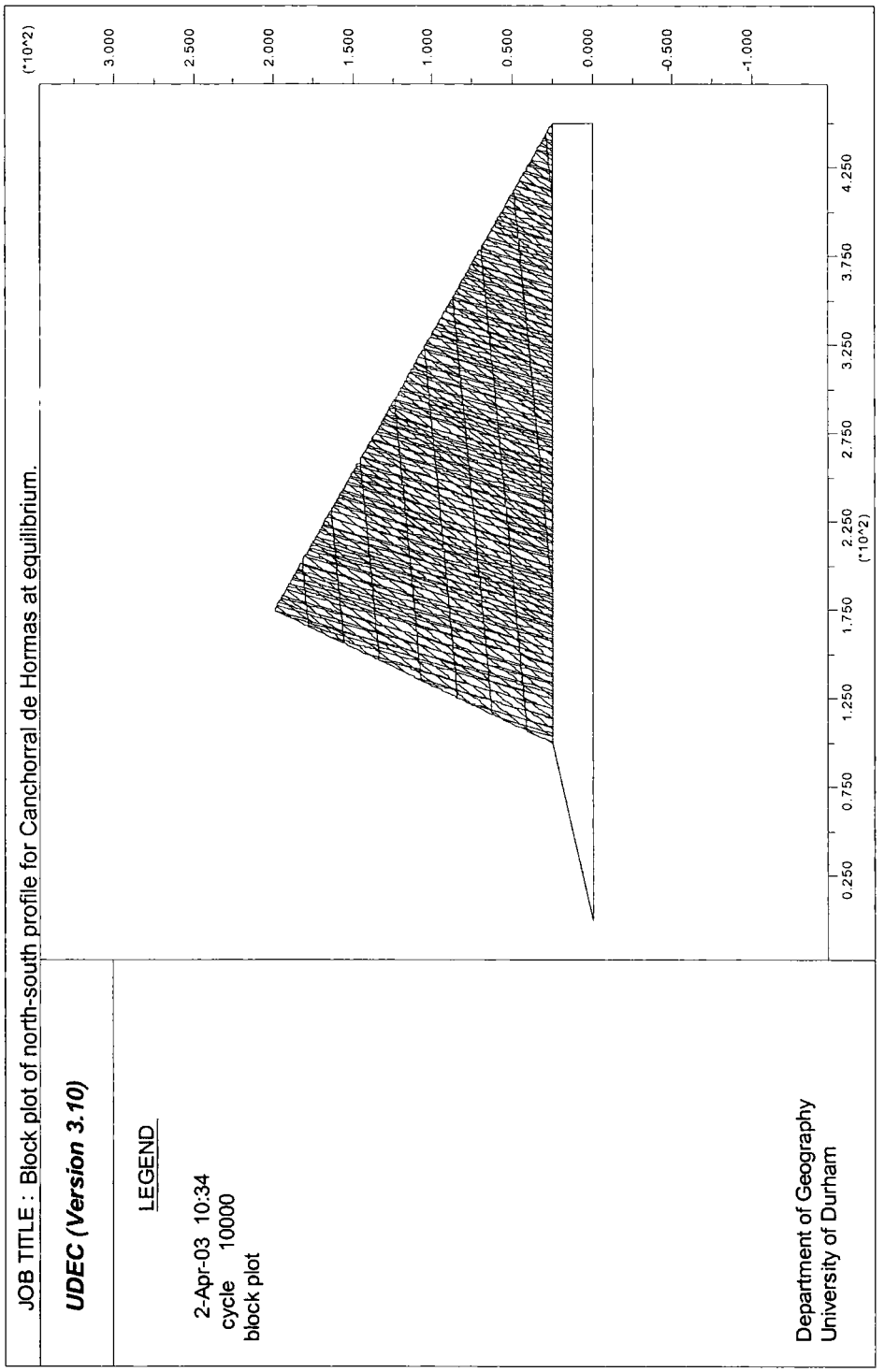

Figure 7.26a: Block plot of the north-south profile of Canchorral de Hormas, Picos de Europa at equilibrium.

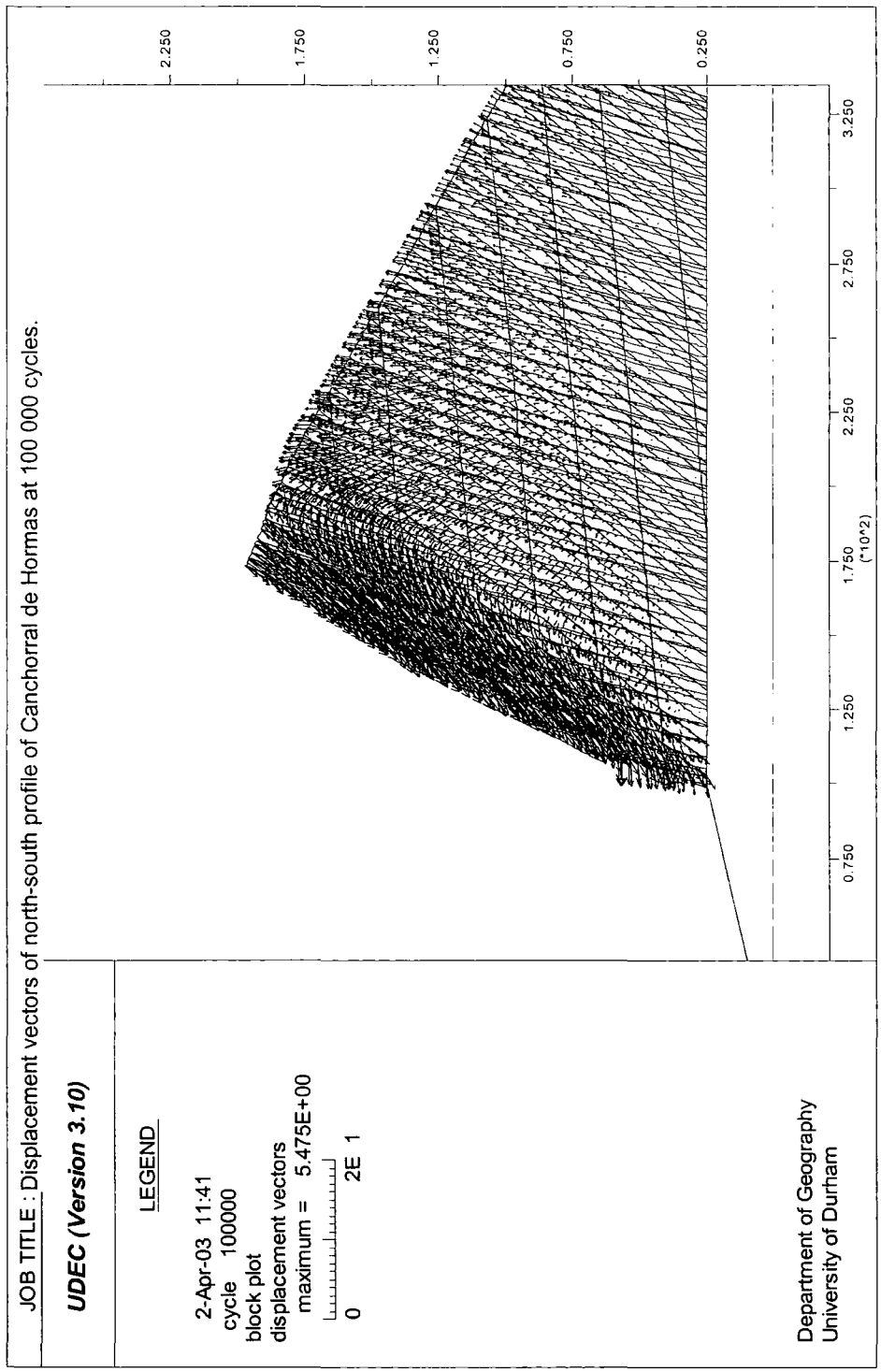

Figure 7.26b: Displacement vectors of the north-south profile of Canchorral de Hormas at 100 000 cycles.

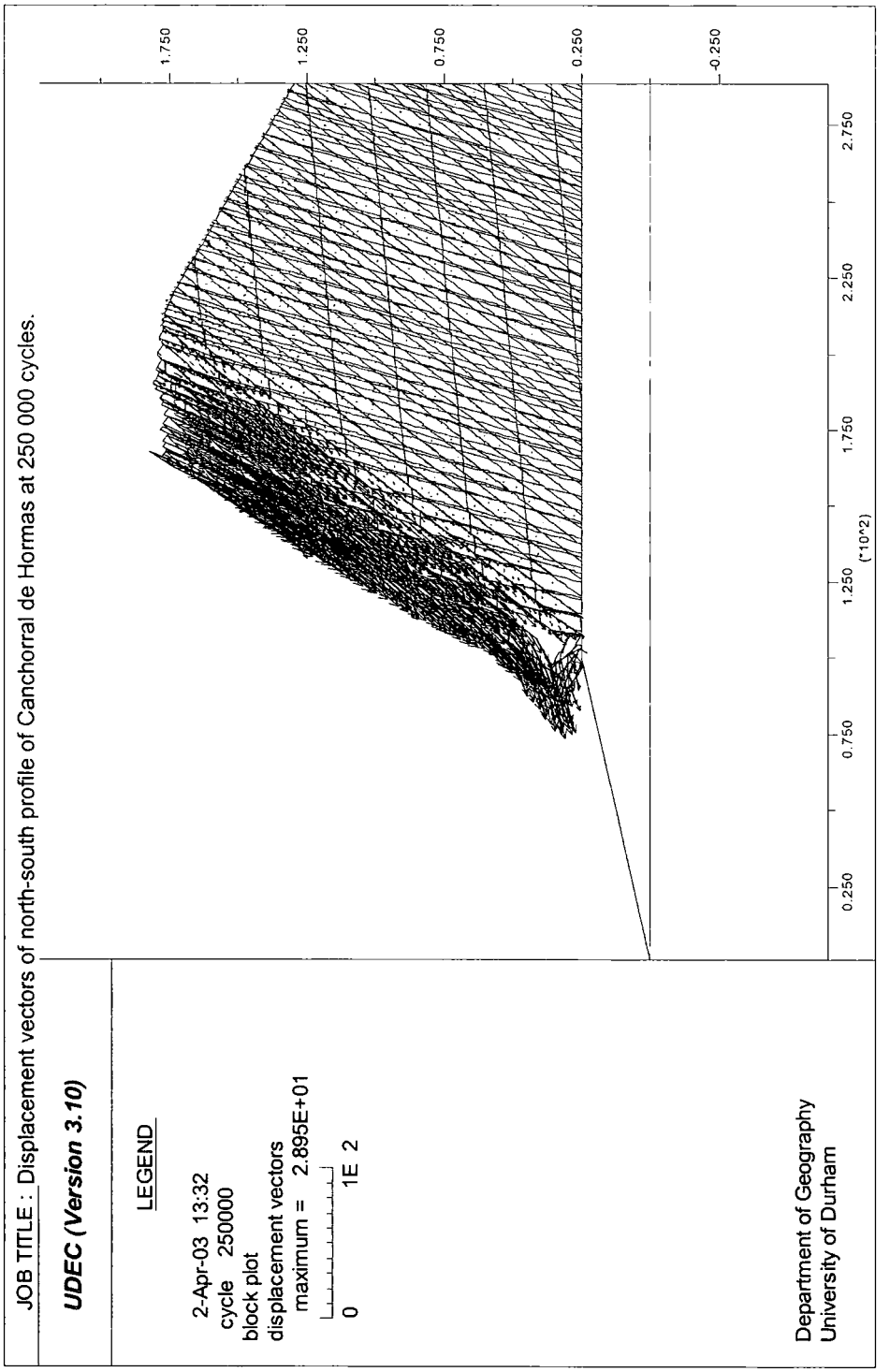

Figure 7.26c: Displacement vectors of the north-south profile of Canchorral de Hormas at 250 000 cycles.

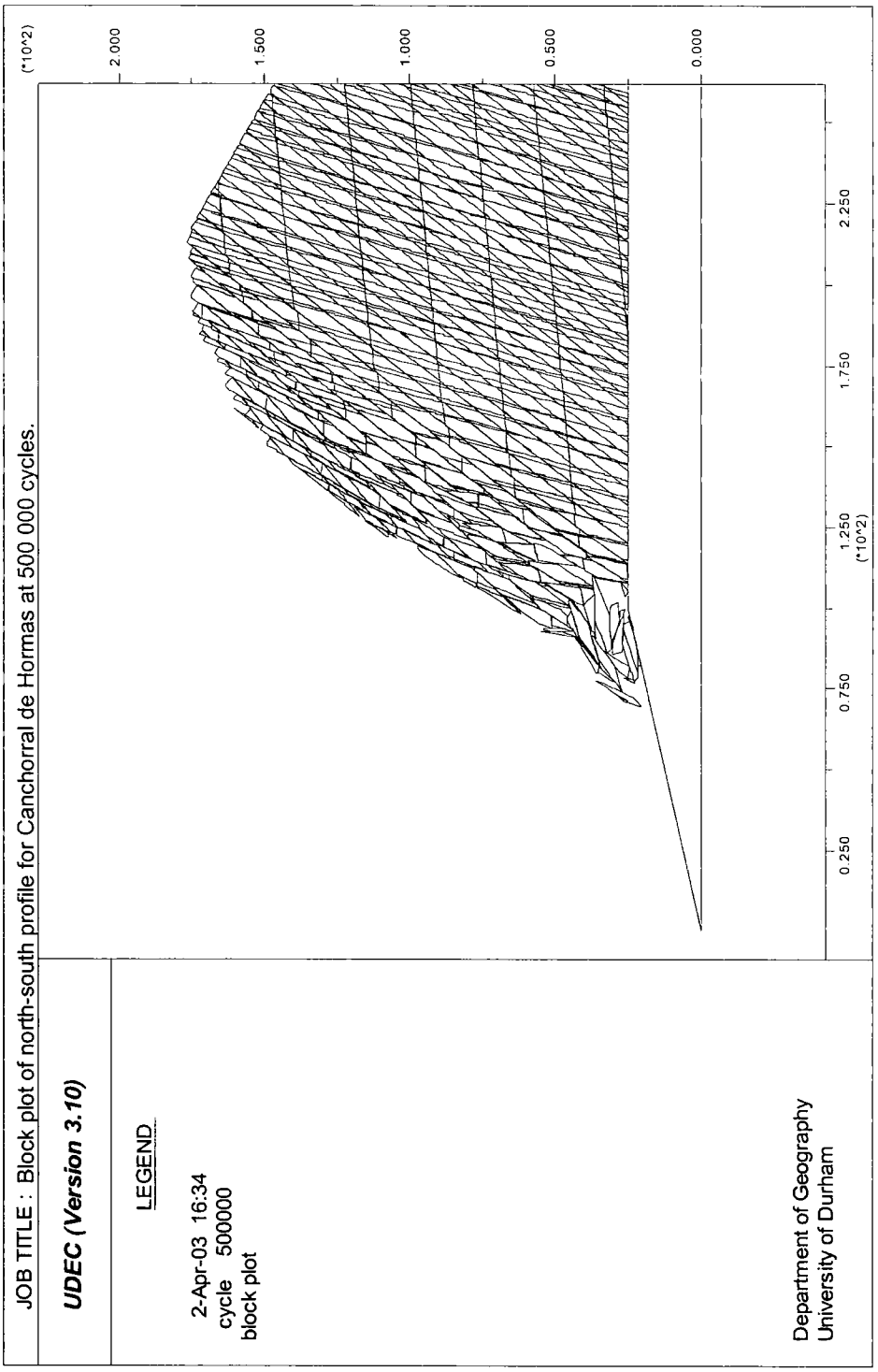

Figure 7.26d: Block plot of the north-south profile of Canchorral de Hormas, Picos de Europa at 500 000 cycles.

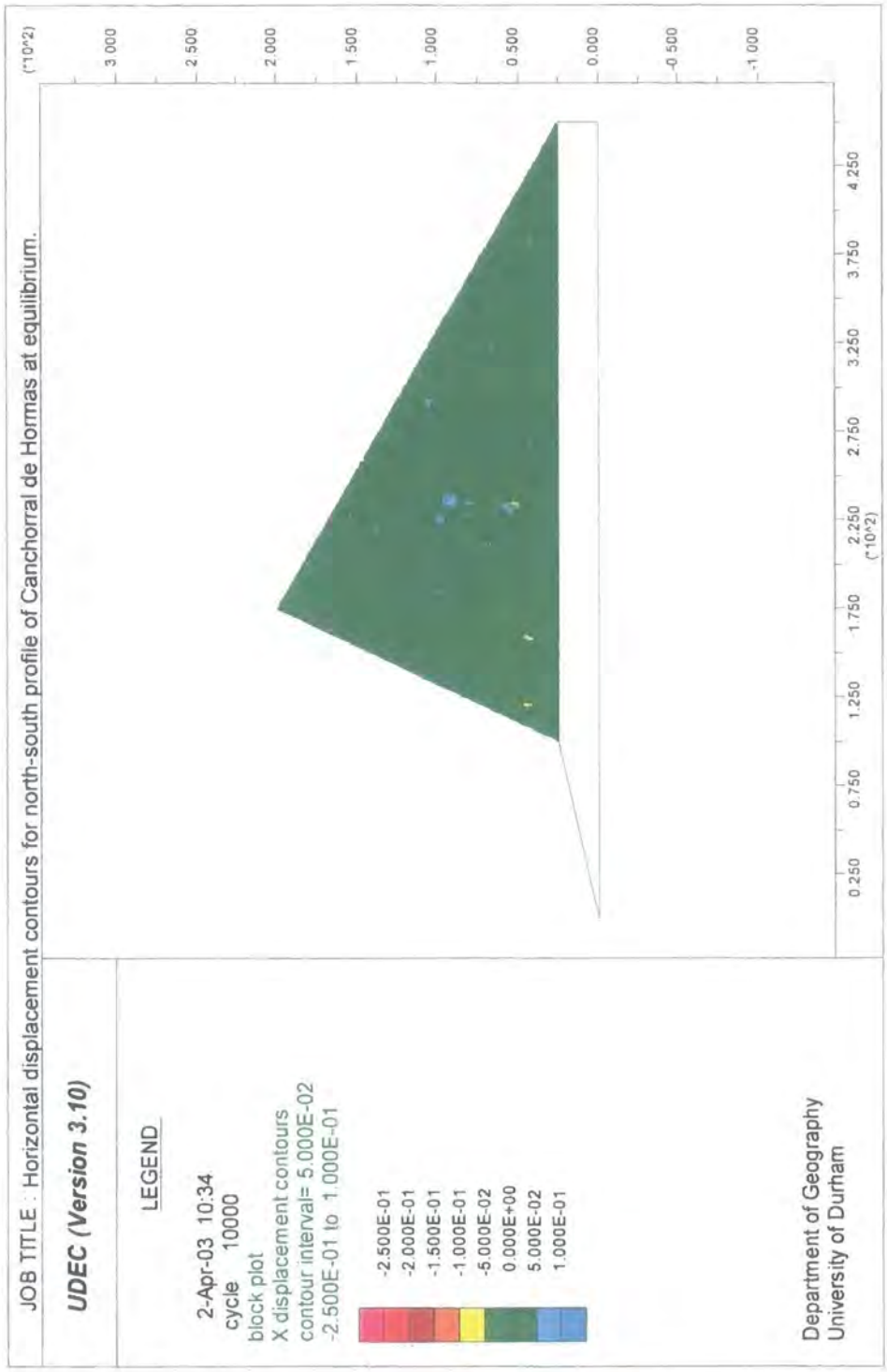

Figure 7.27a: Horizontal displacement contours for the north-south profile of Canchorral de Hormas at equilibrium.

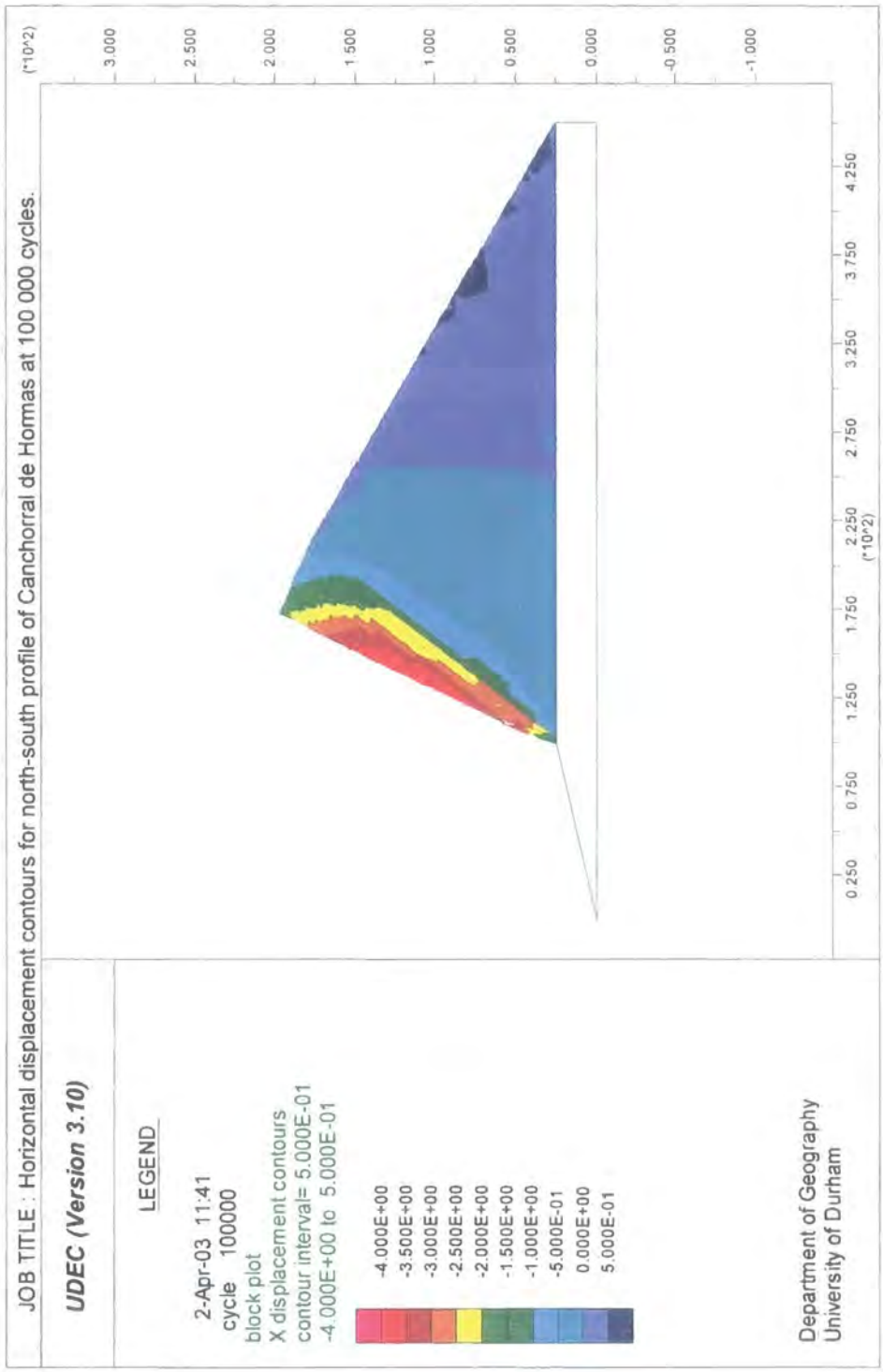

Figure 7.27b: Horizontal displacement contours for the north-south profile of Canchorral de Hormas at 100 000 cycles.

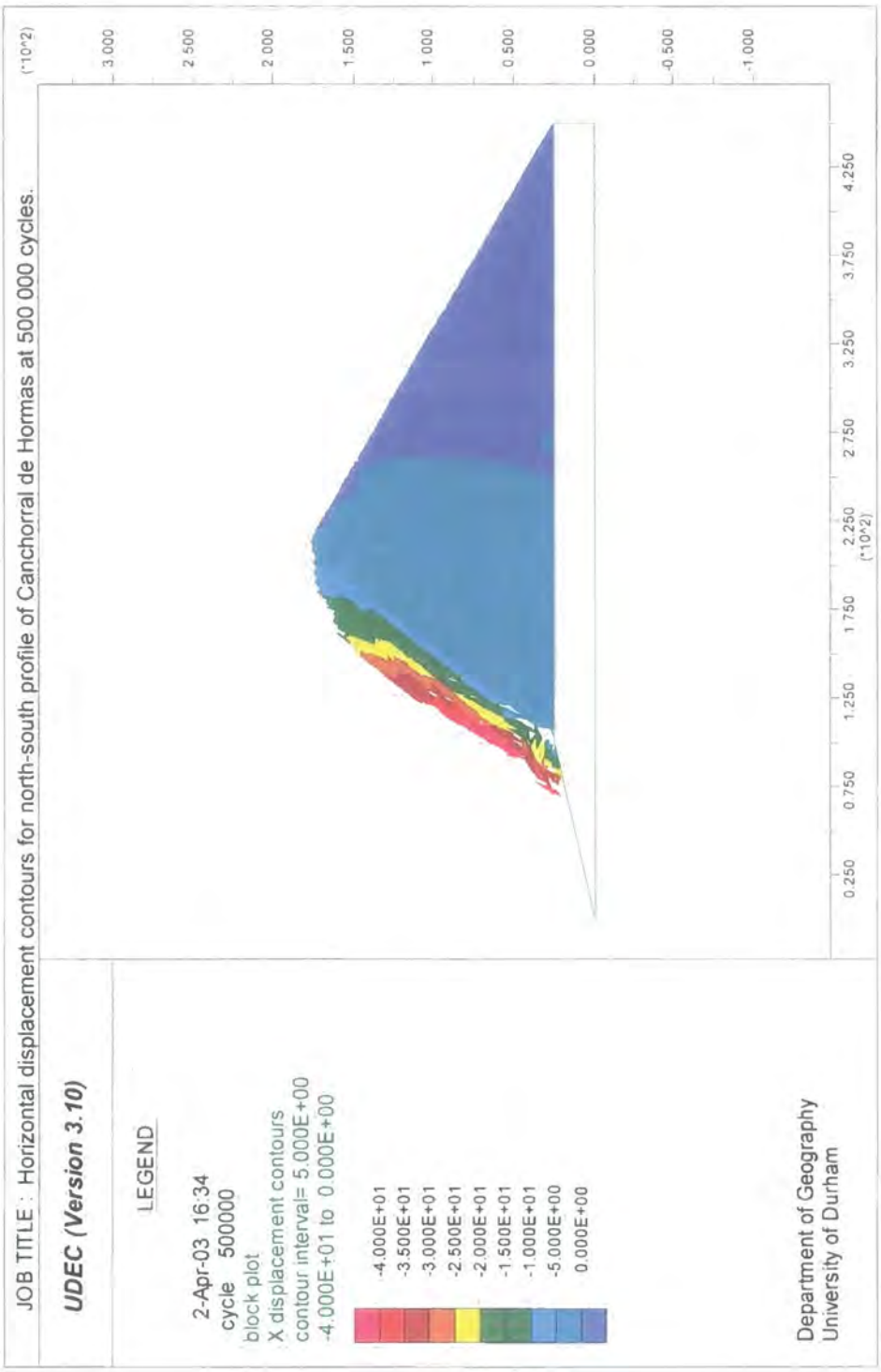

Figure 7.27c: Horizontal displacement contours for the north-south profile of Canchorral de Hormas at 500 000 cycles.

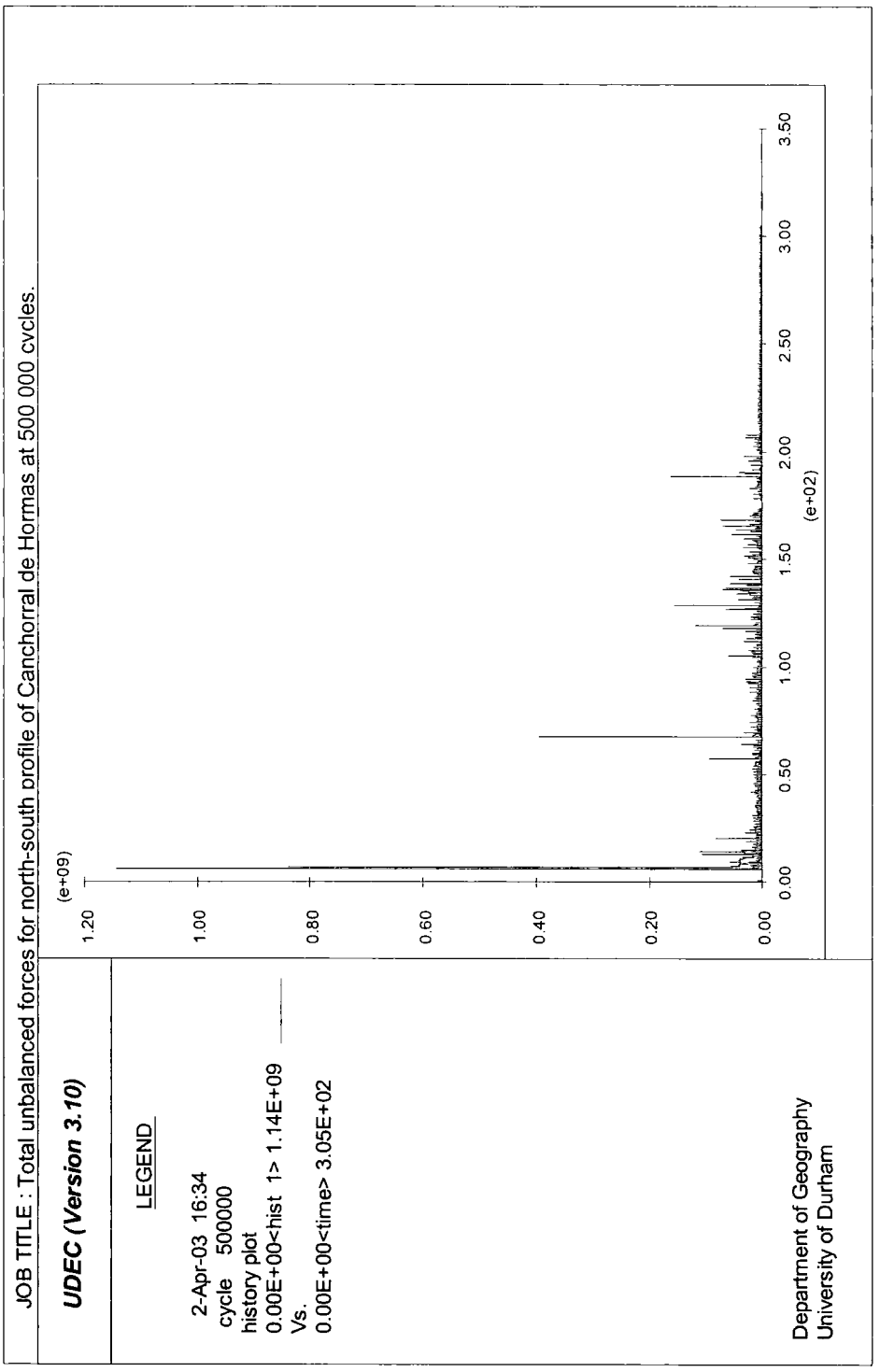

Figure 7.28: Total unbalanced forces for the north-south profile of Canchorral de Hormas, Picos de Europa, at 500 000 cycles.

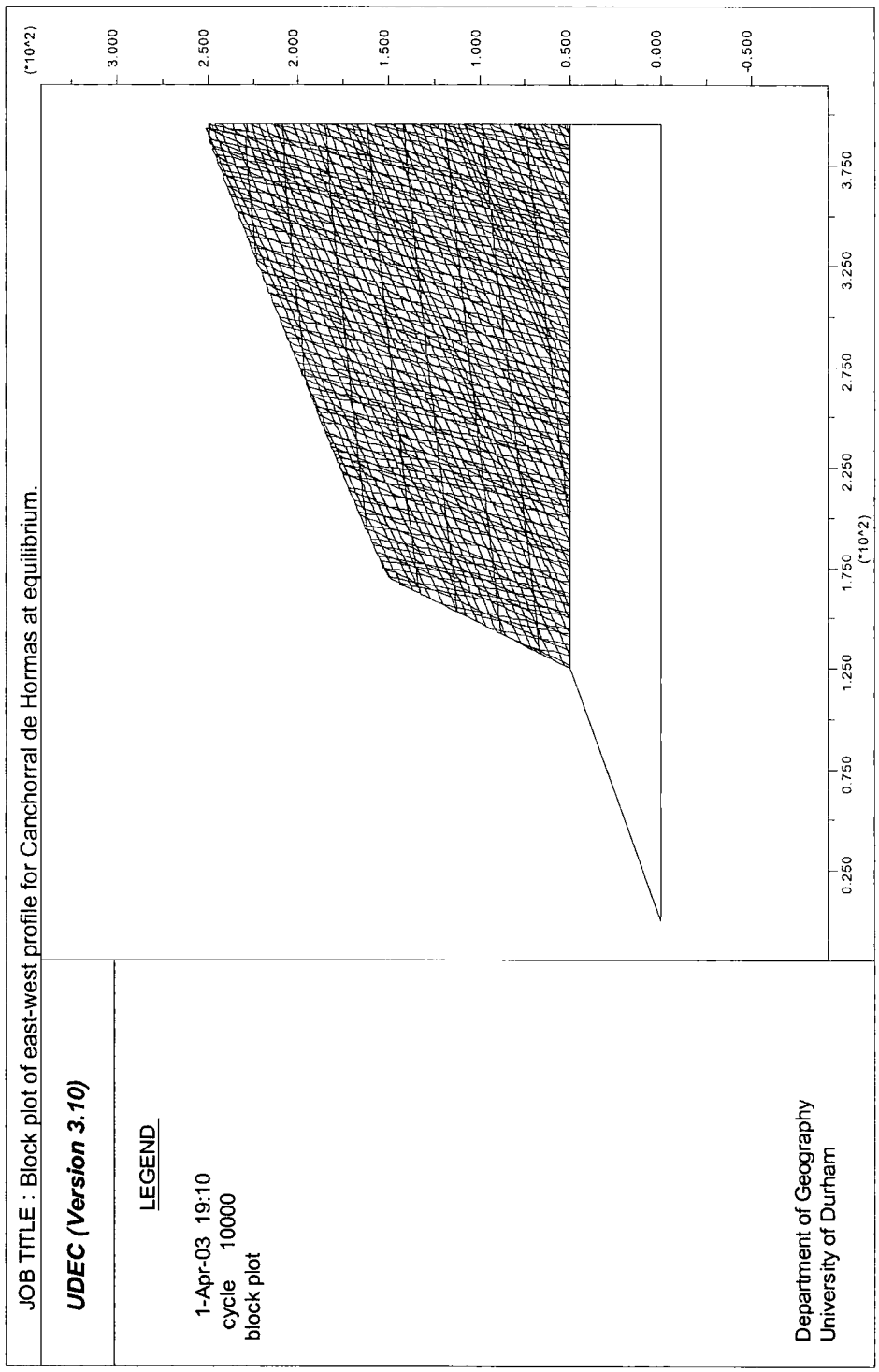

Figure 7.29a: Block plot of the east-west profile of Canchorral de Hormas, Picos de Europa at equilibrium.

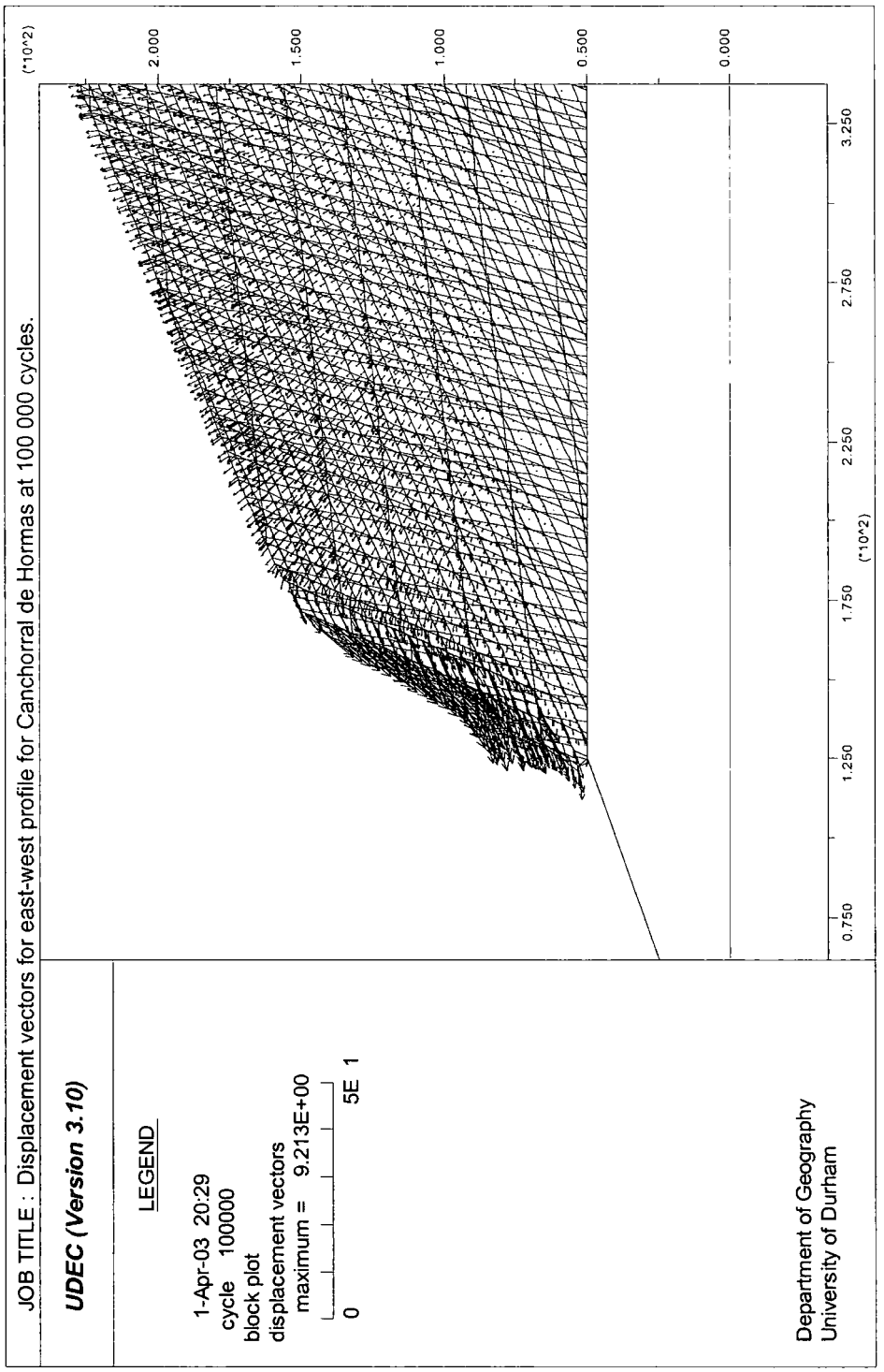

Figure 7.29b: Displacement vectors for the east-west profile of Canchorral de Hormas, Picos de Europa at 100 000 cycles.

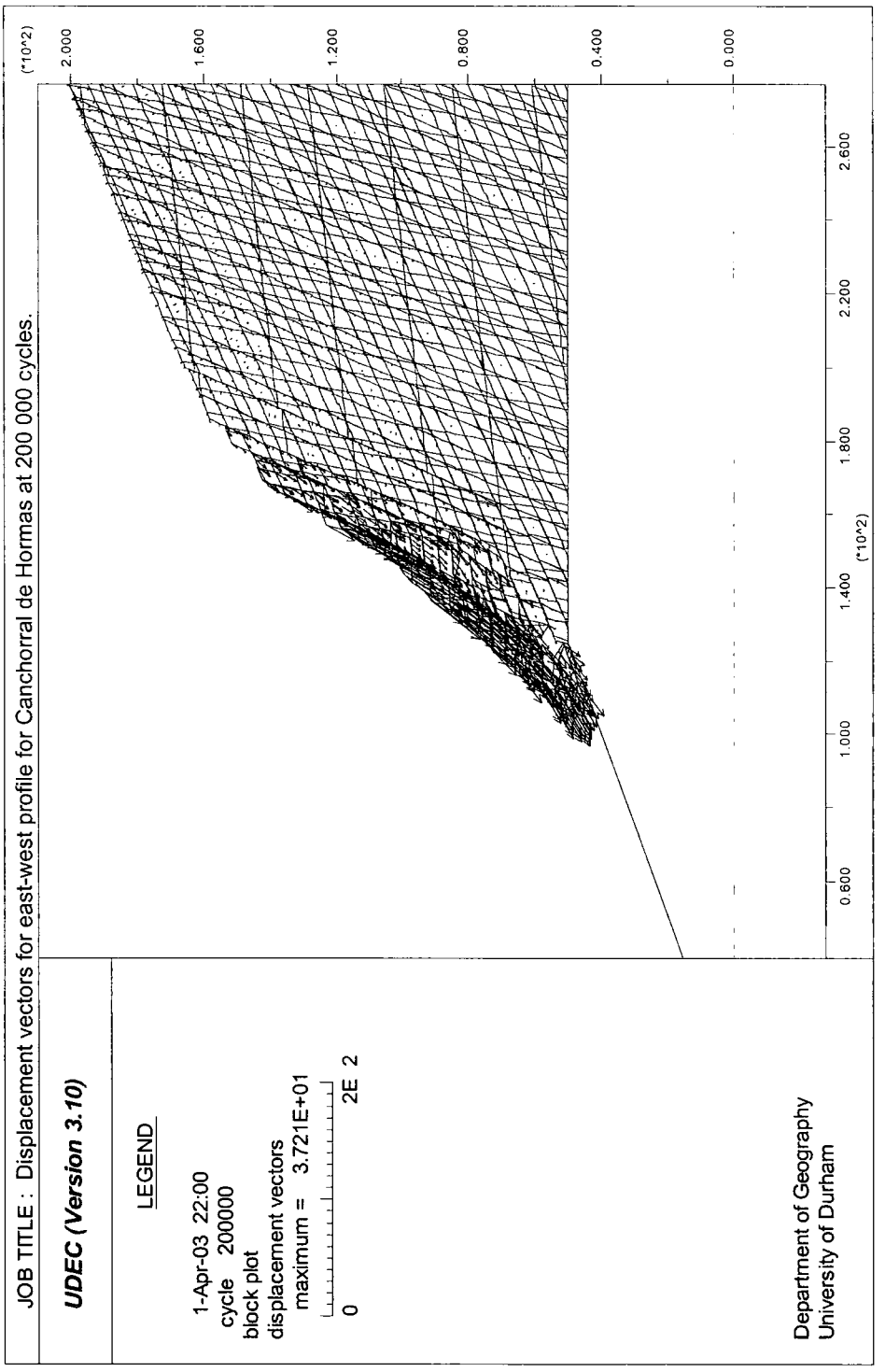

Figure 7.29c: Displacement vectors for the east-west profile of Canchorral de Hormas, Picos de Europa at 200 000 cycles.

Figure 7.29d: Displacement vectors for the east-west profile of Canchorral de Hormas, Picos de Europa at 500 000 cycles.

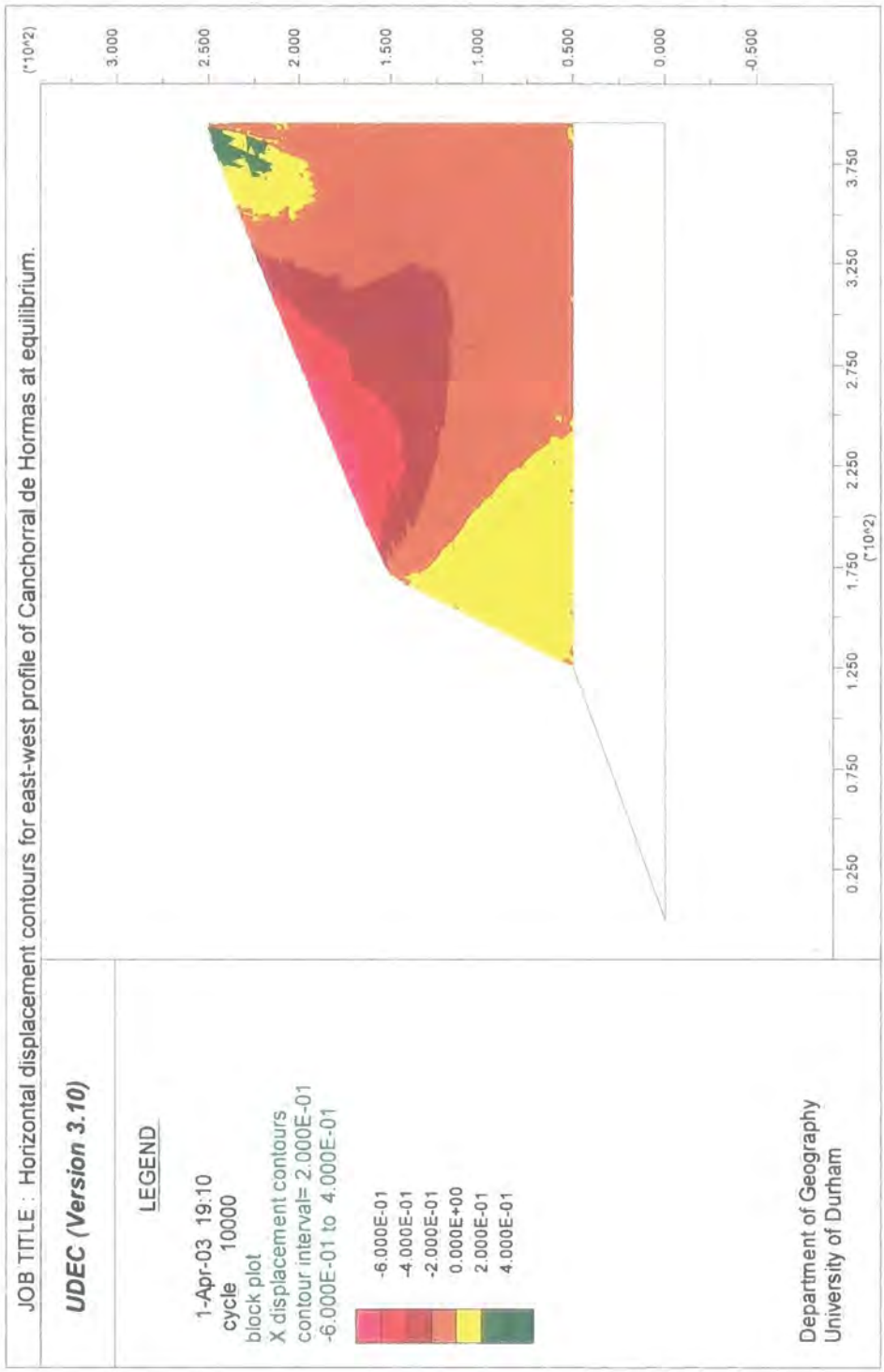

Figure 7.30a: Horizontal displacement contours for the east-west profile of Canchorral de Hormas at equilibrium.

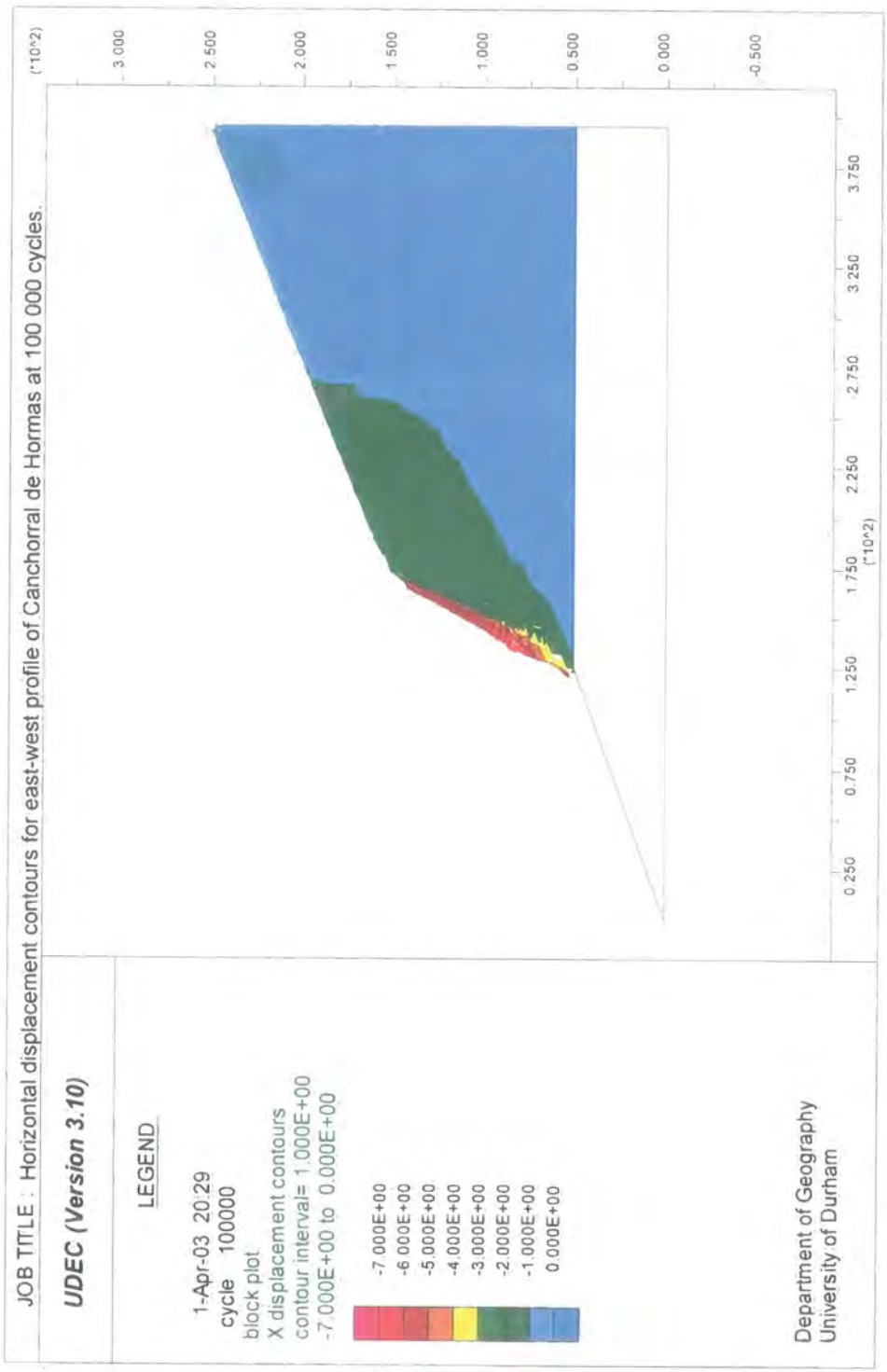

Figure 7.30b: Horizontal displacement contours for the east-west profile of Canchorral de Hormas at 100 000 cycles.

Figure 7.30c: Horizontal displacement contours for the east-west profile of Canchorral de Hormas at 200 000 cycles.

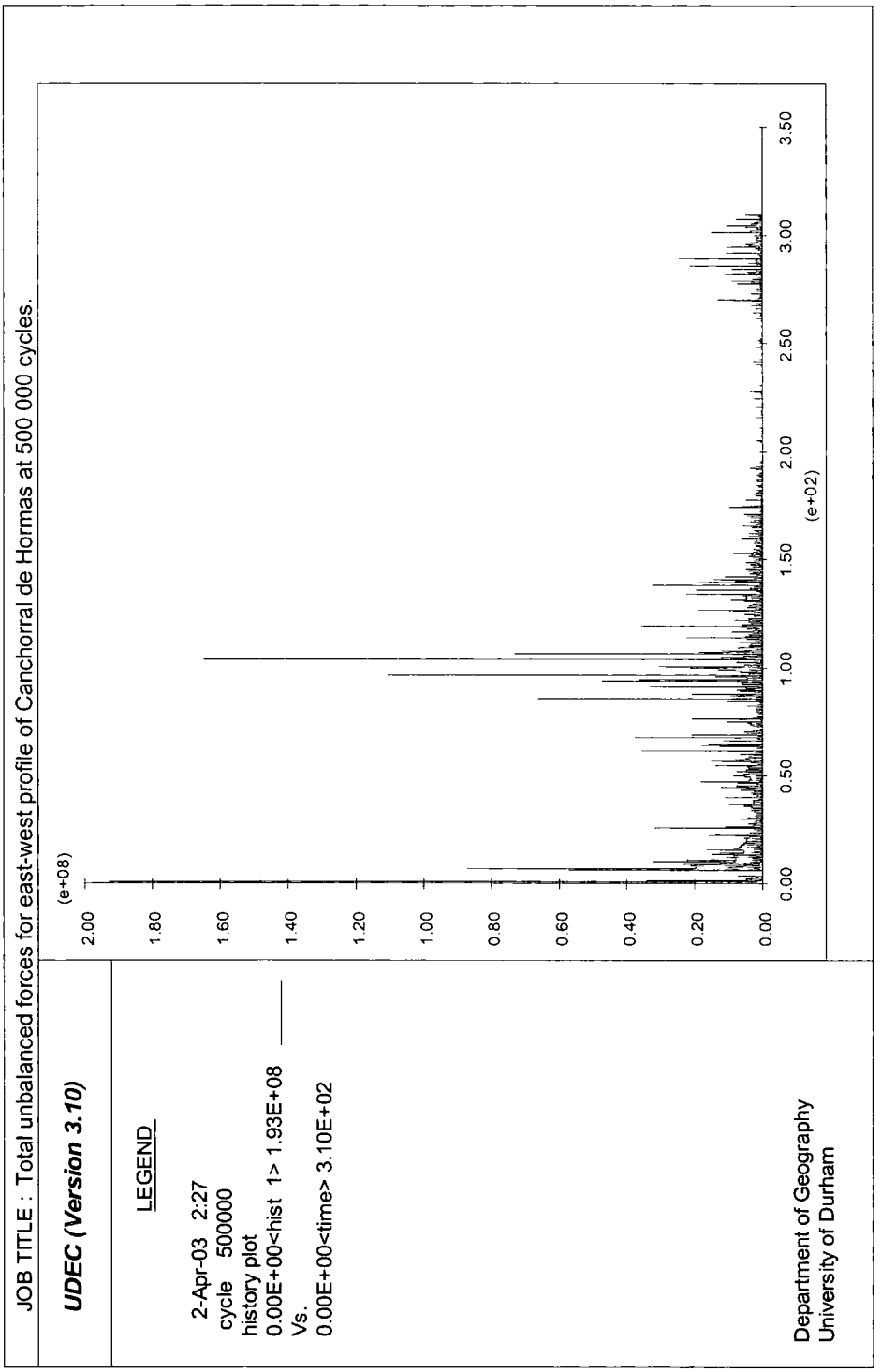

Figure 7.31: Total unbalanced forces for the east-west profile of Canchorral de Hormas at 500 000 cycles.

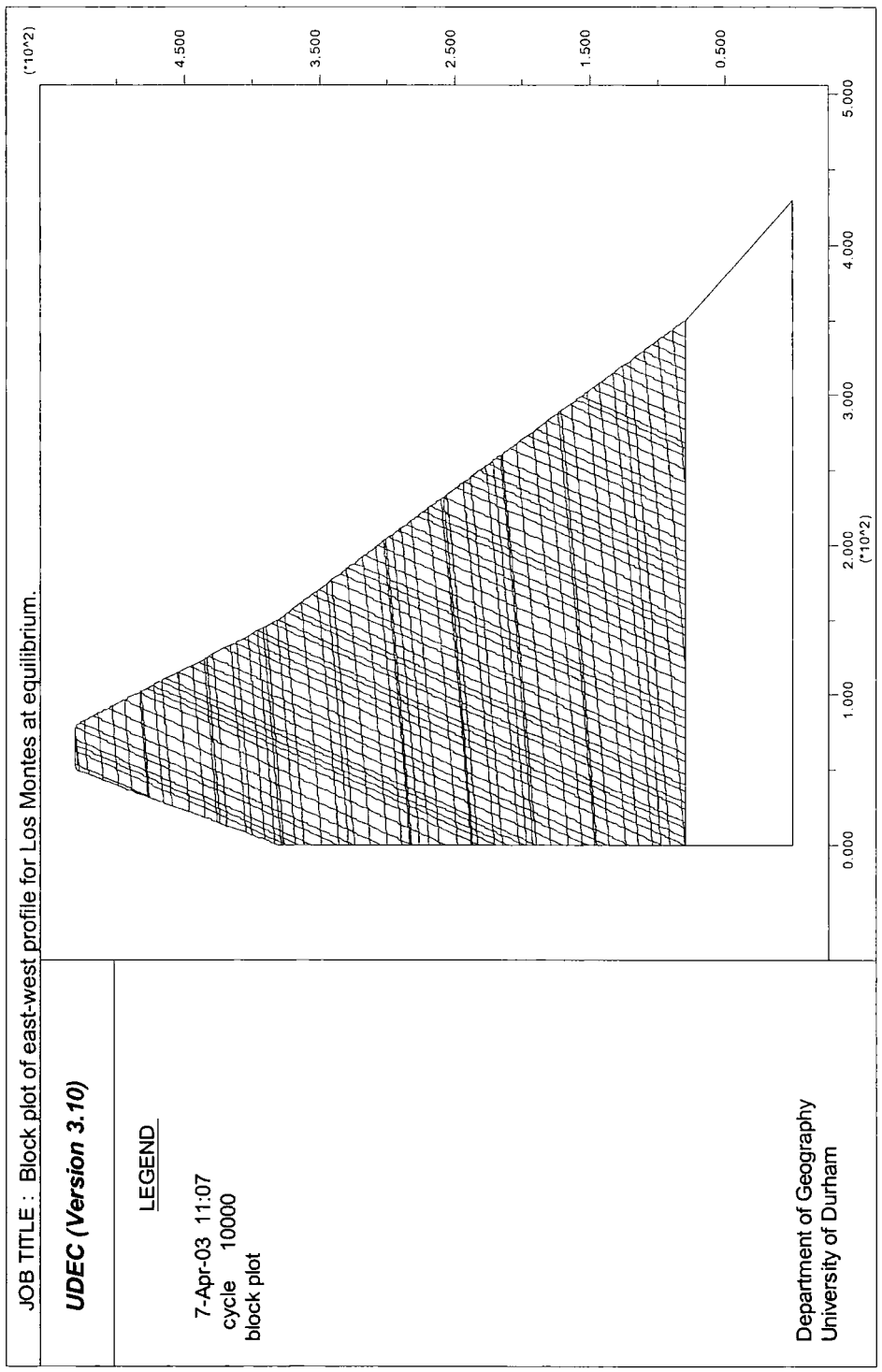

Figure 7.32a: Block plot of the east-west profile of Los Montes, Picos de Europa at equilibrium.

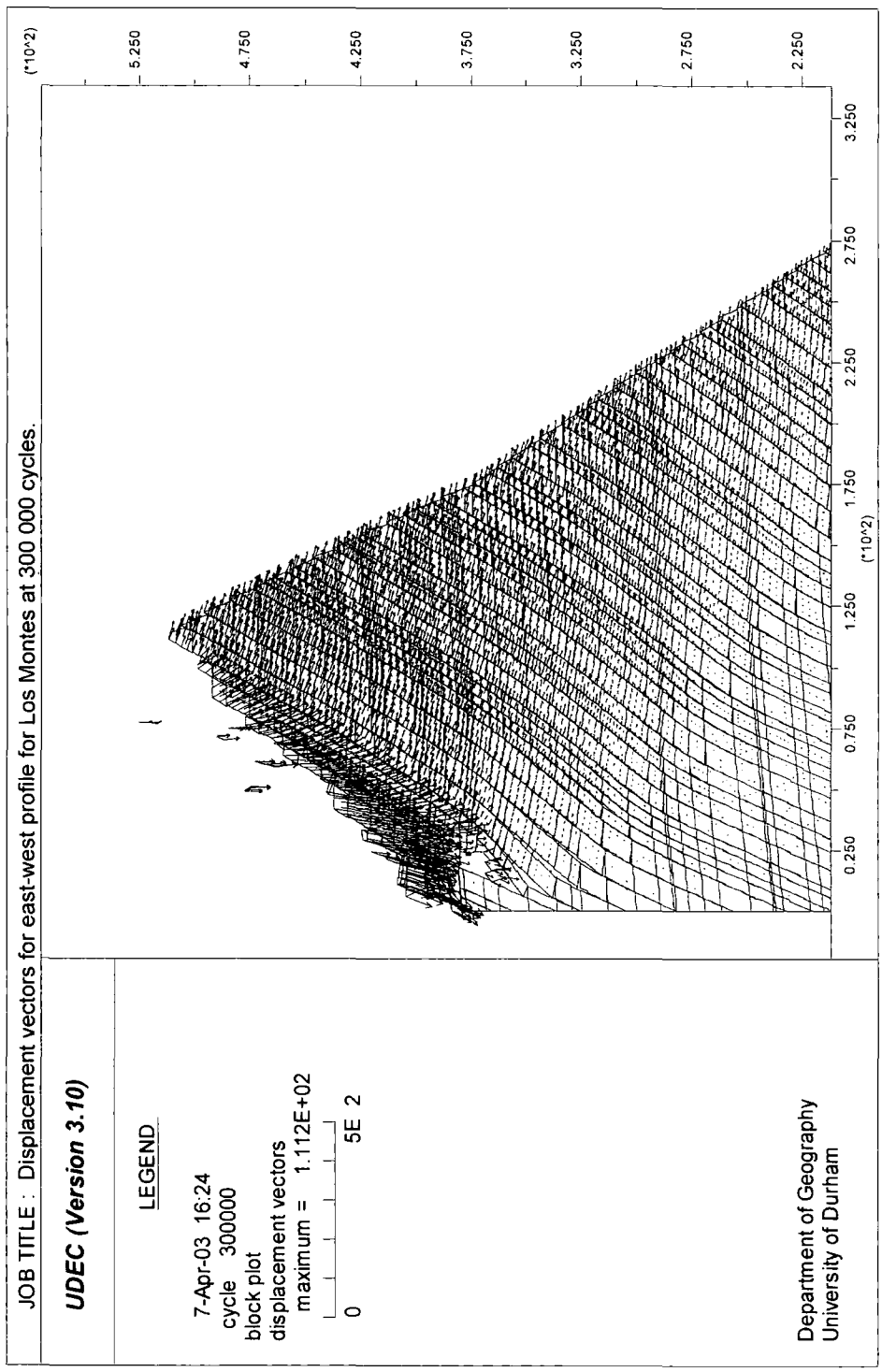

Figure 7.32b: Displacement vector plot for the east-west profile of Los Montes, Picos de Europa at 300 000 cycles.

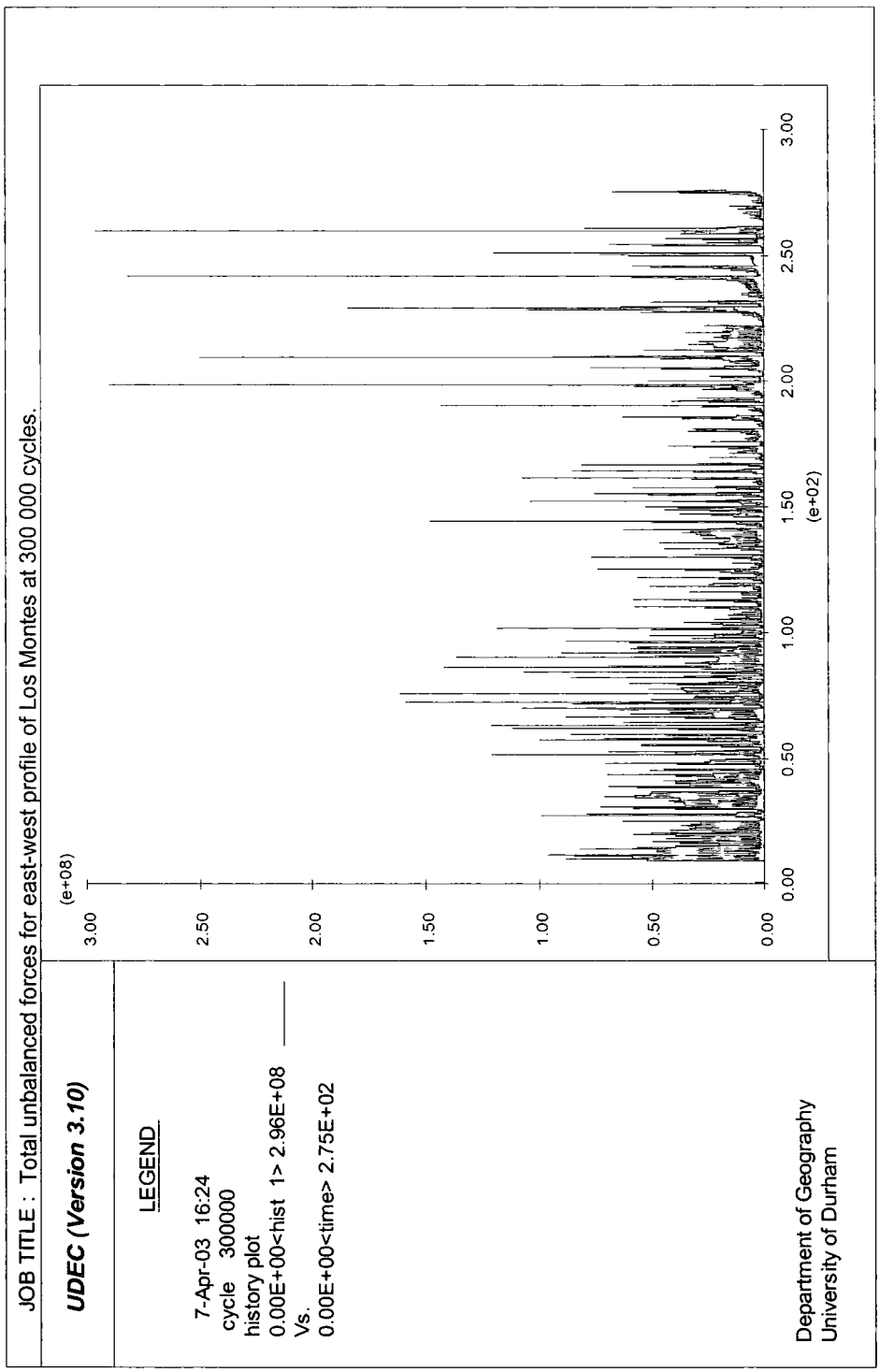

Figure 7.33: Total unbalanced forces for the east-west profile of Los Montes at 300 000 cycles.

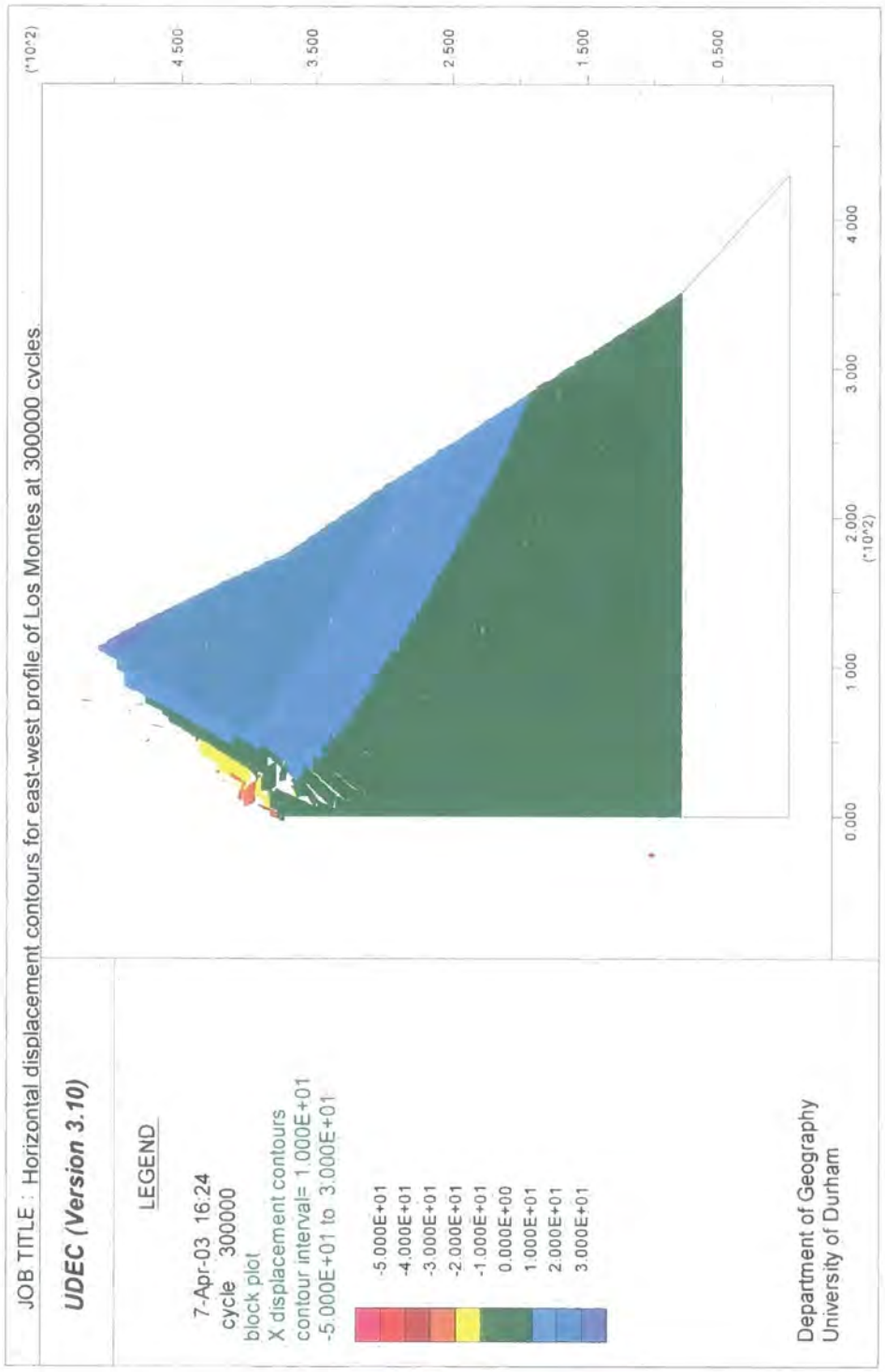

Figure 7.34: Horizontal displacement contours for the east-west profile of Los Montes at 300 000 cycles.

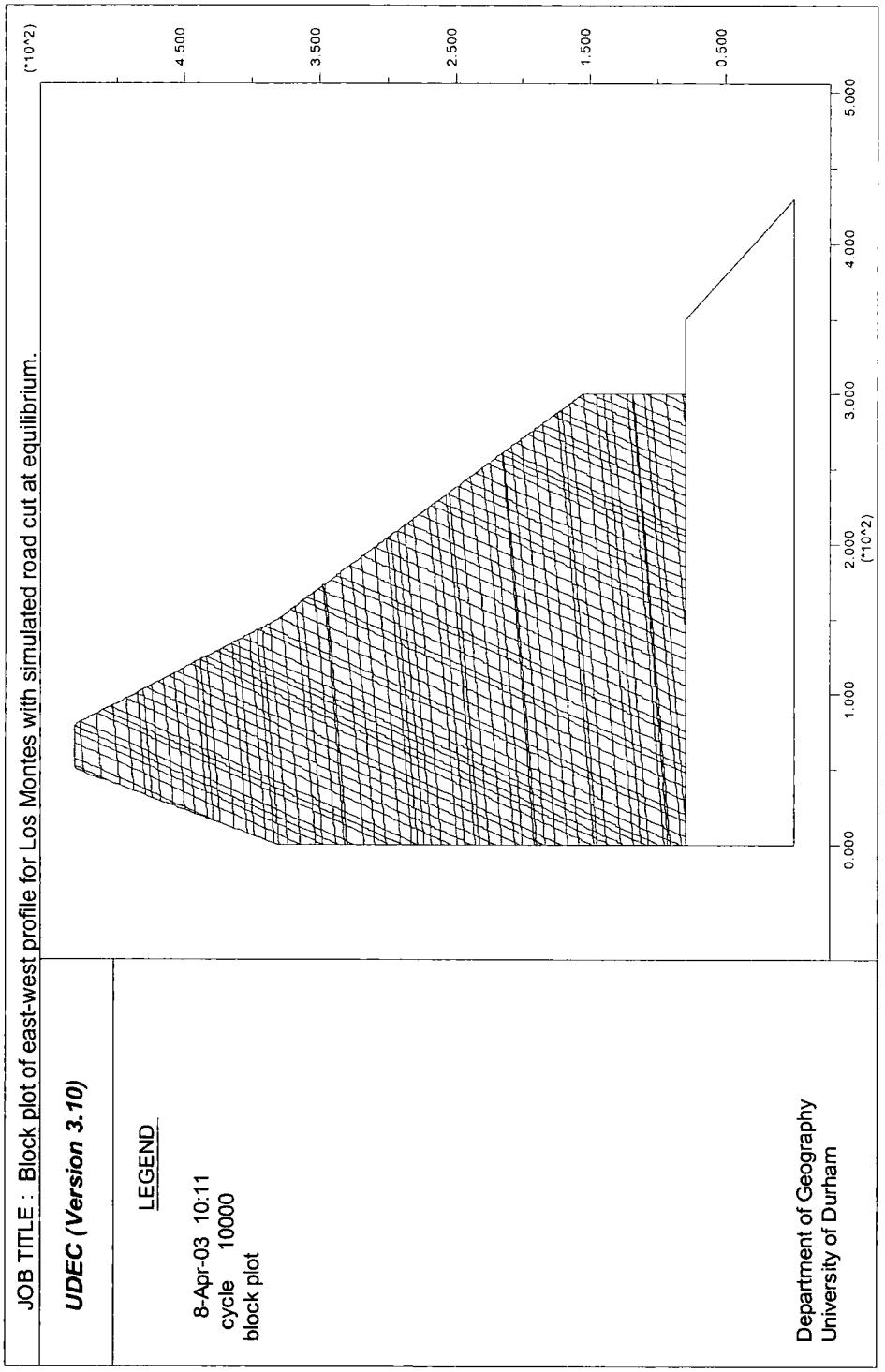

Figure 7.35a: Block plot of the east-west profile of Los Montes, Picos de Europa with a simulated road cut at equilibrium.

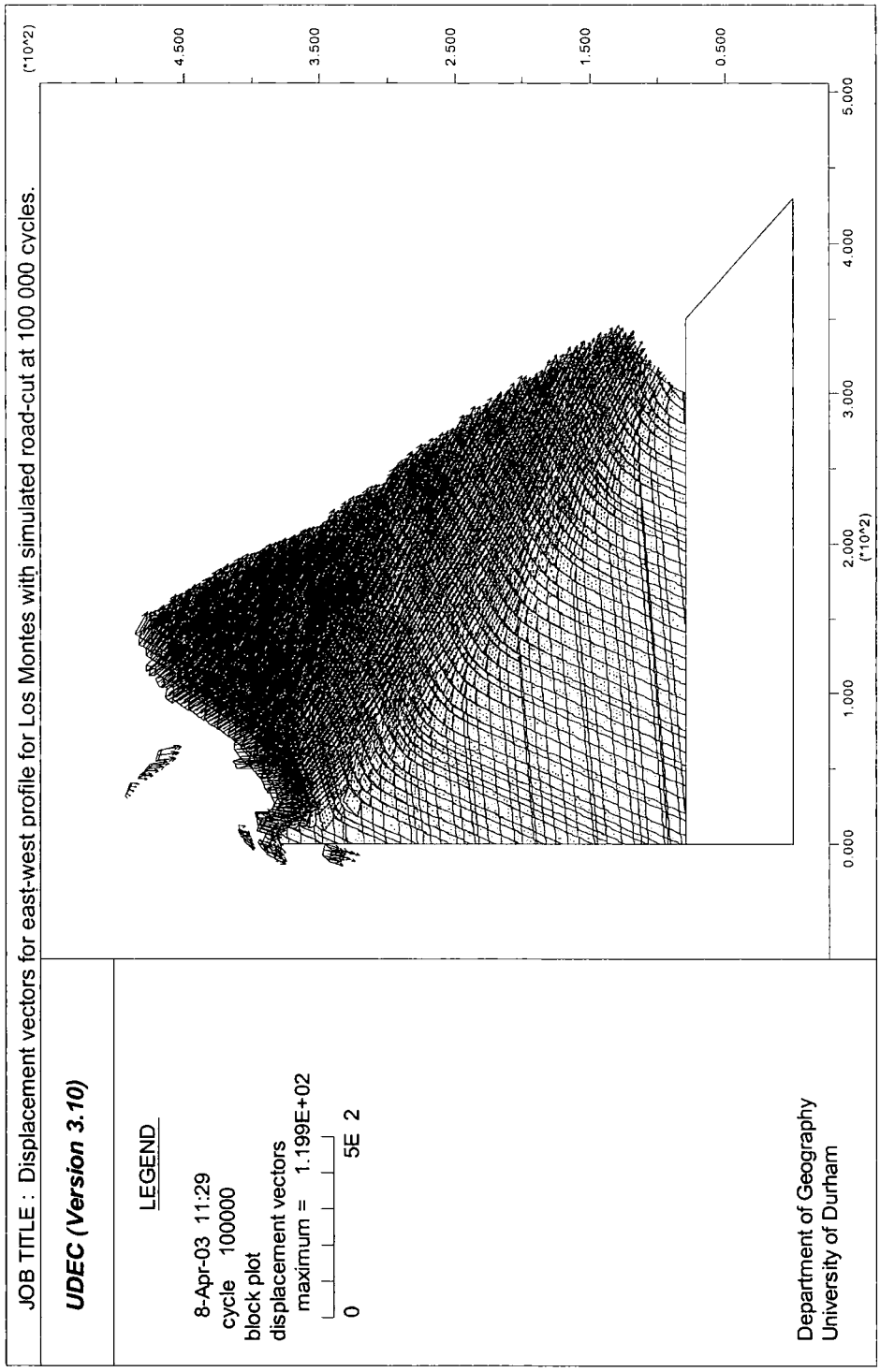

Figure 7.35b: Displacement vectors for the east-west profile of Los Montes, Picos de Europa at 100 000 cycles.

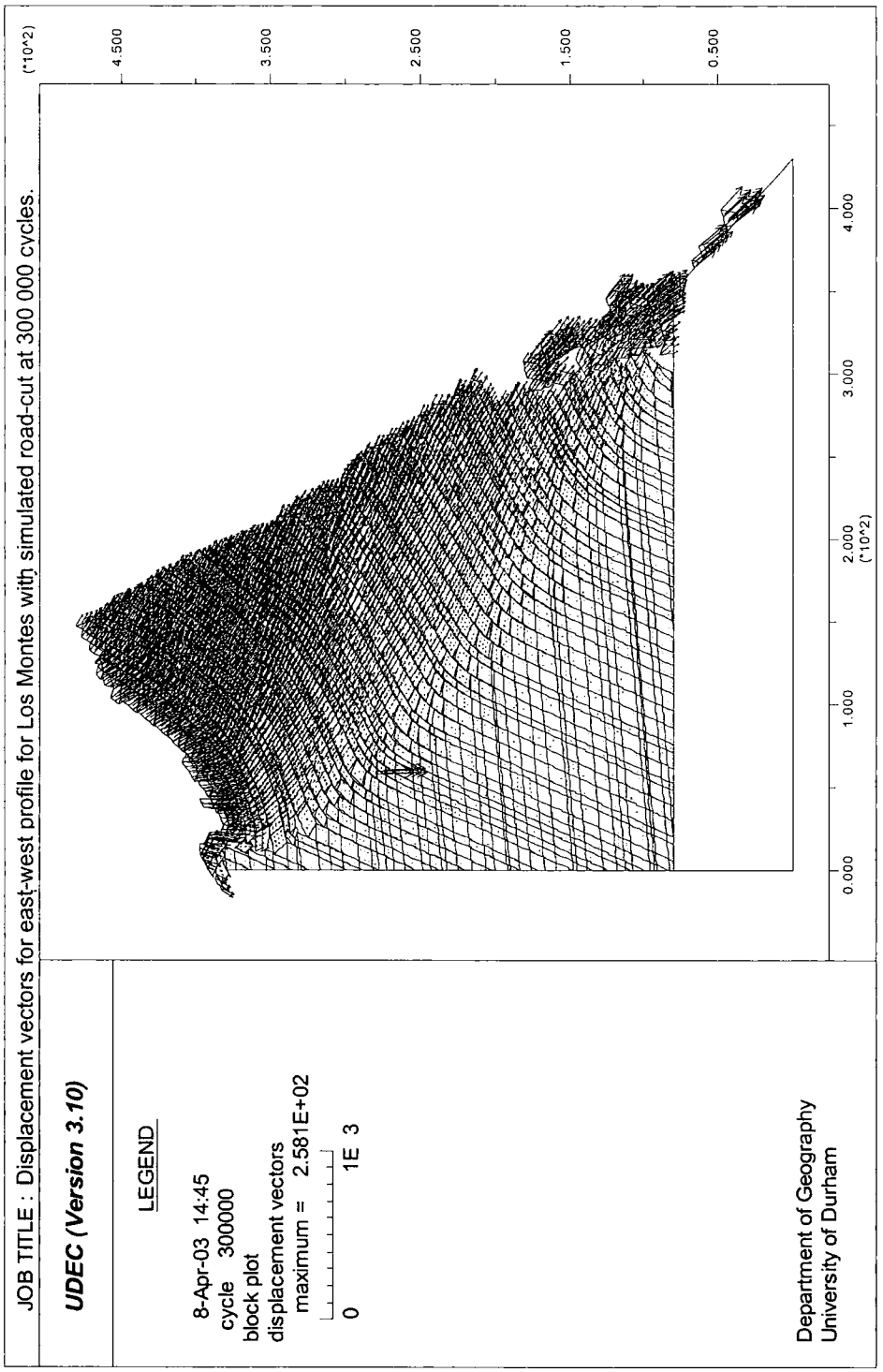

Figure 7.35c: Displacement vectors for the east-west profile of Los Montes, Picos de Europa at 300 000 cycles.

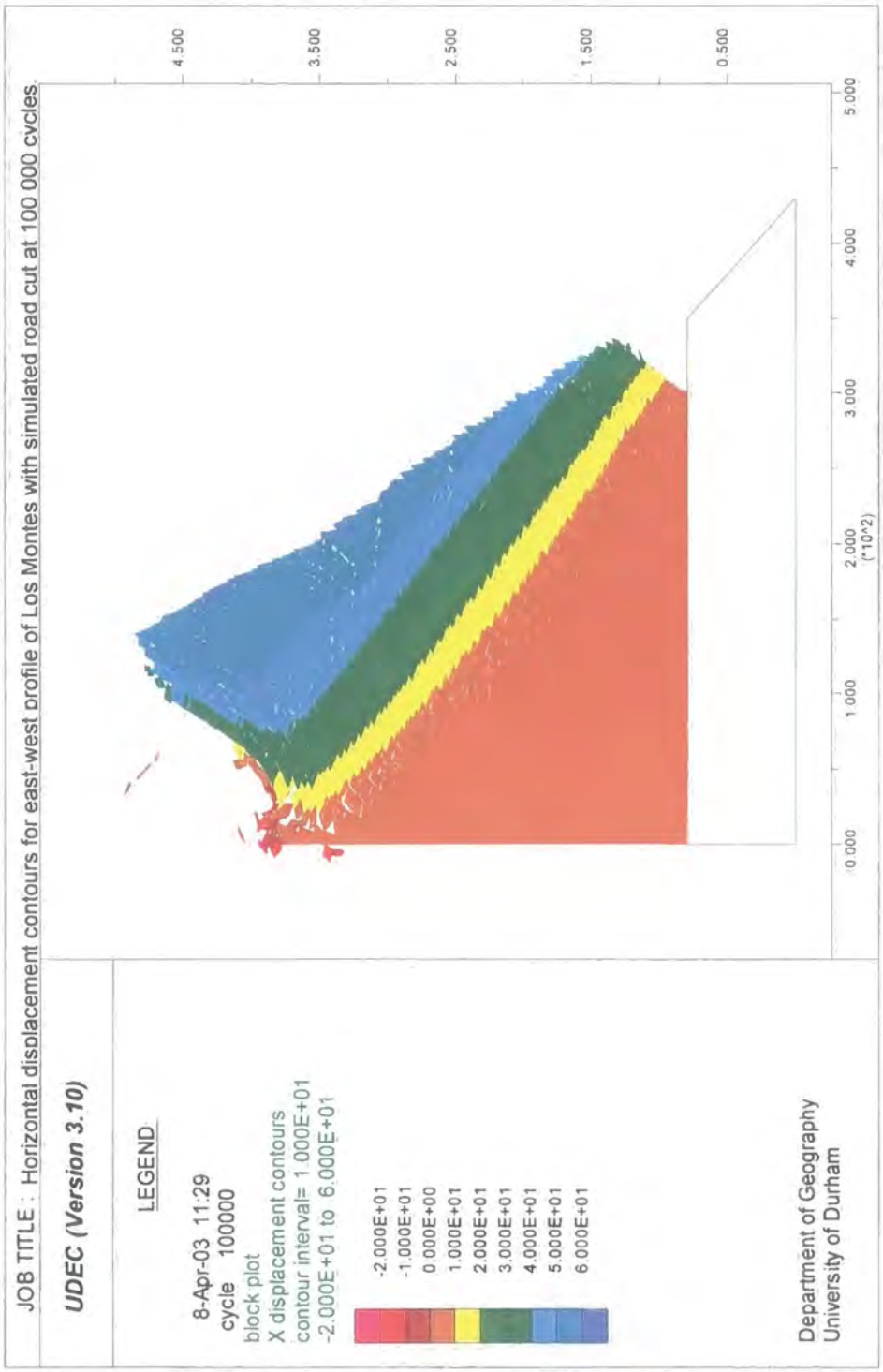

Figure 7.36a: Horizontal displacement contours for the east-west profile of Los Montes with simulated road cut at 100 000 cycles.

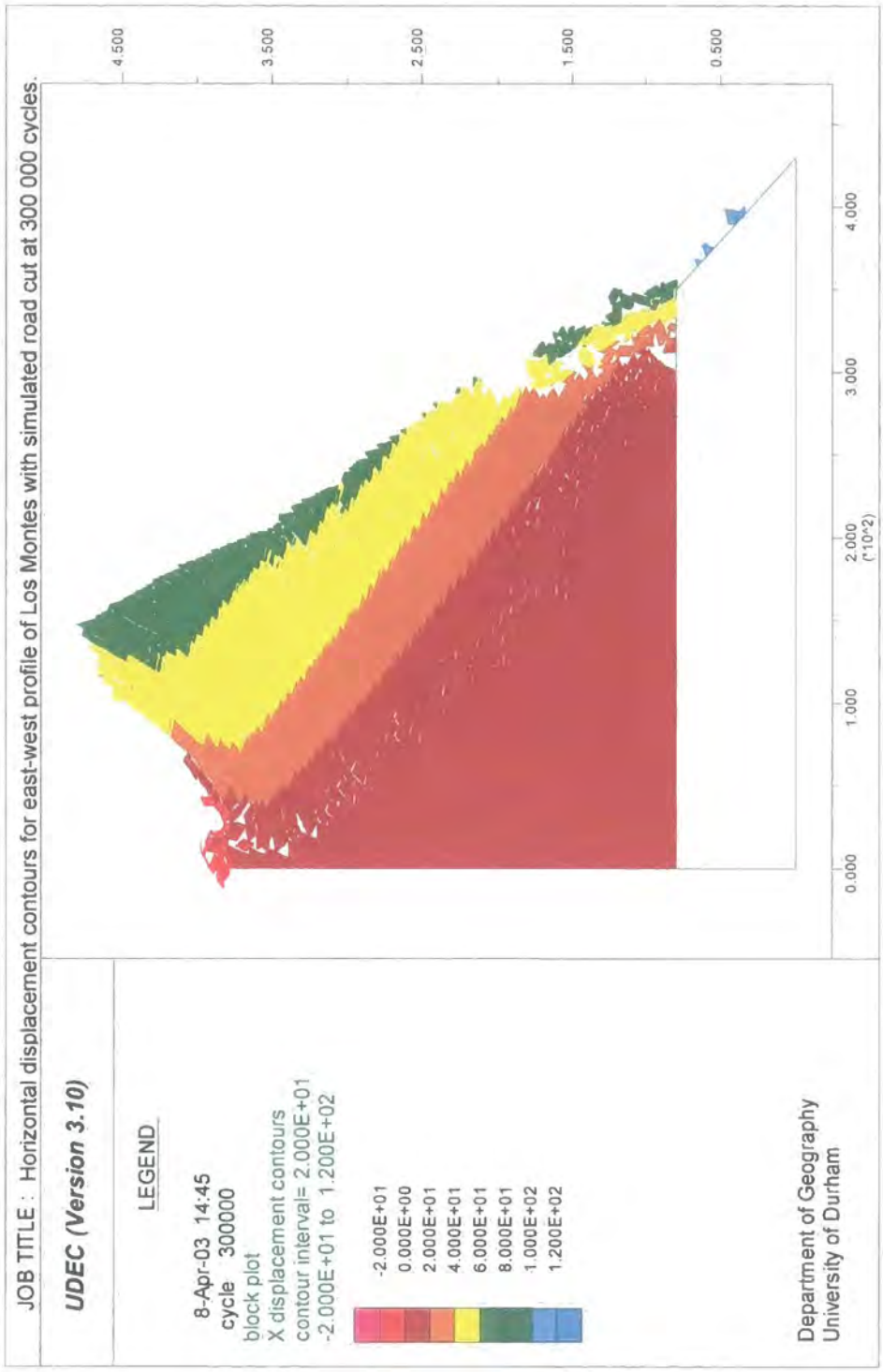

Figure 7.36b: Horizontal displacement contours for the east-west profile of Los Montes with simulated road cut at 300 000 cycles.

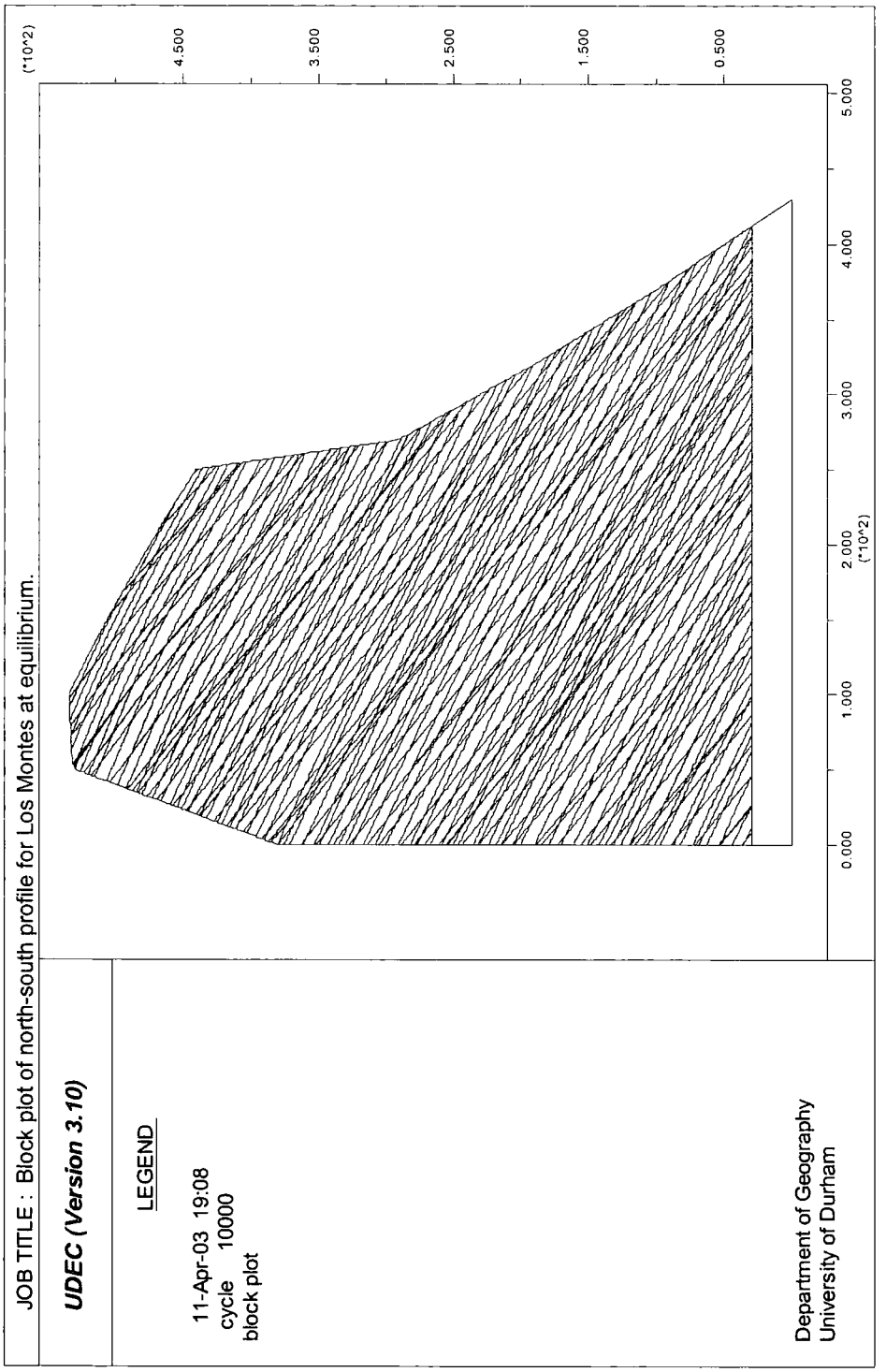

Figure 7.37a: Block plot of the north-south profile of Los Montes, Picos de Europa at equilibrium.

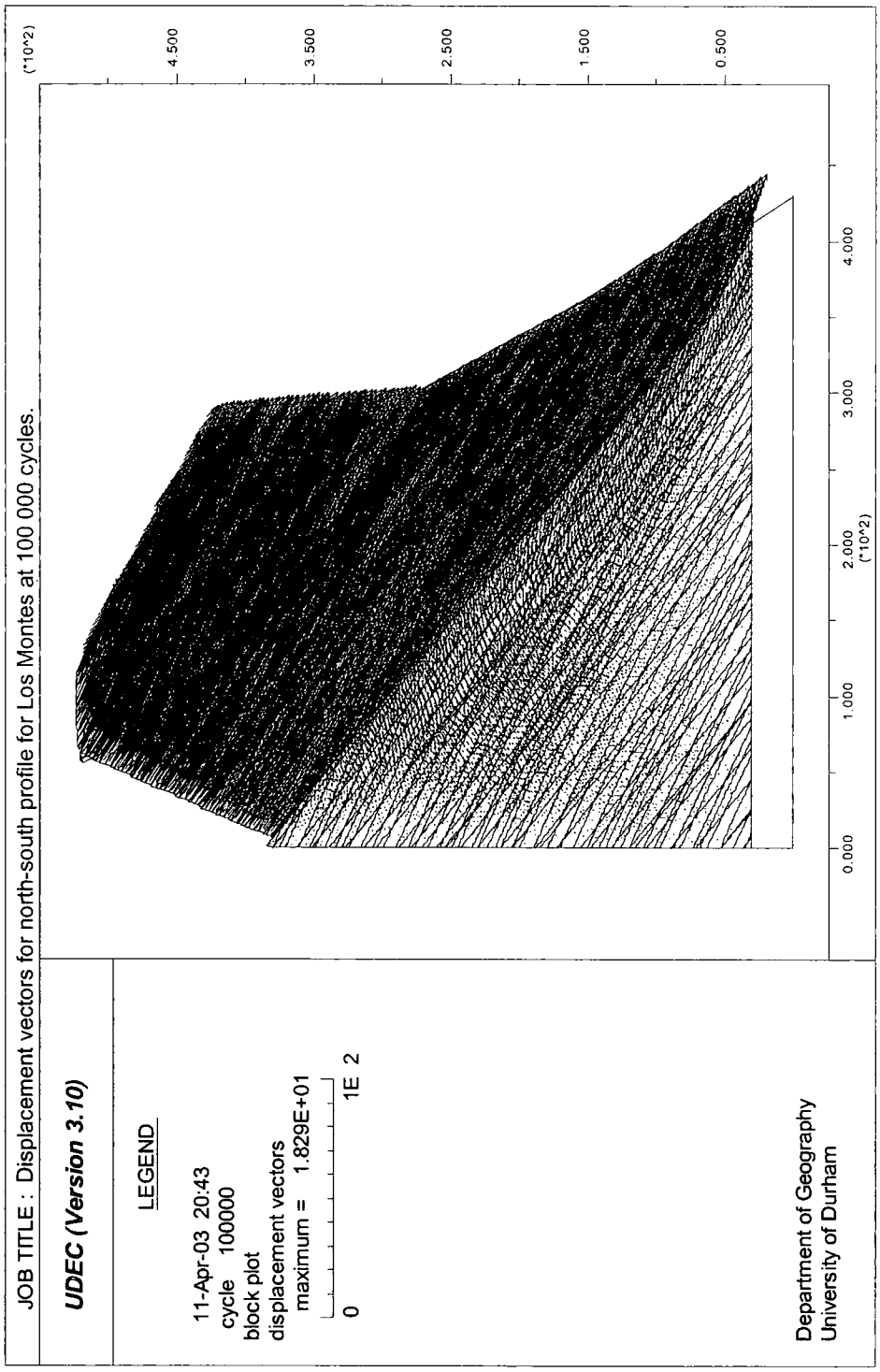

Figure 7.37b: Displacement vectors for the north-south profile of Los Montes, Picos de Europa at 100 000 cycles.

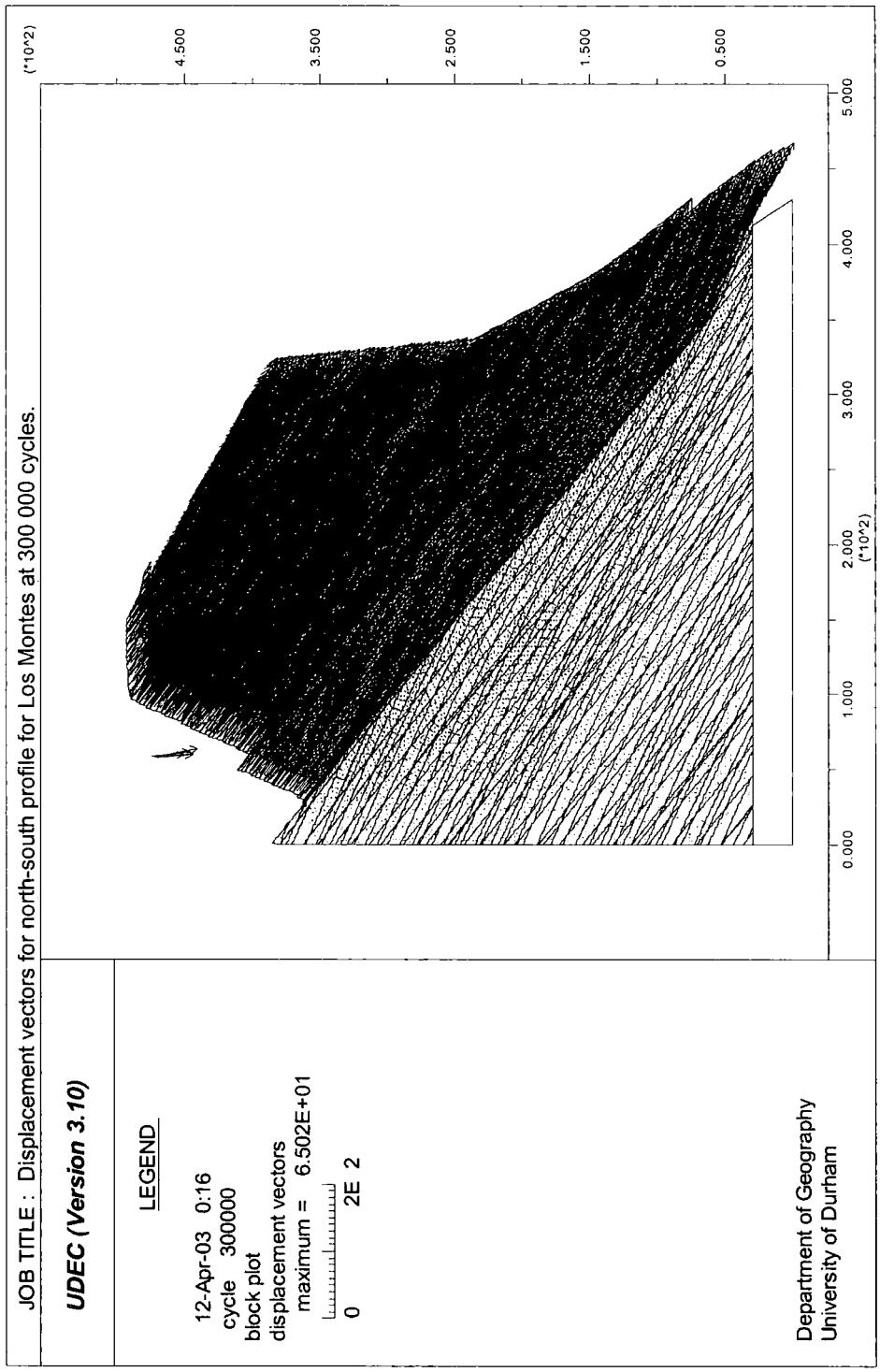

Figure 7.37c: Displacement vectors for the north-south profile of Los Montes, Picos de Europa at 300 000 cycles.

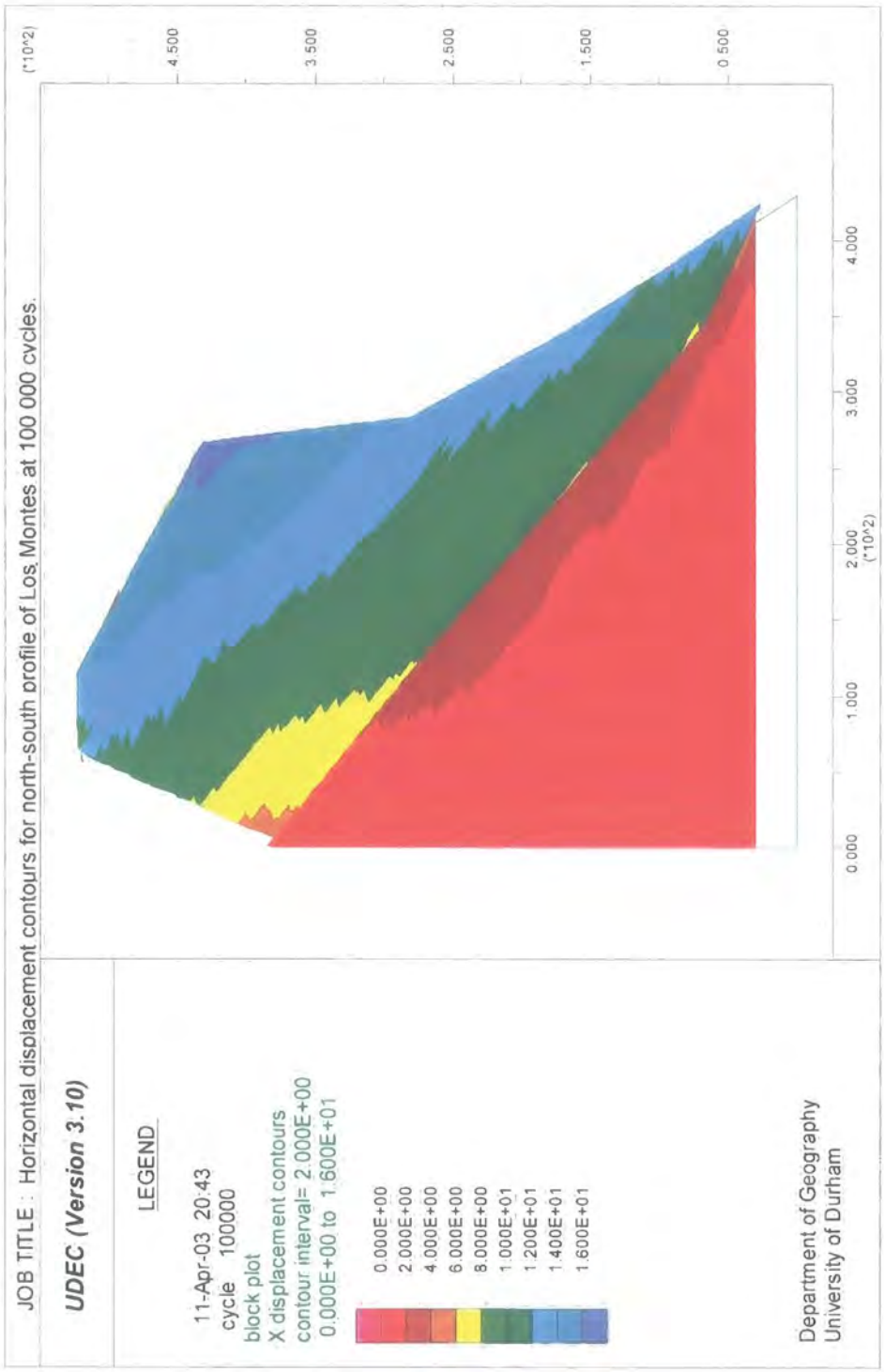

Figure 7.38a: Horizontal displacement contours for the north-south profile of Los Montes at 100 000 cycles.

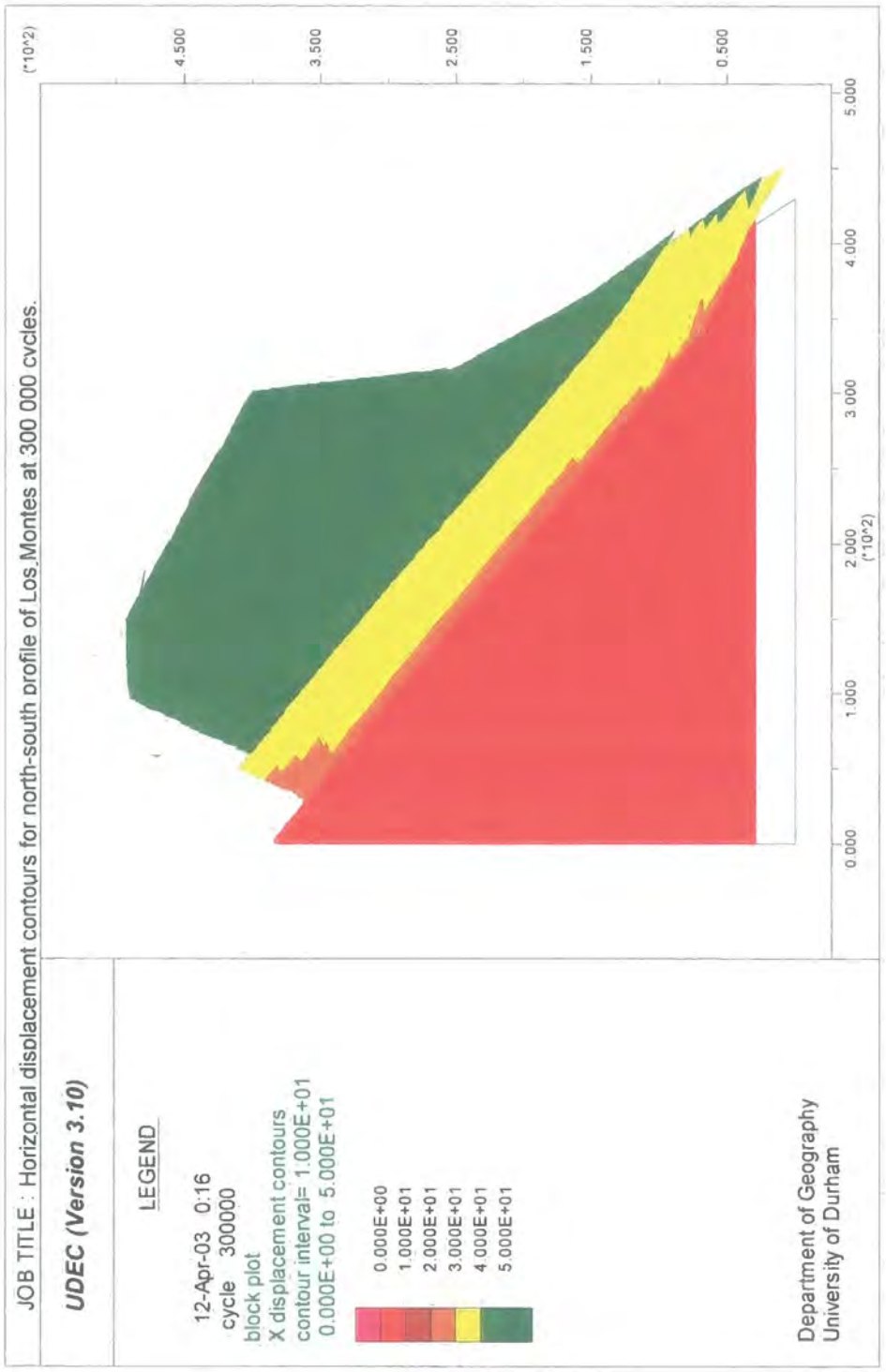

Figure 7.38b: Horizontal displacement contours for the north-south profile of Los Montes at 300 000 cycles.

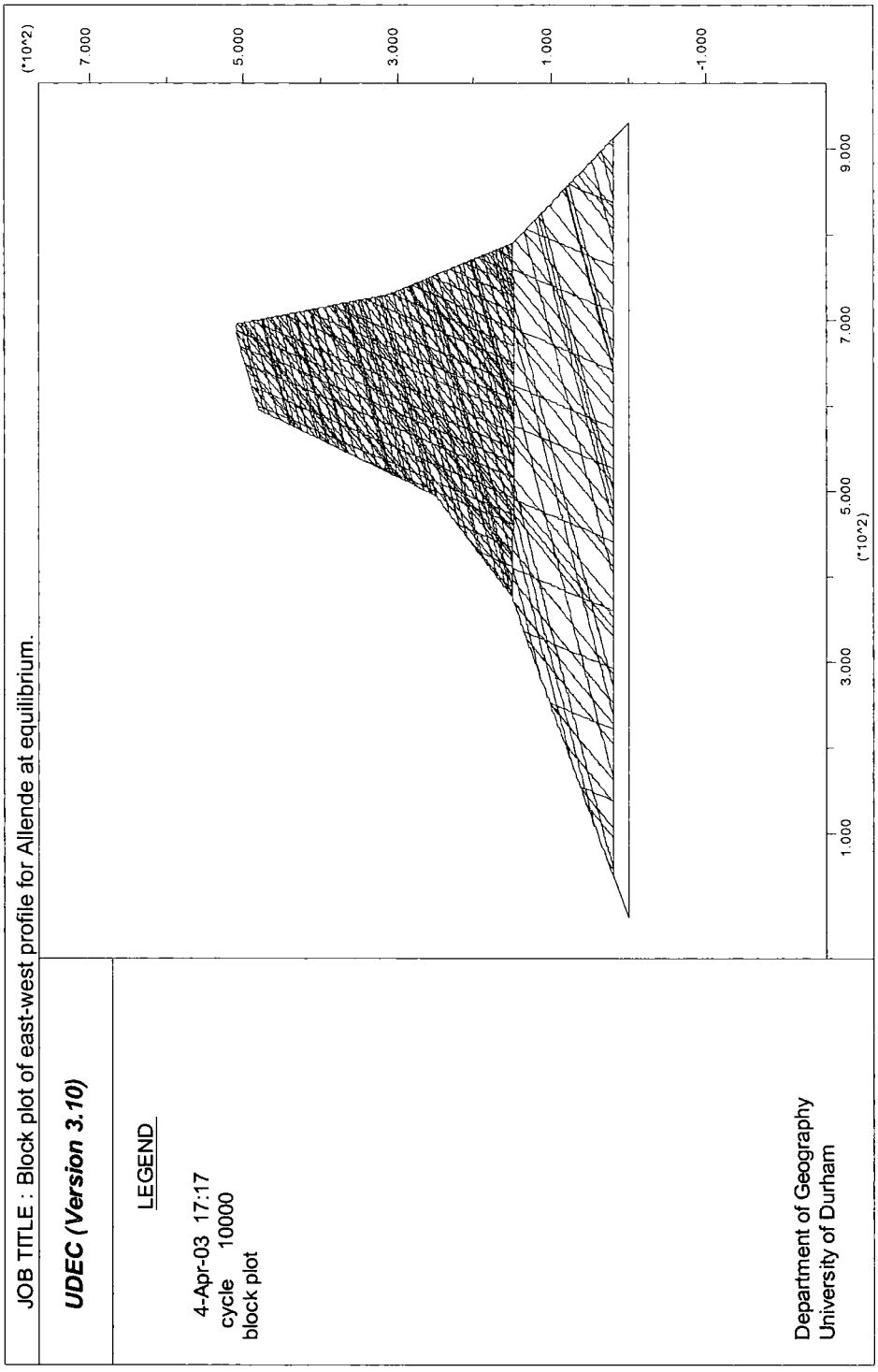

Figure 7.39a: Block plot of the east-west profile of Allende, Picos de Europa at equilibrium.

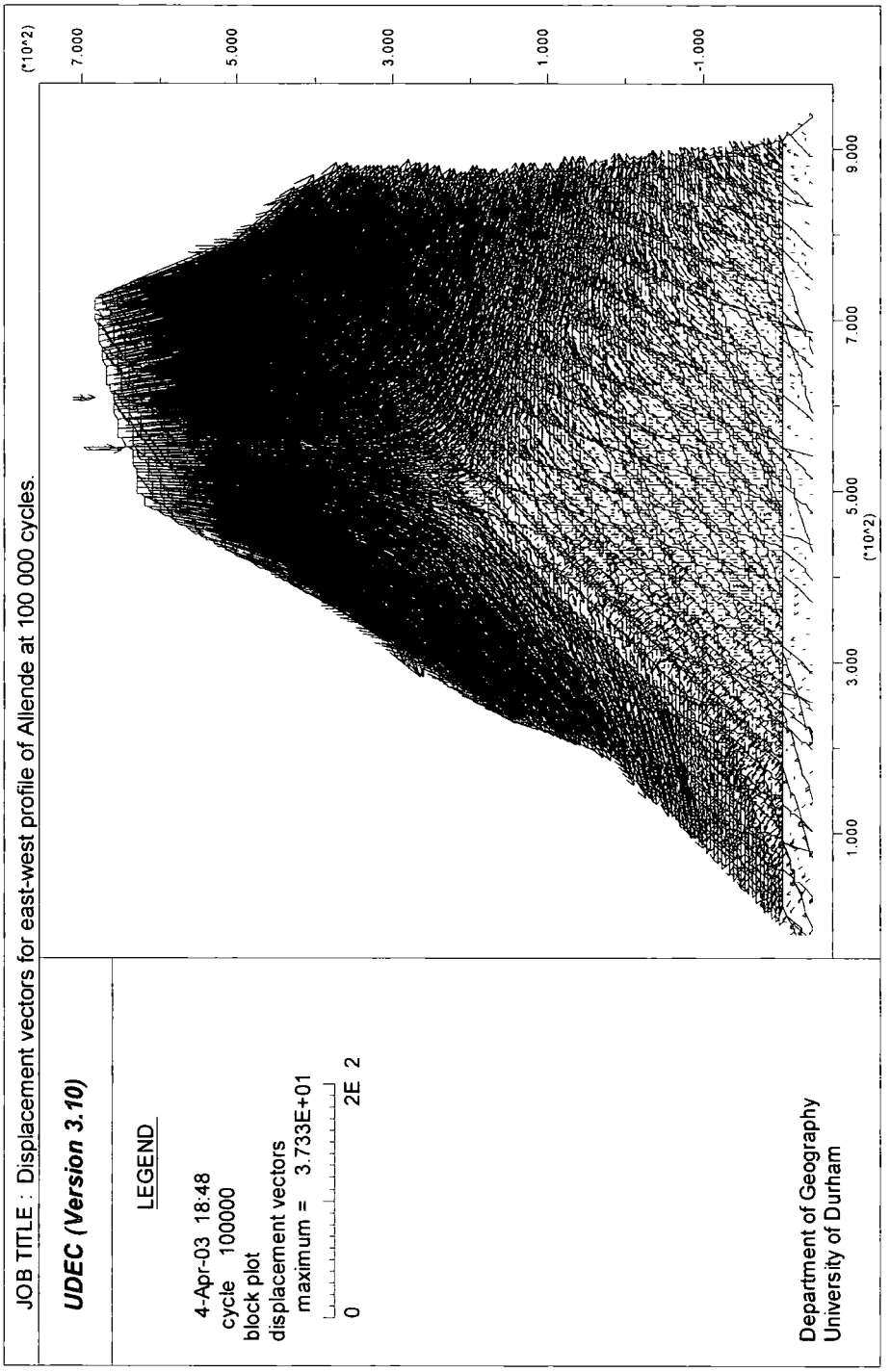

Figure 7.39b: Displacement vectors for the east-west profile of Allende at 100 000 cycles.

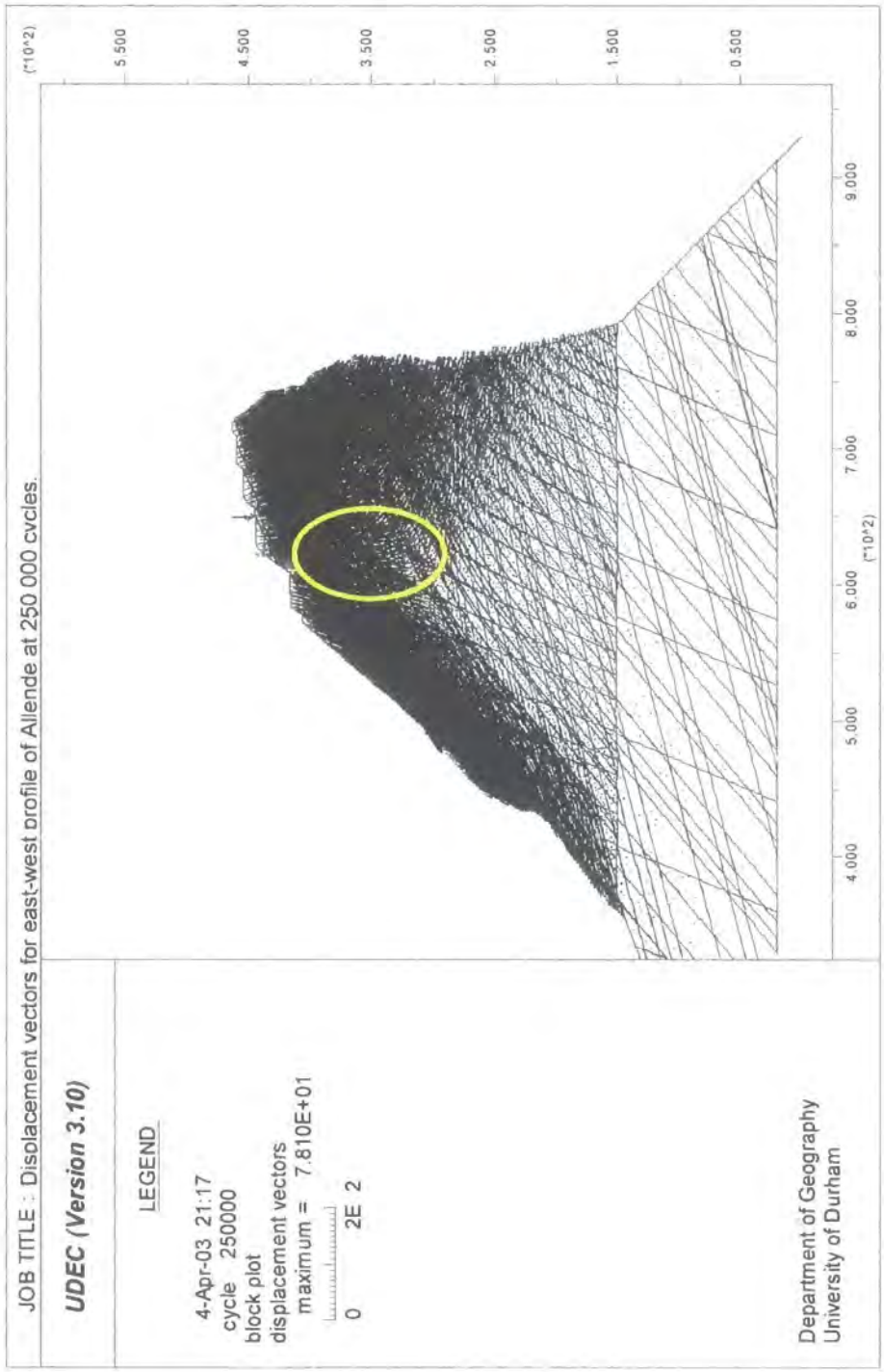

Figure 7.39c: Displacement vectors for the east-west profile of Allende at 250 000 cycles.

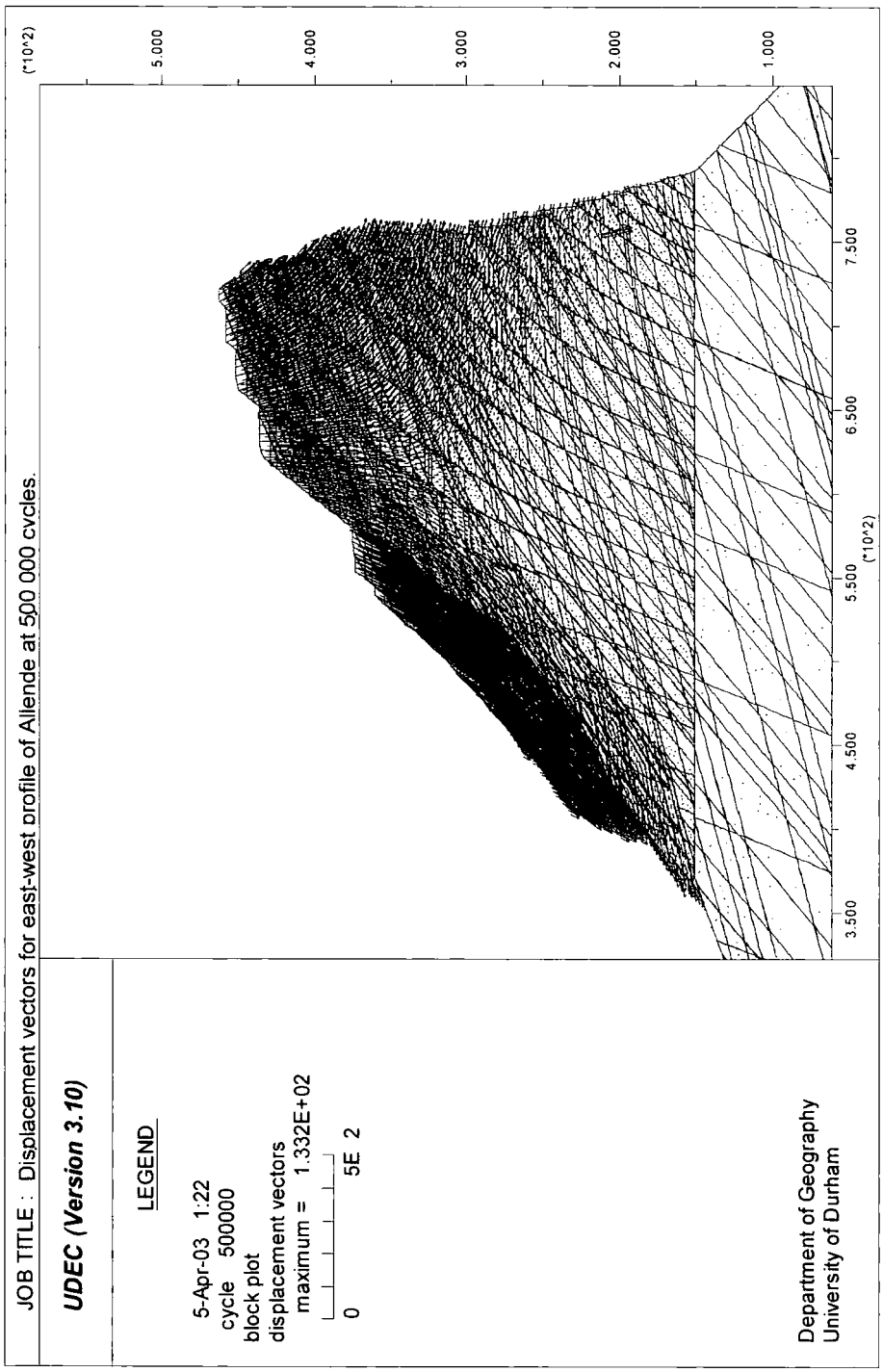

Figure 7.39d: Displacement vectors for the east-west profile of Allende at 500 000 cycles.

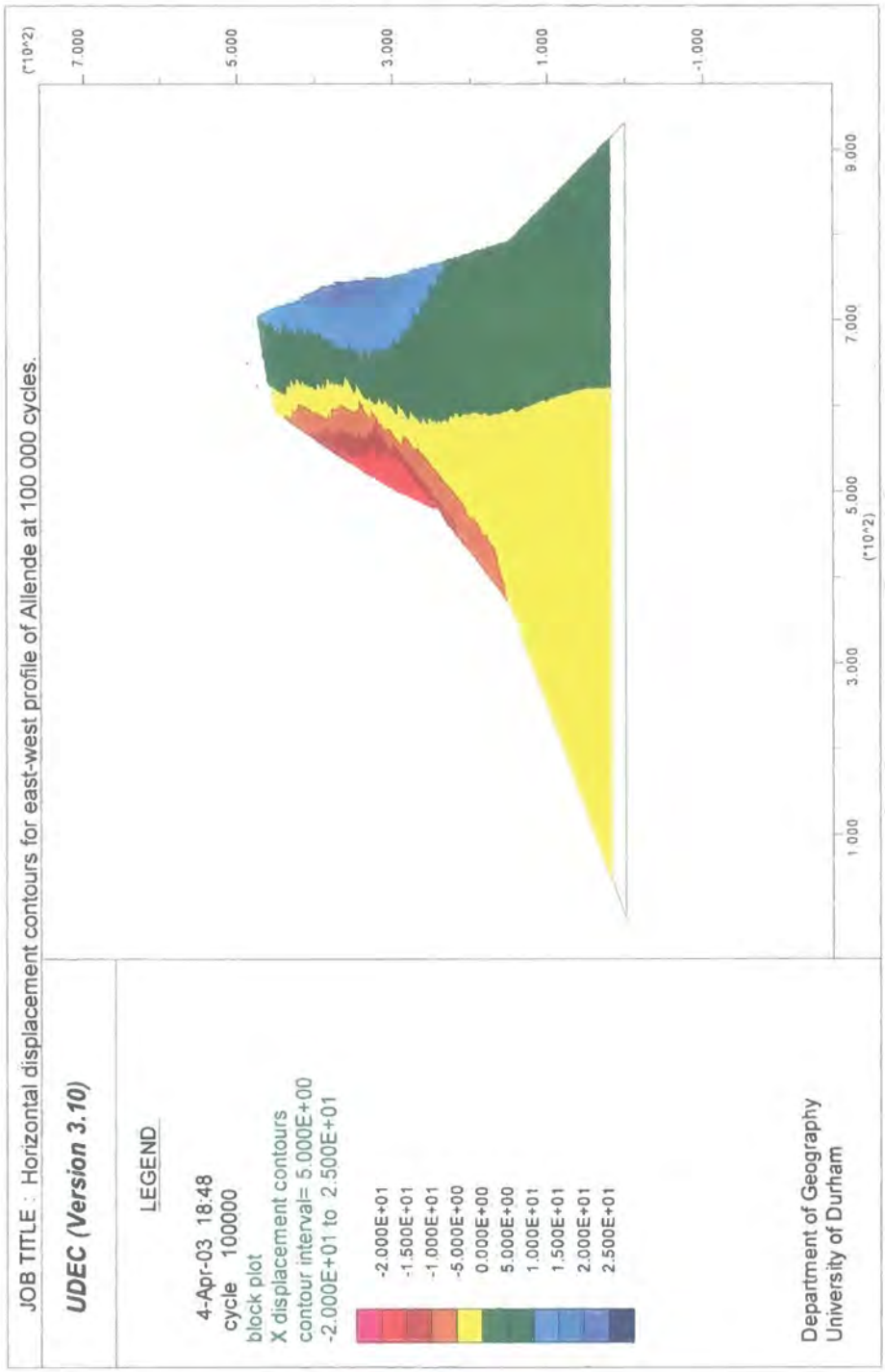

Figure 7.40a: Horizontal displacement contours for the east-west profile of Allende at 100 000 cycles.

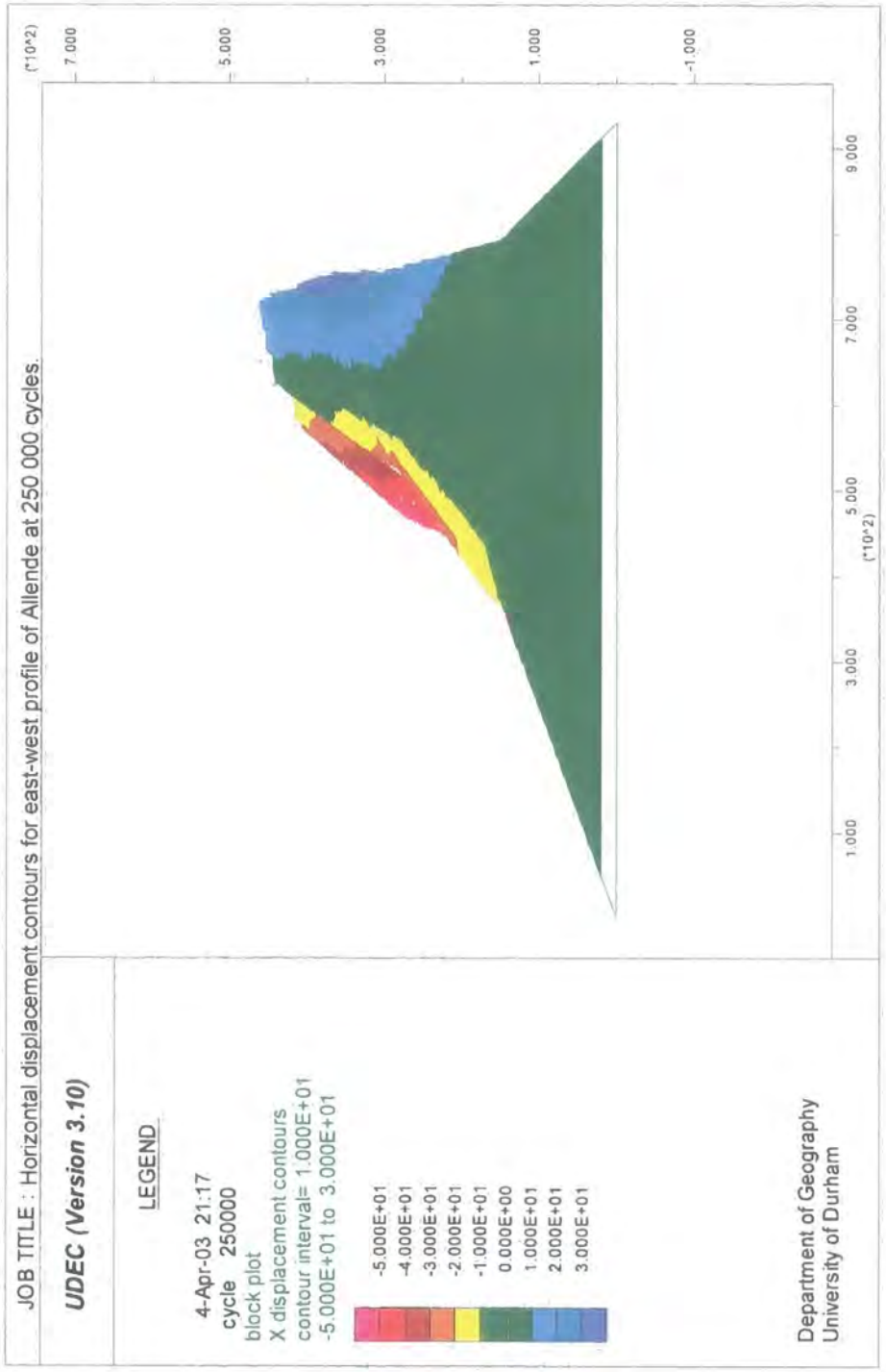

Figure 7.40b: Horizontal displacement contours for the east-west profile of Allende at 250 000 cycles.

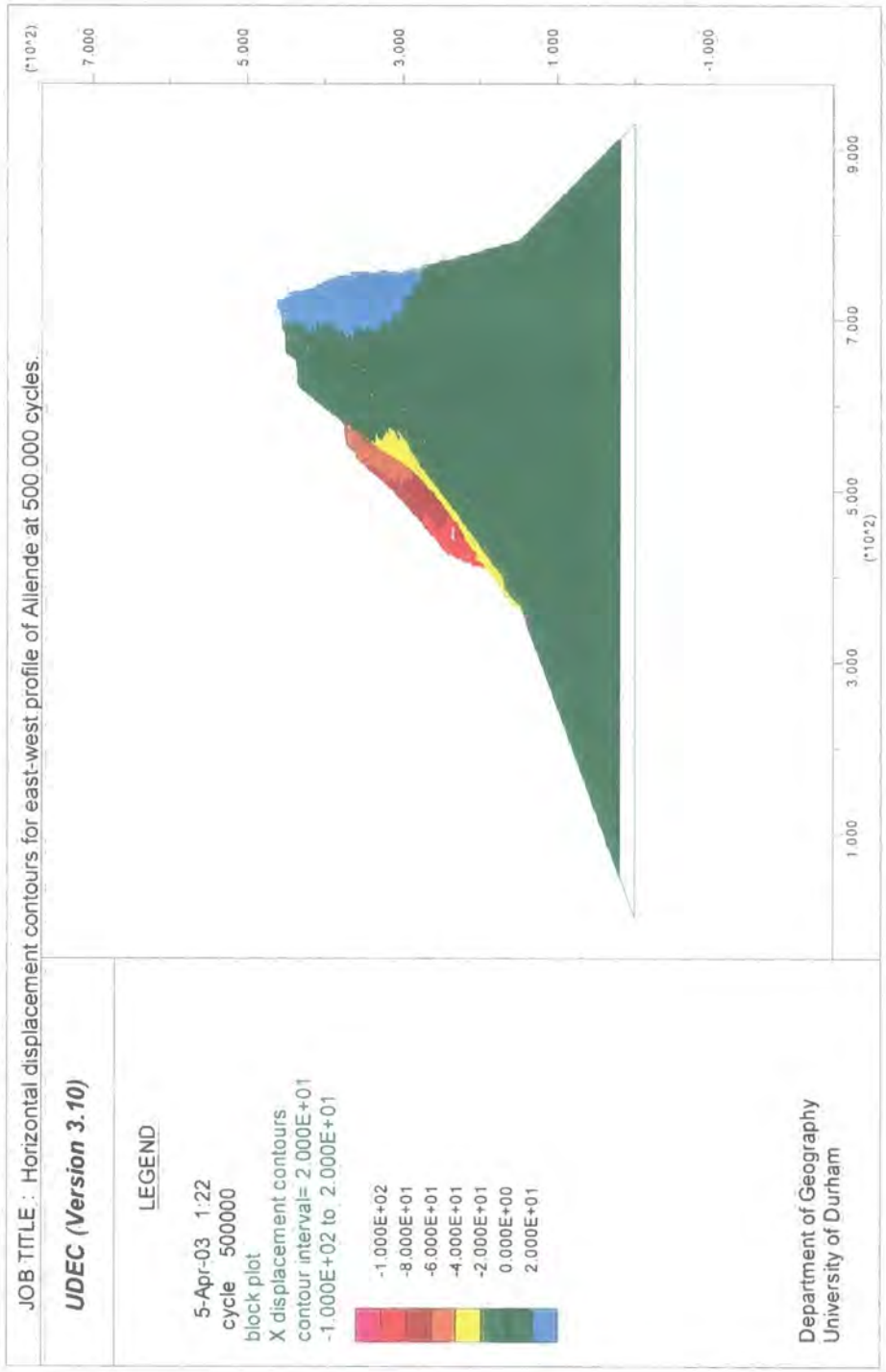

Figure 7.40c: Horizontal displacement contours for the east-west profile of Allende at 500 000 cycles.

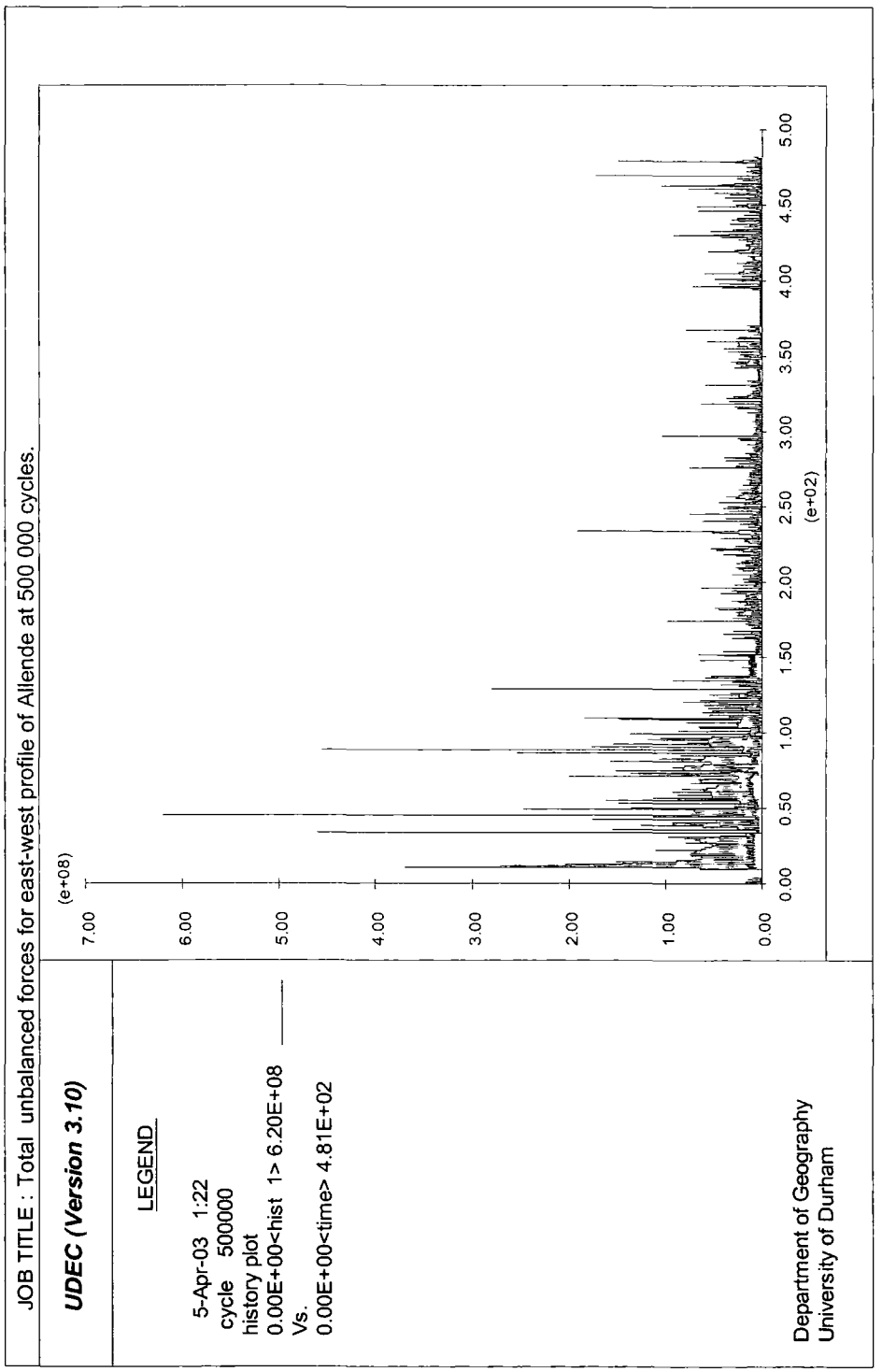

Figure 7.41: Total unbalanced forces for the east-west profile of Allende, Picos de Europa, at 500 000 cycles.

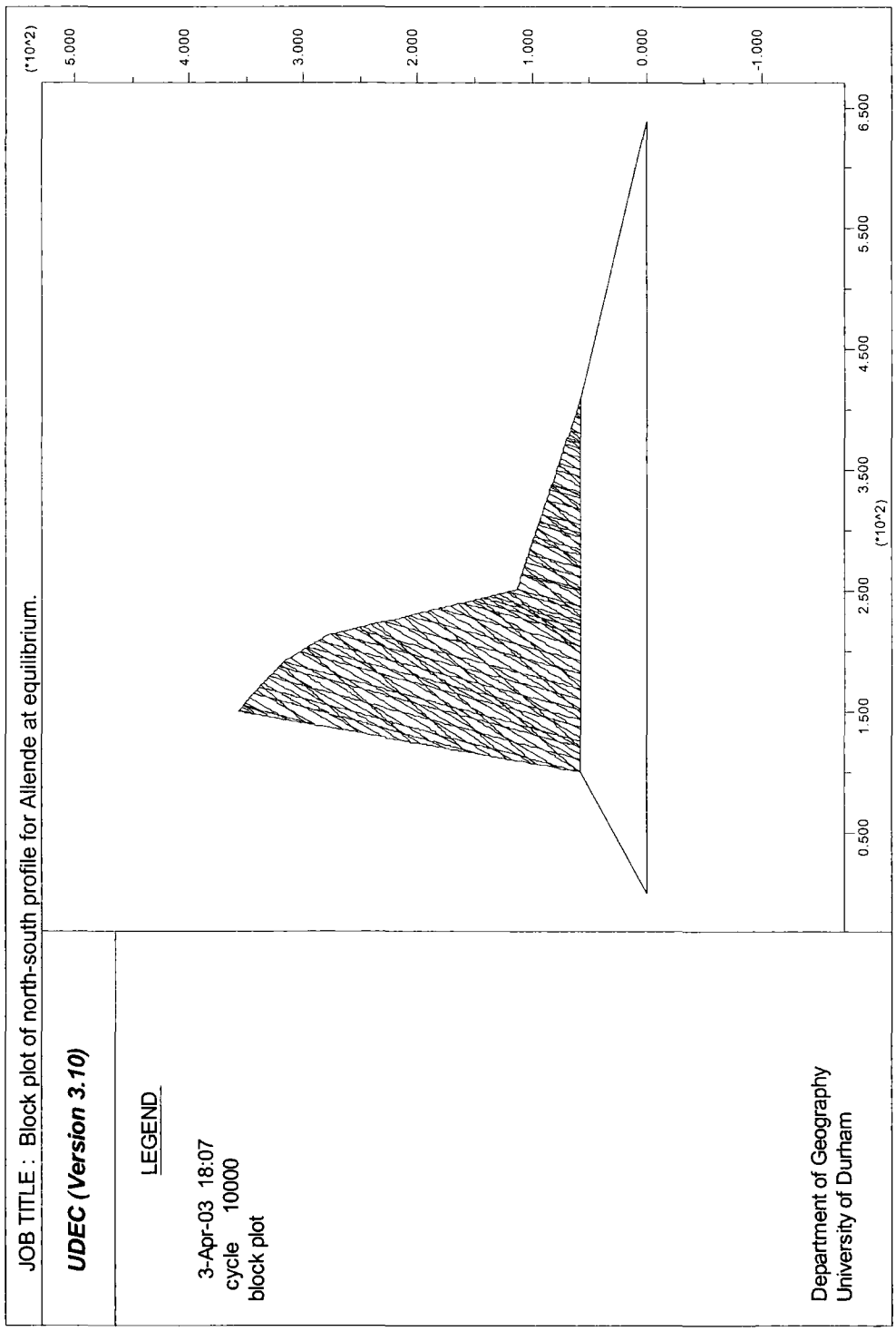

Figure 7.42a: Block plot of the north-south profile of Allende, Picos de Europa at equilibrium.

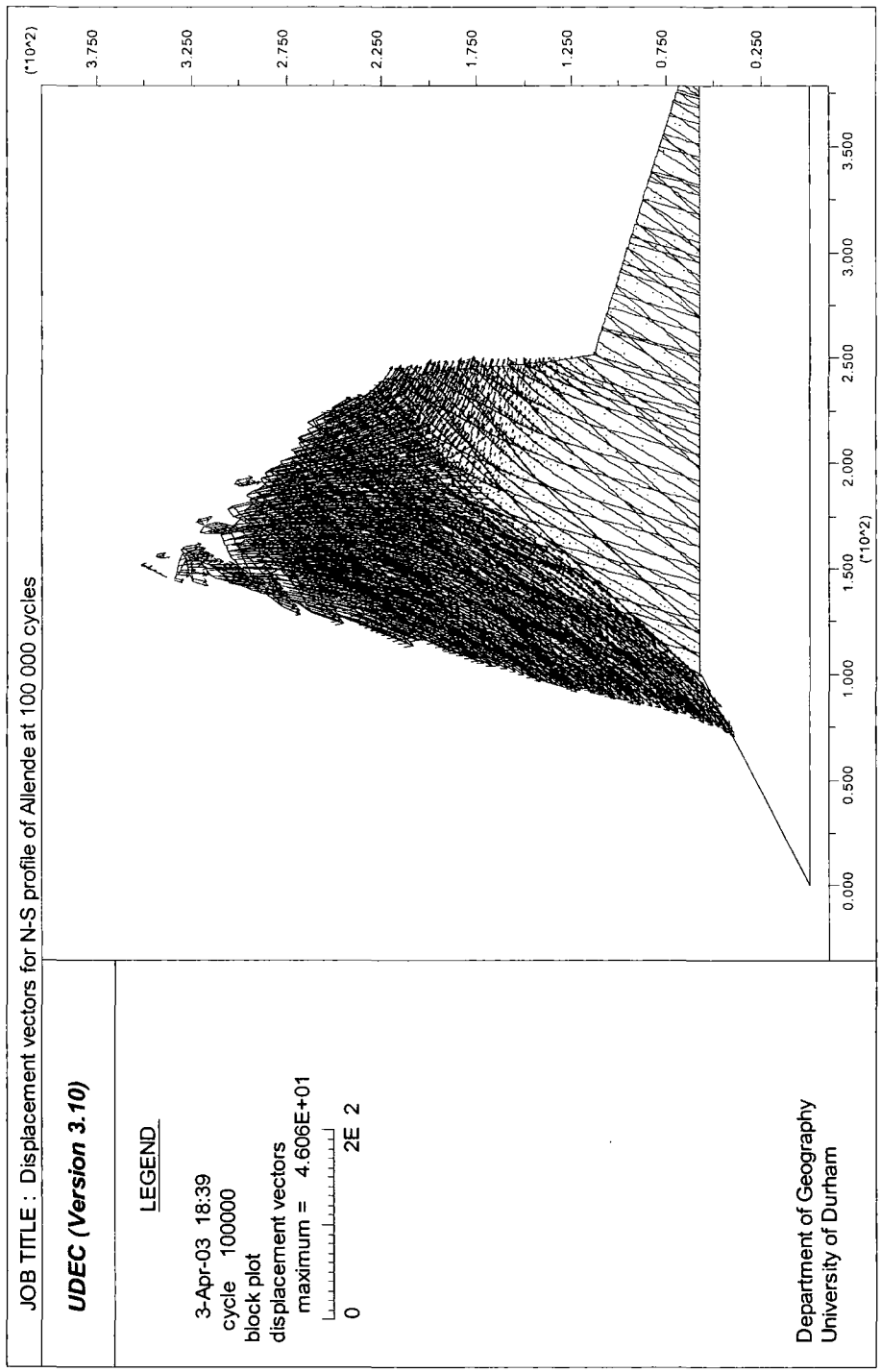

Figure 7.42b: Displacement vectors for the north-south profile of Allende, Picos de Europa at 100 000 cycles.

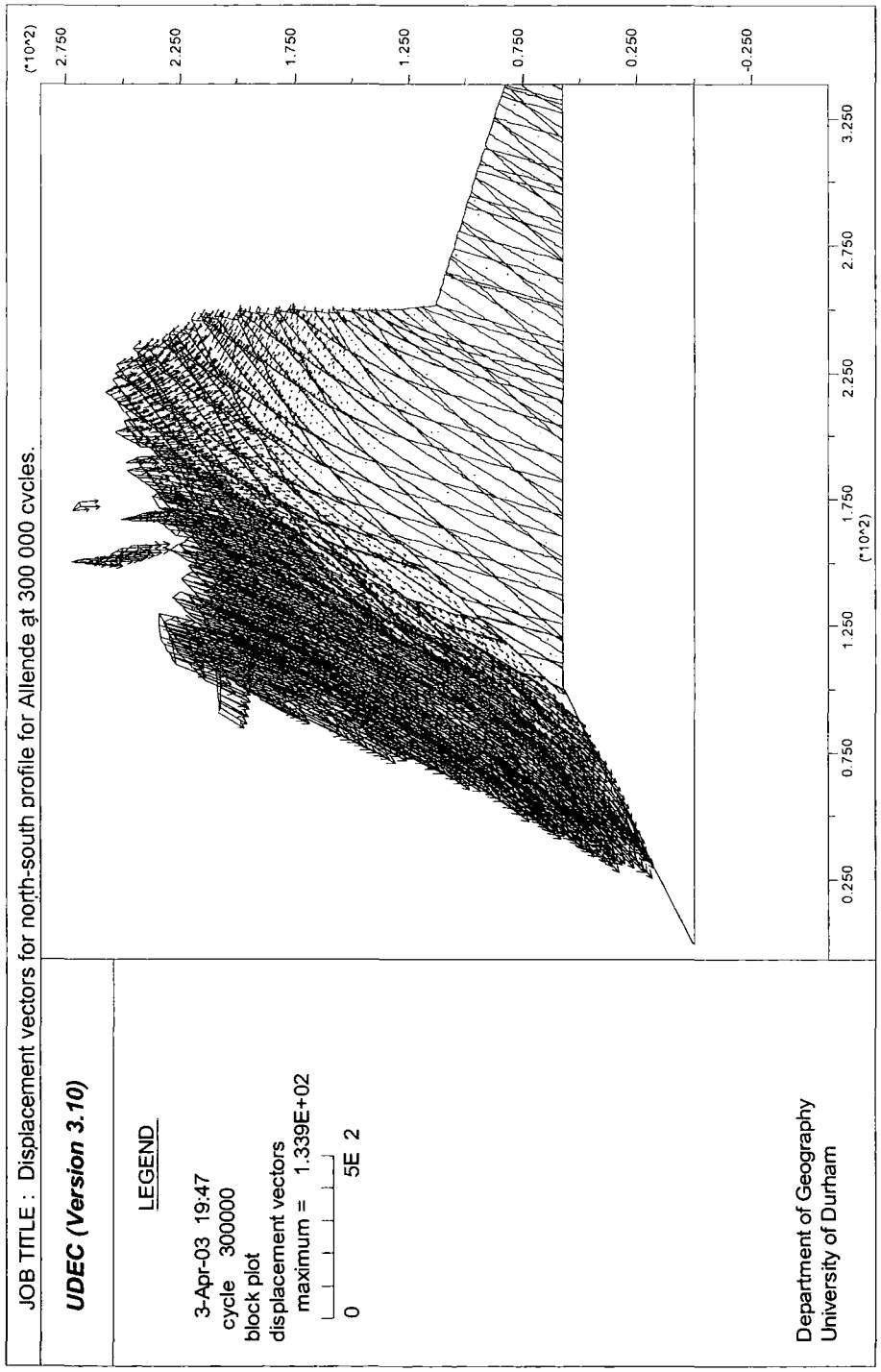

Figure 7.42c: Displacement vectors for the north-south profile of Allende, Picos de Europa at 300 000 cycles.

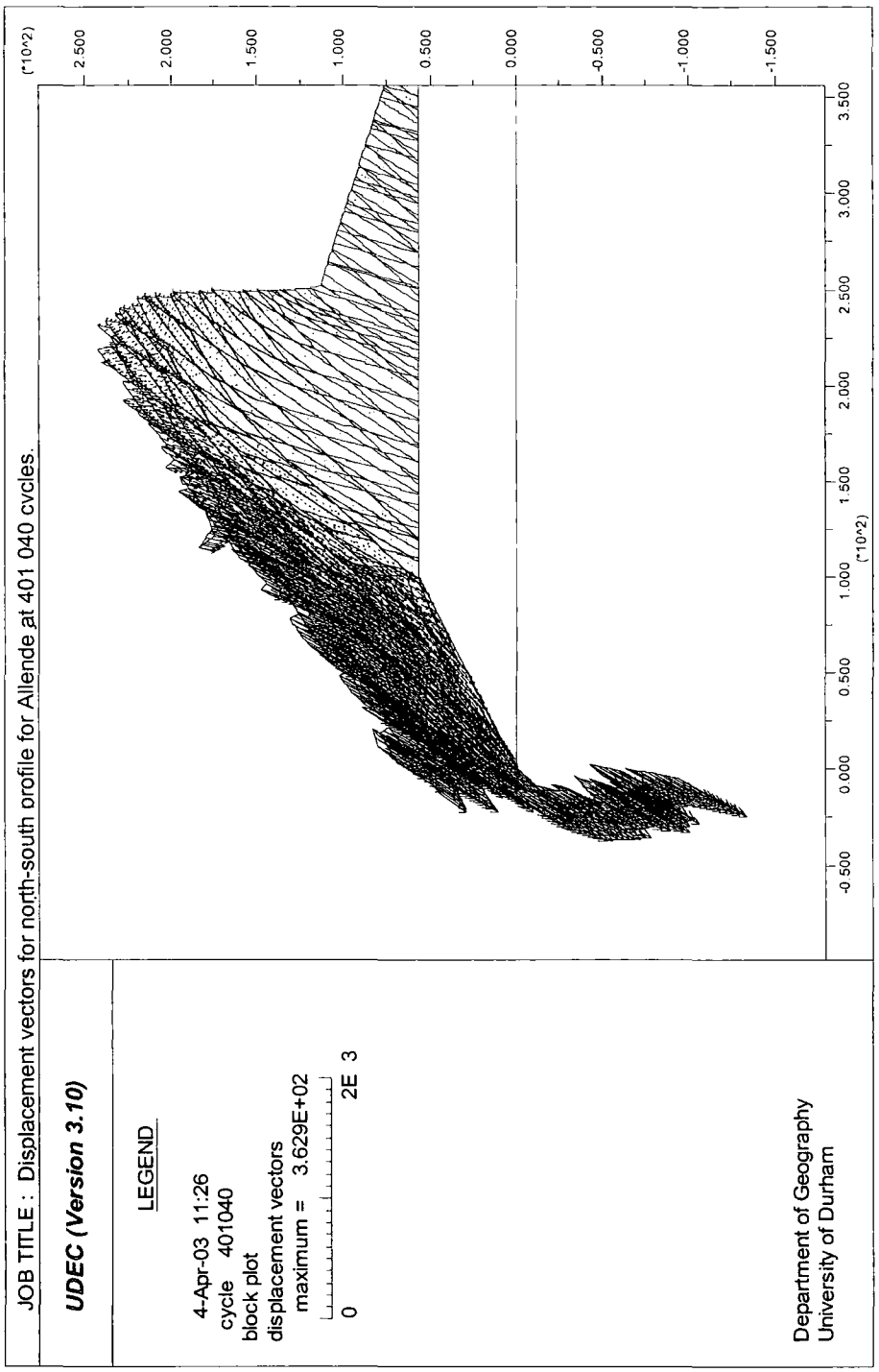

Figure 7.42d: Displacement vectors for the north-south profile of Allende, Picos de Europa at 401 040 cycles.

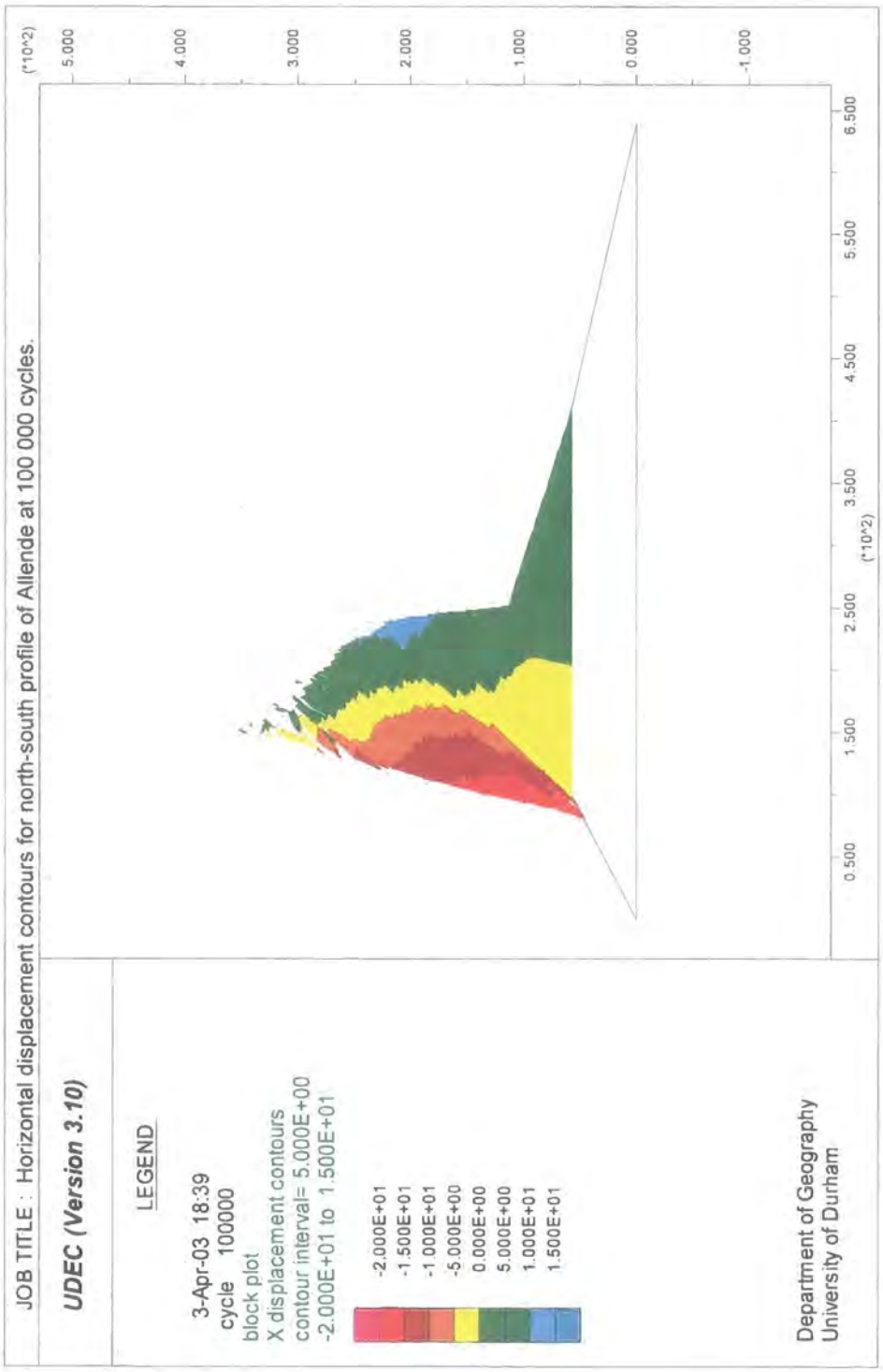

Figure 7.43a: Horizontal displacement contours for the north-south profile of Allende at 100 000 cycles.

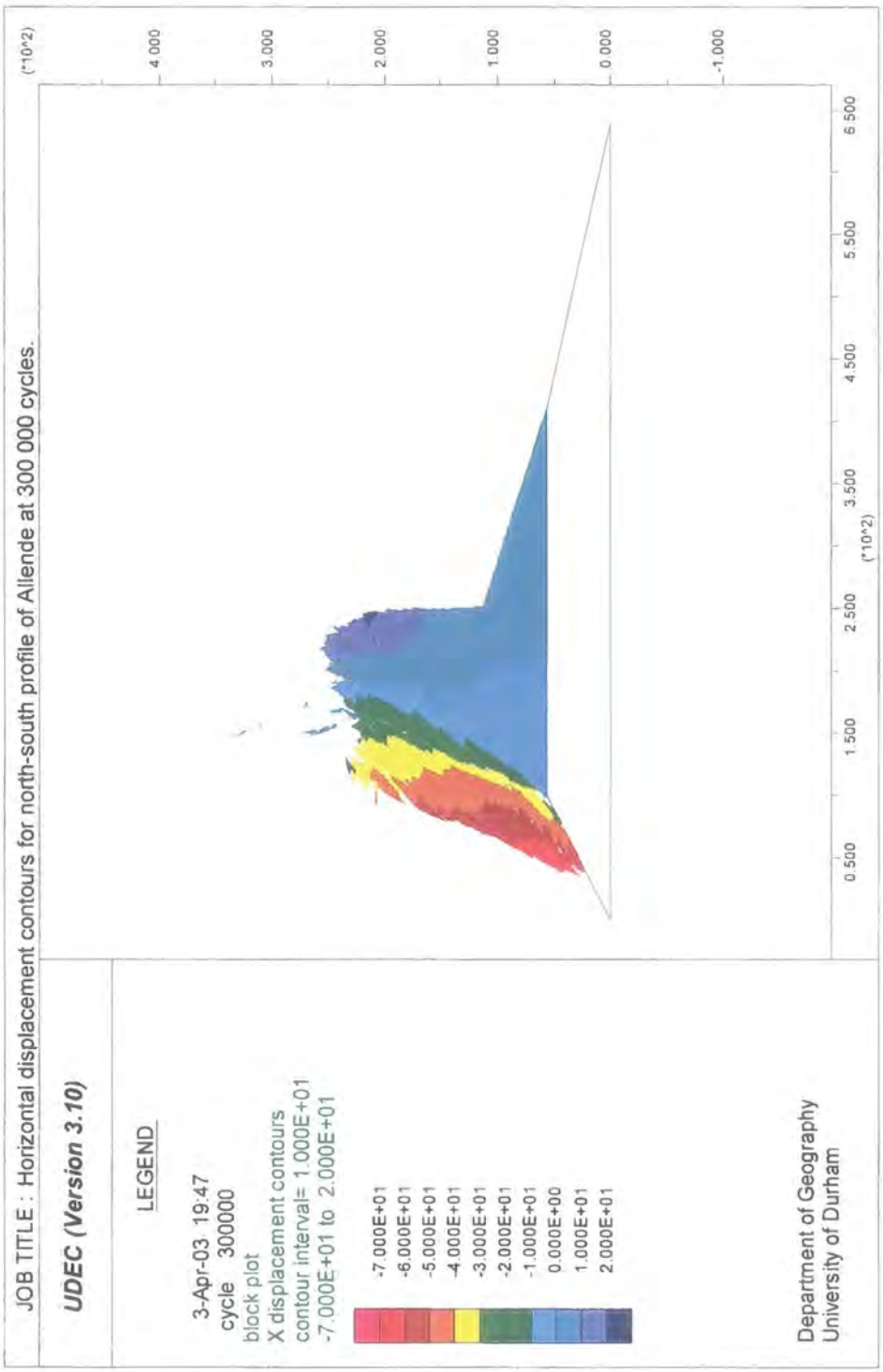

Figure 7.43b: Horizontal displacement contours for the north-south profile of Allende at 300 000 cycles.

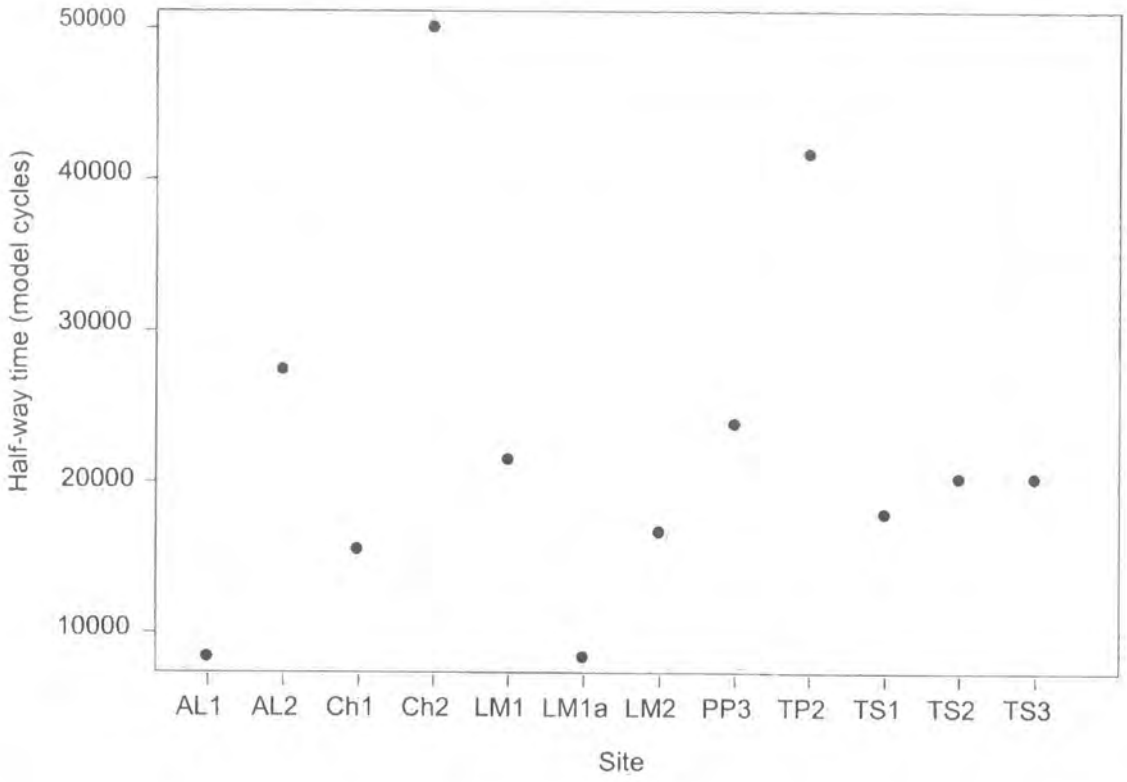

Figure 7.46: Comparison of the half-way time for all failures in the Picos de Europa models.

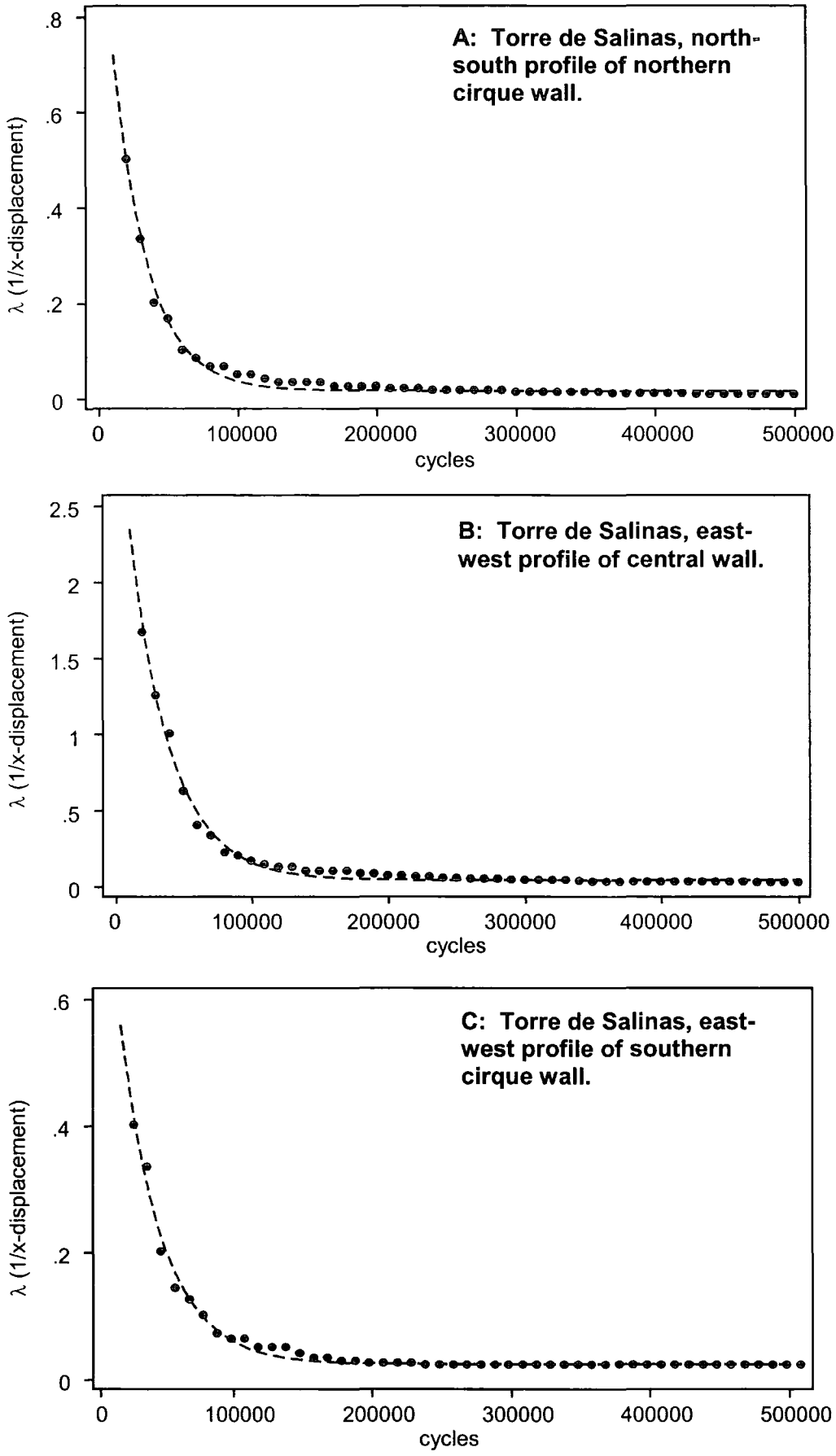

Figure 7.47: Exponential asymptotic model (dashed line) applied to x-displacement data for the failures at Torre de Salinas.

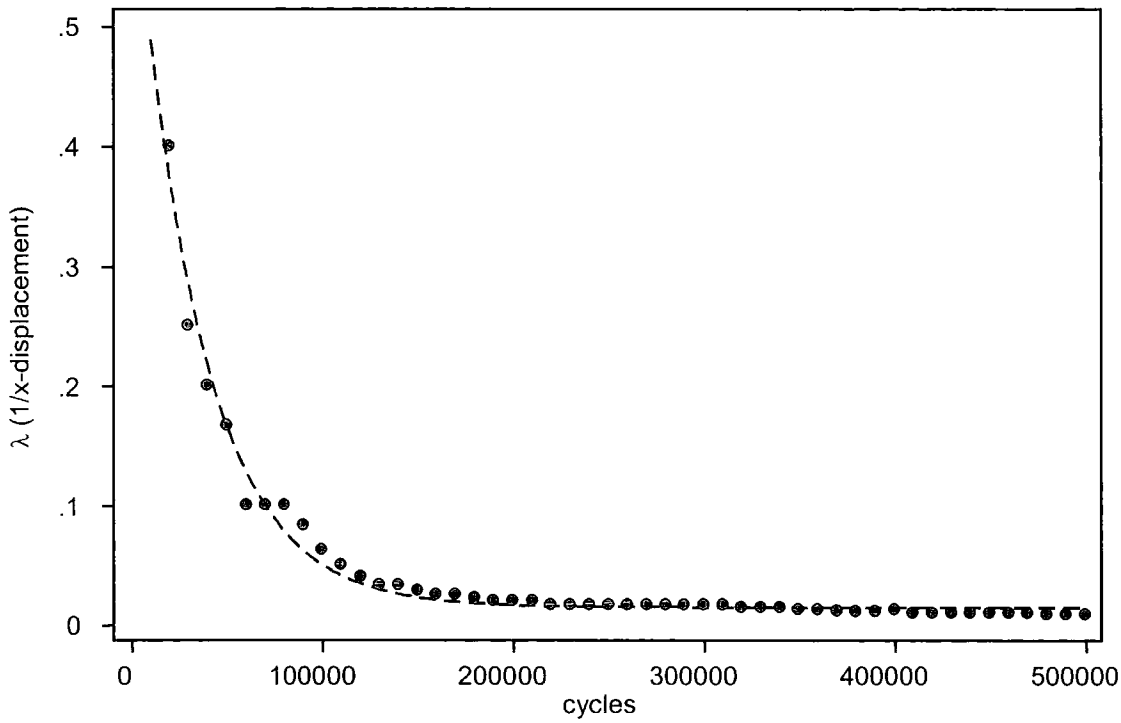

Figure 7.48: Exponential asymptotic model (dashed line) applied to x-displacement data for the failure on the north-south profile of Pico de la Padierna.

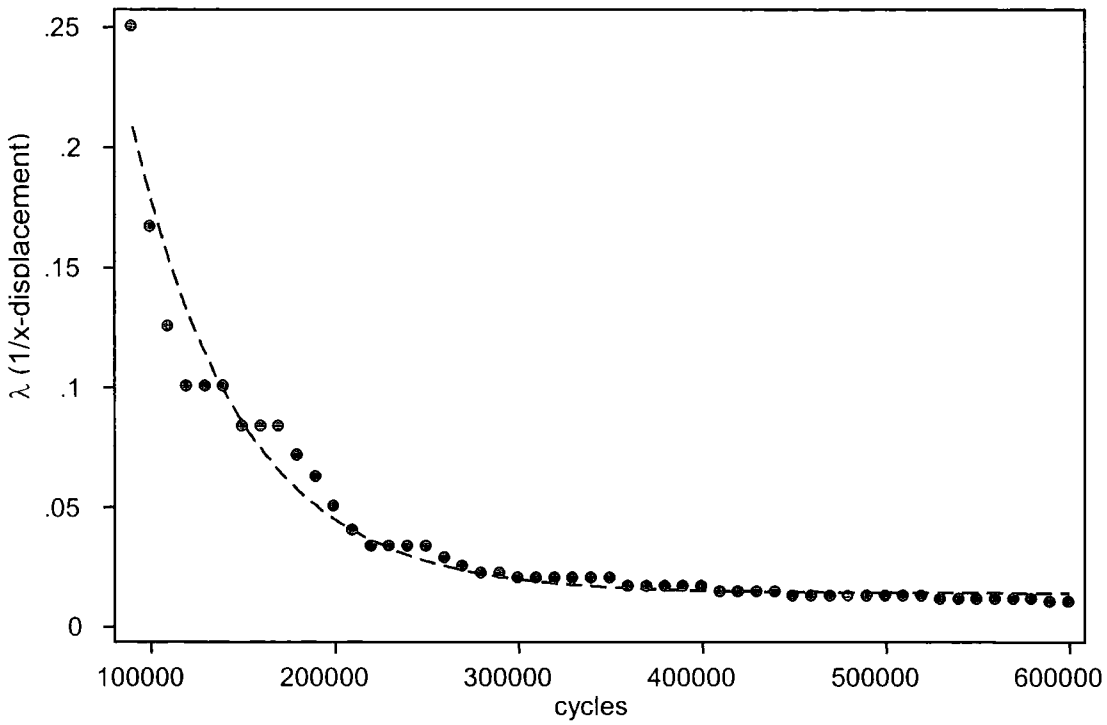

Figure 7.49: Exponential asymptotic (dashed line) applied to x-displacement data (circles) for the east-west profile of Tiro Pedabejo.

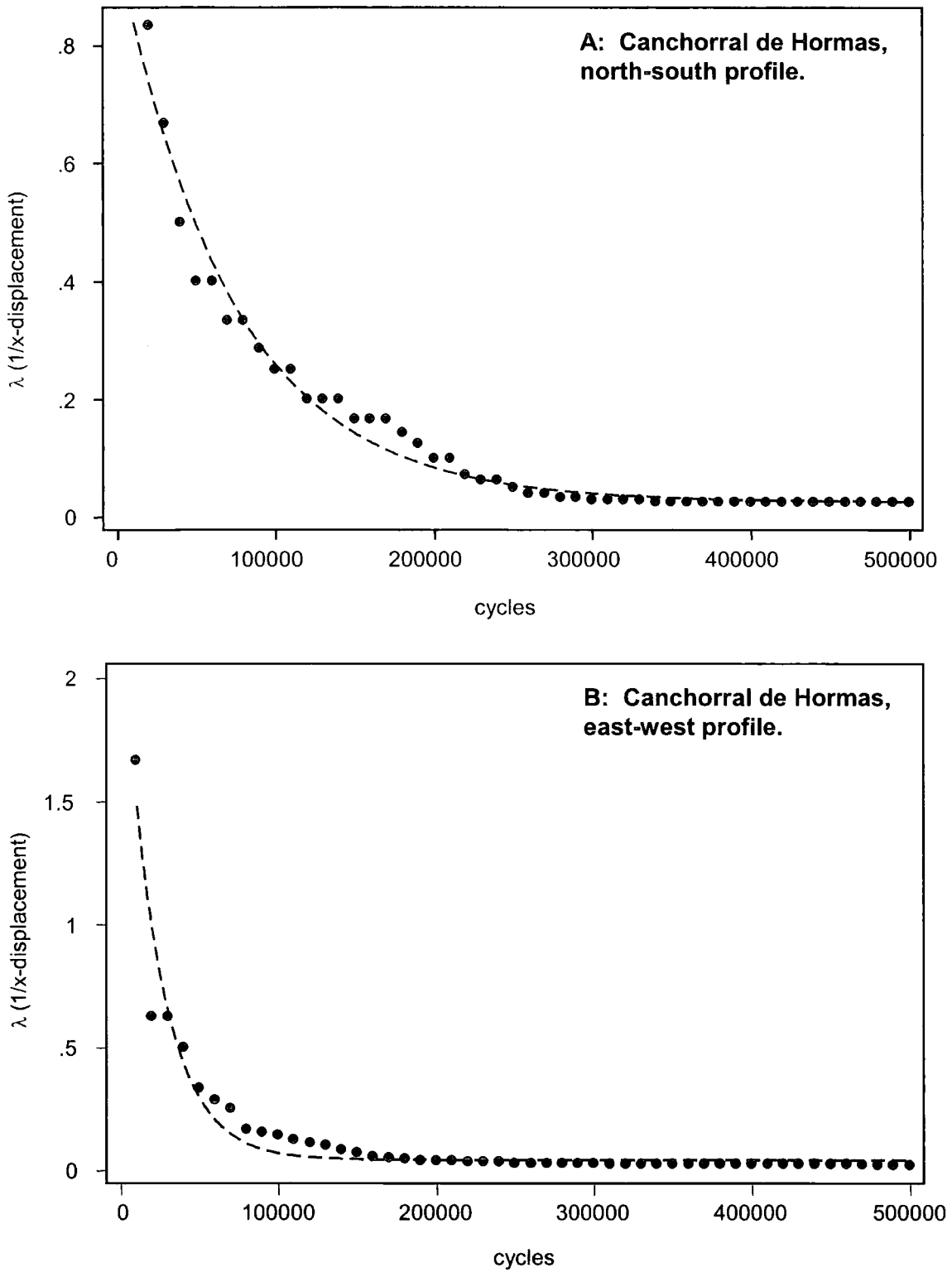

Figure 7.50: Exponential asymptotic model (dashed line) applied to x-displacement data for the failures at Canchorral de Hormas.

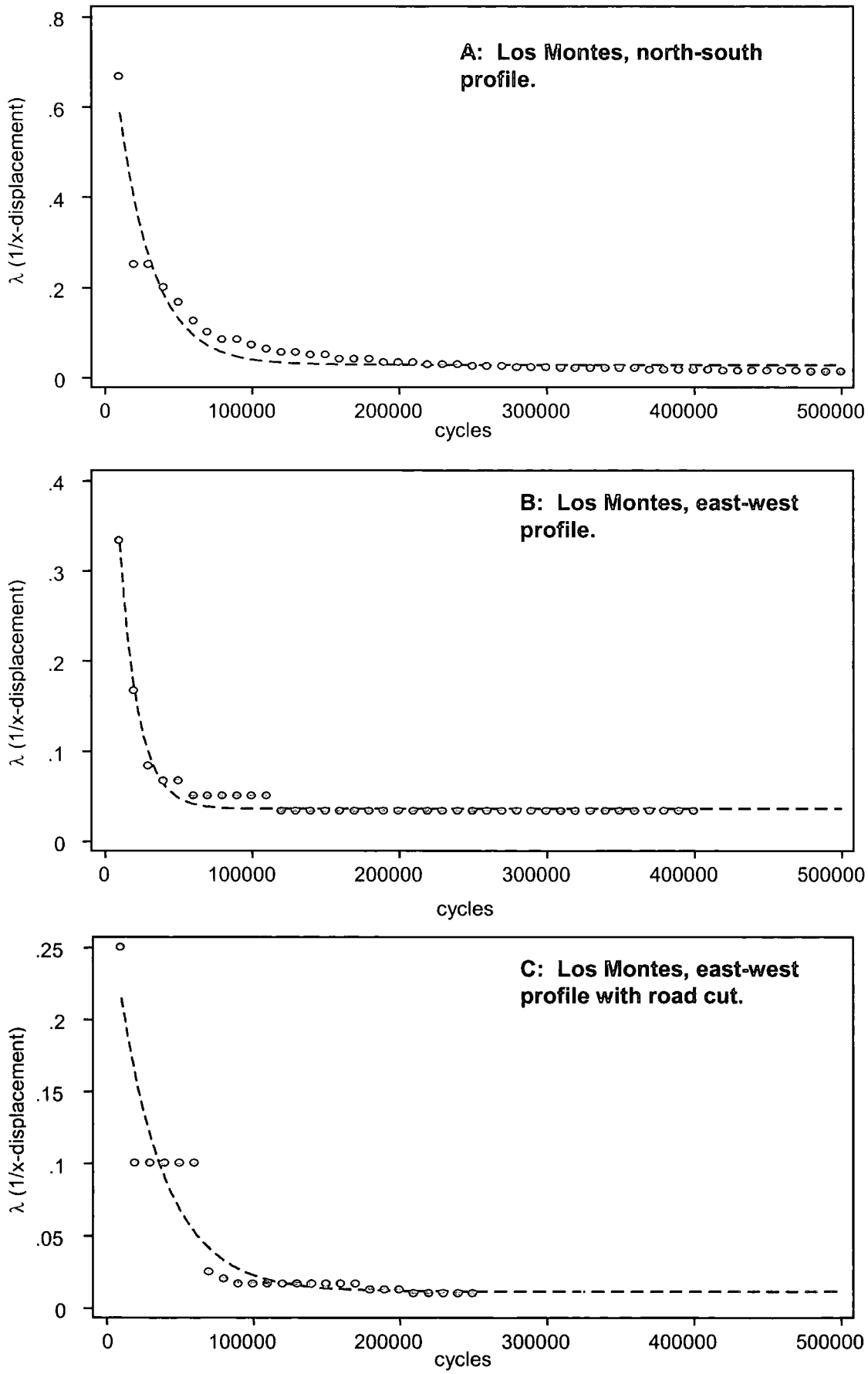

Figure 7.51: Exponential asymptotic model (dashed line) applied to x-displacement data for the failures at Los Montes.

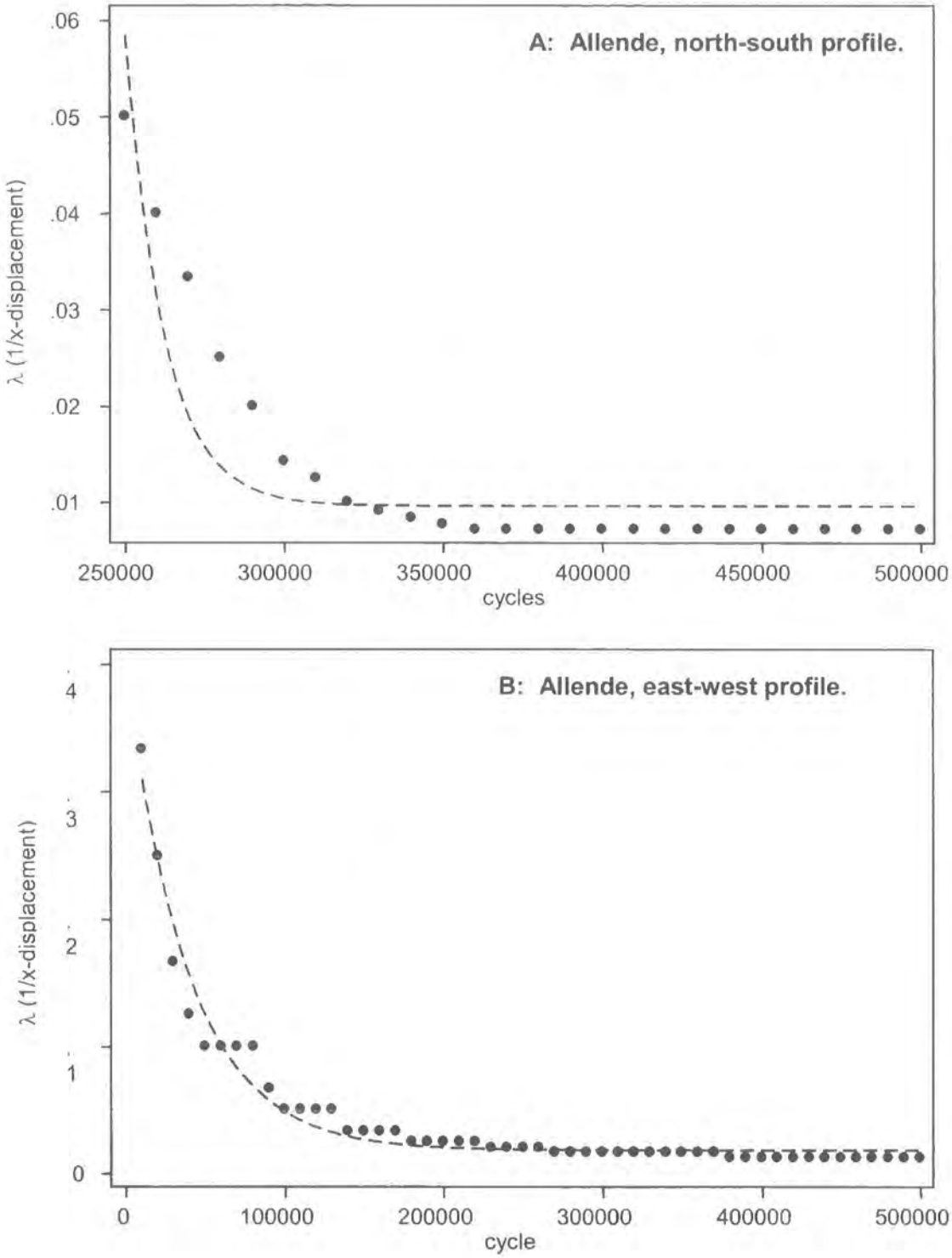

Figure 7.52: Exponential asymptotic model (dashed line) applied to x-displacement data for the failures at Allende.

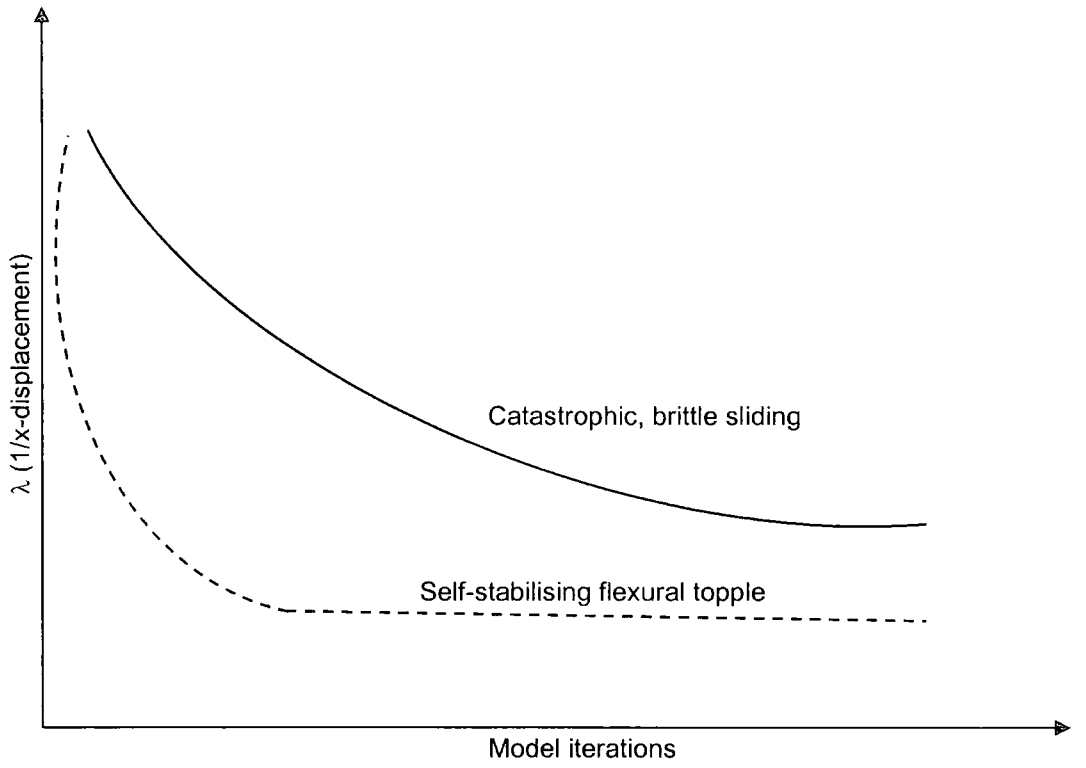

Figure 7.53: Summary of the two main patterns of failure in λ-*t* space associated with brittle, catastrophic failure and self-stabilising flexural toppling failure.

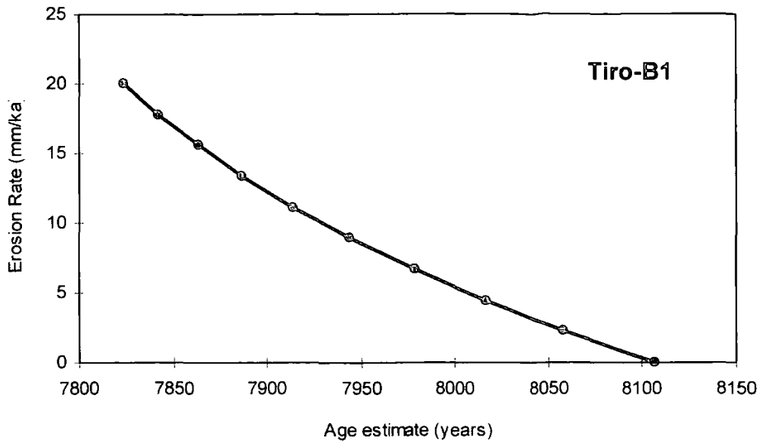

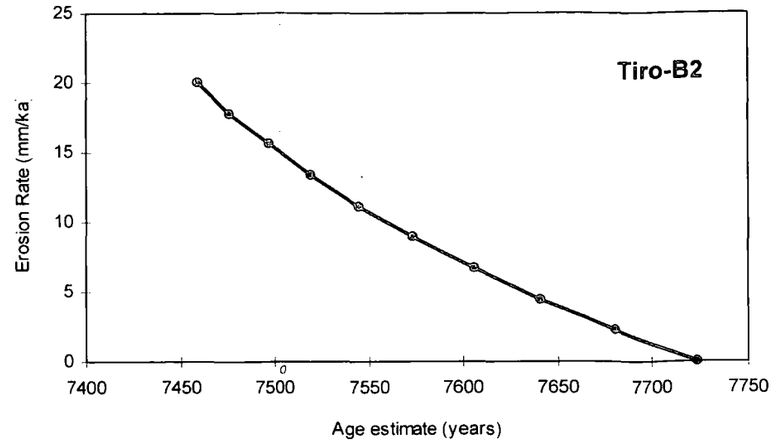

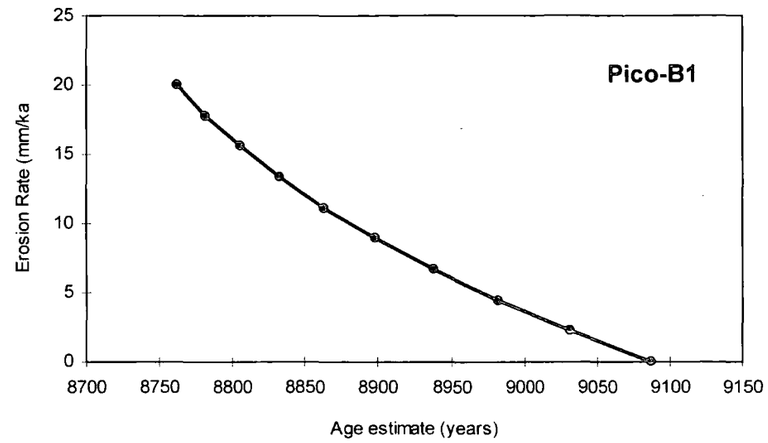

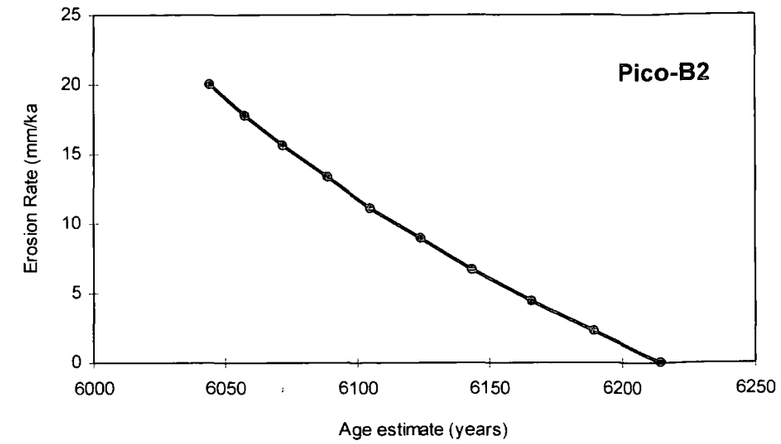

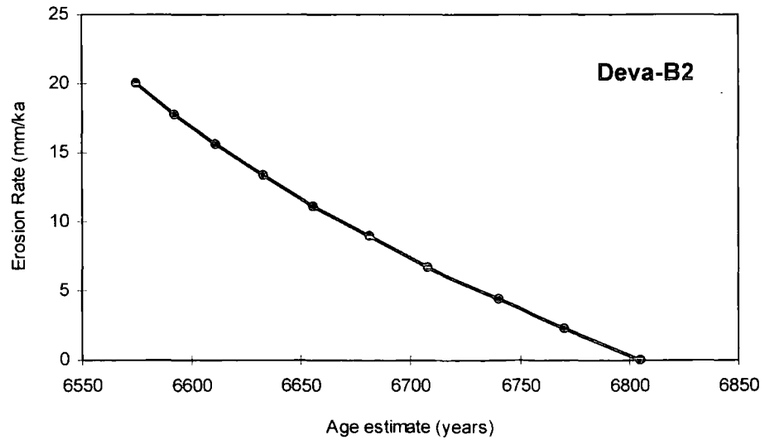

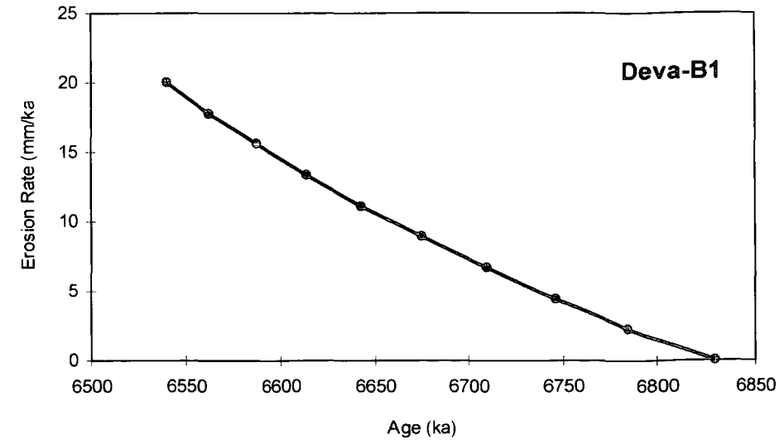

Figure 7.54: Results of erosion rate modelling on the samples selected for ^{36}CL dating. As the erosion rate increases, the applied erosion rate correction decreases the ages of the boulder.

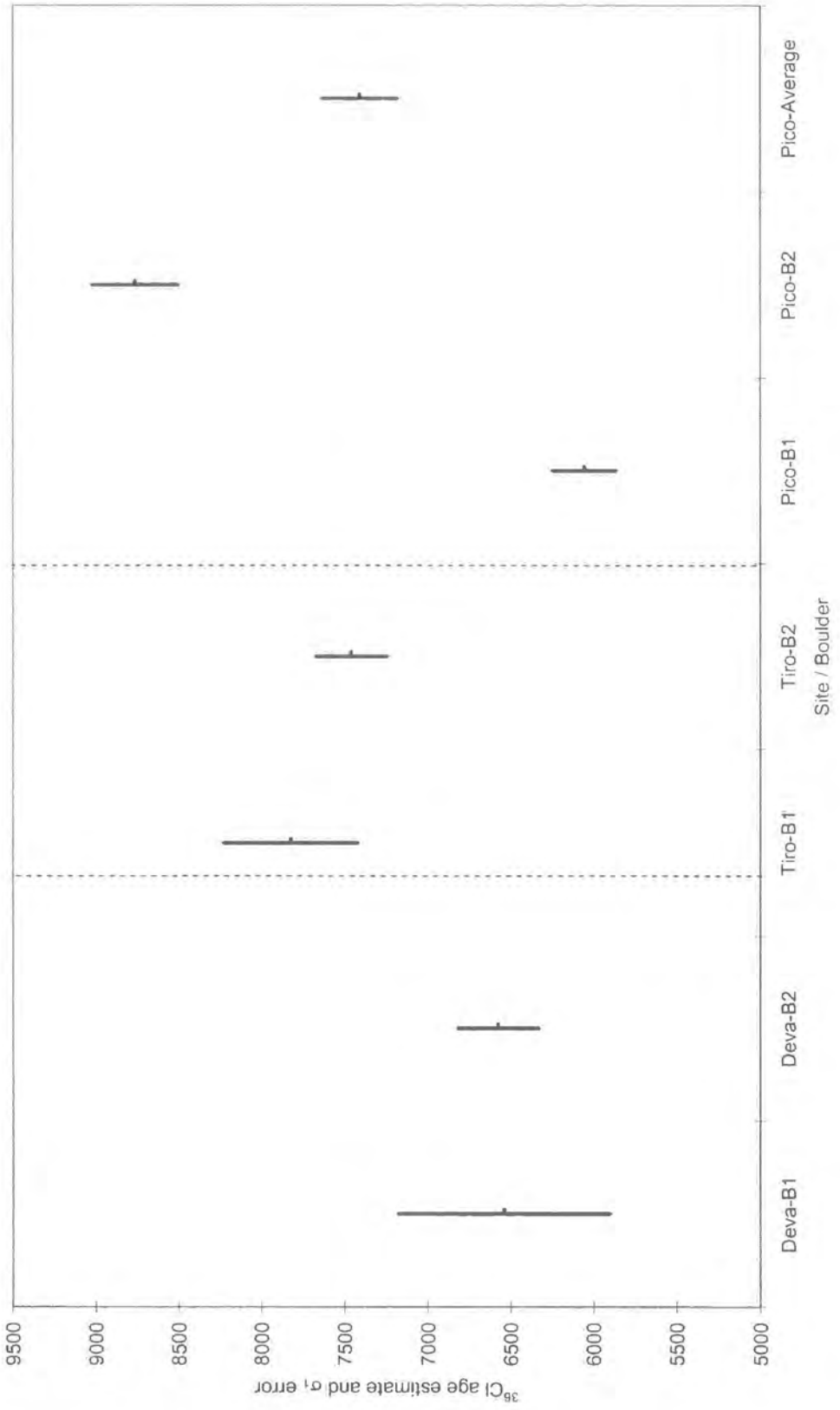

Figure 7.55: Calculated ^{36}Cl dates for rock slope failures in the Picos de Europa. The dates indicate one failure event, with almost synchronous timing.

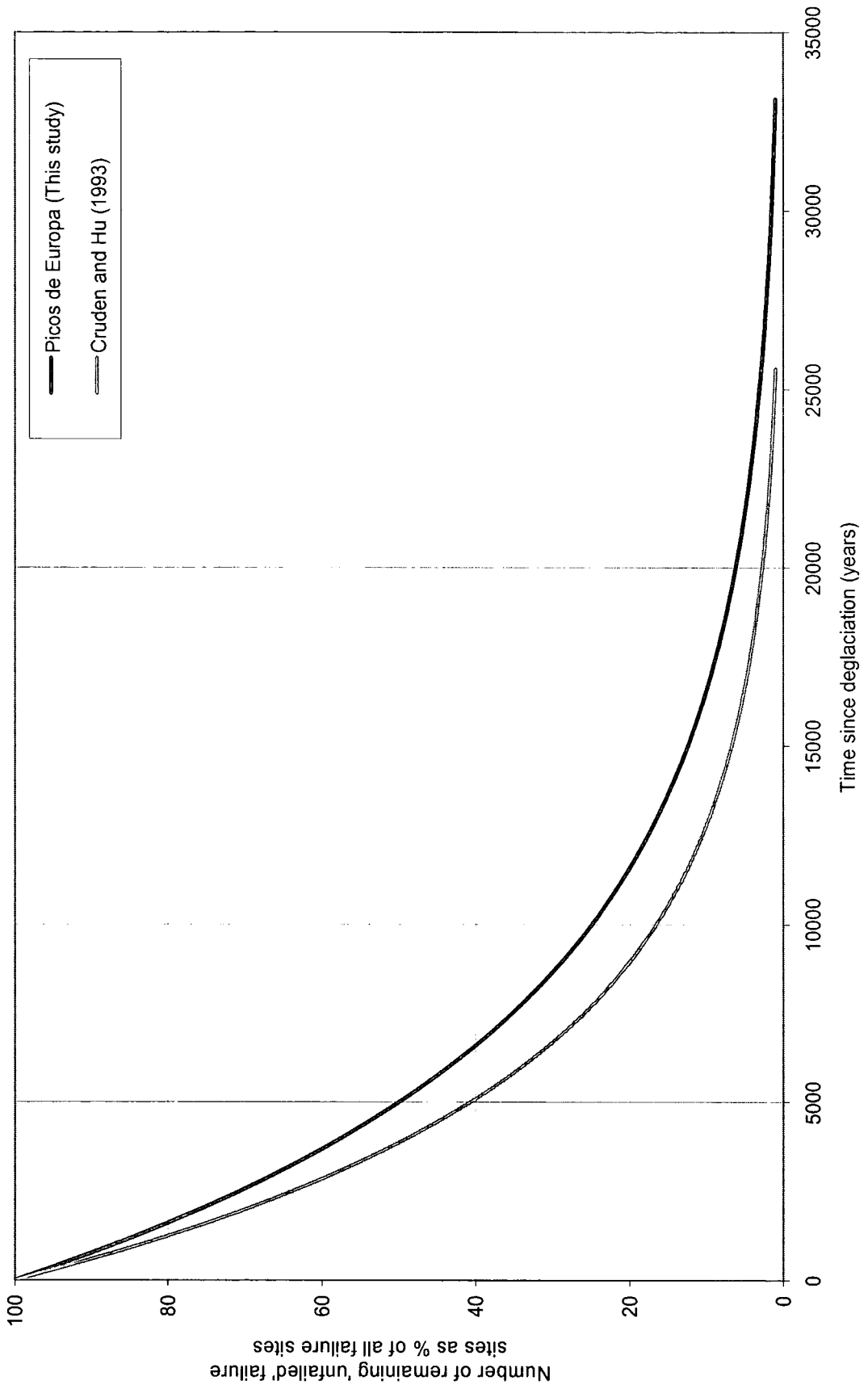

Figure 7.56: Exhaustion model for paraglacial rock slope failure in the Picos de Europa, compared with data from Cruden and Hu (1993) in the Canadian Rockies.

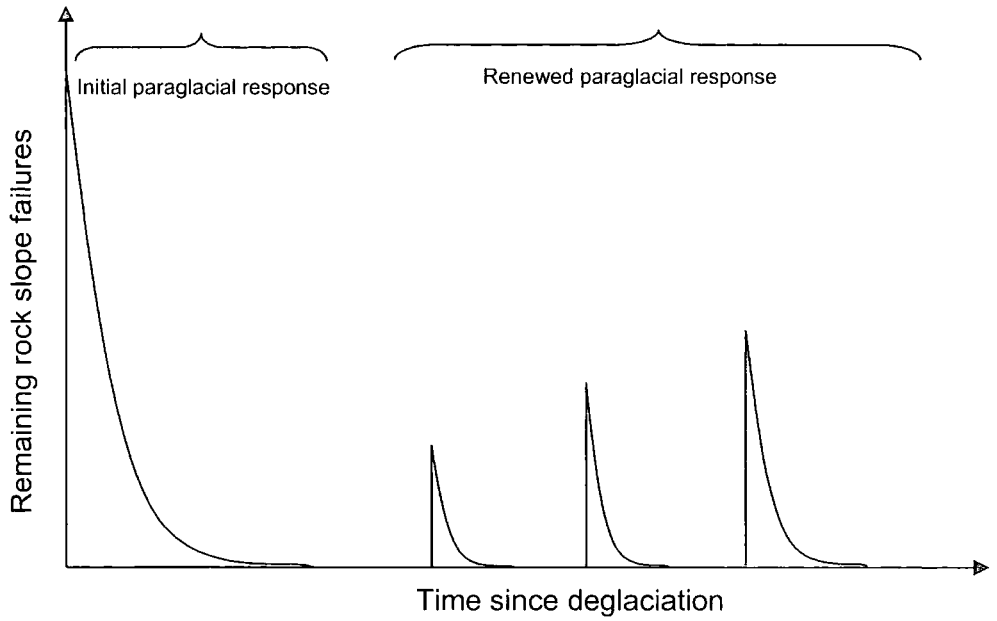

Figure 7.57: Proposed model of paraglacial rock slope evolution for the Picos de Europa based on UDEC modelling, assessment of paraglacial exhaustion models and cosmogenic dating.

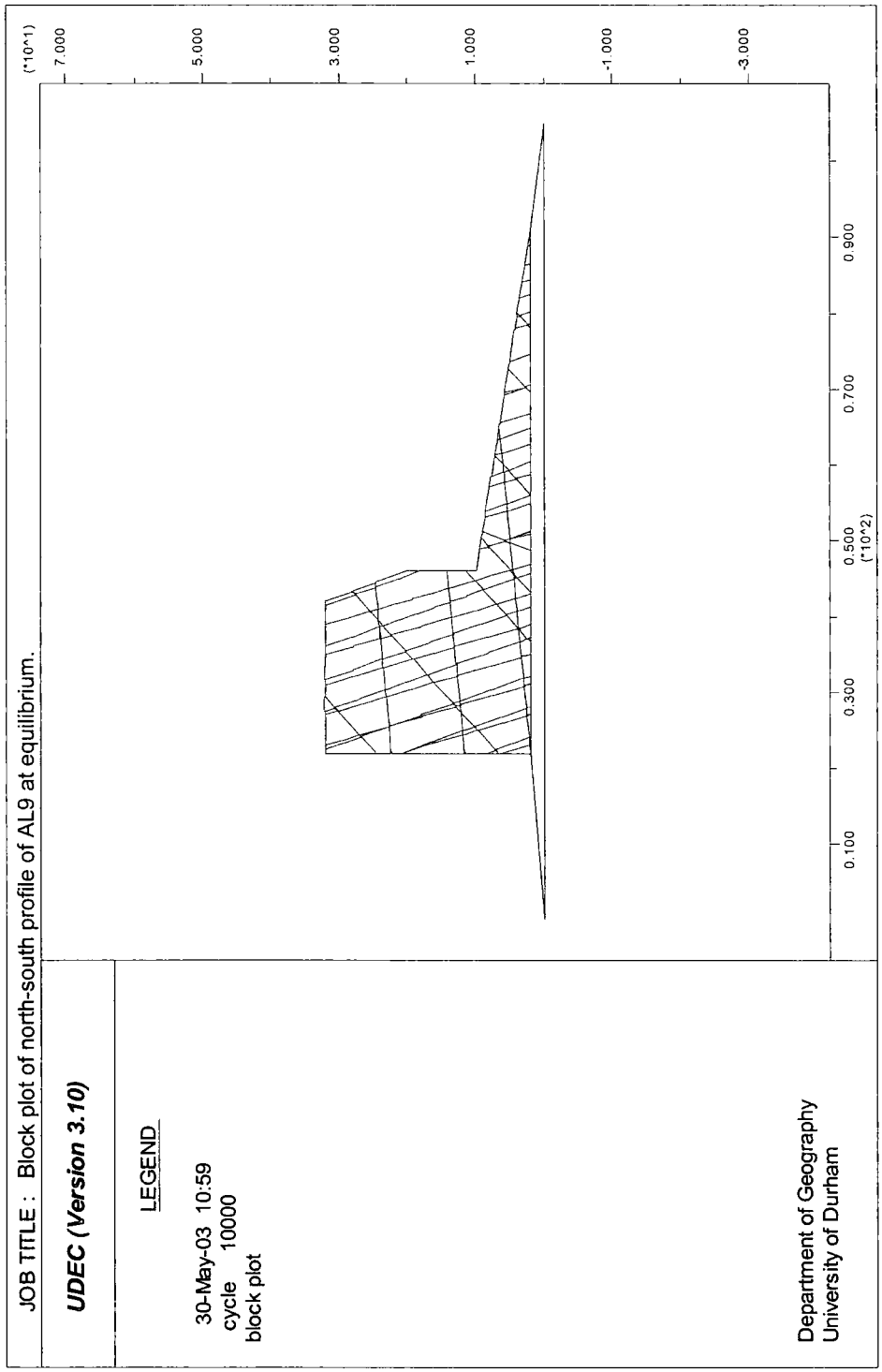

Figure 8.1: Block plot of the north-south profile of AL9 at equilibrium.

Figure 8.2: Total unbalanced forces for the north-south profile of AL9 at equilibrium.

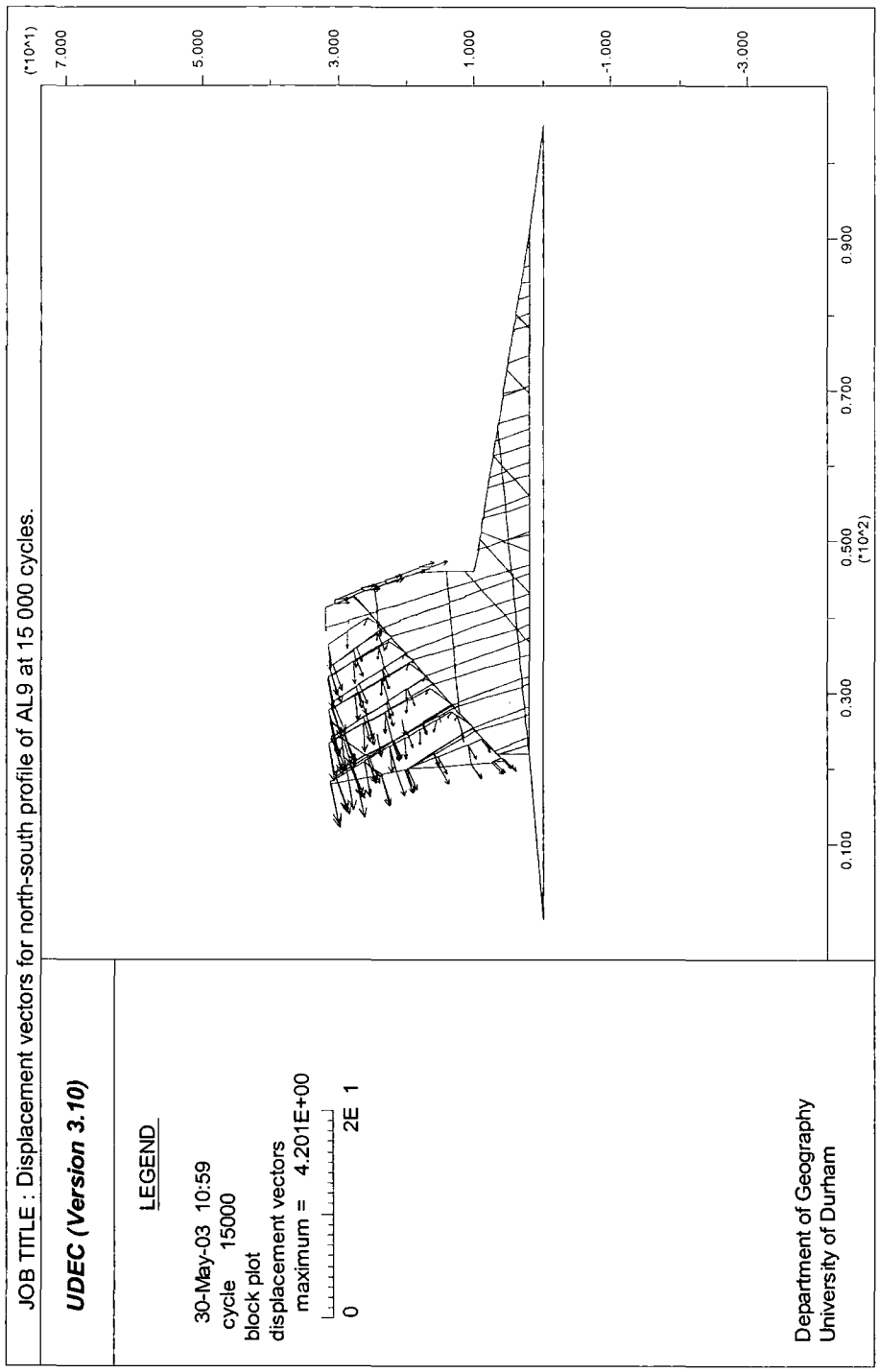

Figure 8.3a: Displacement vectors for the north-south profile of AL9 at 15 000 cycles.

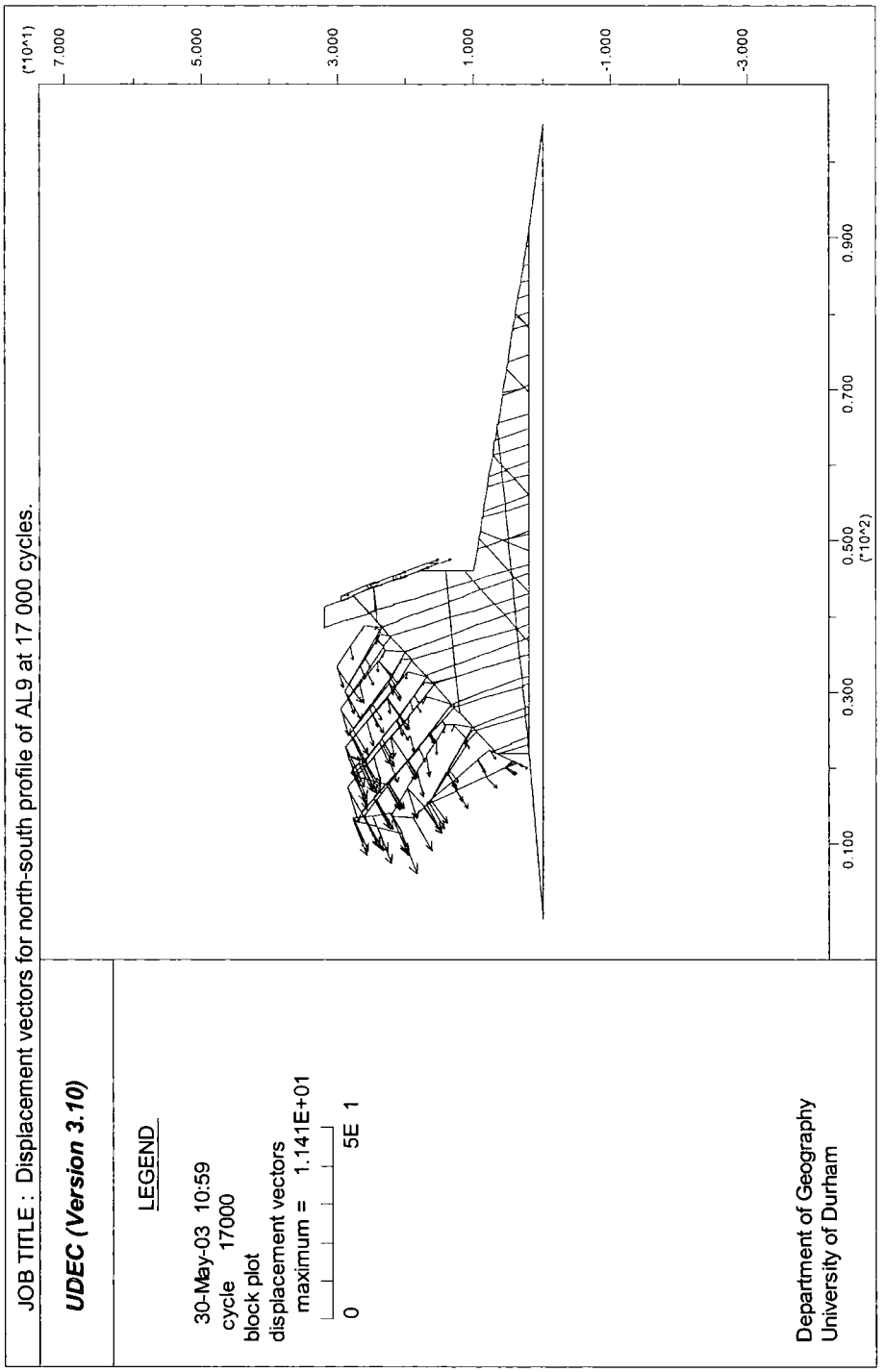

Figure 8.3b: Displacement vectors for the north-south profile of AL9 at 17 000 cycles.

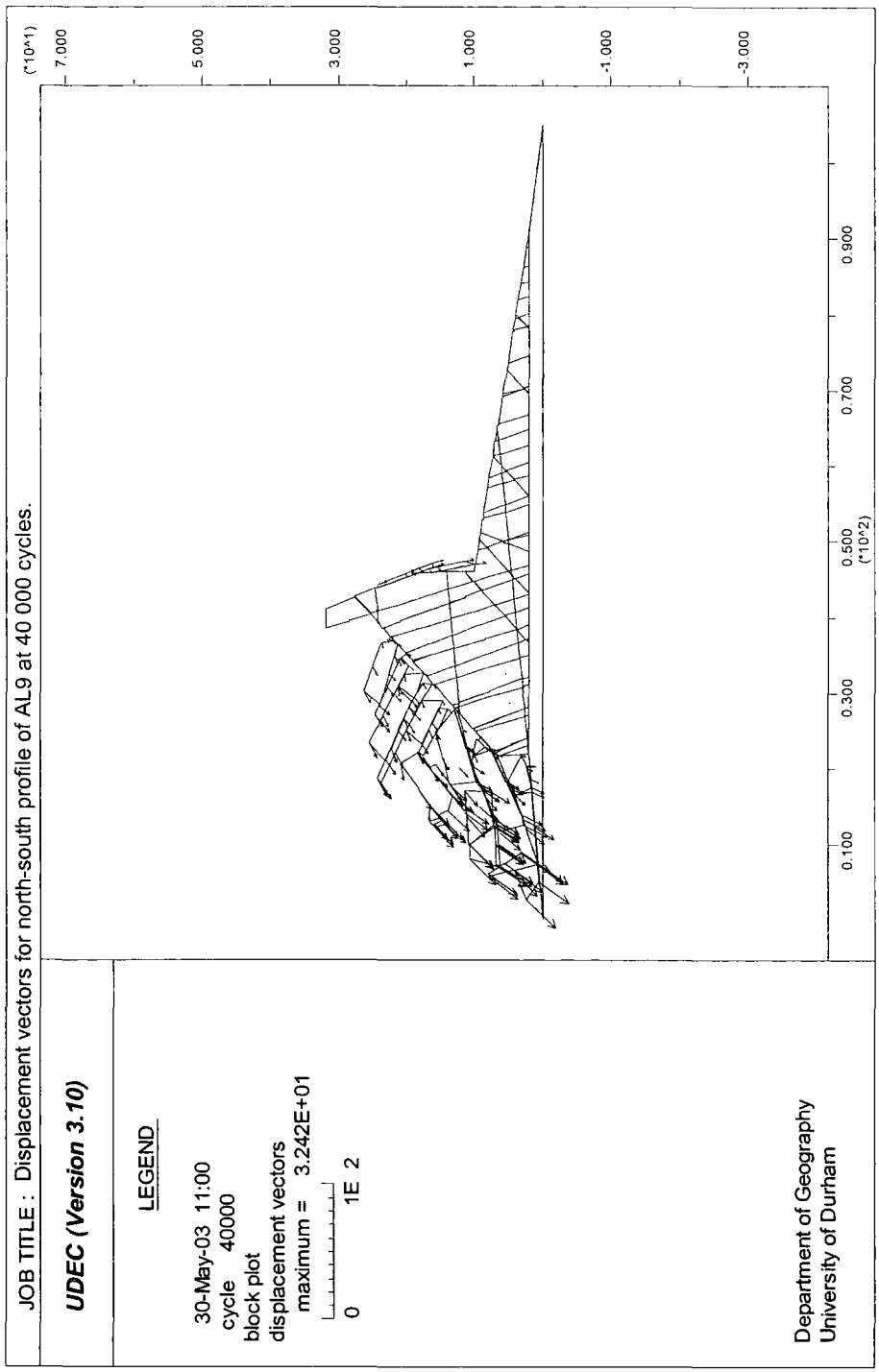

Figure 8.3c: Displacement vectors for the north-south profile of AL9 at 40 000 cycles.

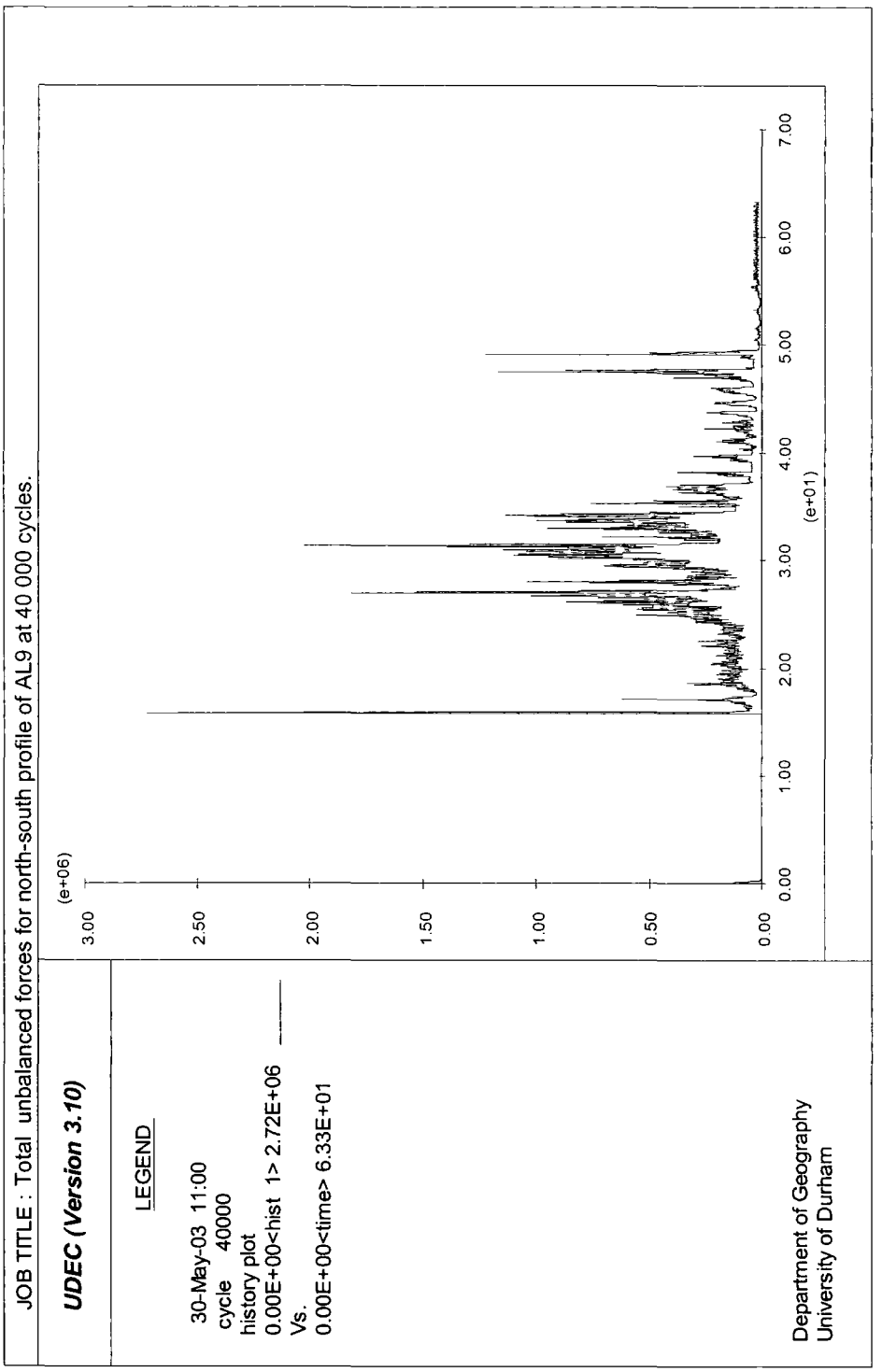

Figure 8.4: Total unbalanced forces for the north-south profile of AL9 at 40 000 cycles.

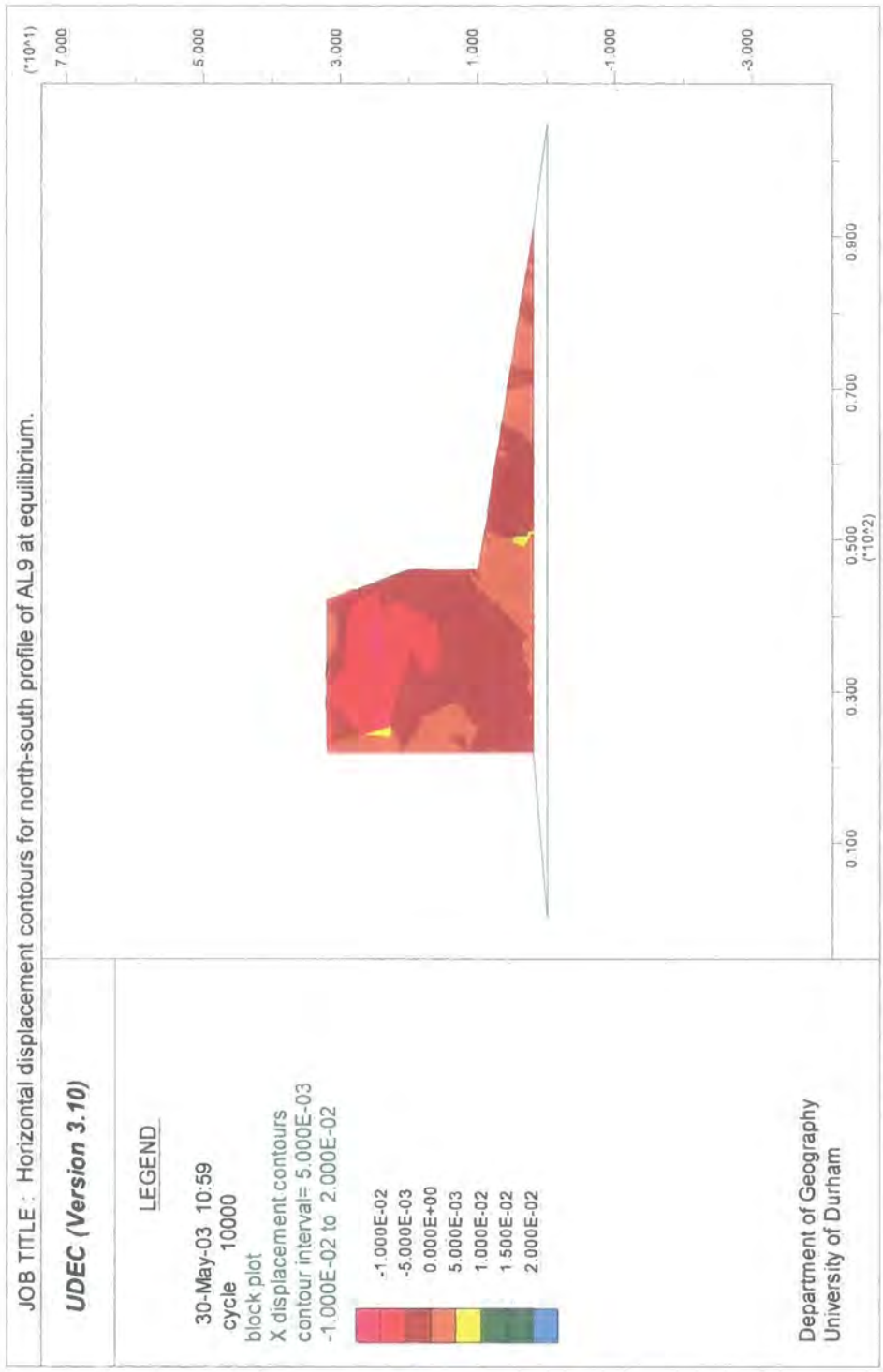

Figure 8.5a: Horizontal displacement contours for the north-south profile of AL9 at equilibrium.

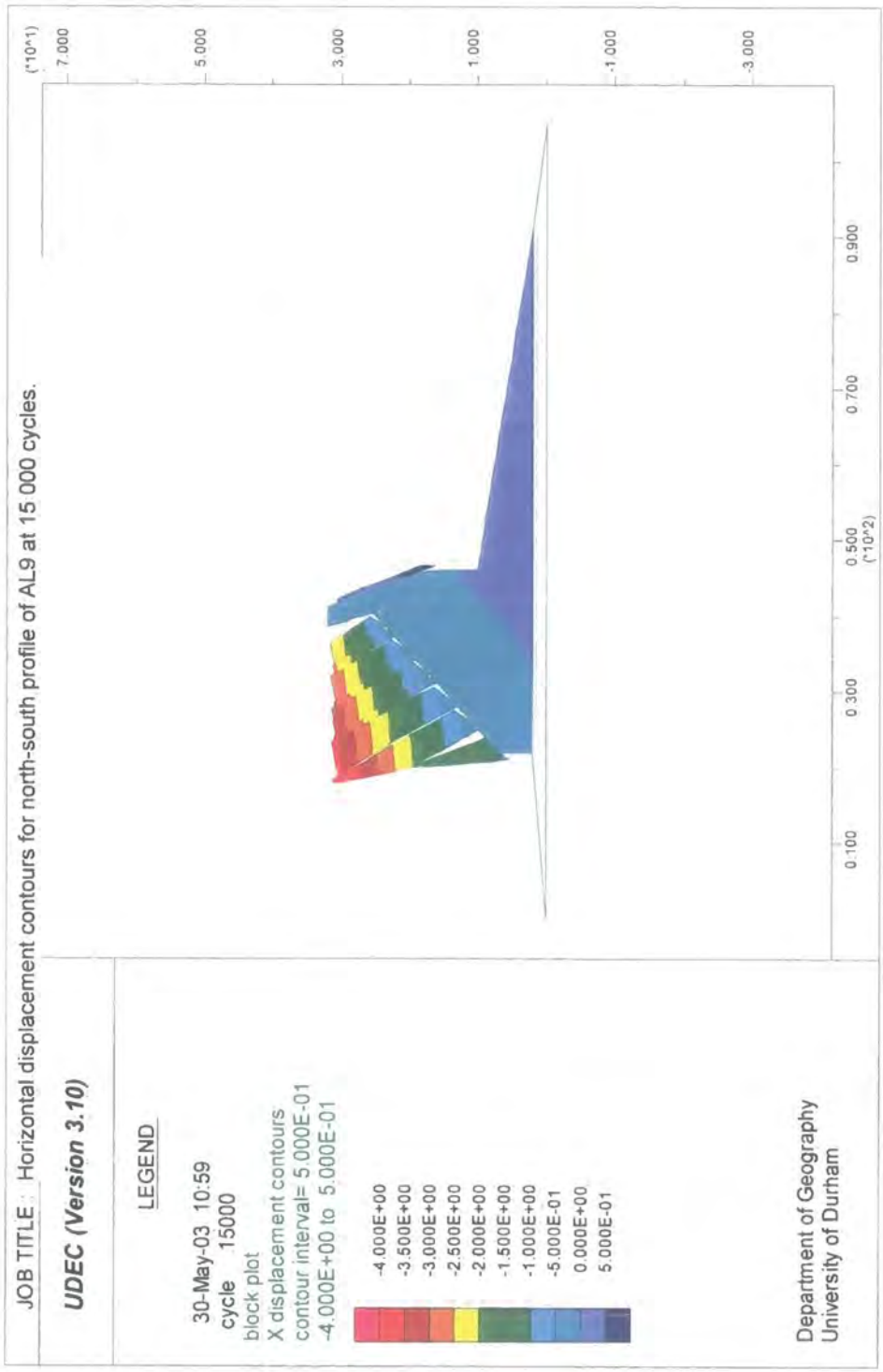

Figure 8.5b: Horizontal displacement contours for the north-south profile of AL9 at 15 000 cycles.

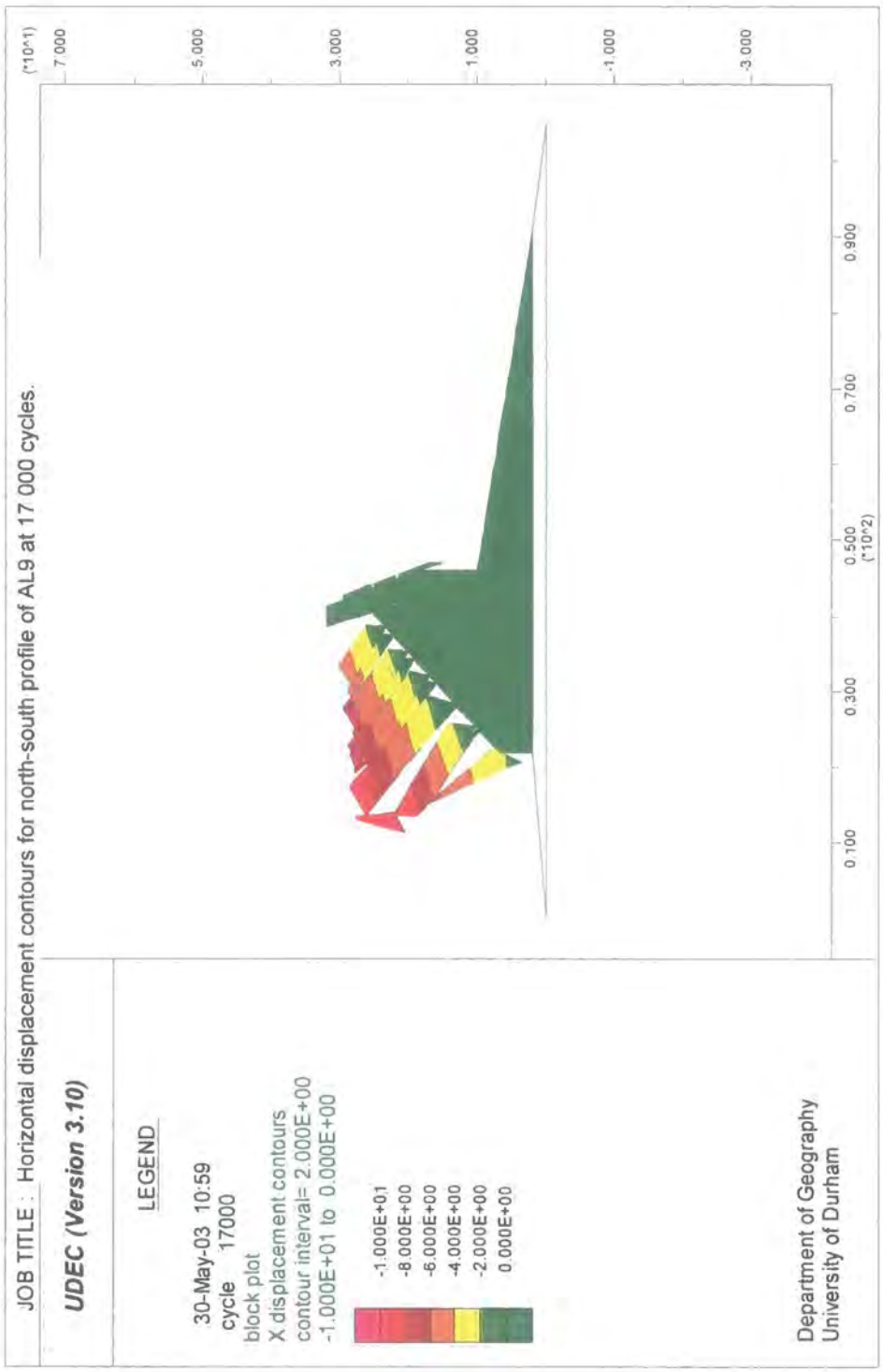

Figure 8.5c: Horizontal displacement contours for the north-south profile of AL9 at 17 000 cycles.

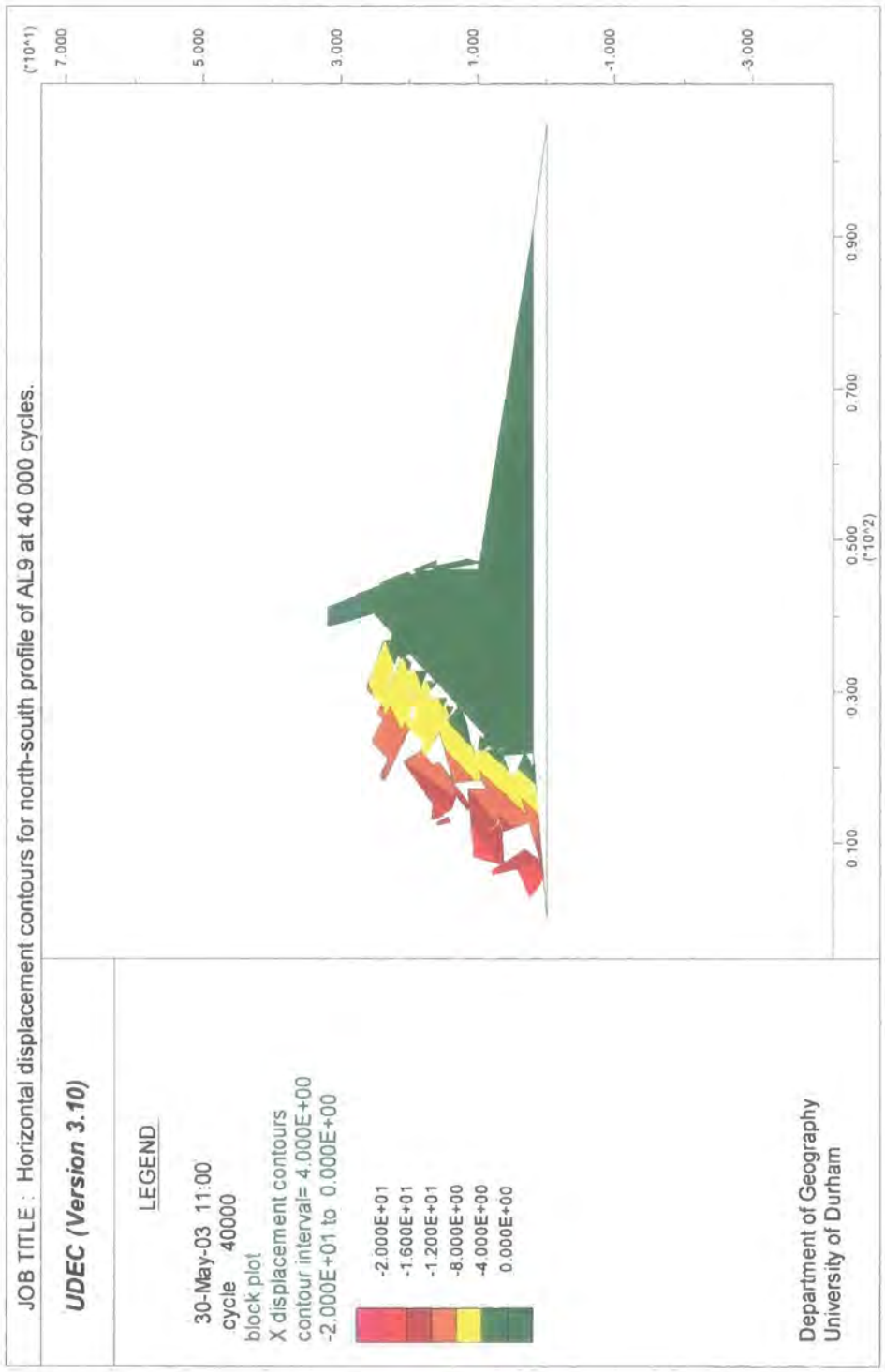

Figure 8.5d: Horizontal displacement contours for the north-south profile of AL9 at 40 000 cycles.

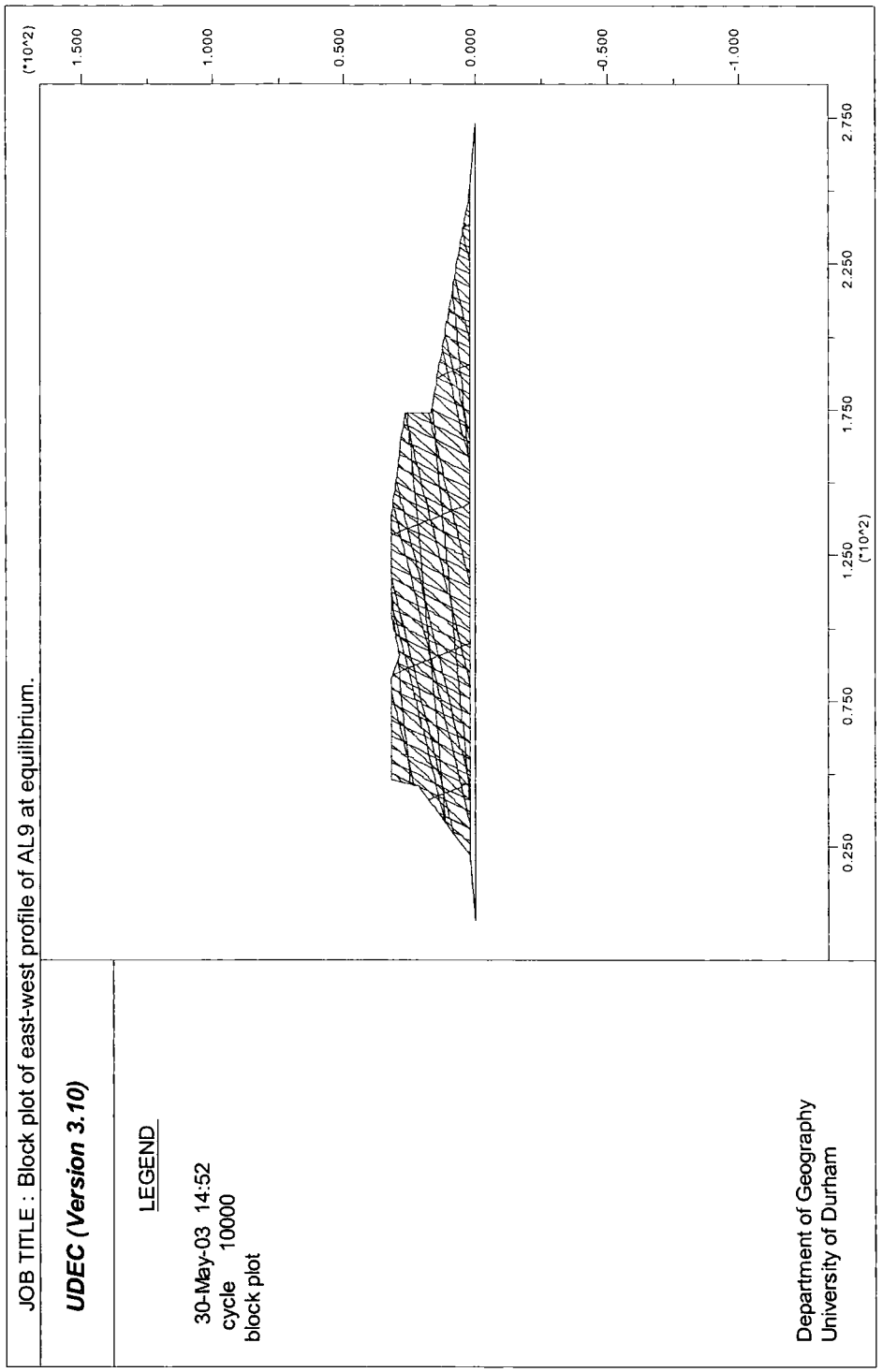

Figure 8.6a: Block plot of the east-west profile of AL9 at equilibrium.

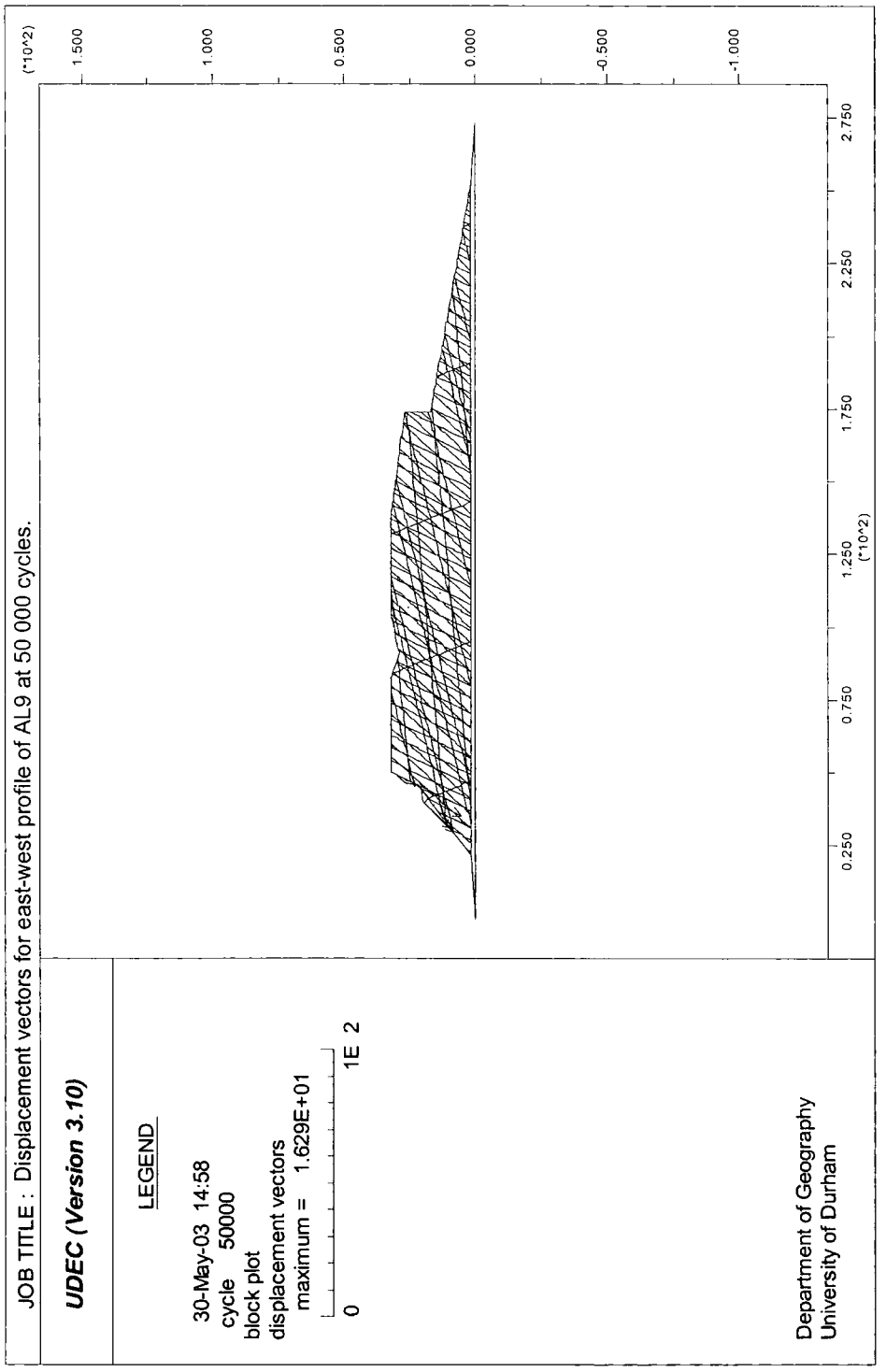

Figure 8.6b: Displacement vectors for the east-west profile of AL9 at 50 000 cycles.

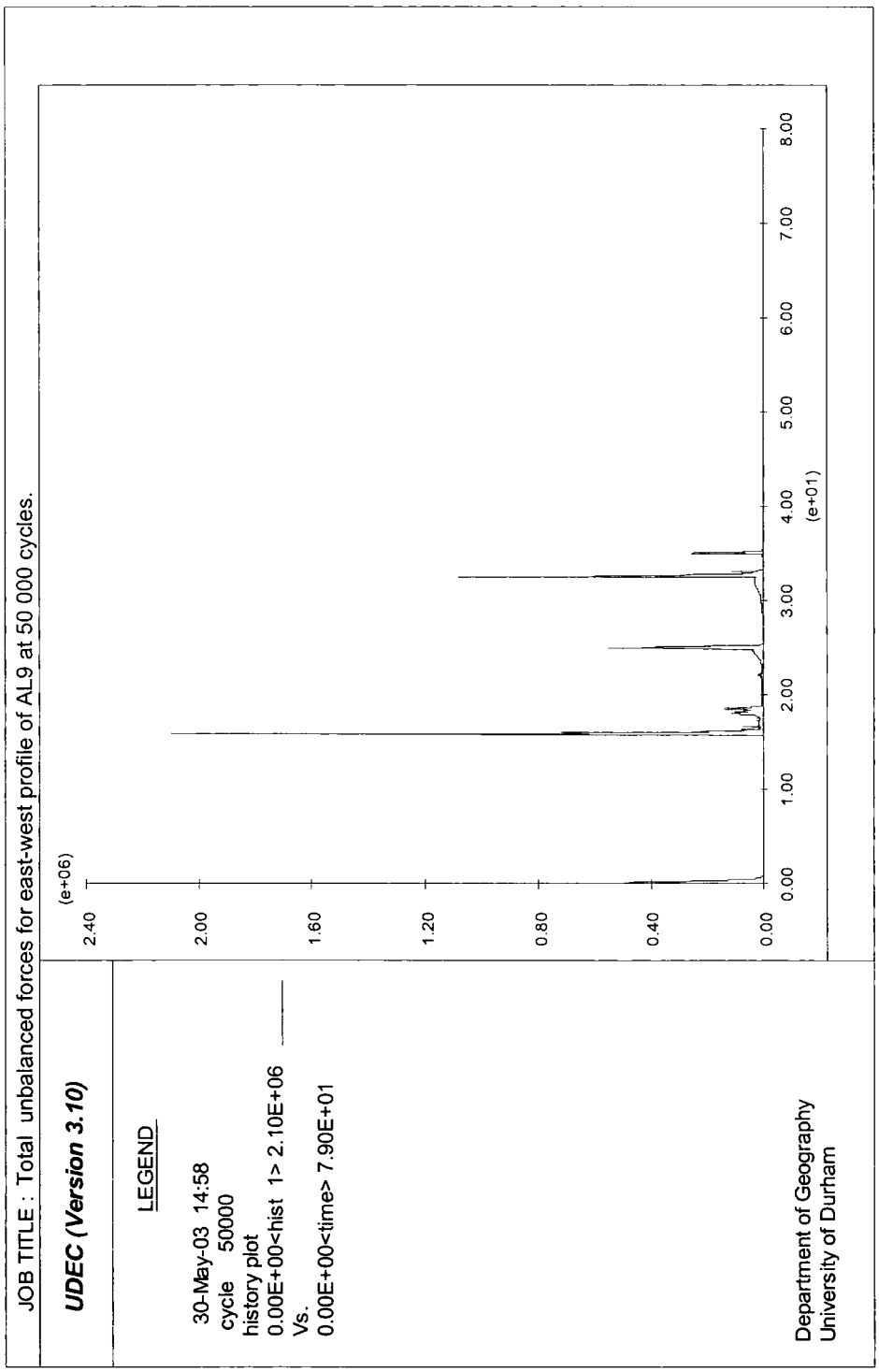

Figure 8.7: Total unbalanced forces for the east-west profile of AL9 at 50 000 cycles.

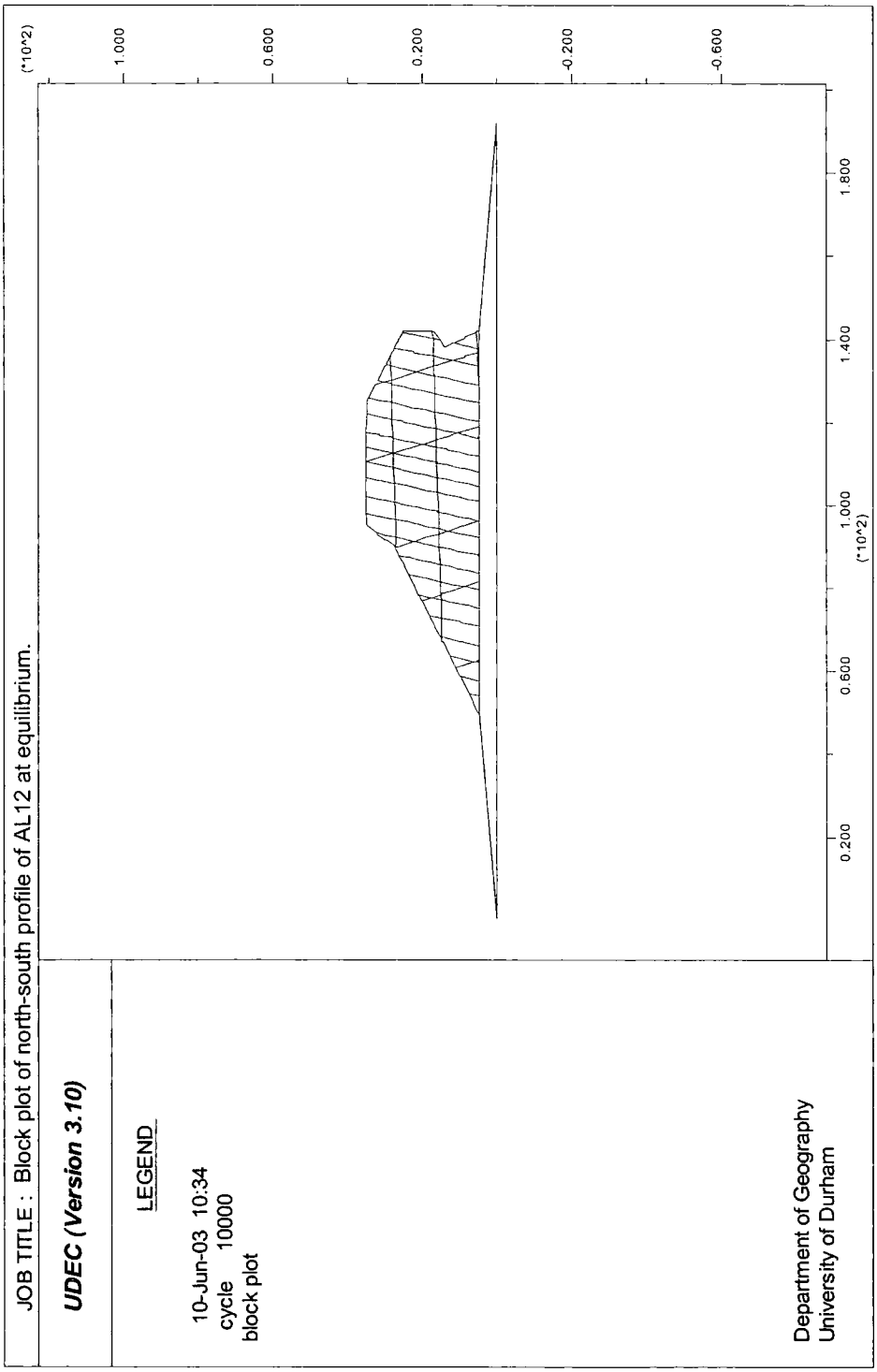

Figure 8.8a: Block plot of the north-south profile of AL12 at equilibrium.

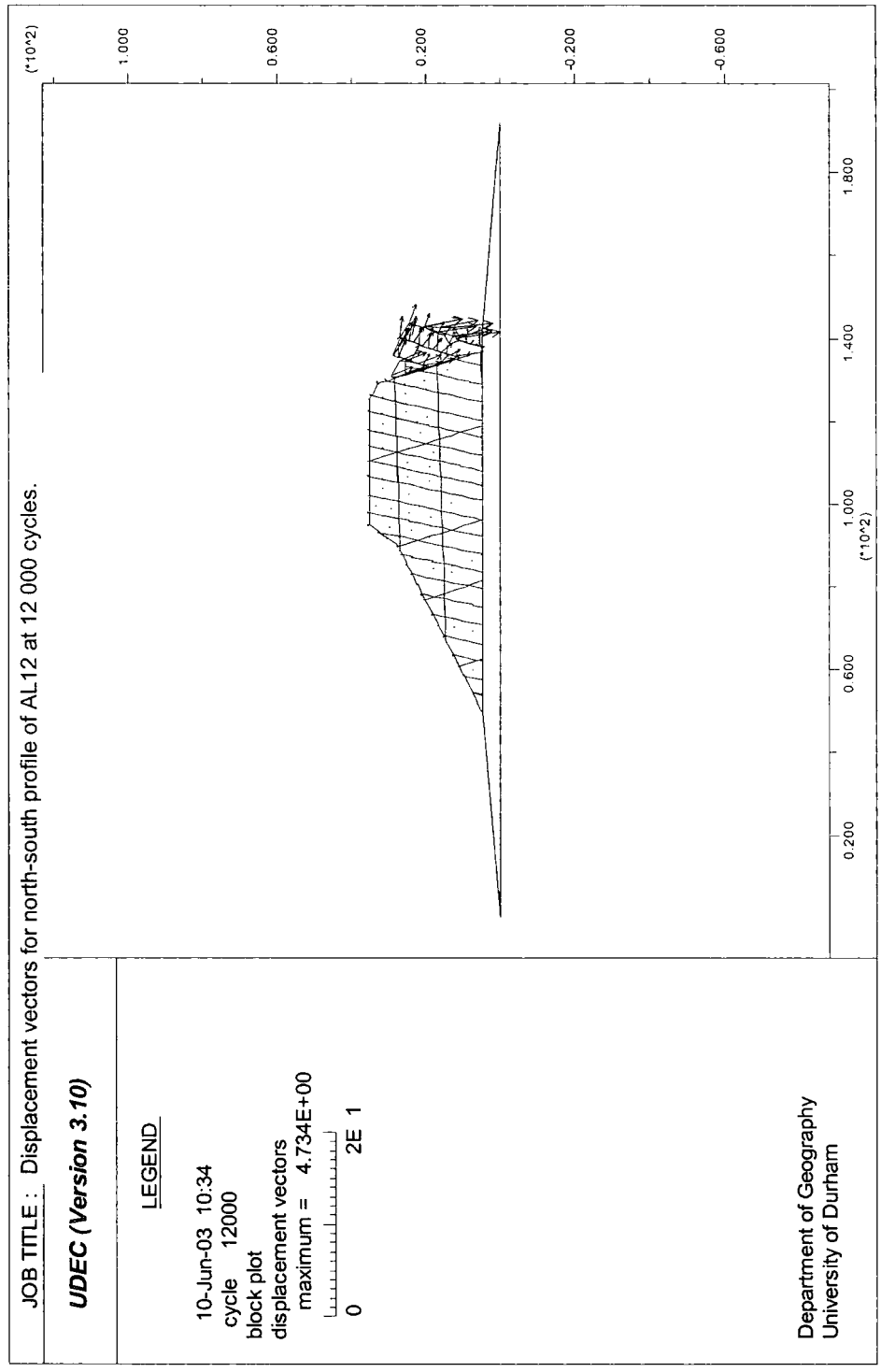

Figure 8.8b: Displacement vectors for the north-south profile of AL12 at 12 000 cycles.

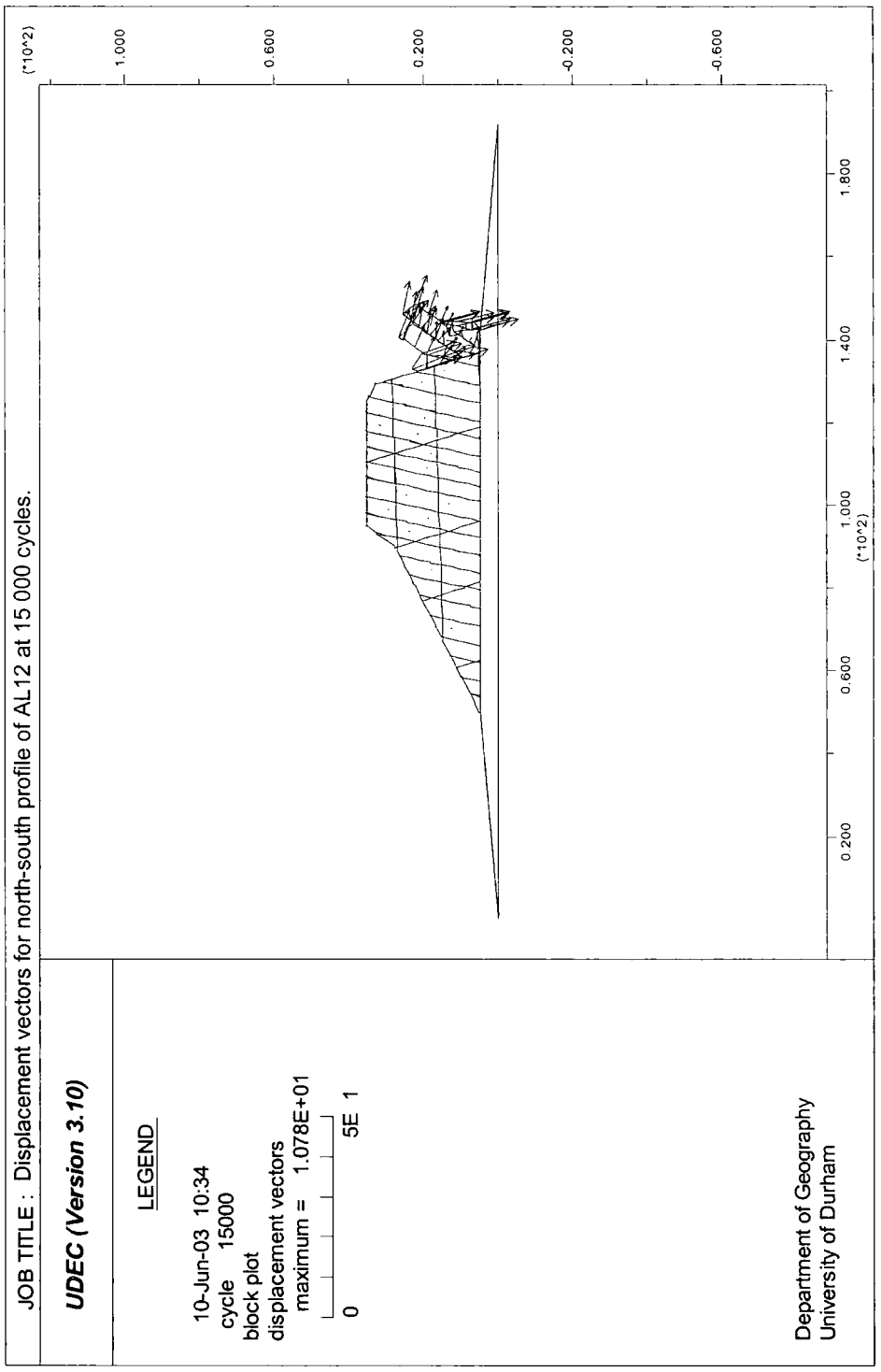

Figure 8.8c: Displacement vectors for the north-south profile of AL12 at 15 000 cycles.

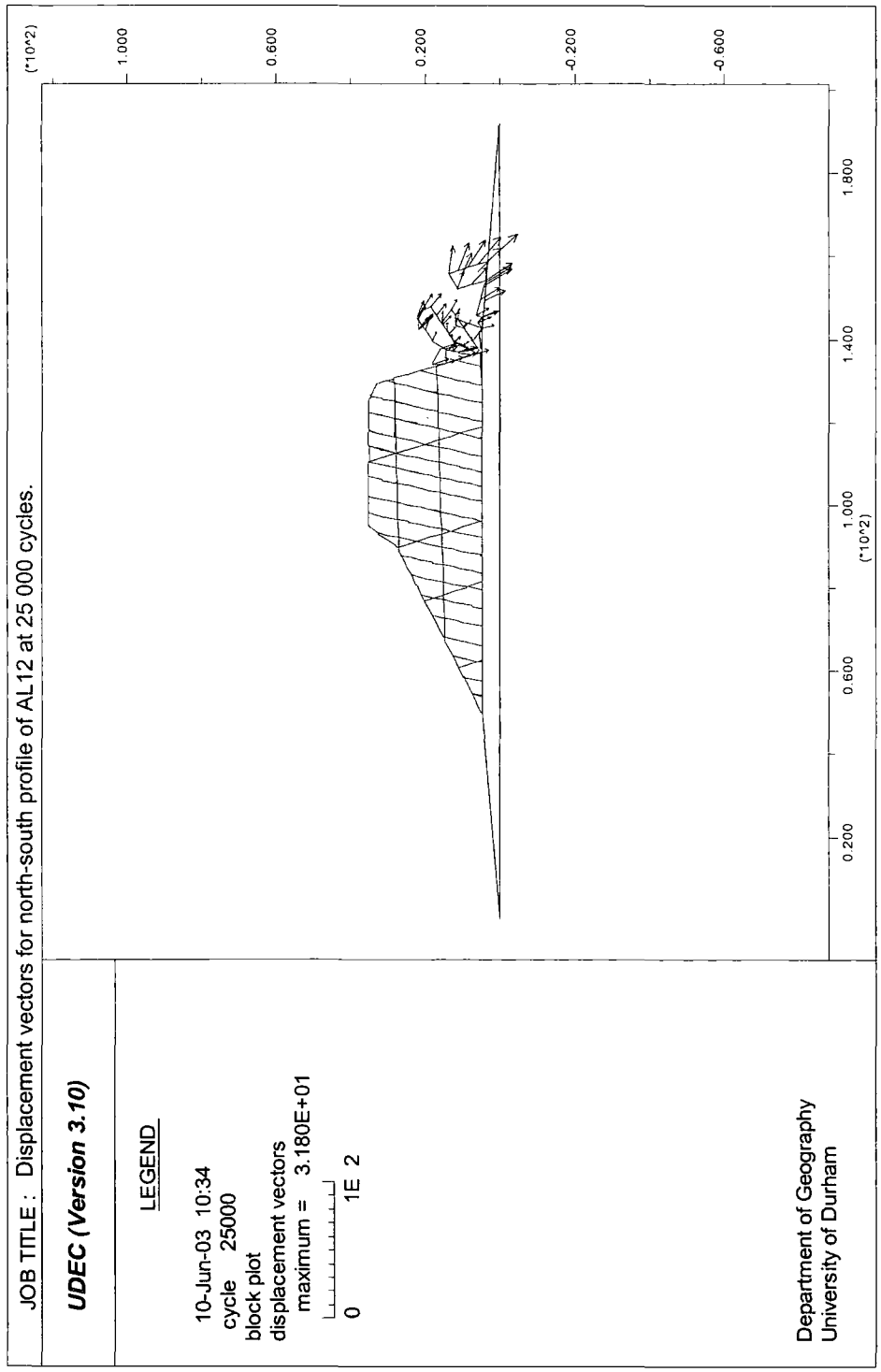

Figure 8.8d: Displacement vectors for the north-south profile of AL12 at 25 000 cycles.

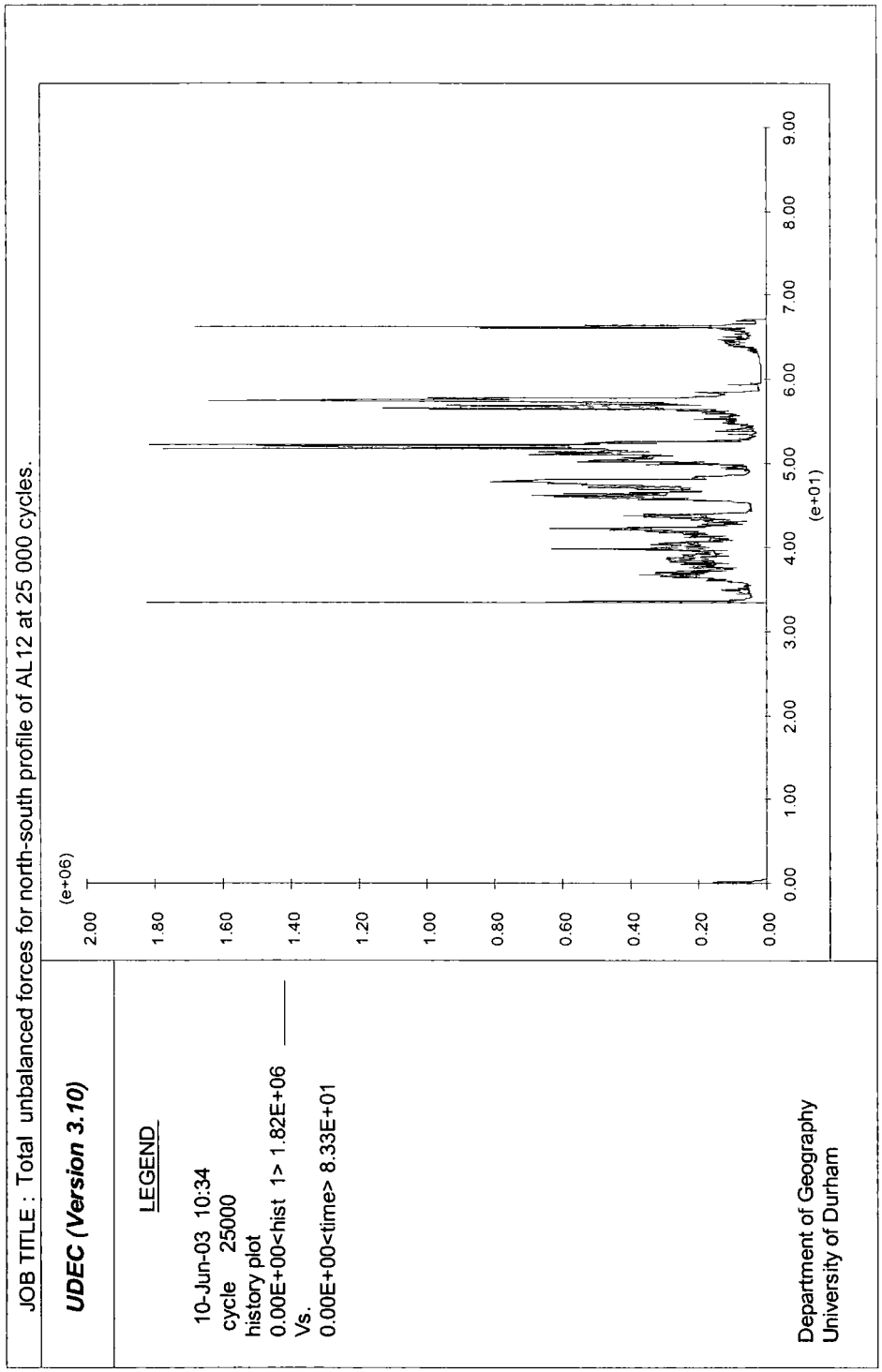

Figure 8.9: Total unbalanced forces for the north-south profile of AL12 at 25 000 cycles.

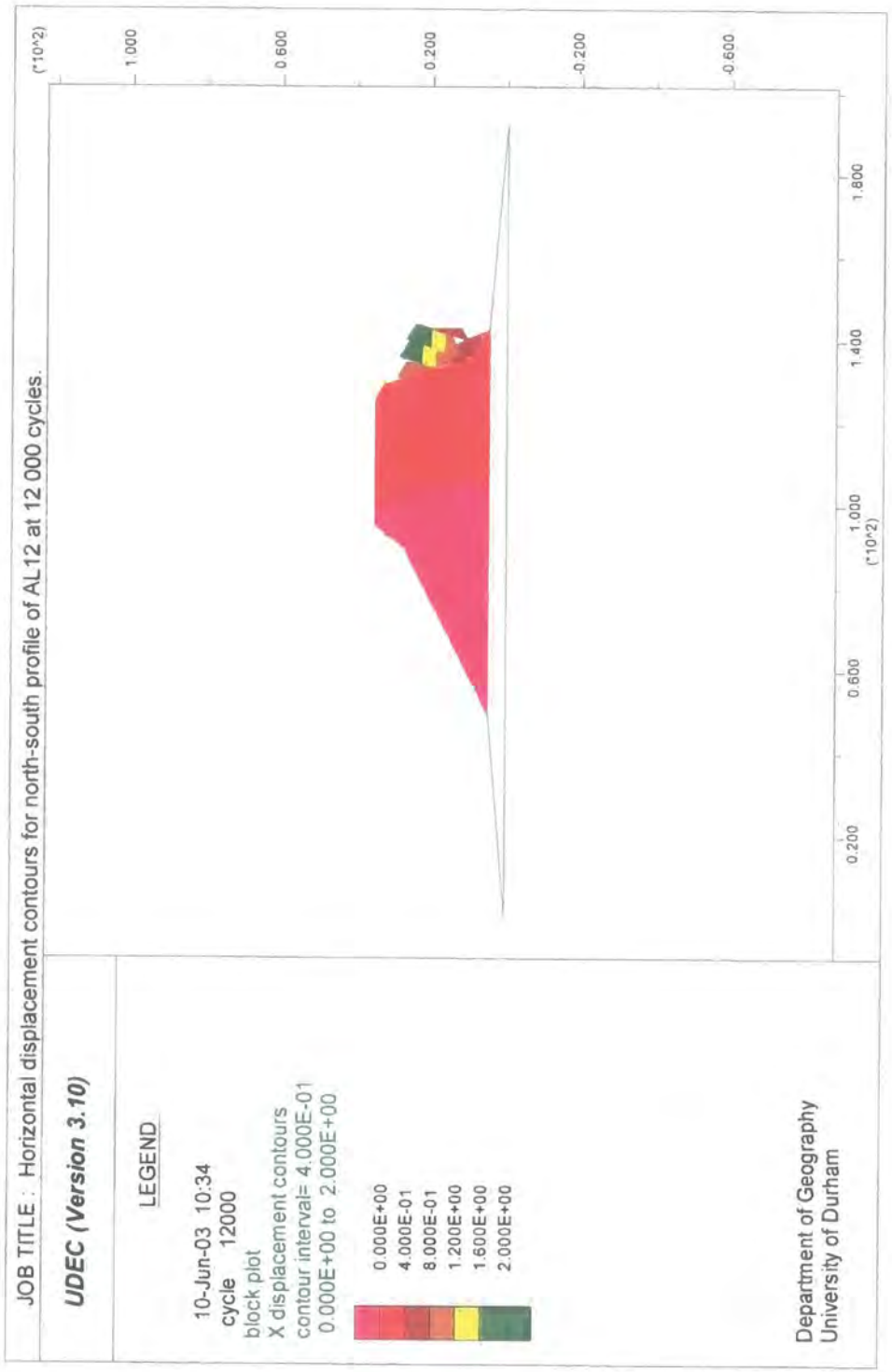

Figure 8.10a: Horizontal displacement contours for the north-south profile of AL12 at 12 000 cycles.

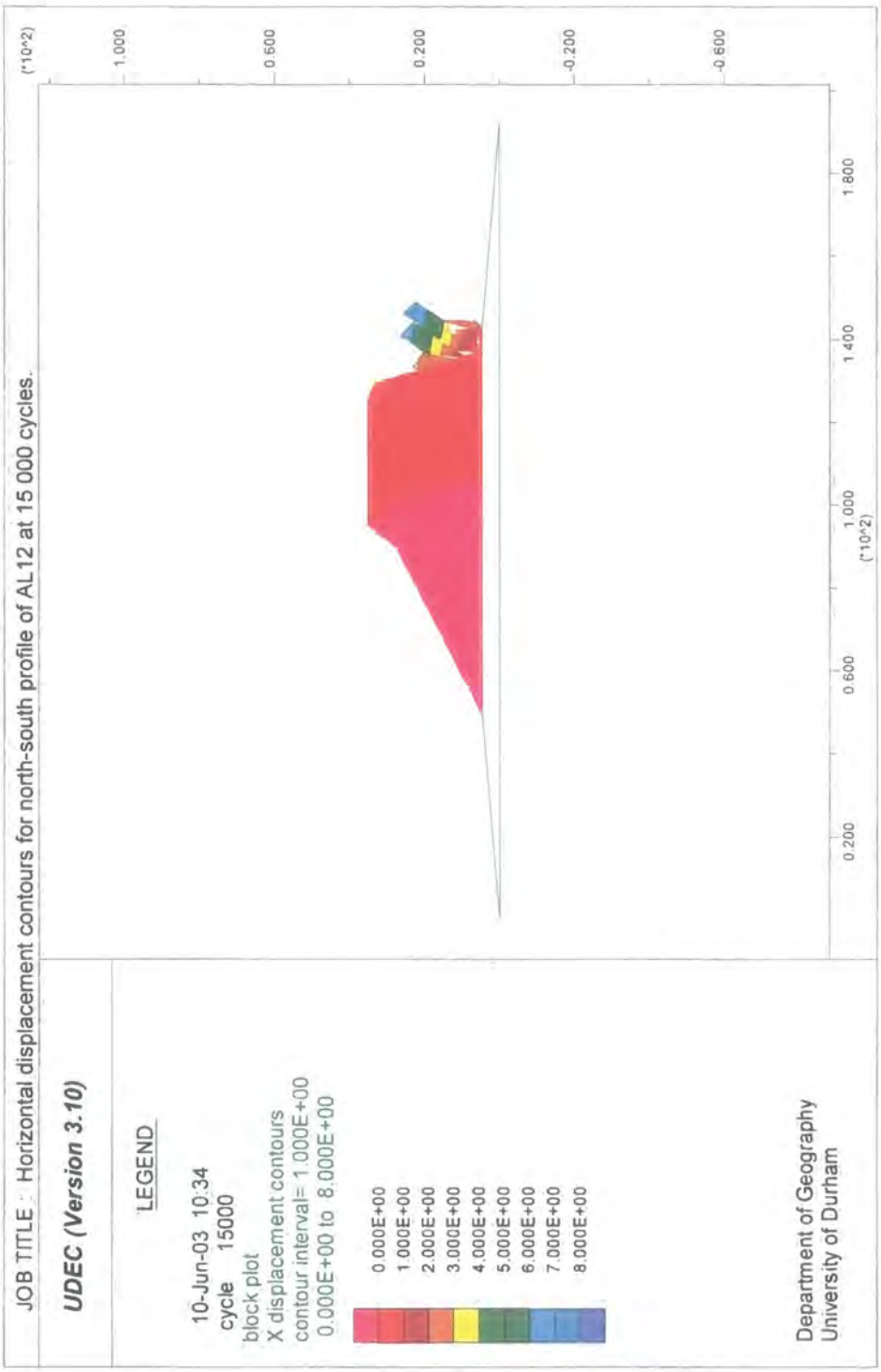

Figure 8.10b: Horizontal displacement contours for the north-south profile of AL12 at 15 000 cycles.

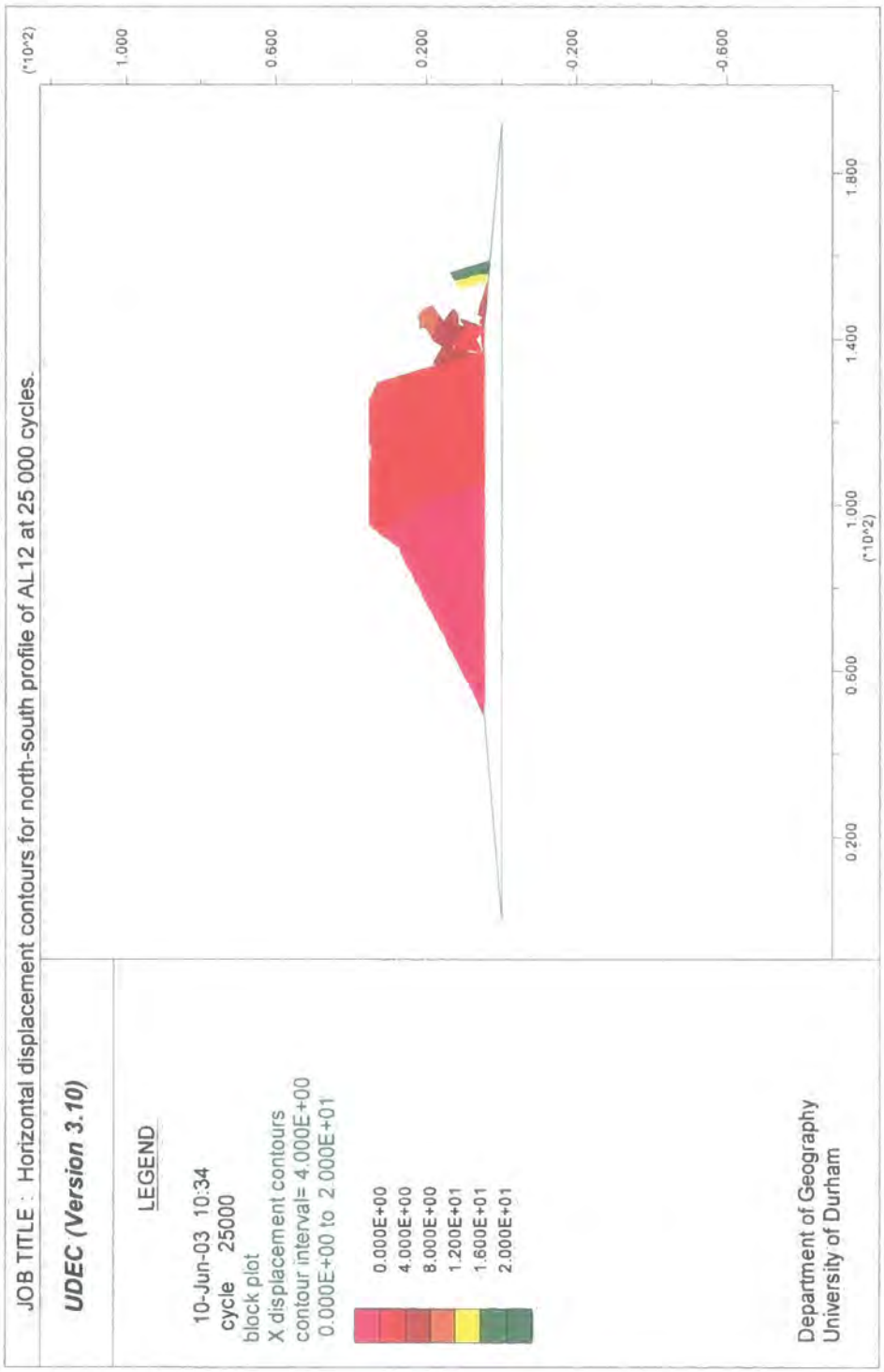

Figure 8.10c: Horizontal displacement contours for the north-south profile of AL12 at 25 000 cycles.

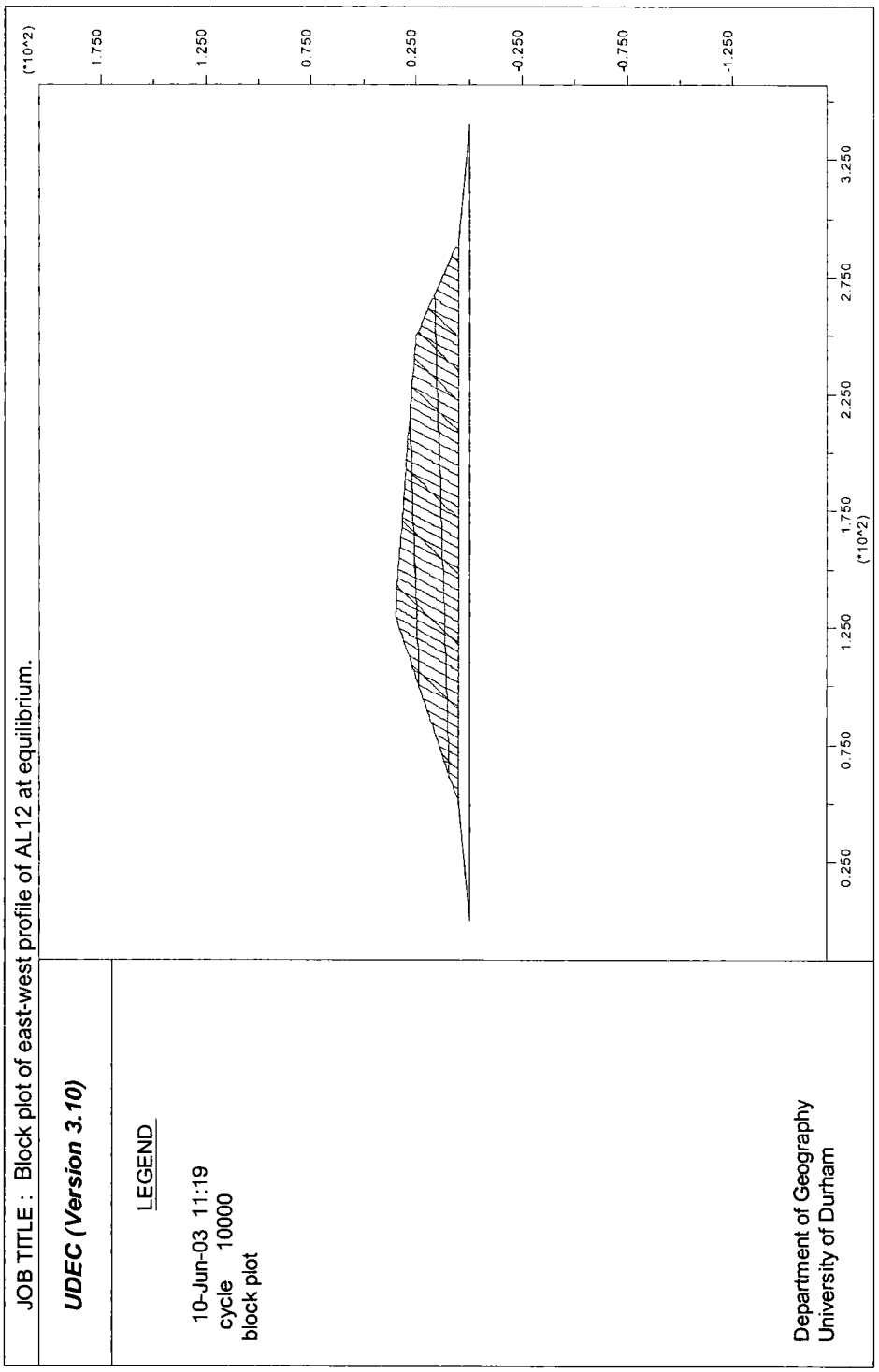

Figure 8.11a: Block plot of the east-west profile of AL12 at equilibrium.

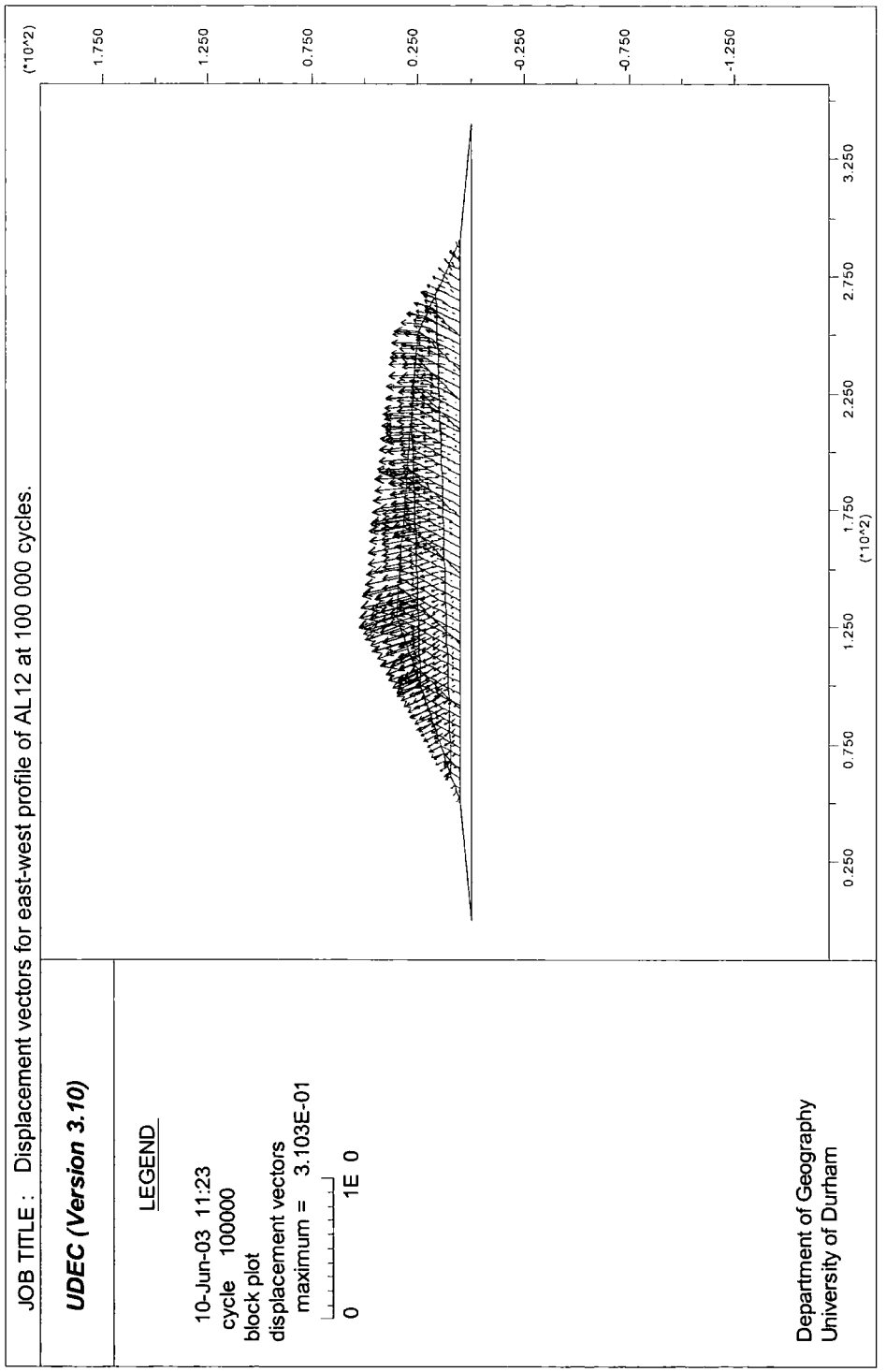

Figure 8.11b: Displacement vectors for the east-west profile of AL12 at 100 000 cycles.

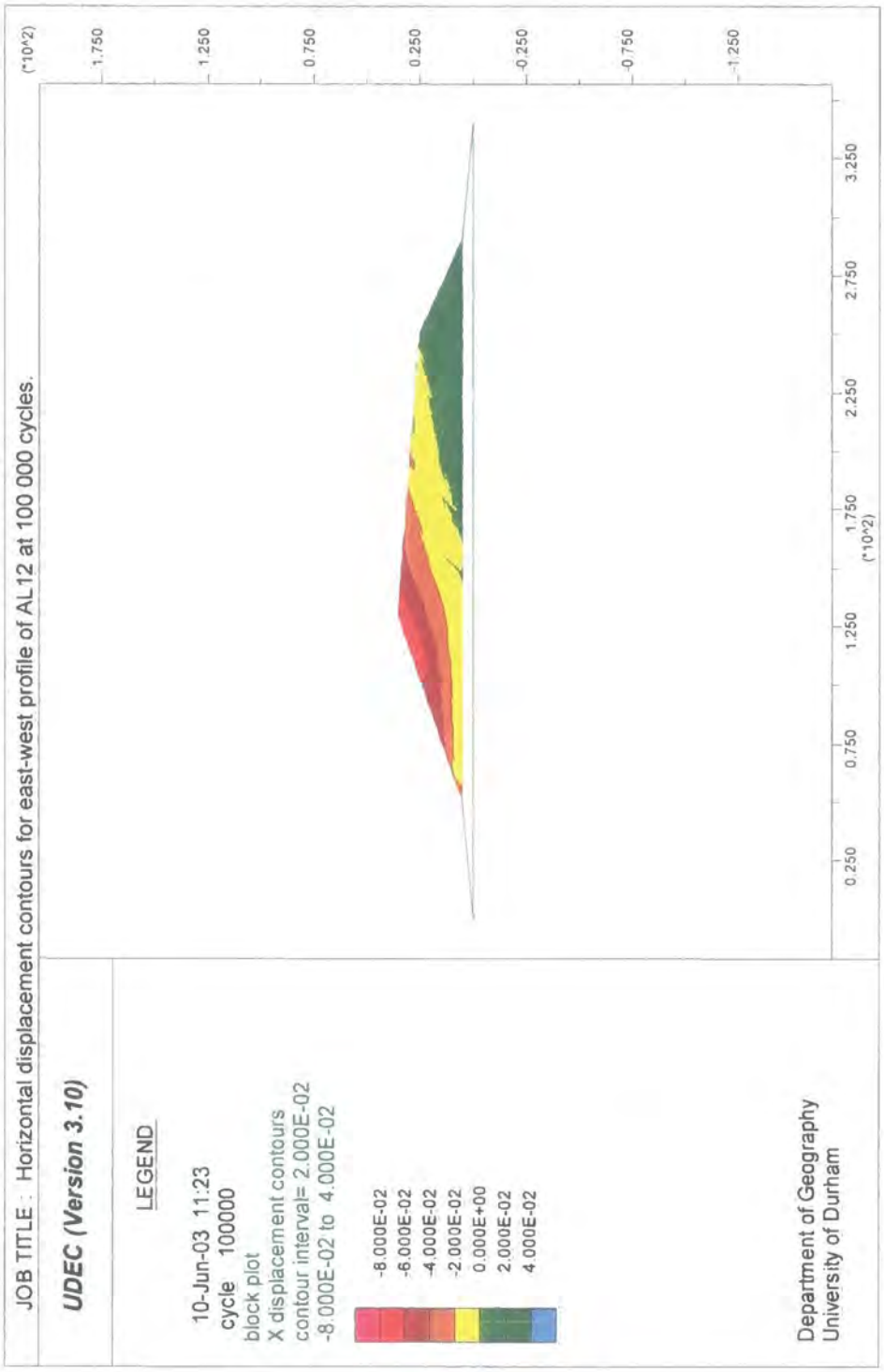

Figure 8.12: Horizontal displacement contours for the east-west profile of AL12 at 100 000 cycles.

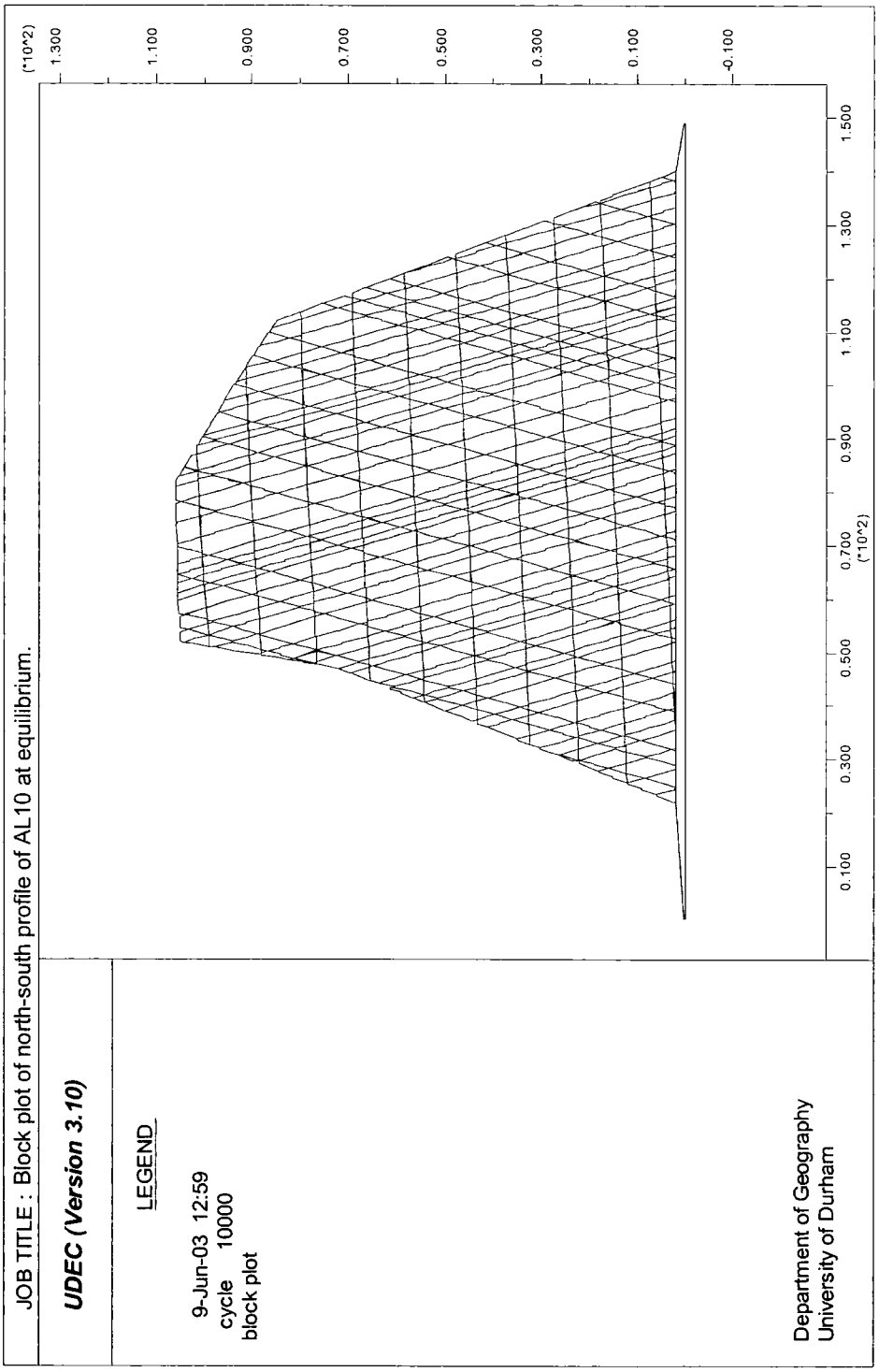

Figure 8.13a: Block plot of the north-south profile of AL10 at equilibrium.

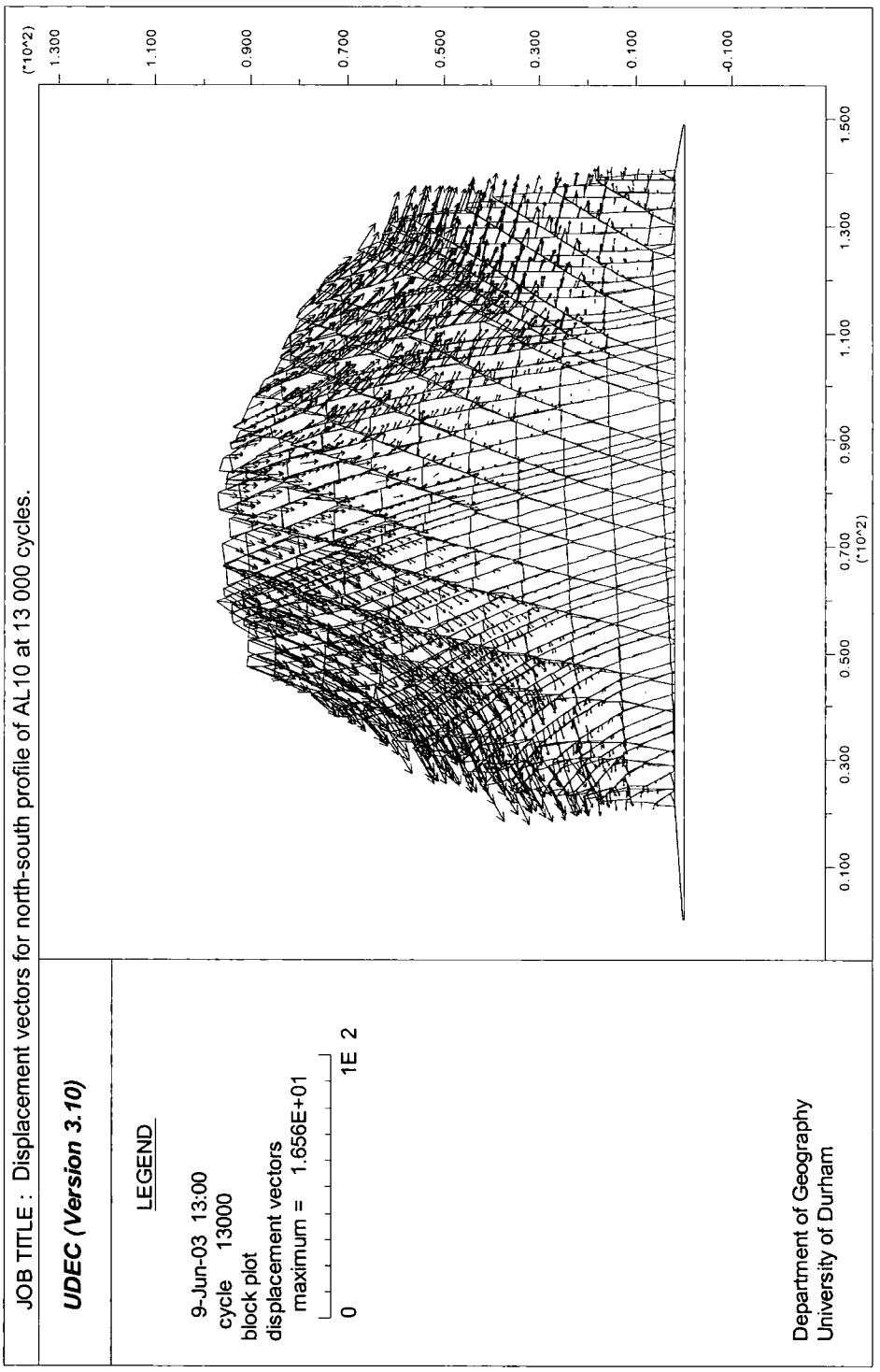

Figure 8.13b: Displacement vectors for the north-south profile of AL10 at 13 000 cycles.

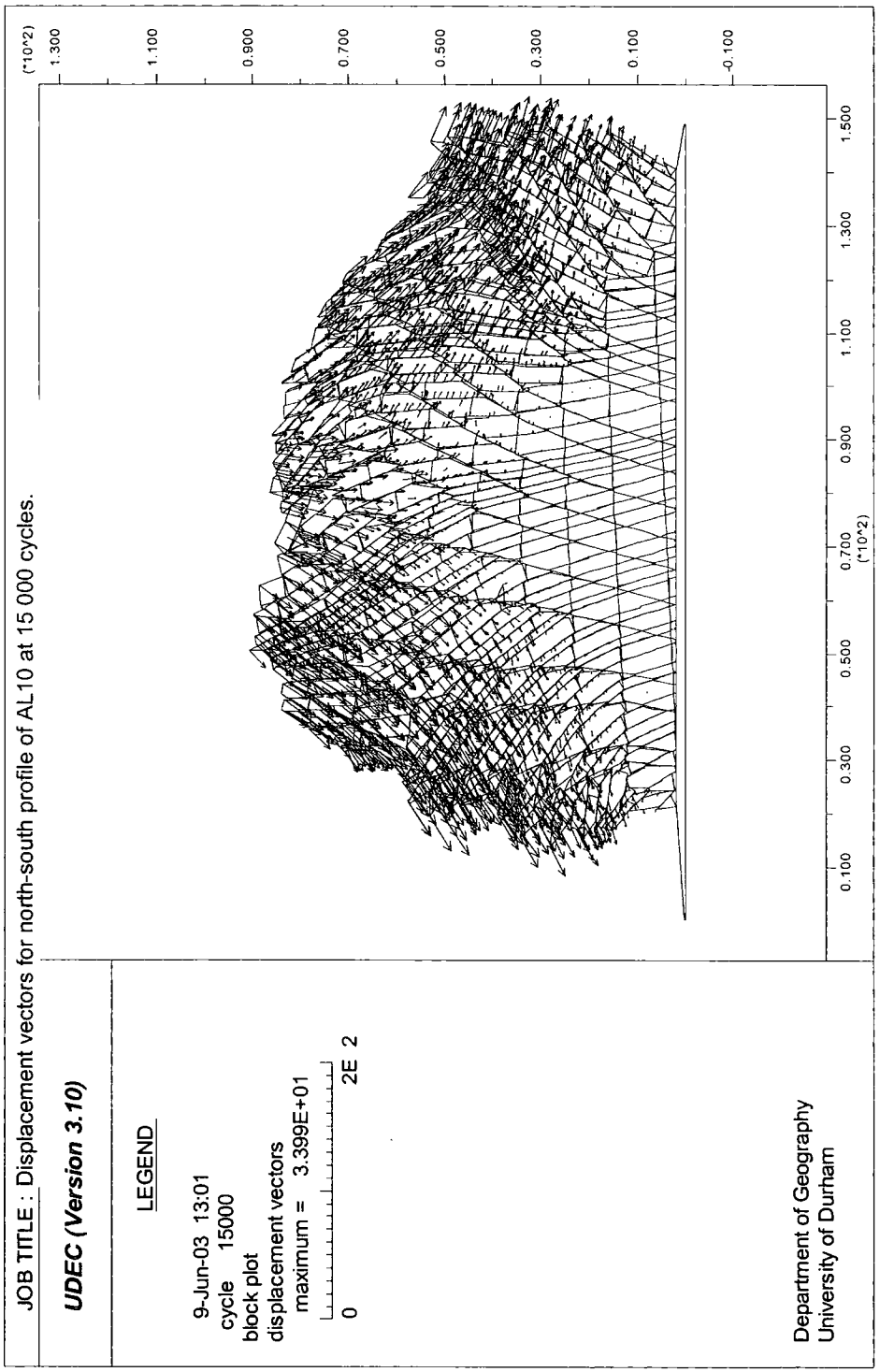

Figure 8.13c: Displacement vectors for the north-south profile of AL10 at 15 000 cycles.

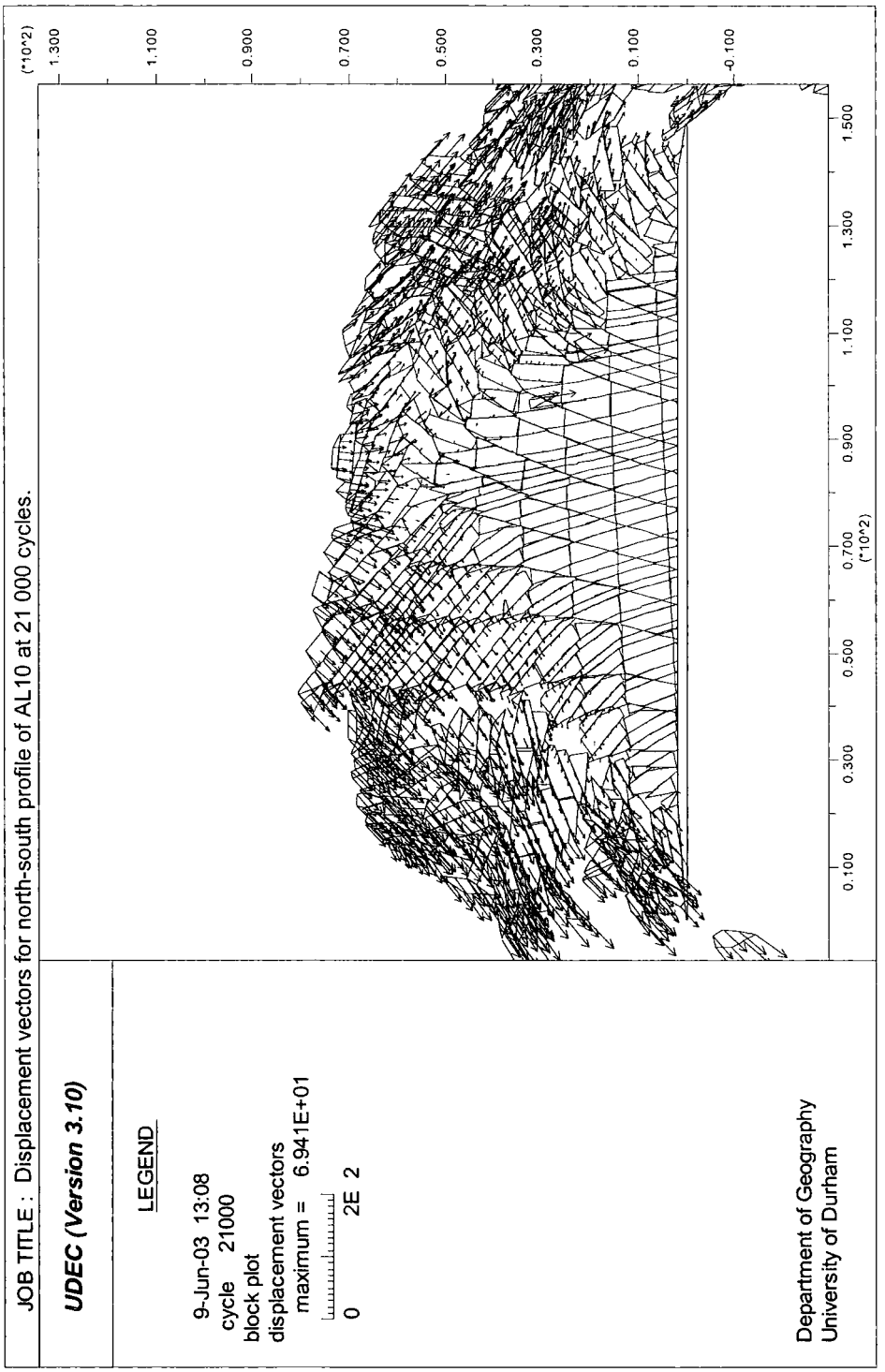

Figure 8.13d: Displacement vectors for the north-south profile of AL10 at 21 000 cycles.

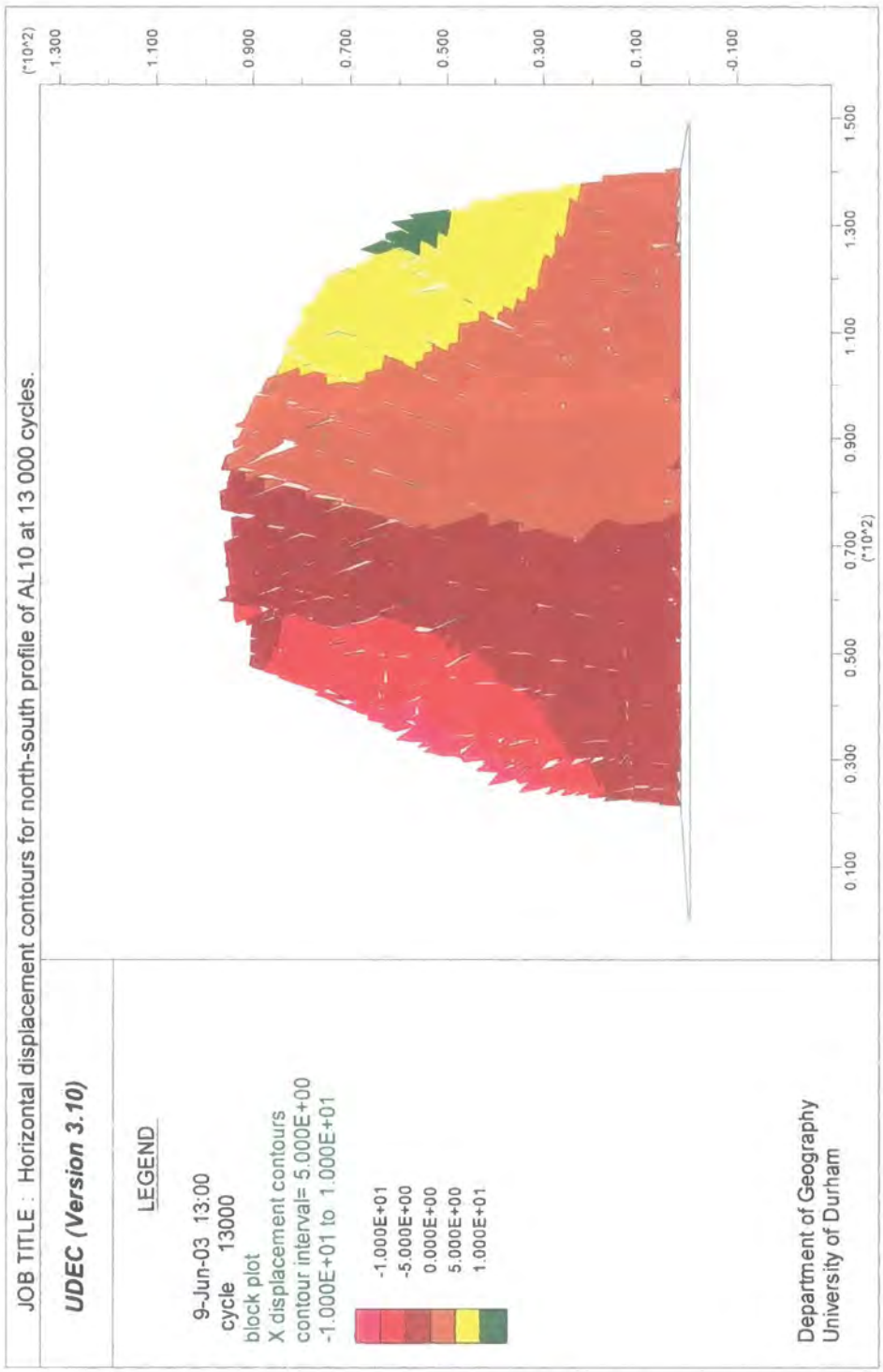

Figure 8.14a: Horizontal displacement contours for the north-south profile of AL10 at 13 000 cycles.

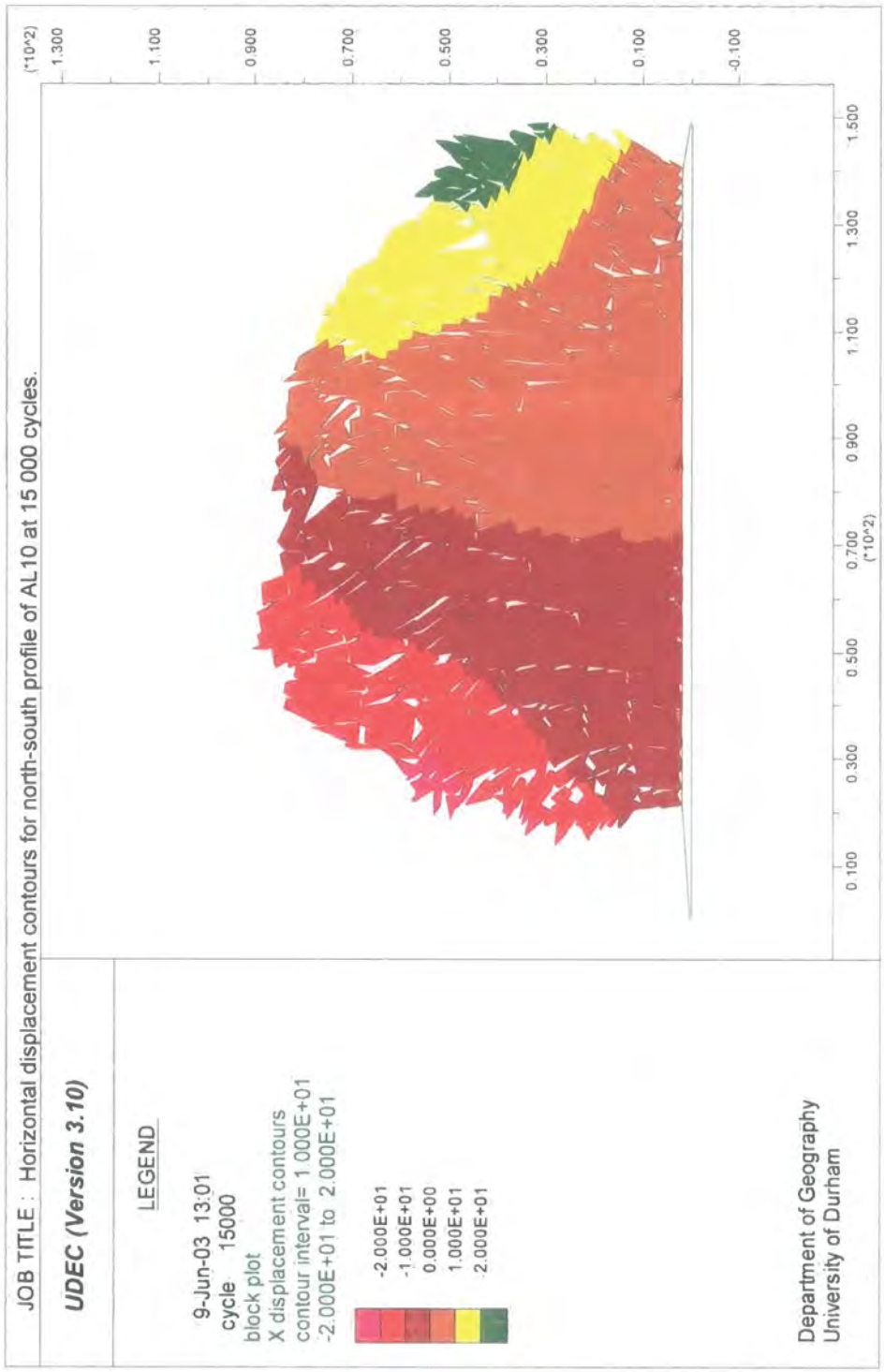

Figure 8.14b: Horizontal displacement contours for the north-south profile of AL10 at 15 000 cycles.

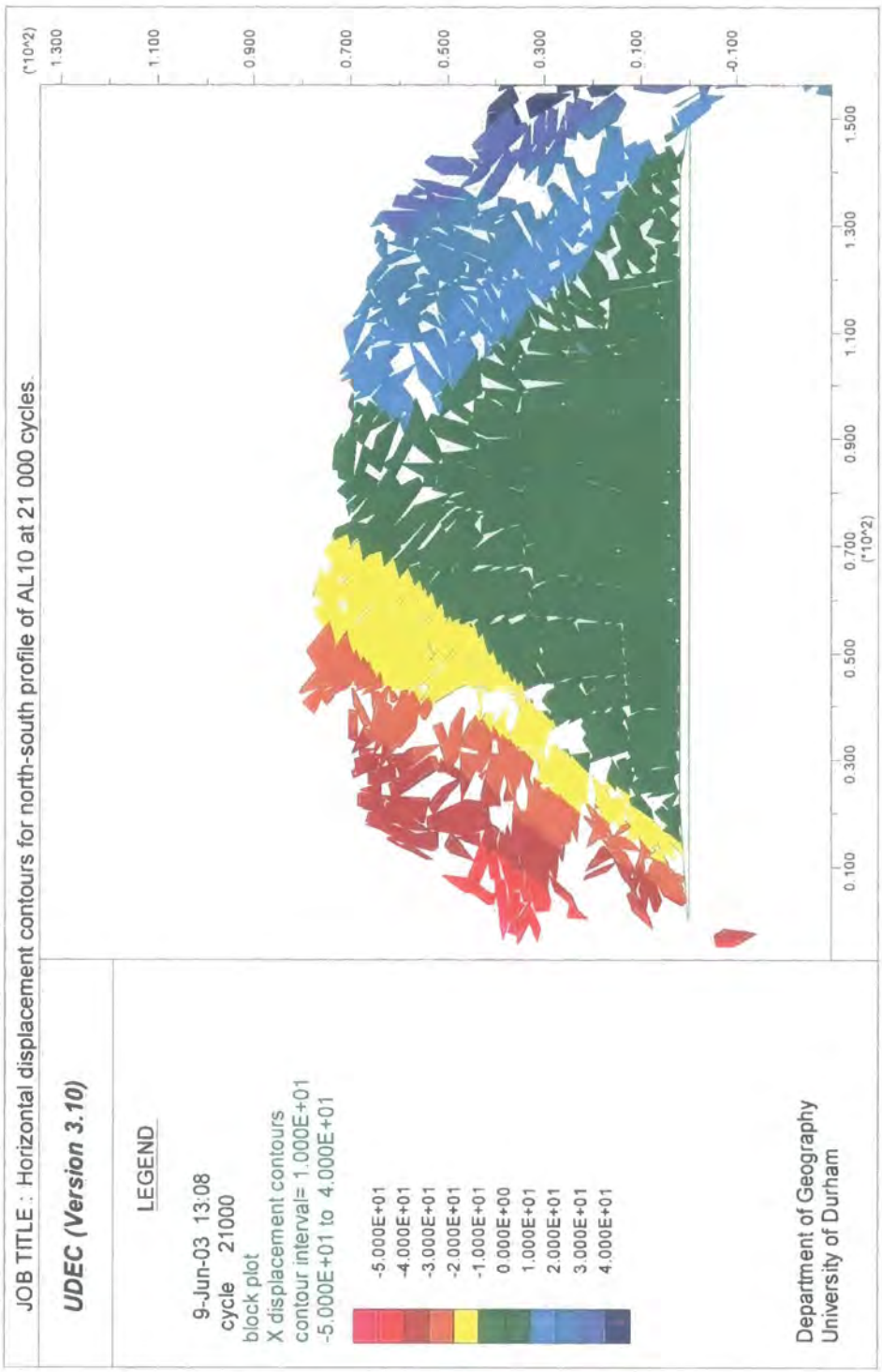

Figure 8.14c: Horizontal displacement contours for the north-south profile of AL10 at 21 000 cycles.

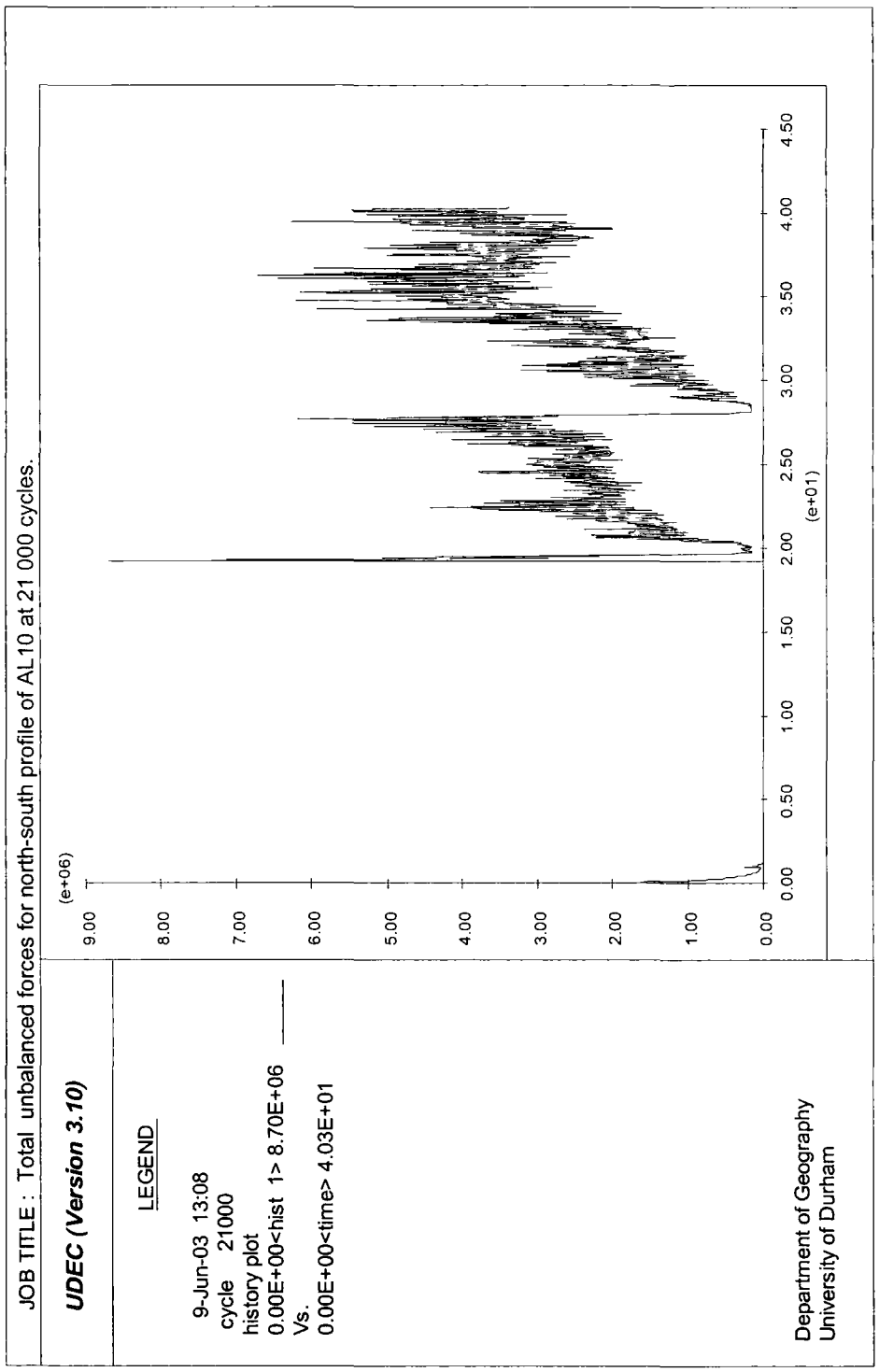

Figure 8.15: Total unbalanced forces for the north-south profile of AL10 at 21 000 cycles.

Figure 8.16a: Block plot of the east-west profile of AL10 at equilibrium.

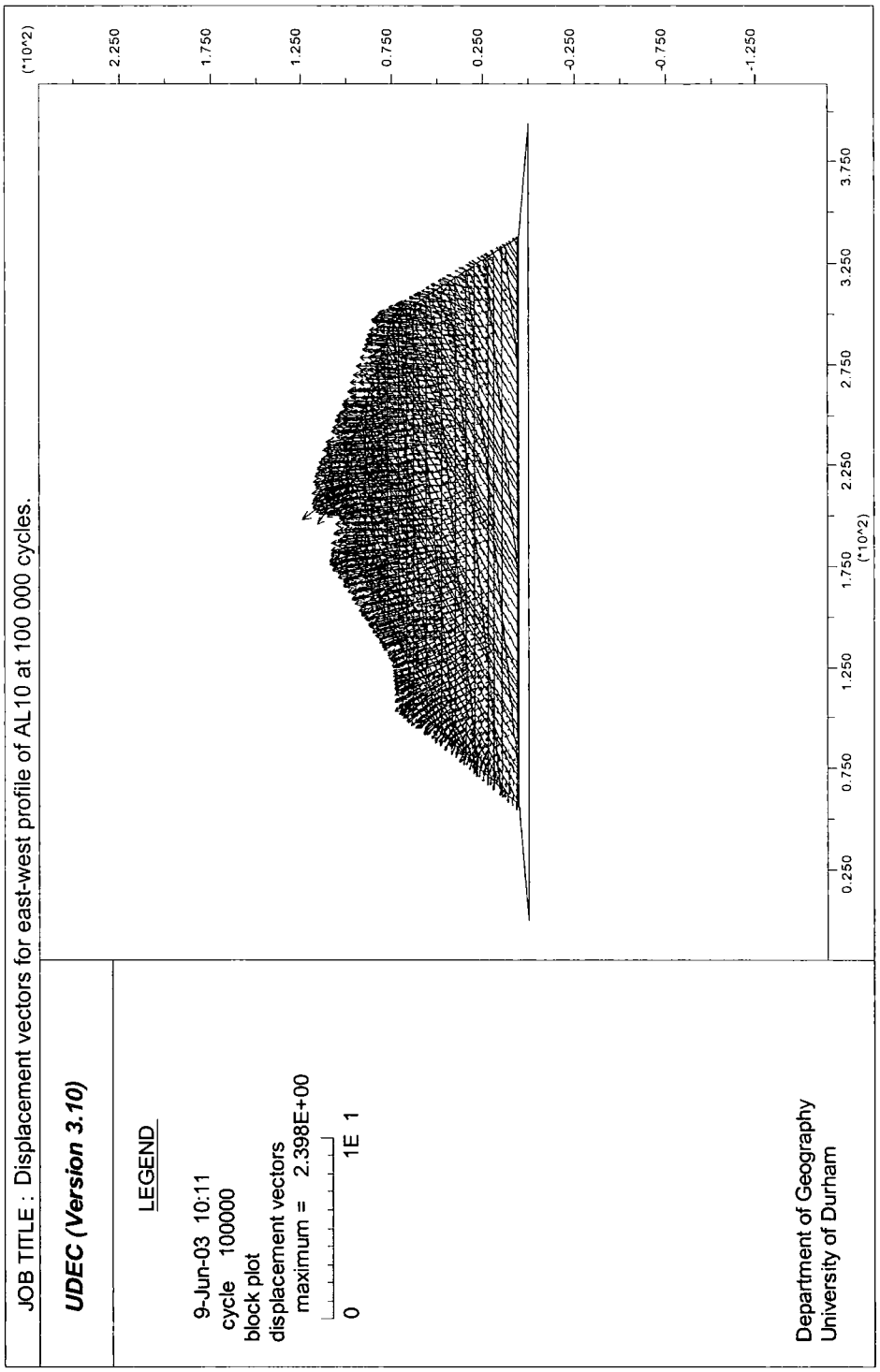

Figure 8.16b: Displacement vectors for the east-west profile of AL10 at 100 000 cycles.

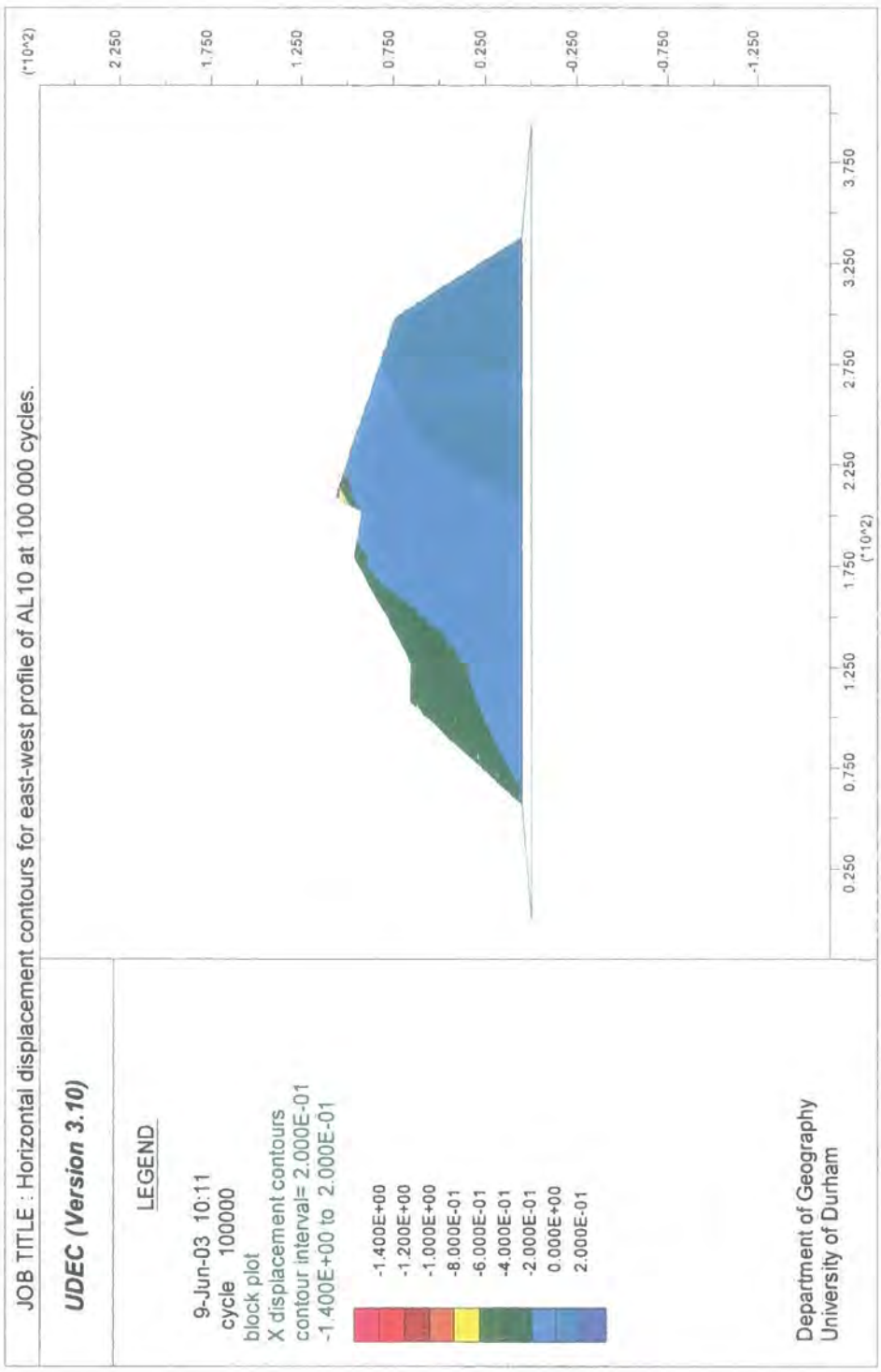

Figure 8.17: Horizontal displacement contours for the east-west profile of AL10 at 100 000 cycles.

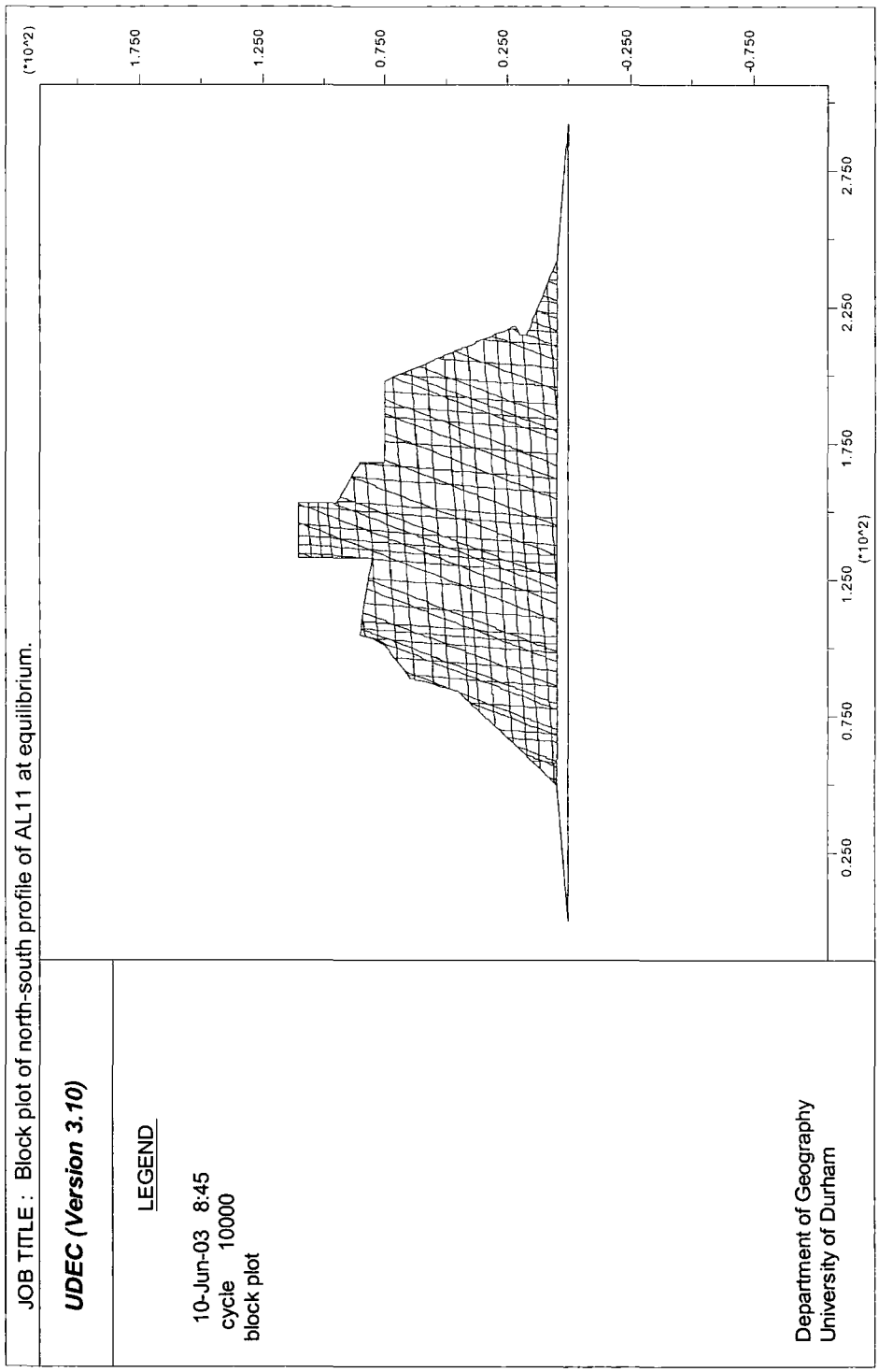

Figure 8.18a: Block plot of the north-south profile of AL11 at equilibrium.

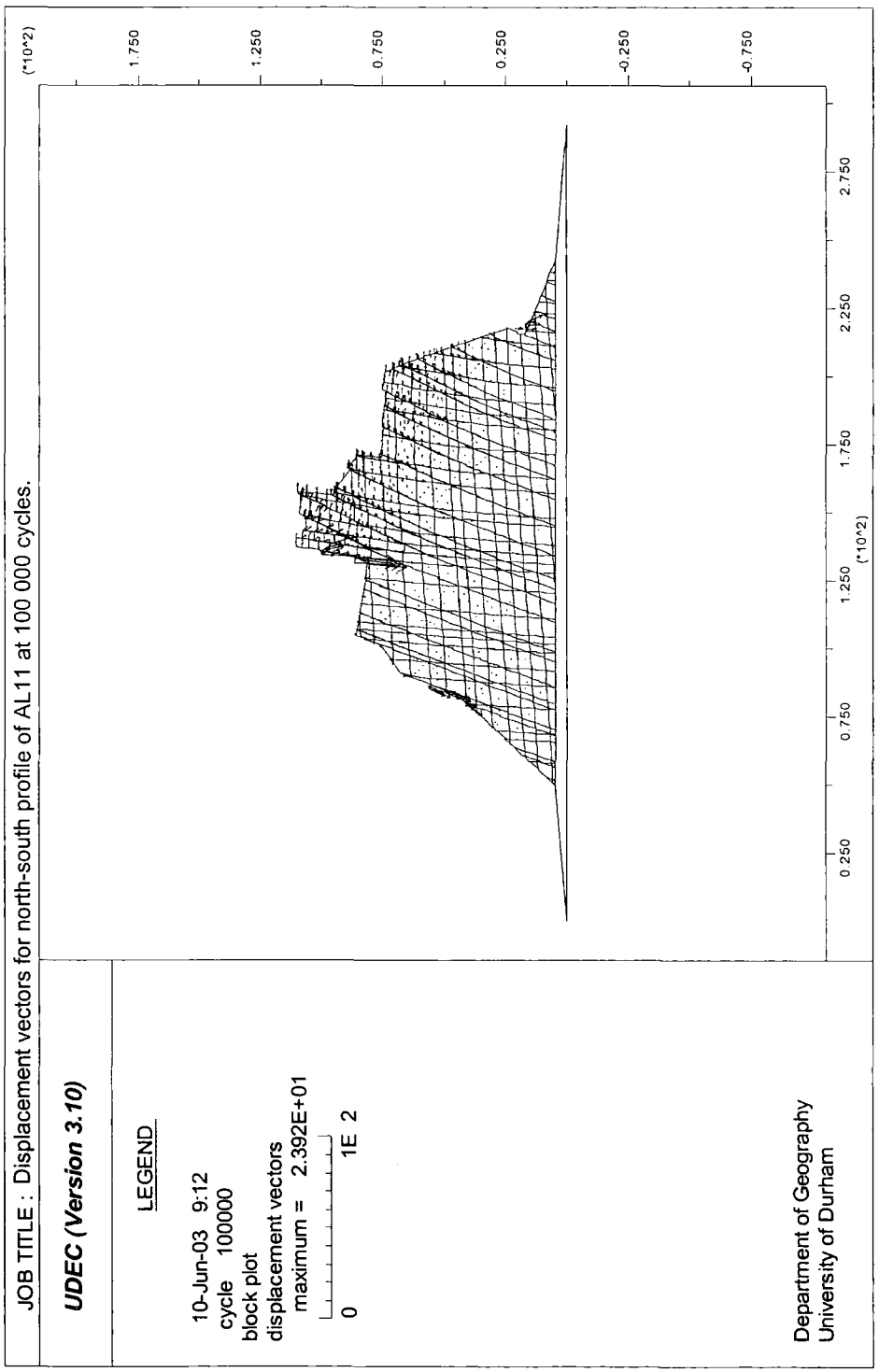

Figure 8.18b: Displacement vectors for the north-south profile of AL11 at 100 000 cycles.

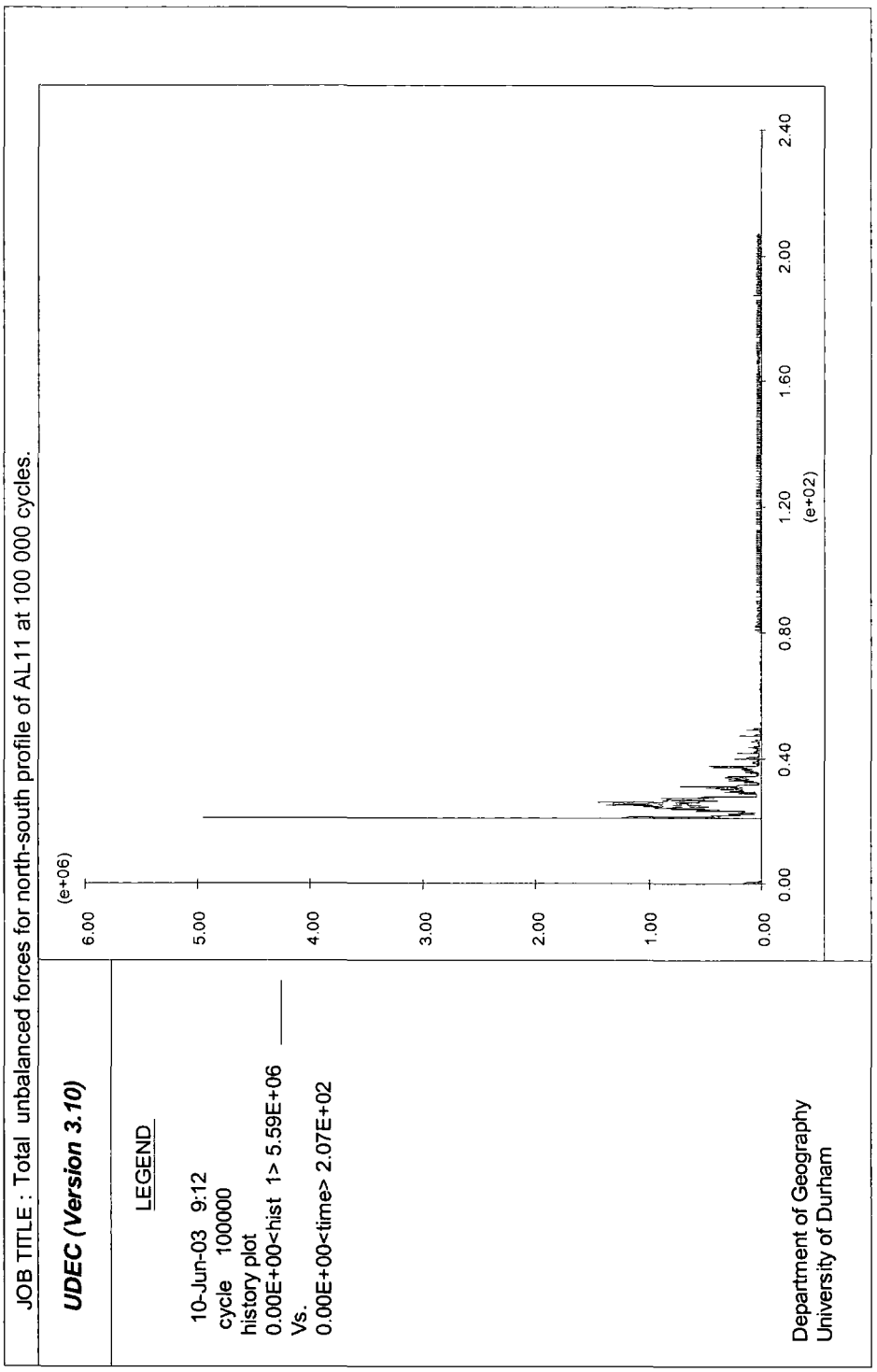

Figure 8.19: Total unbalanced forces for the north-south profile of AL11 at 100 000 cycles.

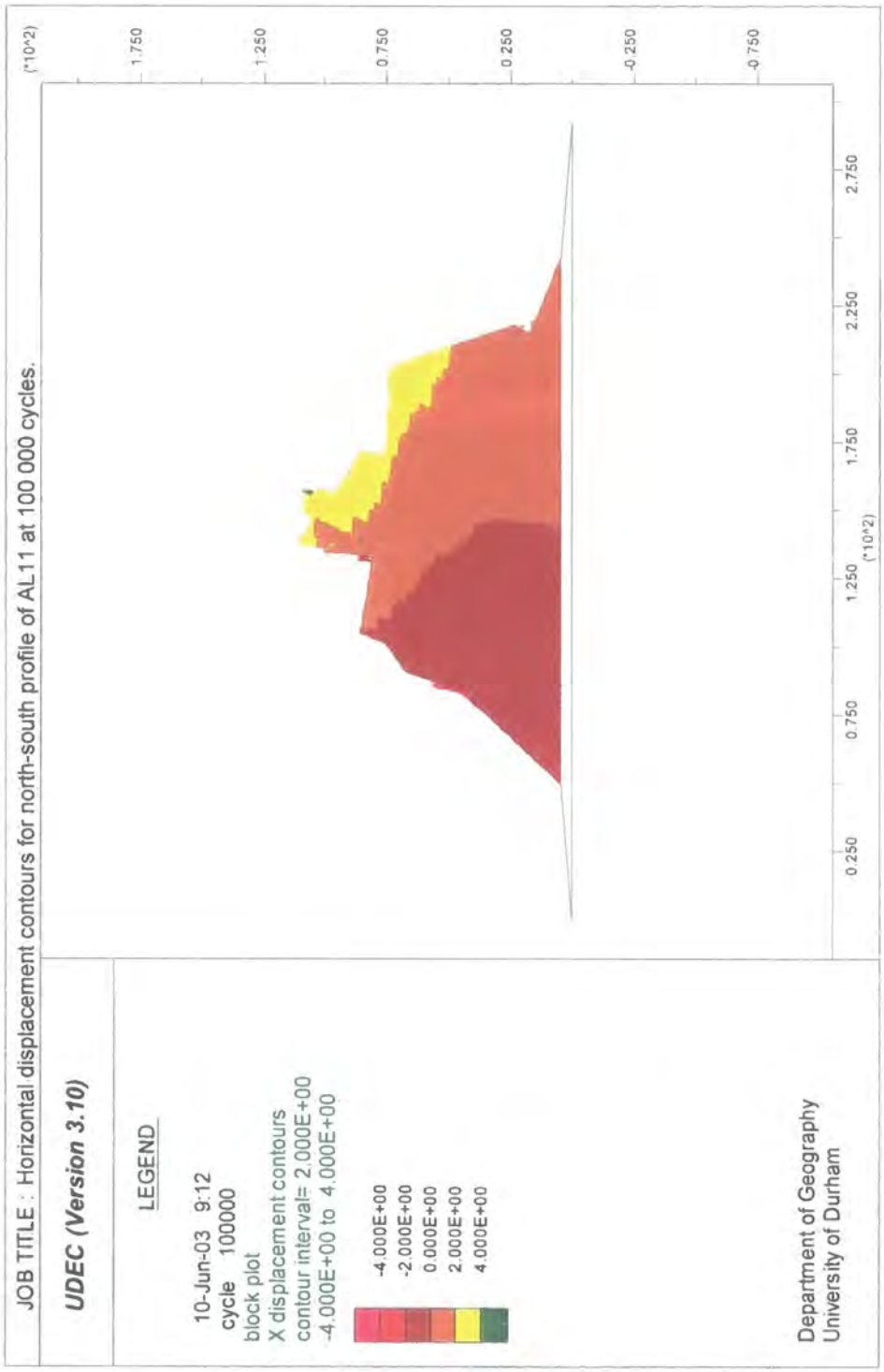

Figure 8.20: Horizontal displacement contours for the east-west profile of AL11 at 100 000 cycles.

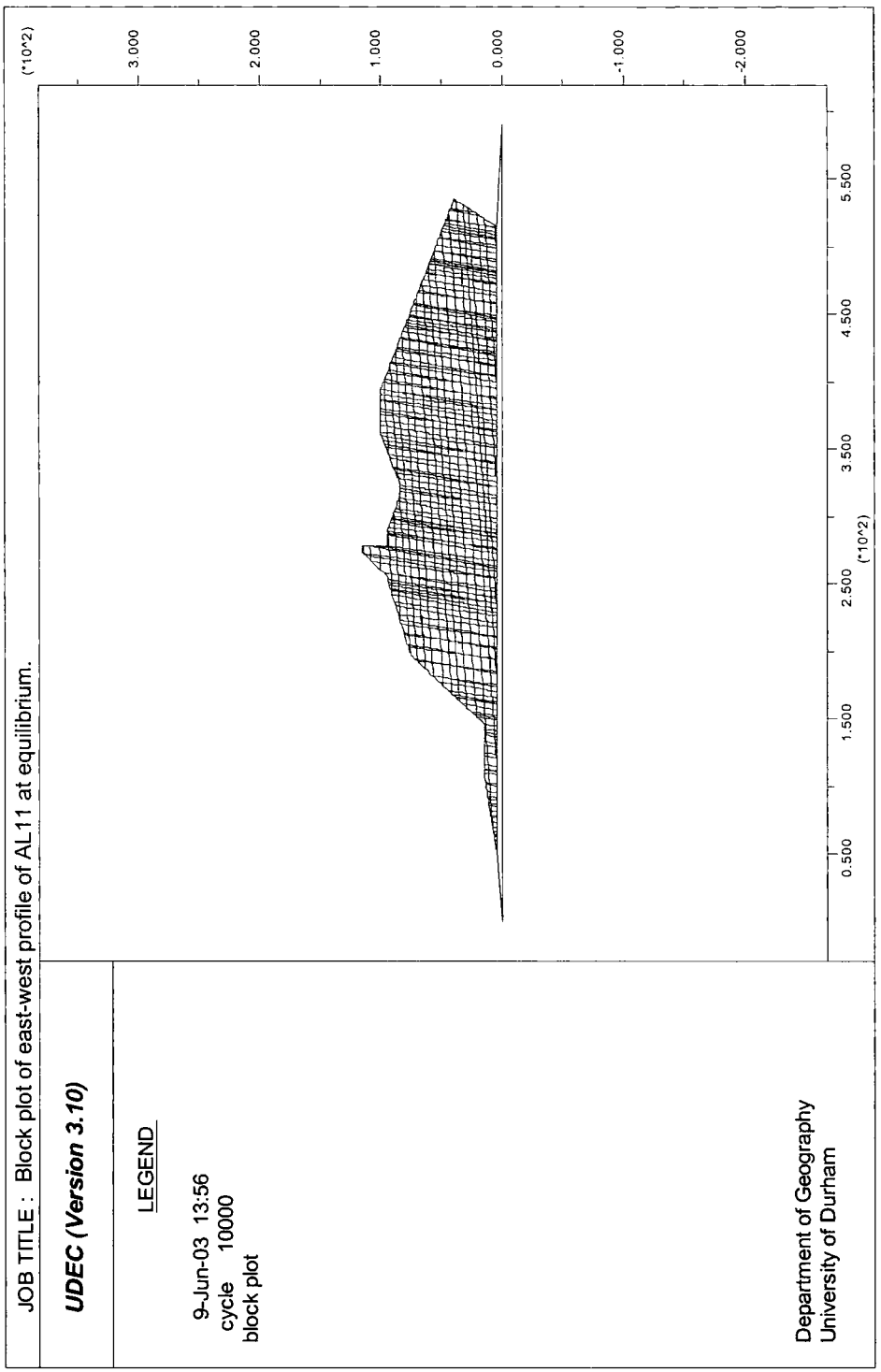

Figure 8.21a: Block plot of the east-west profile of AL11 at equilibrium.

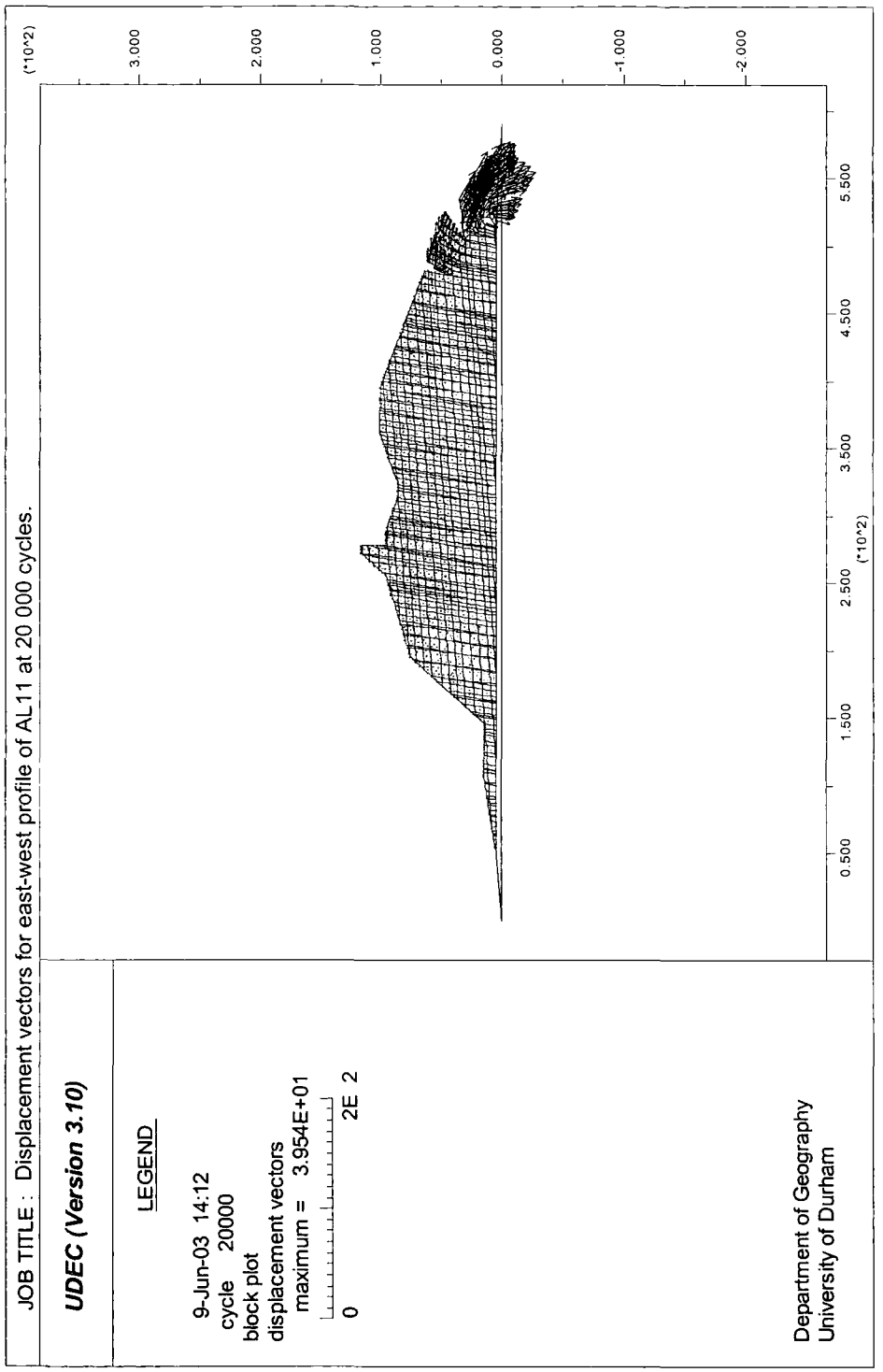

Figure 8.21b: Displacement vectors for the east-west profile of AL11 at 20 000 cycles.

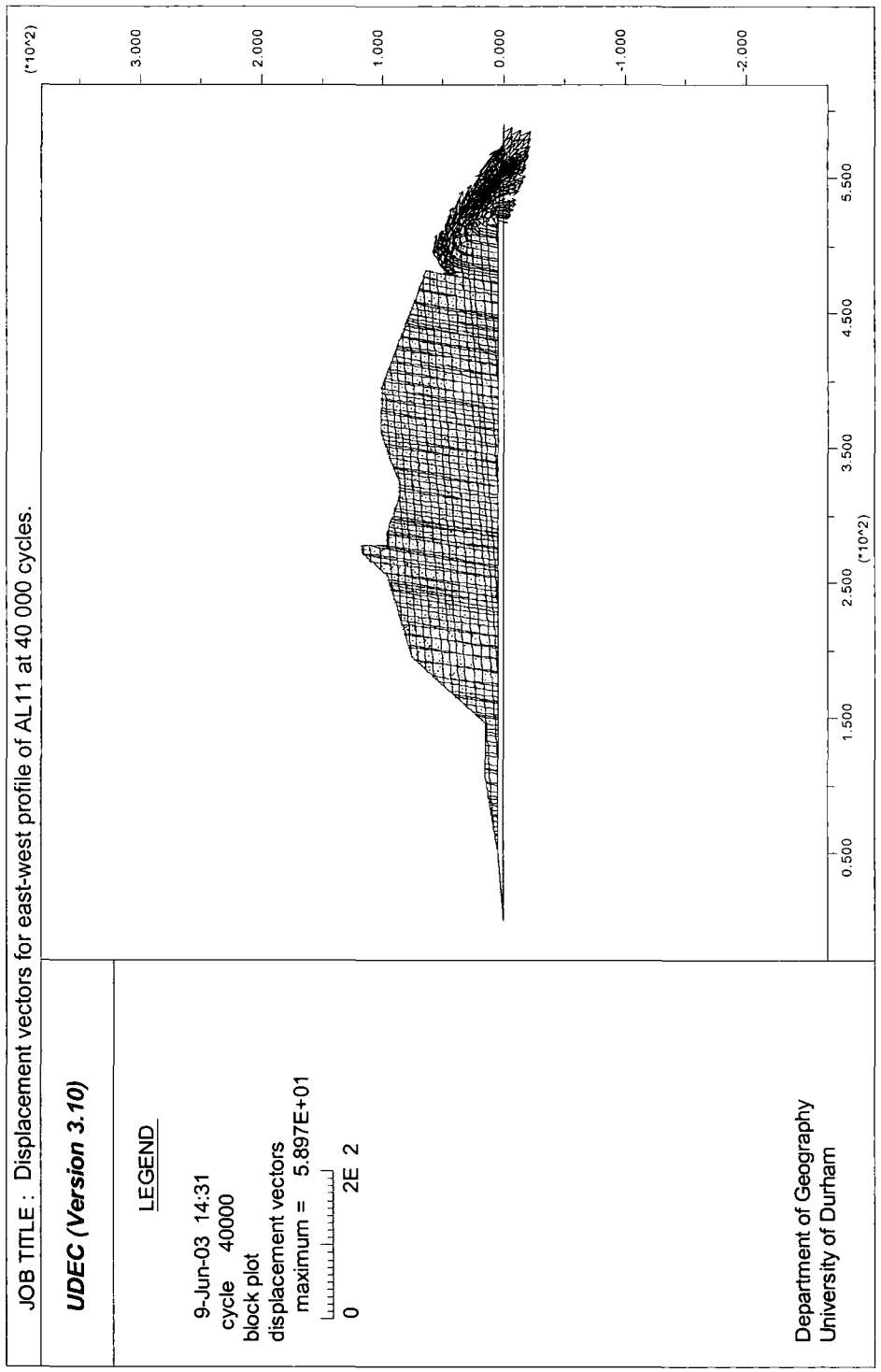

Figure 8.21c: Displacement vectors for the east-west profile of AL11 at 40 000 cycles.

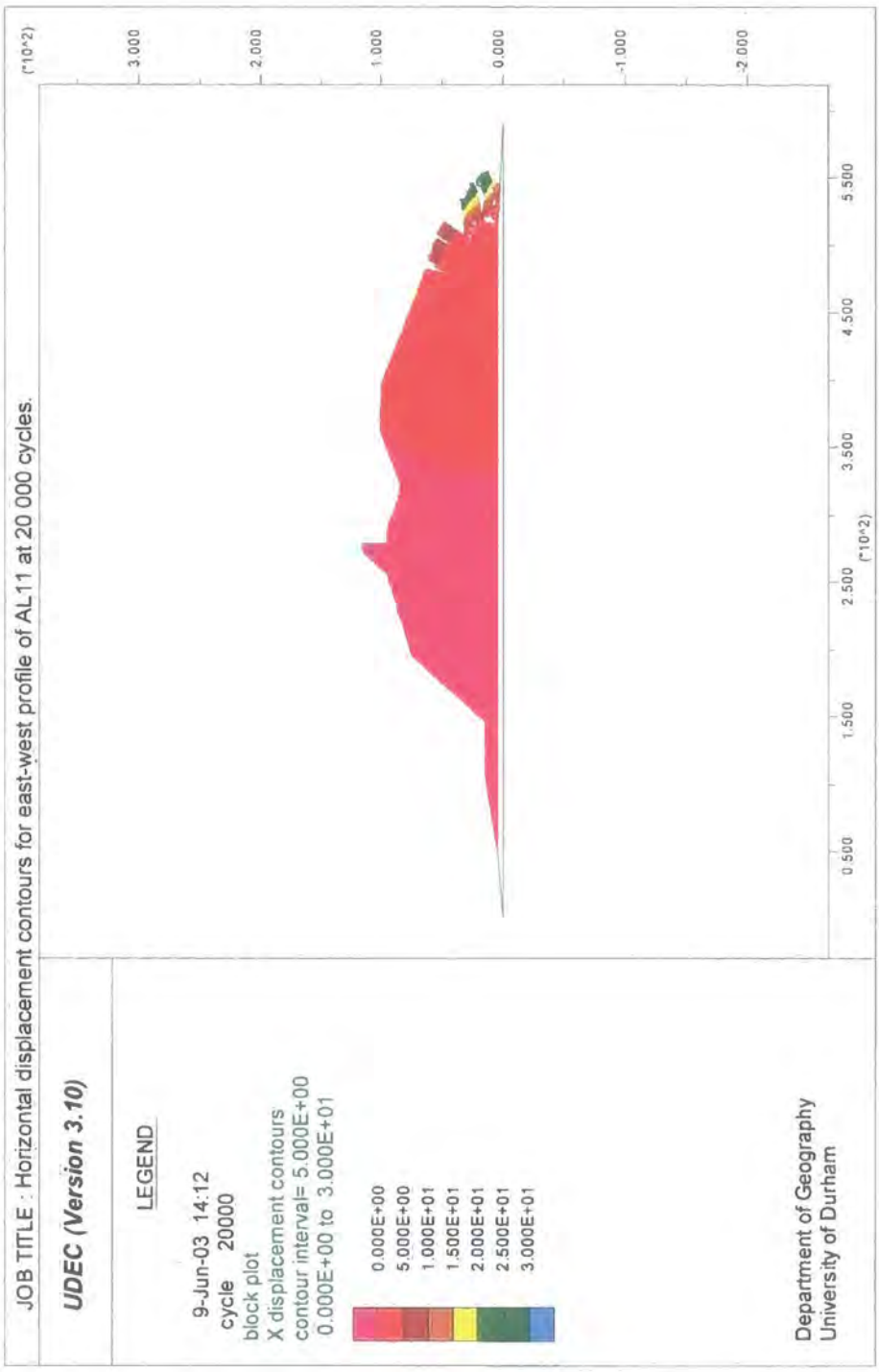

Figure 8.22a: Horizontal displacement contours for the east-west profile of AL11 at 20 000 cycles.

Figure 8.22b: Horizontal displacement contours for the east-west profile of AL11 at 40 000 cycles.

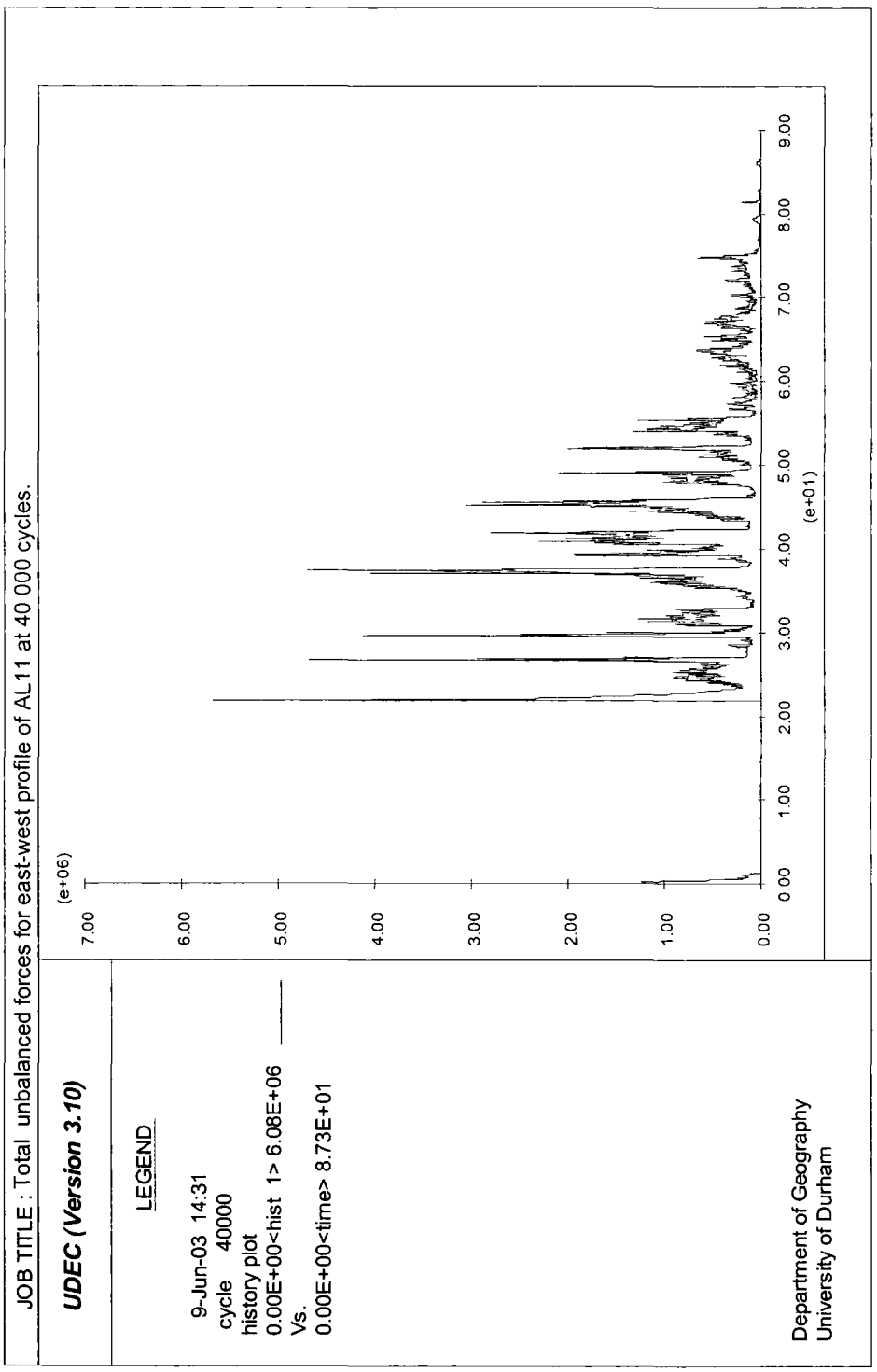

Figure 8.23: Total unbalanced forces for the east-west profile of AL11 at 40 000 cycles.

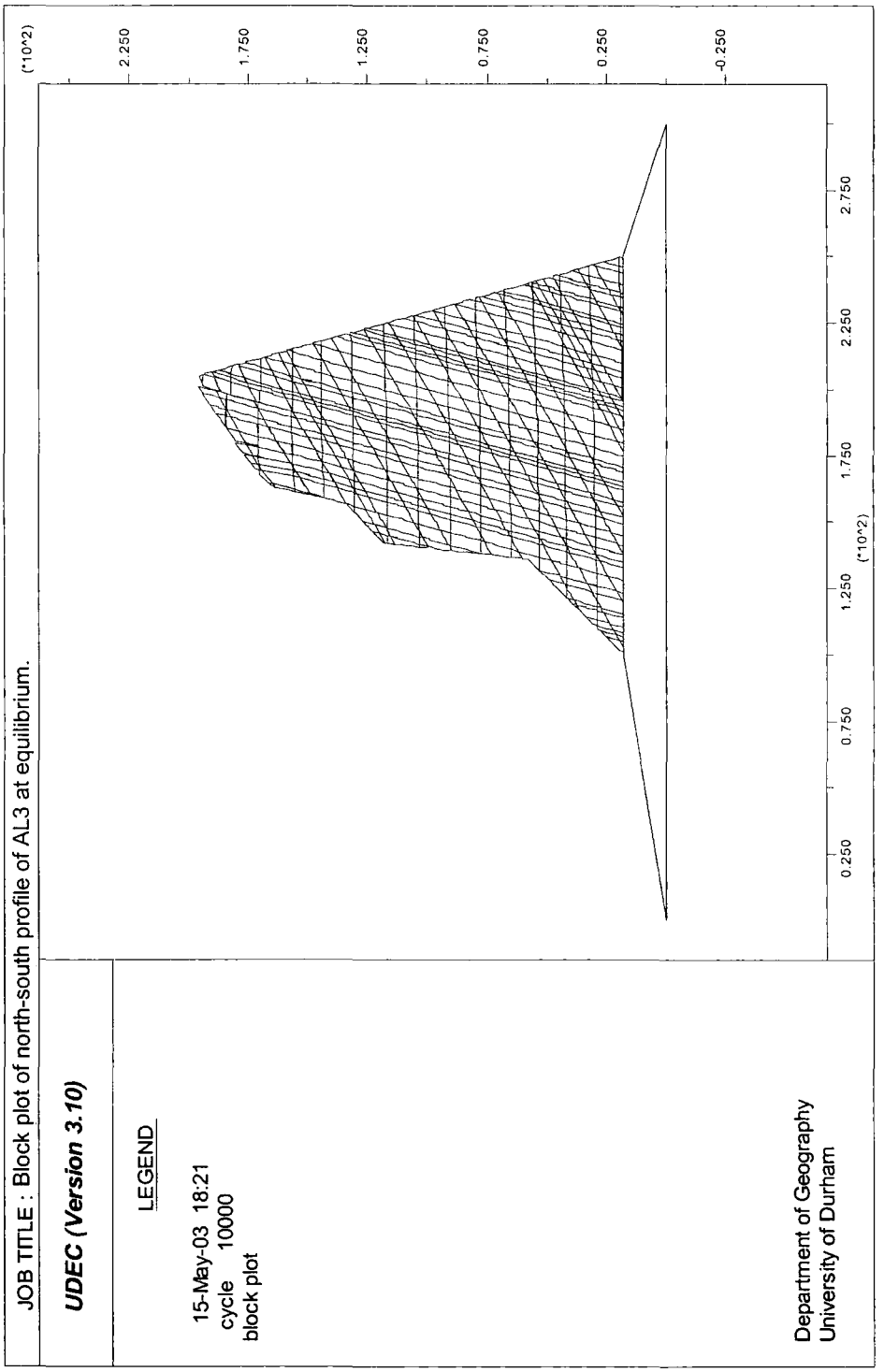

Figure 8.24a: Block plot of the north-south profile of AL3 at equilibrium.

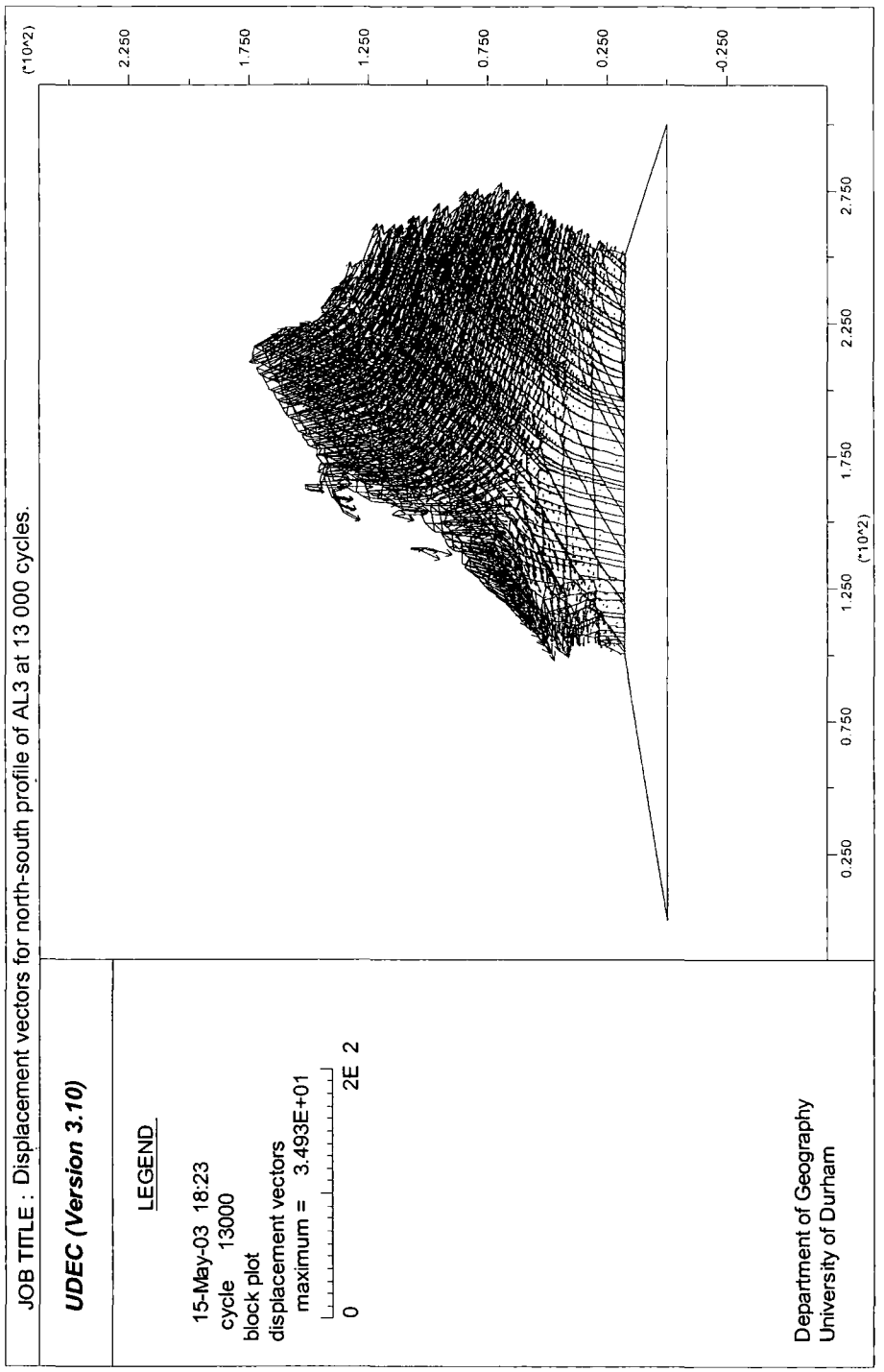

Figure 8.24b: Displacement vectors for the north-south profile of AL3 at 13 000 cycles.

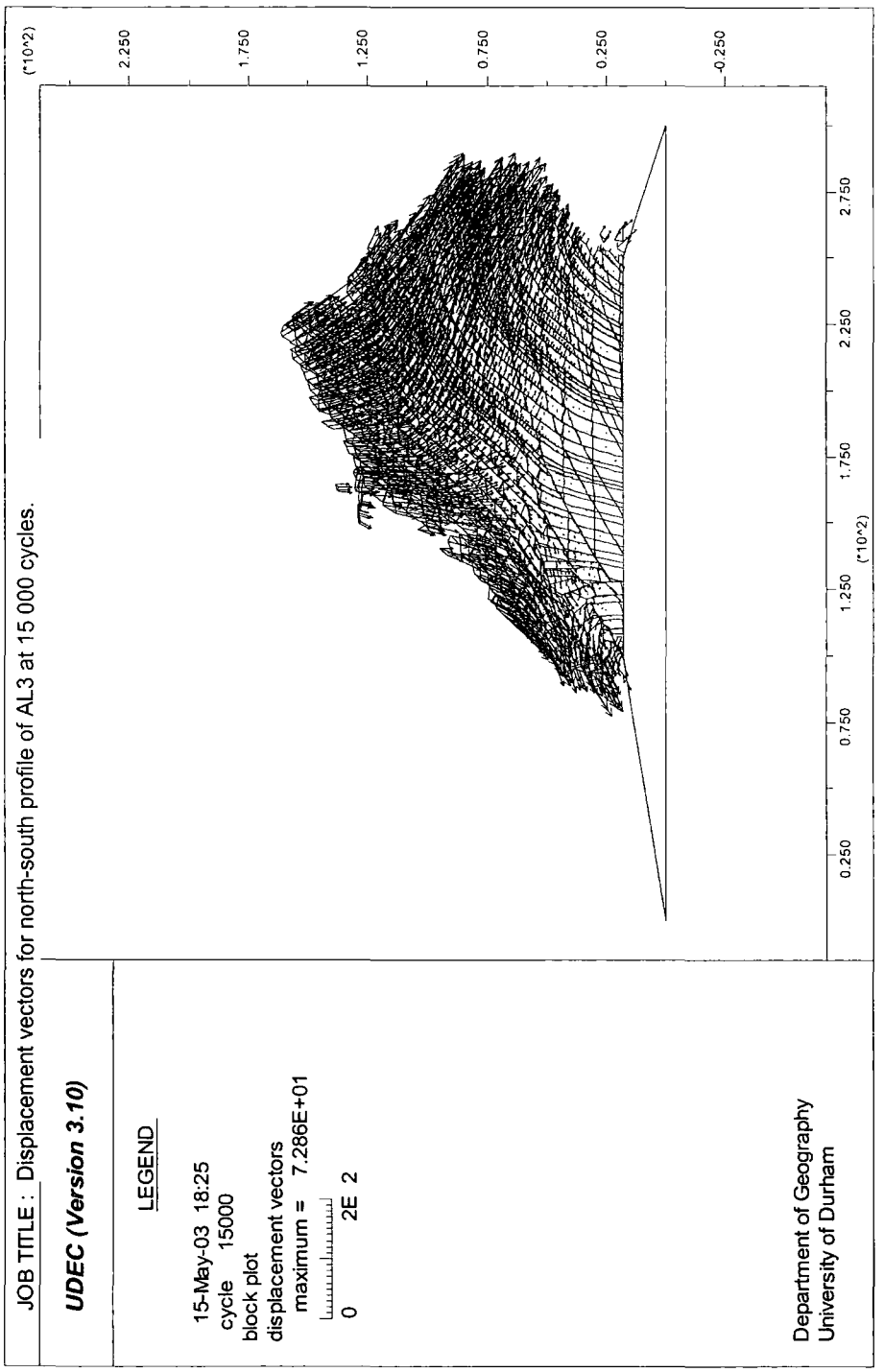

Figure 8.24c: Displacement vectors for the north-south profile of AL3 at 15 000 cycles.

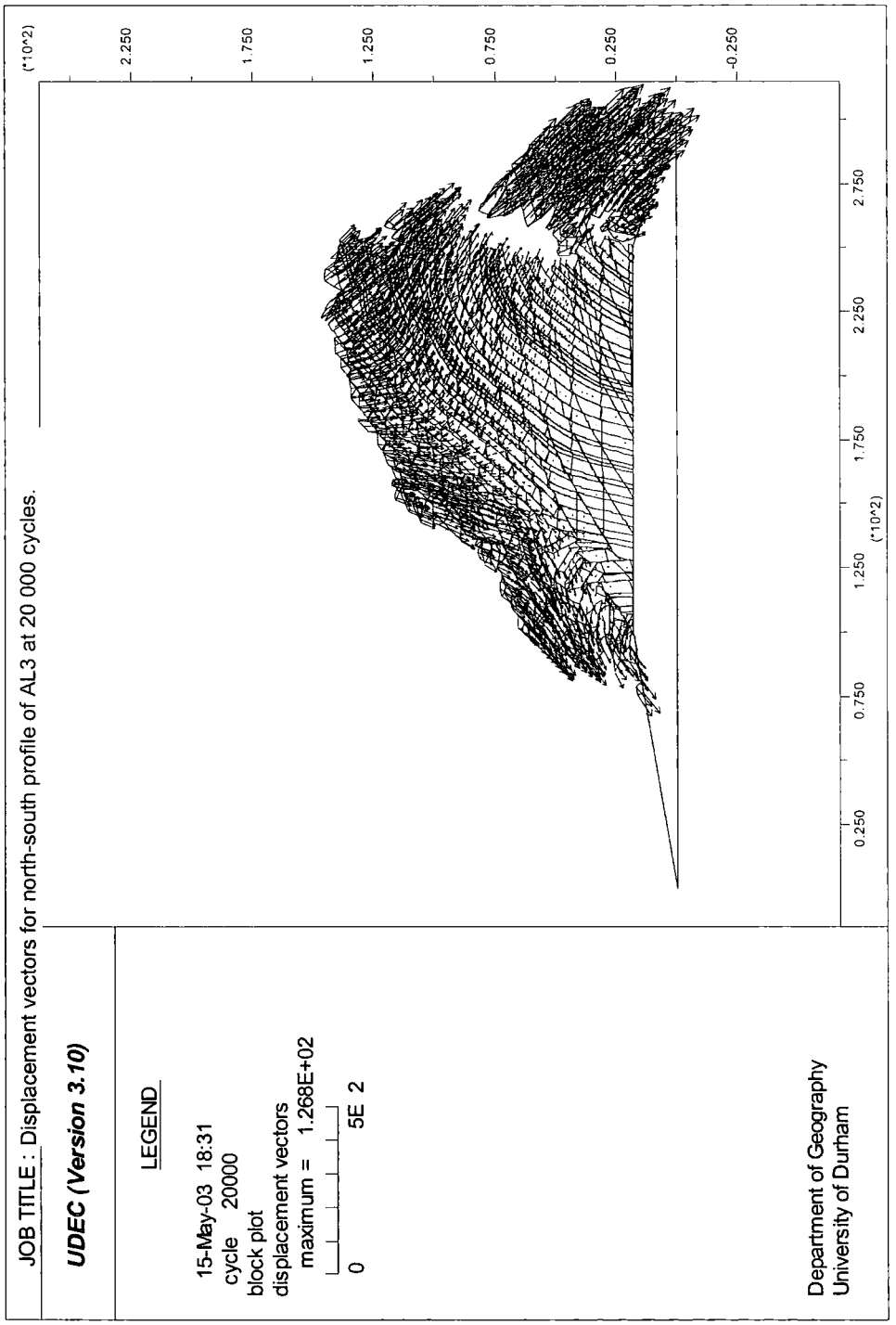

Figure 8.24d: Displacement vectors for the north-south profile of AL3 at 20 000 cycles.

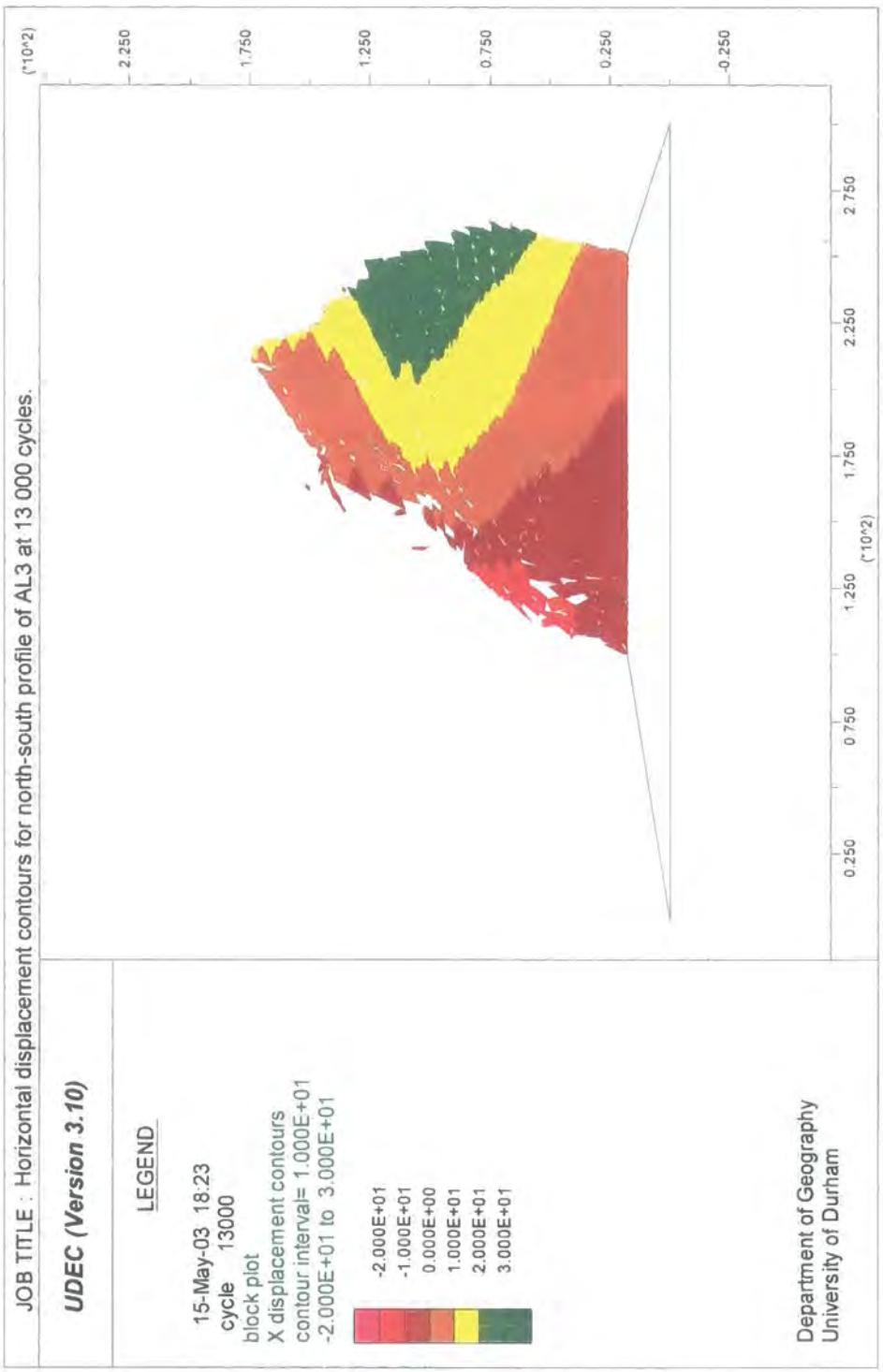

Figure 8.25a: Horizontal displacement contours for the north – south profile of AL3 at 13 000 cycles.

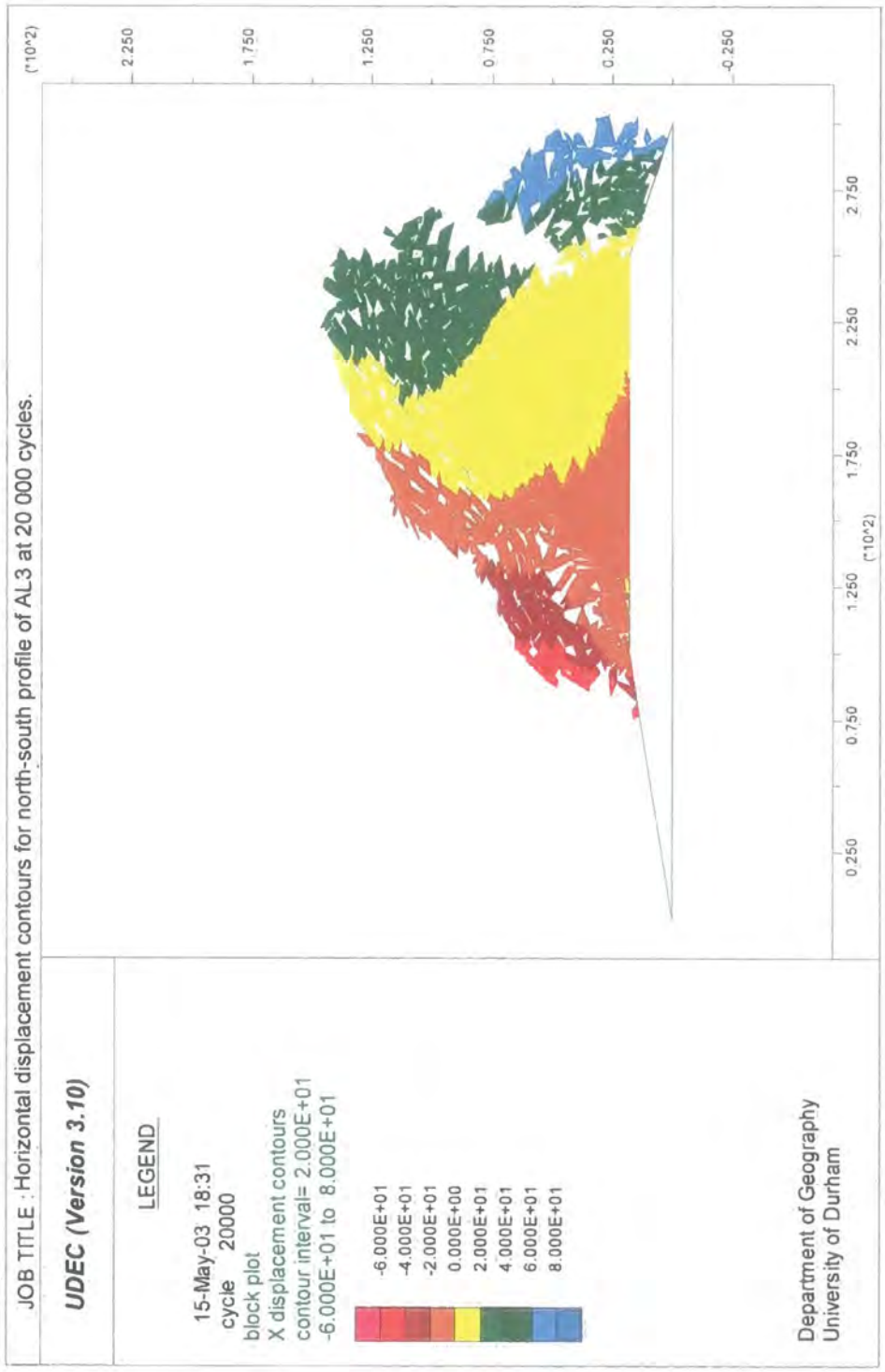

Figure 8.25b: Horizontal displacement contours for the north – south profile of AL3 at 20 000 cycles.

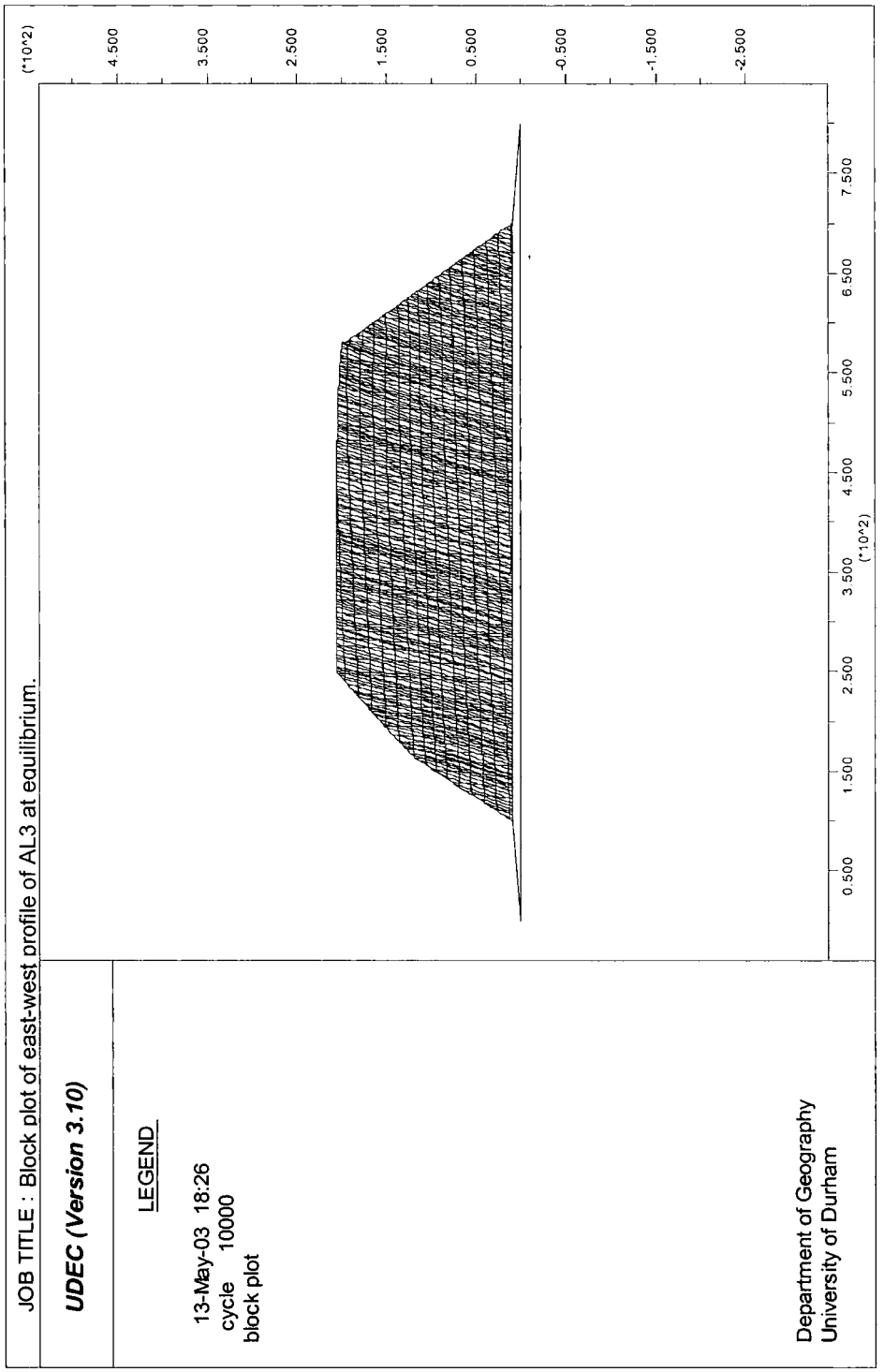

Figure 8.26a: Block plot of the east-west profile of AL3 at equilibrium.

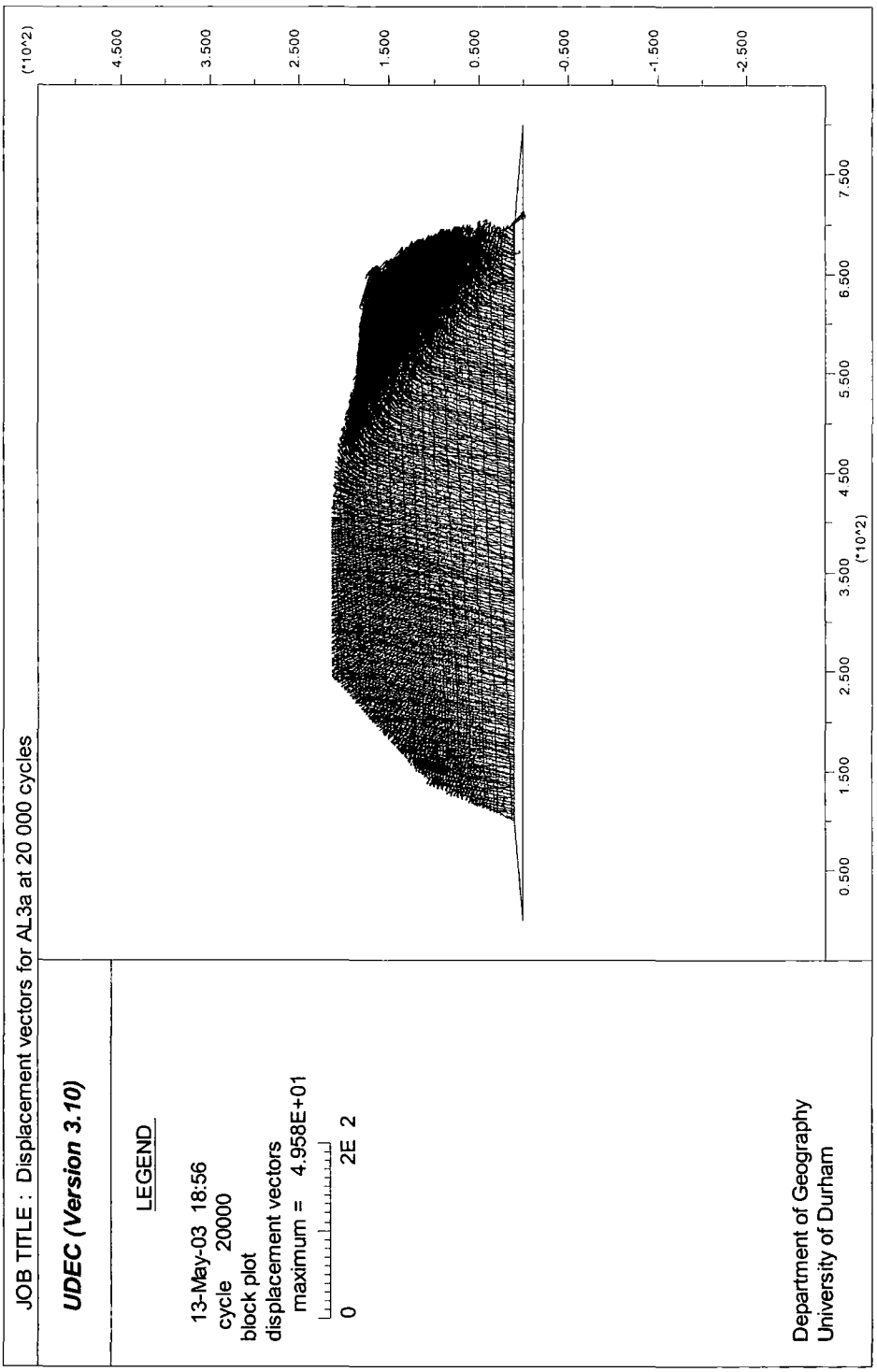

Figure 8.26b: Displacement vectors for the east-west profile of AL3 at 20 000 cycles.

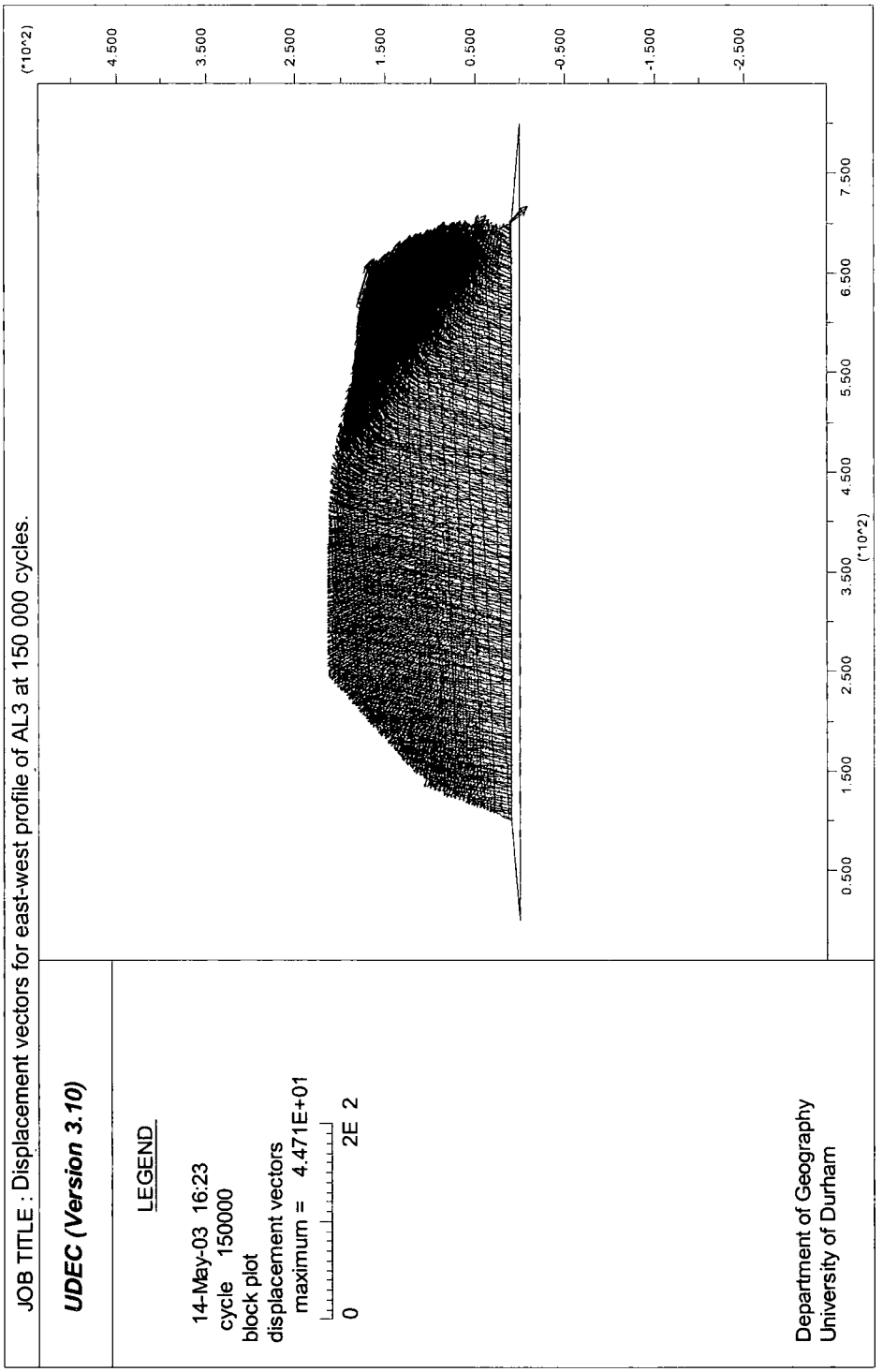

Figure 8.26c: Displacement vectors for the east-west profile of AL3 at 150 000 cycles.

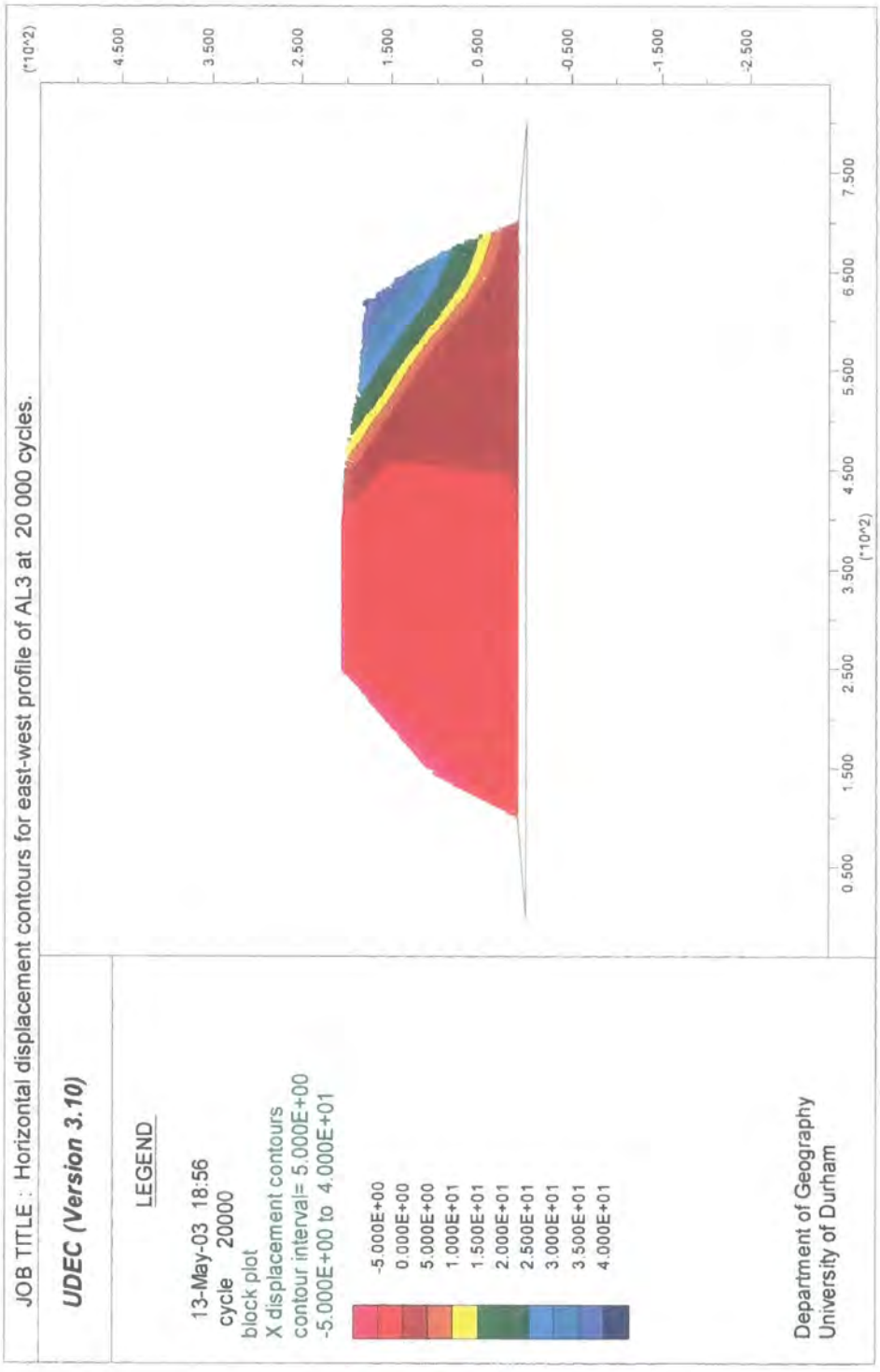

Figure 8.27a: Horizontal displacement contours for the east-west profile of AL3 at 20 000 cycles.

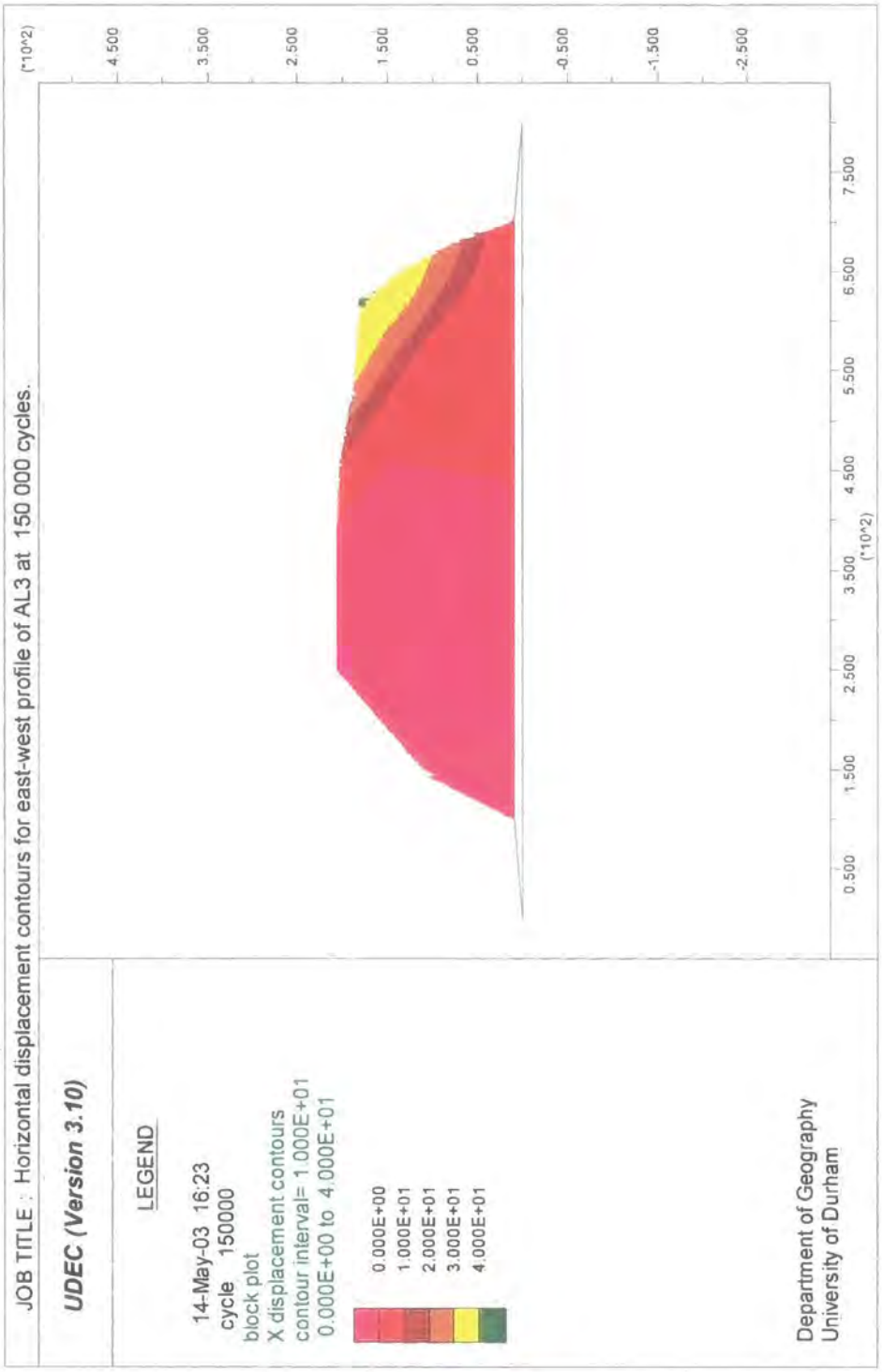

Figure 8.27b: Horizontal displacement contours for the east-west profile of AL3 at 150 000 cycles.

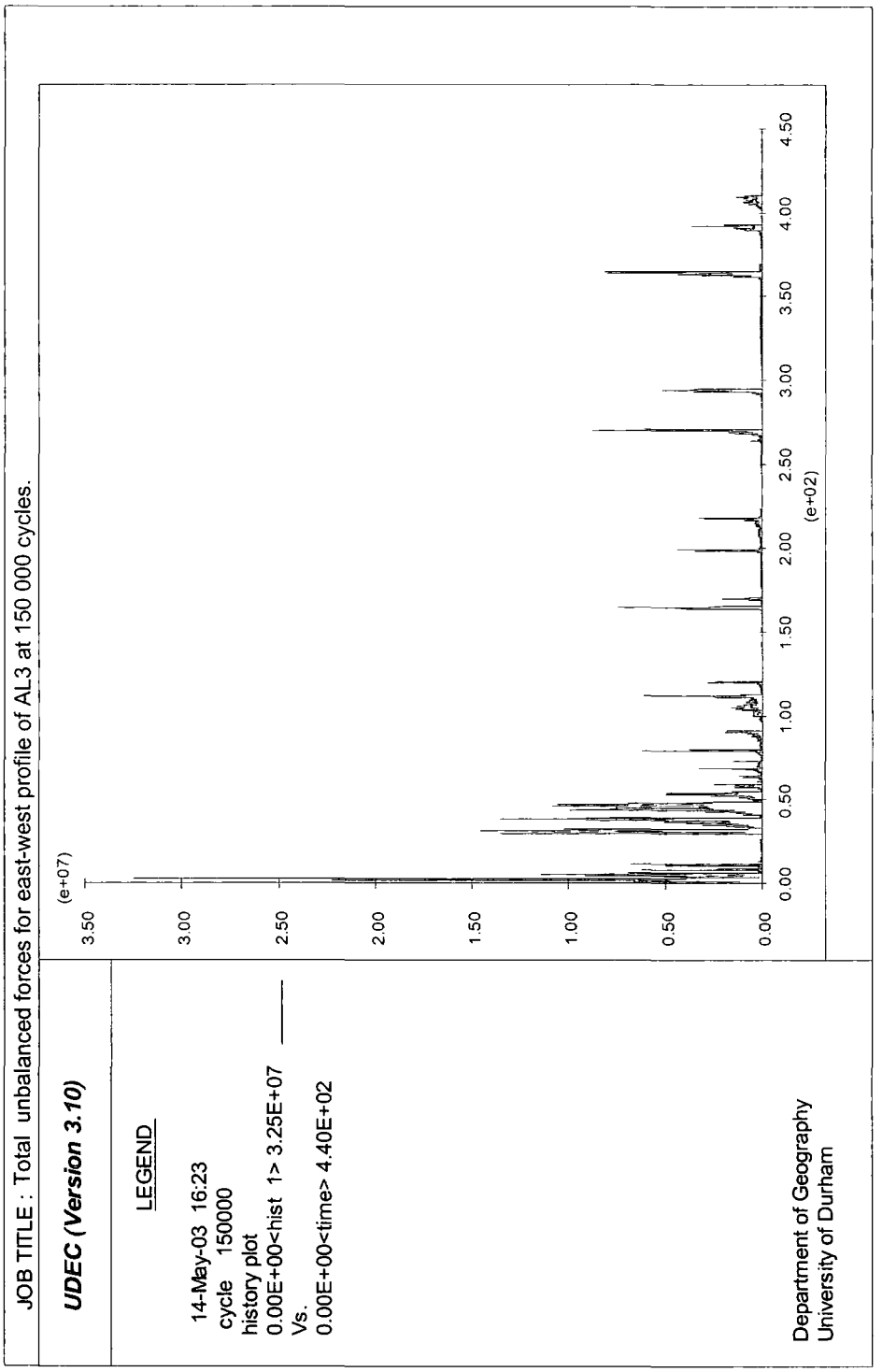

Figure 8.28: Total unbalanced forces for the east-west profile of AL3 at 150 000 cycles.

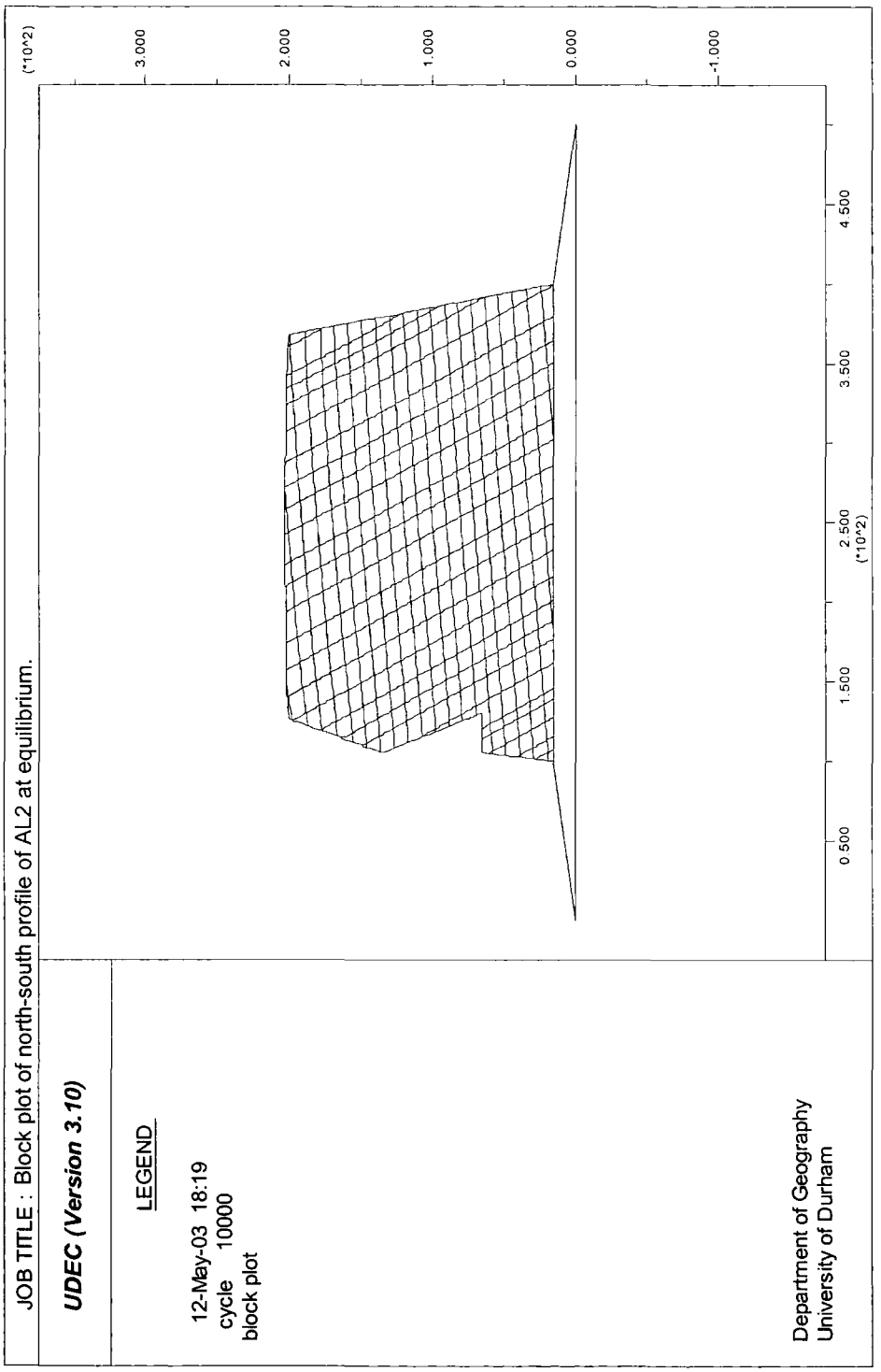

Figure 8.29a: Block plot of the north-south profile of AL2 at equilibrium.

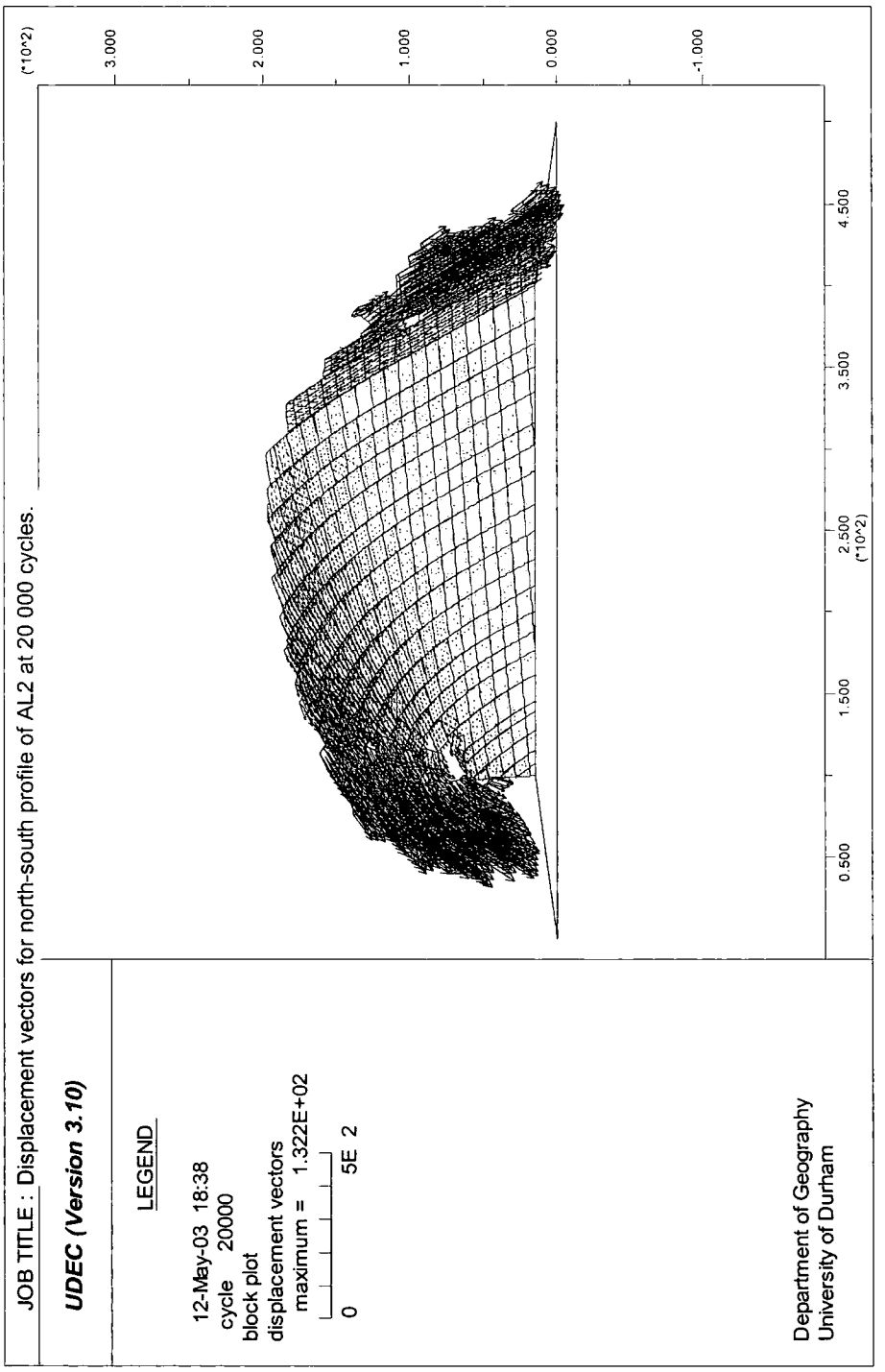

Figure 8.29b: Displacement vectors for the north-south profile of AL2 at 20 000 cycles.

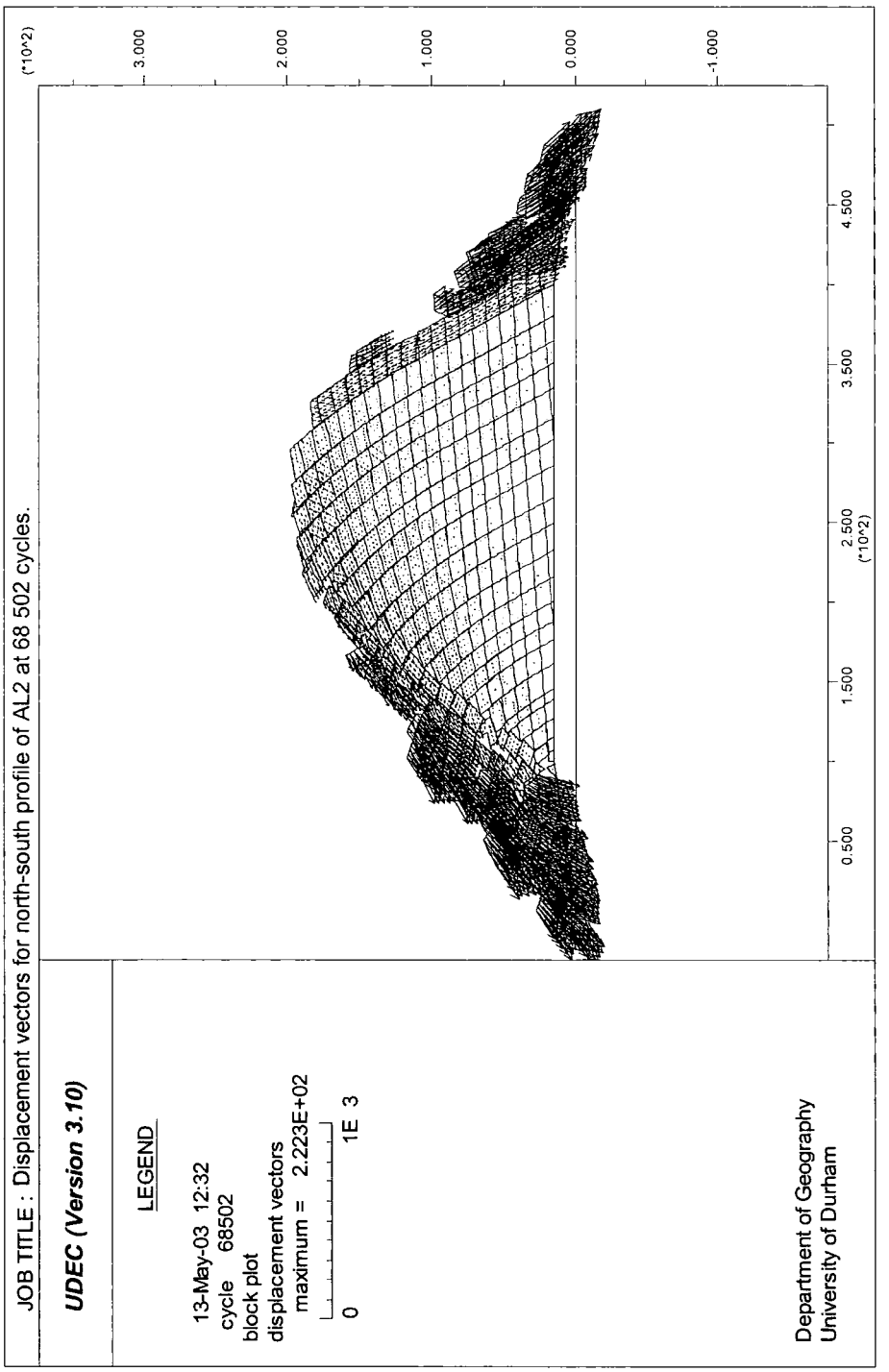

Figure 8.29c: Displacement vectors for the north-south profile of AL2 at 68 502 cycles.

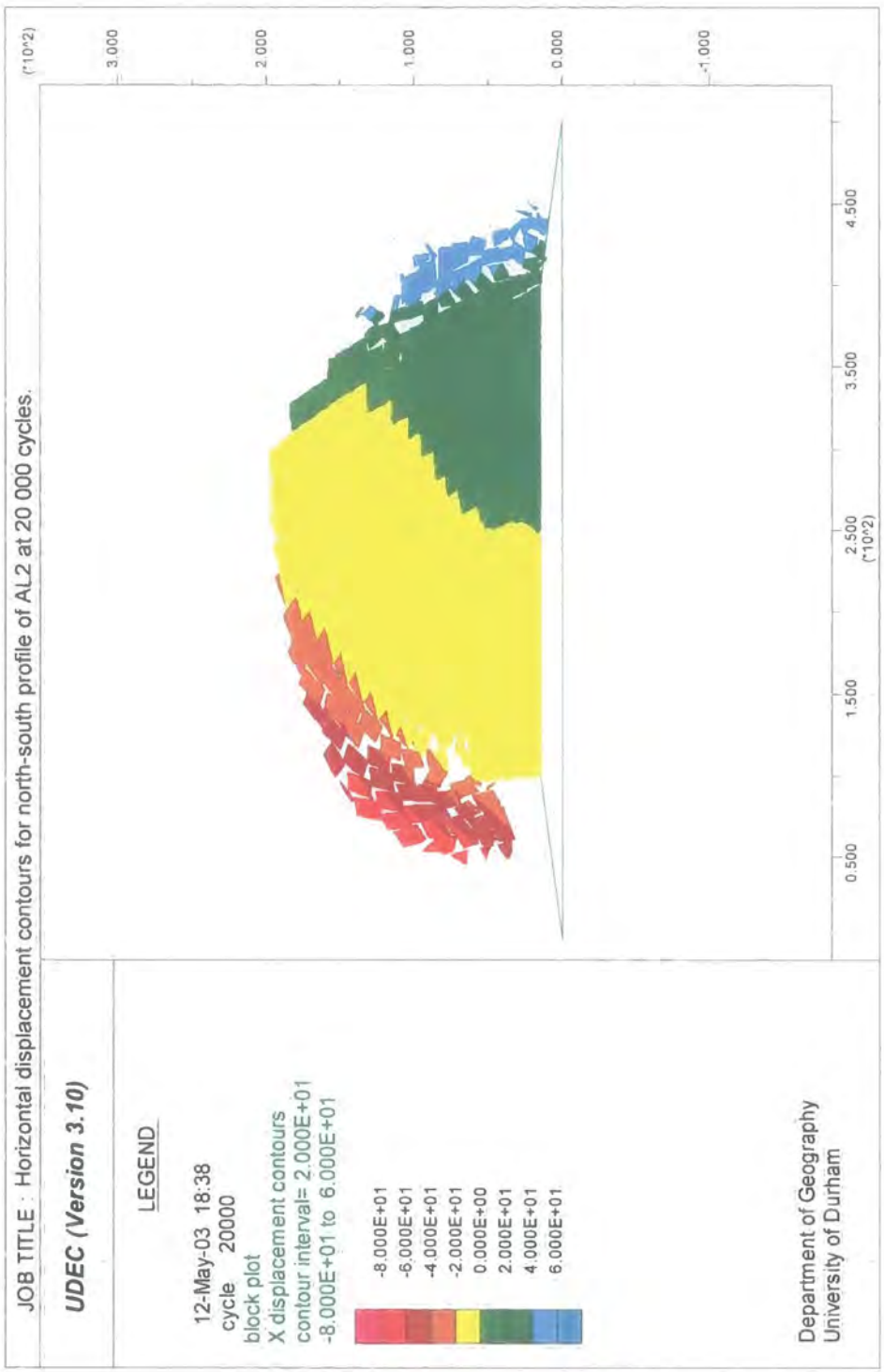

Figure 8.30a: Horizontal displacement contours for the north-south profile of AL2 at 20 000 cycles.

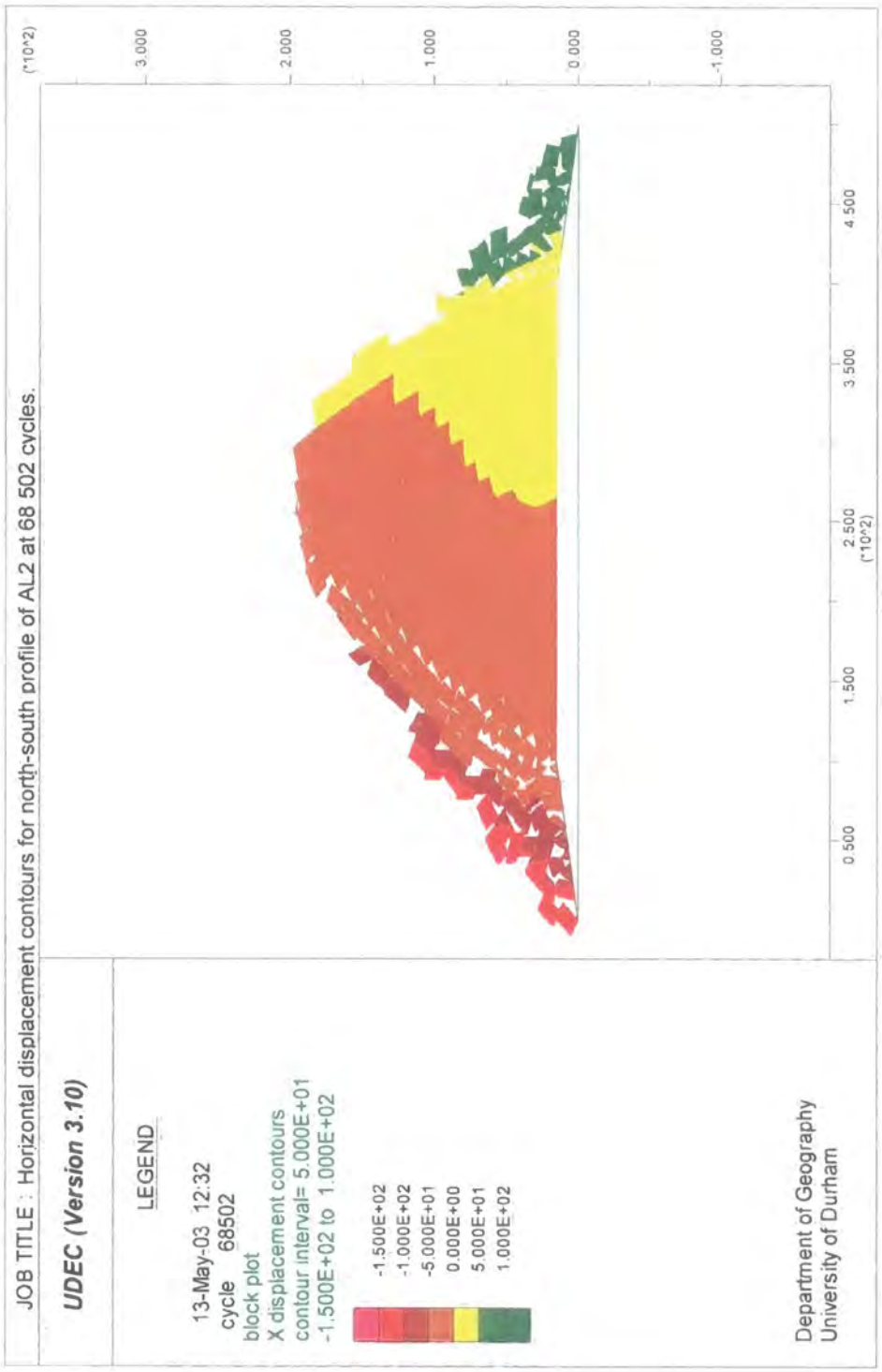

Figure 8.30b: Horizontal displacement contours for the north-south profile of AL2 at 68 502 cycles.

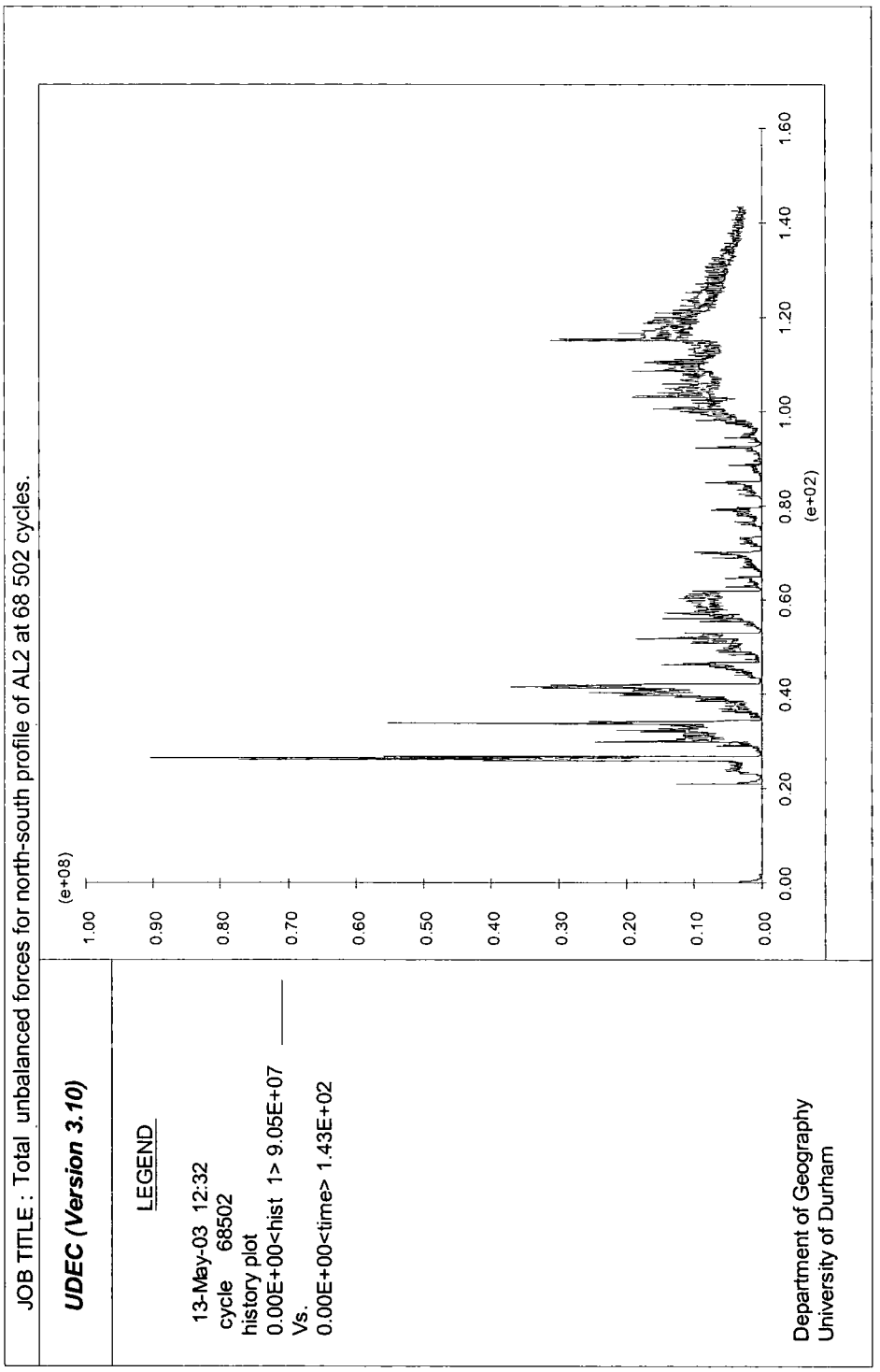

Figure 8.31: Total unbalanced forces for the north-south profile of AL2 at 68 502 cycles.

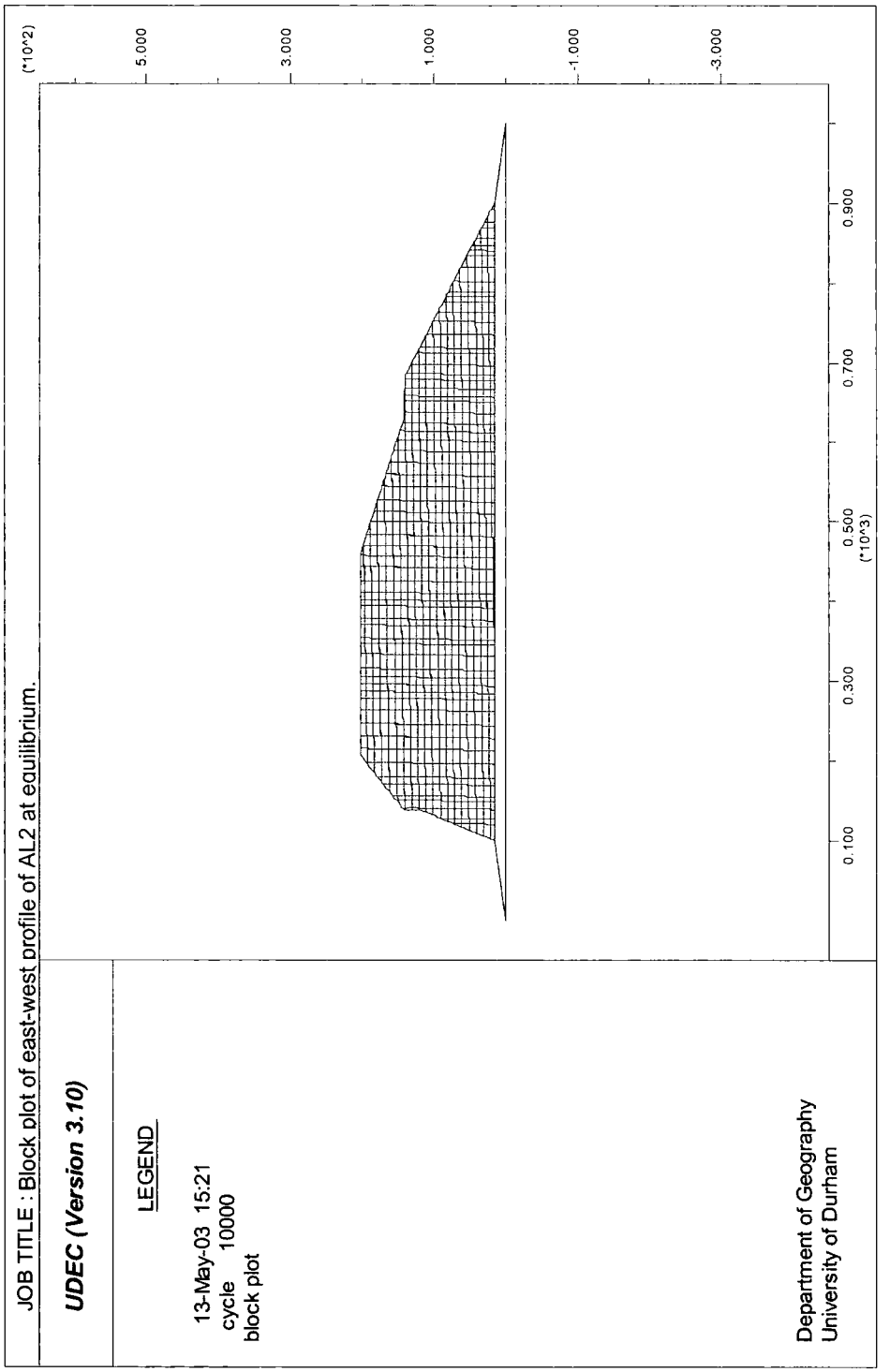

Figure 8.32a: Block plot of the east-west profile of AL2 at equilibrium.

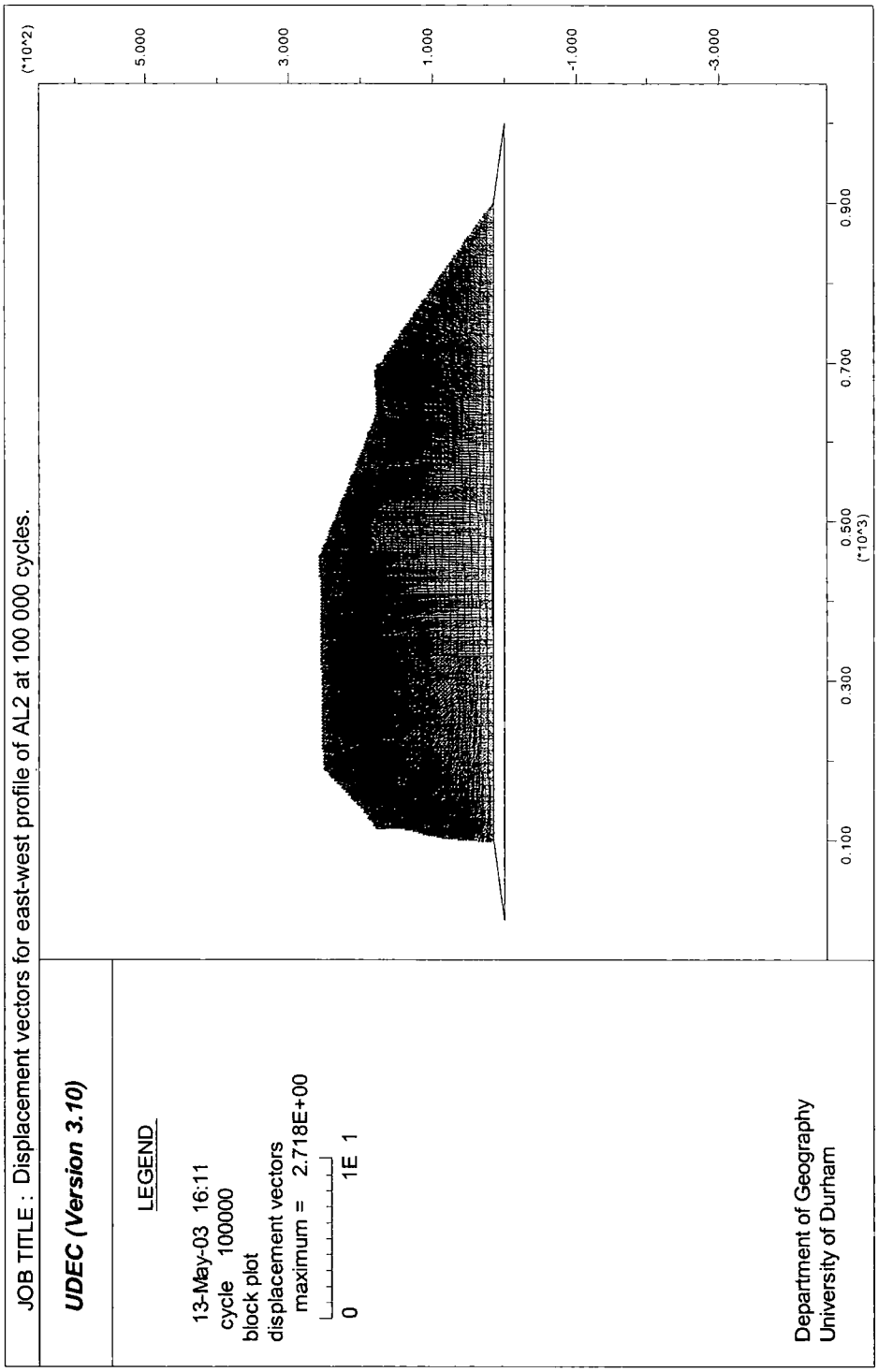

Figure 8.32b: Displacement vectors for the east-west profile of AL2 at 100 000 cycles.

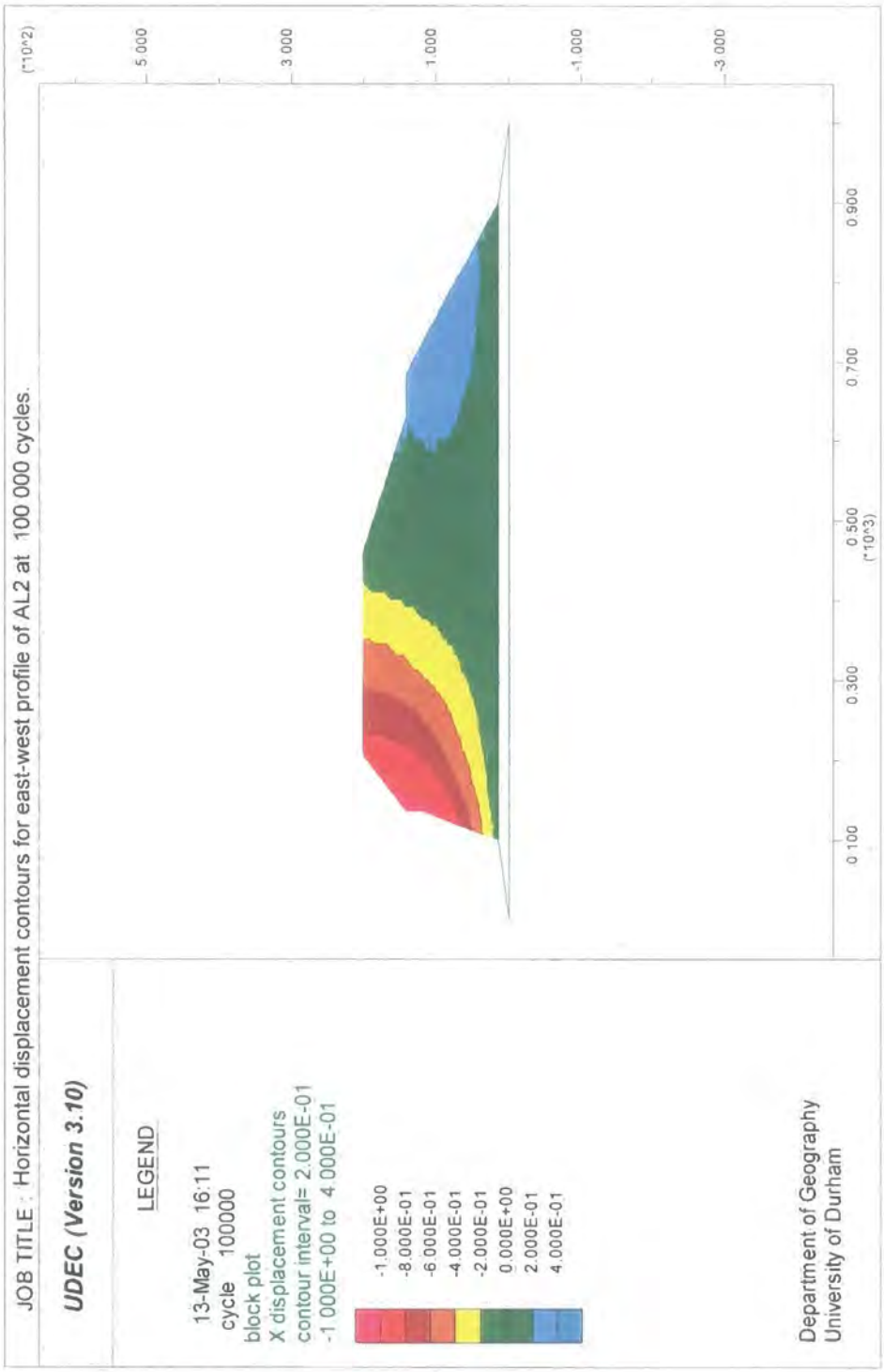

Figure 8.33: Horizontal displacement contours for the east-west profile of AL2 at 100 000 cycles.

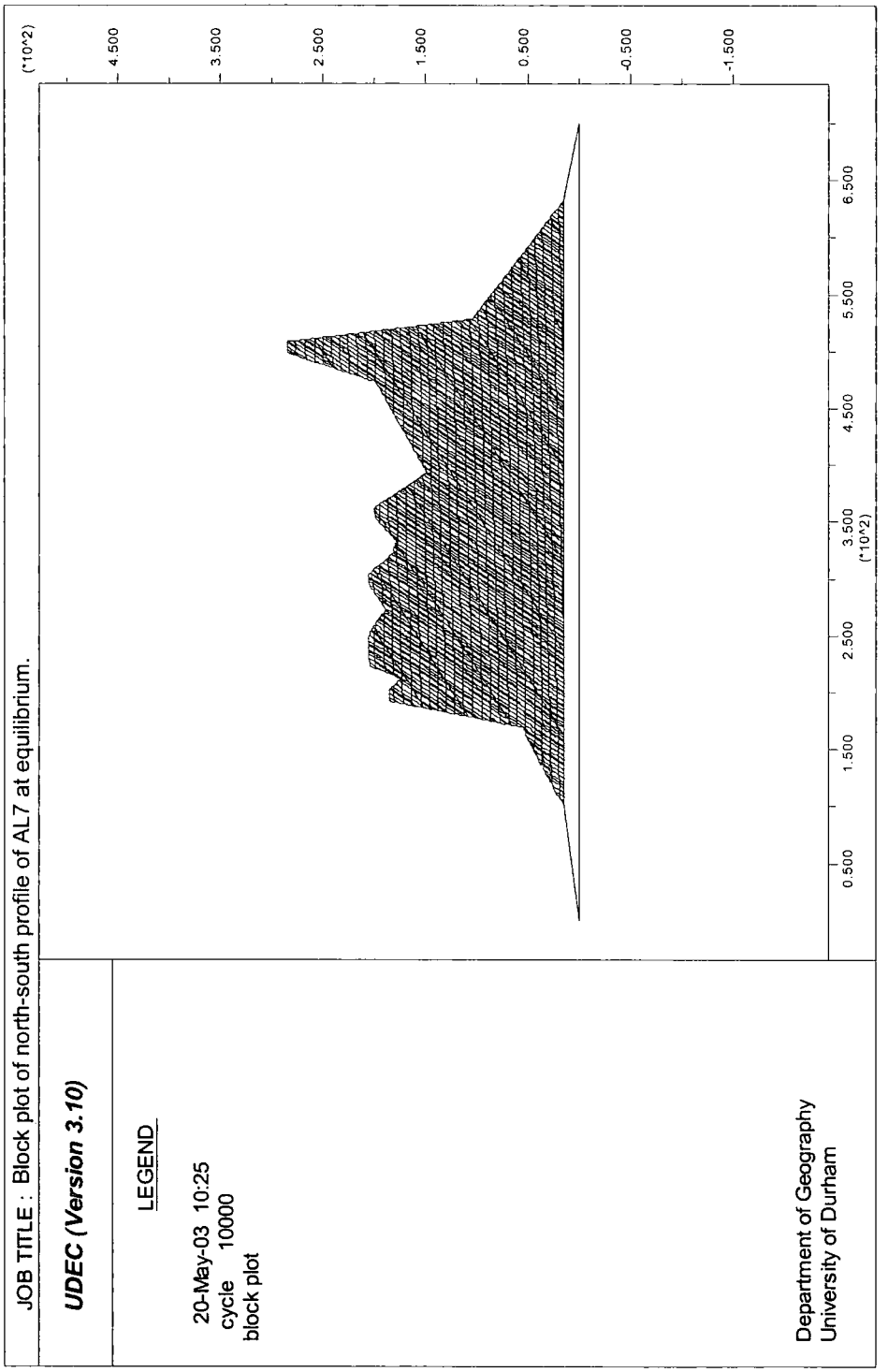

Figure 8.34a: Block plot of the north-south profile of AL7 at equilibrium.

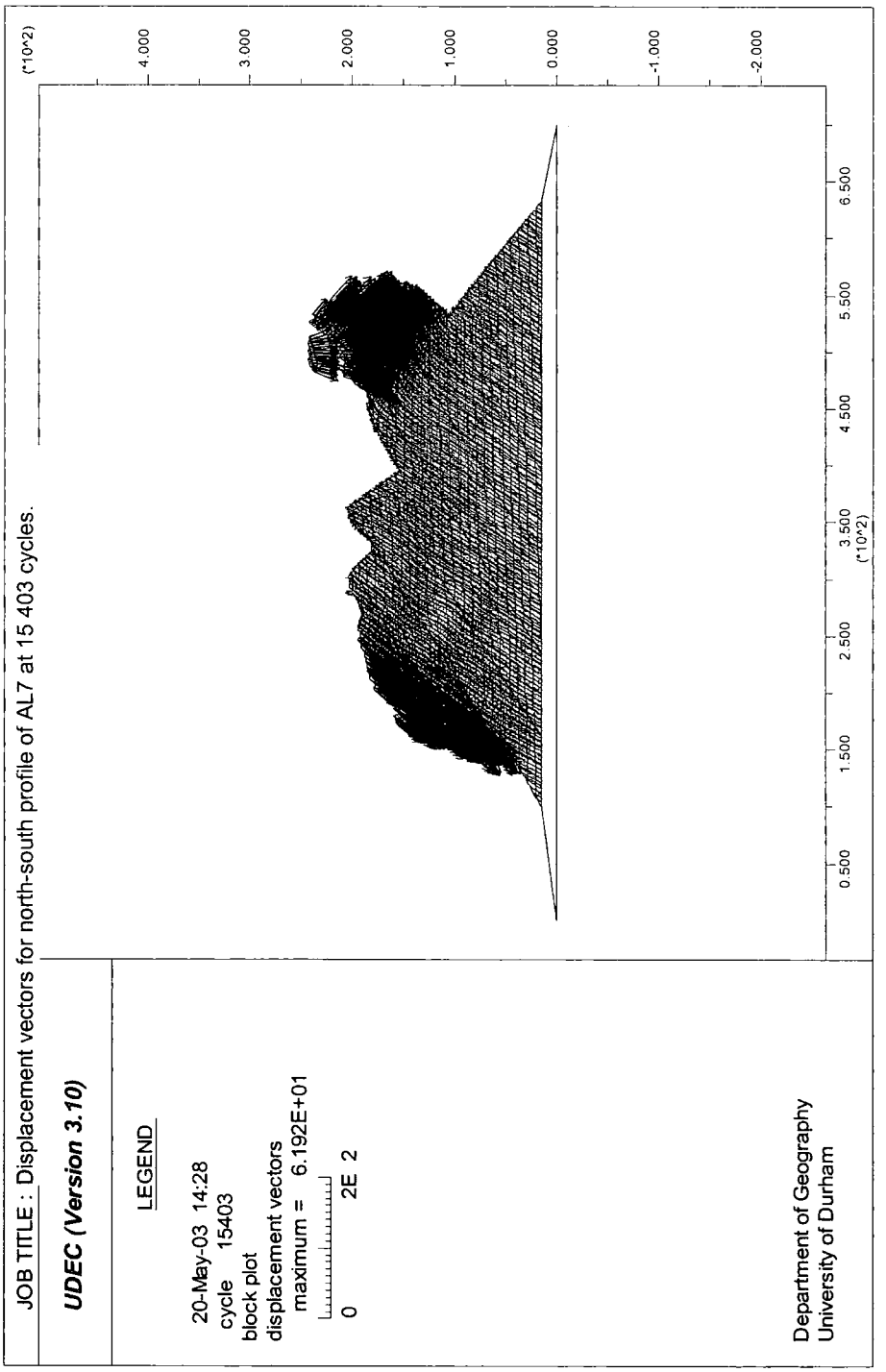

Figure 8.34b: Displacement vectors for the north-south profile of AL7 at 15 403 cycles.

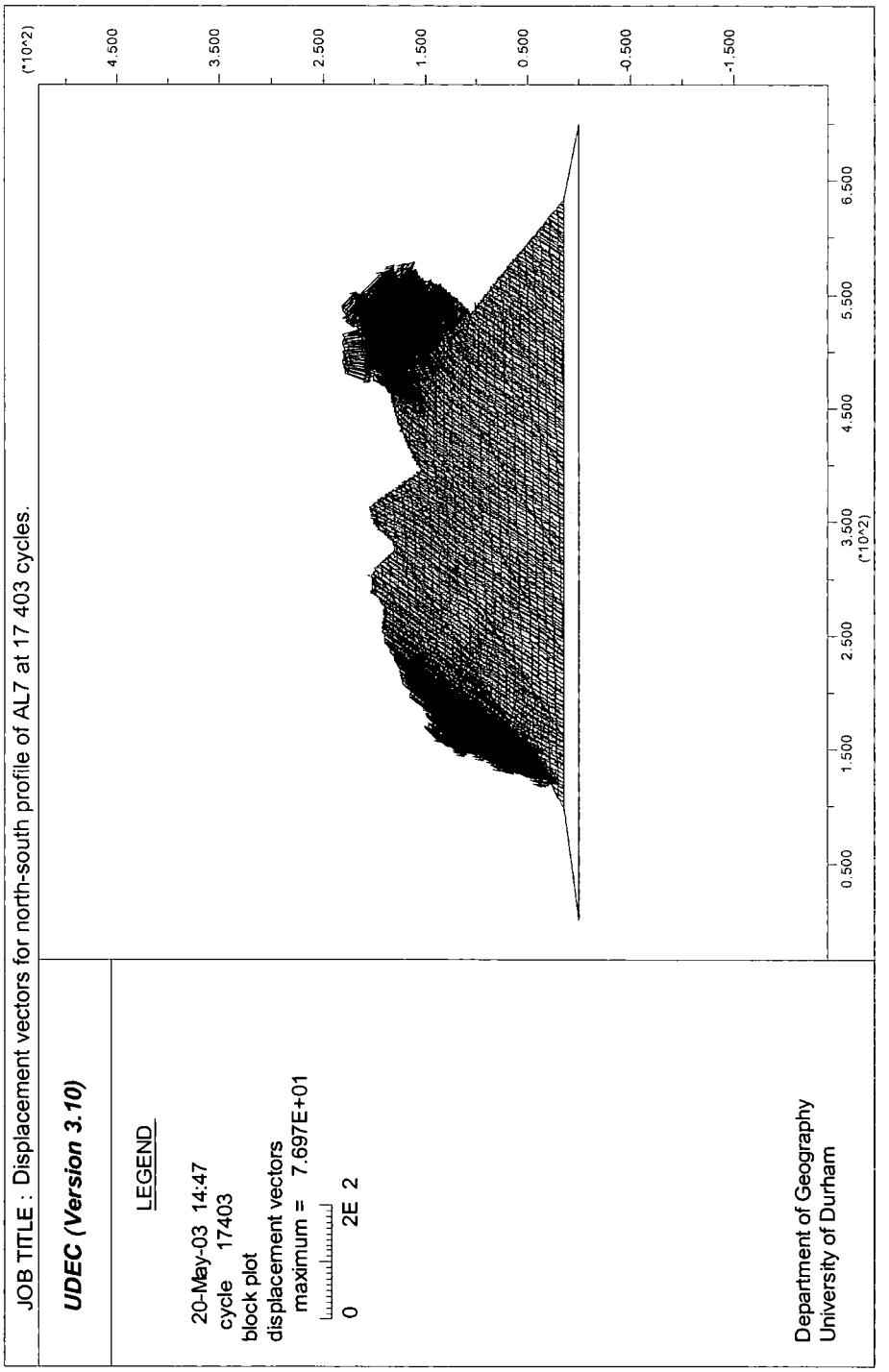

Figure 8.34c: Displacement vectors for the north-south profile of AL7 at 17 403 cycles.

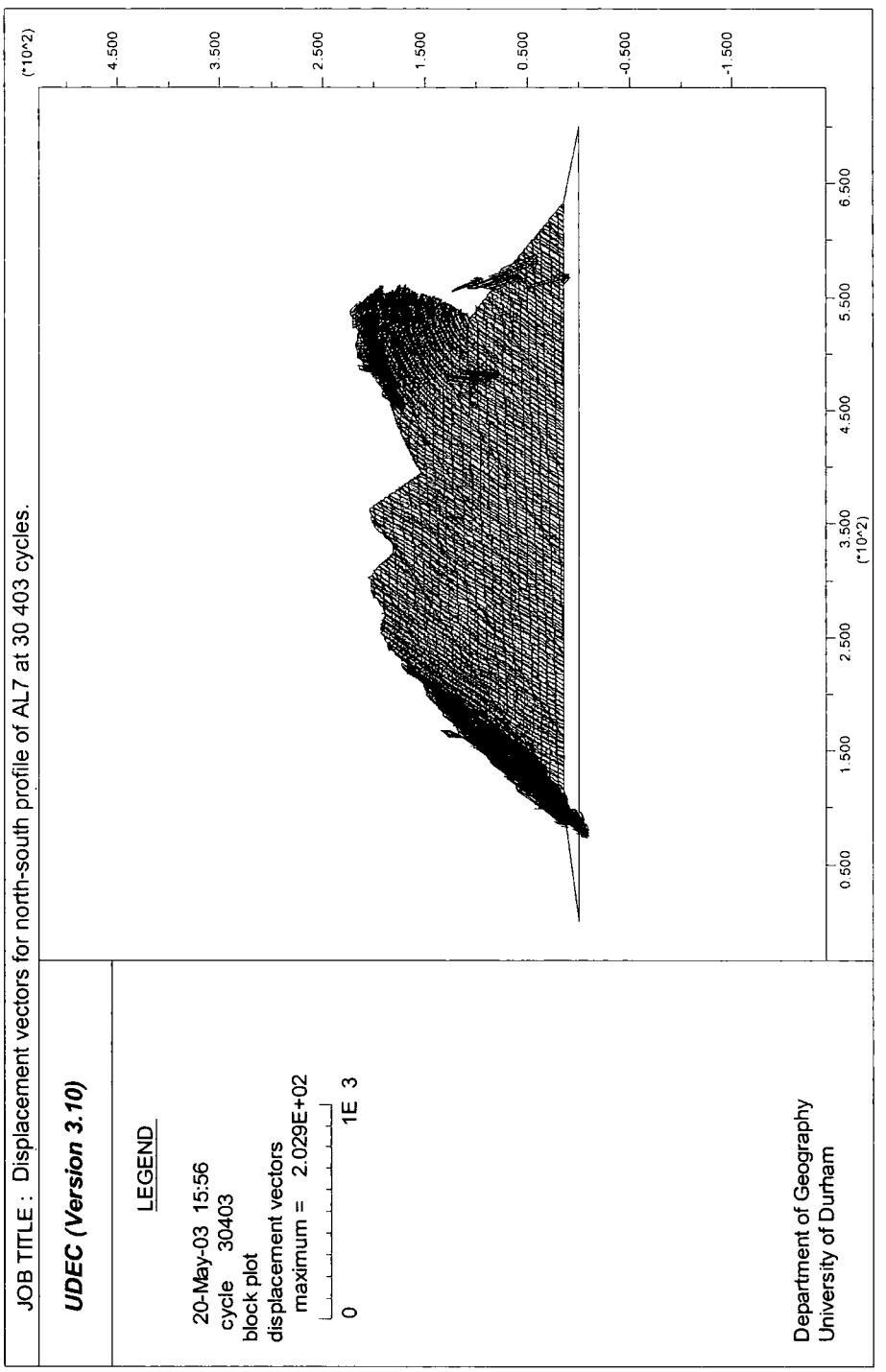

Figure 8.34d: Displacement vectors for the north-south profile of AL7 at 30 056 cycles.

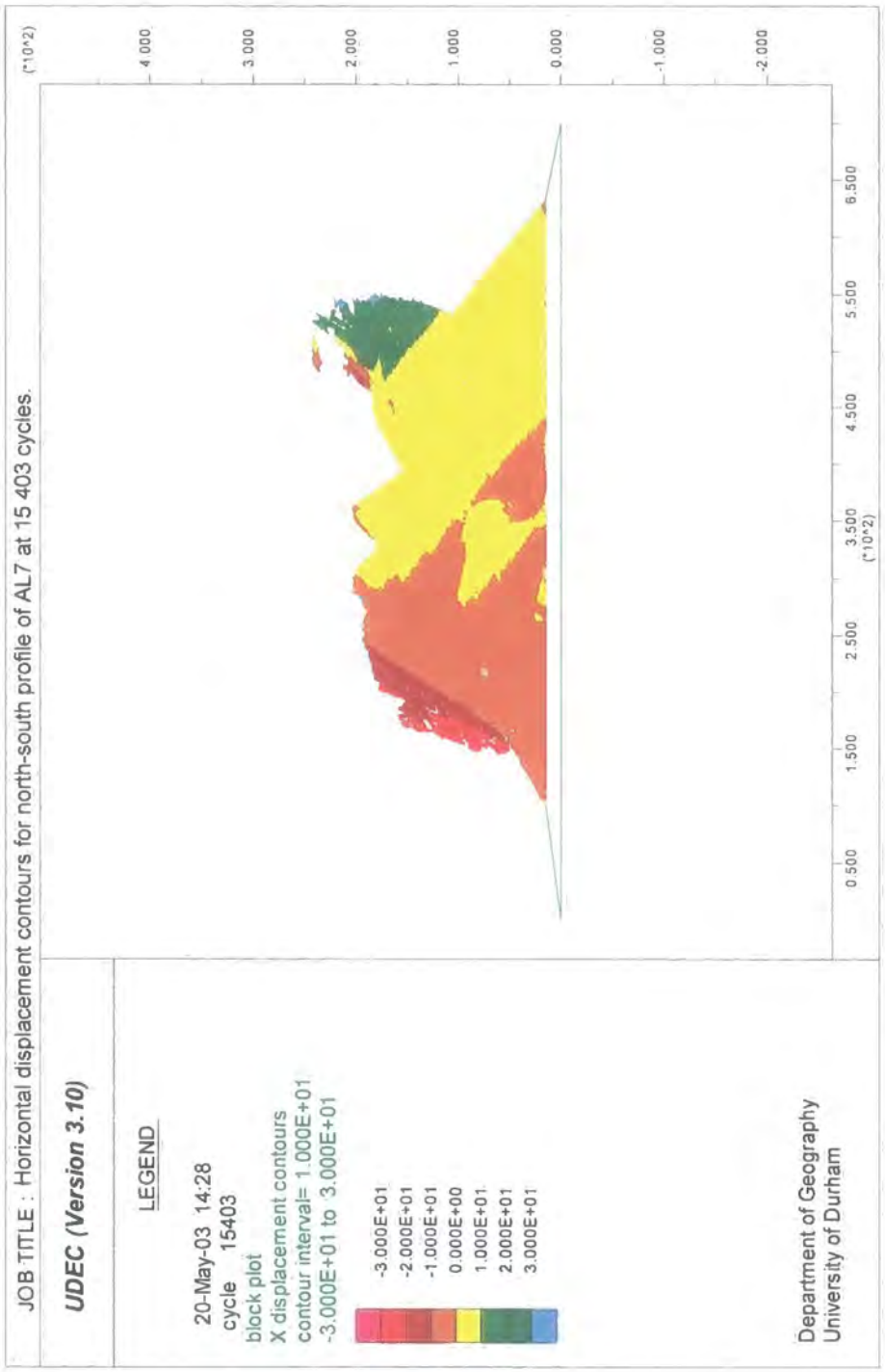

Figure 8.35a: Horizontal displacement contours for the north-south profile of AL7 at 15 403 cycles.

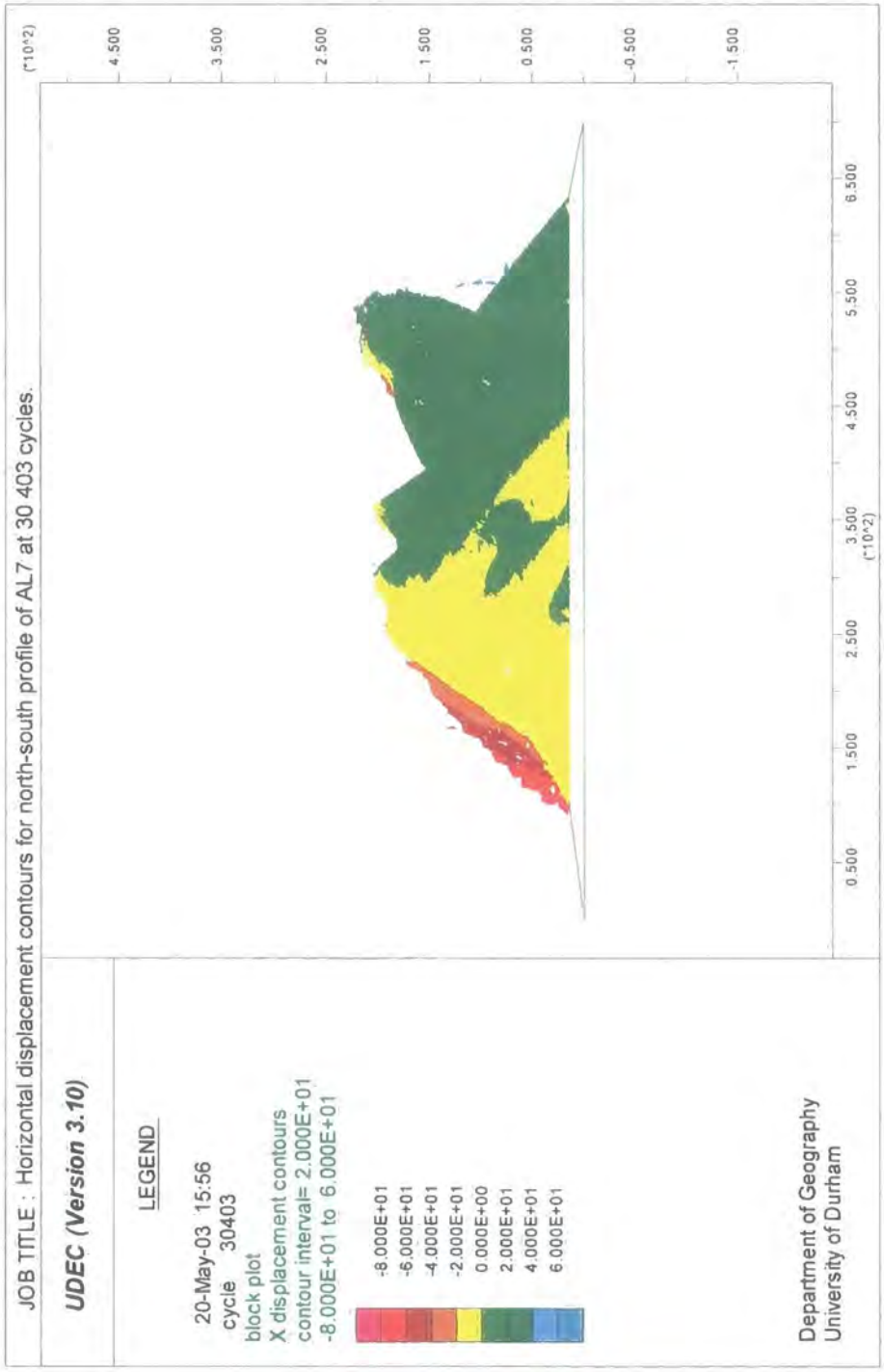

Figure 8.35b: Horizontal displacement contours for the north-south profile of AL7 at 30 403 cycles.

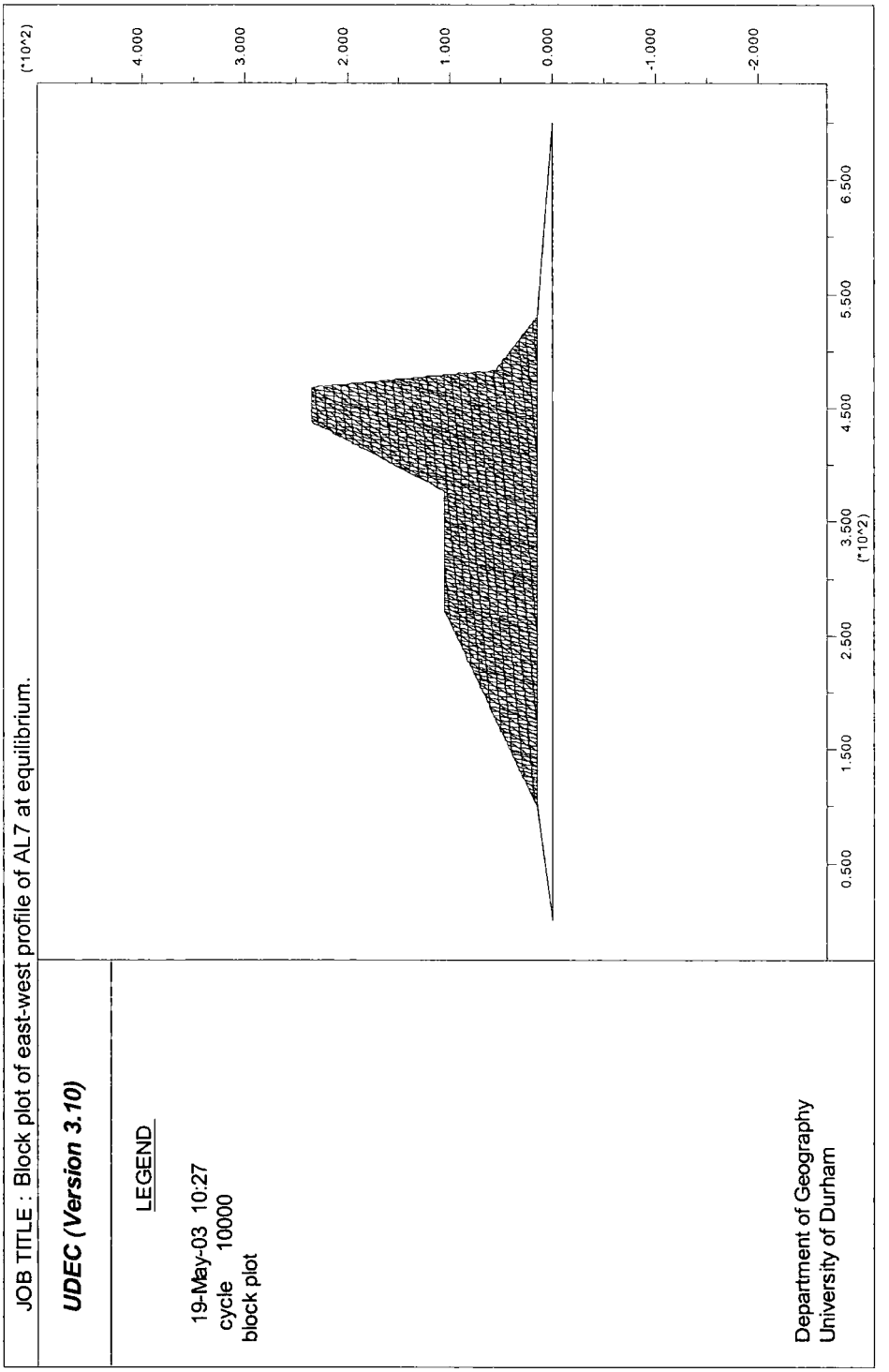

Figure 8.36a: Block plot of the east-west profile of AL7 at equilibrium.

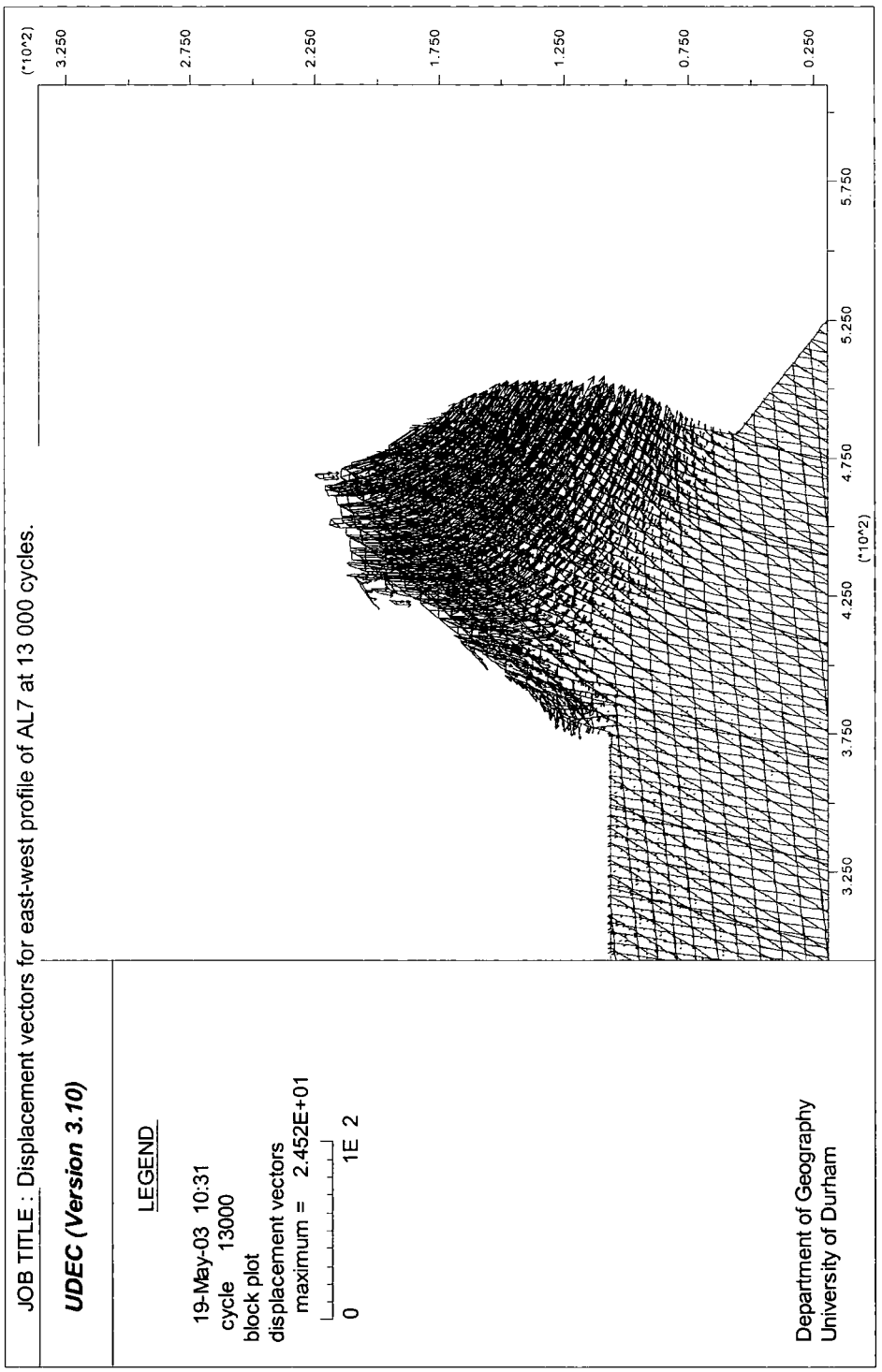

Figure 8.36b: Displacement vectors for the east-west profile of AL7 at 13 000 cycles.

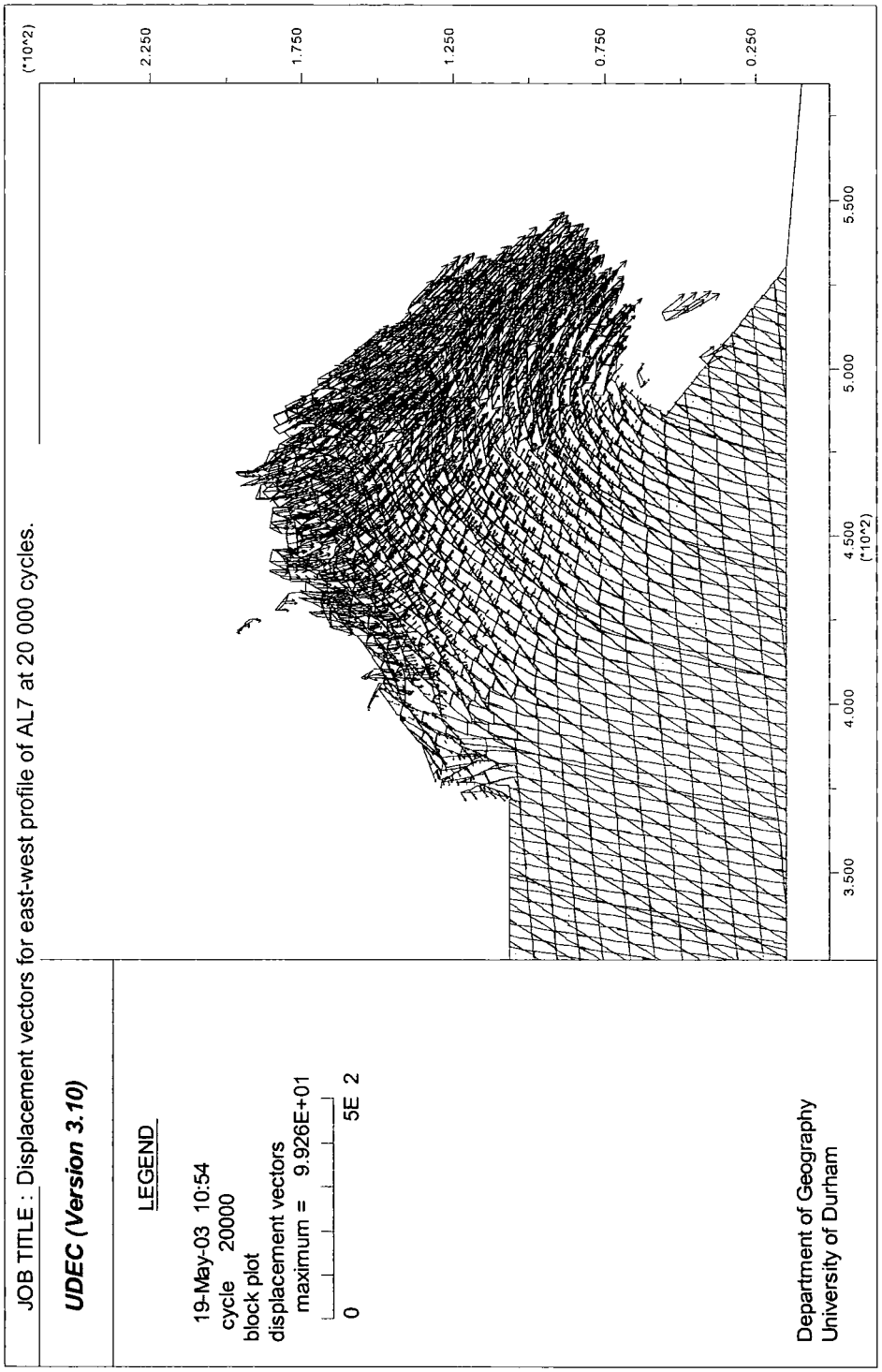

Figure 8.36c: Displacement vectors for the east-west profile of AL7 at 20 000 cycles.

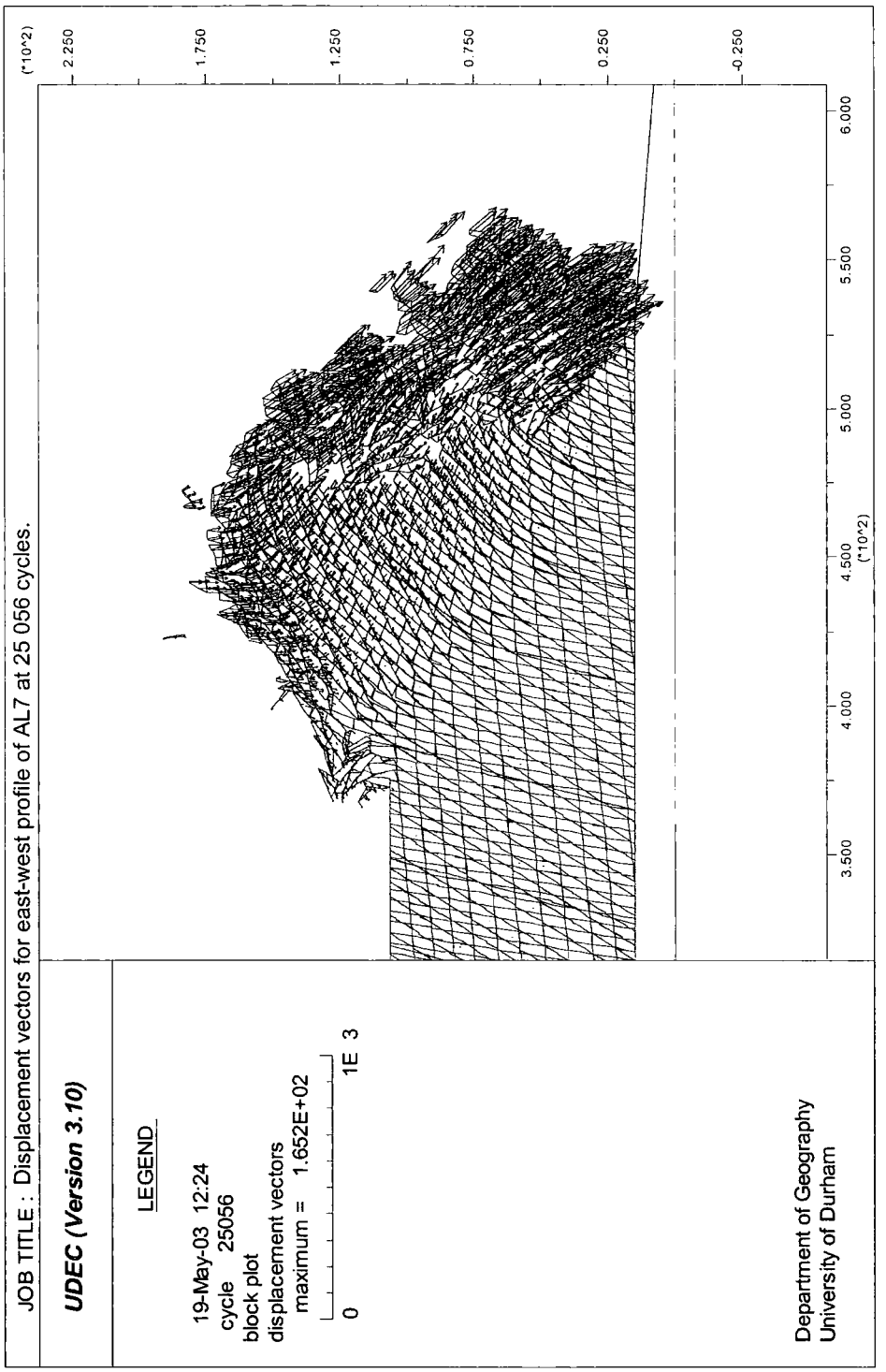

Figure 8.36d: Displacement vectors for the east-west profile of AL7 at 25 056 cycles.

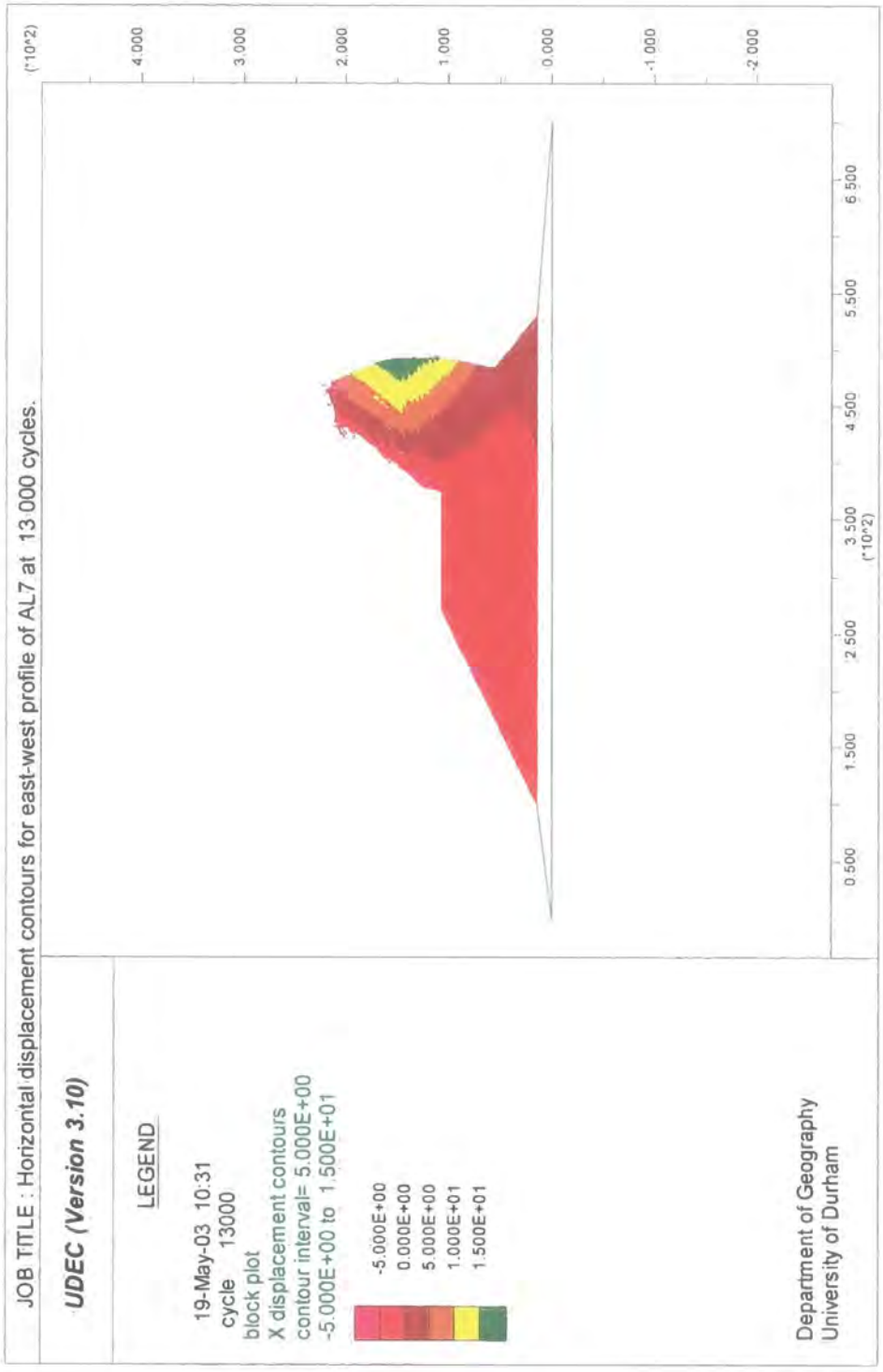

Figure 8.37a: Horizontal displacement contours for the east-west profile of AL7 at 13 000 cycles.

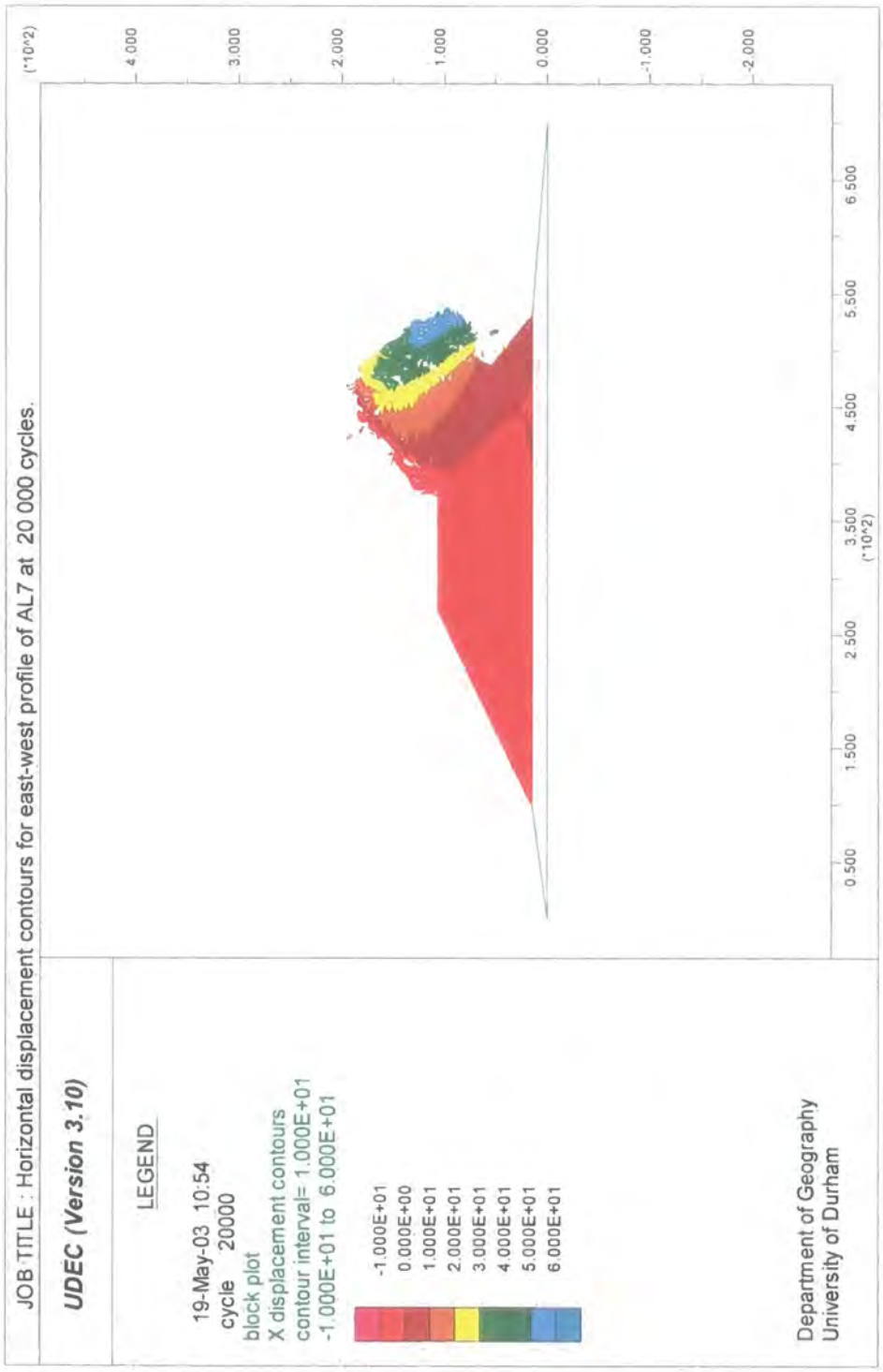

Figure 8.37b: Horizontal displacement contours for the east-west profile of AL7 at 20 000 cycles.

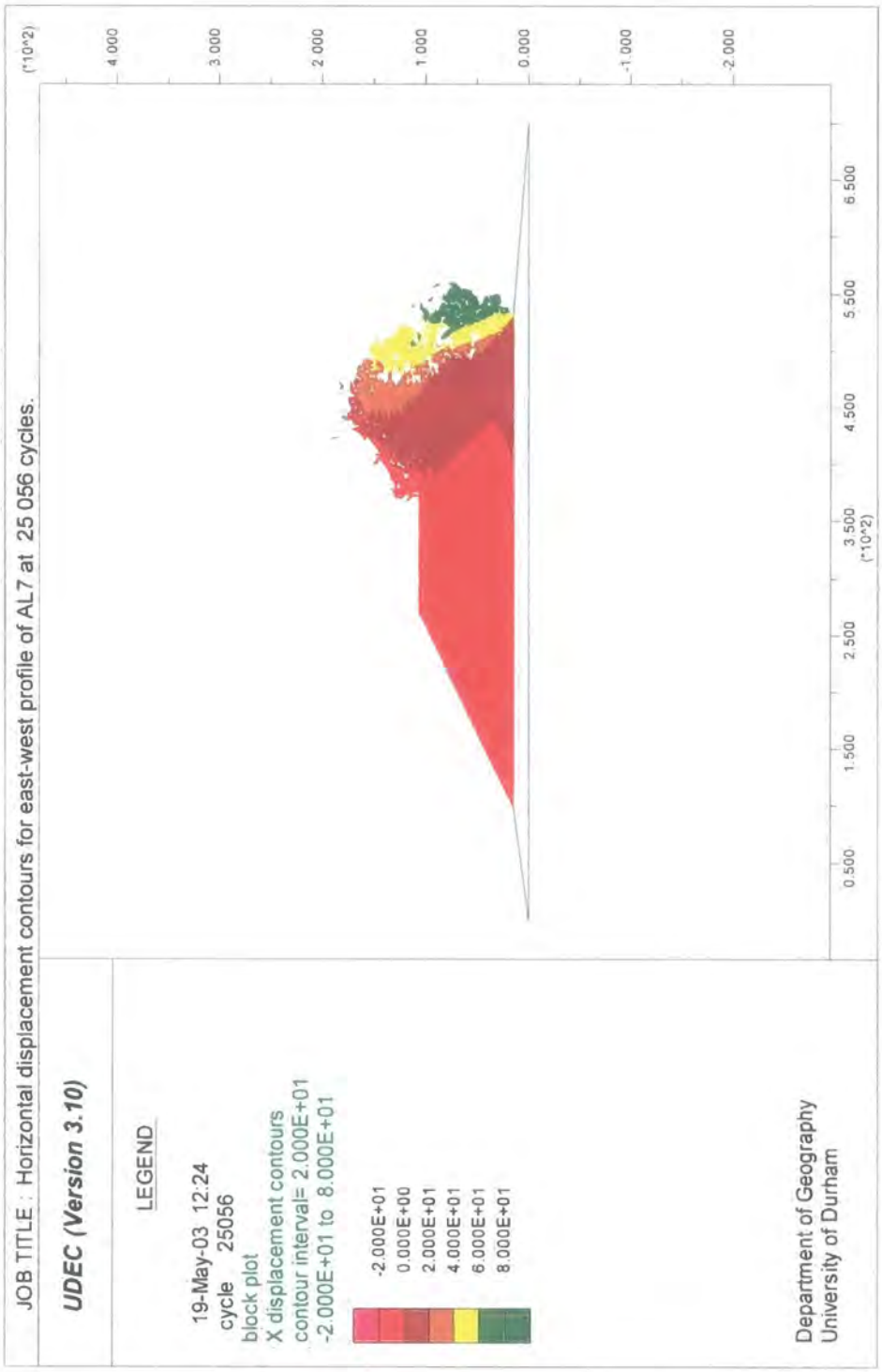

Figure 8.37c: Horizontal displacement contours for the east-west profile of AL7 at 25 056 cycles.

Figure 8.38a: Block plot of the east-west profile of AL17 at equilibrium.

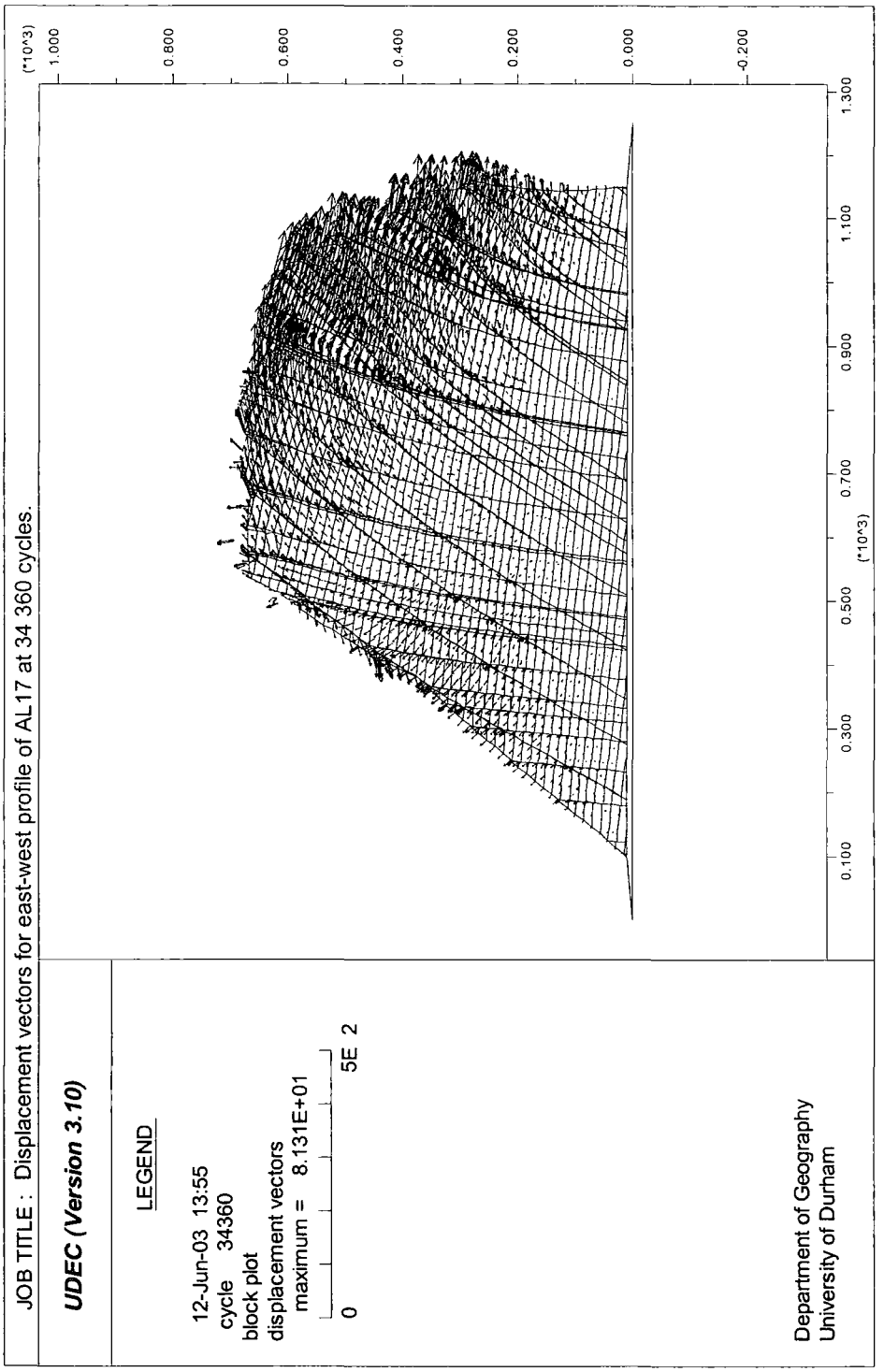

Figure 8.38b: Displacement vectors for the east-west profile of AL17 at 34 360 cycles.

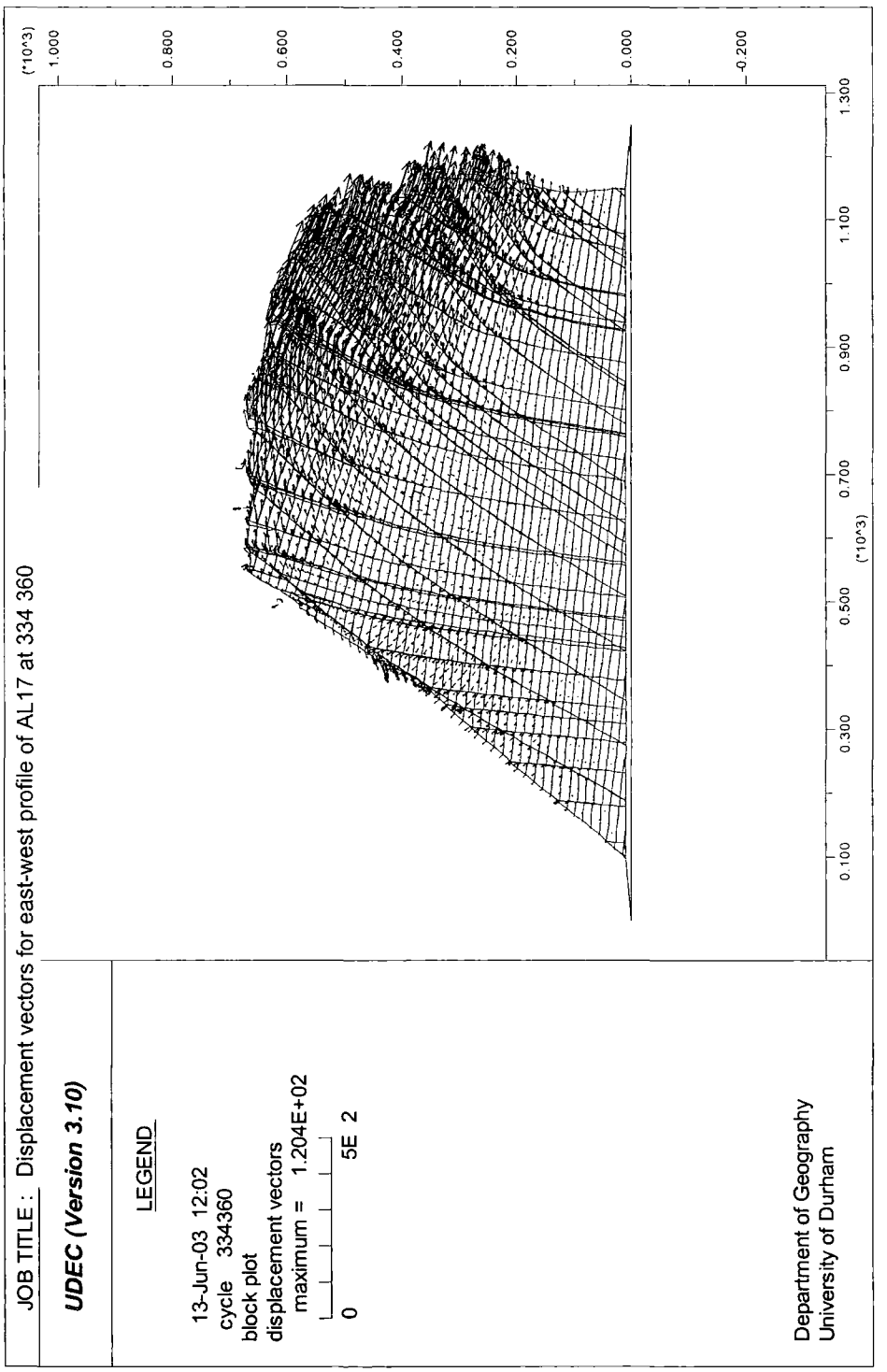

Figure 8.38c: Displacement vectors for the east-west profile of AL17 at 334 360 cycles.

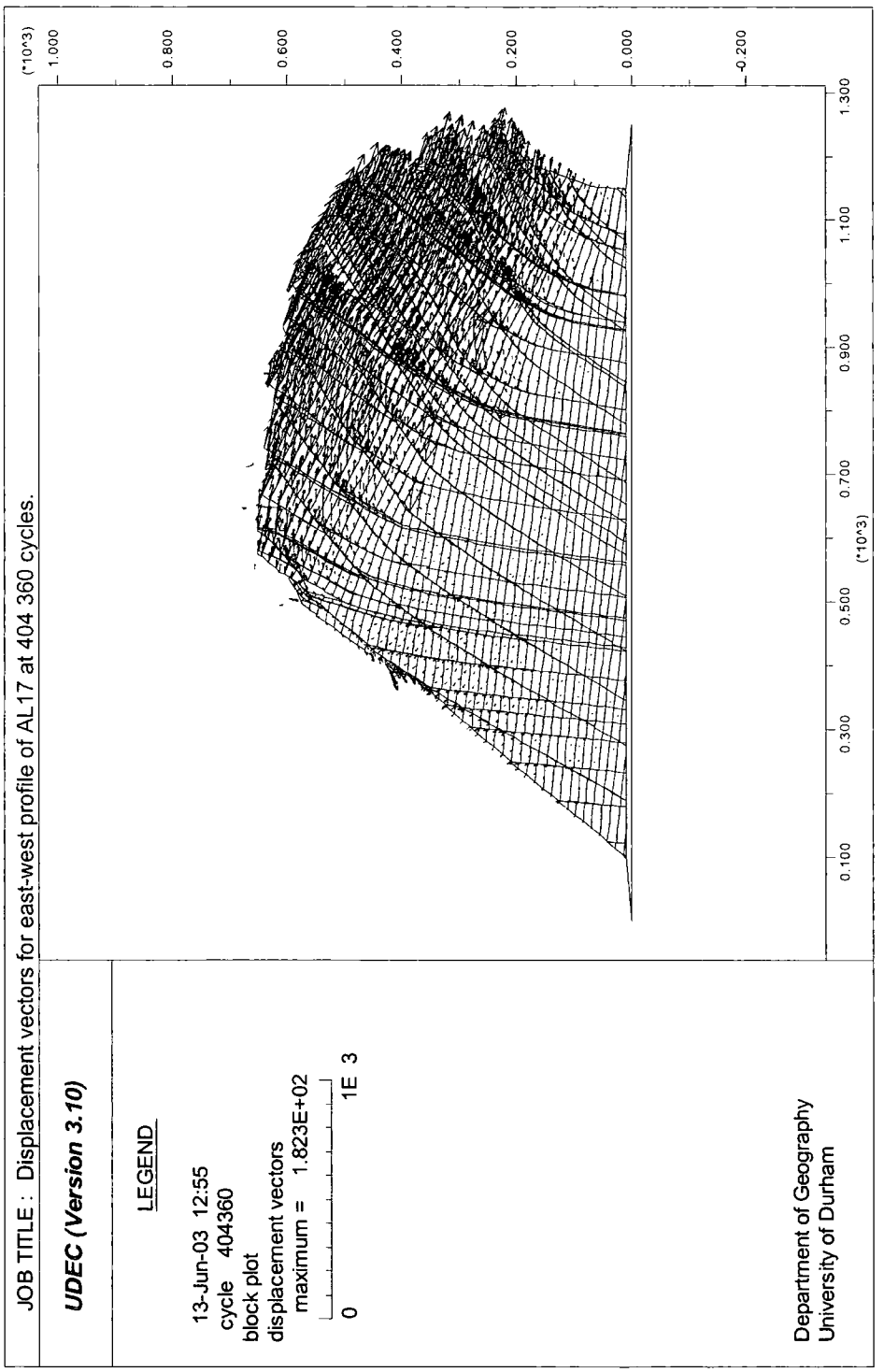

Figure 8.38d: Displacement vectors for the east-west profile of AL17 at 404 360 cycles.

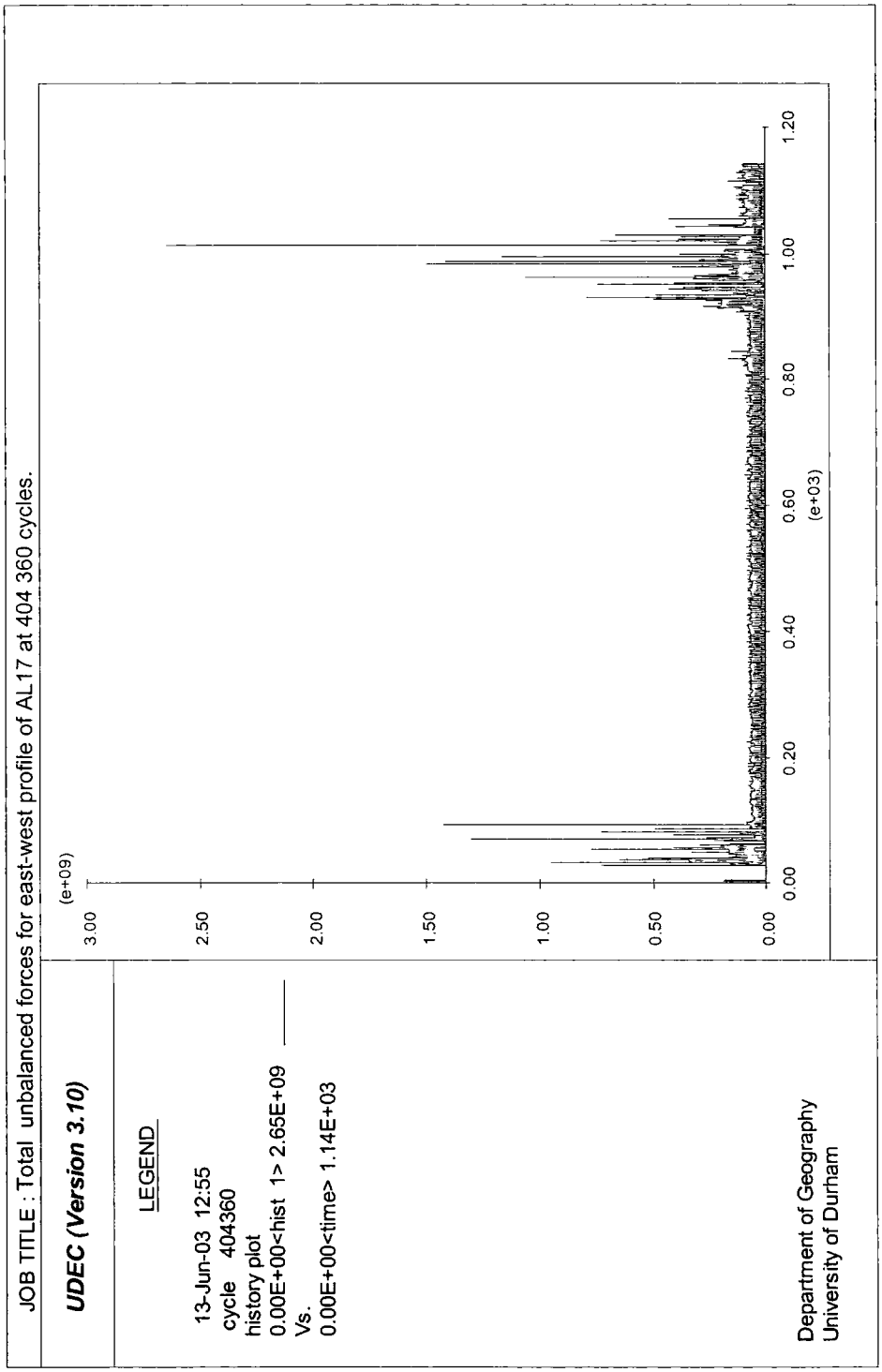

Figure 8.39: Total unbalanced forces for the east-west profile of AL17 at 404 360 cycles.

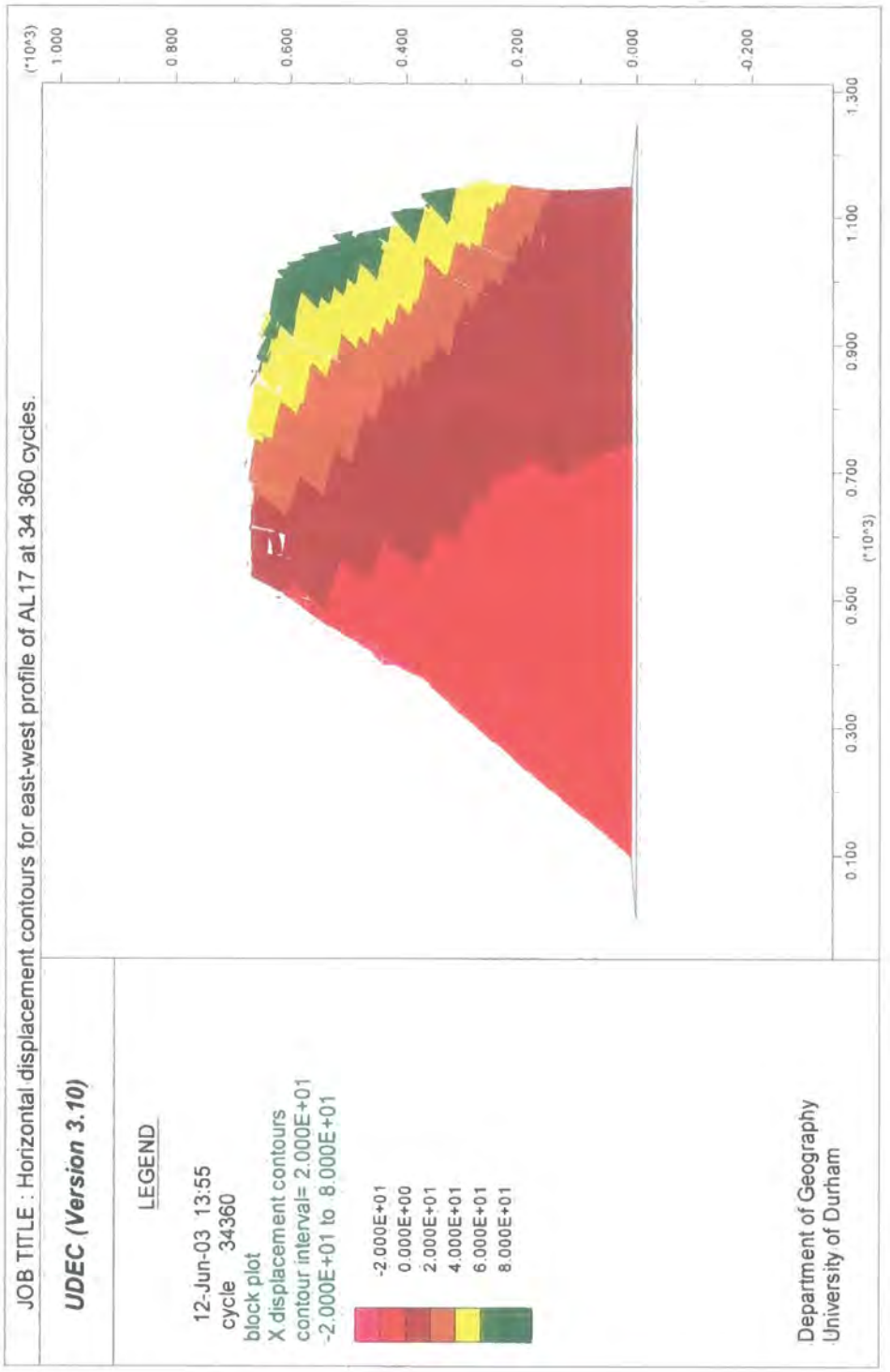

Figure 8.40a: Horizontal displacement contours for the east-west profile of AL17 at 34 360 cycles.

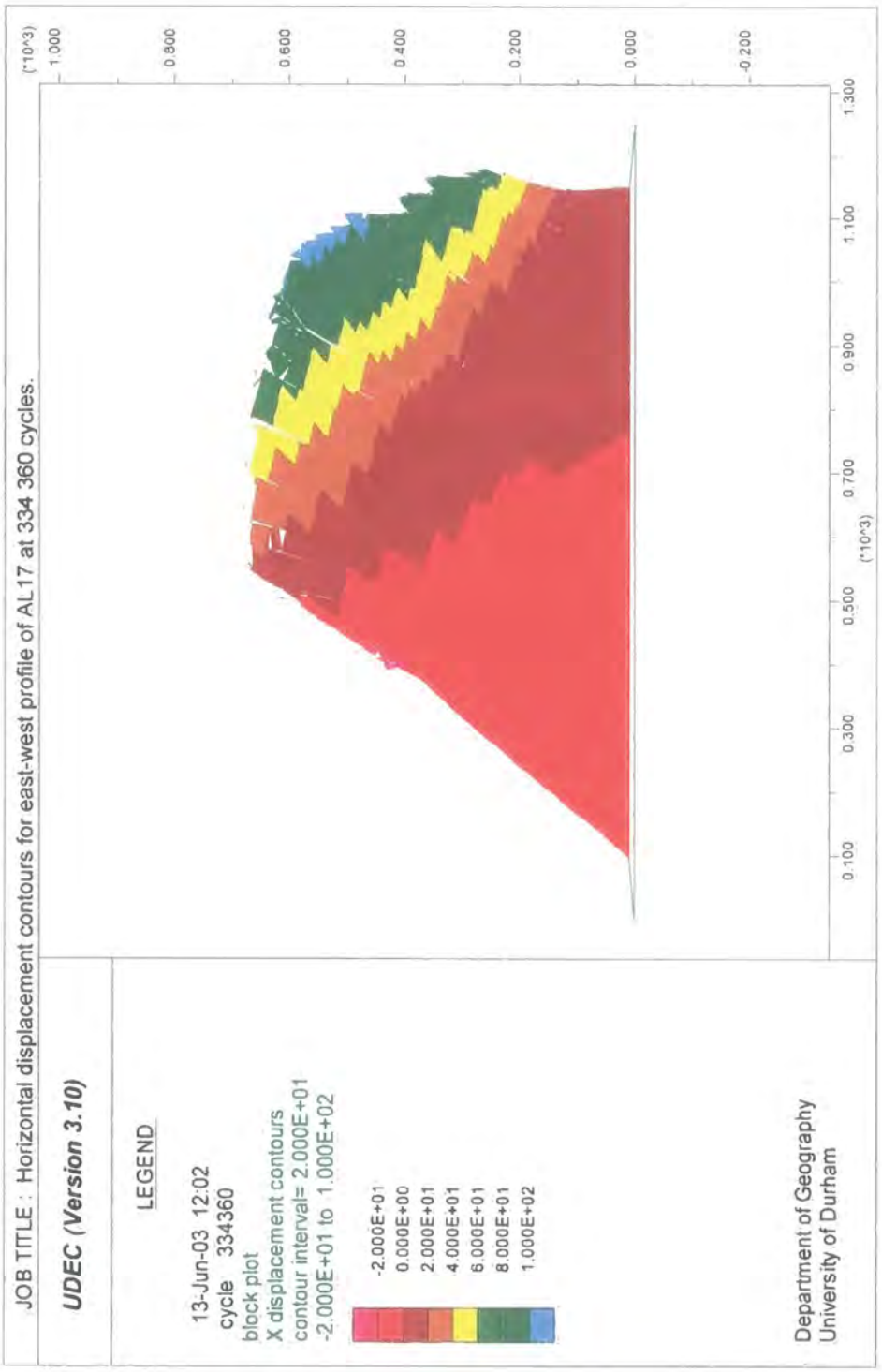

Figure 8.40b: Horizontal displacement contours for the east-west profile of AL17 at 334 360 cycles.

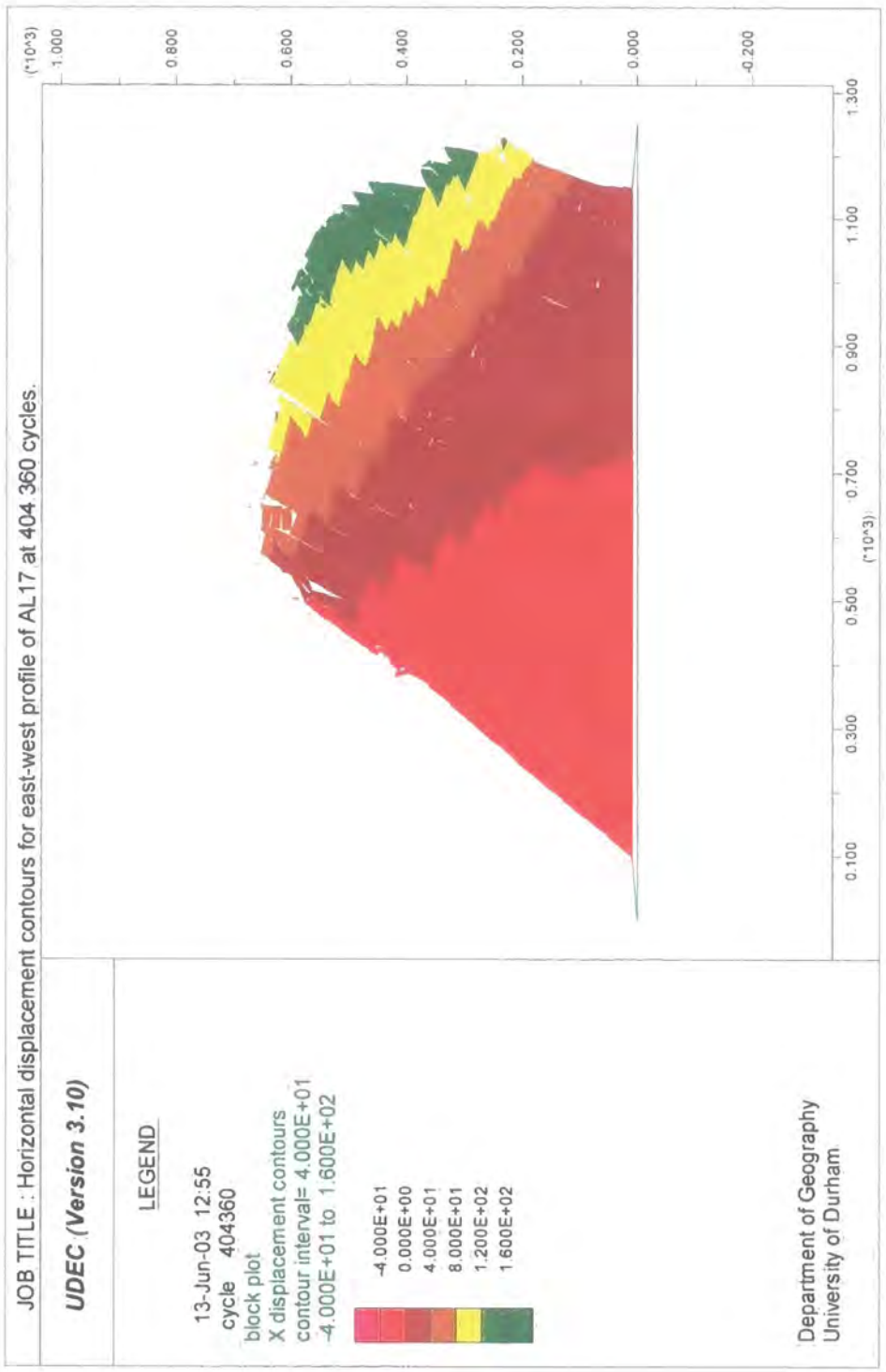

Figure 8.40c: Horizontal displacement contours for the east-west profile of AL17 at 404 360 cycles.

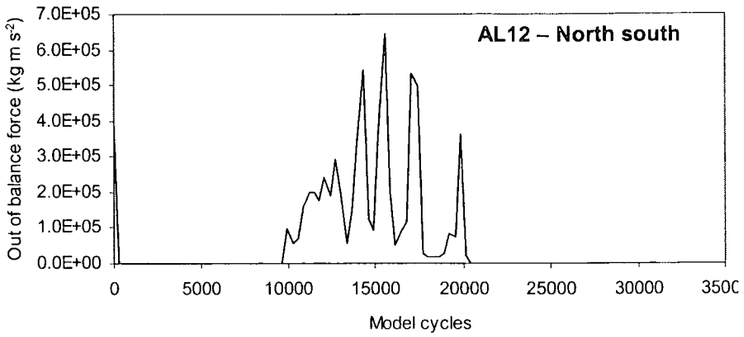

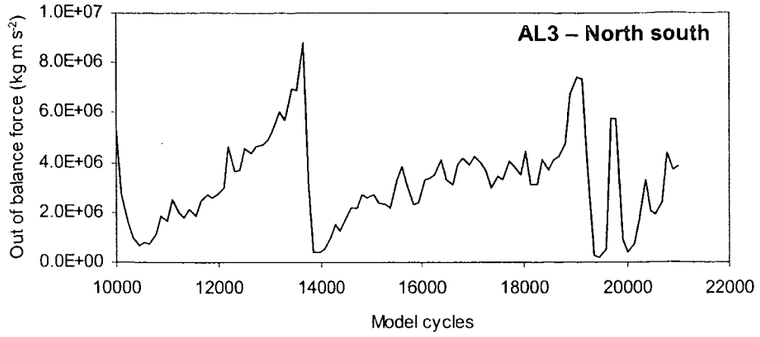

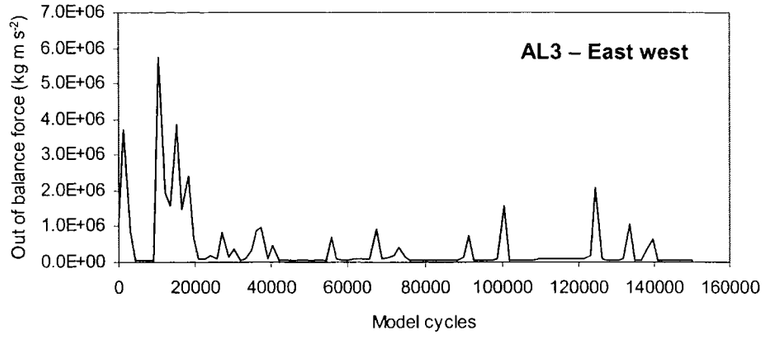

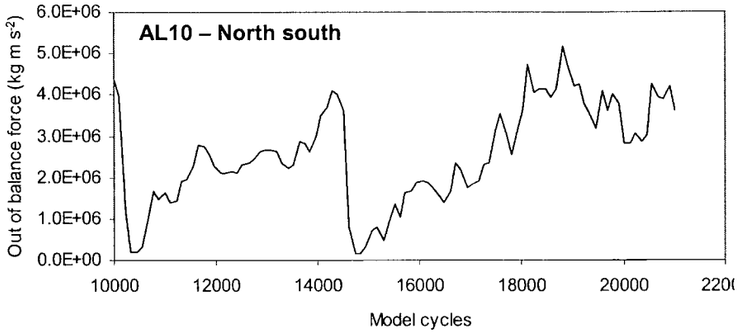

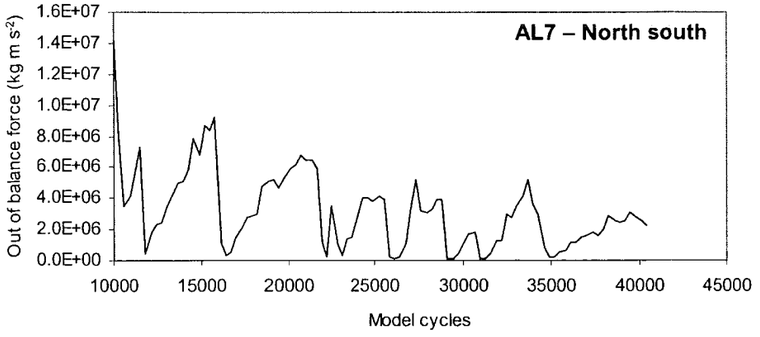

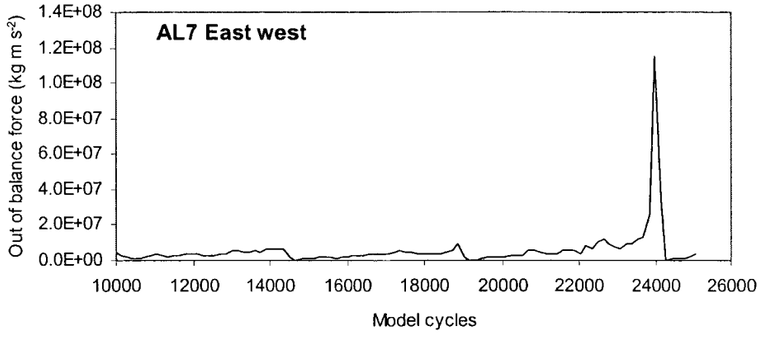

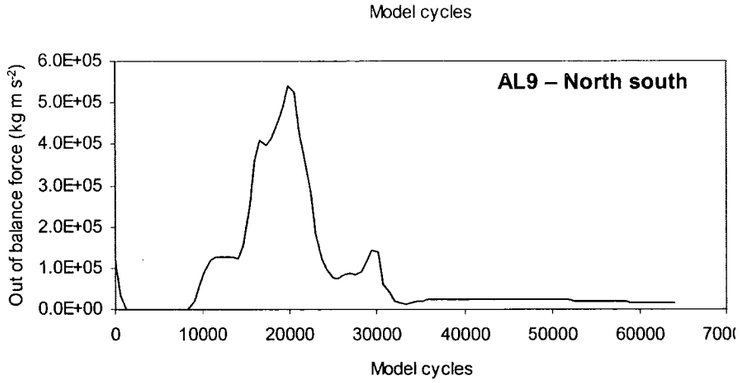

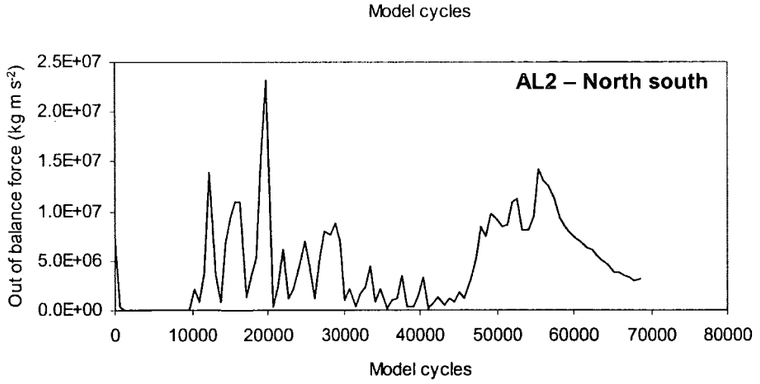

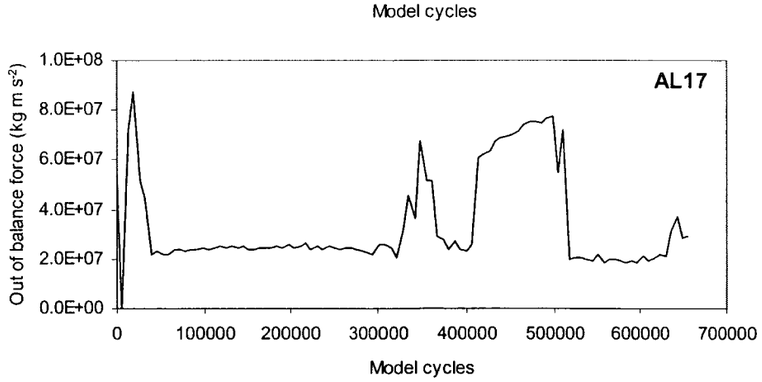

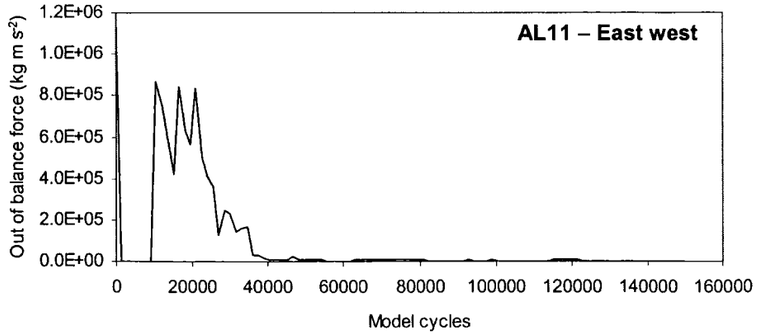

Figure 8.41: Out of balance forces with loess smoothing function applied to pick out the main trends in unbalanced forces.

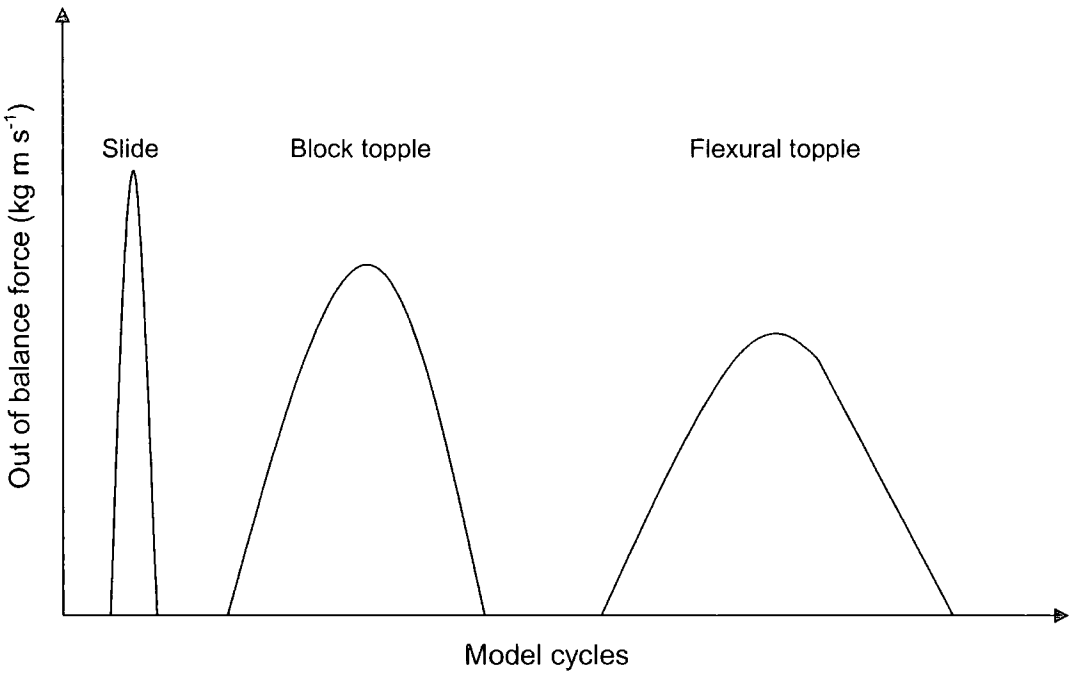

Figure 8.42: Comparison of failure mechanisms compared with the out of balance forces for models simulating the sandstone inselbergs of the Wadi Rum region.

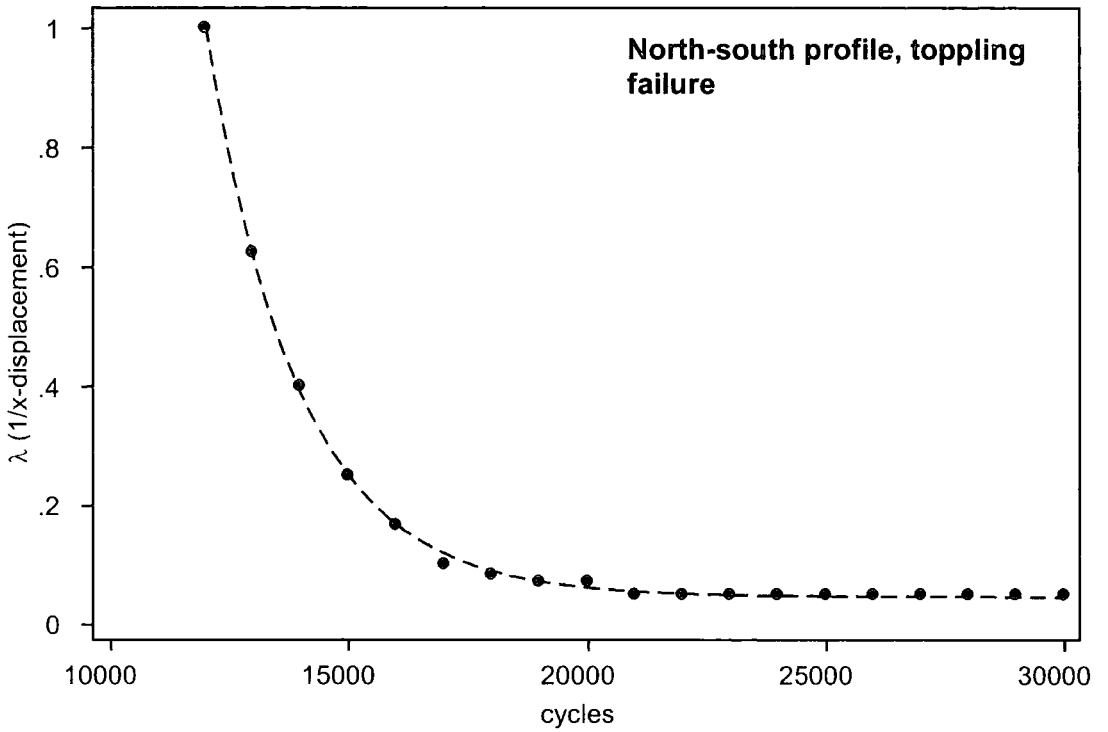

Figure 8.43: Exponential asymptotic model (dashed line) applied to x-displacement data for the toppling failure on the north face of AL9.

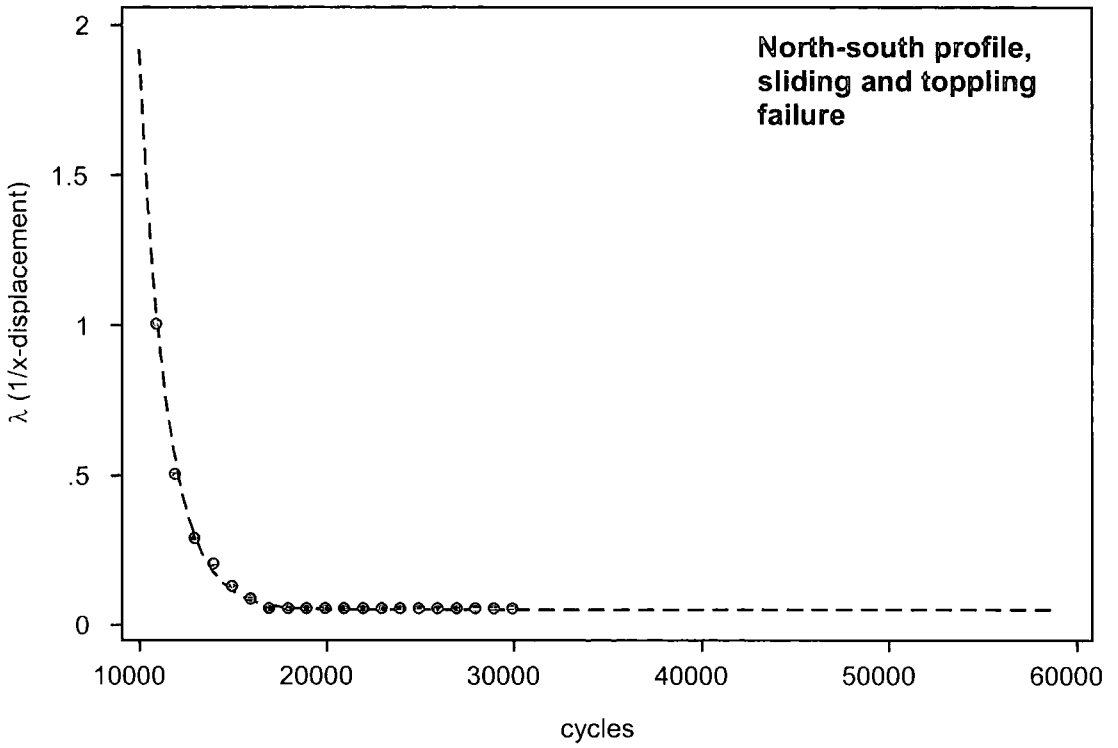

Figure 8.44: Exponential asymptotic model (dashed line) applied to x-displacement data for the failure on the south face of AL12.

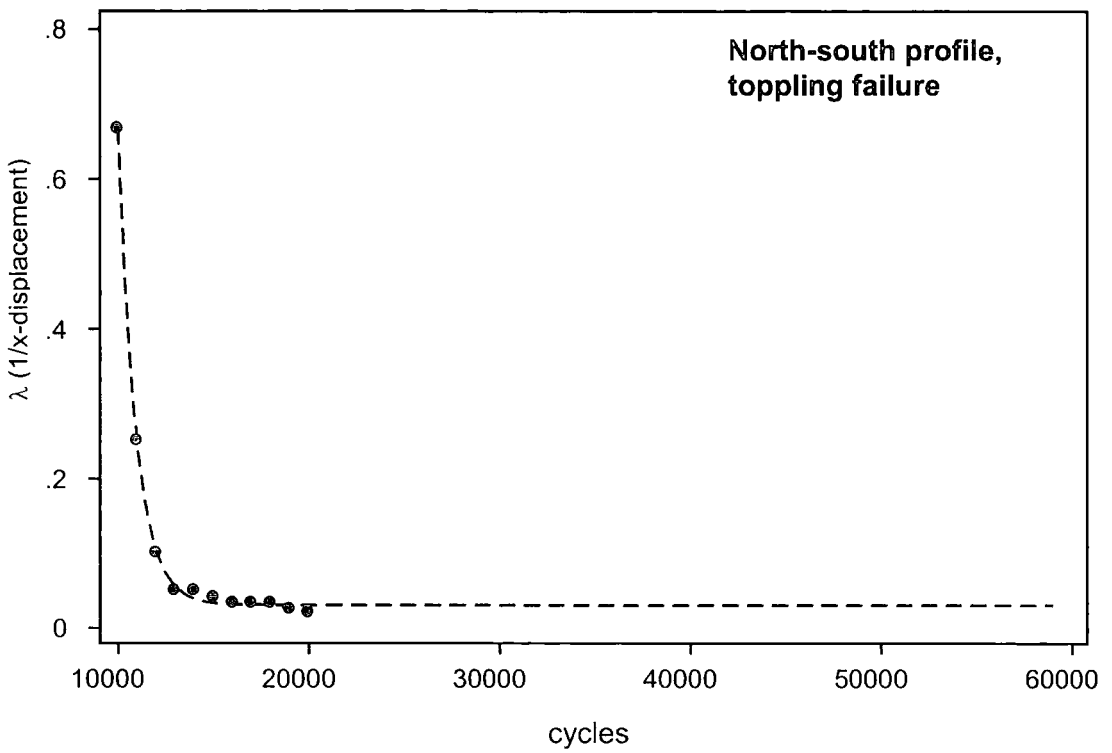

Figure 8.45: Exponential asymptotic model (dashed line) applied to x-displacement data for the toppling failure on the south face of AL10.

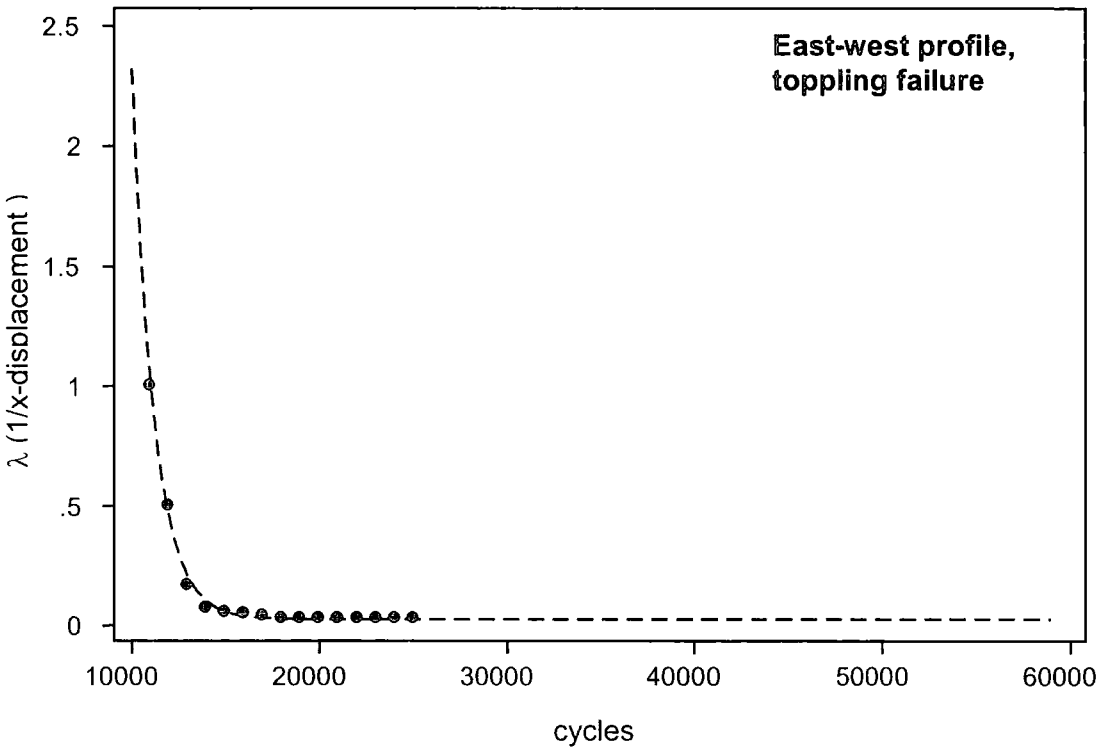

Figure 8.46: Exponential asymptotic model (dashed line) applied to x-displacement data for the failures on the east of AL11.

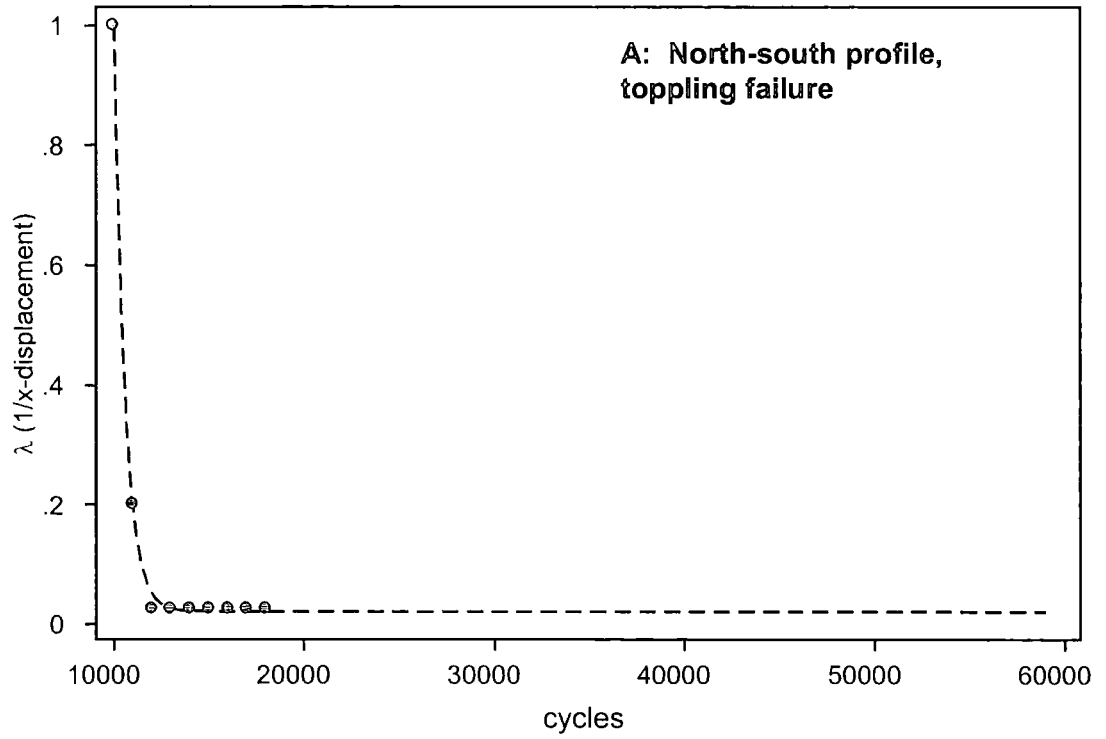

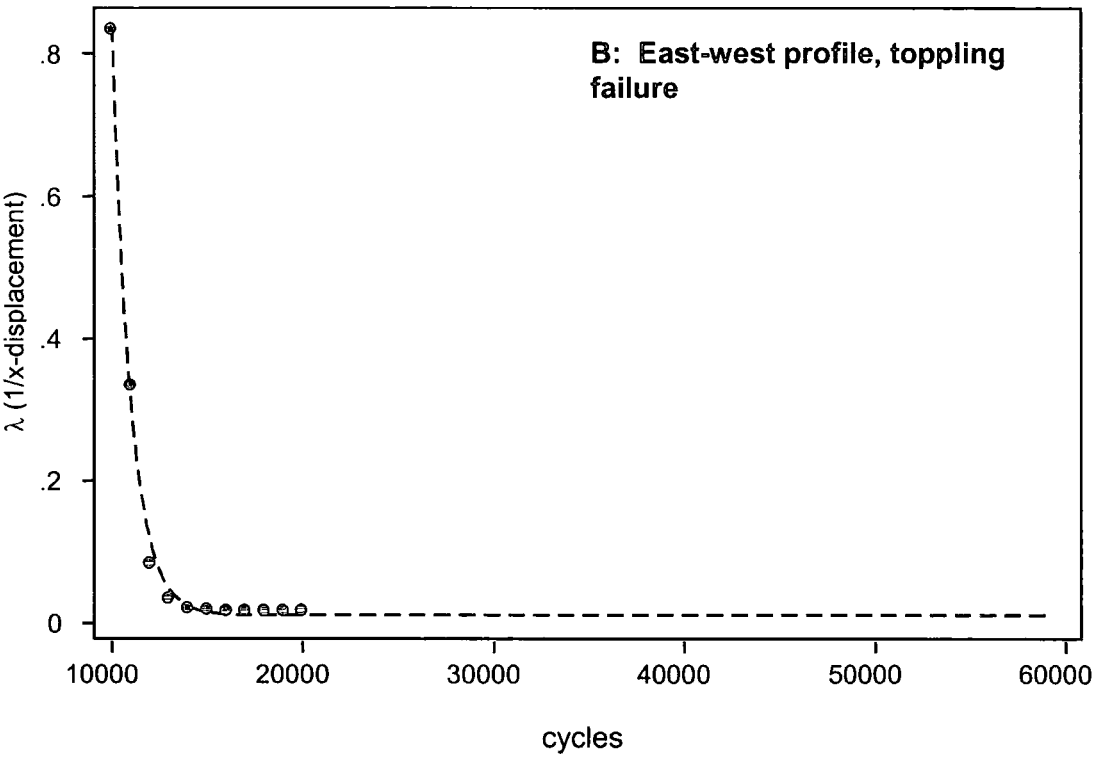

Figure 8.47: Exponential asymptotic model (dashed line) applied to x-displacement data for the failures on the east (a) and south (b) faces.

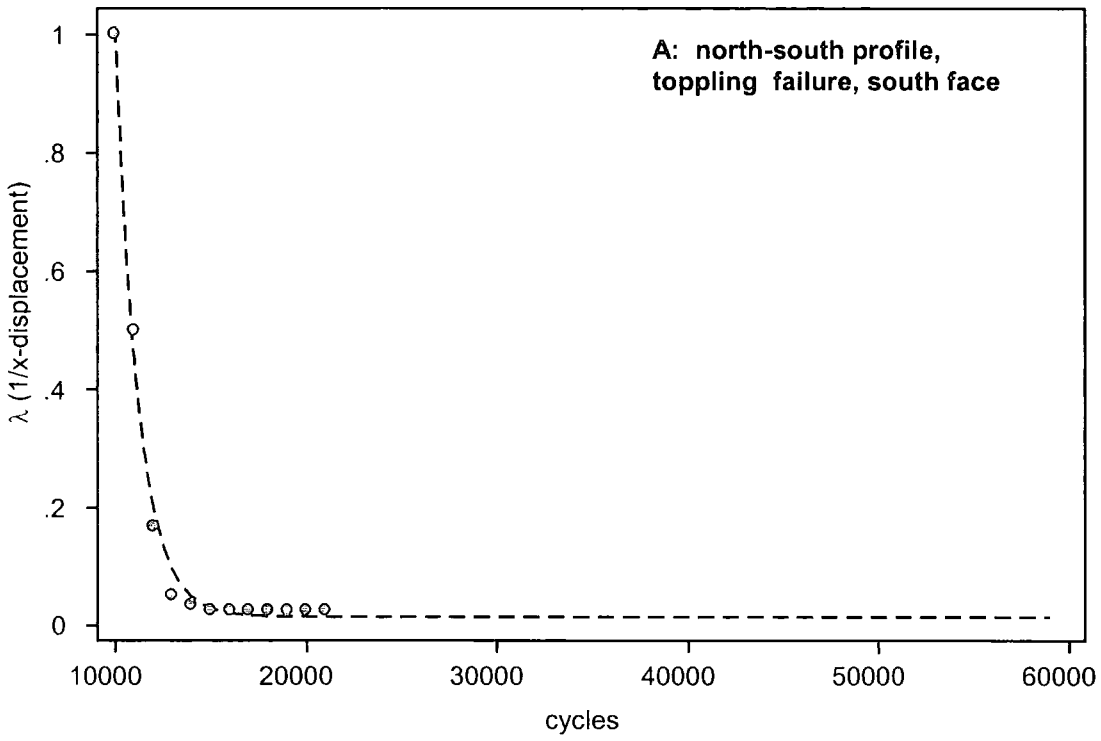

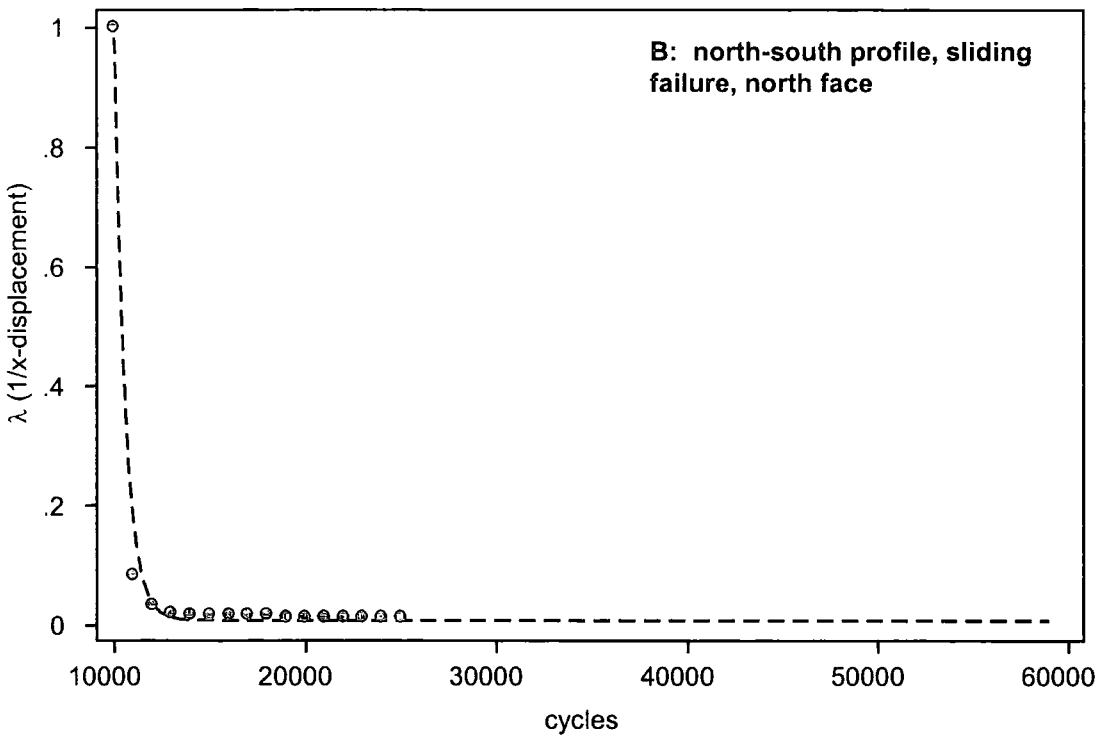

Figure 8.48: Exponential asymptotic model (dashed line) applied to x-displacement data for the failures on the north and south faces of AL2.

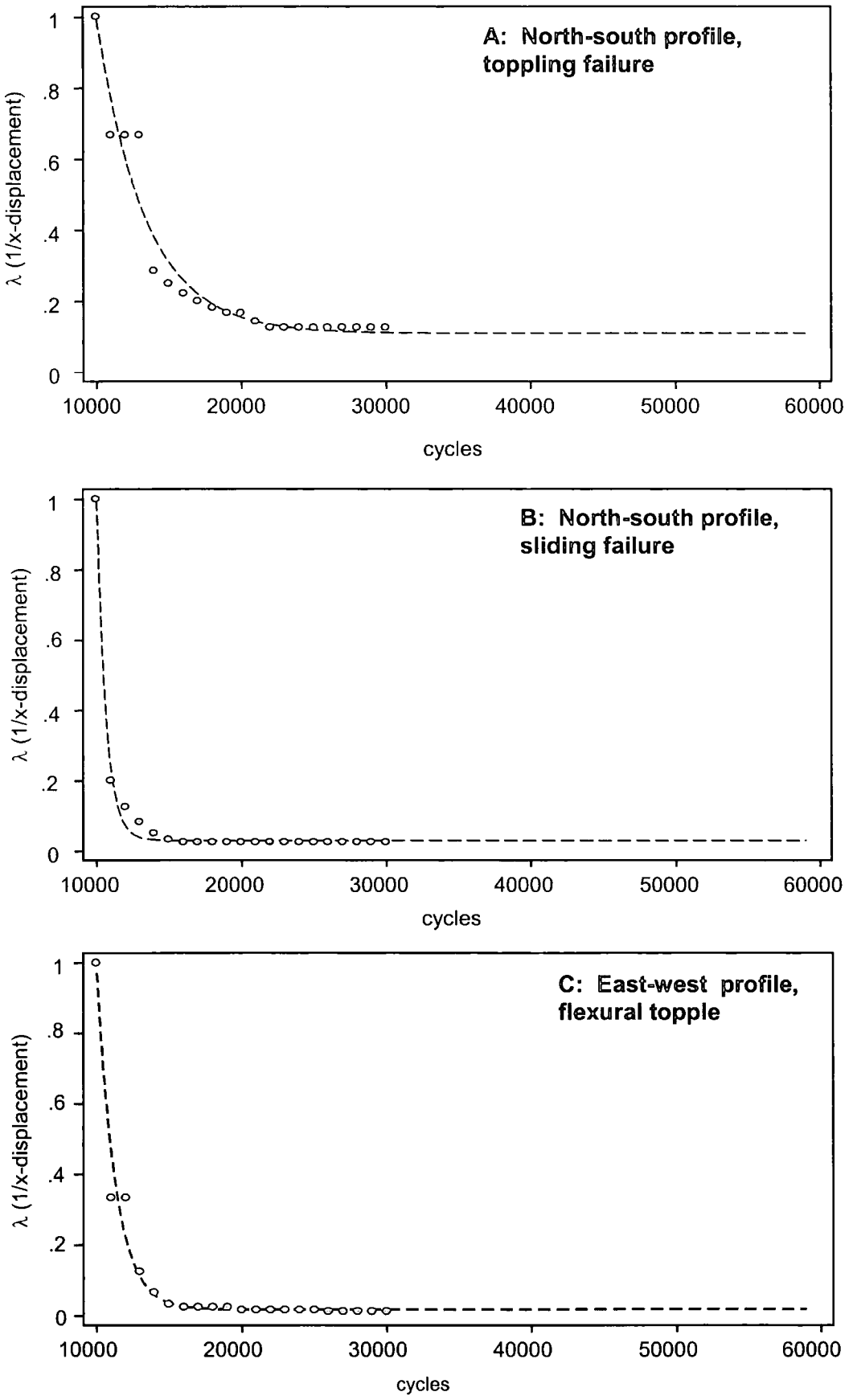

Figure 8.49: Exponential asymptotic model (dashed line) applied to x-displacement data for the failures on the west and south faces of AL7.

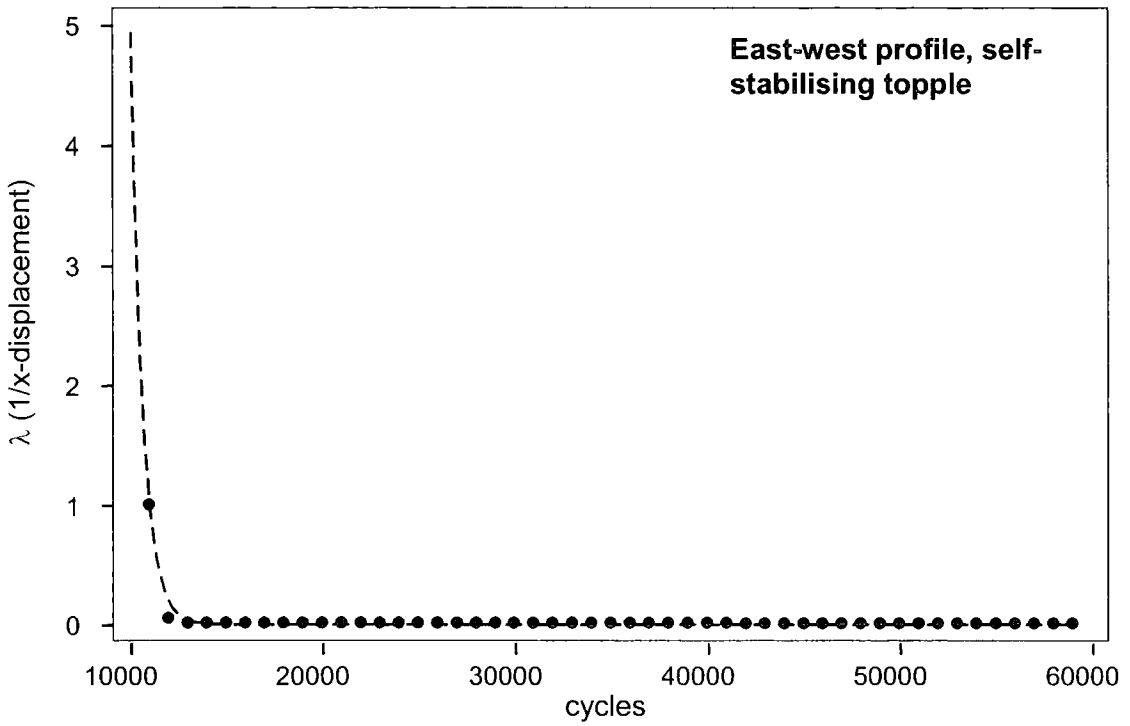

Figure 8.50: Exponential asymptotic model (dashed line) applied to x-displacement data for the failures on the west of AL17.

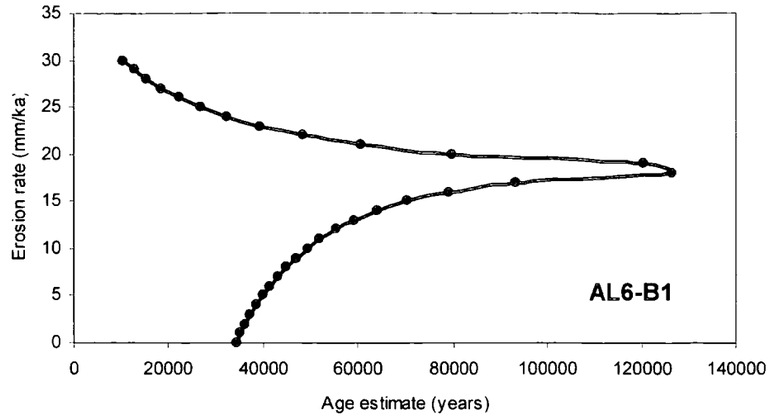

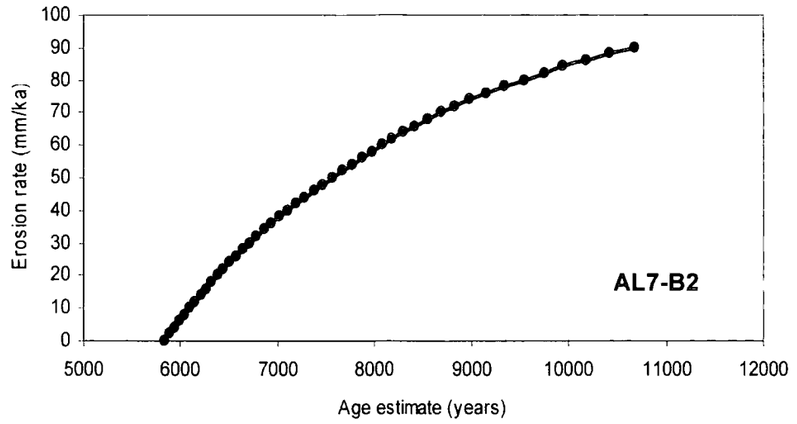

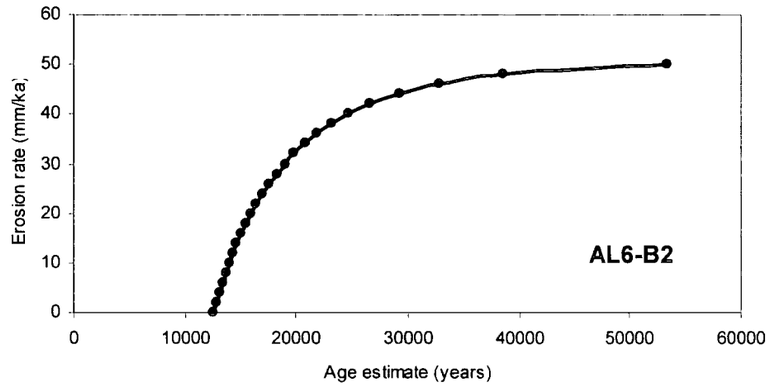

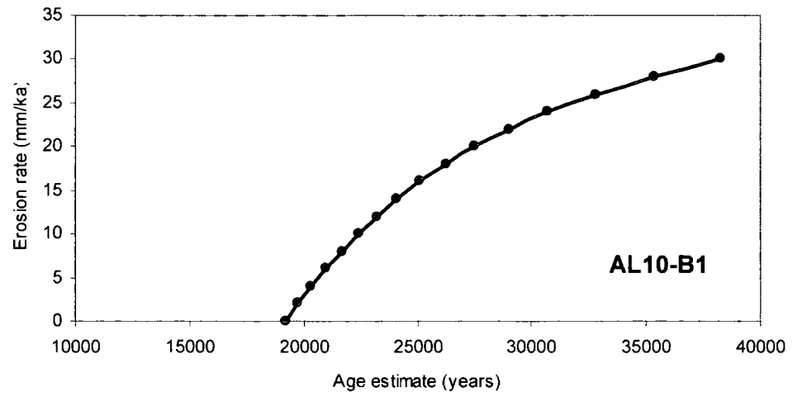

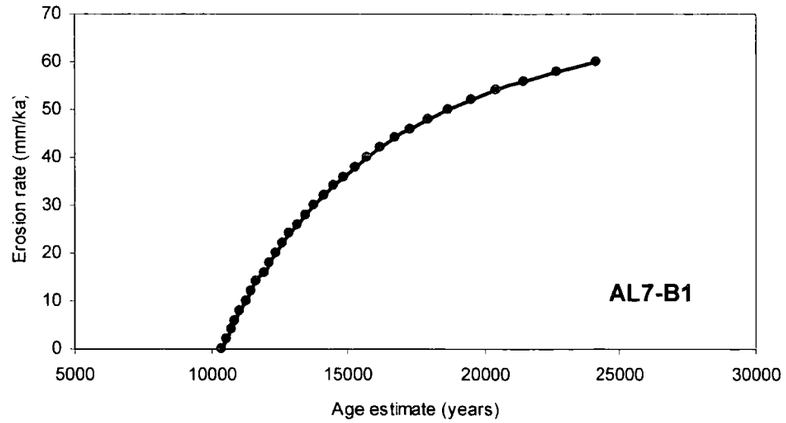

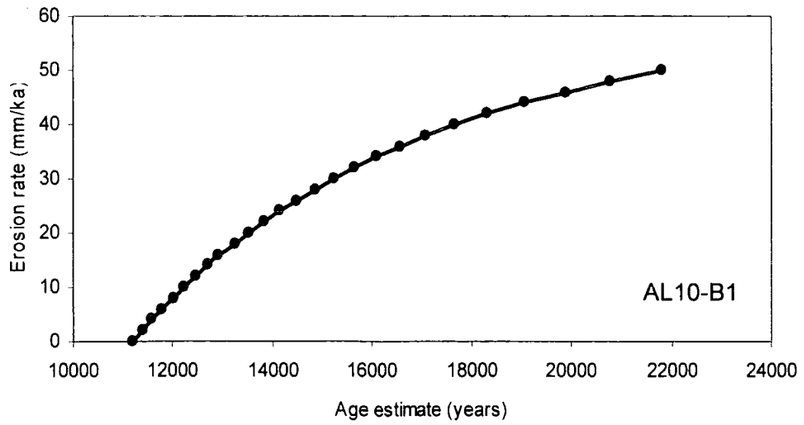

Figure 8.51: Results of erosion rate modelling on the samples selected for ^{10}Be dating. As the erosion rate increases, the applied erosion rate correction increases the ages of the boulder.

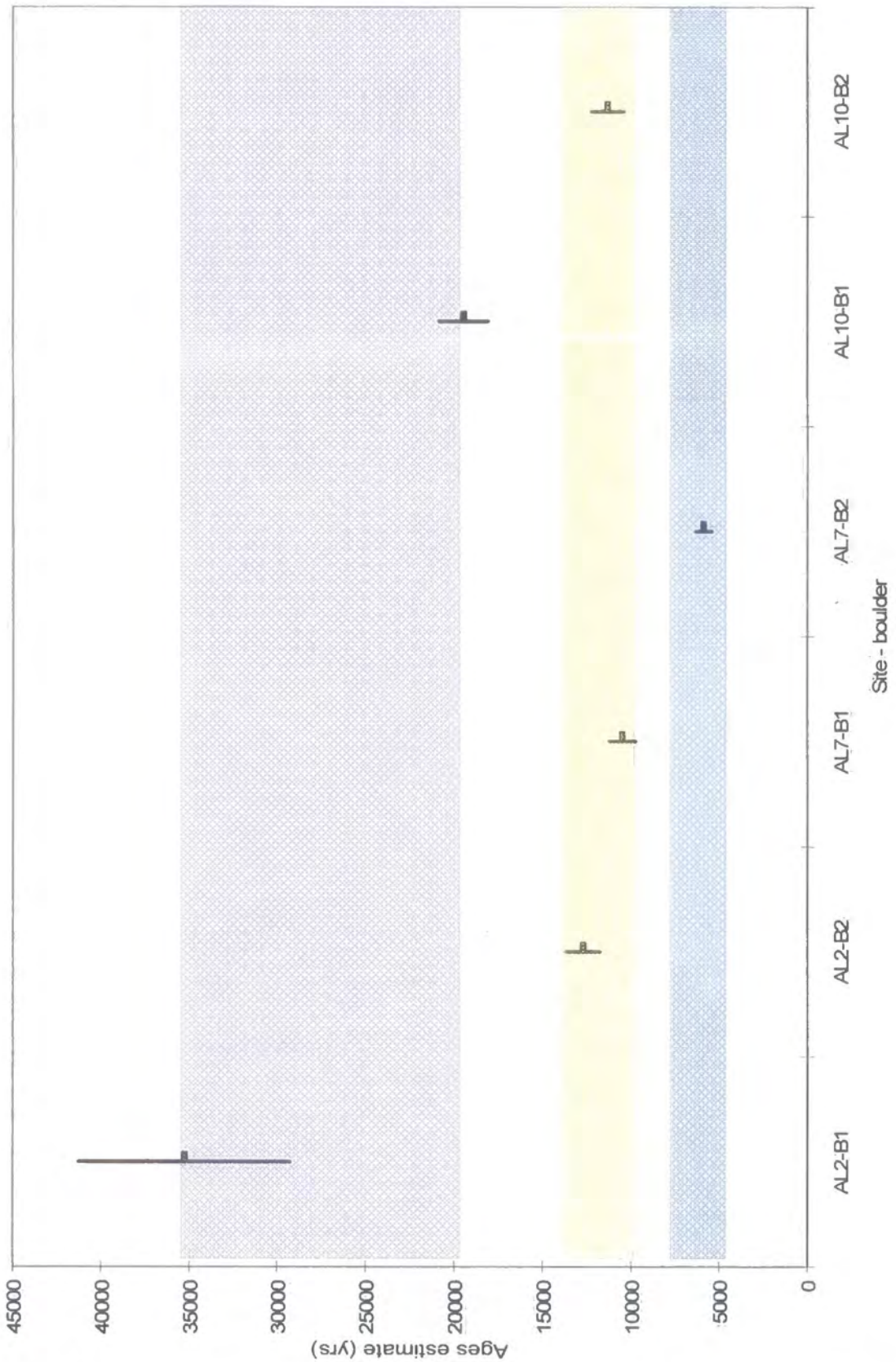

Figure 8.52: ^{10}Be ages estimates for selected rock slope failures in the Wadi Rum region. Purple represents a wet climatic period between 35 000 and 20 000 years B.P., the yellow a wet period between 12 000 and 10 000 years B.P. and the blue the Neolithic wet period between 7000 and 4400 years B.P.

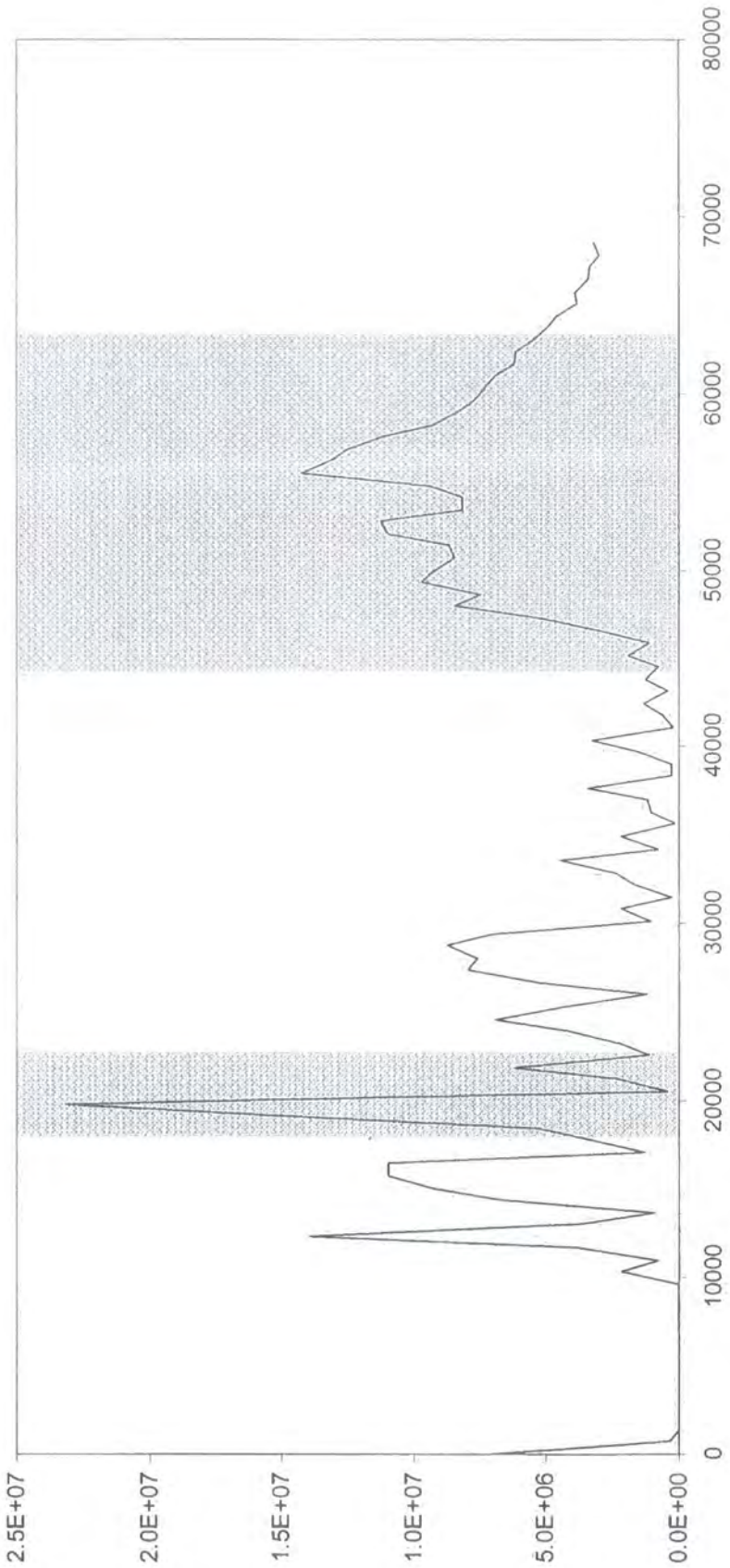

Figure 8.53: Smoothed total unbalanced forces for AL2. ^{10}Be ages and σ_1 error have been overlaid on the graph, based on one year representing 1.5 model cycles.

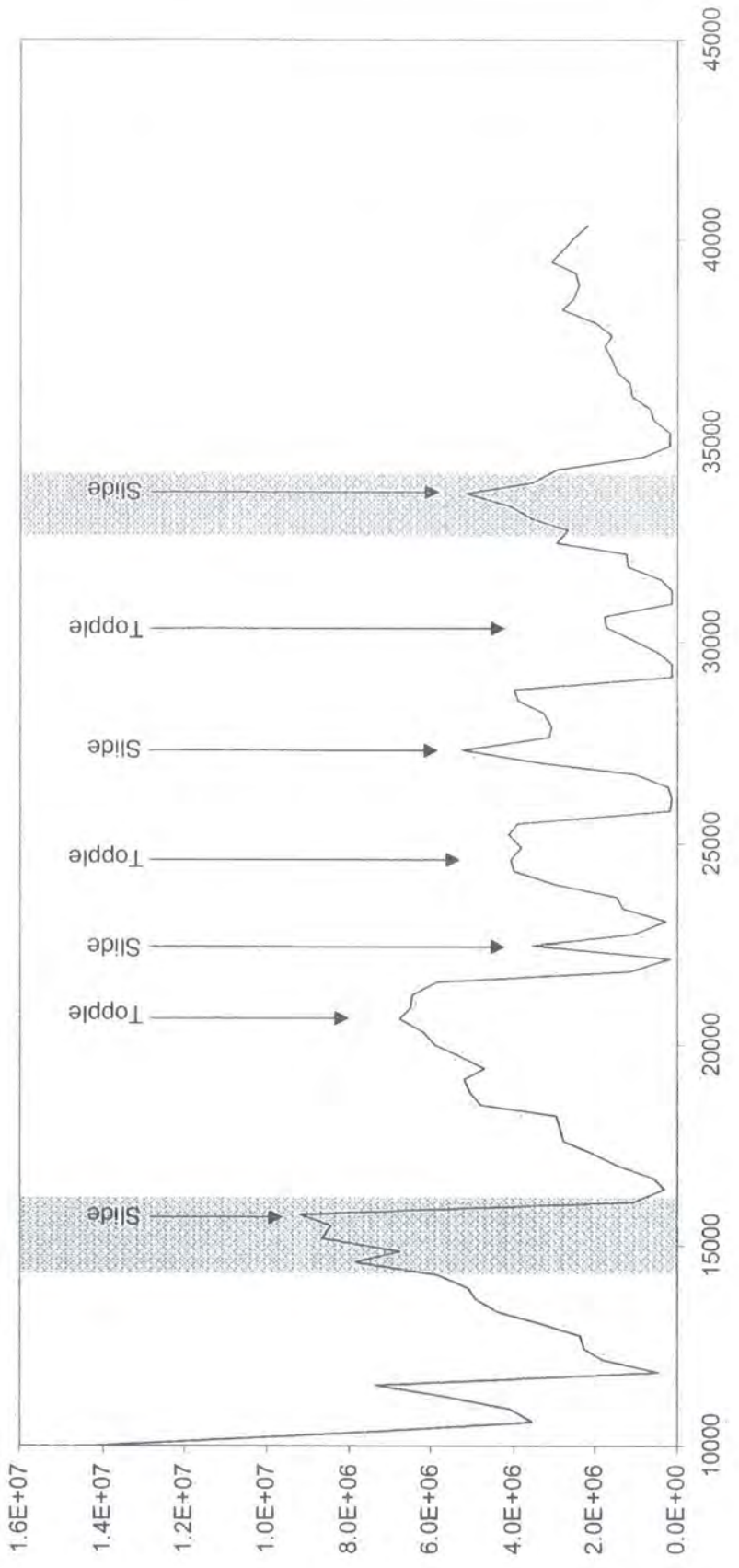

Figure 8.54: Smoothed total unbalanced forces for AL7 ^{10}Be ages and σ_1 error have been overlaid on the graph, based on one model cycle representing 1.5 years.

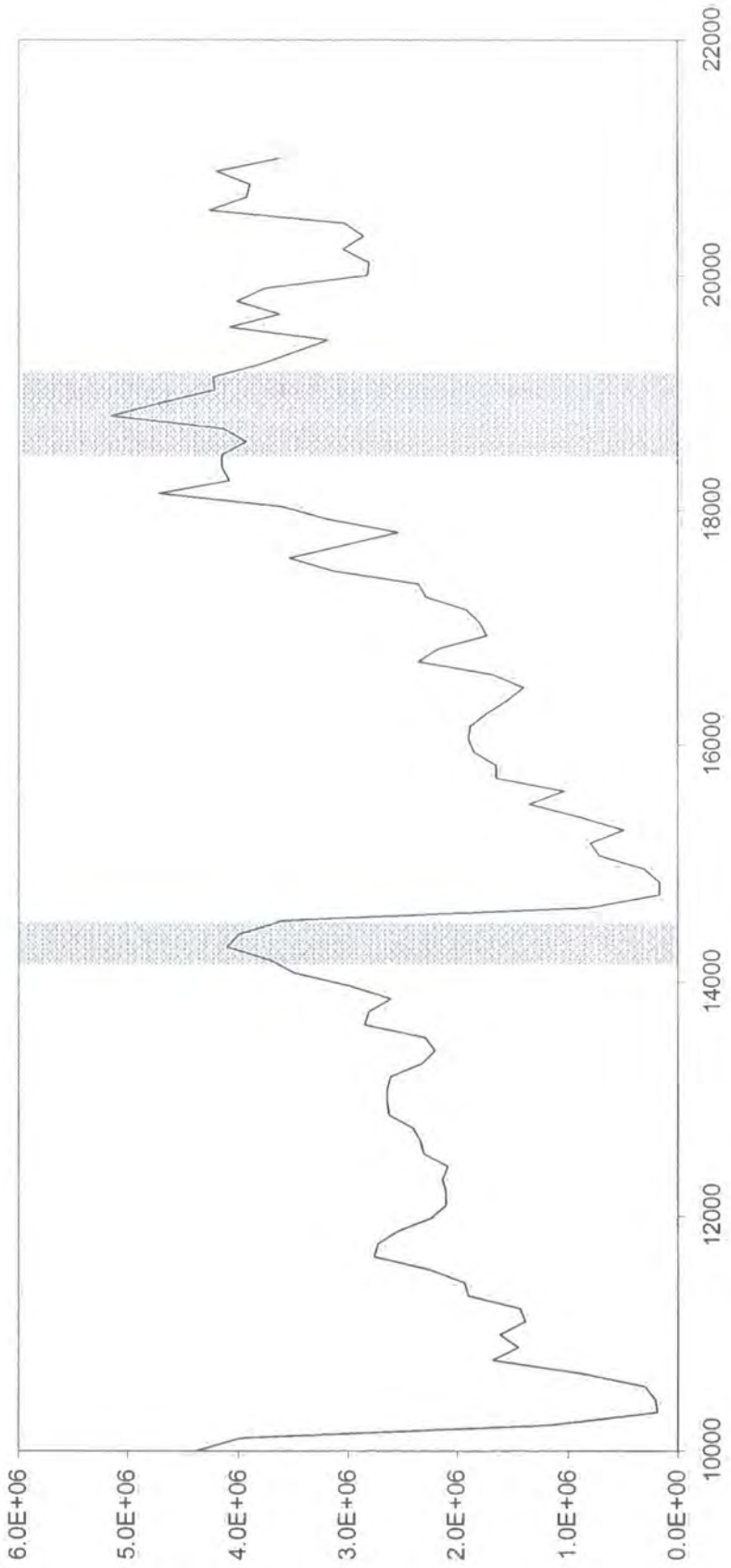

Figure 8.55: Smoothed total unbalanced forces for AL10 ^{10}Be ages and σ_1 error have been overlaid on the graph, based on one model cycle representing 2.3 years.

Plates

Plate 5.1: Incision of the Cares Gorge has divided the Central and Western Picos in to two separate massifs. The peaks surrounding the gorge rise to 2000 m, while the floor is just 400 m above sea level.

Plate 5.2: A relict rock glacier in the Vega de Liordes formed through the downslope transport of failed slope debris. The glacier is largely relict, apart from the active accumulation of debris on the left hand side.

Plate 5.3: Debris flow system in the bottom left of the picture with the Government guesthouse of Fuente De just above. The fan consists of coarse alluvium and is incised in its lower channel. Note also that prominent slope deformation in the middle of the picture. Not a good place to stay during prolonged, heavy rain.

Plate 5.4: The large debris flow system originating at Canchorral de Hormas. The red line traces the approximate source area. Although not visible on the picture, the village of Cabañas is behind the hill at the bottom of the debris flow system.

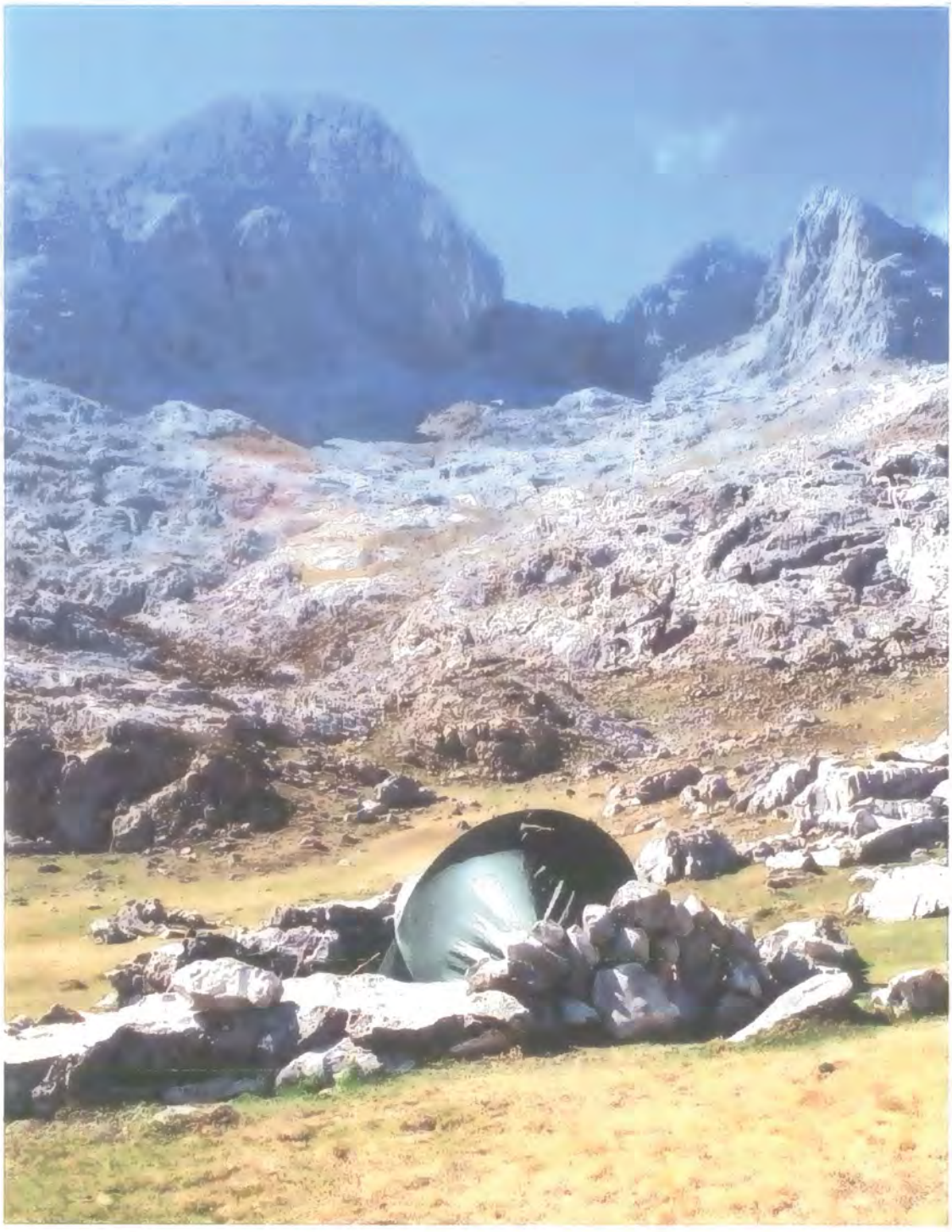

Plate 5.5: The cirque headwalls of Torre de Salinas, viewed from the Vega de Liordes. Torre del Hoyo de Liordes, the cirque reaches a high point of 2474m to the west (left) of the picture.

Plate 5.6: The east-west trending face of Pico de la Padierna. The highest part of the slope occurs to the right of the picture and decreases in height towards the west (left). The red line traces the top of the slope as a bench separates the slope from the peak seen behind, which is some distance away.

Plate 5.7: The north face of Tiro Pedabejo. The north and west faces were the most easily accessible for the collection of discontinuity data. Numerous ploughing blocks occur on the lower slopes.

Plate 5.8: The large block field forming the deposition area for failed material from the headwalls of Canchorral de Hormas. This block field also provides the source area for the large debris flow system seen in plate 5.4.

Plate 5.9: The rock slope investigated at Los Montes in the Deva Gorge. Much remedial work has taken place at the toe of the slope. Plans to widen the highway in the Gorge require cutting back of the slope toe.

Plate 5.10: The rock slope investigated at the crags of Algobras, Allende in the Deva Gorge. The slope is bounded on the left by a large canal, providing access to high level grazing.

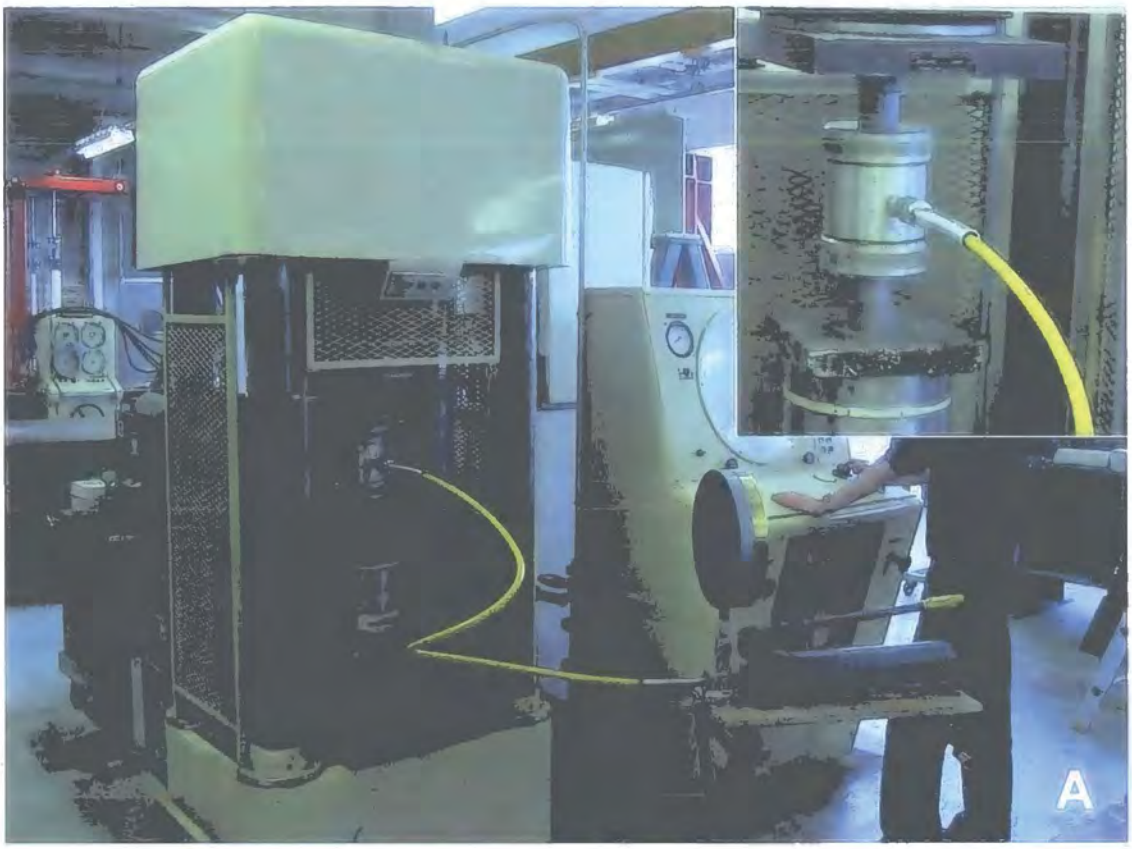

Plate 5.11: Triaxial testing of rock cores in a Hoek Cell (inset) inserted in to a stiff loading frame (A). Confining pressure is applied with a hand pump. Uniaxial testing of cores for defining the unconfined compressive strength (B).

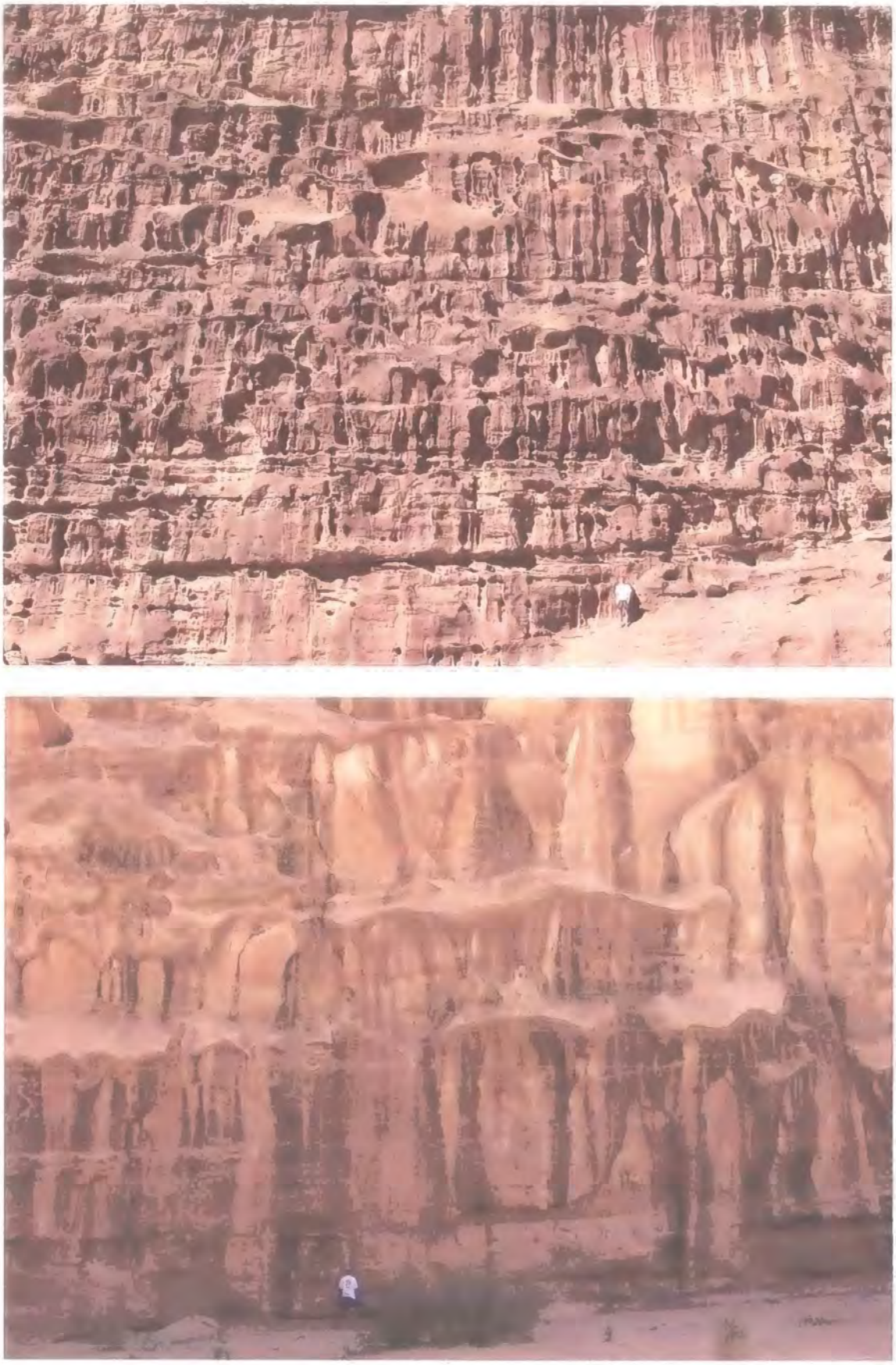

Plate 6.1: Tafoni weathering and case hardening on the sandstone inselbergs of Wadi Rum.

Plate 6.2: Example of rockfall event on the sandstone inselbergs in Wadi Rum.

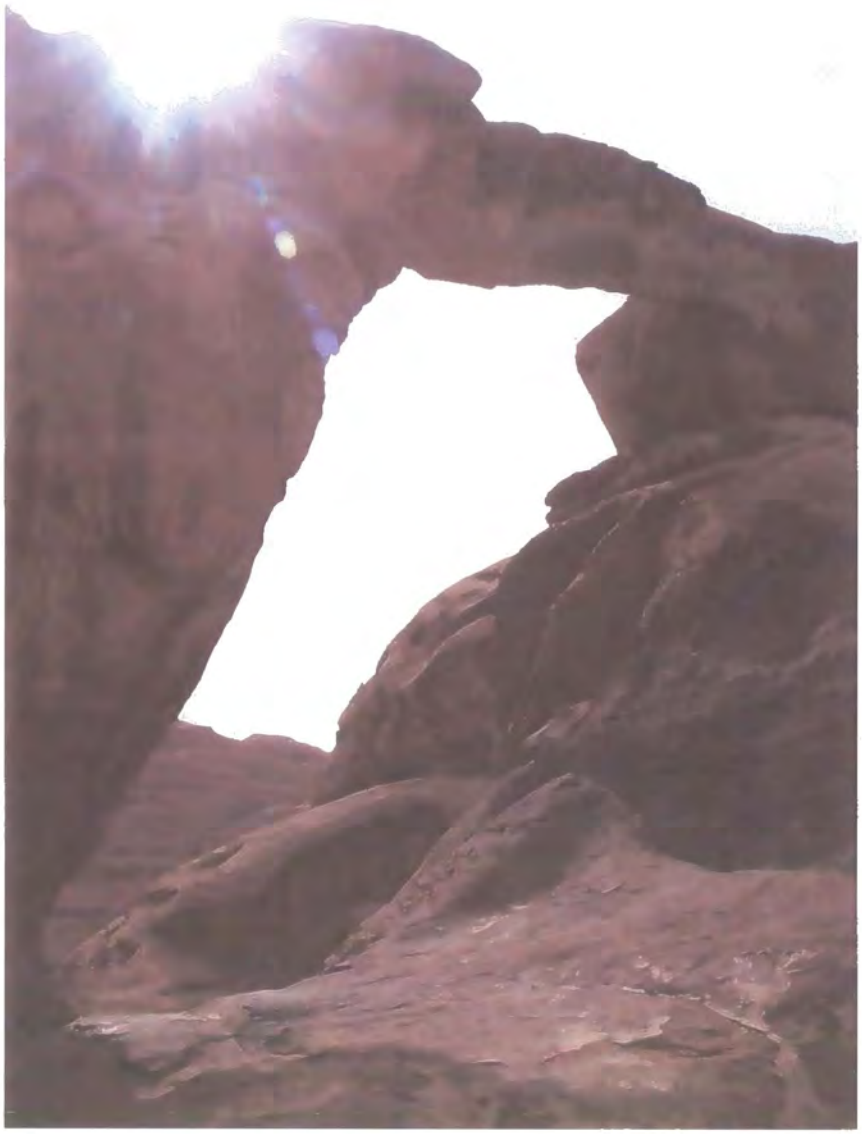

Figure 6.3: A natural rock bridge formed through weathering of the sandstones.

Plate 6.4: Disi and Red Ishrin Sandstone inselbergs. The Red Ishrin Sandstone is much stronger than the Disi, supporting vertical slopes and much higher inselbergs.

Plate 6.5: Rounded domes are characteristic of inselbergs developed in the Disi sandstones.

Plate 6.6: Preferential weathering of 'master' joints leads to the development of columnar inselbergs.

Plate 6.7: Example of tensile failure of sandstone caused by basal slope sapping.

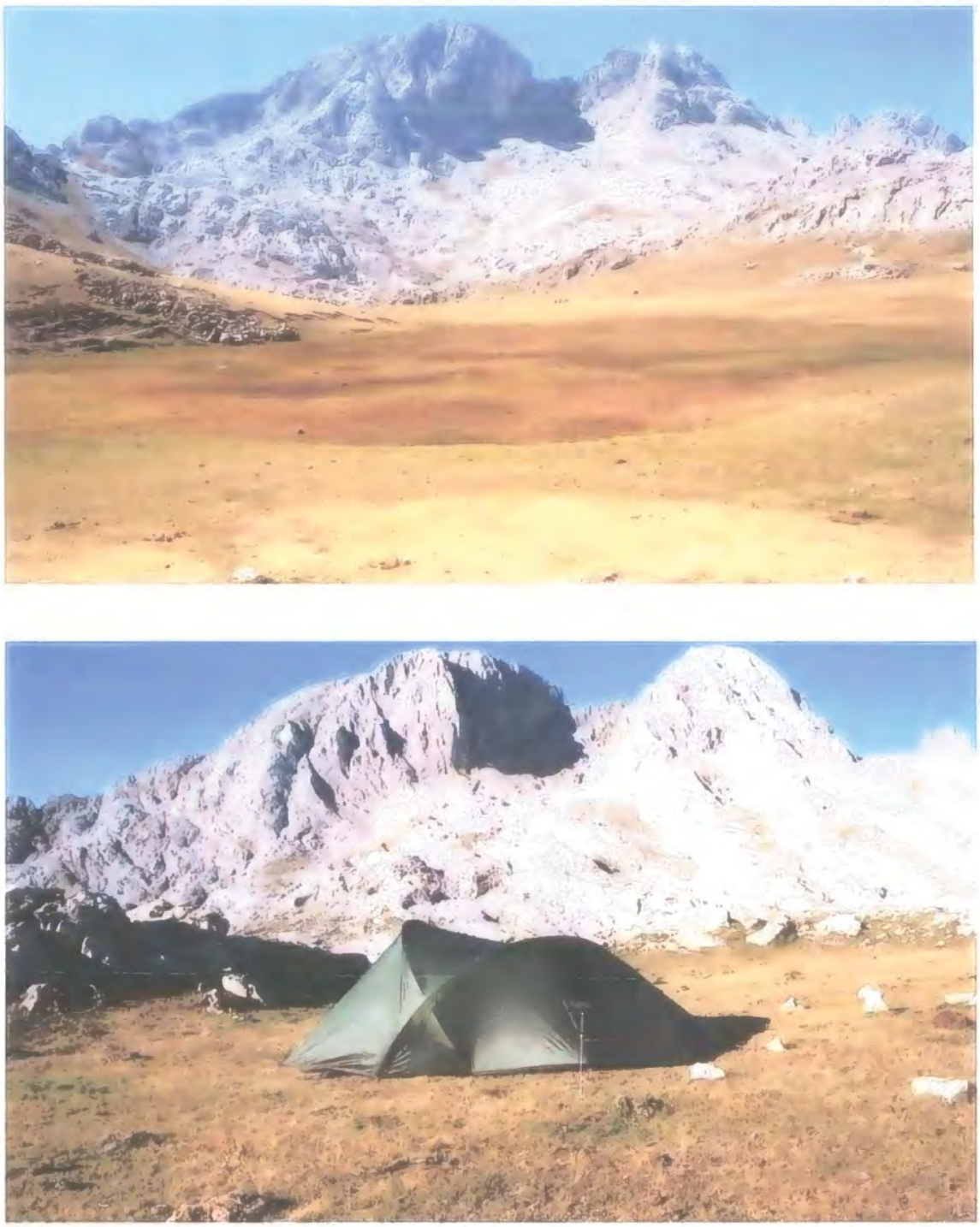

Plate 7.1: Torre de Salinas. The UDEC model meshes were designed to capture the main features of each of the cirque headwall features.

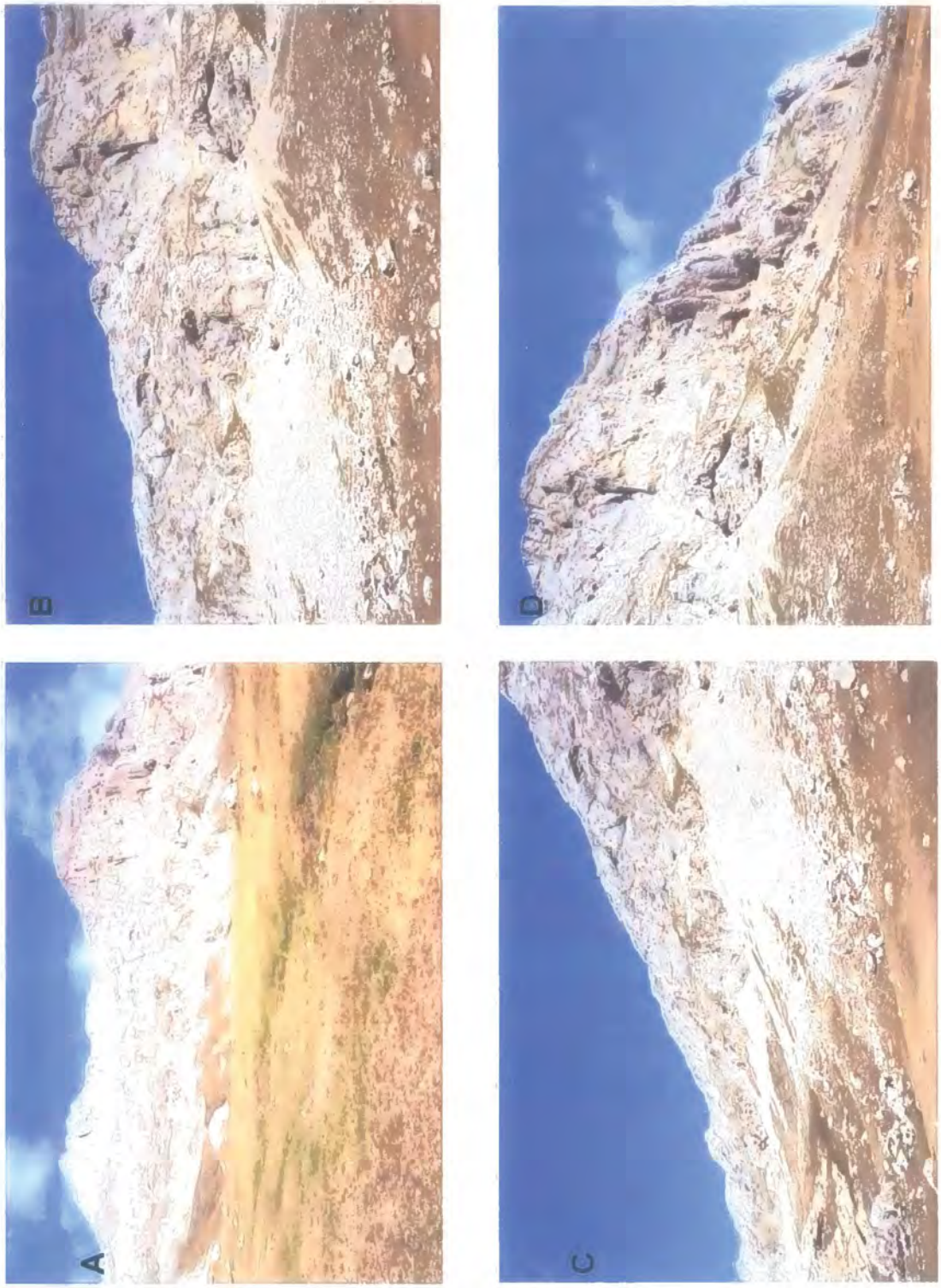

Figure 7.2: Pico de la Padierna. (A) is a view of the whole ridge, (B) the central section, (C) the western portion and (D) the eastern end.

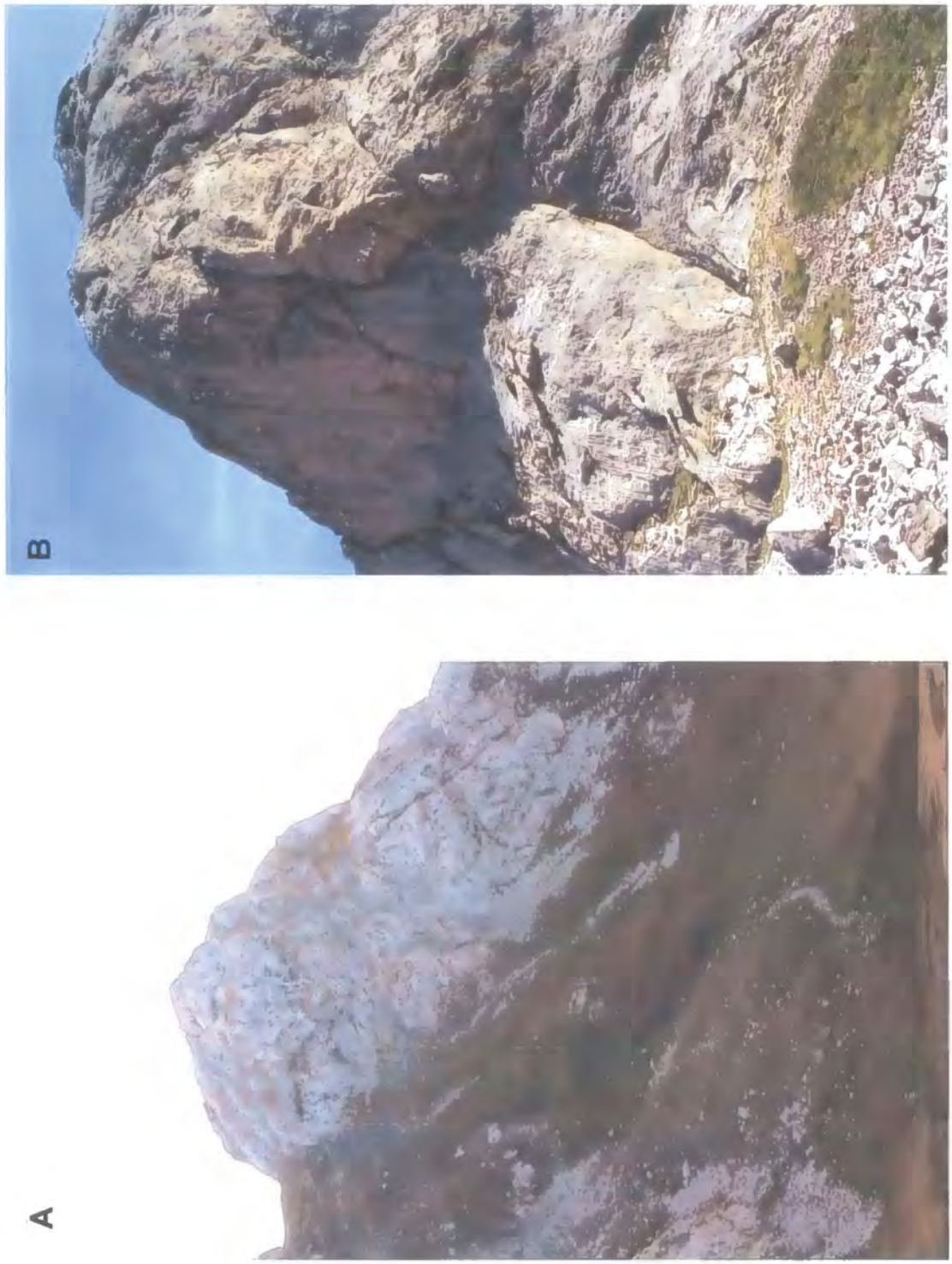

Plate 7.3: (A) The north face of Tiro Pedabejo (B) the south-west face of Tiro Pedabejo from the Canal de Pedabejo. The full free face is just off the picture.

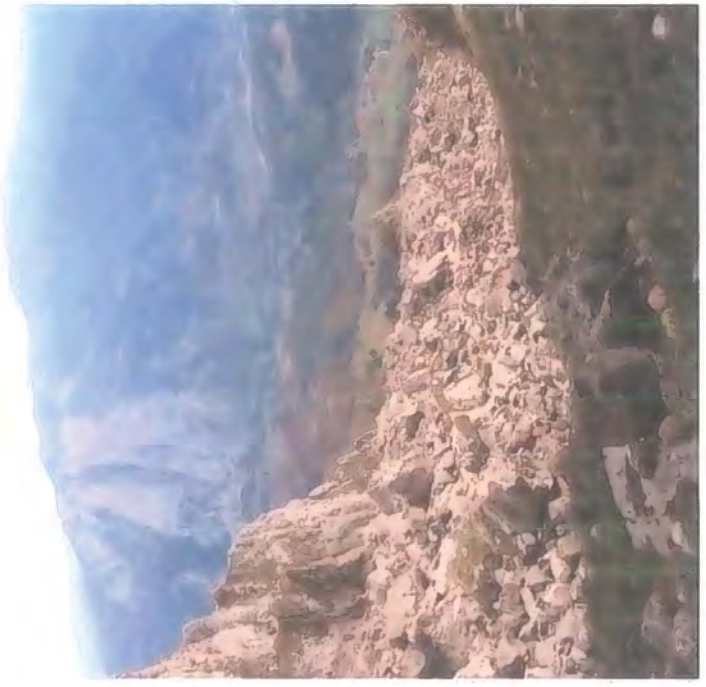

Plate 7.4: Canchorral de Hormas. (A) View of the boulder field (B) View of the site from the end of the Deva Gorge. The red circle marks its location.

Plate 7.5: The east-west profile of Los Montes, Deva Gorge from the south face. The Rio Deva is just off to the right of the picture.

Plate 7.6: (A) General view of Allende from the south showing the west, south and east faces. (B) View of the south face of Allende.

Plate 7.7: The north face of Torre de Salinas from the Collado de Jermoso, Picos de Europa. Antiscarps formed by flexural toppling on the north face can be seen in the centre of the photograph.

Plate 7.8: View of Pena Remona. The back-tilted blocks are formed due to a combination of the nature of the bedding and small rotational movements occurring at the toe of the slope, leading to large-scale deformation.

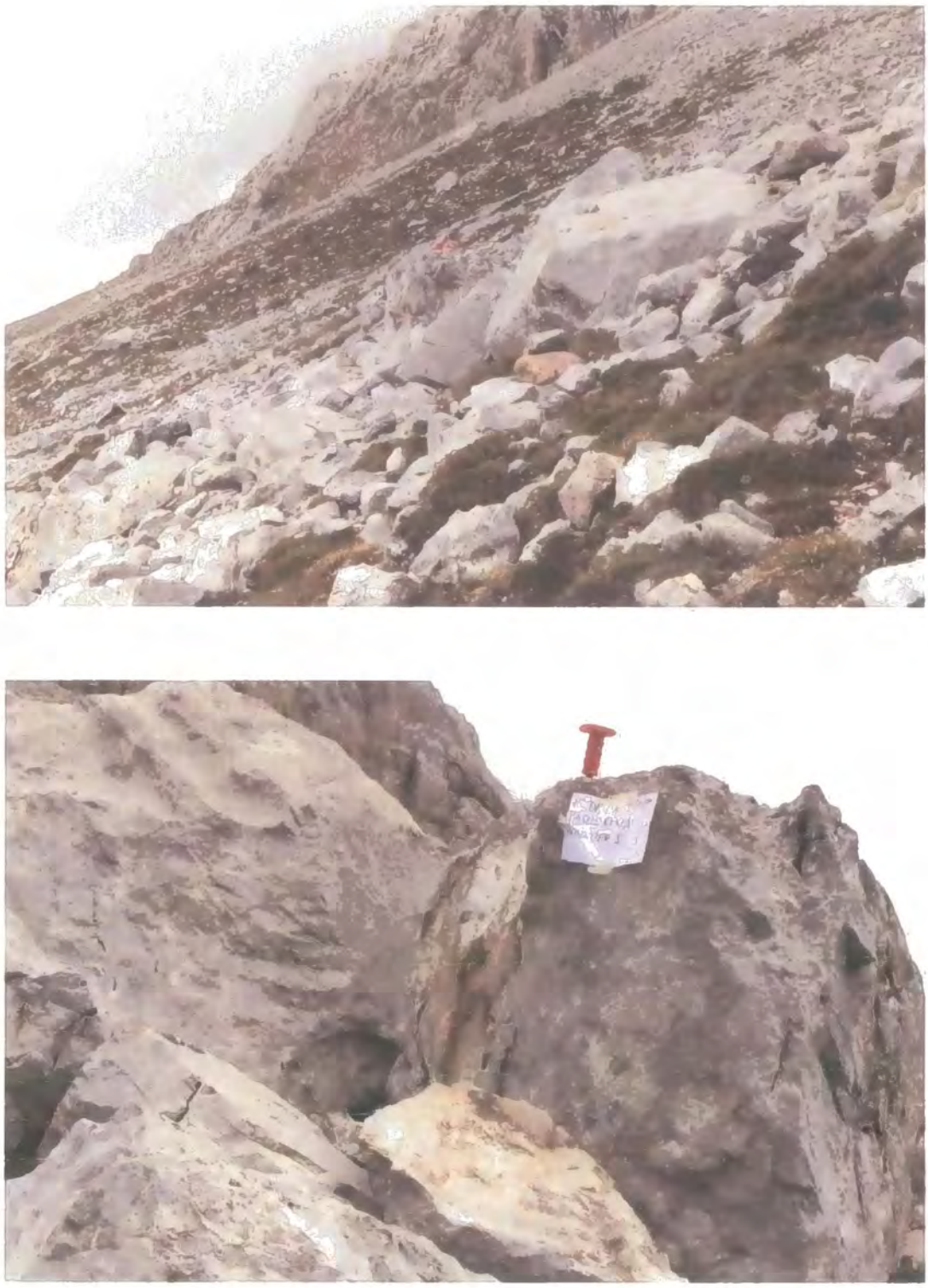

Plate 7.9: Sampling for cosmogenic isotope analysis at Pico de la Padierna.

Plate 7.10: Sampling of boulders for cosmogenic isotope analysis at Tiro Pedabejo. (A) General geomorphic setting of boulders of boulder 2, with an exposure age of 7459 ± 214. (B) close up view of boulder 1, with a calculated exposure age of 7824 ± 403 yrs BP.

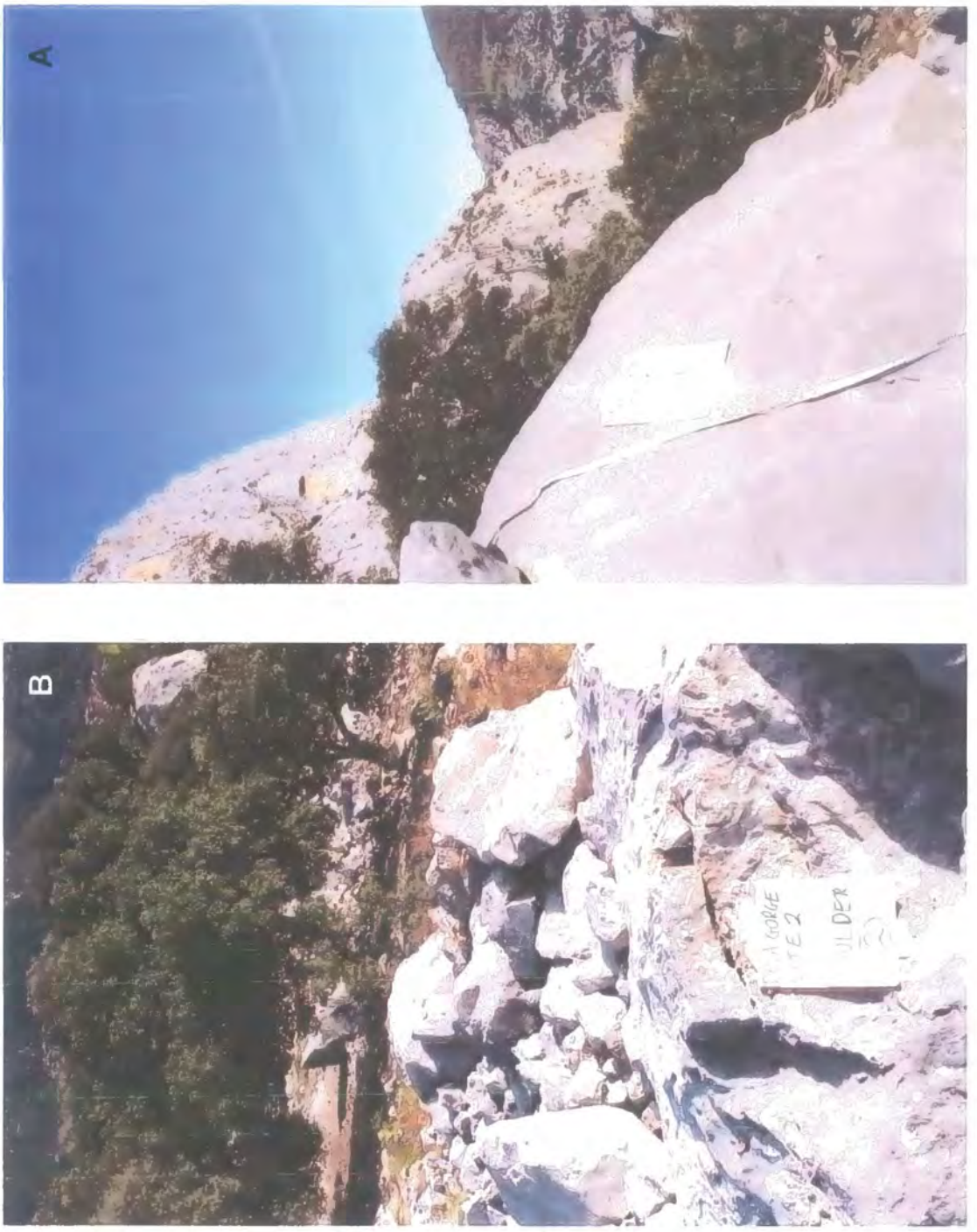

Plate 7.11: Boulders selected for cosmogenic sampling at Allende. (A) Geomorphic setting of boulder 1, with a calculated exposure age of 6540 ± 636 and (B) boulder 2, with a ^{36}Cl exposure age of 6575 ± 242 yrs BP.

Plate 7.12: Evidence that the south face of Pico de la Padierna still represents an overdip slope and that future failures are likely. The angle of the slope is much greater than the friction angle and cohesion of the intact material and discontinuities.

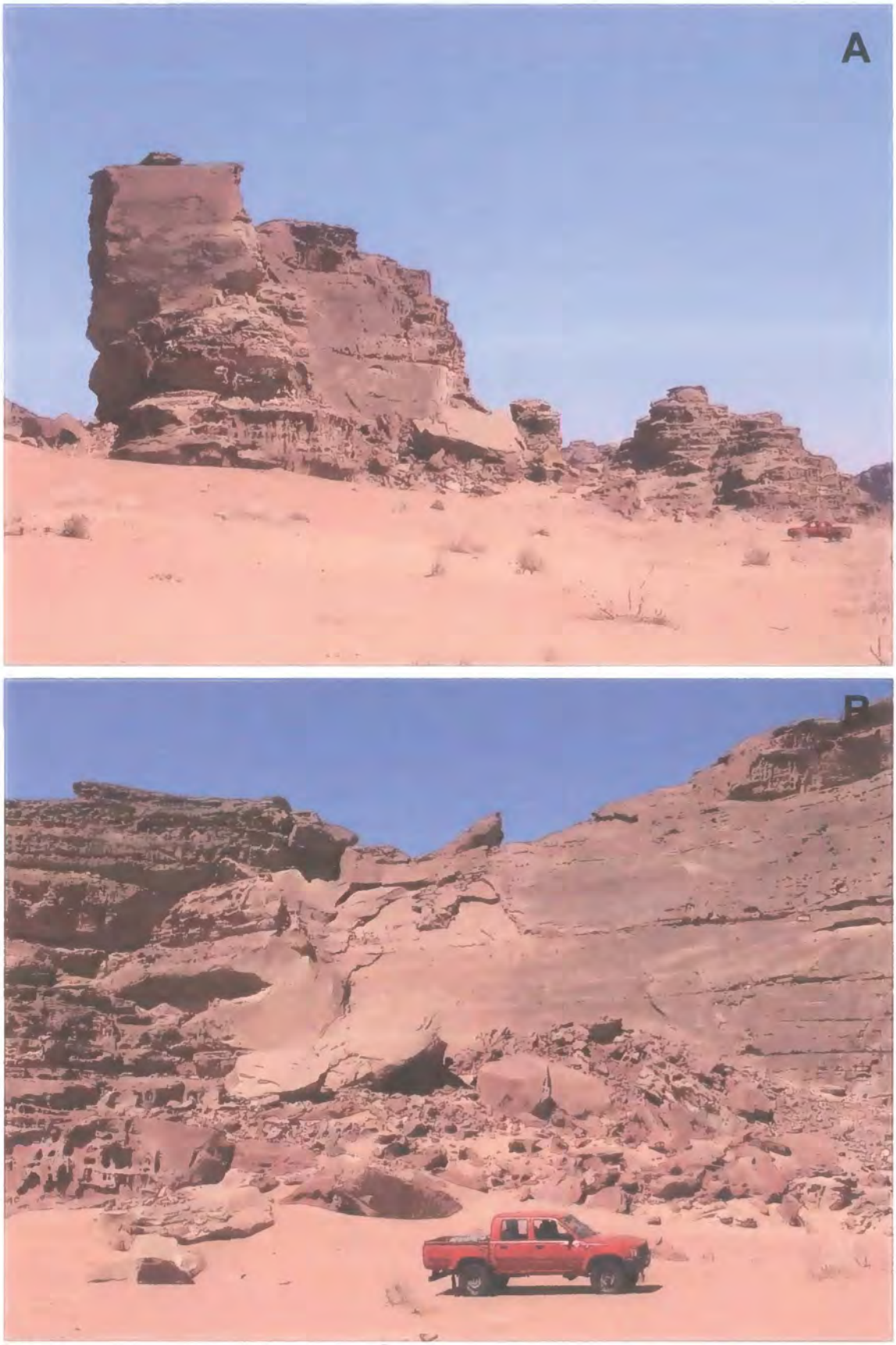

Plate 8.1: North-south profile of AL9 (A), with close up view of the failure on the south face (B).

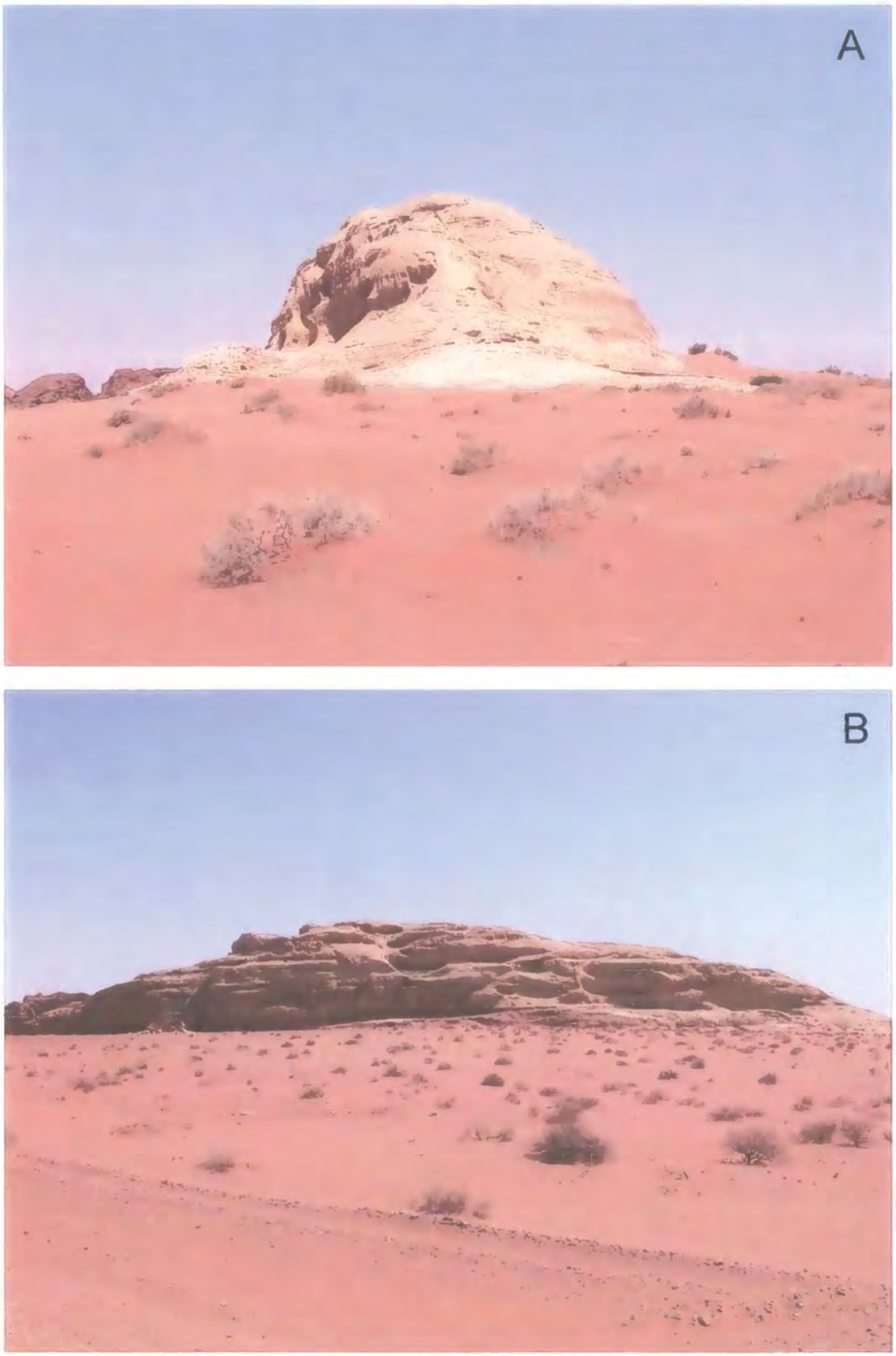

Plate 8.2: North-south profile of AL12 (A) with east-west profile shown in (B). The inselberg is formed in Disi sandstone.

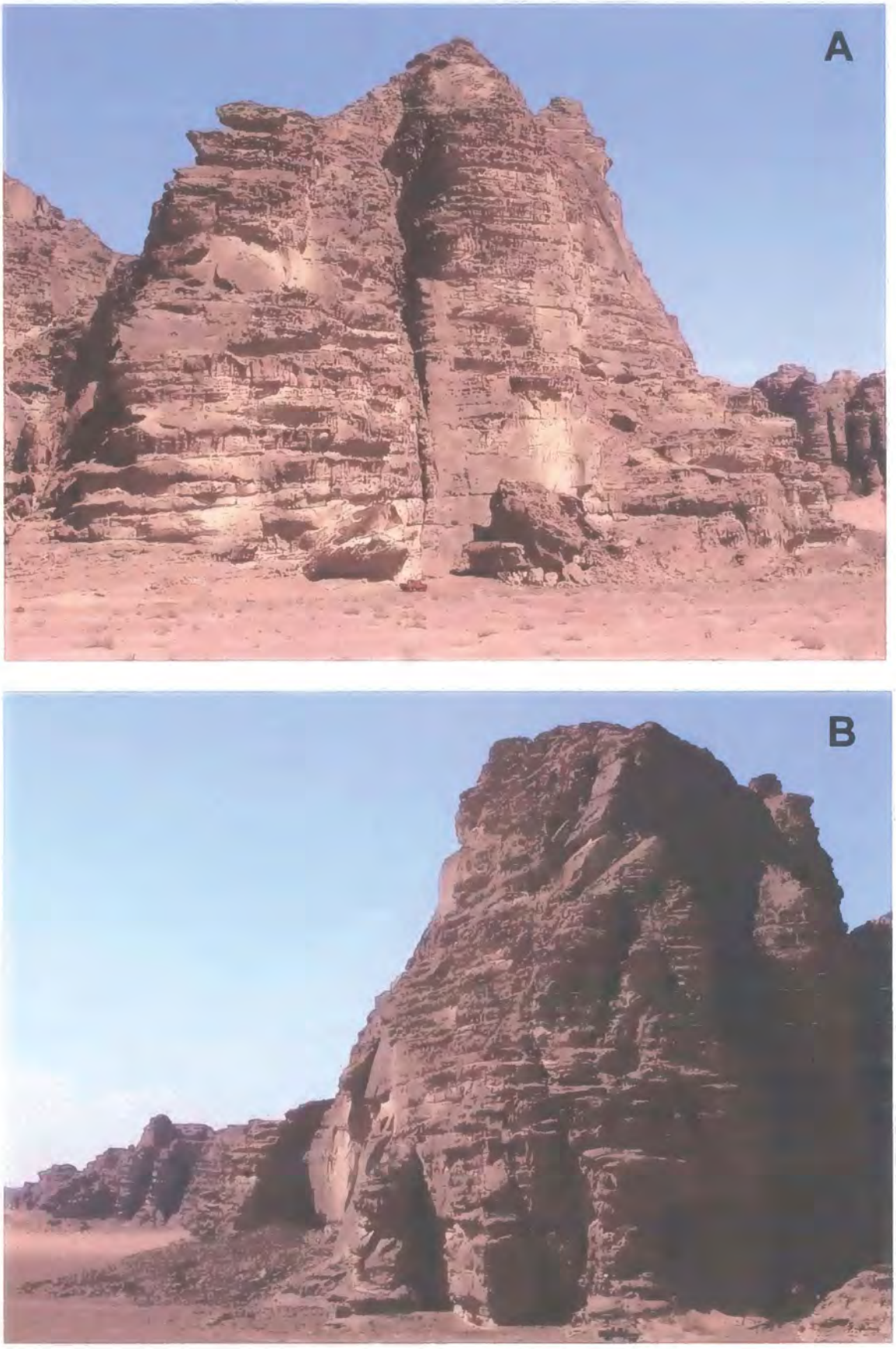

Plate 8.3: North-south profile of AL10 from the west face (A) and the north-south profile showing a large failure on the south face from the eastern end of the inselberg (B).

A

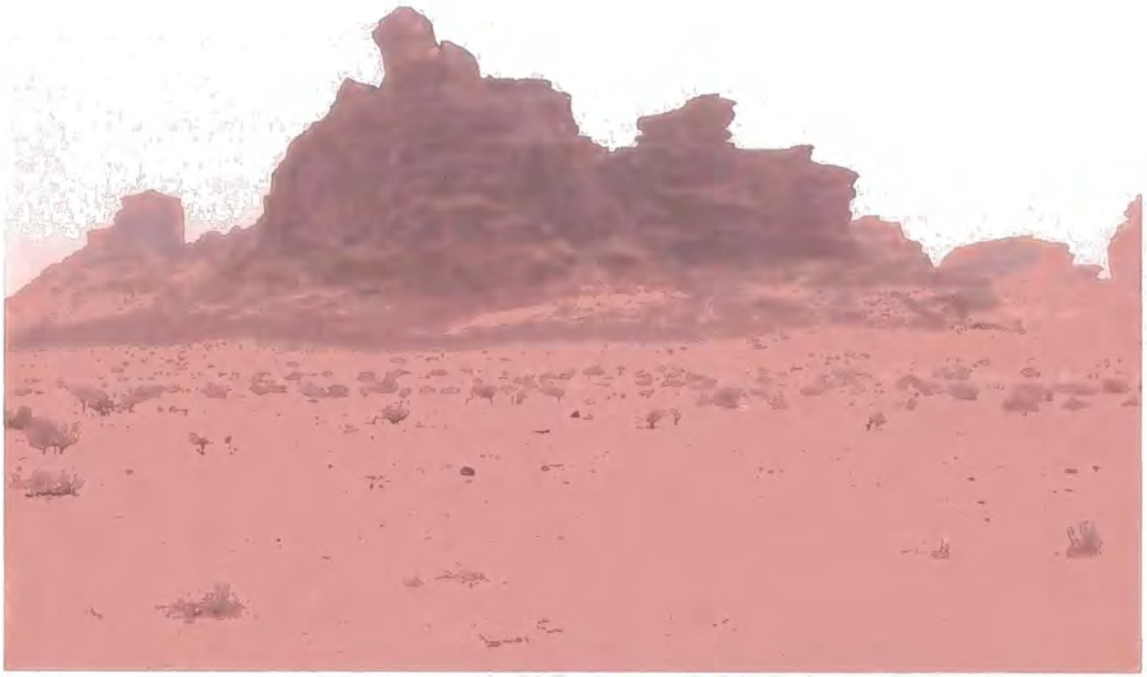

B

Plate 8.4: North-south profile of AL11, from the west face of the inselberg (A), with the east-west profile, taken from the northern end of the inselberg shown in (B).

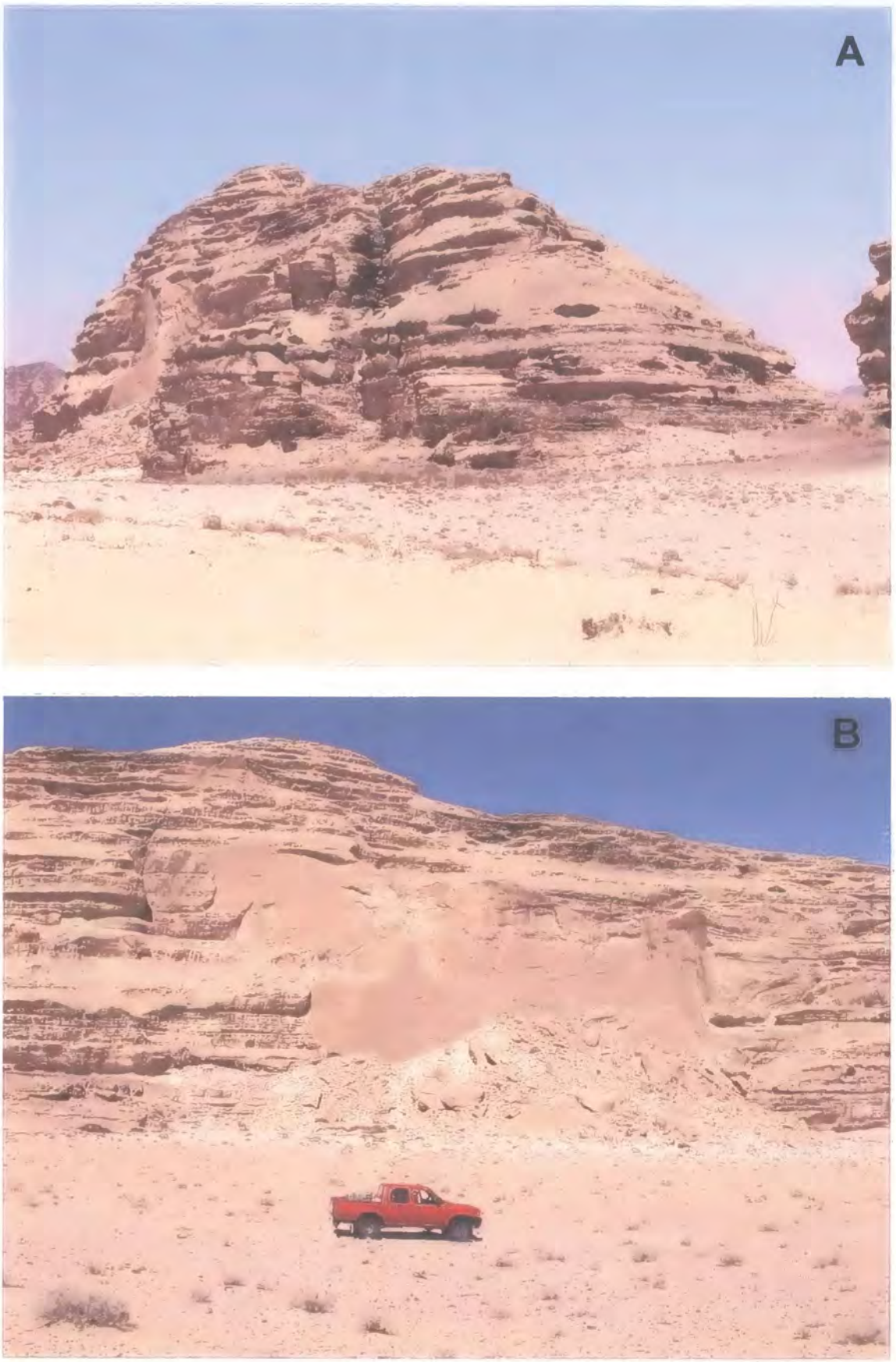

Plate 8.5: East-west profile of AL3, taken from the south face (A). Close up view of the failure on the west face of the inselberg (B). The inselberg is composed entirely of Salib Arkosic sandstone, pushed up due to normal faulting.

Plate 8.6: West face of AL2 (B) showing a small cap of Disi sandstone on the upper part of the inselberg. The north face of AL2 is shown in (B).

Plate 8.7: South face of AL7 showing a large failure and preferential weathering of joints, producing the 'tower' morphology. The actual failure of the rock mass is controlled by joint sets which are much more closely spaced than the preferentially weathered joints. The prominent tower on the east face of the inselberg showed evidence of instability, in addition to the south face.

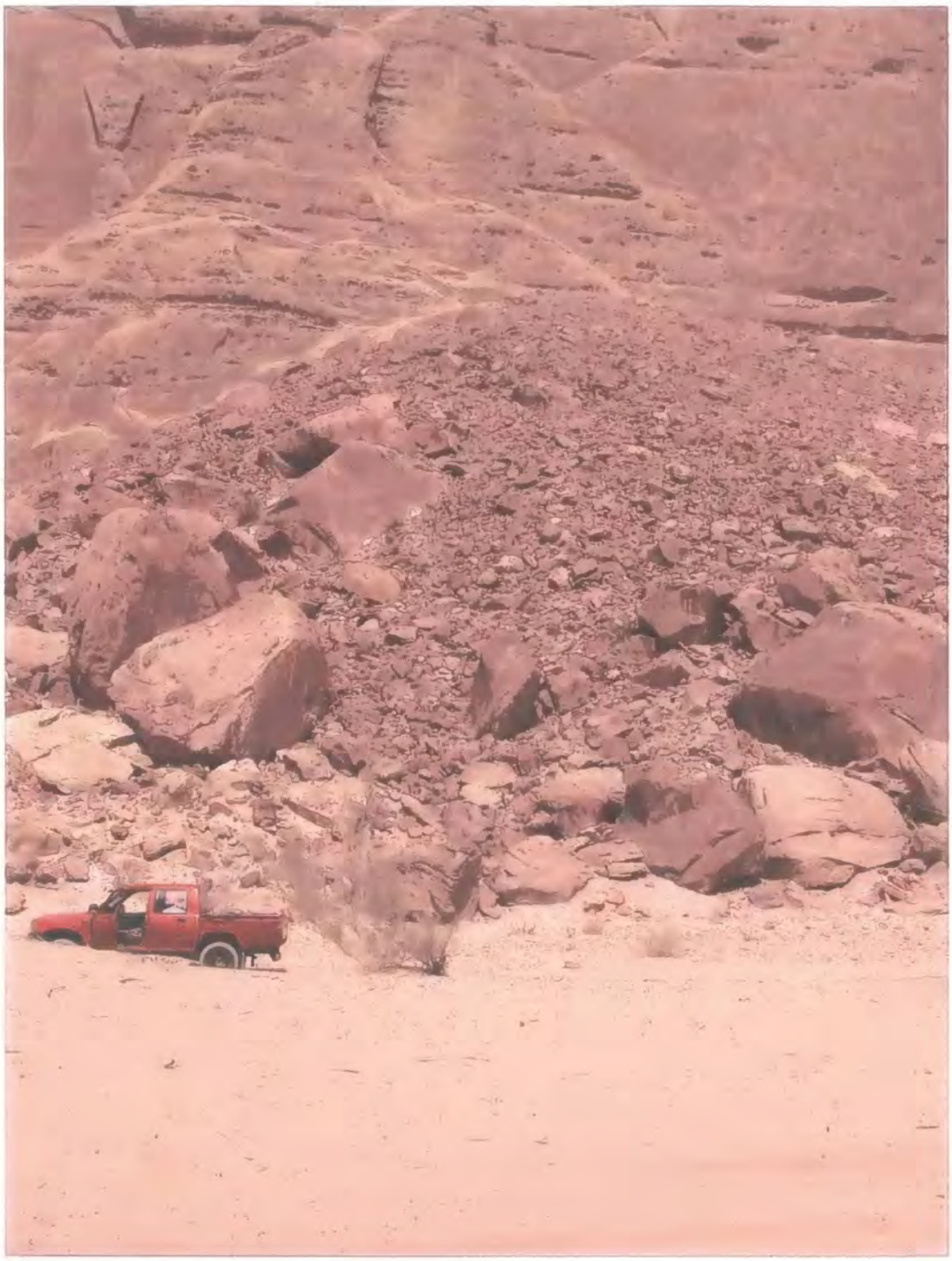

Plate 8.8: The west face of AL17, in the Barra Canyon, showing evidence of large-scale slope collapse. The debris slope is approximately 150 m, indicating a large volume of failed material. The failure was probably initiated by steepening of the slope through fluvial incision during a wetter climatic period.

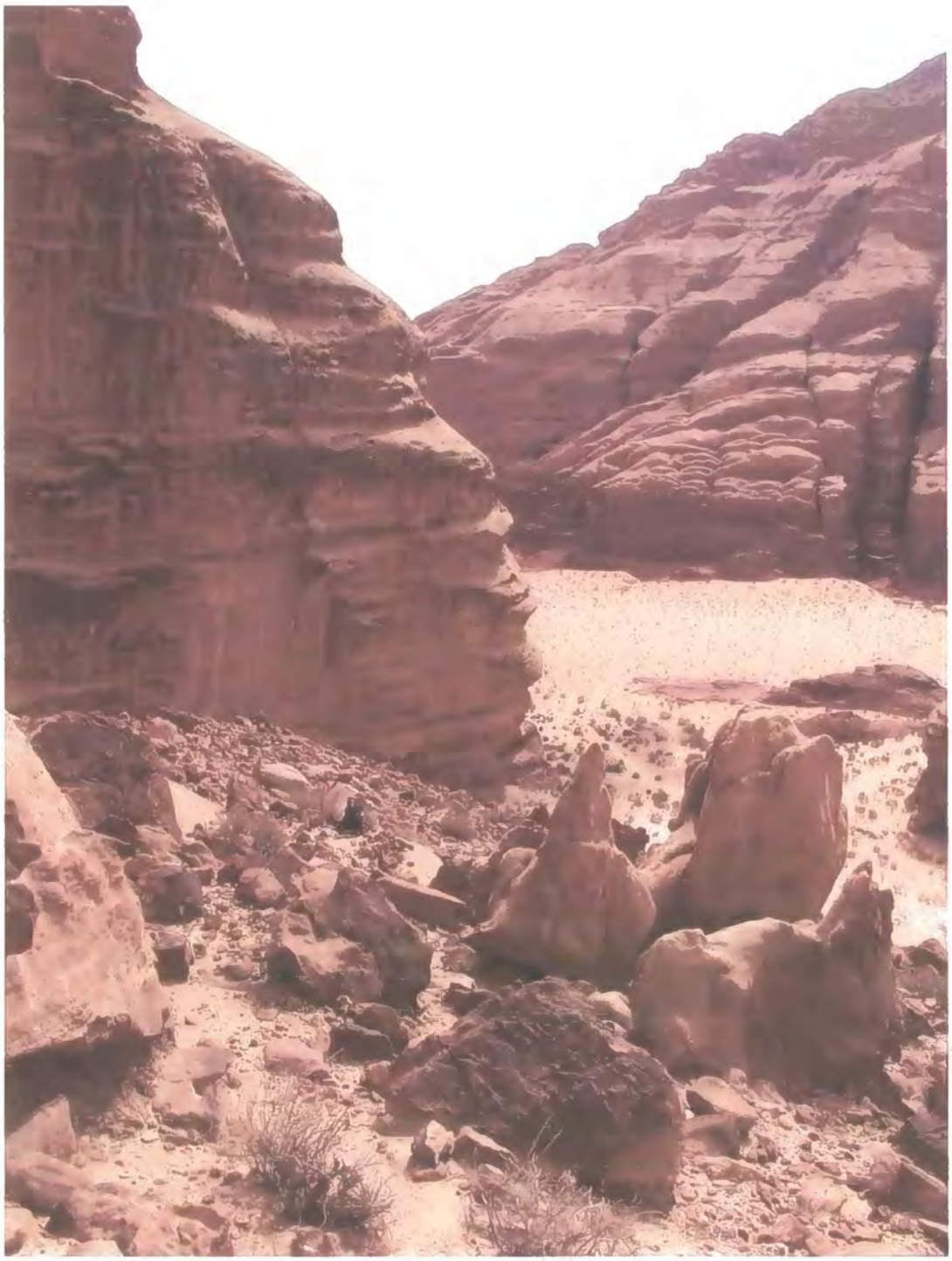

Plate 8.9: View from the top of the rockfall debris on the west face of AL17, with the Barra Canyon located in the centre of the picture. During a wetter climatic period, this canyon was a major fluvial valley.

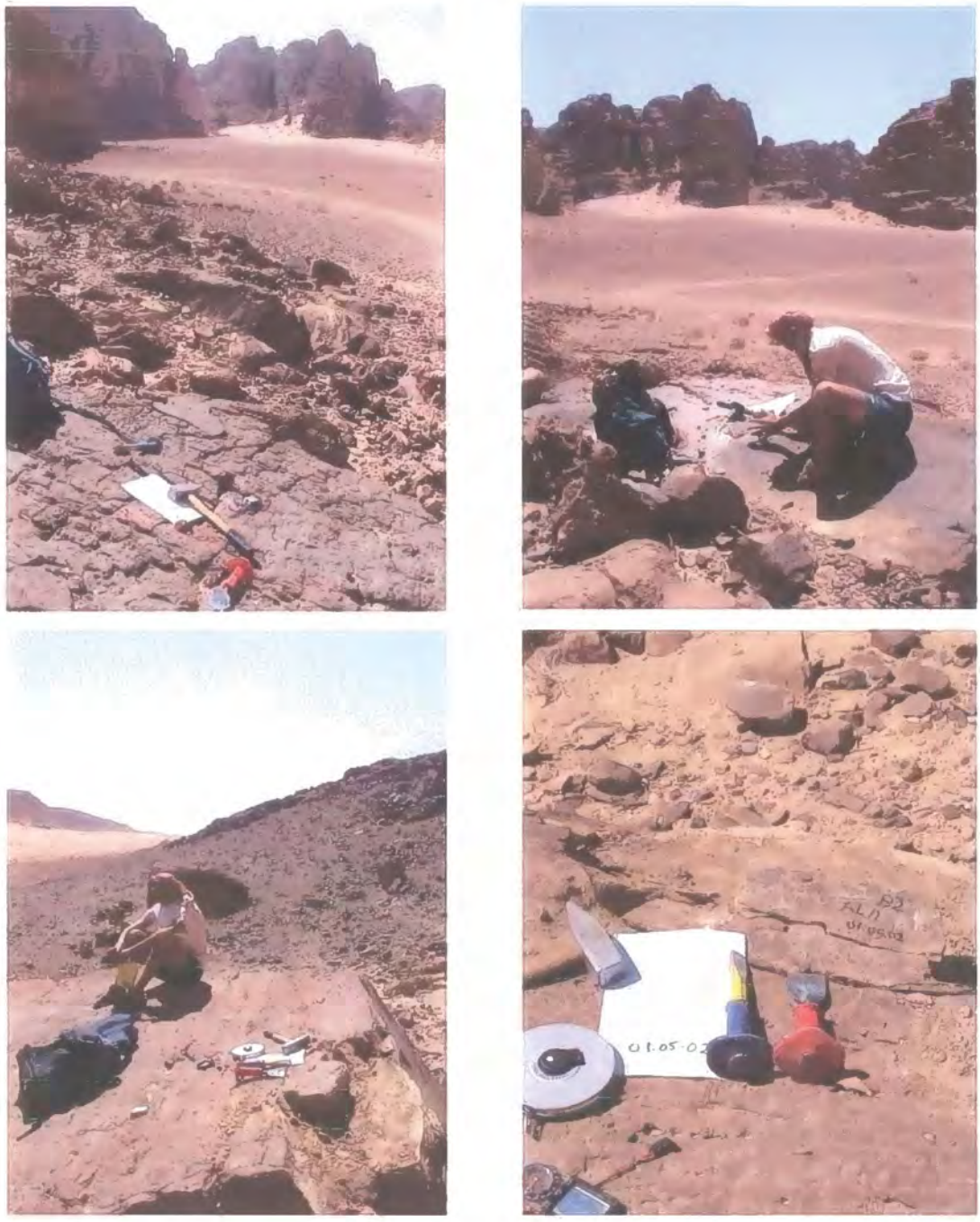

Plate 8.10: Boulders being sampled for cosmogenic dating from failed rock slopes in Wadi Rum, Jordan. Evidence of iron staining can be seen. The surface of the boulders showed only minimal weathering.